Plasmon–soliton waves in metal-nonlinear dielectric planar structures

Wiktor Walasik

AIX–MARSEILLE UNIVERSITY

POLYTECHNIC UNIVERSITY OF CATALONIA

Institut Fresnel

The Institute of Photonic Sciences

PhD thesis

submitted in fulfilment of the requirements for the degree of
Docteur ès Sciences, d'Aix-Marseille Université
and
Doctor per la Universitat Politècnica de Catalunya

PhD School: ED352 Physics and Sciences of Matter
Specialities: Optics, Photonics and Image processing

Wiktor Walasik

Plasmon–soliton waves in metal-nonlinear dielectric planar structures

Defended on the 13th of October 2014 in the presence of the PhD committee:

Kestutis Staliunas	Reviewer	Professor at Universitat Politècnica de Catalunya
Emmanuel Centeno	Reviewer	Professor at Blaise Pascal Université
Juan José Sáenz	Member	Professor at Universidad Autónoma de Madrid
Thibaut Sylvestre	Member	Researcher at FEMTO-ST and Université de Franche-Comté
Yaroslav Kartashov	PhD advisor	Researcher at ICFO
Gilles Renversez	PhD advisor	Professor at Aix-Marseille Université

This document was typeset using LaTeX.

Acknowledgements

First of all I would like to thank my main supervisor, Gilles Renversez, for his constant support and for all the precious time he spent working with me. He always asked the right questions that allowed me to advance in my work. His help has been invaluable during my entire doctoral journey.

I would also like to thank my second supervisor, Yaroslav Kartashov, for his positive criticism toward my work and for investing his time working with me in Barcelona.

I would like to acknowledge Fangwei Ye for providing some of the results about the numerical stability simulations of plasmon–solitons in nonlinear slot waveguide configurations. Additionally, I would like to thank Alejandro Rodriguez for his explanations concerning the MEEP software used for finite-difference time-domain nonlinear simulations presented in the last part of this work.

I am particularly grateful to my colleagues from the PICS Program who have been of immense help with regard to the material and experimental part of the project: Virginie Nazabal, Mathieu Chauvet, and Petr Nemec. The discussions I had with them were very stimulating and sensitized me to the problems encountered during the fabrication of structures and experimental observation of nonlinear waves.

I would like to offer a special thanks to my friends: Susmita, Tasos, Martin, and Siwei for all the entertaining discussions during the many refreshing tea breaks in Institut Fresnel. Thanks to them, for not only helping me maintain my physical form with hours of climbing, ping-pong, biking and billiard, but also giving me some recreation apart from work.

And finally, I would like to express my gratitude to Susmita Sridhar for her persistent efforts to improve my English. I really appreciate the time she spent correcting my language.

This work has been supported by the European Commission through the Erasmus Mundus Joint Doctorate Programme Europhotonics (Grant No. 159224-1-2009-1-FR-ERA MUNDUS-EMJD).

Contents

Abstract

In this PhD thesis, we study properties of transverse magnetic polarized waves in structures composed of a Kerr-type nonlinear dielectric layer, metal and linear dielectric layers. Although these waves, called here plasmon–solitons, have been studied for more than 30 years, there is still no experimental confirmation of their existence. The main reason being that, in all the configurations predicted so far, the nonlinear index modification required to observe plasmon–solitons corresponds to light intensities that are orders of magnitude higher than the damage threshold of typical nonlinear materials. The goal of this PhD thesis is to improve the understanding of plasmon–solitons, so as to design structures that support these nonlinear waves at low power levels.

Firstly, we study configurations with a semi-infinite nonlinear medium. We have developed two semi-analytical models based on Maxwell's equations. The first model treats the Kerr-type nonlinearity in a simplified way, but allows us to obtain analytical expressions for both the field profiles and the nonlinear dispersion relation. The second model treats the nonlinearity in an exact way. It allows us to obtain an analytical expression for the nonlinear dispersion relation, but the field profiles in the nonlinear medium are found numerically. We have studied for the first time three-layer structures (nonlinear dielectric/metal/linear dielectric) for which the linear parts of the permittivities of the dielectric cladding are different on both sides of the metal. In these configurations, we have found narrow regions of structure opto-geometric parameters in which low-power plasmon–solitons exist.

Because our models are formulated for four-layer structures, they allow us to study configurations in which an additional dielectric layer is introduced between the nonlinear dielectric and the metal film for the first time. We have provided dispersion diagrams and field plots for such structures with various parameters. The semi-analytical formulation of our models allows us to rapidly scan the phase space of the structure parameters. Using these scans, we have reported possible four-layer configurations with realistic parameters that support plasmon–solitons for power levels below the material damage threshold.

Secondly, we study configurations called nonlinear slot waveguides, in which a finite-size nonlinear dielectric core is sandwiched between two semi-infinite metal cladding layers. We have developed two models based on Maxwell's equations to study such structures. The first model uses a simplified treatment of the Kerr-type nonlinearity, but provides analytical expressions for the field profiles and the nonlinear dispersion relations expressed in terms of Jacobi elliptic special functions. The second model treats the Kerr-type nonlinearity in the exact way and allows us to obtain an analytical condition that reduces the parameter space in which the solutions for a given structure are numerically computed.

We have studied the dispersion diagrams and the mode transformations along their dispersion curves for the symmetric nonlinear slot waveguides. Except for the first order modes already known in such structures, we have discovered the existence of higher-order modes. All the modes of the nonlinear slot waveguide can be divided in two families: a family of symmetric and antisymmetric modes with nodes that resemble the linear modes of a modified linear slot waveguide; and a family of symmetric and asymmetric node-less modes that do not have linear counterparts. We report that in the node-less family, the symmetric modes appear through a fold bifurcation and the asymmetric modes, that are doubly degenerate, appear from the symmetric modes through a Hopf bifurcation. Using the versatility

of our models, we have also studied the effects of the core size and of the permittivity contrast between the core and the metal cladding on the dispersion diagrams. We have shown that a careful choice of these parameters may lead to nonlinear effects that can be observed at low power levels. We also studied the properties of asymmetric nonlinear slot waveguide structures (with different permittivities of the two metal claddings). Finally, using both theoretical arguments and numerical simulations of the temporal evolution obtained with two different vector methods, we present the first study of the plasmon–soliton stability in nonlinear slot waveguides.

Résumé

Dans cette thèse, nous étudions les propriétés d'ondes transverses magnétiques dans des structures composées d'une couche de diélectrique nonlinéaire de type Kerr et des couches métalliques et diélectriques linéaires. Bien que ces ondes, nommées ici plasmons–solitons, ont été étudiées depuis plus que 30 ans, il n'y a toujours pas de confirmation expérimentale de leurs existences, du fait de l'extrême modification nonlinéaire de l'indice de réfraction requise pour générer ces ondes dans les configurations proposées jusqu'ici. Le but de cette thèse est de développer des modèles analytiques et numériques pour améliorer notre compréhension de ces plasmons–solitons et de concevoir des structures supportant ces ondes nonlinéaires à basse puissance.

Dans la première partie de cette thèse, nous élaborons différents modèles pour étudier les propriétées de plasmons–solitons stationnaires dans deux types de structures : (i) une région diélectrique nonlinéaire semi-infinie en contact avec des couches de métal et de diélectrique linéaires et (ii) une couche de diélectrique nonlinéaire d'épaisseur finie entre deux régions métalliques semi-infinies (guide d'onde métallique à cœur nonlinéaire). Nos modèles nous permettent de calculer des relations de dispersion nonlinéaires et les profils de champ correspondants dans ces structures. Ils généralisent les approches déjà proposées dans la littérature et nous permettent d'étudier des configurations qui ne l'avaient jamais été. Les différents modèles développés ont des niveaux de compléxité différents et font appel à différentes approximations. Par conséquent, ils sont complémentaires dans l'étude des structures visées.

Dans la seconde partie, nous présentons des résultats obtenus pour les deux types de structures mentionnées ci-dessus. Pour le premier, nous montrons qu'en utilisant une structure à quatre couches que nous proposons (avec une couche mince tampon de diélectrique linéaire entre le milieu nonlinéaire et le film métallique), il est possible d'obtenir des plasmons–solitons à des niveaux de puissance déjà utilisés pour des solitons spatiaux dans des guides d'onde purement diélectriques. Du fait de l'efficacité de nos méthodes, nous avons scanné l'espace des paramètres de la structure et nous avons trouvé les configurations les plus adaptées à la première observation expérimentale des plasmons–solitons. Puis, nous étudions les guides d'onde métalliques à cœur nonlinéaire. Pour de tels guides symétriques, nous retrouvons des modes déjà connus dans la littérature et trouvons de nouveaux modes d'ordres supérieurs. Pour certains des modes symétriques, nous observons une bifurcation par brisure de symétrie donnant naissance à des modes asymétriques dans une structure symétrique. Nous étudions les effets du changement de la taille du cœur et du contraste de permittivité sur le seuil requis pour cette bifurcation. Nous présentons aussi la première étude des guides d'onde métalliques à cœur nonlinéaire asymétriques. Finallement, en utilisant à la fois des arguments théoriques et des simulations de l'évolution temporelle réalisées avec deux méthodes numériques différentes, nous réalisons la première étude de la stabilité de ces plasmons–solitons dans des guides d'onde métalliques à cœur nonlinéaire.

List of Figures

List of Tables

Chapter 1

Context

Contents

1.1 Introduction

The field of nonlinear optics [1–3] was born after the appearance of lasers at the beginning of 1960s, when sources of powerful and coherent light required to observe nonlinear effects in optical materials became available. Light with high intensity induces changes of the material properties leading to nonlinear phenomena such as second and third harmonic generation, sum and difference frequency generation, intensity dependent refractive index or two photon absorption and many more.

Spatial optical solitons are closely related to the intensity dependent refractive index. Spatial optical solitons are localized nonlinear electromagnetic excitations for which the diffraction is balanced by the self-focusing nonlinear effect [4]. These waves were extensively studied over the last decades [5–9]. Due to the extraordinary properties of solitons, such as strong localization and ability to propagate undisturbed over large distances, these beams are not only interesting physical objects but also offer a huge application potential in integrated optics and all-optical devices. The field confinement can be further enhanced by using layered structures, so that the total refractive index modification is not only due to the self-induced nonlinear effects but also built-in in the structure. The simplest structure of this type is a single interface between a linear and a nonlinear dielectric.

The first description of optical nonlinear localized surface waves — solitons propagating along a single interface between a linear and a nonlinear dielectric — was given in 1980 by Tomlinson [10]. The single nonlinear/linear dielectric interface configuration was studied in a number of works in the following years where both transverse magnetic (TM) and transverse electric (TE) polarized nonlinear surface waves were studied [11–13]. The nonlinear dispersion relations with more realistic assumptions on the nonlinear term than those used in Ref. [10] were found [14, 15].

Later on, as a natural generalization of Tomlinson's work, solitons in dielectric waveguides with nonlinear cladding were studied. Starting from 1983, configurations with nonlinear cladding on one or on two sides were considered for both TE [16–18] and TM [19–21] light polarizations. Both the cases

of focusing and of defocusing third-order local and instantaneous (Kerr-type) nonlinearity were analyzed. In structures with defocusing nonlinearity, a power cut-off phenomena was observed for guided waves [22]. A comparison of symmetric and asymmetric cladding (in terms of relative permittivity or nonlinear parameters) was presented in Refs. [23, 24]. In the case of symmetric dielectric waveguides, a symmetry-breaking bifurcation was predicted in one-dimensional [24–28] and two-dimensional [29, 30] structures. At the beginning of the 90s, a method to study nonlinear dielectric waveguides based on the variational analysis was presented in Ref. [31]. At approximately the same time, scaling rules [32] and dispersion diagrams in normalized coordinates [33] were introduced to facilitate the comparison between the results obtained for different physical parameters. The numerical analysis of the evolution of nonlinear surface waves in dielectric waveguides with nonlinear cladding was presented in Ref. [34] for a one-dimensional case and in Refs. [35, 36] for the two-dimensional waveguiding structures. For a comprehensive review on the topic of nonlinear waves propagating in planar structures the reader may refer to Ref. [37] where also first preliminary experimental results are shown for system using this type of waves (such as nonlinear guided wave optical limiters, nonlinear coherent directional couplers, and optical switches using bistability in nonlinear planar configurations).

In all the works mentioned previously on single-interface configuration or on the waveguides with nonlinear cladding, the nonlinear medium was semi-infinite. Other type of nonlinear dielectric waveguides has a nonlinear core that is surrounded by linear dielectrics. In such type of structures, the nonlinear medium has a finite size, which requires a more complex treatment of the problem. From the beginning of 80s, dielectric waveguides with a nonlinear core were studied for TE [38–40] and TM [41] polarizations. Nonlinear cores with Kerr-type [42] and saturable [43, 44] nonlinearities were studied. The symmetry-breaking bifurcation was discovered in the dielectric waveguides with a nonlinear dielectric core [38, 39] and a symmetric cladding. Scaling rules for thin-film dielectric optical waveguides with nonlinear core, similar to those presented in Ref. [32] for a single-interface case, were developed in Ref. [45]. Studies of nonlinear waveguides with both nonlinear core and cladding were performed using modal [46], effective-index [27, 47], variational [28, 48–50] and resonant [51] approaches. These works lead to the analysis of multi-layered nonlinear dielectric structures [52–54]. The multi-layered structures may find applications for nonlinear wave splitting and coupling. All the works described above were dealing with fully dielectric structures. Below we will describe studies of structures where nonlinear dielectrics are in contact with metal layers.

Plasmonics is another domain that grew strongly over the last decades [55–64]. Surface plasmon polaritons (shortly called here plasmons) are surface waves localized at an interface between a metal and a dielectric. They propagate along this interface but decay rapidly in the direction perpendicular to the interface. Because of the evanescent nature of the plasmon waves, light is strongly localized close to the interface which results in high field confinement and can lead to the enhancement of nonlinear effects near this interface. Combining the fields of plasmonics and nonlinear optics results in interesting and unusual physical effects [65, 66]. One of the most challenging for observation and at the same time the most attractive phenomenon in nonlinear photonics is the formation of plasmon–solitons — nonlinear waves propagating along an interface between a metal and a nonlinear dielectric that possess both the properties of spatial optical solitons and surface plasmon polaritons. Below we describe the field of plasmon–solitons starting by its historical development and coming to the most recent results in this topic.

The first description of the nonlinear surface plasmon polariton waves confined at an interface between a metal and a nonlinear dielectric was given in 1980. Agranovich *et al.* in the seminal paper [67] developed a vector model for a single interface between a metal and a nonlinear dielectric. The method presented in Ref. [67] is similar to the approaches used for the interface between linear and nonlinear dielectrics [10, 11]. In Ref. [67], and in the majority of works published on plasmon–solitons, a dielectric exhibiting a Kerr-type nonlinearity is considered. The model proposed by Agranovich *et al.* describes a one-dimensional geometry (the structure is invariant along two directions) what allows for the polarization separation of Maxwell's equations. The analytical formulas for the nonlinear dispersion relation and the field profiles for TM polarized waves are derived in Ref. [67] using strong assumptions on the nonlinear term. The nonlinearity in this model depends only on the longitudinal component of

the electric field (that is usually much weaker than the transverse component [68]) and affects only two of the diagonal permittivity tensor components.[1] In reality all the permittivity tensor components depend on both transverse and longitudinal field components. Additionally, this model results in fields localized on the metal/nonlinear dielectric interface only for the defocusing type of nonlinearity that is not an intuitive result.

The model proposed in Ref. [67] was subsequently improved by introducing more realistic assumptions on the nonlinear term (e.g., focusing nonlinearity depending only on the transverse component of the electric field). It was also extended to consider both TE and TM polarized waves as well as focusing and defocusing Kerr-type nonlinearities [14, 68, 69].

A different approach, based on the first integral treatment of Maxwell's equations, was developed in 1987 [15] and allowed for obtaining the exact (under the assumption that Kerr nonlinearity depends on both components of the electric field) dispersion relations for TM case. However, the price to pay was that the field profile in the nonlinear medium was not given by an analytic formula as in the Refs. [68, 69] and had to be calculated numerically. A comparison of the numerical methods treating the Kerr-type nonlinearity in an exact way with the analytical approaches that use approximated treatment of nonlinearity is presented in Ref. [70]. Recently, a model for plasmon–soliton waves at a single metal interface based on the resonant interaction between a linear plasmon and a spatial soliton was developed [71]. The authors used a heuristic, scalar model to describe the resonant interaction between plasmon and soliton beams.

In 2009, plasmon–solitons localized in both transverse (plasmonic localization due to index contrast at the interface) and lateral (solitonic self-focusing) directions were predicted theoretically and confirmed numerically in two-dimensional structures [72]. The method presented in Ref. [72] uses the linear solution of the one-dimensional problem (along the transverse direction) to transform Maxwell's equations into a nonlinear Schrödinger equation. Using this method it was shown that the shape of the solution in the lateral direction was given by the sech function as for the usual one-dimensional solitons. The evolution of the beam during the propagation was studied using the nonlinear Schrödinger equation and the results were compared with two-dimensional numerical simulations obtained using a commercial finite-difference time-domain solver. As a result, the authors obtained the two-dimensional plasmon–soliton beam.

Furthermore, the model of Agranovich *et al.* [67] was expanded to consider nonlinear waves guided by a thin metal film sandwiched between two nonlinear dielectrics (nonlinear dielectric/metal/nonlinear dielectric structure — NMN) [73–75]. In Ref. [73], field profiles of plasmon–solitons on thin metal films were shown for the first time. Ref. [73] provides the analytical formulas for the dispersion relations and the field profiles for the NMN structure as well as for the limiting case where the nonlinearity in one of the dielectrics tends to zero (nonlinear dielectric/metal/linear dielectric structure — NML). Looking at the field profiles shown in Ref. [73] we can distinguish two types of plasmon–solitons: (i) the plasmonic type, for which the field profile resembles that of a linear plasmon [symmetric or antisymmetric plasmon in the linear dielectric/metal/linear (LML) dielectric structure, known also as insulator/metal/insulator structure (IMI)] slightly modified by the presence of nonlinearity in the dielectrics and (ii) the solitonic type, for which the features of both soliton (soliton peak in the nonlinear medium) and plasmon (localization on the metal interface) are visible. There is a smooth transition between the two types with the change of the beam power. This type of structures will be studied in more detail in Section 4.2.

Structures with only one nonlinear dielectric as cladding were studied analytically [76, 77] and numerically [78]. The exact dispersion relation for TM waves in NML structures was found for power-law Kerr nonlinearity with an arbitrary order of electric field power [77]. The method used in Ref. [77] is an extension to three-layer structures of the results shown in Ref. [15] for two-layer structures.

[1] In Ref. [67], x denotes the propagation (longitudinal) direction and z denotes the transverse direction. The structure is invariant along the x and the y (lateral) direction. The electric field of the TM polarized wave has only two components: $\mathbf{E} = [E_x, 0, E_z]$. The transverse field components E_z is the leading electric field component in the type of structures studied in this paper [68]. The nonlinearity is assumed to be of the form $\epsilon_x = \epsilon_y = \epsilon_l + \alpha|E_x|^2$, $\epsilon_z = \epsilon_l$ where ϵ_x, ϵ_y, and ϵ_z are the diagonal elements of the relative permittivity tensor and ϵ_l is the linear value of the relative permittivity.

In Ref. [77], the dispersion relation is given in an analytical form, but the field profiles in the semi-infinite nonlinear layer have to be found numerically by integration of Maxwell's equations. The authors propose that plasmon–solitons could find application in a light-controlled metal transmission devices. The control of the plasmon resonance by the electric field intensity could influence the transmission of the thin metal film.

Recently, in order to facilitate the nonlinear coupling between soliton and plasmon waves, an additional linear dielectric layer between the nonlinear dielectric and the metal film was introduced [79–81]. In Refs [79, 81], we have proposed two complementary approaches based on the modal methods developed in [73, 77]. A detailed description of these two models is presented in Part I of this PhD manuscript. In contrast to these modal methods, the model built in Ref. [80] is based on the resonant approach proposed in Refs. [71, 82]. The models presented in Refs. [71, 80, 82], in contrast to the modal approaches in which plasmon–solitons are treated as a single wave, treat plasmon and soliton as separate entities and the coupling is based on the propagation constant matching of these two waves. In the vicinity of the coupling regime, avoided crossing between the plasmon and soliton dispersion relations can be observed. The Pointing vector distribution maps prove the energy exchange between the plasmon and soliton beams. In Refs. [80, 82], the authors show also that some of the solutions found in modal approaches can be unstable during the propagation.

In Refs. [83, 84], two dimensional plasmonic waveguides were studied numerically in the structures where the stripe metal waveguide is surrounded by a nonlinear dielectric medium.

The most interesting and probably the most promising configuration where plasmon–solitons can be observed is the nonlinear slot waveguide configuration. In this thesis, we define the nonlinear slot waveguide as a structure made of a nonlinear dielectric core sandwiched between two semi-infinite metal layers. With this type of structure, the interest in plasmon–soliton beams started to grow again recently. Dispersion relations for nonlinear slot waveguides were obtained using various approaches. The first attempt to study this type of structures was made in 2007 in Ref. [85], where two dimensional plasmon–solitons were studied. The method presented in Ref. [85] is based on the linear plasmon profile along the transverse direction found in the linear MIM structure. This solution is then used to solve nonlinear Maxwell's equations for the field profile in the lateral direction. In Ref. [85], the authors assumed that even though the field is now localized in both transverse and lateral directions, the TM polarization is still maintained. A method similar to the one used in Ref. [85] was applied later to study nonlinear plasmon–solitons at a single interface between a metal and a nonlinear dielectric [72]. An interesting feature of the plasmon–solitons found in Ref. [85] is their extreme confinement. The effective beam size[2] can be one order of magnitude lower than the diffraction limit. This property results from the strong spatial confinement of the field by the metal slot waveguide in the transverse direction and the solitonic localization in the lateral direction. The results presented in Ref. [85] show that reducing the width of the nonlinear dielectric core of the nonlinear slot waveguide results in the decrease of the effective soliton dimension for all range of the widths studied. On the contrary, for a nonlinear core with dielectric claddings, the effective width of the beam starts to increase below a certain width of the core, as it is well known in linear guided optics [86].

Later, the nonlinear dispersion relations of one-dimensional nonlinear slot waveguides were found numerically and the symmetry-breaking bifurcation was observed for the first order symmetric mode [87], resulting in an appearance of a doubly degenerate asymmetric mode. The approach of Davoyan *et al.* [87] is numerical — the solutions of Maxwell's equations (the effective index of the allowed modes and the corresponding field profiles) are found using the shooting method [88] and the power is calculated by numerical integration. This method, unlike the one presented in Ref. [85], accounts for the Kerr-type nonlinearity influence on the transverse field profiles.

The analytical formulas for the nonlinear dispersion relations of the symmetric and antisymmetric modes of the nonlinear slot waveguides were presented in 2011 in Refs. [89, 90]. In these two references, the dispersion relations are given in a form of an integral that has to be solved numerically. Study of the femtosecond pulses in nonlinear slot waveguide configuration was performed using numerical

[2]The effective beam size D_{eff} is defined as a geometric average of the full-width at half-maximum in the transverse (Δx) and lateral (Δy) directions ($D_{eff} = \sqrt{\Delta x \Delta y}$).

methods in Ref. [91]. Recently, we have developed two new semi-analytical models, which allowed to discover higher-order modes in nonlinear slot waveguides and study the size effects in more detail [92]. A detailed description of these models can be found in Part II of this PhD manuscript.

During the last 5 years, formation of plasmonic solitons was also studied in multi-layer structures with alternating metal and nonlinear dielectric layers [93–95] and plasmonic wire arrays [96–98]. In Ref. [95], the authors obtained a set of discrete excitations of the nonlinear plasmonic waveguides with the envelope of the solitonic shape. The surface plasmonic solitons at the interface between a nonlinear medium and a semi-infinite periodic metal/nonlinear dielectric structure showed higher level of localization compared to infinitely periodic structure. Nonlinear plasmonic couplers, in which the symmetry-breaking bifurcation occurs, were also demonstrated in layered structures where nonlinear metal layers are separated by linear dielectric films [99, 100].

1.2 Aim and structure of the work

As it was stated in the description of the state-of-the-art of the nonlinear plasmon–solitons waves presented in Section 1.1, studies of nonlinear surface waves at metal interfaces started more than thirty years ago. Nevertheless, there is no experimental results on plasmon–soliton waves that would confirm their existence. The main reason is that the nonlinear refractive index change required for the formation of plasmon–solitons in the structures that were proposed in the already published works, is too high for the realistic materials used in integrated and nonlinear optics. The nonlinear refractive index changes at which plasmon–solitons exist in the structures reported until now require the light intensity I that exceeds the damage threshold of the available materials.

The aim of this PhD thesis is to improve the understanding of interactions between plasmon and soliton beams in order to facilitate the experimental observation. of plasmon–soliton waves. We want to provide a direct indication of the types of nonlinear materials and metals involved, their configuration, and parameters domains where observation of plasmon–solitons will be possible at realistic power levels. This goal is achieved by the systematic study of the properties of transverse magnetic polarized light propagating in various structures containing nonlinear and linear dielectric layers, and metal layers.

In Part I of this PhD manuscript, we study structures with a semi-infinite nonlinear medium and metal and linear dielectric layers. In Chapter 2, we develop models describing the light propagation in this type of structures. We derive closed analytical formulas for the dispersion relations and for the field profiles of plasmon–solitons. Derivation of our two semi-analytical models is presented in Sections 2.1 and 2.3. In Sections 2.2 and 2.4, one semi-analytical and one numerical model already known in literature are described because they will be used in order to confirm the validity of our new models. The validity of our semi-analytical models is confirmed in Chapter 3, by comparison of their results with results already reported in literature and by a mutual comparison. In Chapter 4, the results for the dispersion curves and the field profiles of plasmon–solitons obtained using our models are presented. We study simple structures with a single interface between a metal and a nonlinear dielectric (Section 4.1), configurations in which a thin metal film is sandwiched between a linear and a nonlinear dielectric cladding (Section 4.2), and four-layer configurations where an additional linear dielectric layer is introduced between the metal film and the nonlinear dielectric (Section 4.3). In Chapter 5, extensions of one of our models to the case of two-dimensional and transverse electric polarized plasmon–solitons is shown.

In Part II of this PhD manuscript, we focus on the structures where a finite-size nonlinear medium is sandwiched between two semi-infinite metal layers. In Chapter 6, we present a theoretical derivation of a semi-analytical model (Section 6.1) which provides closed analytical formulas for the dispersion relations and the field profiles and a numerical model (Section 6.2) to study plasmon–solitons in nonlinear plasmonic slot waveguide structures. The results obtained using these two models are presented in Chapter 7. The classification of the modes of symmetric nonlinear slot waveguides, based on the dispersion curves and the field profiles, is presented in Section 7.1. In this section, the influence on the dispersion curves of the nonlinear slot waveguide parameters, such as the core width or the permit-

tivity contrast between the core and the metal cladding, is also studied. In Section 7.2, the properties of the asymmetric nonlinear slot waveguides are shortly discussed.

At the end of the manuscript, in Chapter 8, our first preliminary results on the stability of the modes found in Chapters 2 and 6 is made. The stability analysis is performed using a topological criterion which allows us to read the stability of a mode directly from the dispersion diagrams of the structure.

In Chapter 9, concluding remarks are made to sum up the results presented in this PhD manuscript. In Appendix A, details on the intensity dependent refractive index are presented. In Appendices B and C definition and properties of the elliptic integrals and the Jacobi elliptic functions are described. Appendix D shows the study of the propagation losses in the nonlinear slot waveguide configurations. In Appendix E more field profiles obtained using the Jacobi elliptic function based model is presented. Finally, in Appendix F preliminary studies of plasmon–soliton waves using the finite-difference time-domain method are described.

1.3 Maxwell's equations

To study classical electromagnetic problems Maxwell's equations must be solved [101, 102]. Here we will use them as a starting point for our calculations. The general form of Maxwell's equations is:

$$\boldsymbol{\nabla} \times \boldsymbol{\mathscr{E}} = -\frac{\partial \boldsymbol{\mathscr{B}}}{\partial t}, \tag{1.3.1a}$$

$$\boldsymbol{\nabla} \times \boldsymbol{\mathscr{H}} = \boldsymbol{\mathscr{J}}_f + \frac{\partial \boldsymbol{\mathscr{D}}}{\partial t}, \tag{1.3.1b}$$

$$\boldsymbol{\nabla} \cdot \boldsymbol{\mathscr{D}} = \rho_f, \tag{1.3.1c}$$

$$\boldsymbol{\nabla} \cdot \boldsymbol{\mathscr{B}} = 0, \tag{1.3.1d}$$

where $\boldsymbol{\mathscr{E}}$ denotes the electric field, $\boldsymbol{\mathscr{D}}$ denotes the displacement vector, $\boldsymbol{\mathscr{H}}$ denotes the magnetic field, and $\boldsymbol{\mathscr{B}}$ denotes the magnetic induction. Additionally, $\boldsymbol{\mathscr{J}}_f$ denotes the free currents and ρ_f denotes the free charges in the system. In our studies, we will set $\boldsymbol{\mathscr{J}}_f = \mathbf{0}$ because we will look for the solutions in the systems without external sources and $\rho_f = 0$ as no free charges will be considered.

Additionally to Maxwell's equations, the four vector fields are related by the constitutive relations [101]:

$$\boldsymbol{\mathscr{D}} = \epsilon_0 \boldsymbol{\mathscr{E}} + \boldsymbol{\mathscr{P}}, \tag{1.3.2a}$$

$$\boldsymbol{\mathscr{H}} = \frac{1}{\mu_0} \boldsymbol{\mathscr{B}} + \boldsymbol{\mathscr{M}}, \tag{1.3.2b}$$

where the auxiliary fields of polarization $\boldsymbol{\mathscr{P}}$ and magnetization $\boldsymbol{\mathscr{M}}$ appear. Here ϵ_0 denotes the vacuum permittivity and μ_0 denotes the vacuum permeability. In our work we will consider nonmagnetic materials, therefore we set $\boldsymbol{\mathscr{M}} = 0$. Assuming an instantaneous response of the materials, the polarization vector describes the electronic response of the material to the applied electric field and is given by:

$$\boldsymbol{\mathscr{P}} = \epsilon_0 \tilde{\tilde{\chi}} \boldsymbol{\mathscr{E}}, \tag{1.3.3}$$

where $\tilde{\tilde{\chi}} = \tilde{\chi} + i\tilde{\chi}''$ denotes the complex susceptibility tensor of the material, and both $\tilde{\chi}$ and $\tilde{\chi}''$ are real quantities.

Using the definition of the polarization given by Eq. (1.3.3) we can rewrite the expression for the displacement vector [Eq. (1.3.2a)] in the form:

$$\boldsymbol{\mathscr{D}} = \epsilon_0 \left(1 + \tilde{\tilde{\chi}}\right) \boldsymbol{\mathscr{E}}. \tag{1.3.4}$$

Introducing the relation between the complex susceptibility $\tilde{\tilde{\chi}}$ and the relative complex permittivity:[3]

$$\tilde{\tilde{\epsilon}} = \left(1 + \tilde{\tilde{\chi}}\right), \tag{1.3.5}$$

[3] In the following, in order to simplify the nomenclature the relative permittivity ϵ will be shorty called permittivity.

the displacement vector can be written as

$$\boldsymbol{\mathscr{D}} = \epsilon_0 \tilde{\tilde{\epsilon}} \boldsymbol{\mathscr{E}}. \tag{1.3.6}$$

The complex permittivity tensor $\tilde{\tilde{\epsilon}}$ in our work is assumed to be diagonal with isotropic losses [68, 72, 73, 81]:

$$\tilde{\tilde{\epsilon}} = \bar{\bar{\epsilon}} + i\,\bar{\bar{\epsilon}}'' = \begin{pmatrix} \epsilon_x & 0 & 0 \\ 0 & \epsilon_y & 0 \\ 0 & 0 & \epsilon_z \end{pmatrix} + i \begin{pmatrix} \epsilon'' & 0 & 0 \\ 0 & \epsilon'' & 0 \\ 0 & 0 & \epsilon'' \end{pmatrix}. \tag{1.3.7}$$

Here ϵ_j ($j \in \{x, y, z\}$) and ϵ'' are real quantities. The refractive index is defined as $n_j = \sqrt{\epsilon_j}$. Using all the assumptions and definitions given above [Eqs. (1.3.2b) and (1.3.4)] Maxwell equations [Eqs. (1.3.1)] are expressed using the electric field $\boldsymbol{\mathscr{E}}$ and the magnetic field $\boldsymbol{\mathscr{H}}$ only

$$\boldsymbol{\nabla} \times \boldsymbol{\mathscr{E}} = -\mu_0 \frac{\partial \boldsymbol{\mathscr{H}}}{\partial t}, \tag{1.3.8a}$$

$$\boldsymbol{\nabla} \times \boldsymbol{\mathscr{H}} = \epsilon_0 \tilde{\tilde{\epsilon}} \frac{\partial \boldsymbol{\mathscr{E}}}{\partial t}, \tag{1.3.8b}$$

$$\boldsymbol{\nabla} \cdot (\tilde{\tilde{\epsilon}} \boldsymbol{\mathscr{E}}) = 0, \tag{1.3.8c}$$

$$\boldsymbol{\nabla} \cdot \boldsymbol{\mathscr{H}} = 0. \tag{1.3.8d}$$

1.4 Polarization separation in one-dimensional problems

Maxwell's equations [Eqs. (1.3.8)] hold for the general type of three-dimensional electromagnetic problems where all three components of electric and magnetic fields are nonzero. Although, in our work we consider a simpler case of one-dimensional structures in which the refractive index of the structure is modulated only along one direction and therefore, the structure is invariant in two remaining directions. Here we choose the refractive index to be structured along the x direction. This direction will be called the transverse direction. We assume that the light propagates along the z direction, called here the longitudinal direction. Along the remaining direction (y direction called here the lateral direction) the structure is invariant and therefore we will assume that all the y derivatives are equal to zero and that the electromagnetic field distribution will be uniform along this direction. In such configurations, using the scalar component notation of the vector fields, it is possible to split the six Maxwell's equations [Eqs. (1.3.8a) and (1.3.8b)] into two sets of three equations corresponding to the orthogonally polarized electromagnetic fields. This is the well known transverse electric/transverse magnetic separation [101]. The scalar components of the electromagnetic field are defined by

$$\boldsymbol{\mathscr{E}} \equiv [\mathscr{E}_x, \mathscr{E}_y, i\mathscr{E}_z], \tag{1.4.1a}$$

$$\boldsymbol{\mathscr{H}} \equiv [\mathscr{H}_x, \mathscr{H}_y, i\mathscr{H}_z], \tag{1.4.1b}$$

where the imaginary unit i is written explicitly in front of the z field components so as all the quantities: $\mathscr{E}_x$, $\mathscr{E}_y$, $\mathscr{E}_z$, $\mathscr{H}_x$, $\mathscr{H}_y$, and $\mathscr{H}_z$ are real. The first set of three equations:

$$\frac{\partial \mathscr{H}_x}{\partial z} - i\frac{\partial \mathscr{H}_z}{\partial x} = \epsilon_0 \tilde{\epsilon}_y \frac{\partial \mathscr{E}_y}{\partial t}, \tag{1.4.2a}$$

$$\frac{\partial \mathscr{E}_y}{\partial z} = \mu_0 \frac{\partial \mathscr{H}_x}{\partial t}, \tag{1.4.2b}$$

$$\frac{\partial \mathscr{E}_y}{\partial x} = i\mu_0 \frac{\partial \mathscr{H}_z}{\partial t}, \tag{1.4.2c}$$

relates only $\mathscr{E}_y$, $\mathscr{H}_x$, and $\mathscr{H}_z$ field components. Here we introduced the complex permittivity components denoted by $\tilde{\epsilon}_j = \epsilon_j + i\epsilon''$ for $j \in \{x, y, z\}$. The waves possessing only these three nonzero field

components will be called transverse electric (TE) waves. Three equations building the second set:

$$i\frac{\partial \mathscr{E}_z}{\partial x} - \frac{\partial \mathscr{E}_x}{\partial z} = \mu_0 \frac{\partial \mathscr{H}_y}{\partial t}, \tag{1.4.3a}$$

$$-\frac{\partial \mathscr{H}_y}{\partial z} = \epsilon_0 \tilde{\epsilon}_x \frac{\partial \mathscr{E}_x}{\partial t}, \tag{1.4.3b}$$

$$\frac{\partial \mathscr{H}_y}{\partial x} = i\epsilon_0 \tilde{\epsilon}_z \frac{\partial \mathscr{E}_z}{\partial t}, \tag{1.4.3c}$$

relate only $\mathscr{H}_y$, $\mathscr{E}_x$, and $\mathscr{E}_z$ field components. The waves possessing only these three nonzero field components will be called transverse magnetic (TM) waves.

1.5 Transverse magnetic monochromatic waves

The structures that we consider in our work are build of layers of dielectrics and metals. We are interested in observing the waves possessing a plasmonic part in the metal region. Previous linear studies [55–57, 60] have shown that plasmons exist on the metal/dielectric interfaces only for the TM light polarization. Therefore, we will focus our attention on the TM polarized waves. The problem of the TE polarized waves will be shortly discussed in Section 5.2.

In the following, we will work with TM polarized waves where the magnetic field has only one component $\boldsymbol{\mathscr{H}} = [0, \mathscr{H}_y, 0]$ and the electric field has two components $\boldsymbol{\mathscr{E}} = [\mathscr{E}_x, 0, i\mathscr{E}_z]$. The stationary solutions in one-dimensional geometry are sought in the form of monochromatic harmonic waves:

$$\begin{Bmatrix} \boldsymbol{\mathscr{E}}(x,z,t) \\ \boldsymbol{\mathscr{H}}(x,z,t) \end{Bmatrix} = \begin{Bmatrix} \mathbf{E}(x) \\ \mathbf{H}(x) \end{Bmatrix} e^{i(k_0\beta z - \omega t)}. \tag{1.5.1}$$

Here ω denotes the angular frequency of the wave, $k_0 = \omega/c$ denotes the wavenumber in vacuum, c denotes the speed of light in vacuum, and β denotes the effective index of the propagating wave (the propagation constant is expressed as $k_0\beta$). We follow here the notation used in Refs. [18, 21, 22, 25, 32, 35, 36, 68, 73–76, 79, 81] The structure is invariant along the y direction and therefore electromagnetic fields do not carry any y dependency.

The TM approach used here is exact only in case where both the structure and the light distribution are invariant along the lateral y direction. By invariant light distribution we understand the case where light intensity is uniform along the y direction. A good approximation of such an invariant light distribution is obtained if the light intensity varies slowly compared to the scale of the wavelength. This is often the case in linear optics, where beams with large widths are used. In the case of nonlinear studies, the light distribution is often not uniform along the y direction. The nonlinear studies require high light intensities. Experimentally, this is obtained by using powerful lasers and focusing the beam to a spot of the size comparable to the wavelength. This means that the light intensity of the beam varies significantly on the wavelength scales. Additionally, in the frame of the nonlinear optics, properties of the material depend on the impinging light intensity. If the light intensity distribution is not uniform along the y direction, it induces the nonuniform distribution of the material properties (e.g., refractive index) along the y direction. In this case, the structure is no longer invariant in the lateral direction. This explains why the TM approach is only an approximation in the nonlinear case. The quality of this approximation depends on two factors: how fast is the light modulation along the y direction and how large is the modulation amplitude of the material parameters (nonlinear induced refractive index change). To account for this effects, in Section 5.1, we will develop the approximated two-dimensional approach providing the first approximation of the two-dimensional plasmon–solitons. In the studies of one-dimensional plasmon–solitons that propagate in one-dimensional structures we will consider that the light distribution along the y direction is uniform.

In order to solve Maxwell's equations in our structures we use a supplementary assumption. Only the real part of the permittivity tensor $\bar{\bar{\epsilon}}$ is used to find the dispersion relations and to determine the field profiles. The imaginary part of permittivity ϵ'' will be used later to estimate the propagation losses of the nonlinear waves. Identical way of splitting the problem was already used in Refs. [67–69, 73–77].

Using Eq. (1.5.1) the z and time derivatives are eliminated from Eqs. (1.4.3) to finally give

$$k_0\beta E_x - \frac{\mathrm{d}E_z}{\mathrm{d}x} = \omega\mu_0 H_y, \tag{1.5.2a}$$

$$E_x = \frac{\beta}{\epsilon_0\epsilon_x c} H_y, \tag{1.5.2b}$$

$$E_z = \frac{1}{\epsilon_0\epsilon_z\omega}\frac{\mathrm{d}H_y}{\mathrm{d}x}, \tag{1.5.2c}$$

where the x, z, and time dependencies are skipped in the field components and the permittivity in order to simplify the notation. In Eqs. (1.5.2), the complex permittivity tensor components were replaced by their real parts according to the approximation discussed above. Equations (1.5.2) will be used in Sections 2 and 6 as a starting point of the derivations of all the models.

1.6 Kerr effect

In the definitions of the polarization and the displacement vector [Eqs. (1.3.3) and (1.3.4)], we use the total complex susceptibility tensor $\tilde{\bar{\bar{\chi}}} = \bar{\bar{\chi}} + i\bar{\bar{\chi}}''$. The imaginary part $\bar{\bar{\chi}}''$ is proportional to the imaginary part of the permittivity $\bar{\bar{\epsilon}}'' = \epsilon_0\bar{\bar{\chi}}''$. As stated in Section 1.5, the imaginary part of the permittivity will be omitted in the process of Maxwell's equation solutions and will be used only in the losses calculations. In the presentation of the Kerr effect, the imaginary part of the susceptibility tensor will be omitted in a similar manner. In our studies, losses that originate from the nonlinear three photon absorption effect will not considered.

In the derivation of the Kerr effect, we will use different notation for the fields than in Sections 1.3–1.5. As the nonlinear effects can influence the light at frequencies different than the fundamental (excitation) frequency, we will show the time and frequency dependencies explicitly in the notation. The electric field and polarization vectors are denoted here as

$$\widetilde{\boldsymbol{\mathscr{E}}}(t) = \mathbf{E}(\omega)e^{-i\omega t} + \mathbf{E}(\omega)^* e^{i\omega t}, \tag{1.6.1a}$$

$$\widetilde{\boldsymbol{\mathscr{P}}}(t) = \mathbf{P}(\omega)e^{-i\omega t} + \mathbf{P}(\omega)^* e^{i\omega t}, \tag{1.6.1b}$$

where the complex conjugate fields (denoted by *) are included. The notation used here[4] and the derivation of the Kerr effect follow the lines presented in Ref. [2].

In conventional linear optics, the polarization depends linearly on the electric field strength. In the linear case and for instantaneous material response, Eq. (1.3.3) reads

$$\widetilde{\boldsymbol{\mathscr{P}}}(t) = \epsilon_0\bar{\bar{\chi}}^{(1)}\widetilde{\boldsymbol{\mathscr{E}}}(t), \tag{1.6.2}$$

where the proportionality constant $\bar{\bar{\chi}}^{(1)}$ is known as the linear susceptibility tensor. In nonlinear optics, when the field intensities become sufficiently high to induce nonlinear effects, the linear description is no longer accurate [103]. Higher terms of the Taylor expansion of polarization have to be taken into account:

$$\widetilde{\boldsymbol{\mathscr{P}}}(t) = \epsilon_0\left[\bar{\bar{\chi}}^{(1)}\widetilde{\boldsymbol{\mathscr{E}}}(t) + \bar{\bar{\chi}}^{(2)} : \widetilde{\boldsymbol{\mathscr{E}}}(t)\widetilde{\boldsymbol{\mathscr{E}}}(t) + \bar{\bar{\chi}}^{(3)} : \widetilde{\boldsymbol{\mathscr{E}}}(t)\widetilde{\boldsymbol{\mathscr{E}}}(t)\widetilde{\boldsymbol{\mathscr{E}}}(t) + \ldots\right]. \tag{1.6.3}$$

The quantities $\bar{\bar{\chi}}^{(2)}$ and $\bar{\bar{\chi}}^{(3)}$ are known as second- and third-order nonlinear optical susceptibility tensors, respectively.

In centrosymmetric materials, $\bar{\bar{\chi}}^{(2)}$ is equal to zero [1, 2] and the lowest nonlinear contribution to the polarization comes from the third-order nonlinear susceptibility. All the materials considered

[4] In this notation $\mathbf{F}(\omega)$ is equivalent to $\mathbf{F}(x)$ which appeared in Sections 1.3–1.5 (where $\mathbf{F}$ denotes either electric field $\mathbf{E}$ or polarization $\mathbf{P}$). At the beginning of this section we choose to show explicitly only the frequency dependency as we are primarily interested to study effects for this particular frequency. At the end we will come back to $\mathbf{F}(x)$ notation, as we will be more interested in a spatial distribution of the Kerr effect.

in this PhD manuscript will be centrosymmetric. Setting $\overline{\overline{\chi}}^{(2)} = 0$ and inserting Eq. (1.6.1a) into Eq. (1.6.3) yields

$$\begin{aligned}\widetilde{\boldsymbol{\mathscr{P}}}(t) = \epsilon_0 \overline{\overline{\chi}}^{(1)} \left[\mathbf{E}(\omega)e^{-i\omega t} + \mathbf{E}(\omega)^* e^{i\omega t}\right] \\ + \epsilon_0 \overline{\overline{\chi}}^{(3)} \left\{\mathbf{E}(\omega)^3 e^{-3i\omega t} + 3\mathbf{E}(\omega)\mathbf{E}(\omega)^* \left[\mathbf{E}(\omega)e^{-i\omega t} + \mathbf{E}(\omega)^* e^{i\omega t}\right] + \left[\mathbf{E}(\omega)^*\right]^3 e^{3i\omega t}\right\},\end{aligned} \tag{1.6.4}$$

where we limited ourselves to the third-order nonlinear effects. The Kerr effect is induced by a light of frequency ω and influences the behavior of light beams at the same frequency. Therefore, in Eq. (1.6.4) we will keep only the part of nonlinear polarization that is proportional to $e^{\pm i\omega t}$ and omit the two terms connected with third harmonic generation [1, 2]. Equation (1.6.4) is rewritten into a form:

$$\widetilde{\boldsymbol{\mathscr{P}}}(t) = \epsilon_0 \left[\overline{\overline{\chi}}^{(1)} + 3\overline{\overline{\chi}}^{(3)} |\mathbf{E}(\omega)|^2\right] \widetilde{\boldsymbol{\mathscr{E}}}(t), \tag{1.6.5}$$

Using Eqs. (1.6.1) to eliminate the time dependency, Eq. (1.6.5) becomes

$$\mathbf{P}(\omega) = \epsilon_0 \left[\overline{\overline{\chi}}^{(1)} + 3\overline{\overline{\chi}}^{(3)} |\mathbf{E}(\omega)|^2\right] \mathbf{E}(\omega) \tag{1.6.6}$$

Inserting Eq. (1.6.6) into Eq. (1.3.2a) [and using the definitions $\boldsymbol{\mathscr{D}}(x,z,t) \equiv \mathbf{D}(x)e^{i(k_0\beta z - \omega t)}$ and $\boldsymbol{\mathscr{P}}(x,z,t) \equiv \mathbf{P}(x)e^{i(k_0\beta z - \omega t)}$] gives

$$\mathbf{D} = \epsilon_0 \left[\left(1 + \overline{\overline{\chi}}^{(1)}\right) + 3\overline{\overline{\chi}}^{(3)} |\mathbf{E}|^2\right] \mathbf{E}(\omega) = \epsilon_0 \left(\overline{\overline{\epsilon}}_l + 3\overline{\overline{\chi}}^{(3)} |\mathbf{E}|^2\right) \mathbf{E}(\omega), \tag{1.6.7}$$

where the linear part of the permittivity is related to the linear susceptibility by

$$\overline{\overline{\epsilon}}_l = 1 + \overline{\overline{\chi}}^{(1)} \tag{1.6.8}$$

Regrouping terms in Eq. (1.6.7) we can write

$$\mathbf{D} = \epsilon_0 \left(\overline{\overline{\epsilon}}_l + 3\overline{\overline{\chi}}^{(3)} |\mathbf{E}|^2\right) \mathbf{E} = \epsilon_0 \overline{\overline{\epsilon}}\, \mathbf{E}, \tag{1.6.9}$$

In this work, a nonlinear Kerr type dielectric is considered for which the nonlinear third-order susceptibility is isotropic and can be expressed as

$$\overline{\overline{\chi}}^{(3)} = \frac{\alpha}{3}\mathbf{I}. \tag{1.6.10}$$

All the elements of the permittivity tensor depend in identical way on the electric field intensity in the nonlinear medium ($\mathbf{I}$ denotes the identity matrix).

The diagonal elements of the nonlinear Kerr-type permittivity tensor [given by Eq. (1.3.7)] can be written as

$$\epsilon_j(x) = \epsilon_{l,j}(x) + \epsilon_{\mathrm{nl}}(x), \tag{1.6.11}$$

where $j \in \{x, y, z\}$ and $\epsilon_{l,j}$ denotes the linear real part of the permittivity. The nonlinear part of the permittivity, limited to the optical Kerr effect that depends on the electric field intensity, is denoted by

$$\epsilon_{\mathrm{nl}}(x) = \alpha(x)|\mathbf{E}(x)|^2, \tag{1.6.12}$$

where $\alpha(x)$ denotes the function that takes values of the third-order nonlinear susceptibility associated with different layers (in linear materials it is null). Finally the expression for the real part of the permittivity is given by

$$\epsilon_j(x) = \epsilon_{l,j}(x) + \alpha(x)|\mathbf{E}(x)|^2. \tag{1.6.13}$$

In this PhD manuscript, only materials with the focusing Kerr-type nonlinearity ($\alpha > 0$) are studied, although all the models can be reformulated in order to study the defocusing nonlinearity ($\alpha < 0$). In the SI system, the unit of α and $\overline{\overline{\chi}}^{(3)}$ is $\mathrm{m}^2/\mathrm{V}^2$. More about nonlinear coefficients and their units can be found in Section 1.7 and in Appendix A.

The formulation of the Kerr effect given by Eq. (1.6.13) is used in the majority of the works on the nonlinear waveguides and nonlinear surface waves [10–12, 15–49, 67–84, 87, 89, 90]. It describes sufficiently well the nonlinear effects that we will study in this PhD thesis. To describe the physics of our system we do not need to use the more complex form of the Kerr nonlinear term which was used in Refs. [104–106].

1.7 Intensity dependent refractive index

In the majority of works, a common and intuitive measure of the third-order nonlinear effects is the second-order nonlinear refractive index[5] n_2. The intensity dependent refractive index is given by [2]:

$$n = n_0 + n_{\mathrm{nl}} = n_0 + n_2 I, \tag{1.7.1}$$

where n_0 denotes the linear (weak field) refractive index that is related with the linear part of isotropic permittivity by $n_0 = \sqrt{\epsilon_l}$. The light intensity is defined [107] as the energy carried by the electric field

$$U = \frac{\epsilon_0 |\epsilon| |\mathbf{E}|^2}{2} \tag{1.7.2}$$

multiplied by the group wave velocity. For the monochromatic plane waves, the group velocity is given by

$$v = \frac{c}{\beta}, \tag{1.7.3}$$

where the effective index β of a monochromatic plane wave is equal to the refractive index n_0 of the medium in which it propagates. Therefore, the light intensity is given by

$$I = Uv = \frac{\epsilon_0 |\epsilon| c}{2\beta} |\mathbf{E}|^2. \tag{1.7.4}$$

The relation between the refractive index and the permittivity is $\epsilon = n^2$. Using this fact, we compare Eqs. (1.6.13) and (1.7.1) assuming that the permittivity tensor is isotropic ($\epsilon_x = \epsilon_y = \epsilon_z = \epsilon = \epsilon_l + \alpha |\mathbf{E}|^2$). This comparison yields:

$$\epsilon_l + \alpha |\mathbf{E}|^2 = (n_0 + n_2 I)^2. \tag{1.7.5}$$

Inserting the definition of intensity given by Eq. (1.7.4) into Eq. (1.7.5) allows us to relate the values of α and n_2. Using the relation $\epsilon_l = n_0^2$ we obtain

$$\alpha = \frac{\epsilon_0 |\epsilon| c n_2}{\beta} n_0 + \left(\frac{\epsilon_0 |\epsilon| c}{2\beta} \right)^2 n_2^2 |\mathbf{E}|^2 = \frac{\epsilon_0 |\epsilon| c n_2}{\beta} n_0 + \frac{\epsilon_0 |\epsilon| c n_2}{2\beta} n_2 I. \tag{1.7.6}$$

From Eq. (1.7.6), we observe that the value of the nonlinear coefficient α depends on the material parameters (ϵ_l, n_l, n_2), the propagation constant β and on the electric field intensity $|\mathbf{E}|^2$ (or equivalently light intensity I). In order to simplify the formulation of our problem, we will assume that the relation between α and n_2 is not dependent on the electric field intensity $|\mathbf{E}|^2$. In most of this manuscript, we will work with the light intensities for which the nonlinear modification of the refractive index is much lower than the linear part of the refractive index ($n_2 I \ll n_0$). The same is true for the permittivity $\alpha |\mathbf{E}|^2 \ll |\epsilon_l|$. Therefore, we will omit the second term in the sum [Eq. (1.7.6)] that is important only of high light intensities I. Based on the same argument, we will substitute the full nonlinear permittivity ϵ by the linear part of the permittivity ϵ_l in the first term of the sum in Eq. (1.7.6). Finally, for the sake of simplicity, we will substitute the effective index β, in the denominator in the first term of the sum in Eq. (1.7.6), by the linear part of the refractive index n_0. This assumption is well satisfied for the plasmon–solitons waves whose effective index is close to the linear part of the refractive index of the nonlinear material. Thanks to this assumptions we can relate the nonlinear coefficient α with n_2 by a simple linear relation

$$\alpha = \epsilon_0 |\epsilon_l| c n_2. \tag{1.7.7}$$

Equation (1.7.7) implies that to a given value of n_2 and ϵ_l of the nonlinear material corresponds only one value of the nonlinear coefficient α.

[5] The name 'second-order nonlinear refractive index' is used following the formalism used in Ref. [2]. In many articles the n_2 coefficient is simply called 'nonlinear coefficient'. Here we use the former, in order to avoid confusions between n_2 and other nonlinear coefficients, like α or a, introduced later.

In this manuscript, we use Eq. (1.7.7) to relate α with n_2, even for the case of high nonlinear index changes or modes where $\beta \not\approx n_l$. Otherwise we would have to account for the changes of n_2 for a given structure for solutions with different light intensities and effective indices.

Using the notation $\epsilon = n^2$ and Eqs. (1.6.13) and (1.7.1) we can relate the nonlinear refractive index modification n_{nl} and nonlinear permittivity modification ϵ_{nl} by the following formula

$$n_{\mathrm{nl}} = -n_l + \sqrt{n_l^2 + \epsilon_{\mathrm{nl}}}. \tag{1.7.8}$$

Part I

Configurations with semi-infinite nonlinear medium

In this part of the PhD manuscript, we focus our attention on the structures in which the nonlinear medium is semi-infinite. In general, in optical waveguide studies it is easier to model infinite or semi-infinite structures than structures with finite dimensions. In Part I, simple structures with semi-infinite nonlinear medium are studied, where the solutions are expressed in a less complicated mathematical way than is structures with finite dimensions. Simpler mathematical formulation in such structures facilitates understanding of the physical problem and the nature of the nonlinear plasmon–solitons, because the reader is not overwhelmed by the mathematical complexity of the problem. Configurations with the finite-size nonlinear medium, which require more complicated mathematical analysis, will be addressed in Part II of this PhD thesis.

As mentioned in Section 1.1, configurations with semi-infinite nonlinear medium and a metal layer were extensively studied since the beginning of 1980s [67]. Many works appeared that addressed the problem of a single interface between a nonlinear dielectric and a metal [14, 15, 67–72]. Later, structures where a thin metal film is sandwiched between nonlinear dielectrics were studied [73–78].

Even though there is a number of publications describing plasmon–soliton waves in the structures with semi-infinite nonlinear medium, there is still no experimental confirmation of the existence of such nonlinear waves. The main reason for that is that the nonlinear index modification, and therefore the light intensity, required to observe the plasmon–soliton waves predicted theoretically so far, is orders of magnitude higher than the values that can be obtained in modern nonlinear optics laboratories. In Chapter 2, we will develop new models to study transverse magnetic polarized plasmon–soliton waves in the structures with a semi-infinite nonlinear medium. These models will be based on already published approaches, but we will improve and extend them. These extensions will allow us to obtain new results that are interesting both from the theoretical and experimental point of view. The results of our semi-analytical models will be confirmed numerically using a home-made finite element method.

After having confirmed the validity of our models in Chapter 3, in Chapter 4 we will discuss the possibility of existence of various types of plasmon–solitons in the structures build of two, three and four layers, including one semi-infinite nonlinear layer. We will show that in the three-layer structures, using cladding that is asymmetric in terms of linear permittivity, it is possible to obtain solitonic-type plasmon–solitons at the power levels below the damage threshold of common nonlinear materials. We will also show that the use of an additional dielectric layer allows us to obtain low-power solitonic-type solutions in much larger parameter range than in the case of three-layer structures.

In Chapter 5, we will discuss some paths that were initiated during this PhD thesis but were not studied in detail. Firstly, the extension of one of our models to two-dimensions will be discussed. This approach provides a crude approximation on what the two-dimensional plasmon–soliton waves may look like. Secondly, results for the transverse electric polarized surface waves will be presented.

Chapter 2

Theory

Contents

In this chapter, we present three methods based on Maxwell's equations, to study the properties of stationary solutions in one-dimensional structures composed of a semi-infinite nonlinear medium and layers of metal and linear dielectrics. An example of such a structure is presented in Fig. 2.1. This is the most complicated structure that will be studied in this part of the manuscript. Simpler structures will also be considered, however, in all of them, a semi-infinite nonlinear dielectric layer and a metal layer (finite or semi-infinite) will be present. In all the described approaches, only transverse magnetic (TM) polarized waves are considered due to the presence of the metal layer. We found no localized solutions for the transverse electric (TE) polarization, as discussed in Section 5.2.

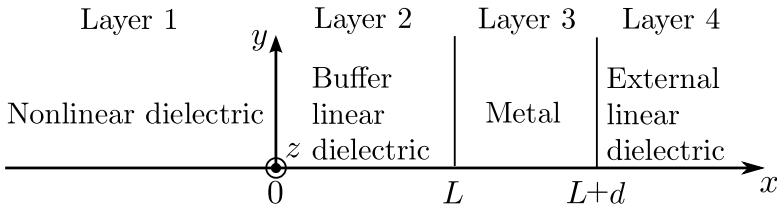

Figure 2.1: Geometry of the four-layer structure with a semi-infinite nonlinear dielectric medium and a metal film.

The first model presented here extends and modifies the approach described in Ref. [73] and uses two assumptions: (i) the nonlinearity depends only on the transverse electric field component and (ii) the nonlinear permittivity modifications are small compared to the linear part of the permittivity. These assumptions allow us to write a single nonlinear wave equation for one of the magnetic field components. This equation is then solved analytically [67], resulting in closed formulas for the nonlinear

dispersion relation and for the electromagnetic field profiles. This model will be called the field based model (FBM).

The second model, named in this work the exact model (EM) because it does not require any of the two above assumptions, is based on the approaches from Refs. [15, 77]. It also provides a closed formula for the nonlinear dispersion relation but the field profiles in the nonlinear medium are not given in an analytical form and have to be computed numerically by solving a system of two coupled first-order nonlinear differential equations derived from Maxwell's equations.

The third model — in contrast with the two previous semi-analytical approaches — uses a numerical finite element method (FEM) to solve the nonlinear scalar TM problem in layered structures. This approach finds the solutions using the fixed power algorithm from Refs. [108–110] adapted to one-dimensional planar metal/nonlinear dielectric structures.

2.1 Field based model

We start by the description of the field based model. At first, the way to transform nonlinear Maxwell's equations for the TM polarized waves into a single nonlinear wave equation is described. Then, using the solution of the nonlinear wave equation, the nonlinear dispersion relations are obtained for four-layer structures. Afterwards, the way of obtaining exact nonlinear field profiles of all the electromagnetic field components is presented. Finally, the analytical expressions for the power and approximated propagation losses of plasmon–solitons are obtained.

2.1.1 Nonlinear wave equation

The derivation of the field based model starts from Maxwell's equations for the TM polarized light given by Eqs. (1.5.2). Basing on these equations, the problem of finding stationary solutions using a nonlinear wave equation is formulated. The derivation presented here is similar to the one proposed by Agranovich *et al.* [67], in which the first description of the nonlinear surface plasmon polariton waves localized at a single interface between a metal and a nonlinear dielectric was given. In this seminal paper, the analytical expressions for the dispersion relation and for the field profiles of the nonlinear solutions in such structures were found in the TM case using strong assumptions on the form of the permittivity tensor components. Later on, this model was improved by introducing more realistic assumptions on the nonlinear term (e.g., focusing nonlinearity depending only on the transverse component of the electric field). It was also extended to consider TE polarized waves as well as focusing and defocusing Kerr nonlinearities [14, 68, 69, 75]. Furthermore, the model of Agranovich *et al.* was expanded to consider nonlinear waves guided by a thin metal film sandwiched between nonlinear dielectrics [73–75].

Our FBM improves and extends the previous approaches in three ways: (i) it improves the nonlinearity treatment so that all the diagonal elements of the permittivity tensor depend on the electric field in a nonlinear manner [Eqs. (1.6.11) and (2.1.5)], (ii) it improves the way the nonlinearity is taken into account in the dispersion relation derivation [Eqs. (2.1.43)–(2.1.47)] and in the electric field profiles calculations (Section 2.1.3), and (iii) it extends the existing model from three-layer structures to four-layer structures (the benefits of using four-layer structures are discussed in Section 4.3). The derivation given below follows the lines presented in Ref. [73] with the improvements mentioned above.

Taking the derivative of Eq. (1.5.2c) with respect to x and using Eqs. (1.5.2a), (1.5.2b), and (1.6.11) gives

$$\frac{\mathrm{d}^2 H_y}{\mathrm{d}x^2} = k_0^2 \left(\frac{\epsilon_z}{\epsilon_x} \beta^2 - \epsilon_z \right) H_y + \epsilon_0 \omega \frac{\mathrm{d}\epsilon_{\mathrm{nl}}}{\mathrm{d}x} E_z. \tag{2.1.1}$$

At this step, we assumed that Maxwell's equations [Eqs. (1.5.2)] are solved separately in each of the layers of the structures (see Fig. 2.1). This allows us to neglect the permittivity discontinuities at the interfaces between the layers that will be treated separately using boundary conditions. Therefore, the last term is proportional only to the x derivative of the nonlinear part of the permittivity ϵ_{nl} and the derivative of the linear part of permittivity is equal to zero. Making use of Eq. (1.5.2c) in the last

term of Eq. (2.1.1) allows us to eliminate the electric field component E_z from this equation, yielding an equation for the magnetic field component:

$$\frac{\mathrm{d}^2 H_y}{\mathrm{d}x^2} = k_0^2 \left(\frac{\epsilon_z}{\epsilon_x} \beta^2 - \epsilon_z \right) H_y + \frac{1}{\epsilon_z} \frac{\mathrm{d}\epsilon_{\mathrm{nl}}}{\mathrm{d}x} \frac{\mathrm{d}H_y}{\mathrm{d}x}. \tag{2.1.2}$$

We remark that in Eq. (2.1.2), the dependency on the electric field is still present, in an implicit way, through the nonlinear permittivity tensor components ϵ_x and ϵ_z [see Eqs. (1.6.11) and (1.6.12)]. This dependency will be eliminated later in the derivation.

At this point, important assumptions about the FBM are made. It is assumed that (i) the nonlinear contribution to the permittivity is small compared to the linear part of the permittivity $|\epsilon_{\mathrm{nl}}| \ll |\epsilon_{l,j}|$ for $j \in \{x, z\}$ and (ii) both ϵ_{nl} and H_y in the nonlinear medium vary in x direction on scales larger than the wavelength. These hypothesis are valid for low-power solutions and are verified *a posteriori* by analyzing the field profiles. If these assumptions are fulfilled the last term in Eq. (2.1.2) is small and it can be omitted. Then the nonlinear wave equation can be written in the simple form:

$$\frac{\mathrm{d}^2 H_y}{\mathrm{d}x^2} = k_0^2 \left(\frac{\epsilon_z}{\epsilon_x} \beta^2 - \epsilon_z \right) H_y. \tag{2.1.3}$$

Solutions of Eq. (2.1.3) in each of the layers of the structure describe the magnetic field profiles in these layers. The approximations made above affect the solutions of Eq. (2.1.3) only in the nonlinear layer. Since they influence the field profile in the nonlinear layer, they will also modify the continuity conditions at the interfaces of this layer and therefore the dispersion relation of the full nonlinear waveguides studied here. The field profiles in the linear layers are found in an exact way.

In the following, only isotropic materials for which $\epsilon_{l,x} = \epsilon_{l,y} = \epsilon_{l,z} \equiv \epsilon_l$ will be considered.[1] For isotropic materials, Eq. (2.1.3) becomes

$$\frac{\mathrm{d}^2 H_y}{\mathrm{d}x^2} = k_0^2 \left(\beta^2 - \epsilon \right) H_y. \tag{2.1.4}$$

The nonlinearity considered in our FBM is of the usual Kerr type, but we assume that only the transverse electric field component E_x contributes to the nonlinear response (this component is usually much stronger than the longitudinal component in the photonic structures studied here [68])

$$\epsilon_x(x) = \epsilon_y(x) = \epsilon_z(x) = \epsilon(x) = \epsilon_l(x) + \alpha(x) E_x^2(x). \tag{2.1.5}$$

Using this form of nonlinearity,[2] and Eq. (1.5.2b), we can express the nonlinear permittivity modification in terms of the magnetic field H_y

$$\epsilon(x) = \epsilon_l(x) + \frac{\beta^2 \alpha(x)}{\left[\epsilon_0 \epsilon_l c\right]^2} H_y^2(x). \tag{2.1.6}$$

Here we used again the assumption that $|\epsilon_{\mathrm{nl}}| \ll |\epsilon_l|$ [this assumption justifies the substitution of $\beta H_y/(\epsilon_0 \epsilon c)$ by $\beta H_y/(\epsilon_0 \epsilon_l c)$ in the nonlinear term]. Using Eq. (2.1.6) in Eq. (2.1.4), the nonlinear wave equation can be rewritten into its final form:

$$\frac{\mathrm{d}^2 H_y}{\mathrm{d}x^2} - k_0^2 q^2(x) H_y + k_0^2 a(x) H_y^3 = 0, \tag{2.1.7a}$$

where

$$q^2(x) = \beta^2 - \epsilon_l(x) \tag{2.1.7b}$$

[1] Actually, this assumption is stronger than the one required to formulate our model. In our case, it is necessary to consider materials in which linear parts of only two permittivity tensor elements are equal $\epsilon_{l,x} = \epsilon_{l,z} = \epsilon_l$. The tensor component $\epsilon_{l,y}$ can have arbitrary values as it does not appear in the model derivation.

[2] As in the case described in Footnote 1 for linear part of permittivity tenor, this assumption is stronger than the one required to formulate the FBM. Here it is necessary to consider materials in which only two diagonal elements of the nonlinear permittivity tensor elements are equal $\epsilon_x = \epsilon_z = \epsilon$. The tensor component ϵ_y can have arbitrary values as it does not appear in the model derivation.

and the function

$$a(x) = \frac{\beta^2 \alpha(x)}{[\epsilon_0 \epsilon_l(x) c]^2} \tag{2.1.7c}$$

is nonzero only in the nonlinear layer. Here, $\epsilon_l(x)$ and $\alpha(x)$ are step-wise functions which take the values indicated in Table 2.1 depending on the layer (see Fig. 2.1 for layer numbers).

Layer	Abscissa	$\epsilon_l(x)$	$\epsilon(x)''$	$\alpha(x)$
1	$x < 0$	$\epsilon_{l,1}$	ϵ_1''	$\epsilon_0 c \epsilon_{l,1} n_2^{(1)} = \alpha_1$
2	$0 \leqslant x < L$	$\epsilon_2 = \epsilon_{l,2}$	ϵ_2''	0
3	$L \leqslant x < L + d$	$\epsilon_3 = \epsilon_{l,3}$	ϵ_3''	0
4	$x \geqslant L + d$	$\epsilon_4 = \epsilon_{l,4}$	ϵ_4''	0

Table 2.1: Values of the functions describing the properties of the materials in different layers. The second-order nonlinear refractive index in layer 1 is denoted by $n_2^{(1)}$. All the quantities presented in this table are real.

Equations (2.1.7) are equivalent to Eqs. (4a) and (4b) in Ref. [73] and to Eq. (14) in Ref. [68] with a slight difference in the nonlinear term due the to more consistent nonlinearity treatment used here. The nonlinear function $a(x)$ differs by a factor β^2/ϵ_l between our approach and the approaches from Refs. [68, 73]. This results in discrepancies between our model and the older models mainly when the effective index of the nonlinear wave is much higher than the linear part of the nonlinear medium refractive index. For the purpose of comparison, the approach from Ref. [73] is presented in more detail in Section 2.2 and the results of the two approaches are directly compared in Section 4.2.1.

2.1.2 Nonlinear dispersion relation

In Section 2.1.1, we derived a single nonlinear wave equation [Eq. (2.1.7a)] for the nonlinear medium where the Kerr-type nonlinearity is treated in a simplified way. In this section, we will find the solutions of this equation for the H_y field component. In the frame of the FBM, the solutions of Eq. (2.1.7a) are studied separately in each layer of the structure. Then the use of boundary and continuity conditions allows us to obtain the nonlinear dispersion relation for the studied problem.

The solution of Eq. (2.1.7a) is well known in literature [11, 16, 19, 67] and is based on the first integral treatment of this equation and formula (2.266)[3] from Ref. [111]. Below we present the procedure to find the solutions of Eq. (2.1.7a).

We consider a nonlinear medium where the nonlinear term in Eq. (2.1.7a) is nonzero. We multiply both sides of Eq. (2.1.7a) by $\mathrm{d}H_y/\mathrm{d}x$ and integrate with respect to x. The integration by parts leads to the following equation

$$\left(\frac{\mathrm{d}H_y}{\mathrm{d}x}\right)^2 - k_0^2 q^2 H_y^2 + \frac{k_0^2 a}{2} H_y^4 = c_0, \tag{2.1.8}$$

where a denotes the constant value of the function $a(x)$ [see Eq. (2.1.7c)] in the considered nonlinear medium and c_0 denotes an integration constant. Due to the fact that only problems where the nonlinear region is semi-infinite are considered in this part of the work, we impose the following boundary

[3] Formula (2.266) from Ref. [111] gives the expression of the integral

$$\int \frac{\mathrm{d}x}{x\sqrt{R}},$$

where R is in the form $R = a + bx + cx^2$ and Δ is defined as $\Delta = 4ac - b^2$, for various combinations of signs of the parameters a and Δ. Here we recall only the case for $a > 0$ and $\Delta < 0$, which it the case in our derivation. For this case the integral results in

$$\int \frac{\mathrm{d}x}{x\sqrt{R}} = -\frac{1}{\sqrt{a}} \ln\left(\frac{2a + bx + 2\sqrt{aR}}{x}\right).$$

conditions on the magnetic field $H_y \xrightarrow{x\to-\infty} 0$ and its derivative $\frac{\mathrm{d}H_y}{\mathrm{d}x} \xrightarrow{x\to-\infty} 0$. These boundary conditions allow us to conclude that the integration constant c_0 should be set to 0. In this case Eq. (2.1.8) can be rewritten into a form:

$$\frac{\mathrm{d}H_y}{H_y\sqrt{Q + A^{-1}H_y^2}} = \mathrm{d}x, \tag{2.1.9}$$

where the reduced parameters Q and A were introduced:

$$Q = k_0^2 q^2, \tag{2.1.10a}$$

$$A = -\left(\frac{k_0^2 a}{2}\right)^{-1}. \tag{2.1.10b}$$

The solutions of Eq. (2.1.9) that fulfill the condition that the quantity under the square-root is positive are sought. This condition, using Eqs. (2.1.10), results in a relation

$$q^2 \geqslant \frac{a}{2}H_y^2. \tag{2.1.11}$$

Using Eq. (2.1.7b), we can find a lower bound of the effective index of the mode for a given mode profile $H_y(x)$

$$\beta^2 \geqslant \epsilon_l + \frac{a}{2}H_y^2(x). \tag{2.1.12}$$

This equation has to be fulfilled for all the x values in the nonlinear region. As there is only one value of the effective index β that corresponds to a mode profile $H_y(x)$ we find that

$$\beta^2 \geqslant \epsilon_l + \frac{a}{2}\max[H_y^2(x)] \tag{2.1.13}$$

which gives us the lower bound of β as a function of the amplitude value of the magnetic field in the nonlinear region.

Integrating Eq. (2.1.9) results in

$$\int \frac{\mathrm{d}H_y}{H_y\sqrt{Q + A^{-1}H_y^2}} = x + F, \tag{2.1.14}$$

where F denotes an arbitrary integration constant. From Eq. (2.1.11), we notice that the sign of q^2 is positive for the focusing Kerr effect ($a > 0$), therefore, with the help of Eq. (2.1.10a), we conclude that $Q > 0$. In this work we consider only the self-focusing Kerr-type nonlinearity ($a > 0$), which together with Eq. (2.1.10b) implies that $A^{-1} < 0$. The left-hand side of Eq. (2.1.14) is integrated using formula (2.266) from Ref. [111] for positive Q and negative value of $\Delta = 4QA^{-1}$ (see Footnote 3 on Page 20):

$$\int \frac{\mathrm{d}H_y}{H_y\sqrt{Q + A^{-1}H_y^2}} = -\frac{1}{\sqrt{Q}}\ln\left(\frac{2Q + 2\sqrt{Q\left(Q + A^{-1}H_y^2\right)}}{H_y}\right). \tag{2.1.15}$$

Inserting Eq. (2.1.15) into Eq. (2.1.14) and reorganizing terms under the natural logarithm one obtains

$$-\frac{1}{\sqrt{Q}}\ln\left[\frac{2Q}{H_y} + 2\sqrt{|A^{-1}|\,Q\left(\frac{Q^2}{|A^{-1}|\,QH_y^2} - 1\right)}\right] = x + F, \tag{2.1.16}$$

where we have substituted A^{-1} with $-|A^{-1}|$. Further algebraic transformation leads to

$$-\frac{1}{\sqrt{Q}}\ln\left[2\sqrt{|A^{-1}|\,Q}\left(\frac{Q}{H_y\sqrt{|A^{-1}|\,Q}} + \sqrt{\frac{Q^2}{|A^{-1}|\,QH_y^2} - 1}\right)\right] = x + F. \tag{2.1.17}$$

Using the fact that $\ln(rp) = \ln(r) + \ln(p)$ we obtain

$$-\frac{1}{\sqrt{Q}}\left[\ln\left(2\sqrt{|A^{-1}|\,Q}\right) + \ln\left(\frac{Q}{H_y\sqrt{|A^{-1}|\,Q}} + \sqrt{\frac{Q^2}{|A^{-1}|\,QH_y^2} - 1}\right)\right] = x + F. \tag{2.1.18}$$

Equation (2.1.18) is transformed using the relation $\ln(r + \sqrt{r^2-1}) = \operatorname{arcosh}(r)$

$$-\frac{1}{\sqrt{Q}}\left[\ln\left(2\sqrt{|A^{-1}|\,Q}\right) + \operatorname{arcosh}\left(\frac{Q}{H_y\sqrt{|A^{-1}|\,Q}}\right)\right] = x + F. \tag{2.1.19}$$

The relation $\ln(r + \sqrt{r^2-1}) = \operatorname{arcosh}(r)$ is only valid for $r \geqslant 1$. In our case, this condition reads $Q/H_y\sqrt{|A^{-1}|\,Q} > 1$ and it is fulfilled because it is equivalent to Eq. (2.1.11).

After some algebra where the parity of the cosine hyperbolic function was used, we find the analytical expression for the magnetic field profile that is the solution of Eq. (2.1.7a):

$$H_y = |A|^{1/2}\frac{\sqrt{Q}}{\cosh\left[\sqrt{Q}\,(x - x_0)\right]}, \tag{2.1.20}$$

where a new variable was introduced:

$$x_0 = -\left[F + \frac{\ln\left(2\sqrt{Q\,|A^{-1}|}\right)}{\sqrt{Q}}\right]. \tag{2.1.21}$$

Because F is an integration constant and its value can be chosen arbitrarily, in further analysis we use x_0 as a new free parameter as it has been done in several already published articles [16, 19, 21–23, 25, 68, 73–75]. This choice is motivated by the physical meaning of x_0 as a center of the soliton beam. Another possible choice of the free parameter in the solution of Eq. (2.1.7a) is the magnetic field at $x = 0$ that is usually chosen to be the interface between the nonlinear medium and other material [10, 11, 16, 67]

$$H_0 = |A|^{1/2}\frac{\sqrt{Q}}{\cosh\left[\sqrt{Q}x_0\right]}. \tag{2.1.22}$$

Expressing the reduced parameters in their explicit form in Eq. (2.1.20) yields the final formula for the magnetic field in the nonlinear region[4]

$$H_y = \sqrt{\frac{2}{a}}\frac{q}{\cosh[k_0 q(x - x_0)]}. \tag{2.1.23}$$

As we have stated at the beginning of this section, the solutions of Eq. (2.1.7a) are sought separately in each of the layers of the structure depicted in Fig. 2.1. In the nonlinear layer, the solution is in the form given by Eq. (2.1.23) (the y subscript of the magnetic field is skipped as in our models for the TM light polarization there is only one magnetic field component, while the subscript 1 indicates the nonlinear layer, see Fig. 2.1):

$$H_1 = \sqrt{\frac{2}{a_1}}\frac{q_1}{\cosh[k_0 q_1(x - x_0)]} \qquad \text{for } x < 0, \tag{2.1.24a}$$

where the x_0 is a free integration parameter that can be arbitrarily chosen and q_k and a_k denote the constant value of the $q(x)$ and $a(x)$ functions [see Eqs. (2.1.7b) and (2.1.7c), respectively] in the k-th layer ($k \in \{1, 2, 3, 4\}$). If x_0 is negative, is has a physical meaning of the soliton peak position in

[4] In this work the following equivalent notation with secant hyperbolic function will be also used:

$$\frac{1}{\cosh(x)} = \operatorname{sech}(x).$$

the nonlinear dielectric. If it is positive, there is no maximum of the H_1 component in the nonlinear layer. In linear layers, the nonlinear term in Eq. (2.1.7a) vanishes and the solutions of the linear wave equation are expressed in a standard form of decreasing and increasing exponentials (for the layer indices see Fig. 2.1):

$$H_2 = A_+ e^{k_0 q_2 x} + A_- e^{-k_0 q_2 x} \qquad \text{for } 0 \leqslant x < L, \tag{2.1.24b}$$

$$H_3 = B_+ e^{k_0 q_3 (x-L)} + B_- e^{-k_0 q_3 (x-L)} \qquad \text{for } L \leqslant x < L + d, \tag{2.1.24c}$$

$$H_4 = C e^{-k_0 q_4 [x-(L+d)]} \qquad \text{for } x \geqslant L + d. \tag{2.1.24d}$$

The use of the boundary condition $H_y \xrightarrow{x\to\infty} 0$ in the layer 4 results in the single term in Eq. (2.1.24d).

Having found the analytical expressions for the magnetic fields in all the layers, we can proceed with the derivation of the nonlinear dispersion relation for the four-layer structure depicted in Fig. 2.1. We will use the continuity conditions for the tangential field components (H_y and E_z) at all the interfaces between media. The expressions for the E_z fields are obtained using Eq. (1.5.2c) and read

$$E_{z,1} = \frac{1}{\epsilon_0 \epsilon_1 \omega} \sqrt{\frac{2}{a_1}} k_0 q_1^2 \frac{\sinh[k_0 q_1 (x - x_0)]}{\cosh^2[k_0 q_1 (x - x_0)]} \qquad \text{for } x < 0, \tag{2.1.25a}$$

$$E_{z,2} = \frac{1}{\epsilon_0 \epsilon_2 \omega} k_0 q_2 \left(A_+ e^{k_0 q_2 x} - A_- e^{-k_0 q_2 x} \right) \qquad \text{for } 0 \leqslant x < L, \tag{2.1.25b}$$

$$E_{z,3} = \frac{1}{\epsilon_0 \epsilon_3 \omega} k_0 q_3 \left[B_+ e^{k_0 q_3 (x-L)} - B_- e^{-k_0 q_3 (x-L)} \right] \qquad \text{for } L \leqslant x < L + d, \tag{2.1.25c}$$

$$E_{z,4} = \frac{-1}{\epsilon_0 \epsilon_4 \omega} k_0 q_4 C e^{-k_0 q_4 [x-(L+d)]} \qquad \text{for } x \geqslant L + d. \tag{2.1.25d}$$

The continuity conditions on the interfaces result in the following relations:

1. At the interface $x = 0$

   (a) The continuity condition for the magnetic field component

   $$H_1|_{x=0^-} = H_2|_{x=0^+} \tag{2.1.26}$$

   yields

   $$H_0 = A_+ + A_-, \tag{2.1.27}$$

   where we introduced the magnetic field intensity at the nonlinear dielectric interface

   $$H_0 = \sqrt{\frac{2}{a_1}} \frac{q_1}{\cosh[k_0 q_1 x_0]}. \tag{2.1.28}$$

   (b) The continuity condition for the tangential electric field component

   $$E_{z,1}|_{x=0^-} = E_{z,2}|_{x=0^+} \tag{2.1.29}$$

   gives

   $$H_0 \frac{\widetilde{q_{1,\mathrm{nl}}}|_{x=0}}{\tilde{q}_2} = A_+ - A_-, \tag{2.1.30}$$

   where

   $$\tilde{q}_k = \frac{q_k}{\epsilon_k} \qquad \text{for } k \in \{1, 2, 3, 4\} \tag{2.1.31}$$

   and

   $$\widetilde{q_{1,\mathrm{nl}}} = \tilde{q}_1 \tanh(k_0 q_1 x_0). \tag{2.1.32}$$

Taking a sum and a difference of Eqs. (2.1.27) and (2.1.30) allows us to find the expressions for the field amplitudes A_+ and A_-

$$A_\pm = \frac{H_0}{2}\left(1 \pm \frac{\widetilde{q_{1,\mathrm{nl}}}|_{x=0}}{\widetilde{q_2}}\right). \tag{2.1.33}$$

2. At the interface $x = L$

   (a) The continuity condition for the magnetic field component

   $$H_2|_{x=L^-} = H_3|_{x=L^+} \tag{2.1.34}$$

   yields

   $$A_+ e^{k_0 q_2 L} + A_- e^{-k_0 q_2 L} = B_+ + B_-. \tag{2.1.35}$$

   (b) The continuity condition for the tangential electric field component

   $$E_{z,2}|_{x=L^-} = E_{z,3}|_{x=L^+} \tag{2.1.36}$$

   gives

   $$\frac{\widetilde{q_2}}{\widetilde{q_3}}\left(A_+ e^{k_0 q_2 L} - A_- e^{-k_0 q_2 L}\right) = B_+ - B_-. \tag{2.1.37}$$

Taking a sum and a difference of Eqs. (2.1.35) and (2.1.37) allows us to find the expressions for the field amplitudes B_+ and B_-

$$B_\pm = \frac{H_0}{2}\left[\left(1 \pm \frac{\widetilde{q_{1,\mathrm{nl}}}|_{x=0}}{\widetilde{q_3}}\right)\cosh(k_0 q_2 L) + \left(\frac{\widetilde{q_{1,\mathrm{nl}}}|_{x=0}}{\widetilde{q_2}} \pm \frac{\widetilde{q_2}}{\widetilde{q_3}}\right)\sinh(k_0 q_2 L)\right]. \tag{2.1.38}$$

3. At the interface $x = L + d$

   (a) The continuity condition for the magnetic field component

   $$H_3|_{x=(L+d)^-} = H_4|_{x=(L+d)^+} \tag{2.1.39}$$

   yields

   $$B_+ e^{k_0 q_3 d} + B_- e^{-k_0 q_3 d} = C. \tag{2.1.40}$$

   (b) The continuity condition for the tangential electric field component

   $$E_{z,3}|_{x=(L+d)^-} = E_{z,4}|_{x=(L+d)^+} \tag{2.1.41}$$

   gives

   $$\frac{\widetilde{q_3}}{\widetilde{q_4}}\left(B_+ e^{k_0 q_2 L} - B_- e^{-k_0 q_2 L}\right) = -C. \tag{2.1.42}$$

Comparison of Eqs. (2.1.40) and (2.1.42) gives the analytical form of the nonlinear dispersion relation of the four-layer structure:

$$\boxed{\Phi_+\left(\widetilde{q_4} + \widetilde{q_3}\right)e^{(2k_0 q_3 d)} + \Phi_-\left(\widetilde{q_4} - \widetilde{q_3}\right) = 0,} \tag{2.1.43a}$$

where

$$\Phi_\pm = \left(1 \pm \frac{\widetilde{q_{1,\mathrm{nl}}}|_{x=0}}{\widetilde{q_3}}\right) + \left(\frac{\widetilde{q_{1,\mathrm{nl}}}|_{x=0}}{\widetilde{q_2}} \pm \frac{\widetilde{q_2}}{\widetilde{q_3}}\right)\tanh(k_0 q_2 L). \tag{2.1.43b}$$

Some assumptions have to be made in order to obtain a closed form of the expression for $\widetilde{q_{1,\mathrm{nl}}}|_{x=0}$ and therefore of the nonlinear dispersion relation. The exact expression for $\widetilde{q_1}$ reads

$$\widetilde{q_1} = \frac{q_1}{\epsilon_1} = \frac{q_1}{\epsilon_{l,1} + \alpha_1 E_x^2} \tag{2.1.44}$$

At this point, the model presented by Ariyasu *et al.* [73] is improved once again. In Ref. [73], the nonlinear term is omitted at this step and $\widetilde{q_1} = q_1/\epsilon_{l,1}$. Nevertheless, one can go beyond and find the first-order approximation for $\widetilde{q_1}$ taking into account the nonlinearity. In our work, $\widetilde{q_1}$ is expressed in terms of the magnetic field H_1. Inserting Eq. (1.5.2b) into Eq. (2.1.44) yields

$$\widetilde{q_1} = \frac{q_1}{\epsilon_{l,1} + \alpha_1 \left(\frac{k_0\beta}{\omega\epsilon_0\epsilon_{l,1}}\right)^2 H_1^2}, \tag{2.1.45}$$

where the assumption that $\epsilon_1 = \epsilon_{l,1}$ was used in the nonlinear term in the denominator of Eq. (2.1.45). Use of Eq. (2.1.24a) and the definition of the function $a(x)$ [Eq. (2.1.7c)] results in

$$\widetilde{q_1} = \frac{q_1}{\epsilon_{l,1} + 2q_1^2 \operatorname{sech}^2[k_0 q_1 (x - x_0)]}. \tag{2.1.46}$$

To obtain the dispersion relation we need to know the value of $\widetilde{q_{1,\mathrm{nl}}}$ at the interface $x = 0$ which is

$$\widetilde{q_{1,\mathrm{nl}}}|_{x=0} = \frac{q_1 \tanh(k_0 q_1 x_0)}{\epsilon_{l,1} + 2q_1^2 \operatorname{sech}^2(k_0 q_1 x_0)}. \tag{2.1.47}$$

After these transformations, the dispersion relation (2.1.43) depends only on the wavenumber k_0, material and structure parameters ($\epsilon_{l,1}$, ϵ_2, ϵ_3, ϵ_4, L, d), the x_0 parameter, and the effective index β. By fixing the values of the material and geometric parameters and x_0, one obtains a nonlinear expression that is satisfied only for a limited set of β values. We are interested only in the solutions with $\beta > \sqrt{\epsilon_{l,1}}$ because the solutions we look for should be localized either in the nonlinear dielectric or at the metal/nonlinear dielectric interface {see the definition of q [Eq. (2.1.7b)] and the field profiles [Eqs. (2.1.24)]}. Moreover, from Eq. (2.1.13) we know that using our procedure we can only find the solutions for which $\beta^2 \geqslant \epsilon_{l,1} + a_1/2H_y(x)^2$ which is coherent with the range of β where the solutions are sought.

It is worth noting that the dispersion relation (2.1.43) depends neither on the nonlinear parameter a_1 nor on the magnetic field amplitude H_y. This is a consequence of the fact that the nonlinear solutions depend on the nonlinear permittivity modification $\epsilon_{\mathrm{nl}} \propto \alpha_1 E_x^2 = a_1 H_y^2$ and not on the field amplitude or nonlinear parameter itself. Changing the nonlinearity coefficient does not result in change of the effective indices that fulfill the dispersion relation (2.1.43), but only in change of the field amplitude as it can be seen by rescaling all the fields by a factor $\sqrt{\alpha_1}$.

2.1.3 Expressions for the electric field components

In our FBM, the wave equation for the H_y magnetic field component [Eq. (2.1.7a)] is solved and the analytical expressions for the field profile of this component are provided [Eqs. (2.1.24)]. In the case of a linear medium, knowing the expression for the magnetic field one can easily calculate the electric field components using Eqs. (1.5.2b) and (1.5.2c). In the nonlinear case, this problem requires precautions. If the permittivity depends on the TM wave electric field components, Eqs. (1.5.2b) and (1.5.2c) form a set of two coupled nonlinear equations:

$$E_x = \frac{\beta}{\epsilon_0 \epsilon_x(E_x, E_z) c} H_y, \tag{2.1.48a}$$

$$E_z = \frac{1}{\epsilon_0 \epsilon_z(E_x, E_z) \omega} \frac{\mathrm{d}H_y}{\mathrm{d}x}. \tag{2.1.48b}$$

However, in the frame of the FBM, a simplified Kerr-type dependency for the permittivity is assumed through Eq. (2.1.5), where the permittivity depends only on the main electric field component E_x. In this case the problem reduces to:

$$E_x = \frac{\beta}{\epsilon_0 \epsilon_x(E_x) c} H_y, \tag{2.1.49a}$$

$$E_z = \frac{1}{\epsilon_0 \epsilon_z(E_x) \omega} \frac{\mathrm{d}H_y}{\mathrm{d}x}. \tag{2.1.49b}$$

The first equation is no longer coupled to the second one and it contains only one unknown quantity (E_x). Therefore, it can be readily solved. Inserting Eq. (2.1.5) into Eq. (2.1.49a) and performing some simple algebra gives

$$E_x^3 + \frac{\epsilon_{l,1}}{\alpha_1} E_x - \frac{\beta H_y}{\epsilon_0 c \alpha_1} = 0 \tag{2.1.50}$$

This equation has in general three roots: one real and a pair of complex conjugate solutions. In our approach the E_x field is assumed to be real so we choose the real root of this equation to be the field profile. The solution is in the form (see formula 3.8.2 in Ref. [112]):

$$E_x = \left(\frac{w}{2} + \sqrt{\frac{v^3}{27} + \frac{w^2}{4}} \right)^{\frac{1}{3}} + \left(\frac{w}{2} - \sqrt{\frac{v^3}{27} + \frac{w^2}{4}} \right)^{\frac{1}{3}}, \tag{2.1.51}$$

with $w = \beta H_y/(\epsilon_0 c \alpha_1)$ and $v = \epsilon_{l,1}/\alpha_1$. Having found the E_x field profile, the E_z dependency is calculated directly using Eq. (2.1.49b). In previous approaches [68, 73], the electric field was calculated using simplified formulas containing only the linear part of the refractive index:

$$E_x = \frac{\beta}{\epsilon_0 \epsilon_{l,x} c} H_y, \tag{2.1.52a}$$

$$E_z = \frac{1}{\epsilon_0 \epsilon_{l,z} \omega} \frac{\mathrm{d}H_y}{\mathrm{d}x}. \tag{2.1.52b}$$

2.1.4 Power calculations

In the FBM, Eq. (2.1.43) allows us to determine the allowed values of the effective indices β. For a given β the analytical expressions for the magnetic field profiles are given by Eqs. (2.1.24), where the coefficients H_0, A_+, A_-, B_+, B_-, and C are found during the procedure of solving the nonlinear dispersion relation [Eqs. (2.1.43)] and are given by Eqs. (2.1.28), (2.1.33), (2.1.38), and (2.1.40).

Based on this results, a closed analytical expression for the approximated power density of the corresponding plasmon–soliton waves can be found. Power density transmitted per unit length along the y direction is expressed as a longitudinal (z) component of the pointing vector

$$\mathbf{S} = \frac{1}{2} \Re e(\mathbf{E} \times \mathbf{H}^*) \tag{2.1.53}$$

integrated over the transverse dimension (x)

$$P_{\mathrm{tot}} = \int_{-\infty}^{+\infty} S_z dx = \frac{1}{2} \int_{-\infty}^{+\infty} E_x H_y^* \, \mathrm{d}x. \tag{2.1.54}$$

Equation (2.1.54) is rewritten using Eq. (1.5.2b) into a form:

$$P_{\mathrm{tot}} = \frac{\beta}{2c\epsilon_0} \int_{-\infty}^{+\infty} \frac{1}{\epsilon_x(x)} |H_y|^2 \, \mathrm{d}x. \tag{2.1.55}$$

In this expression, the dependency of the permittivity on the x coordinate is both due to a layered structure (linear) and due to the field induced changes in the nonlinear layer. Here we use again the assumption that $\epsilon_{\mathrm{nl}} \ll \epsilon_l$ which allows us to approximate the nonlinear permittivity profile $\epsilon_x(x)$ by the linear permittivity profile $\epsilon_l(x)$. Using this assumption the expression for the total approximated power density P_{tot} can be rewritten as a sum of four separate integrals

$$P_{\mathrm{tot}} = \sum_{k=1}^{4} P_k, \tag{2.1.56}$$

where

$$P_k = \frac{\beta}{2c\epsilon_0 \epsilon_{l,k}} \int_{\text{layer } k} |H_k|^2 \, \mathrm{d}x. \tag{2.1.57}$$

Using Eq. (2.1.24) we find the approximate power density in the nonlinear layer

$$P_1 = \frac{\beta}{2c\epsilon_0\epsilon_{l,1}k_0}\frac{H_0^2}{q_1 - q_{1,\mathrm{nl}}}, \tag{2.1.58a}$$

where $q_{1,\mathrm{nl}} = \widetilde{q_{1,\mathrm{nl}}}\epsilon_1$. The expressions for the power densities in the linear layers read:

$$\begin{aligned} P_2 = \frac{\beta}{2c\epsilon_0\epsilon_2}\Bigg[&\frac{A_+^2}{2k_0q_2}\left(e^{2k_0q_2L}-1\right) \\ &+2A_+A_-L - \frac{A_-^2}{2k_0q_2}\left(e^{-2k_0q_2L}-1\right)\Bigg], \end{aligned} \tag{2.1.58b}$$

$$\begin{aligned} P_3 = \frac{\beta}{2c\epsilon_0\epsilon_3}\Bigg[&\frac{B_+^2}{2k_0q_3}\left(e^{2k_0q_3d}-1\right) \\ &+2B_+B_-d - \frac{B_-^2}{2k_0q_3}\left(e^{-2k_0q_3d}-1\right)\Bigg], \end{aligned} \tag{2.1.58c}$$

$$P_4 = \frac{\beta}{2c\epsilon_0\epsilon_4}\frac{C^2}{2k_0q_4}. \tag{2.1.58d}$$

The expressions for the power density in the linear layers are exact. The assumption we made substituting the $\epsilon_x(x)$ by $\epsilon_l(x)$ affects only the nonlinear layer and does not change the values of the permittivity in the linear layers.

2.1.5 Linear losses estimation

An important part of the study of nonlinear wave propagation is the calculation of losses. In our studies we will focus only on the linear losses and the nonlinear effects (such as two photon absorption) will not be taken into account (see Section 1.6). In the FBM, the linear losses are estimated using the approach based on the imaginary part of permittivity and the field profiles. This method is described in the case of linear waveguides in Ref. [113] and has already been used for nonlinear plasmon–soliton studies [68, 69, 79, 81]. The complex permittivity considered here is isotropic and is described by the function $\tilde{\epsilon}(x) = \epsilon(x) + i\epsilon''(x)$ and it takes values given in Table 2.1.

The derivation of the equation describing losses starts by considering the expression $\boldsymbol{\nabla}\cdot\left(\overline{\boldsymbol{\mathscr{E}}}\times\overline{\boldsymbol{\mathscr{H}}_b}^*\right)$, where over-lined quantities still carry the oscillatory z dependency $e^{i\tilde{\beta}z}$:

$$\begin{Bmatrix}\boldsymbol{\mathscr{E}}(\mathbf{r},t)\\ \boldsymbol{\mathscr{H}}(\mathbf{r},t)\end{Bmatrix} = \begin{Bmatrix}\overline{\boldsymbol{\mathscr{E}}}(\mathbf{r})\\ \overline{\boldsymbol{\mathscr{H}}}(\mathbf{r})\end{Bmatrix} e^{-i\omega t} = \begin{Bmatrix}\mathbf{E}(\mathbf{r})e^{ik_0\beta z}\\ \mathbf{H}(\mathbf{r})e^{ik_0\beta z}\end{Bmatrix} e^{-i\omega t}, \tag{2.1.59}$$

and the backward propagating waves are considered:

$$\begin{Bmatrix}\boldsymbol{\mathscr{E}}_b(\mathbf{r},t)\\ \boldsymbol{\mathscr{H}}_b(\mathbf{r},t)\end{Bmatrix} = \begin{Bmatrix}\overline{\boldsymbol{\mathscr{E}}_b}(\mathbf{r})\\ \overline{\boldsymbol{\mathscr{H}}_b}(\mathbf{r})\end{Bmatrix} e^{-i\omega t} = \begin{Bmatrix}\mathbf{E}_b(\mathbf{r})e^{-ik_0\beta z}\\ \mathbf{H}_b(\mathbf{r})e^{-ik_0\beta z}\end{Bmatrix} e^{-i\omega t}. \tag{2.1.60}$$

The relations between the forward and backward propagating field amplitudes are given by [86]:

$$\mathbf{E}_b = -\mathbf{E}, \tag{2.1.61a}$$

$$\mathbf{H}_b = \mathbf{H}. \tag{2.1.61b}$$

Note that this time we consider the effective index to be a complex quantity $\tilde{\beta} = \beta + i\beta''$, where both β and β'' are real. Using the standard vector identity we write:

$$\boldsymbol{\nabla}\cdot\left(\overline{\boldsymbol{\mathscr{E}}}\times\overline{\boldsymbol{\mathscr{H}}_b}^*\right) = \overline{\boldsymbol{\mathscr{H}}_b}^*\left(\boldsymbol{\nabla}\times\overline{\boldsymbol{\mathscr{E}}}\right) - \overline{\boldsymbol{\mathscr{E}}}\left(\boldsymbol{\nabla}\times\overline{\boldsymbol{\mathscr{H}}_b}^*\right). \tag{2.1.62}$$

Inserting Eqs. (2.1.59) and (2.1.60) into Maxwell's equations [Eqs. (1.3.8a) and (1.3.8b)] and performing time derivatives results in:

$$\boldsymbol{\nabla} \times \overline{\boldsymbol{\mathscr{E}}} = i\omega\mu_0 \overline{\boldsymbol{\mathscr{H}}}, \tag{2.1.63a}$$

$$\boldsymbol{\nabla} \times \overline{\boldsymbol{\mathscr{H}}}_b = -i\omega\epsilon_0\tilde{\epsilon}\overline{\boldsymbol{\mathscr{E}}}_b. \tag{2.1.63b}$$

Using Eq. (2.1.63a) and the complex conjugate of Eq. (2.1.63b) in Eq. (2.1.62) we obtain:

$$\boldsymbol{\nabla} \cdot \left(\overline{\boldsymbol{\mathscr{E}}} \times \overline{\boldsymbol{\mathscr{H}}}_b^*\right) = i\omega(\mu_0 \overline{\boldsymbol{\mathscr{H}}}\ \overline{\boldsymbol{\mathscr{H}}}_b^* - \epsilon_0\tilde{\epsilon}\overline{\boldsymbol{\mathscr{E}}}\ \overline{\boldsymbol{\mathscr{E}}}_b^*). \tag{2.1.64}$$

Integrating this equation on a planar surface S perpendicular to the direction of wave propagation results in:

$$\int_S \boldsymbol{\nabla} \cdot \left(\overline{\boldsymbol{\mathscr{E}}} \times \overline{\boldsymbol{\mathscr{H}}}_b^*\right) \mathrm{d}S = i\omega \int_S (\mu_0 \overline{\boldsymbol{\mathscr{H}}}\ \overline{\boldsymbol{\mathscr{H}}}_b^* - \epsilon_0\tilde{\epsilon}\overline{\boldsymbol{\mathscr{E}}}\ \overline{\boldsymbol{\mathscr{E}}}_b^*)\, \mathrm{d}S. \tag{2.1.65}$$

At this step, we use the two-dimensional form of the divergence theorem [Eq. (37–56) in Ref. [86]]:

$$\int_S \boldsymbol{\nabla} \cdot \mathbf{A}\, \mathrm{d}S = \frac{\partial}{\partial z} \int_S \mathbf{A} \cdot \hat{\mathbf{z}}\, \mathrm{d}S + \oint_L \mathbf{A} \cdot \hat{\mathbf{n}}\, \mathrm{d}L, \tag{2.1.66}$$

where S is a planar surface with a perimeter L, on which $\hat{\mathbf{n}}$ is a unit vector normal to L pointing outward, and $\hat{\mathbf{z}}$ is a unit vector orthogonal to S and parallel to the increasing z-direction. In our problem, we use the boundary condition where the field vanishes at infinities. Therefore, we can further simplify this relation by omitting the line integral term (choice of the contour is arbitrary and we can choose it to be infinitely large):

$$\int_S \boldsymbol{\nabla} \cdot \mathbf{A}\, \mathrm{d}S = \frac{\partial}{\partial z} \int_S \mathbf{A} \cdot \hat{\mathbf{z}}\, \mathrm{d}S. \tag{2.1.67}$$

Using Eq. (2.1.67) on the left-hand side of Eq. (2.1.65), we obtain:

$$\frac{\partial}{\partial z} \int_S \left(\overline{\boldsymbol{\mathscr{E}}} \times \overline{\boldsymbol{\mathscr{H}}}_b^*\right) \cdot \hat{\mathbf{z}}\, \mathrm{d}S = i\omega \int_S (\mu_0 \overline{\boldsymbol{\mathscr{H}}}\ \overline{\boldsymbol{\mathscr{H}}}_b^* - \epsilon_0\tilde{\epsilon}\overline{\boldsymbol{\mathscr{E}}}\ \overline{\boldsymbol{\mathscr{E}}}_b^*)\, \mathrm{d}S. \tag{2.1.68}$$

We make use of a fact that the over-lined fields still carry the z dependency $e^{ik_0\tilde{\beta}z}$ and change the order of integral and derivative on the left-hand side. Performing the derivative results in appearance of effective index $\tilde{\beta}$ in the expression. Extracting $\tilde{\beta}$ on the left-hand side yields:

$$\tilde{\beta} = \frac{\omega}{2k_0} \frac{\int_S (\mu_0 \mathbf{H}\, \mathbf{H}_b^* - \epsilon_0\tilde{\epsilon}\mathbf{E}\, \mathbf{E}_b^*)\, \mathrm{d}S}{\int_S (\mathbf{E} \times \mathbf{H}_b^*) \cdot \hat{\mathbf{z}}\, \mathrm{d}S}. \tag{2.1.69}$$

Using Eqs. (2.1.61) to eliminate the fields associated to the backward propagating waves, we obtain

$$\tilde{\beta} = \frac{\omega}{2k_0} \frac{\int_S (\mu_0 |\mathbf{H}|^2 + \epsilon_0\tilde{\epsilon}|\mathbf{E}|^2)\, \mathrm{d}S}{\int_S (\mathbf{E} \times \mathbf{H}^*) \cdot \hat{\mathbf{z}}\, \mathrm{d}S}. \tag{2.1.70}$$

Taking the imaginary part of this equation we can express the imaginary part of $\tilde{\beta}$ as a function of field profiles and of the imaginary part of permittivity:

$$\Im m(\tilde{\beta}) = \frac{\omega\epsilon_0}{2k_0} \frac{\int_S \Im m(\tilde{\epsilon}) |\mathbf{E}|^2\, \mathrm{d}S}{\int_S (\mathbf{E} \times \mathbf{H}^*) \cdot \hat{\mathbf{z}}\, \mathrm{d}S}. \tag{2.1.71}$$

In our one-dimensional problem, the surface integrals that appear in the above expression can be replaced by integrals along x-direction due to the spatial invariance of structure and fields along the y-direction:

$$\Im m(\tilde{\beta}) = \frac{\omega\epsilon_0}{2k_0} \frac{\int_T \Im m(\tilde{\epsilon}) |\mathbf{E}|^2\, \mathrm{d}x}{\int_T (\mathbf{E} \times \mathbf{H}^*) \cdot \hat{\mathbf{z}}\, \mathrm{d}x}, \tag{2.1.72}$$

where T denotes the transverse cross-section of the four layer structure. In the denominator, we recognize the expression for the power density calculated as the integral of the Pointing vector $P_{\text{tot}} = \int_T S_z \,\mathrm{d}x = \frac{1}{2}\int_T \Re e(\mathbf{E}\times\mathbf{H}^*)\cdot\hat{\mathbf{z}}\,\mathrm{d}x$. Finally, the expression of the imaginary part of effective index reads:

$$\Im m(\widetilde{\beta}) = \beta'' = \frac{\epsilon_0 c}{4}\frac{\int_T \epsilon''|\mathbf{E}|^2\,\mathrm{d}x}{P_{\text{tot}}}. \tag{2.1.73}$$

The imaginary part of the refractive index is connected with the losses in decibel per meter ($\mathfrak{L}$) in the following way [114]:

$$\mathfrak{L} = \frac{40\pi}{\ln(10)\lambda}\beta'', \tag{2.1.74}$$

where λ it the free-space wavelength expressed in meters.

2.2 Wave equation for a simplified field based model

In this section, we will describe the derivation of the nonlinear wave equation in the case of a simplified expression for the nonlinear Kerr term. Contrarily to Sec. 2.1, where the nonlinear permittivity tensor is isotropic, here we will consider anisotropic nonlinearity, as it was done in Refs. [68, 73]. We assume that only the ϵ_x and ϵ_y depend on the transverse component of the electric field:[5]

$$\epsilon_x(x) = \epsilon_l(x) + \epsilon_{\text{nl}}[x, |\mathbf{E}(x)|^2], \tag{2.2.1a}$$
$$\epsilon_y(x) = \epsilon_l(x) + \epsilon_{\text{nl}}[x, |\mathbf{E}(x)|^2], \tag{2.2.1b}$$
$$\epsilon_z(x) = \epsilon_l(x) \tag{2.2.1c}$$

This approach was already presented in detail in Refs. [68, 73], but we recall it here shortly, because it will be useful for us for the purpose of comparison presented in Section 4.2.1. Moreover, the results of this approach will be used in the derivation and calculations of the two-dimensional profiles of plasmon–solitons in Section 5.1, where the form of permittivity tensor given by Eq. (2.2.1) is required to obtain analytical results.

The derivation presented here is based on similar methodology as we used in Section 2.1.1 deriving the nonlinear wave equation for the isotropic nonlinear Kerr effect. Taking the derivative of Eq. (1.5.2c) with respect to x and using Eqs. (1.5.2a), (1.5.2b), and the definition of the simplified permittivity tensor (2.2.1) gives

$$\frac{\mathrm{d}^2 H_y}{\mathrm{d}x^2} = k_0^2\left(\frac{\epsilon_z}{\epsilon_x}\beta^2 - \epsilon_z\right)H_y. \tag{2.2.2}$$

Comparing with Eqs. (2.2.2) and (2.1.1), we notice that Eq. (2.2.2) does not contain the term with the x-derivative of the nonlinear permittivity ϵ_{nl}. This is caused by the fact that, ϵ_z does not depend on the electric field. Using Eq. (2.2.1), we can rewrite Eq. (2.2.2) to a form:

$$\frac{\mathrm{d}^2 H_y}{\mathrm{d}x^2} = \epsilon_l k_0^2\left(1 - \frac{\beta^2}{\epsilon_l}\frac{1}{1+\frac{\epsilon_{\text{nl}}}{\epsilon_l}}\right)H_y. \tag{2.2.3}$$

Assuming that the nonlinear correction to the permittivity is small with respect to the linear permittivity $\epsilon_{\text{nl}}/\epsilon_l \ll 1$ we can expand the nonlinear term in a Taylor series:

$$\frac{1}{1+\frac{\epsilon_{\text{nl}}}{\epsilon_l}} = \left(1 - \frac{\epsilon_{\text{nl}}}{\epsilon_l}\right) + \mathcal{O}\left[\left(\frac{\epsilon_{\text{nl}}}{\epsilon_l}\right)^2\right]. \tag{2.2.4}$$

[5] There is a difference in notation between our work and Refs. [68, 73]. In our case x is the transverse direction and z is the longitudinal direction. In Refs. [68, 73] the situation is reversed. There z is the transverse direction and x is the longitudinal direction. Therefore, the components E_x and E_z are interchanged in the expression presented in this sections and the original expressions in Refs. [68, 73].

Keeping just the first-order terms we obtain

$$\frac{1}{1+\frac{\epsilon_{\mathrm{nl}}}{\epsilon_l}} \approx \left(1-\frac{\epsilon_{\mathrm{nl}}}{\epsilon_l}\right). \tag{2.2.5}$$

Inserting Eq. (2.2.5) into Eq. (2.2.3) yields

$$\frac{\mathrm{d}^2 H_y}{\mathrm{d}x^2} = \epsilon_l k_0^2 \left[1-\frac{\beta^2}{\epsilon_l}\left(1-\frac{\epsilon_{\mathrm{nl}}}{\epsilon_l}\right)\right] H_y. \tag{2.2.6}$$

Using the definition of the nonlinear correction to the permittivity

$$\epsilon_{\mathrm{nl}} = \alpha(x) E_x^2(x) \tag{2.2.7}$$

and Eq. (1.5.2b) one obtains

$$\frac{\mathrm{d}^2 H_y}{\mathrm{d}x^2} - k_0^2 q(x)^2 H_y + k_0^2 \frac{\beta^4 \alpha(x)}{\epsilon_z [\epsilon_0 \epsilon_l(x) c]^2} H_y^3 = 0. \tag{2.2.8}$$

Using again the approximation $\epsilon_{\mathrm{nl}}/\epsilon_l \ll 1$, we can replace now ϵ_z by ϵ_l in the denominator of the nonlinear term. Finally, we obtain

$$\frac{\mathrm{d}^2 H_y}{\mathrm{d}x^2} - k_0^2 q(x)^2 H_y + k_0^2 a^{(s)}(x) H_y^3 = 0, \tag{2.2.9a}$$

where

$$a^{(s)}(x) = \frac{\beta^4 \alpha(x)}{\epsilon_l [\epsilon_0 \epsilon_l(x) c]^2}. \tag{2.2.9b}$$

Equation (2.2.9a) has identical form as Eq. (2.1.7a), but the nonlinear term is different. Function $a(x)$ is replaced by $a^{(s)}(x)$ and the ratio between these two quantities is

$$\frac{a^{(s)}(x)}{a(x)} = \frac{\beta^2}{\epsilon_l}. \tag{2.2.10}$$

It can be a matter of discussion which of these two formulations is better. In the FBM derived in Section 2.1, we had to skip one of the nonlinear terms (term containing the derivative of the nonlinear permittivity). In the simplified field based model (SFBM) presented in this section, we use the Taylor expansion of the nonlinear term, and omit the higher-order terms. For weakly nonlinear solutions, the effective index β is close to the refractive index of the nonlinear material. Therefore, the ratio of the two nonlinear parameters $a^{(s)}(x)/a(x)$ is close to 1 and both approaches give very similar results. For higher effective indices β, the discrepancy between the two approaches increases as it will be visible during the comparison of the results obtained using the two models (FBM and SFBM) in Section 4.2.1.

In order to obtain the dispersion relations and the field profiles in the SFBM one can follow the lines of the derivation presented in Section 2.1.2. To obtain the formulas for SFBM one has to substitute function $a(x)$ by $a^{(s)}(x)$.

2.3 Exact model

In this section, the derivation of the exact model (EM) will be presented. This model, on the contrary to the FBM, does not require any additional assumptions on the form of the Kerr-type nonlinearity. First, we will describe the method of solution of Maxwell's equations in the nonlinear region that allows for the exact treatment of the nonlinear Kerr effect. Then the method to obtain the analytical formulas for the nonlinear dispersion relation in four-layer structures will be presented.

2.3.1 First integral method for nonlinear medium treatment

Below we present the derivation of the model that allows for the exact treatment of the Kerr nonlinearity. This derivation is based on the approaches presented by Mihalache *et al.* [15] for a single interface between a Kerr-type nonlinear material and a linear material, later extended to three-layer configurations and generalized to the case of power-law Kerr nonlinearity by Yin *et al.* [77]. Here we extend the approach from Ref. [77] to a four-layer configuration.

The derivation of the EM starts from Maxwell's equations [Eqs. (1.5.2)]. In this approach the magnetic field is eliminated from these equations. The use of Eq. (1.5.2b) in Eqs. (1.5.2a) and (1.5.2c) gives

$$\frac{\mathrm{d}E_z}{\mathrm{d}x} = k_0\left(\beta - \frac{\epsilon_x}{\beta}\right)E_x, \tag{2.3.1a}$$

$$\frac{\mathrm{d}(\epsilon_x E_x)}{\mathrm{d}x} = \beta k_0 \epsilon_z E_z. \tag{2.3.1b}$$

Equation (2.3.1a) is derived with respect to x and the last term is replaced using Eq. (2.3.1b) resulting in

$$\frac{\mathrm{d}^2E_z}{\mathrm{d}x^2} = \beta k_0 \frac{\mathrm{d}E_x}{\mathrm{d}x} - k_0^2\epsilon_z E_z. \tag{2.3.2}$$

Multiplying Eq. (2.3.2) by $\mathrm{d}E_z/\mathrm{d}x$ and using Eq. (2.3.1a) once more, gives

$$\frac{\mathrm{d}^2E_z}{\mathrm{d}x^2}\frac{\mathrm{d}E_z}{\mathrm{d}x} = \beta k_0^2 \frac{\mathrm{d}E_x}{\mathrm{d}x}\left(\beta - \frac{\epsilon_x}{\beta}\right)E_x - k_0^2\epsilon_z E_z\frac{\mathrm{d}E_z}{\mathrm{d}x}. \tag{2.3.3}$$

In this approach, a full power-law Kerr dependency of the permittivity of the following form is assumed in the nonlinear layer [compare with Eqs. (1.6.11) and (2.1.5)]:

$$\epsilon_x = \epsilon_y = \epsilon_z = \epsilon_1 = \epsilon_{l,1} + \alpha_1|\mathbf{E}|^\kappa = \epsilon_{l,1} + \alpha_1\left(E_x^2 + E_z^2\right)^{\frac{\kappa}{2}}. \tag{2.3.4}$$

The nonlinear term in the EM depends both on the transverse and the longitudinal components of electric field. The derivation will be conducted for an arbitrary value of κ resulting in the nonlinear treatment of Maxwell's equations in the nonlinear medium with a power-law Kerr nonlinearity. For $\kappa = 2$ we recover results for the standard cubic Kerr-type nonlinearity.

Inserting Eq. (2.3.4) into Eq. (2.3.3) one obtains

$$\begin{aligned}\frac{\mathrm{d}^2E_z}{\mathrm{d}x^2}\frac{\mathrm{d}E_z}{\mathrm{d}x} = (\beta k_0)^2 E_x\frac{\mathrm{d}E_x}{\mathrm{d}x} - k_0^2\epsilon_{l,1}\left(E_x\frac{\mathrm{d}E_x}{\mathrm{d}x} + E_z\frac{\mathrm{d}E_z}{\mathrm{d}x}\right)\\ - k_0^2\alpha_1\left(E_x^2 + E_z^2\right)^{\frac{\kappa}{2}}\left(E_x\frac{\mathrm{d}E_x}{\mathrm{d}x} + E_z\frac{\mathrm{d}E_z}{\mathrm{d}x}\right).\end{aligned} \tag{2.3.5}$$

Integrating this equation with respect to x gives

$$\left(\frac{\mathrm{d}E_z}{\mathrm{d}x}\right)^2 = (\beta k_0)^2 E_x^2 - k_0^2\epsilon_{l,1}\left(E_x^2 + E_z^2\right) - k_0^2\frac{2\alpha_1}{\kappa+2}\left(E_x^2 + E_z^2\right)^{\frac{\kappa}{2}+1} + C_0, \tag{2.3.6}$$

where C_0 is the integration constant. The first three terms of Eq. (2.3.5) were integrated by parts using the identity

$$\int f(x)\frac{\mathrm{d}f(x)}{\mathrm{d}x}\,\mathrm{d}x = \frac{1}{2}f^2(x). \tag{2.3.7}$$

The last (nonlinear) term was integrated using the following change of variables:

$$\begin{aligned}\int\left(E_x^2 + E_z^2\right)^{\frac{\kappa}{2}}\left(E_x\frac{\mathrm{d}E_x}{\mathrm{d}x} + E_z\frac{\mathrm{d}E_z}{\mathrm{d}x}\right)\mathrm{d}x &= \left|\begin{array}{l} Y = E_x^2 + E_z^2 \\ \mathrm{d}Y = 2\left(E_x\frac{\mathrm{d}E_x}{\mathrm{d}x} + E_z\frac{\mathrm{d}E_z}{\mathrm{d}x}\right)\mathrm{d}x\end{array}\right| \\ &= \frac{1}{2}\int Y^{\frac{\kappa}{2}}\,\mathrm{d}Y = \frac{1}{\kappa+2}Y^{\frac{\kappa}{2}+1} = \frac{1}{\kappa+2}\left(E_x^2 + E_z^2\right)^{\frac{\kappa}{2}+1}.\end{aligned} \tag{2.3.8}$$

In Eq. (2.3.6), the integration constant C_0 is set to 0 taking into consideration the fact that a semi-infinite nonlinear medium is studied, where the electric fields E_x, E_z, and their x-derivatives vanish as $x \to -\infty$. The final step of this derivation is to compare the right-hand side of Eq. (2.3.6) with the square of the right-hand side of Eq. (2.3.1a). This comparison yields

$$\left(\frac{\epsilon_1^2}{\beta^2} - 2\epsilon_1\right) E_x^2 + \epsilon_{l,1}\left(E_x^2 + E_z^2\right) + \frac{2\alpha_1}{\kappa+2}(E_x^2 + E_z^2)^{\frac{\kappa}{2}+1} = 0, \tag{2.3.9}$$

which is the first step in order to obtain the nonlinear dispersion relation in the frame of the EM.

2.3.2 Nonlinear dispersion relation and field profiles

In the previous paragraph, a method that allows for the treatment of the nonlinearity in an exact manner, without the approximations used in the FBM, was presented. Besides, there is no difficulty in solving Maxwell's equations in the linear layers. In these layers, the electric field components are solutions to the linear wave equations. These wave equations are derived from Maxwell's equations [Eqs. (1.5.2)] and read:

$$\frac{\mathrm{d}^2 E_x}{\mathrm{d}x^2} - k_0^2 q^2(x) E_x = 0, \tag{2.3.10a}$$

$$\frac{\mathrm{d}^2 E_z}{\mathrm{d}x^2} - k_0^2 q^2(x) E_z = 0. \tag{2.3.10b}$$

The general solution of these wave equations is a combination of decreasing and increasing exponential functions of the form $Ae^{k_0 q x} + Be^{-k_0 q x}$. In the following, the two electric field components in the linear layers are expressed in this form:

1. in the buffer linear dielectric ($0 \leqslant x < L$ — layer 2)

$$E_{x,2} = A_x e^{k_0 q_2 x} + B_x e^{-k_0 q_2 x}, \tag{2.3.11a}$$

$$E_{z,2} = A_z e^{k_0 q_2 x} + B_z e^{-k_0 q_2 x}, \tag{2.3.11b}$$

2. in the metal ($L \leqslant x < L + d$ — layer 3)

$$E_{x,3} = C_x e^{k_0 q_3 (x-L)} + D_x e^{-k_0 q_3 (x-L)}, \tag{2.3.12a}$$

$$E_{z,3} = C_z e^{k_0 q_3 (x-L)} + D_z e^{-k_0 q_3 (x-L)}, \tag{2.3.12b}$$

3. in the external linear dielectric ($x \geqslant L + d$ — layer 4)

$$E_{x,4} = F_x e^{-k_0 q_4 [x-(L+d)]}, \tag{2.3.13a}$$

$$E_{z,4} = F_z e^{-k_0 q_4 [x-(L+d)]}. \tag{2.3.13b}$$

In order to derive the nonlinear dispersion relation in the frame of the exact model, several relationships between field amplitudes in the linear layers are needed. Using Eq. (2.3.1b) separately in each of the linear and uniform layers, relations between the amplitudes of the x and z components of the fields defined by Eqs. (2.3.11)–(2.3.13) are found. Inserting Eqs. (2.3.11a) and (2.3.11b) into Eq. (2.3.1b) yields the relation for the field amplitudes in layer 2:

$$\beta(A_z e^{k_0 q_2 x} + B_z e^{-k_0 q_2 x}) = q_2(A_x e^{k_0 q_2 x} - B_x e^{-k_0 q_2 x}). \tag{2.3.14}$$

Because Eq. (2.3.14) has to be fulfilled for each value of $x \in (0, L)$ we separately solve this equations for the terms proportional to $e^{k_0 q_2 x}$ and $e^{-k_0 q_2 x}$. As a result one obtains

$$\begin{cases} A_x = \dfrac{\beta}{q_2} A_z, \\ B_x = -\dfrac{\beta}{q_2} B_z. \end{cases} \tag{2.3.15}$$

Applying a similar procedure to the expressions of the fields in other linear layers leads to

$$\begin{cases} C_x = \dfrac{\beta}{q_3} C_z, \\ D_x = -\dfrac{\beta}{q_3} D_z, \end{cases} \tag{2.3.16}$$

$$F_x = -\frac{\beta}{q_4} F_z. \tag{2.3.17}$$

We will use the continuity conditions for the tangential components of the fields (E_z and H_y) in order to obtain the analytical expression for the nonlinear dispersion relation. The H_y field components, according to Eq. (1.5.2b), are proportional to the E_x field multiplied by the permittivity of the medium.

The continuity conditions on the interfaces result in the following:

1. Continuity conditions at $x = 0$

   (a) The continuity condition for the magnetic field component

   $$H_1|_{x=0^-} = H_2|_{x=0^+} \tag{2.3.18}$$

   yields

   $$\epsilon_{1,0} E_{x,0} = \epsilon_2 (A_x + B_x), \tag{2.3.19}$$

   where the transverse electric field component in the nonlinear medium at the interface $x = 0$ is denoted by $E_x(x = 0^-) = E_{x,0}$ and the value of the nonlinear permittivity at this interface is denoted by $\epsilon_{1,0}$.

   (b) The continuity condition for the tangential electric field component

   $$E_{z,1}|_{x=0^-} = E_{z,2}|_{x=0^+} \tag{2.3.20}$$

   yields

   $$E_{z,0} = A_z + B_z, \tag{2.3.21}$$

   where the longitudinal electric field component in the nonlinear medium at the interface $x = 0$ is denoted by $E_z(x = 0^-) = E_{z,0}$.

2. Continuity conditions at $x = L$

   (a) The continuity condition for the magnetic field component

   $$H_2|_{x=L^-} = H_3|_{x=L^+} \tag{2.3.22}$$

   yields

   $$\epsilon_2 (A_x e^{k_0 q_2 L} + B_x e^{-k_0 q_2 L}) = \epsilon_3 (C_x + D_x). \tag{2.3.23}$$

   (b) The continuity condition for the tangential electric field component

   $$E_{z,2}|_{x=L^-} = E_{z,3}|_{x=L^+} \tag{2.3.24}$$

   yields

   $$A_z e^{k_0 q_2 L} + B_z e^{-k_0 q_2 L} = C_z + D_z. \tag{2.3.25}$$

3. Continuity conditions at $x = L + d$

   (a) The continuity condition for the magnetic field component

   $$H_3|_{x=(L+d)^-} = H_4|_{x=(L+d)^+} \tag{2.3.26}$$

   yields

   $$\epsilon_3 (C_x e^{k_0 q_3 d} + D_x e^{-k_0 q_3 d}) = \epsilon_4 F_x. \tag{2.3.27}$$

(b) The continuity condition for the tangential electric field component

$$E_{z,3}|_{x=(L+d)^-} = E_{z,4}|_{x=(L+d)^+} \tag{2.3.28}$$

yields

$$C_z e^{k_0 q_3 d} + D_z e^{-k_0 q_3 d} = F_z. \tag{2.3.29}$$

At first, wherever it is possible, we will eliminate the amplitudes of the transverse field components E_x in Eqs. (2.3.19), (2.3.21), (2.3.23), (2.3.25), (2.3.27), and (2.3.29). To this end we will use the relations given by Eqs. (2.3.15)–(2.3.17). Inserting Eqs. (2.3.15) into Eq. (2.3.19) we obtain

$$\epsilon_{1,0} E_{x,0} = \frac{\beta \epsilon_2}{q_2}(A_z - B_z). \tag{2.3.30}$$

Inserting Eqs. (2.3.15) and (2.3.16) into Eq. (2.3.23) we obtain

$$\frac{\epsilon_2}{q_2}\left(A_z e^{k_0 q_2 L} - B_z e^{-k_0 q_2 L}\right) = \frac{\epsilon_3}{q_3}(C_z - D_z). \tag{2.3.31}$$

Inserting Eqs. (2.3.16) and (2.3.17) into Eq. (2.3.27) we obtain

$$\frac{\epsilon_3}{q_3}\left(C_z e^{k_0 q_3 d} - D_z e^{-k_0 q_3 d}\right) = -\frac{\epsilon_4}{q_4} F_z. \tag{2.3.32}$$

Inserting Eq. (2.3.29) into Eq. (2.3.32), after some algebra yields

$$D_z = \frac{\frac{\epsilon_3}{q_3} + \frac{\epsilon_4}{q_4}}{\frac{\epsilon_3}{q_3} - \frac{\epsilon_4}{q_4}} C_z e^{2 q_3 d}. \tag{2.3.33}$$

Taking a sum and a difference of Eq. (2.3.31) and Eq. (2.3.25) multiplied by ϵ_3/q_3 gives

$$2\frac{\epsilon_3}{q_3} C_z = A_z \left(\frac{\epsilon_2}{q_2} + \frac{\epsilon_3}{q_3}\right) e^{k_0 q_2 L} + B_z \left(\frac{\epsilon_3}{q_3} - \frac{\epsilon_2}{q_2}\right) e^{-k_0 q_2 L} \tag{2.3.34}$$

$$2\frac{\epsilon_3}{q_3} D_z = A_z \left(\frac{\epsilon_3}{q_3} - \frac{\epsilon_2}{q_2}\right) e^{k_0 q_2 L} + B_z \left(\frac{\epsilon_2}{q_2} + \frac{\epsilon_3}{q_3}\right) e^{-k_0 q_2 L} \tag{2.3.35}$$

Inserting Eqs. (2.3.34) and (2.3.35) into Eq. (2.3.33) and performing some lengthy but elementary algebra results in the relation between A_z and B_z

$$A_z = \phi B_z, \tag{2.3.36}$$

where we introduce the following notation:

$$\phi = \frac{\Psi_+^+ e^{-k_0 q_2 L - k_0 q_3 d} + \Psi_-^- e^{-k_0 q_2 L + k_0 q_3 d}}{\Psi_-^+ e^{k_0 q_2 L + k_0 q_3 d} + \Psi_+^- e^{k_0 q_2 L - k_0 q_3 d}}, \tag{2.3.37a}$$

and

$$\Psi_{\mathrm{sgn}(p)}^{\mathrm{sgn}(m)} = \frac{\epsilon_2/q_2 + m\epsilon_3/q_3}{\epsilon_3/q_3 + p\epsilon_4/q_4}, \quad \text{where } \{m, p\} = \{1, -1\}, \tag{2.3.37b}$$

Inserting Eq. (2.3.36) into Eqs. (2.3.21) and (2.3.30) results in

$$E_{z,0} = (\phi + 1) B_z, \tag{2.3.38}$$

$$\epsilon_{1,0} E_{x,0} = \frac{\beta \epsilon_2}{q_2}(\phi - 1) B_z. \tag{2.3.39}$$

Eliminating B_z from Eq. (2.3.38) with the help of Eq. (2.3.39), we obtain the relation between the amplitudes of the electric field components in the nonlinear dielectric at the interface $x = 0$

$$E_{z,0} = \frac{\epsilon_{1,0} q_2 (\phi + 1)}{\epsilon_2 \beta (\phi - 1)} E_{x,0}. \tag{2.3.40}$$

The total electric field amplitude in the nonlinear medium at the interface $x = 0$, denoted by E_0, is defined by

$$E_0^2 = E_{x,0}^2 + E_{z,0}^2. \tag{2.3.41}$$

Using Eqs. (2.3.40) and (2.3.41) we can express the electric field amplitude $E_{x,0}$ as a function of the total electric field amplitude

$$E_{x,0}^2 = \frac{(\epsilon_2\beta)^2 (1-\phi)^2}{(\epsilon_{1,0}q_2)^2 (1+\phi)^2 + (\epsilon_2\beta)^2 (1-\phi)^2} E_0^2. \tag{2.3.42}$$

Using Eqs. (2.3.42) and (2.3.41) to eliminate E_x and E_z from Eq. (2.3.9) taken at $x = 0^-$ results in the final form of the nonlinear dispersion relation for the four-layer structure in the frame of the EM:

$$\boxed{\left(\frac{\epsilon_{1,0}\epsilon_2}{q_2}\right)^2 - 2\epsilon_{1,0}\left(\frac{\epsilon_2\beta}{q_2}\right)^2 + \left(\epsilon_{l,1} + \frac{2\alpha_1}{\kappa+2}E_0^\kappa\right)\left[\epsilon_{1,0}^2\left(\frac{1+\phi}{1-\phi}\right)^2 + \left(\frac{\epsilon_2\beta}{q_2}\right)^2\right] = 0,} \tag{2.3.43}$$

where ϕ is defined by Eqs. (2.3.37). For a given set of opto-geometric parameters ($\epsilon_{l,1}$, α_1, ϵ_2, ϵ_3, ϵ_4, L, d) and a given wavelength (λ), it contains as a unique free parameter the total electric field amplitude at the nonlinear interface E_0. Fixing arbitrarily E_0 allows for solving this equation for all the possible values of β.

After obtaining the effective indices of the nonlinear waves propagating in a given structure, the field profiles corresponding to these values of β are calculated. In the EM, contrarily to the FBM, no analytical formulas for the field profiles in the nonlinear layer are provided. However, a system of two coupled first-order differential equations for the electric field components can be derived to allow field profile computations. Equation (2.3.1b) is written in the form:

$$\frac{\mathrm{d}\epsilon_x}{\mathrm{d}x}E_x + \frac{\mathrm{d}E_x}{\mathrm{d}x}\epsilon_x = \beta k_0 \epsilon_z E_z. \tag{2.3.44}$$

Using Eq. (2.3.4) in the first term and calculating the derivative gives

$$2\alpha_1\left(E_x\frac{\mathrm{d}E_x}{\mathrm{d}x} + E_z\frac{\mathrm{d}E_z}{\mathrm{d}x}\right)E_x + \frac{\mathrm{d}E_x}{\mathrm{d}x}\epsilon_1 = \beta k_0 \epsilon_1 E_z. \tag{2.3.45}$$

Replacing $\mathrm{d}E_z/\mathrm{d}x$ using Eq. (2.3.1a) and reorganizing the terms result in the first coupled differential equation

$$\frac{\mathrm{d}E_x}{\mathrm{d}x} = \frac{\beta k_0 \epsilon_1 E_z - 2k_0\alpha_1 E_z E_x^2\left(\beta - \frac{\epsilon_1}{\beta}\right)}{\epsilon_1 + 2\alpha_1 E_x^2}. \tag{2.3.46}$$

The second coupled differential equation used to calculate the field profiles is Eq. (2.3.1a).

2.4 Finite element method

In this section, the finite element method (FEM) based approach used to compute the stationary solutions propagating in the structure depicted in Fig. 2.1 is described. The FEM [115] has already been used to study stationary solutions in nonlinear waveguides since at least the end of the eighties [116–118]. For a general and recent review of FEM in the frame of optical waveguides, the reader can refer to Ref. [119]. In the present case, the problem is relatively simple since it is both one-dimensional and is reduced to a scalar case.

The FEM is an approximative method used to solve partial differential equations. In the frame of the FEM, the physical problem is written in a variational formulation, which is equivalent to the initial formulation of the problem. In order to obtain the variational formulation also called a

weak formulation, the initial partial differential equations are multiplied by chosen form functions that belong to a particular function space depending notably on the used boundary conditions and the type of partial differential equations. The next step to establish the FEM is the discretization, in which one shifts from an infinite-dimension functional space to a finite-size one that allow the numerical resolution. It must be pointed out that, the weak formulation of the scalar problem for the full structure, deduced from Eq. (2.1.3) or its approximated form given by Eq. (2.1.7a), must take into account all the continuity relations fulfilled by the electromagnetic field at the structure interfaces. This implies that the full TM wave equation for H_y component must be used to obtain the correct weak formulation that deals with both the inhomogeneous permittivity term induced by the nonlinearity and the structure interfaces. The corresponding weak formulation is given by:

$$-\int_F \frac{1}{k_0^2\epsilon(x)}\boldsymbol{\nabla}\phi(x)\cdot\boldsymbol{\nabla}\phi'(x)\,\mathrm{d}x+\int_F \phi(x)\phi'(x)\,\mathrm{d}x = \beta^2\int_F \frac{1}{\epsilon(x)}\phi(x)\phi'(x)\,\mathrm{d}x \qquad \forall\phi'\in\mathcal{H}_0^1(F) \text{ and } \phi\in\mathcal{H}_0^1(F), \tag{2.4.1}$$

where $\mathcal{H}_0^1(F)$ is the Sobolev space of the order 1 with the null Dirichlet boundary conditions on the domain of integration F (in the present case the full x cross-section of the structure). In the above equation, ϕ stands for the H_y component and ϕ' denotes the test form functions.

After Eq. (2.4.1) is solved for the H_y field profiles in the four-layer structure, the electric field components are calculated using Eqs. (1.5.2b) and (1.5.2c) with the method described in Section 2.1.3. The FEM is implemented using the free softwares Gmsh as a mesh generator and GetDP as a solver [120–122]. These softwares have already been used to solve both two-dimensional scalar and vector nonlinear electromagnetic waveguide problems [110, 123]. The nonlinearity considered in these two references was of the simplified Kerr type given by Eq. (2.1.7a).

The algorithm used for this plasmon–soliton study is the fixed power one [108–110] in which, for a given structure, the wave power is the input parameter and the outputs are the propagation constant and the corresponding field profiles. This algorithm involves an iterative process requiring successive resolutions of generalized linear eigenvalue problems, where the square of the propagation constant $(k_0\beta)^2$ is the eigenvalue and the field profile H_y is the eigenvector. The iterative process is stopped when an arbitrary criterion on the convergence of the propagation constant is reached. Typically, $|(\beta_n-\beta_{n-1})/\beta_n|<\delta$, where n denotes the step number in the procedure, and $\delta=10^{-6}$ is chosen in the present work. To fulfill this criterion between 10 and 15 steps are needed depending on the structure parameters and the used initial field. It is worth noticing that, in the frame of the fixed power algorithm, different initial fields provide at the end of the iterative process the same results except if the structure exhibits multiple solutions for identical power. In this last case, the obtained solution at the end of the iterative process depends on the initial field.

Chapter 3

Limiting cases for semi-analytical models

Contents

In this chapter, we will present a validation of our models. Their validity will be confirmed on two levels: formulation and implementation. First, the formulation will be verified by analyzing the limiting cases that will lead to dispersion formulas for simpler structures already studied in literature. The validation of the implementation of the models will be done later, together with the presentation of the results in Chapter 4. The implementation verification will be based on the comparison between the results obtained using our codes and the previously published results for identical structures (see Section 4.2.1) and by a mutual comparison between our models (see Section 4.3.2).

Here the formulations of the semi-analytical models for four-layer structure are verified. The validation is made by comparison of the analytical formulas obtained in other works for simpler structures (three- and two- layer) and for the linear case, with the corresponding formulas obtained by taking limiting cases of the dispersion relations provided by our models. At first, the field based model (FBM) and later the exact model (EM) will be analyzed.

3.1 Field based model

In order to verify our analytical results for the FBM, several comparisons with the formulas from previous works for simpler structures are realized in this section. The dispersion relations obtained in the frame of the FBM are considered in three limiting cases:

3.1.1 Three-layer structure

To consider a three-layer structure, we need to reduce by one the number of linear layers of the structure presented in Fig. 2.1. One way to do, it is to assume that $L \to 0$. In this case we consider a structure where the metal film of the thickness d (layer 3) is sandwiched between a nonlinear dielectric layer 1 and a linear dielectric layer 4. Letting $L \to 0$, one notices immediately that $\tanh(k_0 q_2 L) \to 0$ in Eq. (2.1.43b) and this equation simplifies to

$$\Phi_{\pm} = \left(1 \pm \frac{\widetilde{q_{1,\mathrm{nl}}}|_{x=0}}{\widetilde{q}_3}\right). \tag{3.1.1}$$

Inserting Eq. (3.1.1) into Eq. (2.1.43a), after some simple algebra, yields

$$\tanh(k_0 q_3 d) = -\frac{\widetilde{q_3}(\widetilde{q_{1,\mathrm{nl}}}|_{x=0} + \widetilde{q_4})}{\widetilde{q_3}^2 + \widetilde{q_4}\widetilde{q_{1,\mathrm{nl}}}|_{x=0}}. \tag{3.1.2}$$

If in Eq. (3.1.2), the nonlinear permittivity is approximated by its linear value (see discussion in Section 2.1.2 on Page 24) then $\widetilde{q_{1,\mathrm{nl}}}|_{x=0}$ becomes $q_1 \tanh(k_0 q_1 x_0)/\epsilon_{l,1}$. Upon this assumption, Eq. (3.1.2) is identical to Eq. (8) in Ref. [73] that gives the nonlinear dispersion relation for the three-layer structure, where the metal film is sandwiched between linear and nonlinear dielectrics.[1]

3.1.2 Two-layer structure

An elegant way of finding the dispersion relation for two-layer structures is to infinitely separate both interfaces of the three-layer structure. This is done by letting $d \to \infty$. Upon this assumption $\tanh(k_0 q_3 d) \to 1$ in Eq. (3.1.2) and this equation becomes

$$(\widetilde{q_{1,\mathrm{nl}}}|_{x=0} + \widetilde{q_3})(\widetilde{q_3} + \widetilde{q_4}) = 0. \tag{3.1.3}$$

Equation (3.1.3) has two solutions. The first one,

$$\widetilde{q_{1,\mathrm{nl}}}|_{x=0} = -\widetilde{q_3}, \tag{3.1.4}$$

describes the nonlinear dispersion relation for the waves localized at the interface between the semi-infinite nonlinear layer 1 and the semi-infinite linear layer 3. This equation has a structure that resembles Eq. (7) in Ref. [67]. The differences between the two expressions result from different assumptions on the type of the nonlinearity used, as described on Pages 3 and 18. The second solution,

$$\widetilde{q_3} = -\widetilde{q_4}, \tag{3.1.5}$$

gives the linear dispersion relation for a plasmon at the interface between two linear layers (3 and 4). Equation (3.1.5) is equivalent to Eq. (2.12) in Ref. [55].

3.1.3 Linear case

Consider a limiting case of a linear structure $\{\alpha_1 \to 0$ and therefore $a_1 \to 0$ [see Eq. (2.1.7c)]$\}$. The nonlinear dispersion relation (2.1.43a) does not depend on the value of the nonlinear parameter a_1 as discussed at the end of Section 2.1.2. The only free parameter on which the dispersion relation depends is x_0. Therefore, we need to find a relation between a_1 and x_0 in order to be able to formally calculate the limiting expression for the dispersion relation in the linear case.

In the frame of the FBM the magnetic field profile in the nonlinear medium is given by Eq. (2.1.24a.) We recall this expression here expressing the cosine hyperbolic using exponential functions:

$$H_1 = \sqrt{\frac{2}{a_1}}\frac{2q_1}{e^{k_0 q_1 (x-x_0)} + e^{-k_0 q_1 (x-x_0)}}. \tag{3.1.6}$$

[1] Other ways to obtain the three-layer limit of Eq. (2.1.43) also exist. The way presented here (letting $L \to 0$) does not require a lot of algebra. Another simple way to consider a three layer structure is to assume that $\epsilon_4 = \epsilon_3$. In this case, a four-layer structure from Fig. 2.1 transforms into a structure where a film with the thickness L (layer 2) is sandwiched between the nonlinear dielectric layer 1 and a linear layer 3 (that is now semi-infinite because of its merging with layer 4). In this case, the dispersion relation for the limiting case of a three layer structure is given by

$$\tanh(k_0 q_2 L) = -\frac{\widetilde{q_2}(\widetilde{q_{1,\mathrm{nl}}}|_{x=0} + \widetilde{q_3})}{\widetilde{q_2}^2 + \widetilde{q_3}\widetilde{q_{1,\mathrm{nl}}}|_{x=0}},$$

which is equivalent to Eq. (3.1.2). It is also possible to obtain the limiting case of a three-layer structure either by letting $d \to 0$ or assuming $\epsilon_2 = \epsilon_3$. However, these approaches require a bit longer algebraic transformations in order to recover the dispersion formula in the form given by Eq. (3.1.2).

We cannot simply set $a_1 = 0$ in this expression because it would lead to infinite values of the magnetic field, which is an unphysical result. Although, we can find a way to relate a_1 parameter and x_0 parameter in such a way that setting $a_1 = 0$ and a proper value of x_0 will keep the magnetic field value finite.

At first, we notice that for a linear semi-infinite medium (layer 1), the solution of Maxwell's equations in this layer should be given by a single exponential function decaying toward $x = -\infty$. We just keep the second exponential function in the denominator of Eq. (3.1.6) so that the expression for the magnetic field in layer 1 reads:

$$H_1 \approx 2q_1\sqrt{\frac{2}{a_1}}e^{k_0 q_1 (x-x_0)}. \tag{3.1.7}$$

This approximation is valid only when the values of the first exponential term in the denominator of Eq. (3.1.6) are much lower than the values of the second exponential term ($e^{k_0 q_1 (x-x_0)} \ll e^{-k_0 q_1 (x-x_0)}$). At the end of this derivation, we will see that this approximation is satisfied in the limiting case of the linear structure.

Equation (3.1.6) gives us the exponentially decaying field profile in the linear layer 1. We fix now the magnetic field intensity at the interface $x = 0$ to be equal to H_{lin}:

$$H_{\text{lin}} = 2q_1\sqrt{\frac{2}{a_1}}e^{-k_0 q_1 x_0}. \tag{3.1.8}$$

Taking the natural logarithm of Eq. (3.1.8) results in the relation that a_1 and x_0 have to fulfill in order to keep the value of the magnetic field at $x = 0$ equal to H_{lin}:

$$x_0 = \frac{1}{k_0 q_1}\ln\left(\frac{2\sqrt{2}q_1}{\sqrt{a_1}H_{\text{lin}}}\right). \tag{3.1.9}$$

From Eq. (3.1.9) it follows that in the FBM, in order to obtain the limiting case where $a_1 \to 0$, one should have $x_0 \to +\infty$. This result is in agreement with the assumption made in order to transform Eq. (3.1.6) into Eq. (3.1.7). For $x_0 \to +\infty$ the first exponential term in the denominator of Eq. (3.1.6) tends to zero.

The dispersion relation in the limiting case for three- and two-layer structures in the linear regime can be now computed. For the case of three-layer structure, we proceed in the following way. Letting $x_0 \to +\infty$, from Eq. (2.1.32) one obtains that $\widetilde{q_{1,\text{nl}}} \to \tilde{q_1}$. In this case, Eq. (3.1.2) becomes

$$\tanh(k_0 q_3 d) = -\frac{\tilde{q_3}(\tilde{q_1} + \tilde{q_4})}{\tilde{q_3}^2 + \tilde{q_4}\tilde{q_1}}. \tag{3.1.10}$$

After some algebra, it transforms to

$$e^{-2k_0 q_3 d} = \frac{(\tilde{q_3} + \tilde{q_1})(\tilde{q_3} + \tilde{q_4})}{(\tilde{q_3} - \tilde{q_1})(\tilde{q_3} - \tilde{q_4})}, \tag{3.1.11}$$

which is equivalent to Eq. (2.28) in Ref. [55] giving the dispersion relation for linear plasmons on a metallic film sandwiched between two linear dielectrics (IMI — insulator/metal/insulator structure) or of a dielectric film sandwiched between two metals (MIM — metal/insulator/metal structure). For two-layer structure it is now straightforward to see that if $\widetilde{q_{1,\text{nl}}} \to \tilde{q_1}$ then Eq. (3.1.4) is reduced to the dispersion relation of the linear case [Eq. (3.1.5)].

The three limiting cases considered here show that our extended FBM fully recovers already known dispersion relations, including nonlinear ones, for simpler structures. In the next section, we will present the verification of the nonlinear dispersion relations obtained using the EM.

3.2 Exact model

In order to check the agreement between the results of our EM and the previously published results [77] the limiting case of the nonlinear dispersion relation (2.3.43) for the three-layer structure is considered. In a similar manner as for the FBM, in order to transform the four-layer structure from Fig. 2.1 into a three-layer structure, we assume that $L \to 0$. Then Eq. (2.3.37a) simplifies to

$$\phi = \frac{\Psi_+^+ e^{-k_0 q_3 d} + \Psi_-^- e^{k_0 q_3 d}}{\Psi_-^+ e^{k_0 q_3 d} + \Psi_+^- e^{-k_0 q_3 d}}. \tag{3.2.1}$$

As an intermediate step,on the right-hand side of Eq. (2.3.42) both numerator and denominator are divided by ϕ to give

$$E_{x,0}^2 = \frac{(\epsilon_2\beta)^2 \left(\frac{1}{\phi} - 1\right)^2}{(\epsilon_{1,0} q_2)^2 \left(\frac{1}{\phi} + 1\right)^2 + (\epsilon_2\beta)^2 \left(\frac{1}{\phi} - 1\right)^2} E_0^2. \tag{3.2.2}$$

In the next step, the expressions $(1/\phi - 1)$ and $(1/\phi + 1)$ appearing in Eq. (3.2.2) are expanded. Using Eqs. (3.2.1) and (2.3.37b), after lengthy but simple algebra one obtains

$$\frac{1}{\phi} - 1 = 2M\bar{\epsilon}_3[\bar{\epsilon}_3 \sinh(k_0 q_3 d) + \bar{\epsilon}_4 \cosh(k_0 q_3 d)], \tag{3.2.3a}$$

$$\frac{1}{\phi} + 1 = 2M\bar{\epsilon}_3[\bar{\epsilon}_3 \cosh(k_0 q_3 d) + \bar{\epsilon}_4 \sinh(k_0 q_3 d)], \tag{3.2.3b}$$

where $\bar{\epsilon}_k = \epsilon_k / q_k$ (for $k \in \{2, 3, 4\}$) and

$$M = \frac{1}{(\bar{\epsilon}_2 - \bar{\epsilon}_3)(\bar{\epsilon}_3 + \bar{\epsilon}_4) e^{k_0 q_3 d} + (\bar{\epsilon}_2 + \bar{\epsilon}_3)(\bar{\epsilon}_3 - \bar{\epsilon}_4) e^{-k_0 q_3 d}}. \tag{3.2.4}$$

Inserting Eqs. (3.2.3) into Eq. (3.2.2) and defining

$$R = q_4\epsilon_3 \tanh(k_0 q_3 d) + q_3\epsilon_4, \tag{3.2.5a}$$

$$T = q_4\epsilon_3 + q_3\epsilon_4 \tanh(k_0 q_3 d) \tag{3.2.5b}$$

one obtains

$$E_{x,0}^2 = \frac{(\beta\epsilon_3 R)^2}{(\beta\epsilon_3 R)^2 + (q_3\epsilon_{1,0} T)^2} E_0^2. \tag{3.2.6}$$

Equation (3.2.6) is identical to formula (11) in Ref. [77], which was obtained for a three-layer structure with a semi-infinite nonlinear medium. The dispersion relation for the three-layer structure is then obtained by inserting Eq. (3.2.6) into Eq. (2.3.9) and reads

$$(\epsilon_{1,0}\epsilon_3 R)^2 - 2\epsilon_{1,0} (\beta\epsilon_3 R)^2 + \left(\epsilon_{l,1} + \frac{2\alpha_1}{\kappa + 2} E_0^\kappa\right) \left[(\beta\epsilon_3 R)^2 + (q_3\epsilon_1 T)^2\right] = 0 \tag{3.2.7}$$

Equation (3.2.7) is equivalent to Eq. (12) in Ref. [77], which was obtained for a three-layer structure. This proves that in the limiting case our EM for four-layer structures reproduces results for simpler structures. The procedure of transforming Eq. (3.2.7) to obtain two separate dispersion relations, on a linear/nonlinear interface and a linear/linear interfaces ($d \to \infty$), is described in Ref. [77].

Chapter 4

Numerical results

Contents

As it was already mentioned in Section 1.1, theoretical studies of plasmon–solitons or more generally nonlinear localized surface waves started more than 30 years ago with the seminal paper of Agranovich *et al.* [67]. However, no experimental results confirming the existence of these nonlinear waves propagating in metal–nonlinear dielectric structures have been provided. Consequently, from the modeling point of view, the main challenge is to design a feasible structure that enables the experimental realization of plasmon–soliton coupling.

To reach this goal, several conditions must be satisfied simultaneously. Firstly, a structure that supports plasmon–solitons of a solitonic type (with a pronounced soliton peak inside a nonlinear dielectric which facilitates experimentally both its excitation and its discrimination from linear waves) must be found. Secondly, solutions should appear for physically realistic combinations of material parameters, beam power, and nonlinear coefficient. The last, more practical and supplementary requirement is to design a structure in which the plasmon field is accessible both for measurements using the tip of a scanning near-field optical microscope and for potential applications such as sensing [124–130].

This chapter gives a complete description of nonlinear stationary solutions that can be generated in planar structures made of a combination of semi-infinite nonlinear dielectric, metal film, and linear dielectric layers. It starts with the section describing configurations with two layers and finishes with the results for a four-layer structure, which is shown to be the simplest configuration that fulfills all the requirements to facilitate the experimental observation of plasmon–solitons defined above.

4.1 Two-layer configuration

In two-layer configurations (single interface between a nonlinear dielectric and a metal), the only nonlinear solutions that we are able to find using our three models are of the plasmonic type (no pronounced soliton peak in the nonlinear medium). This results are in agreement with the conclusions

drawn by looking at the field shapes obtained using the FBM and the continuity conditions for the tangential electromagnetic field components at the interface. The main results from the FBM for a single-interface configuration are summarized here:

- the field in the nonlinear material is described by the formula (2.1.24a) with the free parameter x_0,
- the field in the metal is given by the exponential function (2.1.24d) (with $L = d = 0$) and decreases to zero as x tends to infinity to satisfy the boundary condition $H_y \xrightarrow{x\to+\infty} 0$,
- in order to obtain the nonlinear dispersion relation we use the conditions for the continuity of the fields at the interface $x = 0$:
  1. for the magnetic field $H_1 = H_4$, so that in Eq. (2.1.24d) $C = H_0$,
  2. for the longitudinal component of the electric field $E_{z,1} = E_{z,4}$, which using Eq. (1.5.2c) is expressed in terms of the x-derivative of H_y and the permittivity of the media:

$$\frac{1}{\epsilon_1}\frac{\mathrm{d}H_1}{\mathrm{d}x} = \frac{1}{\epsilon_4}\frac{\mathrm{d}H_4}{\mathrm{d}x}. \tag{4.1.1}$$

Because the permittivities of the metal and the nonlinear dielectric have opposite signs ($\epsilon_1\epsilon_4 < 0$), from the continuity condition 2 we notice that the derivatives of H_y must have opposite signs at both sides of the interface. From Eq. (2.1.24d), it follows that $(\mathrm{d}H_4/\mathrm{d}x)|_{x=0^+} < 0$. This implies that the derivative on the nonlinear side of the interface has to be positive $(\mathrm{d}H_1/\mathrm{d}x)\,|_{x=0^-} > 0$. By looking at Eq. (2.1.24a) one can see that this condition is fulfilled only if $x_0 > 0$. This allows us to conclude that only the plasmonic-type solutions exist on a single metal/nonlinear dielectric interface.

4.2 Three-layer configuration

In this section, results obtained for three-layer configurations (L is set to 0, see Fig. 2.1) are presented. Firstly, to confirm the validity of our FBM, its results are compared with the results from Ref. [73]. Then the general classification of nonlinear solution types is described and illustrated. Finally, the structure parameter scans are performed in order to find configurations supporting low-power plasmon–solitons.

4.2.1 Comparison between the field based model and older works

In Section 3.1, it was shown that the nonlinear dispersion relation for the four-layer FBM in the limiting cases reproduces analytically several known analytical results including these for the three-layer model proposed in Ref. [73]. In order to check the correctness of the implementation of our FBM, the graphical comparisons between the nonlinear dispersion curves for the three-layer structure presented in Ref. [73] and the results of our modeling are presented. The parameters used in our simulations are identical to those in Fig. 1 of Ref. [73]. The linear part of the nonlinear medium permittivity is $\tilde{\epsilon}_{l,1} = 16 + 0.0096i$, metal permittivity is $\tilde{\epsilon}_3 = -1000 + 160i$, and the linear dielectric permittivity is $\tilde{\epsilon}_4 = 16$. The thickness of the metal film is set to $d = 50$ nm, the wavelength used is $\lambda = 5.5$ μm, and the second-order nonlinear refractive index is $n_2^{(1)} = 10^{-7}$ m^2/W.[1]

Figures 4.1(a) and (c) show the dispersion relation in which the real part of the effective index β is plotted as a function of the power density of the nonlinear wave P_{tot}. The original results from Ref. [73] are depicted by the red solid curve. The results obtained using our FBM for the three-layer structure are presented by the green dashed curve. In our approach, the effective index values were calculated using Eq. (3.1.2) with the definitions given is Section 2.1. The power was calculated using

[1] The value of the second-order nonlinear refractive index used here and in Ref. [73] is extremely high. Typical values of n_2 for highly nonlinear glasses [131–136] or hydrogenated amorphous silicon [137–142] at the telecommunication wavelength are of the order of 10^{-17} m^2/W.

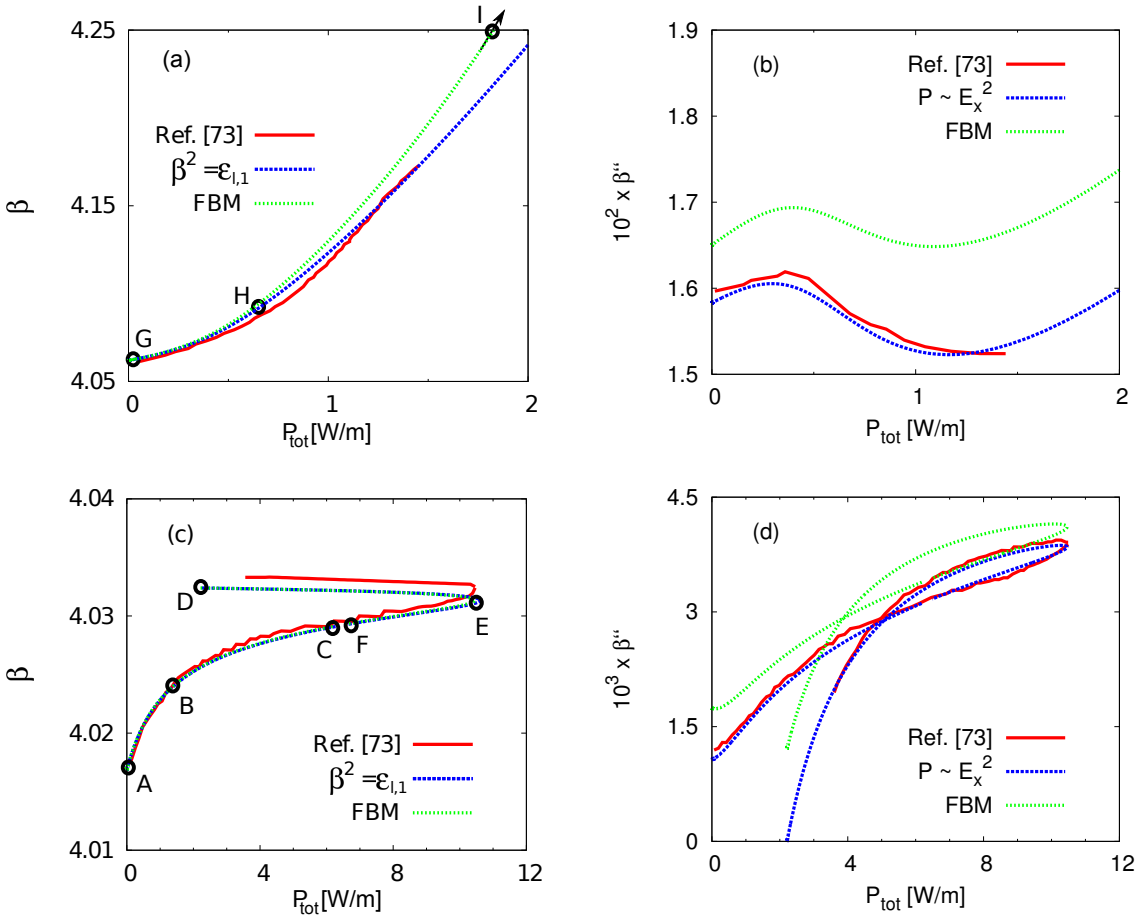

Figure 4.1: Comparison of the original results from the article of Ariyasu *et al.* [73] (Fig. 1 digitized) (red solid curve) and results obtained using our FBM (green dashed curve) with some specific approximations (blue dotted curve) (see the text for more details). (a), (c) Real part and (b), (d) imaginary part of the dispersion relation for the three-layer structure. In panel (c) the green and blue curves overlap perfectly. The labeled points A–I correspond to the field profiles depicted in Figs. 4.2–4.4. Point I lays out of the plotting range (see Section 4.2.2 for explanation).

the approximated analytical formulas derived in Section 2.1.4. The blue dashed curves depict the results obtained using our FBM using some special assumptions discussed later, while commenting on the results.

The plot presenting dispersion curves is separated into two regions. Figure 4.1(a) shows the high-index branch of plasmon–solitons and Fig. 4.1(b) shows the low-index branch. Here we will not discuss in detail the nature and the behavior of the dispersion curves. The detailed discussion will be presented in Section 4.2.2. Here we are interested only in the agreement between the numerical results of our FBM and the results presented in Ref. [73].

In Fig. 4.1, we observe that for the low effective index branch the two curves are in relatively good agreement. On the other hand, for the high effective index branch small discrepancy between the results appears. Two reasons explain the differences between these curves. Firstly, a different form of the nonlinear permittivity tensor is used in Ref. [73] as discussed in Sections 2.1.1 and 2.2. As a consequence, the FBM uses the values of the effective nonlinear function $a(x)$ in Eq. (2.1.7), whereas in Ref. [73], the value $a^{(s)}(x)$ is used [see Eq. (2.2.9) and compare with α' defined in Eq. (4b) in Ref. [73]]. The ratio of the two nonlinear functions is equal to β^2/ϵ_1 and is low for the parameter range, where the effective index is close to the linear refractive index of the nonlinear material and it becomes larger for higher values of the effective index. For this reason, we observe a good agreement between the red and green curve for the solutions where $\beta^2 \gtrapprox \epsilon_1$ [see Fig. 4.1(c)] and a worse agreement for

higher values of β [Fig. 4.1(a)]. This is in full agreement with the explanation presented at the end of Section 2.1.1. Secondly, a closer examination of Eq. (4b) and Eqs. (9)–(11) in Ref. [73] reveals that to compute the power density P_{tot}, the authors made the approximation $\beta^2 = \epsilon_{l,1}$. To reproduce the original results provided in Fig. 1 in Ref. [73] this approximation for power calculations is used in our model for the test purpose. The corresponding blue dotted curve in Fig. 4.1(a) is closer to the original results than the green curve obtained using our full FBM that uses the expressions for power described in Section 2.1.4 without any additional assumptions.

Figures 4.1(b) and (d) show the comparison of the original results from Ref. [73] and our results for the dependency of the imaginary part of the effective index β'' as a function of the power density. The results of our FBM were obtained using Eq. (2.1.73) and are presented by a green dashed curve. This curve lays slightly above the original results from Ref. [73] (red solid curve). The comparison of the formulas used to calculate losses {Eq. (8) in Ref. [68] and Eq. (2.1.73) for our formulation} shows that losses are calculated in different ways. In Ref. [73], authors use Eq. (8) from Ref. [68], where losses are proportional to the product of the imaginary part of permittivity with the power P in each layer ($\beta'' \propto \int \epsilon'' P dx$). The power is proportional to the Pointing vector and in the frame of a linear approximation $P \propto E_x^2$. In our formulation [Eq. (2.1.73)], the losses [green curve in Figs. 4.1(b) and (d)] depend on both components of the electric field [$\beta'' \propto \int \epsilon''(E_x^2 + E_z^2)dx$]. If a formulation in which the losses are proportional only to the transverse field component is used in our FBM, a very good agreement with the original results is reached [see the blue dotted curve in Figs. 4.1(b) and (d)].

Even if small numerical discrepancies between our improved approach and the original results of Ariyasu *et al.* appear due to different approximations used, they are fully understood. Our extended FBM is able to reproduce the results published in Ref. [73] with a good agreement.

4.2.2 Classification of the nonlinear wave types

In this section, a classification of the types of solutions that exist in the three-layer structures is presented. It is useful for the remaining part of this work to classify and name different types of solutions as they will be similar in four-layer configurations. In Fig. 4.1, nine points were labeled from A to I in order to describe the type and the transformation of solutions along the nonlinear dispersion curves. The magnetic field profiles corresponding to these points are shown in Figs. 4.2–4.4.

Using the analytical considerations presented in Section 3.1.3, we have already concluded that for $x_0 \to +\infty$, the solutions correspond to the limiting case of the linear structure. In the linear symmetric three-layer IMI structure, two solutions exist: a symmetric (long range) plasmon and an antisymmetric (short range) plasmon [55, 60, 64]. Points A and G were obtained for $x_0 = \lambda = 5.5$ μm and the corresponding solutions are close to the linear ones. For both solutions the power density is relatively low $P_{\text{tot}} < 0.1$ W/m (this type of solution is obtained for even lower powers if one selects larger values of x_0). The corresponding field profiles resemble the linear solutions. Figures 4.2(a), (d) that correspond to point A present electromagnetic field profiles that are very close to the symmetric linear plasmon. Figures 4.4(a), (d) that correspond to point G show electromagnetic field profile very similar to the antisymmetric linear plasmon.

In the following, the field transformation along the dispersion curves is described in detail. At first, the transformation of the symmetric plasmonic-type solutions, located at the lower branch of the dispersion curve, is studied. For $x_0 = 5.5$ μm field profiles represented in Figs. 4.2(a), (d) and corresponding to point A in Fig. 4.1 are obtained. Decreasing the value of x_0 to 1 μm (all other parameters being identical) we obtain the field profiles corresponding to the point B [see Figs. 4.2(b), (e)]. The power density of this nonlinear wave is $P_{\text{tot}} \approx 2$ W/m and the field profiles still resemble the symmetric linear plasmon but the field is now asymmetric and the energy is more localized on the interface between the metal film and the linear dielectric. Upon further decrease of the value of x_0 to 0.1 μm (point C) the power density of the solution increases to ≈ 5.5 W/m and the field profiles become even more asymmetric. The electromagnetic field profiles corresponding to point C are shown in Figs. 4.2(c), (f). The solutions described above are referred as symmetric-like nonlinear plasmons.

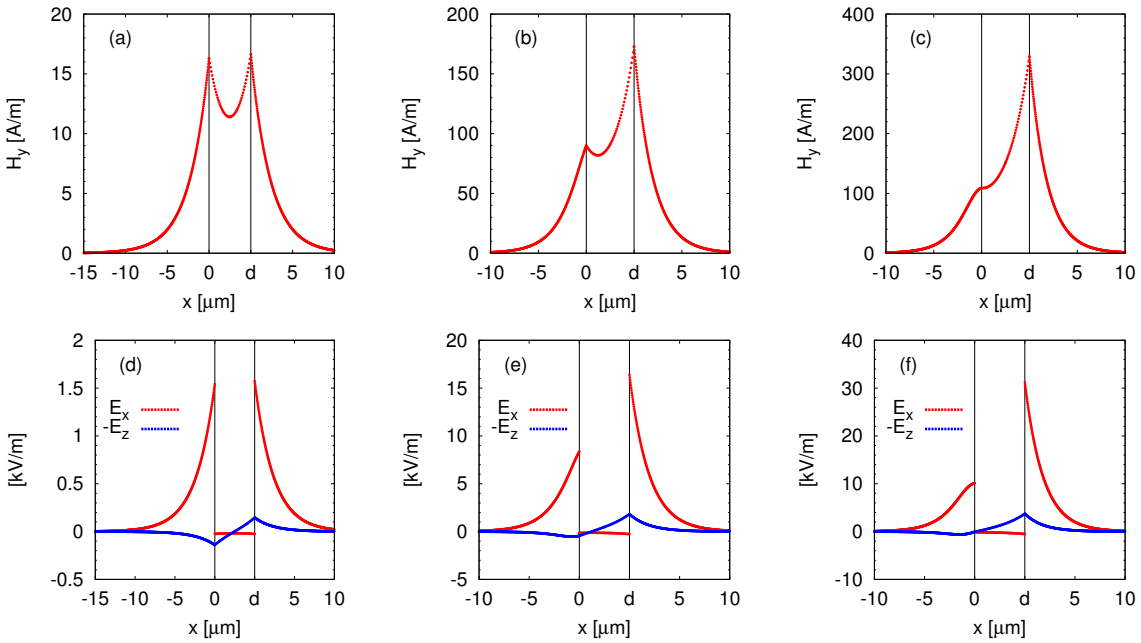

Figure 4.2: Profiles of (a)–(c) magnetic field component H_y and (d)–(f) electric field components E_x and $-E_z$ for symmetric-like nonlinear plasmons in the three-layer structure described in Section 4.2.1 corresponding to points A–C indicated on the dispersion plot in Fig. 4.1. The columns correspond to different values of x_0: the first column to 5.5 μm (point A), the second column to 1 μm (point B), the third column to 0.1 μm (point C). In all the figures showing field profiles in this chapter, the x coordinate inside the thin intermediate films are not at the same scale as those used in the other layers for a better visibility of the field behavior. In this figure, the x coordinate inside the thin metal film is magnified 100 times.

When x_0 becomes negative, a new class of solutions appears, for which the local magnetic field maxima are located both at the interface between the metal film and the linear dielectric and inside the nonlinear medium. Upon the decrease of the x_0 parameter down to -0.1 μm, the power density still increases [to around 7.5 W/m corresponding to point F for which the field profiles are presented in Figs. 4.3(c), (f)] and reaches its maximum at the point E [see Figs. 4.3(b), (e)] for $x_0 = -1$ μm. Further reduction of x_0 leads to the decrease of the total power density ($P_{\text{tot}} \approx 2.5$ W/m for point D corresponding to $x_0 = -5.5$ μm). Point D, for which the field profiles are shown in Figs. 4.3(a), (d), lays close to the end of the branch corresponding to $x_0 \to -\infty$ associated with the isolated classical soliton that does not interact with the metal film.

Even though the field profiles corresponding to points C [Figs. 4.2(c), (f)] and F [Figs. 4.3(c), (f)] at the first glance look almost identical, there is an important qualitative difference between them. On one hand, profile corresponding to point C ($x_0 = 0.1$ μm) is classified as plasmonic-type solution because there is no field maximum in the nonlinear layer. On the other hand, profile F ($x_0 = -0.1$ μm) does have a local maximum in the nonlinear layer (located close to the metal interface) and therefore it belongs to another class of solutions.

For all the solutions presented in Fig. 4.3, the peak amplitude of the solitonic part (in the nonlinear dielectric) remains at approximately the same level and only the maximum of the plasmon field on the metal/linear dielectric interface changes with the decrease of x_0 value. All the solutions shown in Fig. 4.3 will be called solitonic-type solutions.

It is worth noting that, the solitonic-type solution can not be obtained at any desired power density. Following the dashed green curve in Fig. 4.1(c) and knowing the field profiles one can see that for power densities between 6.5 W/m and 10.5 W/m two solitonic-type solutions with different x_0 correspond to one power density. For power densities between 2.5 W/m and 6.5 W/m and for a maximum power

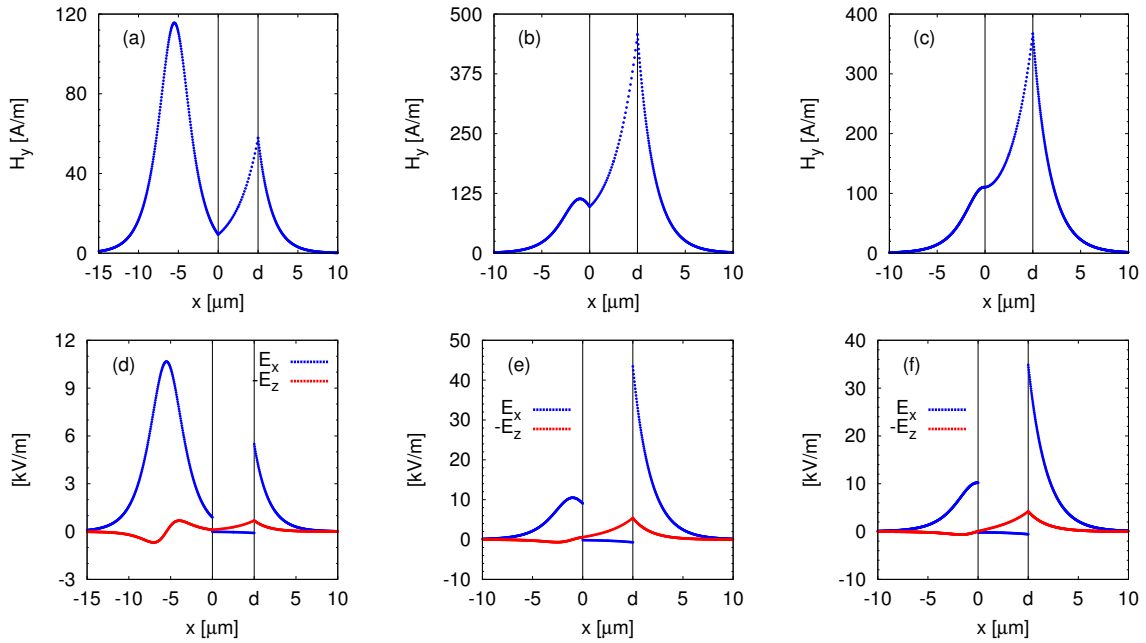

Figure 4.3: Profiles of (a)–(c) magnetic field component H_y and (d)–(f) electric field components E_x and $-E_z$ for solitonic-type solutions in the three-layer structure described in Section 4.2.1 corresponding to points D–F indicated on the dispersion plot in Fig. 4.1. In this figure, the x coordinate inside the thin metal film is magnified 100 times. The columns correspond to different values of x_0: the first column to -5.5 μm (point D), the second column to -1 μm (point E), the third column to -0.1 μm (point F).

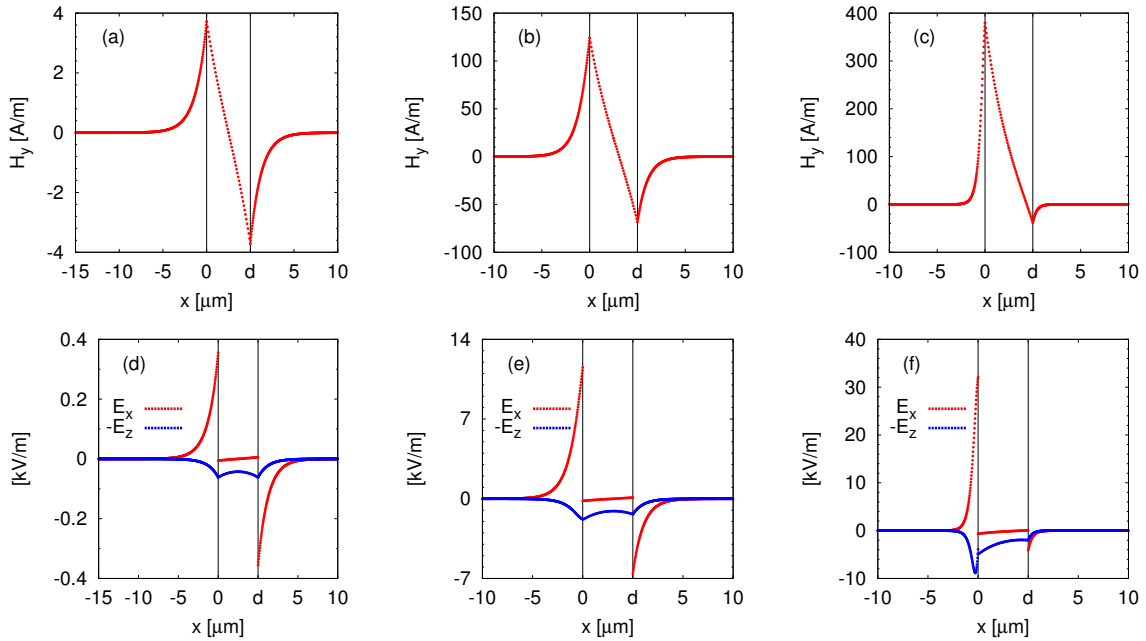

Figure 4.4: Profiles of (a)–(c) magnetic field component H_y and (d)–(f) electric field components E_x and $-E_z$ for antisymmetric-like nonlinear plasmons in the three-layer structure described in Section 4.2.1 corresponding to points G–I indicated on the dispersion plot in Fig. 4.1. In this figure, the x coordinate inside the thin metal film is magnified 100 times. The columns correspond to different values of x_0: the first column to 5.5 μm (point G), the second column to 1 μm (point H), the third column to 0.1 μm (point I).

density of 10.5 W/m there is only one solitonic-type solution corresponding to each power density. Below 2.5 W/m and above 10.5 W/m no solitonic-type solution exists.

Finally, the transformation of solutions laying along the upper branch of the dispersion relation [see Fig. 4.1(a)] is described. The field profiles corresponding to this branch are shown in Fig. 4.4. The branch starts with the solution described above, very similar to the antisymmetric linear plasmon [point G, at which the field profiles are presented in Figs. 4.4(a), (d) corresponding to $x_0 = 5.5$ μm]. Decreasing the value of x_0 to 1 μm, results in the field profiles corresponding to point H shown in Figs. 4.4(b), (e). The field profiles of this solution resemble the antisymmetric linear solution but are distorted. The field distribution is asymmetric and this time the field is more localized at the metal/nonlinear dielectric interface (contrarily to the case of symmetric type solutions, where the field tends to localize on the opposite metal interface). Decreasing x_0 even further, down to 0.1 μm, we obtain the field profiles corresponding to point I in Fig. 4.1 presented in Figs. 4.4(c), (f). Here the field is almost entirely localized at the metal/nonlinear dielectric interface and therefore it is even more asymmetric. The corresponding power density is 2.5 W/m and the effective index is so high ($\beta \approx 4.57$) that it is outside of the plotting range in Fig. 4.1(a). The solutions presented in Figs. 4.4 will be called antisymmetric-like nonlinear plasmons.

4.2.3 Low-power solution search

The simplest structures in which it is possible to obtain the plasmon–solitons of the solitonic type are three-layer structures, as it has been shown in Sections 4.1 and 4.2.2. The study of solitonic type plasmon–solitons presented in Ref. [73] deals only with configurations, where the linear parts of the permittivities of linear and nonlinear dielectrics are equal. Below a more general case is studied, in which a permittivity contrast between the linear and the nonlinear dielectric is introduced. For this study the FBM limited to three-layers (L is set to 0 and only layers 1, 3 and 4 are present as described in Section 3.1) is used. The configurations where $\epsilon_{l,1} \geqslant \epsilon_4$ are chosen to guarantee that the solutions are localized at the interface between layers 3 and 4 as $\beta \geqslant \sqrt{\epsilon_{l,1}}$ [see Eqs. (2.1.7b), (2.1.13) and (2.1.24d)]. From the practical point of view, this condition can also be justified by looking at the properties of typical nonlinear materials. For the glasses it is known that, in most cases, the second-order nonlinear refractive index n_2 increases with the increase of the linear refractive index [132, 135]. This justifies our choice to consider a linear permittivity of the linear layer to be lower than that of the nonlinear layer.

In order to obtain color maps in this section and in Section 4.3, the scans over parameters were performed using the FBM in such a way that, only solutions with the effective index $\beta \in [\sqrt{\epsilon_{l,1}}, 4\sqrt{\epsilon_{l,1}}]$ were sought. For lower effective indices no localized solution exists as pointed out at the end of Section 2.1.2 (see discussion on Page 25) and higher effective indices are not interesting for our purpose, because the corresponding solutions have extremely high power density and the nonlinear index modification is too high to be physically meaningful.

Figure 4.5(a) shows the dependency of the total number of solutions on the parameter x_0 and on the linear external dielectric refractive index $\sqrt{\epsilon_4}$ (other parameters of the structure are indicated in the figure caption). For the symmetric structure ($\sqrt{\epsilon_4} = \sqrt{\epsilon_{l,1}} = 2.4$) (as discussed in Section 4.2.2) and for quasi-symmetric configurations with low refractive index contrast $\Delta\epsilon = \epsilon_{l,1} - \epsilon_4 \lesssim 0.16$ one solitonic-type solution (region A) and two (a symmetric-like and an antisymmetric-like) plasmonic solutions (region B) exist. Upon the decrease of the linear layer refractive index $\sqrt{\epsilon_4}$ (increasing the index contrast between the nonlinear and the external dielectric) a narrow region (C) with two solitonic-type solutions appears. These solutions do not exist for negative values of x_0 close to zero. Further decrease of the linear layer refractive index causes both solitonic-type solutions to vanish around $\sqrt{\epsilon_4} = 2.22$. In the case of plasmonic-type solutions ($x_0 > 0$), the decrease of the linear layer refractive index causes symmetric-like solution to vanish (at a cut-off index value of $\sqrt{\epsilon_4} \approx 2.24$) and only the antisymmetric-like solution remains (region D) (even for $\sqrt{\epsilon_4} = 1$ which is not shown on this plot).

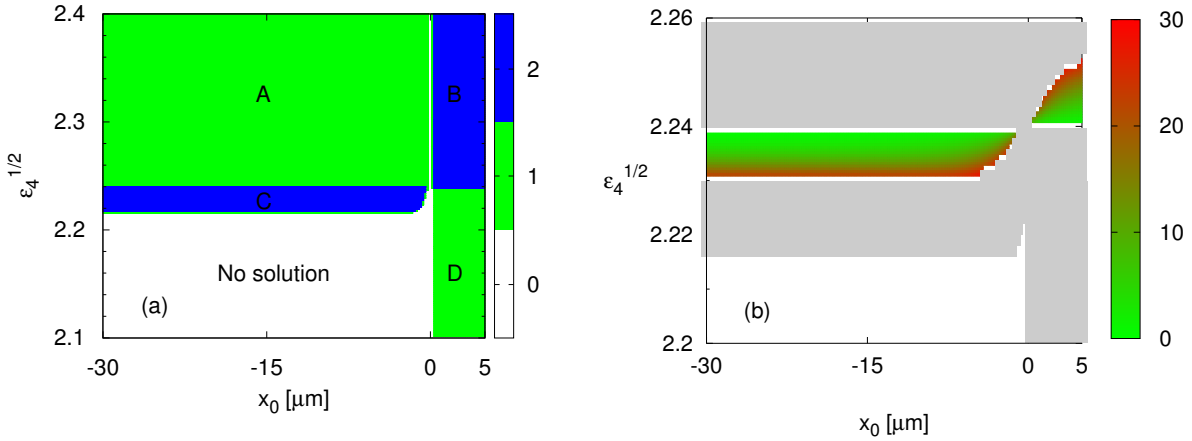

Figure 4.5: (a) Number of solutions as a function of x_0 parameter and of the external linear layer refractive index $\sqrt{\epsilon_4}$. (b) Peak power [GW/cm^2] for the low-power solutions close to the cut-off value of $\sqrt{\epsilon_4}$. In this and in all the following peak power color maps in this paper, only solutions with peak power below 30 GW/cm^2 are plotted. The existence of solutions with higher peak power is marked with the gray color. White color denotes regions with no solutions. The parameters of the structure are: $\epsilon_{l,1} = 2.4^2$, $n_2^{(1)} = 10^{-17}$ m^2/W, $d = 40$ nm, $\epsilon_3 = -20$, and $\lambda = 1.55$ μm.

Figure 4.5(b) presents the peak power of the solutions in a transition region close to the cut-off value of the linear layer refractive index. The maximum peak power was set to 30 GW/cm^2. This value of the peak power, taking into account the nonlinearity parameter used $n_2^{(1)} = 10^{-17}$ m^2/W, involves a maximum nonlinear index modification $\Delta n \leqslant 3 \cdot 10^{-3}$. The value of n_2 used here is typical for chalcogenide glasses [131–136] or for hydrogenated amorphous silicon which seems to be a promising material for nonlinear integrated optics [137–142]. In Fig. 4.5(b), it can be observed that the low-power solutions exist only in a very narrow range of $\sqrt{\epsilon_4}$ values. The value of the linear layer refractive index $\sqrt{\epsilon_4}$ has to be chosen with the precision of 0.01 in order to ensure the peak power below 30 GW/cm^2. The solitonic-type solutions have their lowest peak powers slightly below the cut-off index. On the contrary, the plasmonic-type solutions have their lowest peak powers above this value, as it is illustrated in Fig. 4.5(b).

The study presented in Fig. 4.5 confirms and completes the analysis of the number of solutions in various structures presented in Table I in Ref. [73]. We confirm the result presented in line 5 of table I in Ref. [73] for symmetric configurations ($\epsilon_4 = \epsilon_{l,1}$) and complete the results presented in this table by including the results for a more general case of asymmetric three-layer structures ($\epsilon_4 \neq \epsilon_{l,1}$).

Figure 4.6 shows the comparison of the magnetic field H_y and of the electric field components E_x and E_z for the solitonic-type solutions that appear in the three-layer structure for identical value of x_0 [region C in Fig. 4.5(a)]. Here the parameters are $\epsilon_4 = 2.23^2$ and $x_0 = -1$ μm. The solution with the lower effective index β has a lower peak amplitude of the solitonic part than the one of the higher effective index solution. The solitonic part is broader and the plasmonic part peak amplitude is slightly higher in the former case. Looking at Fig. 4.6 we also conclude that, the ratio between the electric field components $\max(|E_x|)/\max(|E_z|)$ in the nonlinear dielectric layer is higher for low-power solutions (with low β values and broad solitonic peaks) than for the solutions with higher power. This fact confirms the validity of the approximation made in the FEM on the nonlinear Kerr term. In the frame of the FEM, we have assumed that only transverse electric field component E_x contributes to the nonlinear permittivity change [see Eq. (2.1.5)]. As it can be inferred from Fig. 4.6, this assumption is well satisfied for low-power solutions.

Here the influence of the metal permittivity changes on the behavior of the solitonic-type solutions in three-layer structures is analyzed. The center of the solitonic part is set to be at the distance of 10 wavelengths from the metal film ($x_0 = -15.5$ μm). The number of solutions as a function of the metal

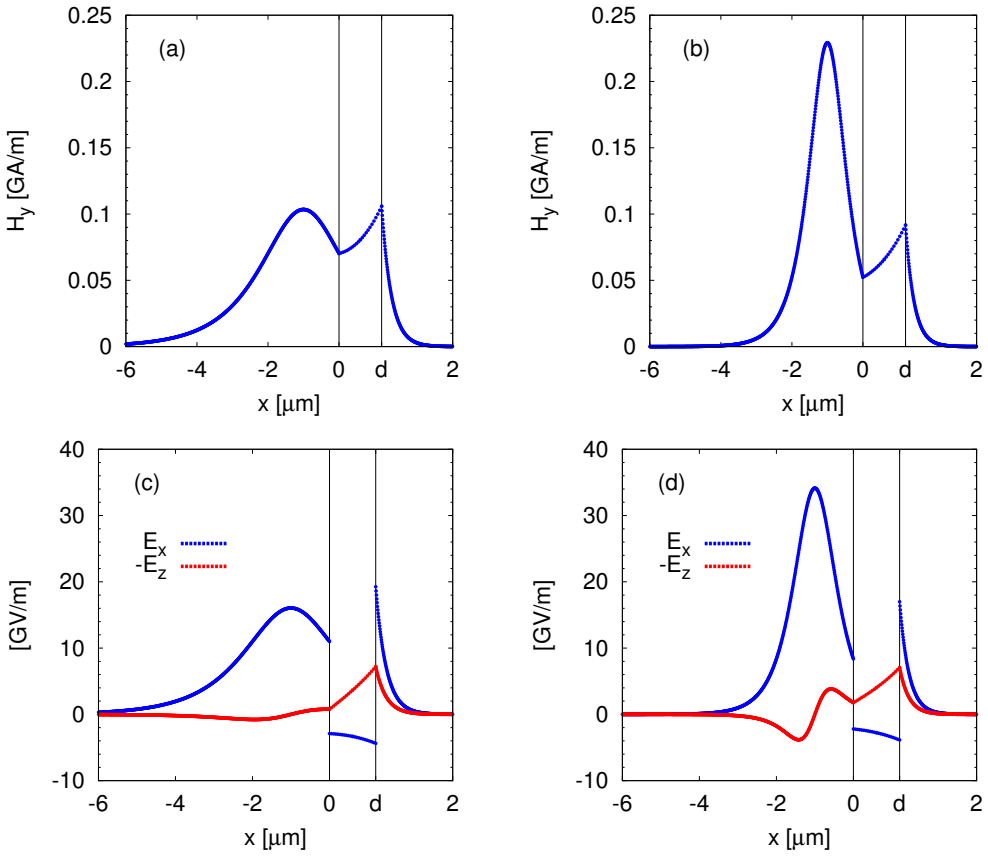

Figure 4.6: Comparison of the field profiles (a) $H_y(x)$ and (b) $E_z(x)$ for the two plasmon–solitons existing in region C in Fig. 4.5(a) for identical x_0 value. The x coordinate inside the thin metal film is magnified 30 times.

permittivity and of the linear dielectric permittivity is studied. From Fig. 4.7(a) it can be seen that two effects occur with the increase (decrease of the absolute value) of the metal permittivity. Firstly, the index contrast between layers 1 and 4 for which solutions can be found increases. Secondly, the allowed external dielectric permittivity range where two solitonic-type solutions occur for one value of x_0 expands. There is also a cut-off metal permittivity above which no solution exists. This cut-off occurs when $|\epsilon_3| \approx \epsilon_4$. From Fig. 4.7(b) that shows the peak power for low-power plasmon–solitons, it can be seen that the low-power solutions lay in a very narrow region close to the line separating regions with one and two solutions.

Summarizing the result of this section, we observe that asymmetric structures (with $\epsilon_{l,1} > \epsilon_4$) are able to support the solitonic-type solutions at much lower powers than symmetric structures. However, in order to obtain really low power densities the index contrast between the two dielectrics has to be precisely chosen [see Figs. 4.5(b) and 4.7(b)]. The asymmetric three-layer configurations fulfill two out of three conditions set at the beginning of this section: they support both plasmonic- and solitonic-type plasmon–solitons and it is possible to obtain low-power solitonic-type solutions. However, these solutions are obtained for configurations in which the linear medium refractive index is close to the linear part of the nonlinear material refractive index. Highly nonlinear glasses [131–136] and hydrogenated amorphous silicon [137–142] that can be used as a nonlinear medium, have high refractive index $\sqrt{\epsilon_{l,1}} > 2$. Therefore, the linear dielectric has to be also a high-index material. Consequently, the last goal can not be fulfilled — it is not possible to access or measure directly the plasmonic part of the solution if the external layer is filled with a solid. In order to reach this goal, a configuration where the linear refractive index of the external layer is low enough $\sqrt{\epsilon_4} \lesssim 1.3$ needs to be found, so that this external medium can be e.g., water or air. This last problem is solved by the use of four-layer structures, as shown in Section 4.3.

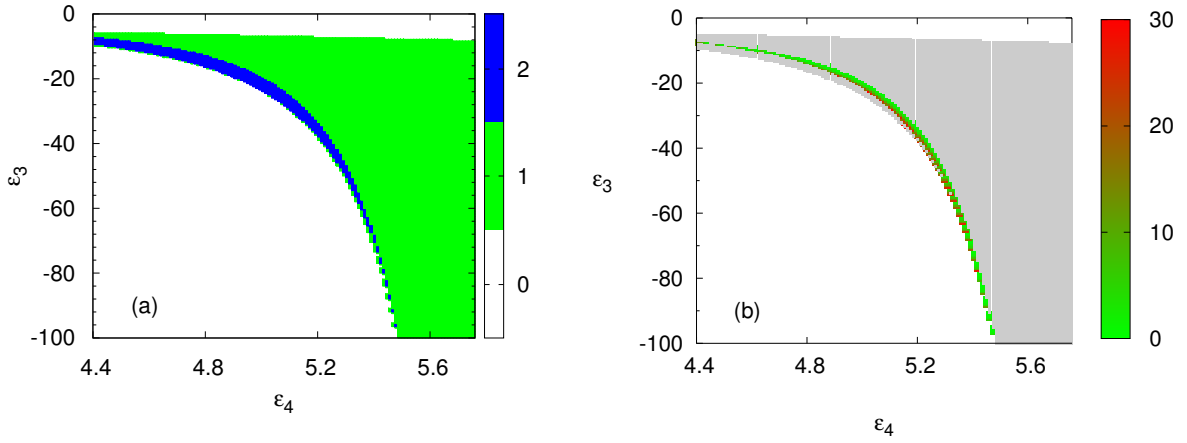

Figure 4.7: (a) Number of solitonic-type solutions in a three-layer structure with identical parameters as in Fig. 4.5 but for a fixed $x_0 = -15.5$ μm, as a function of the metal permittivity ϵ_3 and of the linear dielectric permittivity ϵ_4. (b) Peak power [GW/cm^2] for the low-power solutions.

4.3 Four-layer configuration

In this section, the results obtained using our three models for four-layer configurations are presented. The four-layer configuration is built by extending a three layer configurations discussed in Section 4.2. An additional thin layer of a linear dielectric is introduced between the nonlinear medium and the metal film. This layer will be called a buffer layer. At the beginning, we show and analyze, for the first time, typical dispersion curves of four-layer configurations. Then the comparison between the results obtained using our three models is performed. The very good agreement between these results confirms the validity of our models. Afterwards, the analysis of the structure parameters is performed and the ranges where low-power plasmon–solitons exist are identified. Later, the advantages of the four-layer structures over three-layer structures are discussed. Finally, the influence of the two geometric parameters of the structure (metal thickness d and the buffer layer thickness L — see Fig. 2.1) on the plasmon–solitons properties is presented.

4.3.1 Nonlinear dispersion diagrams

Here we will present for the first time the dispersion relations for the four-layer structure. The four-layer structure with parameters $\tilde{\epsilon}_{l,1} = 2.47^2 + 10^{-5}i$, $n_2^{(1)} = 10^{-17}$ m^2/W (chalcogenide glass) [131–136], $\tilde{\epsilon}_2 = 1.44^2 + 10^{-5}i$ (silica), $\tilde{\epsilon}_3 = -96 + 10i$ (gold) [143–145], $\tilde{\epsilon}_4 = 2.47^2 + 10^{-5}i$, $L = 15$ nm, $d = 40$ nm, and $\lambda = 1.55$ μm is considered. In Fig. 4.8, the dispersion diagrams $\beta(P)$ and $\beta''(P)$ for this configuration are presented.

Firstly, we will analyze the plots of the real part of the effective index presented in the first column in Fig. 4.8. There are two separate branches on these plots: the low-effective-index branch build uniquely of the solitonic-type solutions and the high-effective-index branch that has a plasmonic character in its bottom part and it changes its character to solitonic in its upper part.

At first, we discuss the high-effective-index branch. It starts in the linear regime [point Pa[2] in Fig. 4.8(c)] with the plasmonic-type solution [P-type, red dotted curve in Fig. 4.8(c)]. The corre-

[2]The names of the pints in Fig. 4.8 are constructed using the following rules. The first capital letter denotes the type of the solution (P for plasmonic and S for solitonic). For the plasmonic solutions there is only one branch and only one solution correspond to a given value of x_0. Therefore, we second letter denotes the solutions obtained for different x_0 values. There are two solitonic branches. The points laying on the high-effective-index solitonic branch are denoted by the second letter h. On this branch there is only one solution corresponding to one value of x_0. The third letter denotes solutions obtained for different x_0 values. On the low-effective-index solitonic branch (second letter l) there are two solutions that correspond to one value of x_0. They are denoted by a number. The letter on the last position denotes solutions obtained for different x_0 values.

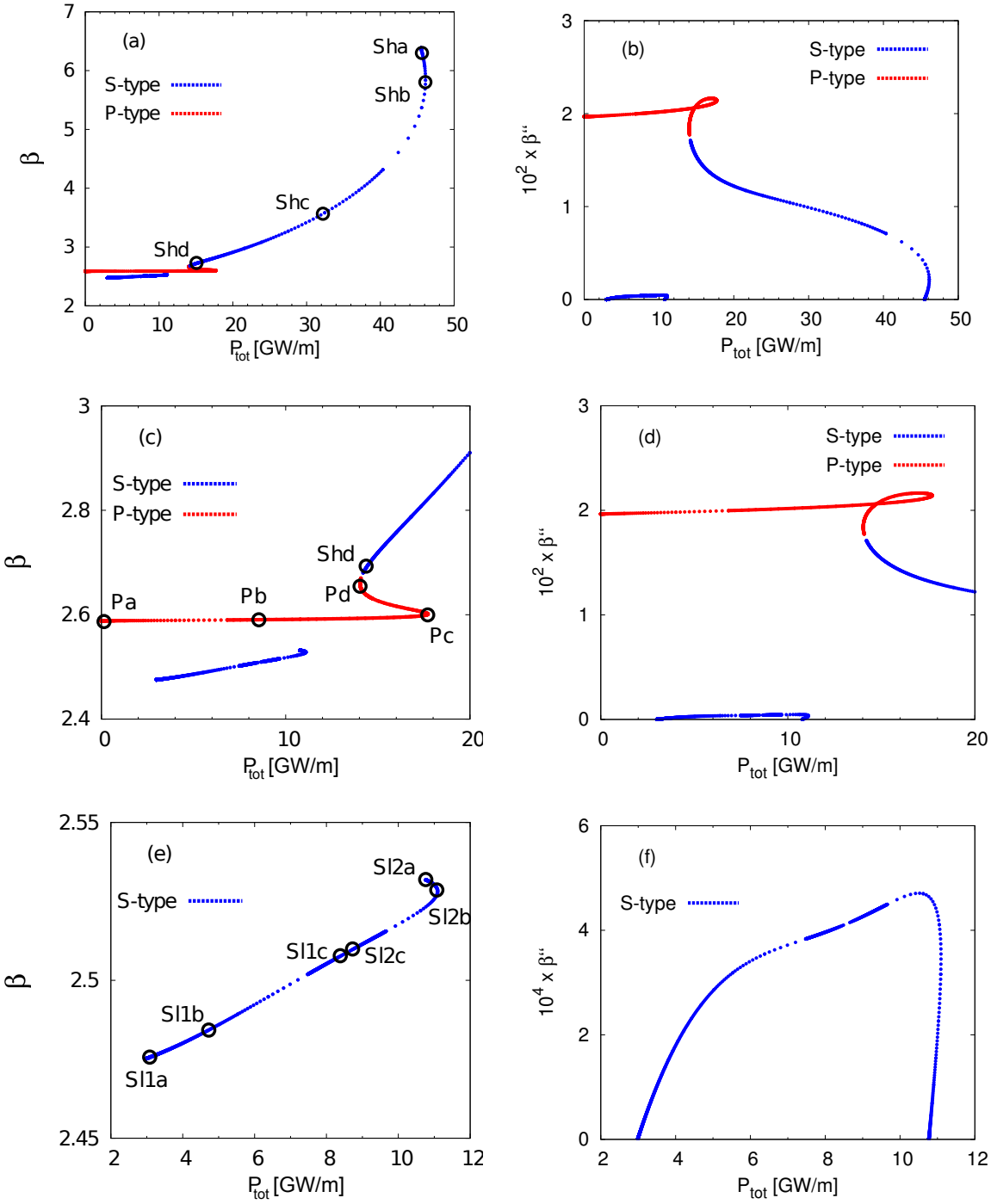

Figure 4.8: Nonlinear dispersion diagrams for the (a), (c), (e) real and (b), (d), (f) imaginary parts of the effective index in the four-layer structure with $\epsilon_4 = \epsilon_{l,1} = 2.47^2$ as a function of power density P_{tot}. Plasmonic-type solutions are denoted by a red dotted line and solitonic-type solutions by a blue dotted line. Full range of effective indices and power densities is presented in panels (a) and (b). Panels (c) and (d) present zooms on the plasmonic branch and its solitonic continuation. Panels (e) and (f) present zooms on the low-effective-index solitonic branch. The labeled points indicated on the dispersion curves correspond to the field profiles presented in Figs. 4.10–4.11.

sponding magnetic field profile is shown in Fig. 4.9(a) and the x_0 parameter for this solution in equal to 5 μm. As the four-layer structures studied in this thesis are asymmetric, we will no longer distinguish between the symmetric-like and antisymmetric-like plasmonics-type solutions. The field

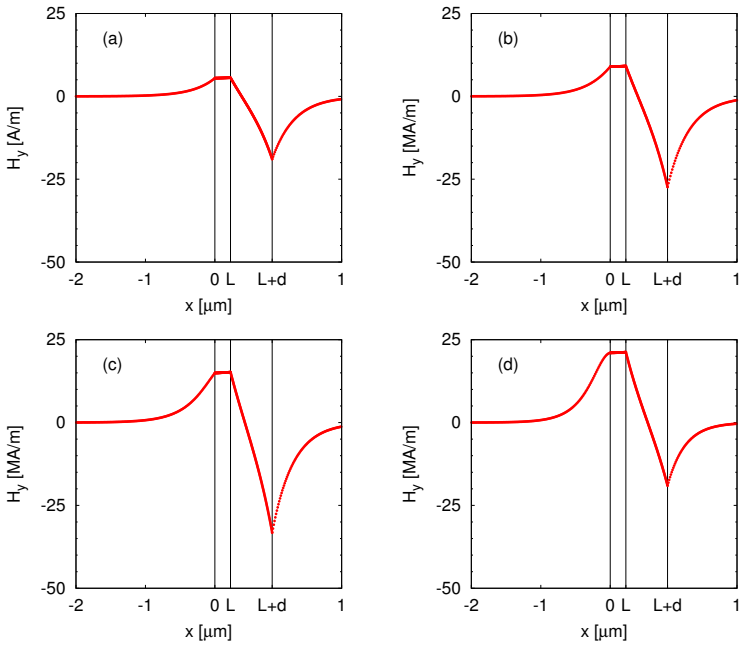

Figure 4.9: Magnetic field profiles corresponding to the plasmonic-type solutions marked by points (a) Pa, (b) Pb, (c) Pc, and (d) Pd in Fig. 4.8(c). The x coordinate inside the thin films is magnified 50 times.

profile presented in Fig. 4.9(a) is qualitatively closer to the antisymmetric-like plasmonic solution. This fact is in agreement with the observation made in Section 4.2.3 where, upon the increase of the asymmetry of the three-layer structure, we observed the symmetric-like plasmonic solution to vanish (only asymmetric-like plasmonic solution remained). With the increase of the power, the propagation constant of the plasmonic-type solution increases slowly and its magnetic field amplitude on the metal/external linear dielectric interface increases [see point Pb in Fig. 4.9(a) and the corresponding field profile in Fig. 4.9(b)]. At point Pb, the value of x_0 was set to 400 nm. The highest power density of the plasmonic-type solution is equal to $P_{\text{tot}} \approx 18$ GW/m and is reached at point Pc for $x_0 = 184$ nm. The corresponding field profiles are shown in Fig. 4.9(c). Further increase of the propagation constant is accompanied by the decrease of the power density until $P_{\text{tot}} \approx 14$ GW/m, where another turning point occurs. The field profile at the second turning point (denoted as Pd for which $x_0 = 11$ nm) is presented in Fig. 4.9(d). We notice that during the field transformation between points Pc and Pd the field amplitude at the nonlinear interface $x = 0$ increases and the field amplitude at the interface between the metal and the external linear dielectric $x = L + d$ decreases. The combination of these two effects accounts for the decrease in the total power of the solution at point Pd.

For effective indices slightly above the second bend denoted by point Pd, the solution changes its type to solitonic (S-type, blue dotted curve in Fig. 4.8). Field profile corresponding to point Shd is presented in Fig. 4.10(d) and the soliton peak in the nonlinear medium of this solution is located at $x_0 = -11$ nm. The solitonic-type solution increases its power density with the increase of β [through point Shc, see Fig. 4.10(c) for the corresponding field profile] until it reaches the maximum of the power density at $\beta \approx 6$ and $P_{\text{tot}} \approx 47$ GW/m [point Shb for which $x_0 = -70$ nm and the corresponding field profile is presented in Fig. 4.10(b)]. Above this point, the power decreases again with the increase of the effective index. The solitonic branch ends at the point where $\beta \approx 6.5$ and $P_{\text{tot}} \approx 45$ GW/m which correspond to a soliton that does not interact with the structured interface ($x_0 \to -\infty$). Point Sha is located close to the end of the dispersion curve, even if the peak of the solitonic part of this solution in only at $x_0 = -150$ nm. Because the high effective index branch has very high power densities, the solutions lying on this branch have very narrow solitonic parts. Therefore, even for $x_0 = -150$ nm, the interaction with the metal layer is weak and this solution resembles the bulk soliton for which $x_0 \to -\infty$.

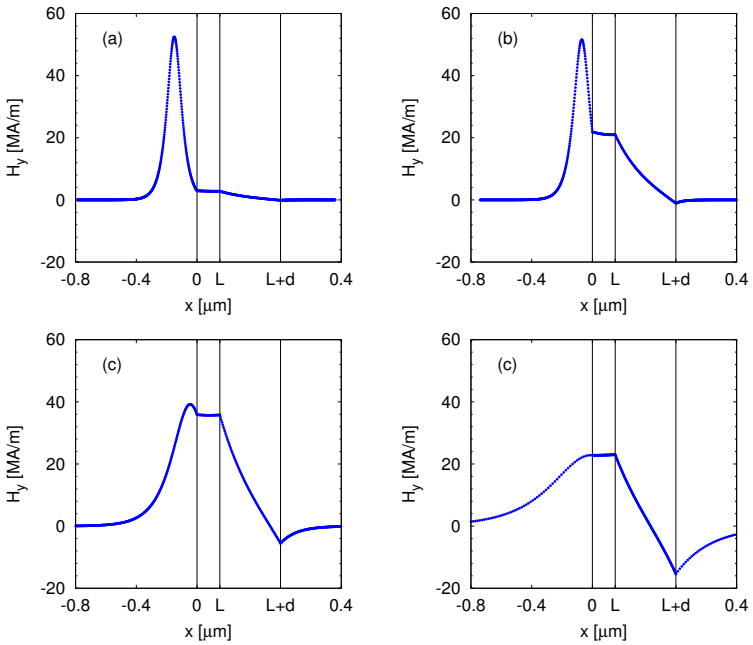

Figure 4.10: Magnetic field profiles corresponding to the high-index solitonic-type solutions marked by points (a) Sha, (b) Shb, (c) Shc, and (d) Shd in Fig. 4.8(a). The x coordinate inside the thin films is magnified 50 times.

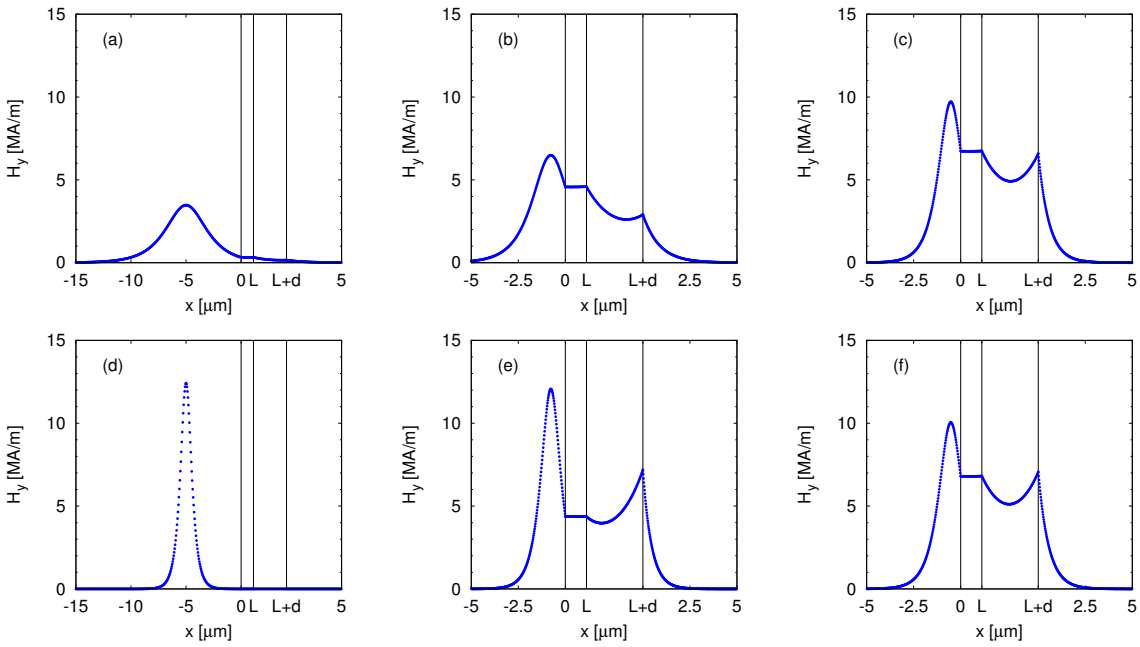

Figure 4.11: Magnetic field profiles corresponding to the low-index solitonic-type solutions marked by points (a) Sl1a, (b) Sl1b, (c) Sl1c, (d) Sl2a, (e) Sl2b, and (f) Sl2c in Fig. 4.8(e). The x coordinate inside the thin films is magnified 50 times.

The low-effective-index branch of the dispersion diagram is purely of the solitonic type [see Figs. 4.8(a) and (e)]. This branch can also be separated in two parts in terms of the x_0. To each value of x_0 correspond two different solutions laying on this low-effective-index branch. We start with the solutions weakly interacting with the metal interface. These solutions are labeled Sl1a and Sl2a and are shown in Figs. 4.11(a) and (d), respectively. For both of them $x_0 = -5$ μm. We notice that the solution with low power density $P_{\text{tot}} \approx 3$ GW/m and low effective index value ($\beta \approx 2.475$) has much

broader solitonic peak and therefore interacts more strongly with the metal interface than the high power density solution Sl2a. Both solutions lay close to the ending points of the low-effective-index branch that correspond to $x_0 \to -\infty$. Increasing the value of x_0 to -770 nm causes the increase of the power density on both parts of the branch. At $x_0 = -770$ nm we obtain points Sl1b and Sl2b for which the corresponding field profiles are shown in Figs. 4.11(b) and (e), respectively. Point Sl2b represents the solution with the highest power density attainable on the low-effective-index solitonic branch. Increasing x_0 even more, to $x_0 = -530$ nm causes the increase of the power density on the lower part of the solitonic-type branch (transformation from Sl1b to Sl1c) and the decrease of the power density on the upper part of the solitonic branch (transformation from Sl2b to Sl2c). Field profiles corresponding to points Sl1c and Sl2c are shown in Figs. 4.11(c) and (f). These field profiles are very similar to each other, because they correspond the the value of $x_0 = -530$, which is very close to the point at which these two solutions merge into one solitonic solution ($x_0 = -525$ nm). For x_0 above -525 nm there is no solitonic solutions on the low-effective-index branch (there are only solutions laying on the high-effective-index branch like those presented in Fig. 4.10)

In the second column in Fig. 4.8, the imaginary part of the effective index β'' is shown. It can be seen that the low-effective-index solitonic branch is a long range one. It has low losses because the solutions laying on this branch are mainly localized in the nonlinear dielectric. The level of losses of this branch is two orders of magnitude lower than that of the plasmonic branch. The high-effective-index plasmonic branch and its solitonic continuation are short range solutions (the high losses of these solutions originate from the fact that an important part of the field of these solutions is localized on the lossy metal film). Only the high-effective-index end of the upper solitonic branch has low losses as for these solutions most of the field is localized in the nonlinear dielectric.

4.3.2 Comparison between the results of the three models

In Fig. 4.12, the dispersion curve obtained using the FBM for a four-layer structure similar to the one presented in Section 4.3.1 is shown. Only the permittivity of the external linear layer ϵ_4 is modified. The parameters of the structure are: $\tilde{\epsilon}_1 = 2.47^2 + 10^{-5}i$, $n_2^{(1)} = 10^{17}$ m^2/W (chalcogenide glass), $\tilde{\epsilon}_2 = 1.44 + 10^{-5}i$ (silica), $\tilde{\epsilon}_3 = -96 + 10i$ (gold), $\tilde{\epsilon}_4 = 1 + 10^{-5}i$ (air), $L = 15$ nm, $d = 40$ nm, and $\lambda = 1.55$ μm. The parameters used here are identical to these of the structures that we have studied in Ref. [79].

This structure supports only solitonic-type solutions. There exist two solutions corresponding to one x_0 value. The solutions for low values of x_0 (x_0 highly negative) correspond to plasmon–solitons weakly interacting with the metal interface are located at the low-β and high-β ends of the dispersion

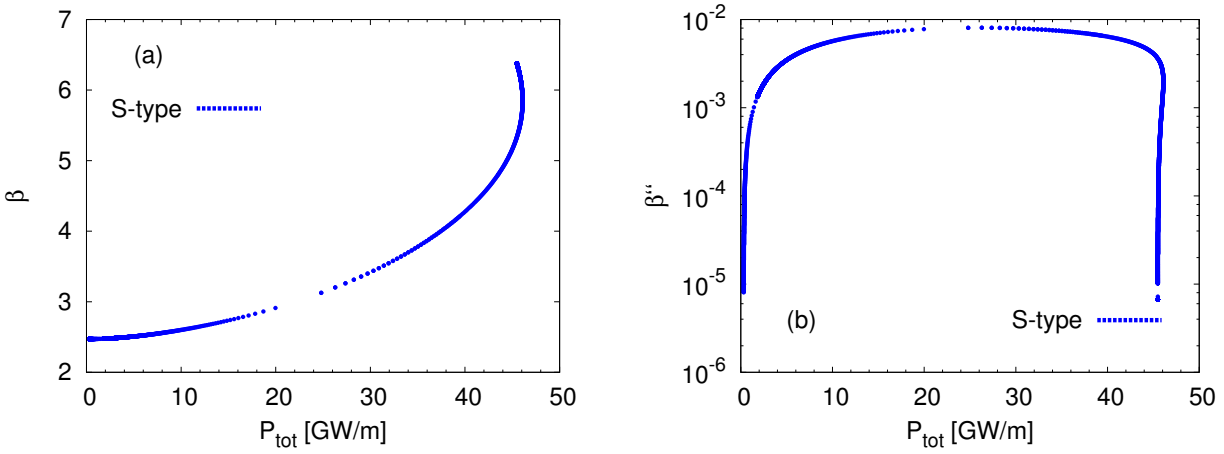

Figure 4.12: Nonlinear dispersion diagrams for the (a) real and (b) imaginary parts of the effective index in the four-layer structure with $\epsilon_{l,1} = 2.47^2$ and $\epsilon_4 = 1$ as a function of power density P_{tot}.

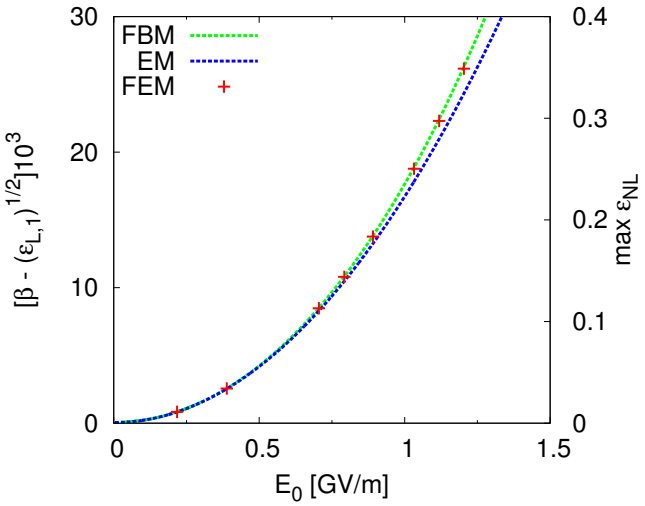

Figure 4.13: Comparison of the nonlinear dispersion curves obtained from: the EM (red solid curve), the FBM (black dashed curve), and the FEM based model (red crosses) for a four-layer structure with parameters from Ref. [79]. The nonlinear variation of the effective index ($\beta - \sqrt{\epsilon_{l,1}}$) is presented in the left vertical axis as a function of the electric field amplitude E_0 at the buffer linear dielectric/nonlinear dielectric interface ($x = 0$). On the right vertical axis the maximum nonlinear permittivity change corresponding to the soliton peak is shown.

curve [in Fig. 4.12(a)]. With the increase of x_0, the two solutions corresponding to identical value of x_0 become similar and they merge into a single solution at $x_0 = 0$, which corresponds to $P_{\text{tot}} \approx 23$ [GW/m].

Figure 4.13 presents a comparison of the results for the four-layer configuration obtained using the three different models described in section Chapter 2: the field based model (FBM — green line), the exact model (EM — blue line), and the finite element method based model (FEM — red crosses). For this comparison only the lowest branch of solitonic-type solutions in this structure is presented for relatively low powers densities ($P_{\text{tot}} < 5$ GW/m). The dispersion diagram presented in Fig. 4.13 shows the effective index of the mode as a function of the total electric field amplitude at the interface between the nonlinear dielectric and a linear buffer layer $E_0 = \sqrt{E_x^2(0) + E_z^2(0)}$ [see Eq. (2.3.41)].

Firstly, the results provided by the two semi-analytical models are compared. For the low total electric field amplitudes $E_0 \lesssim 0.75$ GV/m, and therefore small maximum nonlinear permittivity changes ($\epsilon_{\text{nl}} \lesssim 0.1$), both models are in a very good agreement. For higher values of E_0 the discrepancy between the FBM and the EM appears. This discrepancy can be explained by looking at the assumptions that were used to built the models. As described in Section 2.1, the FBM was formulated by assuming that the nonlinear refractive index changes are small. In this case, it is possible to omit one term in the nonlinear wave equation [see Eq. (2.1.2)] and neglect the longitudinal component of the electric field (E_z) in the nonlinear contribution to the permittivity [see Eq. (2.1.5)], because it is much lower than the transverse component (E_x). For higher nonlinear index modifications both fields contribute with a comparable weight to the nonlinear effects and the assumptions made in the FEM are no longer valid. For this reason the results of the FBM differ from those obtained using the EM that takes both electric field components into account. The highest maximum permittivity change shown in Fig. 4.13 is of the order of 0.3. Even for such high ϵ_{nl} the electric field component ratio is $|E_x/E_z| \approx 10/1$. This justifies the assumption used in the FBM that allowed us to neglect the longitudinal field in the nonlinear contribution to the permittivity. The maximal relative difference between the results provided by the two models for the effective index variation $\beta - \sqrt{\epsilon_{l,1}}$ is of the order of 10% for $E_0 \approx 1.4$ GV/m.

The results of the FEM based model shown in Fig. 4.13 overlap with the FBM results. This is due to the choice made for the used FEM algorithm which takes into account only the transverse component of the electric field while computing the nonlinear effects. The FEM method solves numer-

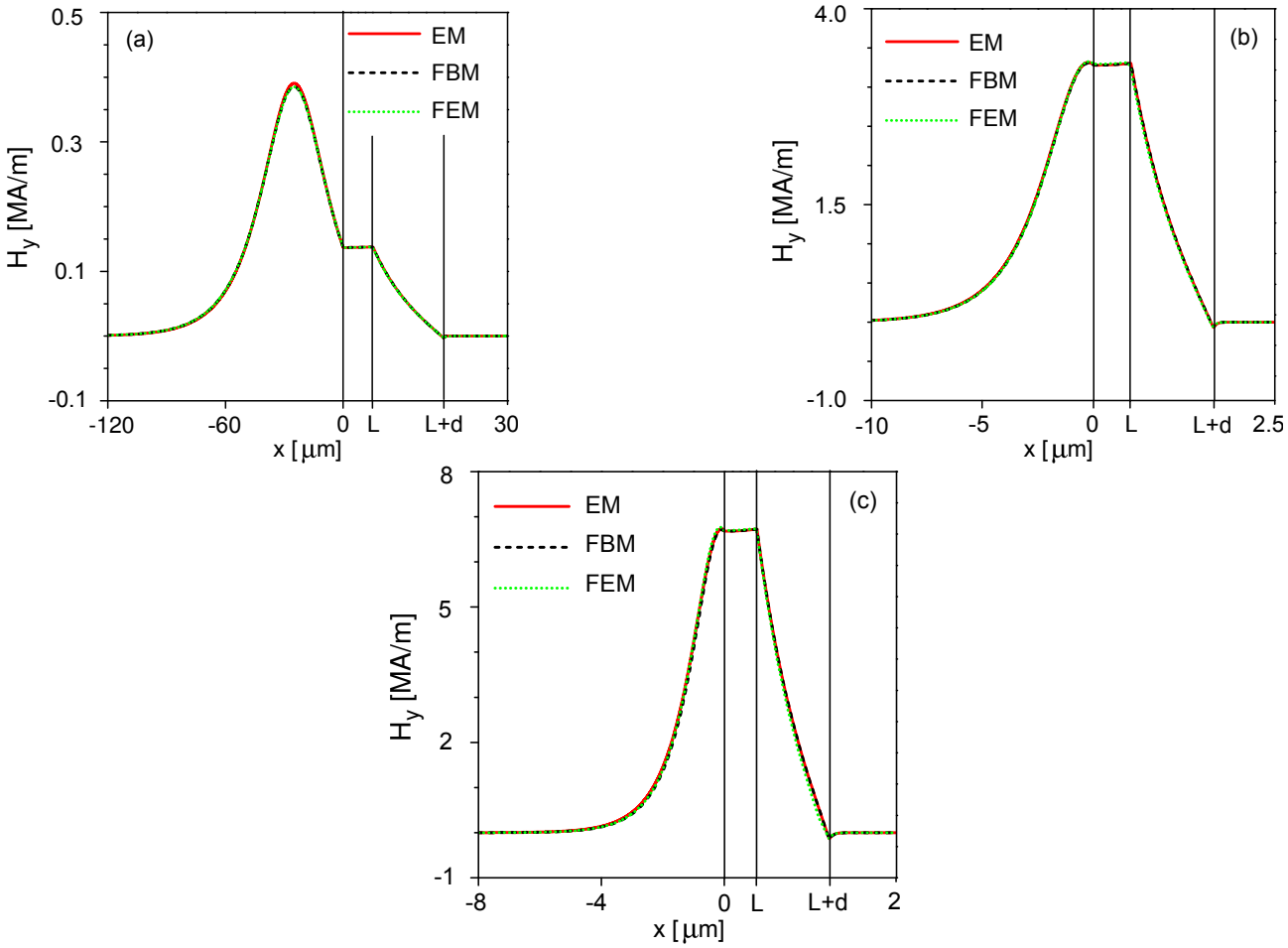

Figure 4.14: Comparison of the magnetic field profiles obtained using the EM (red solid curve), the FBM (black dashed curve), and the FEM based method (green dotted curve) for E_0 values: (a) 0.02 GV/m, (b) 0.5 GV/m, (c) and 1 GV/m.

ically the nonlinear wave equation [Eq. (2.1.7a)] which is the heart of the FBM. For these reasons it is understandable that the FEM based model nicely reproduces the results of the FBM.

In Fig. 4.14, the comparison of the field profiles obtained using our three models is presented. Only the H_y field component is shown because all the important observations can be made using this component. The analysis of the electric field components E_x and E_z will be done only in one case presented in Fig. 4.15. As described in Section 2.3.2, the field profiles in the nonlinear layer in the EM are not given by an analytical formula but are described by the system of the first-order differential equations [Eqs. (2.3.1a) and (2.3.46)]. This system is solved using a home-made 4^{th}-order Runge–Kutta method [88] and confirmed by the built-in ordinary differential equation solver in SCILAB called `ode` [146]. The boundary conditions, allowing to solve this system of equations, take into account the values of the electric field components ($E_{x,0}$ and $E_{z,0}$) at the interface between the nonlinear dielectric and the buffer linear dielectric film (layer 2 in Fig. 2.1). These values are found for a given value of E_0 using Eqs. (2.3.41) and (2.3.42).

In Fig. 4.14(a), the field profiles for $E_0 = 0.02$ GV/m are presented. Panels (b) and (c) present the field profiles corresponding to $E_0 = 0.5$ GV/m and $E_0 = 1$ GV/m, respectively. In all the cases, the fields obtained using the FBM and the FEM based method are in a very good agreement. The fields obtained using the EM also overlap very well with the previous ones despite the small discrepancies of the corresponding propagation constants.

In Fig. 4.15, field profiles of a low-power plasmon–soliton is illustrated in more detail. This solution corresponds to $E_0 = 0.04$ GV/m in Fig. 4.13. In subplots (a) and (b), the profiles of the magnetic field

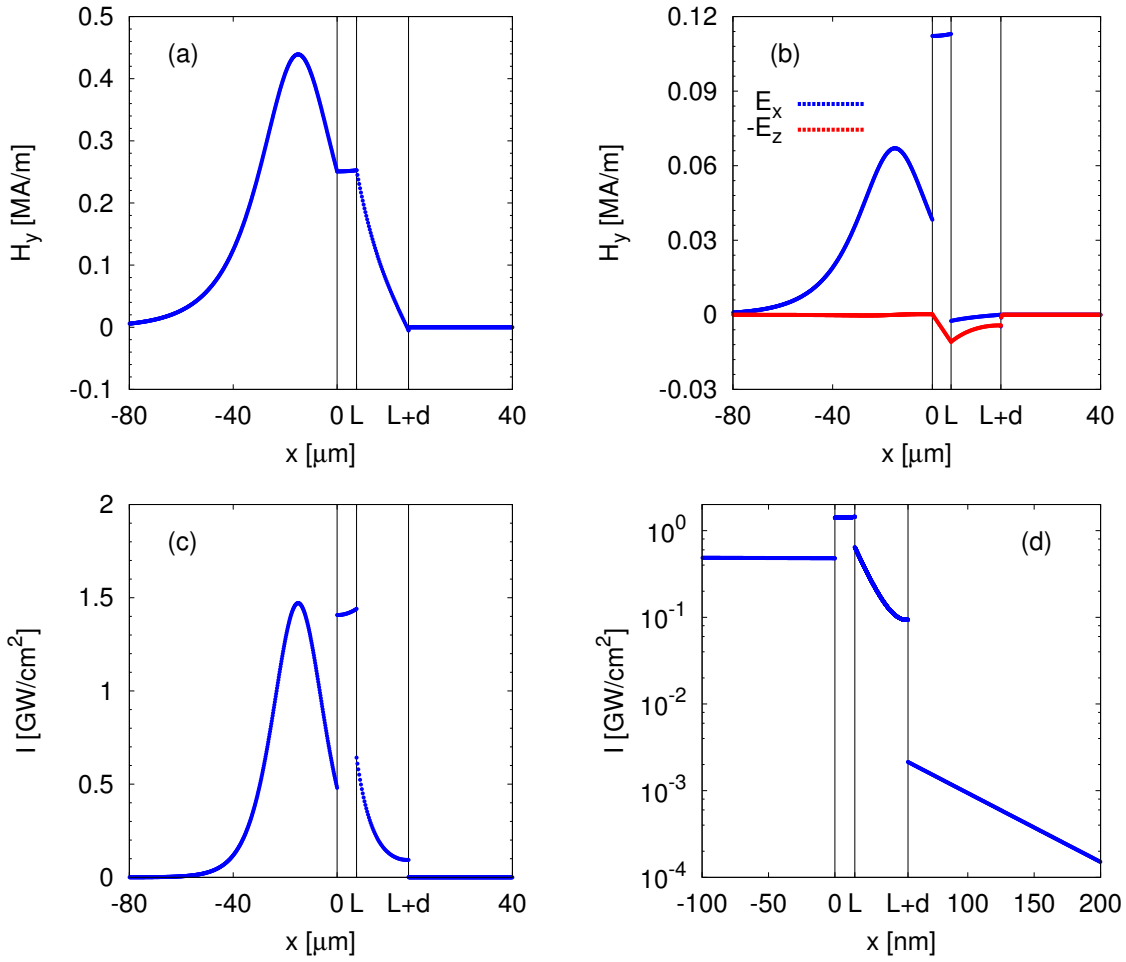

Figure 4.15: Profiles of (a) magnetic field H_y, (b) electric field components E_x and E_z, and (c), (d) light intensity [defined by Eq. (1.7.4)] for a low-power plasmon–soliton in the structure for which the dispersion diagram is shown in Fig. 4.13. Subplot (d) shows the light intensity in the vicinity of the metal film in log scale. The x coordinate inside the thin films is magnified 500 times in panels (a), (b), and (c) and. In panel (d) the x scale is identical in all the layers.

component H_y and the electric field components E_x and E_z are shown. We notice that for low-power solutions, the assumption made in the FBM, stating that the amplitude of the transverse electric field component is much larger than the amplitude of the longitudinal field component ($|E_x/E_z| \gg 1$) is fulfilled very well. For that reason, the simplified Kerr-type nonlinearity treatment used in the FBM [see Eq. (2.1.5)] is not far from the exact description used in the EM [see Eqs. (1.6.13) and (2.3.4)], and there is a good agreement between the results of the FBM and the EM for low light intensities.

In Figs. 4.15(c) and (d), the light intensity distribution for the low-power plasmon–soliton is shown. The peak intensity is at the level of 1.5 GW/cm^2. Due to high index contrast between the nonlinear and linear dielectrics there is an intensity jump [(see definition of the intensity given by Eq. (1.7.4)] and the intensity in the linear dielectric film is comparable to the peak intensity of the solitonic part. In Fig. 4.15(d), a zoom on the plasmonic part of the low-power plasmon–soliton is shown. The intensity is shown in log scale. We clearly see exponentially decaying plasmonic field in the external dielectric layer ($x > L + d$). The intensity of the plasmonic part in the external layer is approximately two and a half orders of magnitude lower than the intensity of the solitonic part.

The imaginary part of the effective index β'' of the solution presented in Fig. 4.15 is equal to $\beta'' = 0.8 \cdot 10^{-5}$. Using Eq. (2.1.74), we can express losses of this low-power solution in dB/cm. The corresponding attenuation $\mathfrak{L} = 2.8$ dB/cm. This value of attenuation allows for observation of the propagation of such waves for tens of micrometers which should be sufficient for experimental purposes.

4.3.3 Toward low-power solutions

In the summary of Section 4.2.3, we have stated that the three-layer configurations support low-power solitonic-type plasmon–solitons only for low values of index contras between the nonlinear medium and the external linear dielectric. Therefore, only two out of three conditions facilitating experimental observations of plasmon–solitons (listed at the beginning of Chapter 4) were satisfied. Some exemplary results on low-power solitonic-type plasmon–solitons in four-layer structures have already been presented in Section 4.3.2. In this section, a systematic study of the properties of four-layer configurations for various structure parameters is performed, in order to find low-power solitonic-type solutions for the configurations with a high index contrast between the nonlinear dielectric and the linear external dielectric. This analysis will help us to find the parameter regions, in which all three conditions listed at the beginning of Chapter 4 are fulfilled.

In this section, the parameters used to obtain all the color maps (two-parameter scans performed with the FBM) are identical to these in Ref. [79] and in Section 4.3.2 except if explicitly stated or if the parameters are on the axes of the plot. We have chosen $x_0 = -15.5$ μm value for all the illustrations. In all the plots, only the effective indices in the range $\beta \in [\sqrt{\epsilon_{l,1}}, 4\sqrt{\epsilon_{l,1}}]$ are shown (like in Section 4.2.3).

Firstly, the evolution of the number of solitonic-type solutions as a function of the linear buffer layer thickness L and of the external layer refractive index $\sqrt{\epsilon_4}$ is analyzed. It is seen from Fig. 4.16 that for low buffer-layer thickness $0 < L \lesssim 9$ nm the four-layer structure presents a similar behavior as the three-layer structure (see Figs. 4.5 and 4.7). There is one solitonic-type solution for the quasi-symmetric case $\sqrt{\epsilon_4}_{\text{cut-off}} \approx 2.4 < \sqrt{\epsilon_{l,1}}$ and no solitonic-type solutions for higher index contrasts between the external layer and the nonlinear dielectric. These two cases are separated by a narrow region with two solutions that becomes broader with the increase of the buffer thickness [see Fig. 4.16(b)]. For buffer thickness between 9 nm and 30 nm, there is up to three solitonic-type solutions possible for low index-contrast regime $\sqrt{\epsilon_4} > n_{\text{cut-off}}$ an even up to four solutions [yellow region in Fig. 4.16(b)] in a small region for a moderate index contrast configuration. For the buffer thickness above 30 nm, only a single solitonic-type solution exists in low and moderate index-contrast regimes.

In the region with three or four solitonic-type solutions occurring for identical x_0 value, two of the corresponding field profiles are similar to those presented in Fig. 4.11. The other solutions have even higher effective indices β and therefore even narrower solitonic parts and higher peak powers than the two previously mentioned solutions.

In Fig. 4.17(a), we show the total number of solutions as a function of the external layer refractive index $\sqrt{\epsilon_4}$ and of the x_0 parameter [in analogy to Fig. 4.5(a) for three-layer structures] for the structure with $L = 15$ nm. In this case, we see that in a quasi-symmetric structure ($\epsilon_4 \approx \epsilon_{l,1}$) there are three (region A) or one (for negative x_0 values close to zero — top right corner of region B) solitonic-type

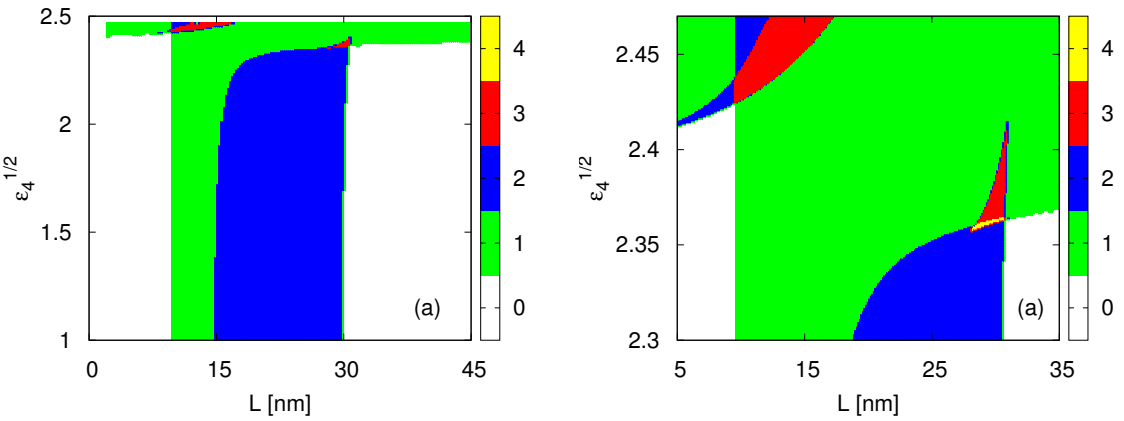

Figure 4.16: (a) Number of solitonic-type solutions in a four-layer structure as a function of the buffer layer thickness L and of the external layer refractive index $\sqrt{\epsilon_4}$. (b) The zoom on the most complex part of the plot presented in panel (a).

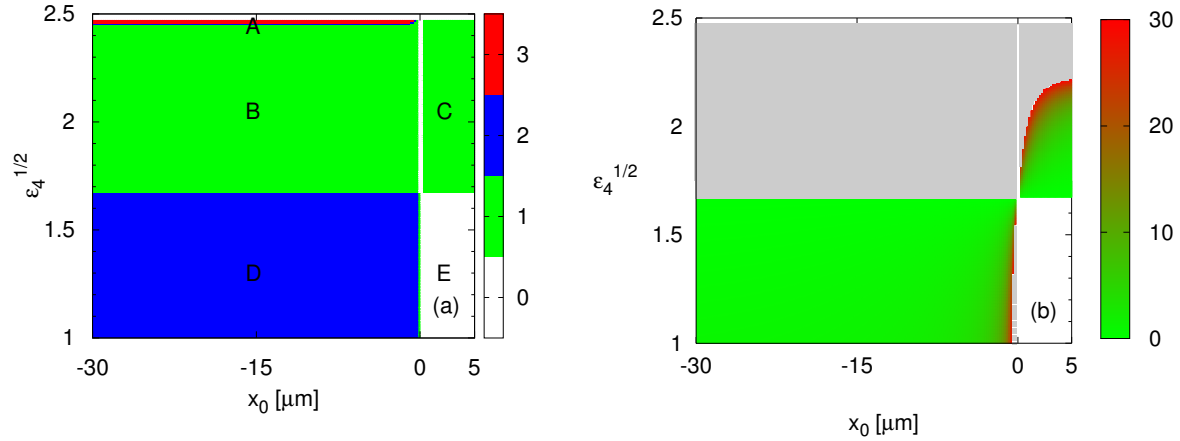

Figure 4.17: (a) Number of solutions in a four-layer structure with $L = 15$ nm as a function of the external layer refractive index $\sqrt{\epsilon_4}$ and of the parameter x_0. (b) Peak power [GW/cm^2] for the low-power solutions. The existence of solutions with peak power higher than 30 GW/cm^2 is marked with the gray color.

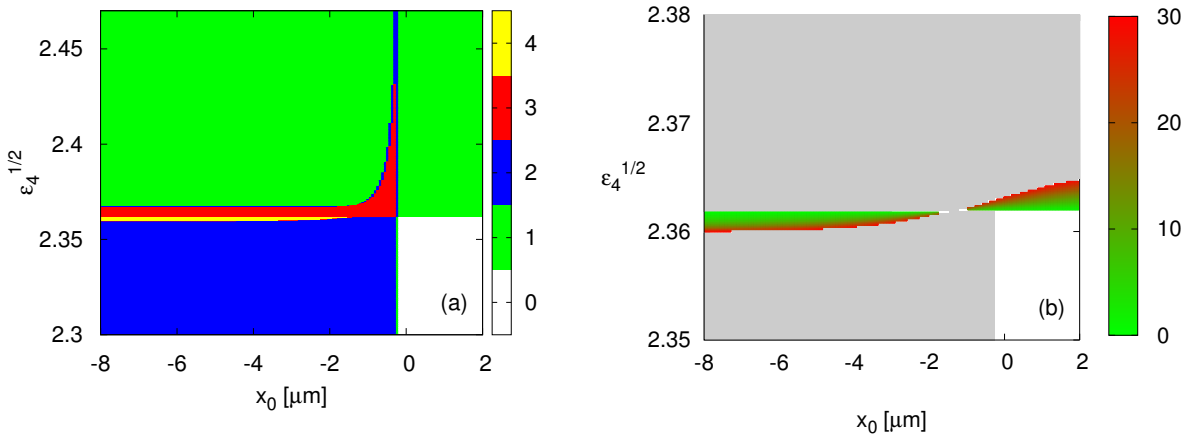

Figure 4.18: (a) Number of solutions in a four-layer structure with $L = 29$ nm as a function of the external layer refractive index $\sqrt{\epsilon_4}$ and of the parameter x_0. (b) Peak power [GW/cm^2] for the low-power solutions in the vicinity of the region with four solitonic-type solutions. The existence of solutions with higher peak power is marked with the gray color.

solutions, and one plasmonic-type solution (top of the region C). For the region with a moderate index contrast ($1.7 \lesssim \sqrt{\epsilon_4} \lesssim 2.4$), there is one solitonic-type solution (region B) and one plasmonic-type solution (region C). Finally for high index contrast ($\sqrt{\epsilon_4} \lesssim 1.7$) there exist two solitonic-type solutions (region D) and no plasmonic-type solution (region E). The value of $\sqrt{\epsilon_4} \approx 1.7$ is a cut-off limit both in the case of solitonic and plasmonic-type solutions. One one hand, increasing $\sqrt{\epsilon_4}$ for positive x_0 values causes the appearance of a plasmonic-type solution. On the other hand, for negative values of x_0 it causes a reduction of the number of solitonic-type solutions from two to one.

Figure 4.17(b) shows the peak power of the solutions in four-layer configurations in the same coordinates as Fig. 4.17(a). Similar to the three-layer case shown in Fig. 4.5(b), the lowest peak intensities occur below the cut-off index for solitonic-type solutions and above this value for plasmonic-type solutions. However, for plasmon–solitons in four-layer structures, the region of low-power solutions extends to much lower external layer refractive indices than in the case of a three-layer configuration.

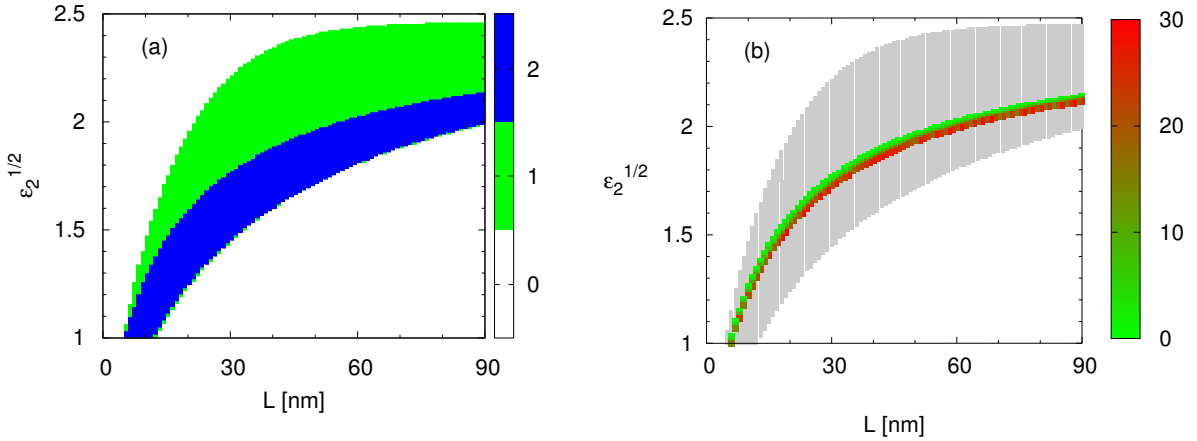

Figure 4.19: (a) Number of solitonic-type solutions as a function of the buffer layer thickness L and of the refractive index of this layer $\sqrt{\epsilon_2}$. (b) Peak power [GW/cm^2] for the low-power solutions.

This means that, in a four-layer configuration, we are not only able to find plasmon–solitons for high index-contrast configurations but also that these solutions have low peak intensities.

It must be pointed out that the maps presented in Fig. 4.17(a) have been obtained for a value of $L = 15$ nm which corresponds to a cut in a region of the map provided in Fig. 4.16 where the maximum number of solitonic-type solutions is equal to three. More complicated maps can be obtained for specific L values. Figure 4.18 shows a cut at $L = 29$ nm. For this case, we first discuss the region of low values of x_0 [$x_0 \in (-8, -2)$ μm]. For low permittivity contrast $\sqrt{\epsilon_{l,1}} - \sqrt{\epsilon_4}$, there is one solitonic-type solution (green region). Around $\sqrt{\epsilon_4} = 2.37$ a region with three solutions appears (red region). Then, at $\sqrt{\epsilon_4} \approx 2.36$ a narrow region for which four solitonic-type solutions can be obtained for identical value of x_0 parameter (yellow region). For lower values of $\sqrt{\epsilon_4}$ two solitonic-type solution exist (blue region). For higher values of x_0 [$x_0 \in (-2, 0)$ μm], the region with three solutions expands to higher and slightly lower values of $\sqrt{\epsilon_4}$ and the region with four solitonic-type solutions vanishes. The behavior of the plasmonic-type solutions remains unchanged with respect to the configuration presented in Fig. 4.17(a), except for the location of the solution cut-off. For the buffer layer thickness $L = 29$ nm, the plasmonic solution exists only for $\sqrt{\epsilon_4} \gtrapprox 2.36$.

Figure 4.18(b) shows the peak power of the solutions indicated in Fig. 4.18(a). We see that now the region where solitonic solutions with low peak power can be obtained is much narrower than in the case presented in Fig. 4.17. This low peak-power region is located close to the top boundary of the region with four solutions [yellow region in Fig. 4.18(a)].

Figure 4.19(a) shows the number of solitonic-type solutions as a function of the buffer layer thickness L and of the refractive index of this layer $\sqrt{\epsilon_2}$. It can be seen that for low buffer layer refractive index ($\sqrt{\epsilon_2} = 1$), the range of thicknesses where one or two solutions exist is quite narrow (5–15 nm). Increasing the buffer layer refractive index, the range of the buffer thicknesses where the solutions exist expands (it becomes approximately 45–80 nm for $\sqrt{\epsilon_2} = 1.75$).

Figure 4.19(b) shows the plasmon–soliton peak power in the same coordinates as those used in panel (a). The region where plasmon–solitons have low peak intensities is very narrow and is located close to the line separating regions with one and two solutions. Increasing the buffer layer refractive index, allows for an increase of the buffer layer thickness required to obtain solutions with low peak power, which is interesting from a technological point of view (i.e., it is challenging to fabricate uniform, high quality thin films on top of chalcogenide glasses [147]).

Figure 4.20(a) presents the number of solitonic-type solutions as a function of the metal layer permittivity ϵ_3 and of the external medium permittivity ϵ_4 [it can be compared with Fig. 4.7(a) presenting similar dependency for a three-layer structure]. The main advantage of the four-layer structure compared to the three-layer one is that, even for very low permittivities of the external medium (like 1 for air or 1.3^2 for water at $\lambda = 1.55$ μm), resulting in high index contrast between the nonlinear

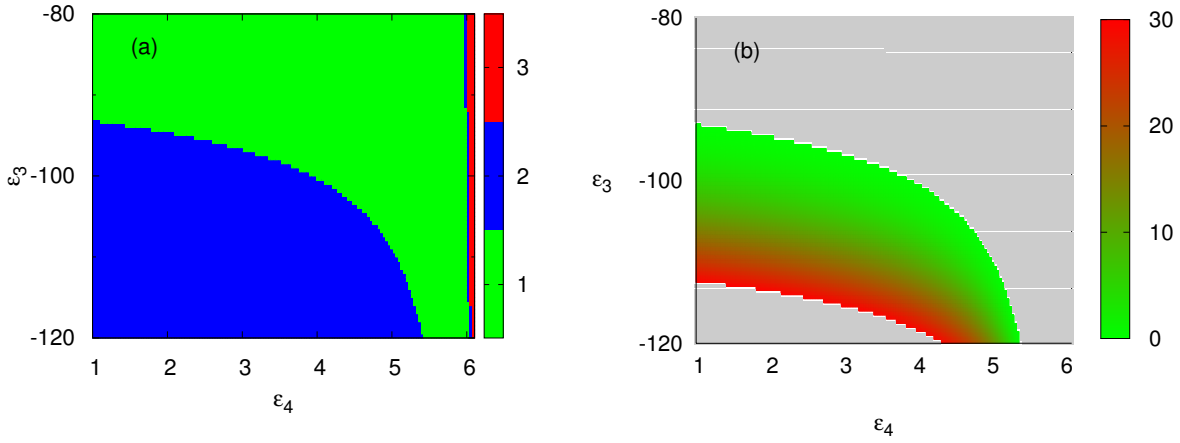

Figure 4.20: (a) Number of solitonic-type solutions as a function of the metal layer permittivity ϵ_3 and of the external medium permittivity ϵ_4. (b) Peak power [GW/cm^2] for the low-power solutions.

and the external linear dielectrics, the solitonic-type solutions exist. There is two of them for low metal permittivity values and one for higher metal permittivity values. In four-layer structures where $\epsilon_4 \approx \epsilon_{l,1}$ even three solitonic-type solutions exist for identical value of the x_0 parameter [the red region in Fig. 4.20(a)].

Figure 4.20(b) shows the peak power of the solitonic-type solutions in the same coordinates as those used in panel (a). Comparing this figure with the corresponding one for a three-layer structure in Fig. 4.7(b), it can be seen that in the case of four-layer configuration, low-power solutions exist for wider ranges of both ϵ_3 and ϵ_4 which broadens the choice of possible parameter combinations. This property may facilitate the fabrication of the structure.

4.3.4 Optimization of the four-layer structure

In this section, a more detailed investigation of the influence of the two geometrical parameters of the four-layer structure (the metal layer thickness d and the buffer layer thickness L — see Fig. 2.1) is shown. Figure 4.21(a) shows the number of solitonic-type solutions as a function of these two parameters. For low values of the thickness of both layers, only one solution is obtained. For higher values of dielectric buffer thickness L, there exist a region for which two solutions appear. For even higher values of L, both solutions disappear. The evolution of the solutions can be followed by looking at Fig. 4.21(b) which corresponds to a cut of Fig. 4.21(a) at $d = 20$ nm. For low values of L, only a high effective index solution exists. $L \approx 21$ nm is a cut-off buffer thickness for a second solitonic-type solution. At this thickness, a low effective index solution appears. As the buffer layer thickness increases, these two solutions become closer to each other and finally merge into one solution for a particular value of $L \approx 34$ nm. Above this value, no solitonic-type solution exists.

In Fig. 4.22(a), the total power density for the solitonic-type solution with the lower β is shown in the same coordinates as those used in Fig. 4.21(a). The solutions with the lowest power density are located close to the cut-off buffer thickness [boundary between the green and blue regions in Fig. 4.21(a)]. In Fig. 4.22(b), the peak power for the low-power solutions is shown. Plasmon–solitons with the lowest peak intensities are located in a narrow region where the total power density is the lowest (i.e., close to the cut-off buffer thickness L for the low-power solution). This shows that in order to obtain solutions with the peak power levels that are attainable by modern high-power commercial lasers the couple L and d has to be precisely chosen. Even a small deviation of the buffer film thickness (e.g., 2 nm) may lead to the change of the peak power of the supported solution by one order of magnitude (e.g., from 3 to 30 GW/cm^2).

Figure 4.23(a) shows the peak power of the solitonic part of the solution as a function of the metal thickness d and x_0 parameter for a fixed buffer thickness $L = 16$ nm. With the increase of the metal

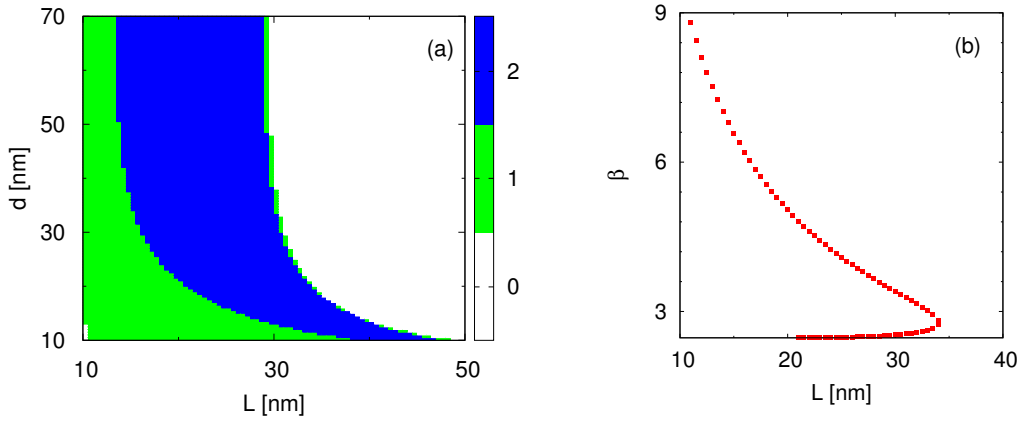

Figure 4.21: (a) Number of solitonic-type solutions as a function of the metal film thickness d and of the buffer layer thickness L. (b) The effective index β as a function of the buffer layer thickness L for a fixed metal thickness $d = 20$ nm.

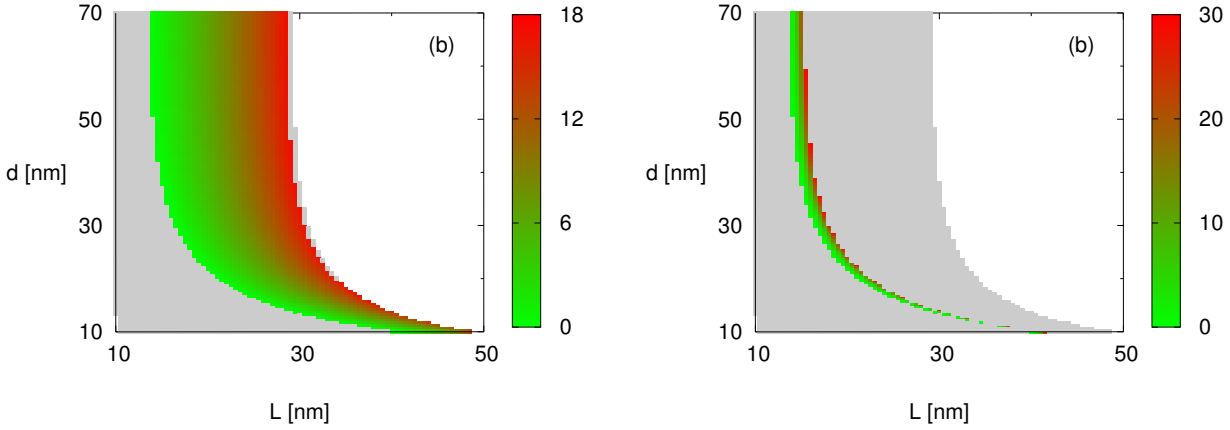

Figure 4.22: (a) Total power density [GW/m] of the low β solitonic-type solution. (b) Peak power [GW/cm^2] for the low-power solutions.

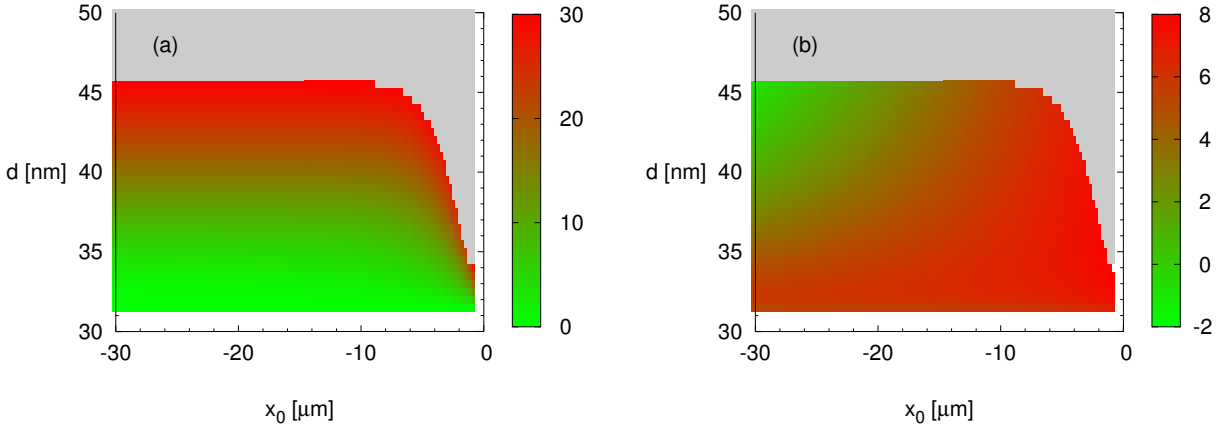

Figure 4.23: (a) Peak power of the solitonic part [GW/cm^2] and (b) decimal logarithm of the peak power of the plasmonic part $I_{\text{plas}} \equiv I(x = L + d)$: $\log_{10}[I_{\text{plas}}/(\text{Wcm}^{-2})]$ for the low-power solitonic-type solutions as a function of the metal thickness d and of the parameter x_0 for the buffer thickness fixed at $L = 16$ nm. Solutions with solitonic part peak power below 30 GW/cm^2 are plotted in color.

thickness or with the increase of the x_0 parameter (decrease in absolute value), the peak power of the solitonic part increases. Besides the peak power of the solitonic part that should be kept low, there is another important parameter that should be taken into account. It is interesting to have a strong plasmonic field at the interface between the metal film and the external medium, in order to facilitate its recording or to use it in some plasmonic devices. Figure 4.23(b) shows the decimal logarithm of the maximum peak power of the plasmonic part as a function of the metal thickness d and x_0 parameter. The lowest values of plasmonic part peak power are obtained for thick metal film and solitonic peak located far from the metal interface. On one hand, for large metal thickness values, bringing the solitonic part closer to the metal interface results in a drastic increase (few orders of magnitude) of the peak power in the external layer. On the other hand, for thin metal films, the peak power in the external layer is relatively high and the changes with the x_0 parameter are much slower.

Chapter 5

Extensions of the field based model

Contents

In this chapter, two extensions of the field based model (FBM) that was developed in Section 2.1 are presented. The FBM was developed for transverse magnetic (TM) light polarization and it allowed us to find one-dimensional stationary solutions in structures with a semi-infinite nonlinear medium. Here we will extend this model to treat a more complicated and general problems. In Section 5.1, we will present a method to compute in an approximate way the dispersion relation and the field profiles of two-dimensional plasmon–solitons in structures with a semi-infinite nonlinear medium. In Section 5.2, the field based model will be formulated for transverse electric (TE) light polarization. It will be shown that for TE polarized light, metal/nonlinear dielectric structures studied in Part I of this PhD manuscript do not support plasmon–soliton waves.

5.1 Model for two-dimensional plasmon–solitons

In this section, we will show how, using Maxwell's equations, it is possible to find two-dimensional plasmon–solitons, knowing the solutions of the one-dimensional problem. In Section 5.1.1 the derivation of the formulas for the dispersion relation and the field profiles of two-dimensional plasmon–solitons will be presented. The approach presented in Section 5.1.1, uses strong assumptions about the nature of the electromagnetic field and provides only the first approximation of the results for the two-dimensional plasmon–solitons. The effective index of the two-dimensional solution will be expressed as the effective index of the one-dimensional solution found using the FEM modified with a correction term. This correction term will be calculated numerically using integrals of the one-dimensional solution field profiles. Furthermore, the lateral[1] field profile of the two-dimensional plasmon–soliton will be found and its width will be expressed using integrals of the one-dimensional solution field profiles. In Section 5.1.2 results for two-dimensional plasmon–solitons will be presented for realistic structure parameters and power levels.

5.1.1 Model formulation

In the two-dimensional problem, we will assume that the electric field $\mathscr{E}(x, y, z, t)$ depends on all three spatial coordinates and time. In the one-dimensional approach we skipped the y dependency due to

[1] In the frame of the FEM, the field profiles in the transverse (x) direction were found. The lateral direction is the second direction (y) that is perpendicular to the direction of light propagation (z).

the structure invariance in this direction (see the discussion in Section 1.5). Here the structure is still invariant in the y direction but the two-dimensional model accounts for the self-focusing of the field in this direction.

The derivation of the two-dimensional model requires the knowledge of the field profiles $E_x(x), E_z(x)$ and the corresponding effective index β values, which can be found using the one-dimensional models described above in Sections 2.1 and 2.2. The following derivation is valid only in the case of the specific assumptions on the form of the nonlinear permittivity. Only two components of the nonlinear permittivity tensor depend on the electric field in the following way [see also Eq. (2.2.1) and Section 1.6]:

$$\epsilon_x = \epsilon_y = \epsilon_l + \alpha |E_x|^2. \tag{5.1.1a}$$

The third component does not depend on the field intensity

$$\epsilon_z = \epsilon_l. \tag{5.1.1b}$$

The formulation of the one-dimensional model using assumption expressed by Eq. (5.1.1) on the form of the nonlinear permittivity tensor is described in Section 2.2.

The derivation of the model for two-dimensional plasmon–solitons starts from Maxwell's equations [Eqs. (1.3.1)]. Mixing Eqs. (1.3.1a) and (1.3.1b) we obtain

$$\boldsymbol{\nabla} \times \boldsymbol{\nabla} \times \boldsymbol{\mathscr{E}} - k_0^2 \epsilon \boldsymbol{\mathscr{E}} = 0 \tag{5.1.2}$$

Assuming that the TM fields, found using the one-dimensional FBM, remain TM polarized also in the two-dimensional case, Eq. (5.1.2) can be rewritten as:

$$\begin{bmatrix} i\partial_{xz}^2 \mathscr{E}_z - \partial_{yy}^2 \mathscr{E}_x - \partial_{zz}^2 \mathscr{E}_x \\ i\partial_{yz}^2 \mathscr{E}_z + \partial_{xy}^2 \mathscr{E}_x \\ -i\partial_{xx}^2 \mathscr{E}_z - i\partial_{yy}^2 \mathscr{E}_z + \partial_{xz}^2 \mathscr{E}_x \end{bmatrix} = k_0^2 \begin{bmatrix} \epsilon_x \mathscr{E}_x \\ 0 \\ \epsilon_z \mathscr{E}_z \end{bmatrix}, \tag{5.1.3}$$

where

$$\partial_{jk}^2 = \frac{\partial}{\partial k}\left(\frac{\partial}{\partial j}\right) \tag{5.1.4}$$

and j and $k \in \{x, y, z\}$. We will use Eq. (1.3.1c) that, due to the form of the permittivity tensor that we use [given by Eq. (5.1.1)], can be written in the form

$$\partial_z \mathscr{E}_z = -\frac{\partial_x \epsilon_x \mathscr{E}_x}{\epsilon_l}, \tag{5.1.5}$$

where

$$\partial_j = \frac{\partial}{\partial j}, \tag{5.1.6}$$

for $j \in \{x, y, z\}$. Inserting Eq. (5.1.5) into the first equation given in Eq. (5.1.3) one obtain the equation that depends only on the transverse component of the electric field $\mathscr{E}_x$:

$$\frac{\partial_{xx}^2(\epsilon_x \mathscr{E}_x)}{\epsilon_l} + \partial_{yy}^2 \mathscr{E}_x + \partial_{zz}^2 \mathscr{E}_x + \epsilon_x k_0^2 \mathscr{E}_x = 0. \tag{5.1.7}$$

Substituting ϵ_x in Eq. (5.1.7) by the expression given by Eq. (5.1.1a), Eq. (5.1.7) can be rewritten into a form:

$$\left(1 + \frac{3\alpha \mathscr{E}_x^2}{\epsilon_l}\right) \frac{\partial^2 \mathscr{E}_x}{\partial x^2} + 6\frac{\alpha}{\epsilon_l}\left(\frac{\partial \mathscr{E}_x}{\partial x}\right)^2 \mathscr{E}_x + \frac{\partial^2 \mathscr{E}_x}{\partial y^2} + \frac{\partial^2 \mathscr{E}_x}{\partial z^2} + k_0^2 \left(\epsilon_l + \alpha \mathscr{E}_x^2\right) \mathscr{E}_x = 0. \tag{5.1.8}$$

In the following, we will assume that in the dependency of the electric field on the spatial coordinates, we can separate the x dependency in the following way:

$$\mathscr{E}_x = E_{\mathrm{NL}}(x) \psi(y, z) e^{i(\beta_{\mathrm{NL}} k_0 z - \omega t)}, \tag{5.1.9}$$

where the $E_{\mathrm{NL}}(x)$ is the field profile found using the one-dimensional FBM and β_{NL} is the corresponding effective index. Inserting Eq. (5.1.9) into Eq. (5.1.8) yields

$$\left(1+\frac{3\alpha E_{\mathrm{NL}}^2\psi^2}{\epsilon_l}\right)\psi\frac{\mathrm{d}^2E_{\mathrm{NL}}}{\mathrm{d}x^2}+6\frac{\alpha}{\epsilon_l}\psi^3\left(\frac{\mathrm{d}E_{\mathrm{NL}}}{\mathrm{d}x}\right)^2E_{\mathrm{NL}}+\frac{\partial^2\psi}{\partial y^2}E_{\mathrm{NL}}+\left(\frac{\partial^2\psi}{\partial z^2}+2i\beta_{\mathrm{NL}}k_0\frac{\partial\psi}{\partial z}-\beta_{\mathrm{NL}}^2k_0^2\psi\right)E_{\mathrm{NL}}+k_0^2\left(\epsilon_l+\alpha E_{\mathrm{NL}}^2\psi^2\right)E_{\mathrm{NL}}\psi=0, \tag{5.1.10}$$

where the x and z dependency in ψ was dropped. Next, we assume that

$$\psi(y,z)=\phi(y)e^{i\Delta\beta k_0z}, \tag{5.1.11}$$

where ϕ is the lateral profile of the two-dimensional plasmon–solitons that we are looking for and $\Delta\beta$ denotes the unknown correction to the effective index that is introduced when we take into account the two dimensional profile. Introducing Eq. (5.1.11) into Eq. (5.1.10) yields

$$\left[\frac{\mathrm{d}^2E_{\mathrm{NL}}}{\mathrm{d}x^2}-k_0^2\left(\beta_{\mathrm{NL}}+\Delta\beta\right)^2E_{\mathrm{NL}}+k_0^2\epsilon_lE_{\mathrm{NL}}\right]\phi+\left\{\frac{3\alpha E_{\mathrm{NL}}}{\epsilon_l}\left[E_{\mathrm{NL}}\frac{\mathrm{d}^2E_{\mathrm{NL}}}{\mathrm{d}x^2}+2\left(\frac{\mathrm{d}E_{\mathrm{NL}}}{\mathrm{d}x}\right)^2\right]+k_0^2\alpha E_{\mathrm{NL}}^3\right\}\phi^3+E_{\mathrm{NL}}\frac{\mathrm{d}^2\phi}{\mathrm{d}y^2}=0. \tag{5.1.12}$$

We multiple Eq. (5.1.12) by E_{NL}/k_0^2 and integrate with respect to x

$$\left[\frac{1}{k_0^2}\int_{-\infty}^{\infty}E_{\mathrm{NL}}\frac{\mathrm{d}^2E_{\mathrm{NL}}}{\mathrm{d}x^2}\,\mathrm{d}x-\left(\beta_{\mathrm{NL}}+\Delta\beta\right)^2\int_{-\infty}^{\infty}E_{\mathrm{NL}}^2\,\mathrm{d}x+\int_{-\infty}^{\infty}\epsilon_l(x)E_{\mathrm{NL}}^2\,\mathrm{d}x\right]\phi+\left\{\int_{-\infty}^{\infty}\left[\frac{3\alpha E_{\mathrm{NL}}^2}{k_0^2\epsilon_l}\left(E_{\mathrm{NL}}\frac{\mathrm{d}^2E_{\mathrm{NL}}}{\mathrm{d}x^2}+2\left(\frac{\mathrm{d}E_{\mathrm{NL}}}{\mathrm{d}x}\right)^2\right)+\alpha E_{\mathrm{NL}}^4\right]\mathrm{d}x\right\}\phi^3+\frac{1}{k_0^2}\int_{-\infty}^{\infty}E_{\mathrm{NL}}^2\,\mathrm{d}x\frac{\mathrm{d}^2\phi}{\mathrm{d}y^2}=0. \tag{5.1.13}$$

Dividing Eq. (5.1.13) by $\int_{-\infty}^{\infty}E_{\mathrm{NL}}^2\,\mathrm{d}x$ results in

$$\left[G-\left(\beta_{\mathrm{NL}}+\Delta\beta\right)^2\right]\phi+\frac{1}{k_0^2}\frac{\mathrm{d}^2\phi}{\mathrm{d}y^2}+A\phi^3=0, \tag{5.1.14}$$

where

$$G=\frac{\int_{-\infty}^{\infty}\left(\frac{E_{\mathrm{NL}}}{k_0^2}\frac{\mathrm{d}^2E_{\mathrm{NL}}}{\mathrm{d}x^2}+\epsilon_l(x)E_{\mathrm{NL}}^2\right)\mathrm{d}x}{\int_{-\infty}^{\infty}E_{\mathrm{NL}}^2\,\mathrm{d}x}, \tag{5.1.15a}$$

$$A=\frac{\int_{-\infty}^{\infty}\left[\frac{3\alpha E_{\mathrm{NL}}^2}{k_0^2\epsilon_l}\left(E_{\mathrm{NL}}\frac{\mathrm{d}^2E_{\mathrm{NL}}}{\mathrm{d}x^2}+2\left(\frac{\mathrm{d}E_{\mathrm{NL}}}{\mathrm{d}x}\right)^2\right)+\alpha E_{\mathrm{NL}}^4\right]\mathrm{d}x}{\int_{-\infty}^{\infty}E_{\mathrm{NL}}^2\,\mathrm{d}x}=\frac{\alpha\int_0^d\left[\frac{3E_{\mathrm{NL}}^2}{k_0^2\epsilon_l}\left(E_{\mathrm{NL}}\frac{\mathrm{d}^2E_{\mathrm{NL}}}{\mathrm{d}x^2}+2\left(\frac{\mathrm{d}E_{\mathrm{NL}}}{\mathrm{d}x}\right)^2\right)+E_{\mathrm{NL}}^4\right]\mathrm{d}x}{\int_{-\infty}^{\infty}E_{\mathrm{NL}}^2\,\mathrm{d}x} \tag{5.1.15b}$$

In Section 2.1.2, we have shown that the solution of the equation of the type: $\mathrm{d}^2\phi/\mathrm{d}y^2+b_1\phi+b_3\phi^3=0$ is given by a secant hyperbolic function. Therefore, we solve Eq. (5.1.14) using the test function $\phi(y)=\mathrm{sech}(y/\omega_y)$. Inserting this test function into Eq. (5.1.14) yields

$$\left[G-\left(\beta_{\mathrm{NL}}+\Delta\beta\right)^2+\frac{1}{k_0^2\omega_y^2}\right]+\left(A-\frac{2}{k_0^2\omega_y^2}\right)\mathrm{sech}^2\left(\frac{y}{\omega_y}\right)=0. \tag{5.1.16}$$

The first term of the sum on the left-hand side of Eq. (5.1.16) is constant (does not depend on y) and the second term of the sum is a constant multiplied by a function of y. As a result, in order for this sum to be equal to zero for any value of y, both terms of the sum must be equal to zero. This results in two conditions:

$$G - (\beta_{\mathrm{NL}} + \Delta\beta)^2 + \frac{1}{k_0^2 \omega_y^2} = 0 \tag{5.1.17a}$$

and

$$A - \frac{2}{k_0^2 \omega_y^2} = 0. \tag{5.1.17b}$$

The second condition provides the expression for the width in the lateral direction ω_y of our two-dimensional plasmon–soliton:

$$\omega_y = \frac{1}{k_0}\sqrt{\frac{2}{A}}. \tag{5.1.18}$$

The first condition gives the expression for the corrected effective index

$$\beta_{\mathrm{2D}} = \beta_{\mathrm{NL}} + \Delta\beta = \sqrt{G + \frac{A}{2}} = \sqrt{G + \frac{1}{k_0^2 \omega_y^2}} \tag{5.1.19}$$

As it can be seen from the definitions of parameters A and G given by Eqs. (5.1.15), the parameters of the two-dimensional plasmon–soliton (ω_y and β_{2D}) depend only on the integrals of the field profiles of the one-dimensional solution and the corresponding effective index β_{NL}.

We stress on the fact that, the model for the two-dimensional plasmon–solitons derived here is not fully rigorous and gives only approximated results. There are several important assumptions made during the derivation of this model. We have assumed that the Kerr-type nonlinearity is described using Eq. (5.1.1) instead of the full expression given by Eq. (1.6.13). Moreover, we assumed that the electromagnetic field remains TM polarized, even if it is not invariant in the lateral direction. The last approximation we have made, is the fact that that we have integrated the one-dimensional field profiles in the transverse direction [see Eq. (5.1.13)] in order to obtain the parameters of the two-dimensional solution. This integration represents an averaging operation. The validity of this operation in case of solitonic-type plasmon–solitons was not justified.

Similar models have been developed for two-dimensional plasmon–solitons of the plasmonic type [72] and for plasmon–solitons in nonlinear slot waveguides (nonlinear dielectric core sandwiched between two metal claddings) [85]. In Ref. [85], authors state that the averaging operation, similar to the one used in Eq. (5.1.13), is adequate when the transverse mode cross-section is smaller the the lateral one. In our case, both cross-sections are comparable.

5.1.2 Results

In Fig. 5.1, dispersion diagrams of the two-dimensional plasmon–solitons are shown for identical parameters of the structure as used in Section 4.3.2. This time the dispersion curves are represented in the coordinates of the effective index β and the total power of the beam

$$P_{\mathrm{2D}} = \int_{-\infty}^{+\infty} \int_{-\infty}^{+\infty} P(x, y)\, \mathrm{d}x\, \mathrm{d}y, \tag{5.1.20}$$

where $P(x, y)$ is expressed as a funtion of the transverse component of the electric field $E_x(x, y) = E_{\mathrm{NL}}(x)\phi(y)$ with the help of Eqs. (2.1.54) and (1.5.2b):

$$P(x, y) = \frac{\epsilon_0 \epsilon(x, y) c}{2\beta} E_x^2(x, y). \tag{5.1.21}$$

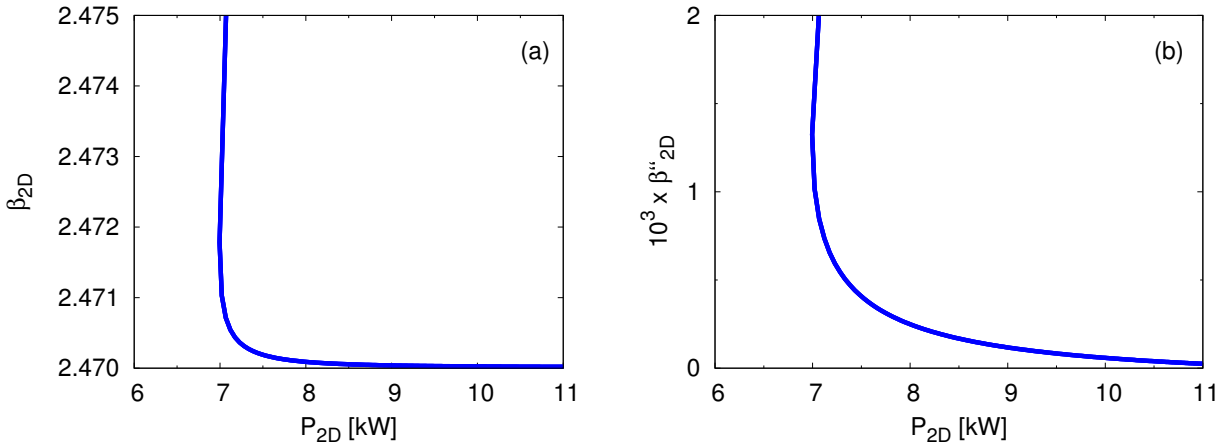

Figure 5.1: Nonlinear dispersion curve of the two-dimensional plasmon–soliton in a four-layer configuration with parameters: $\tilde{\epsilon}_1 = 2.47^2 + 10^5 i$, $n_2^{(1)} = 10^{17}$ m^2/W (chalcogenide glass), $\tilde{\epsilon}_2 = 1.44 + 10^5 i$ (silica), $\tilde{\epsilon}_3 = -96 + 10i$ (gold), $\tilde{\epsilon}_4 = 1 + 10^5 i$ (air), $L = 15$ nm, $d = 40$ nm, and $\lambda = 1.55$ μm. (a) Real and (b) imaginary parts of the effective index are presented as a function of the total power.

The dispersion curves of the two-dimensional plasmon–soliton presented in Fig. 5.1 can be compared with the dispersion curves of the one-dimensional solution obtained for the configuration with identical material parameters, which is presented in Fig. 4.12. The dispersion curves of the one-dimensional solution presents the effective index β_{NL} as a function of the power density P_{tot} expressed in W/m. In this coordinates, the increase of the effective index of the one-dimensional plasmon–soliton is accompanied by the monotonous increase of the power density. In case of the two-dimensional solutions, with the increase of the effective index $\beta_{2\mathrm{D}}$ the total power $P_{2\mathrm{D}}$ decreases for low values of $\beta_{2\mathrm{D}}$ until it reaches its minimum at $P_{2\mathrm{D}} \approx 7$ kW corresponding to $\beta_{2\mathrm{D}} \approx 2.472$. Above this value of the effective index, the total power slowly decreases with the increase of $\beta_{2\mathrm{D}}$. The imaginary part to the effective index shows a behavior similar to the real part [see Fig. 5.1(b)].

In Fig. 5.2, a comparison of the dispersion curves obtained using the one-dimensional model (the FBM) and the two-dimensional model is shown where the effective index is presented as a function of the peak intensity of the solitonic part of plasmon–soliton. We observe that the effective index of the two-dimensional solution is lower than the one of the one dimensional plasmon–soliton which means

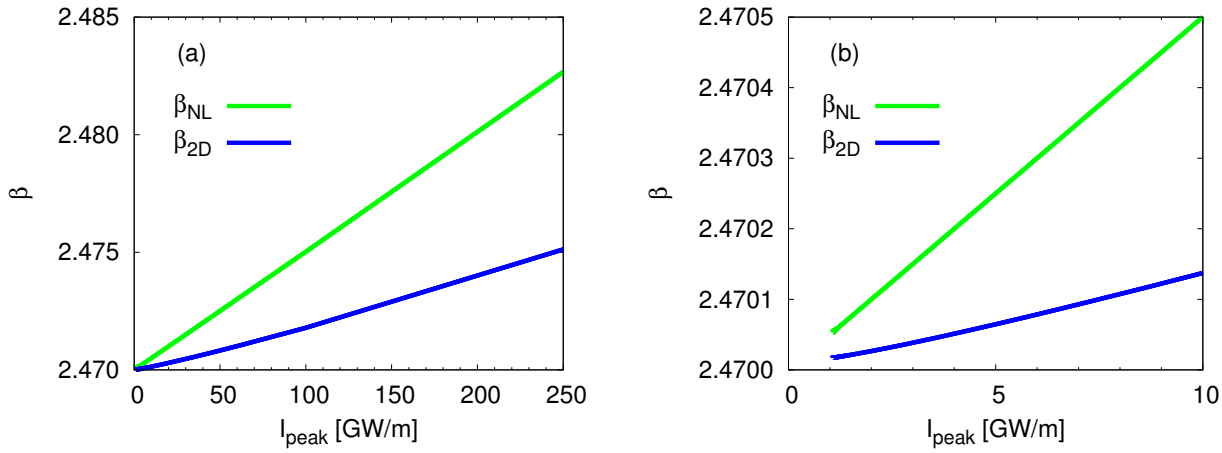

Figure 5.2: Nonlinear dispersion curves $\beta(I_{\mathrm{peak}})$ for one- and two-dimensional plasmon–solitons. (a) Full curve and (b) zoom on the region with low peak intensity.

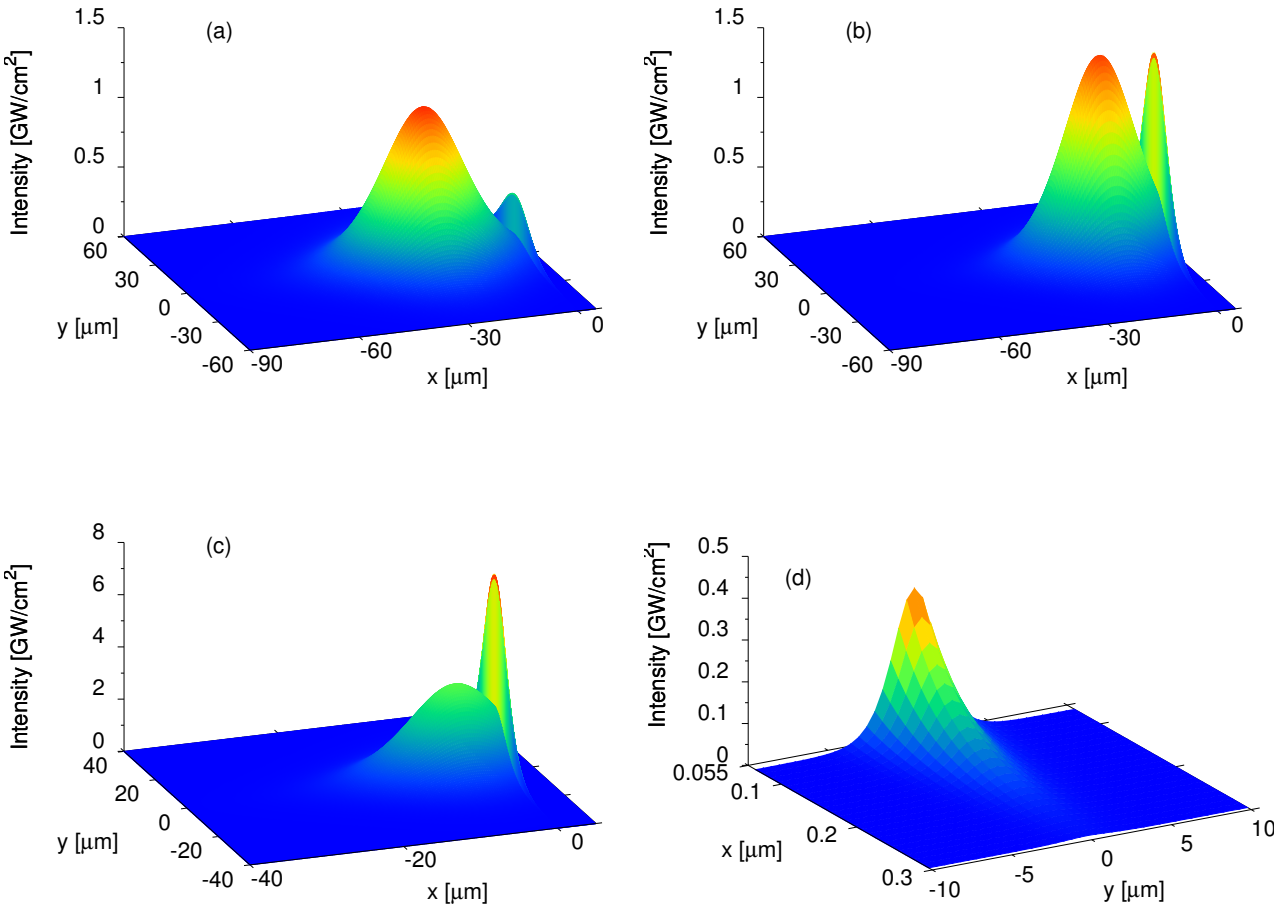

Figure 5.3: Two-dimensional profiles of plasmon–solitons in a four-layer structure with the parameters identical to these in Fig. 5.1. Low-power solutions with (a) peak intensity 1.2 GW/cm^2 and $x_0 = -25$ μm; (b) peak intensity 1.5 GW/cm^2 and $x_0 = -15$ μm; and (c), (d) a moderate-power solution with peak intensity 3.5 GW/cm^2 and $x_0 = -5$ μm. (d) Zoom on the plasmonic tail in the external dielectric layer ($x > 55$ nm) of the profile shown in subplot (c).

that the correction $\Delta\beta$ defined in Eqs. (5.1.11) and (5.1.19) is negative. Both the effective index of the one-dimensional plasmon–soliton β_{NL} and two-dimensional solution β_{2D} are linear functions of the solitonic part peak intensity.

In Fig. 5.3, exemplary two-dimensional profiles of the intensity of plasmon–solitons are presented. In panel (a), the solution with the solitonic peak centered at $x_0 = -25$ μm is shown, for which the peak intensity is at the level of $I_{\mathrm{peak}} \approx 1.2$ GW/cm^2. This solution interacts weakly with the metal film and the plasmonic part has low intensity. In panel (b), the center of the solitonic part of the solution is brought closer to the metal film ($x_0 = -15$ μm). This results in the increase of the effective index of the solution and therefore, the increase of the peak intensity (to $I_{\mathrm{peak}} \approx 1.5$ GW/cm^2). The solution is now more localized in both x and y directions and it interacts strongly with the metal film. The intensity of the plasmonic part is now equal to the peak intensity of the solitonic part. Finally, the solution with the solitonic part centered at $x_0 = -5$ μm is presented in panel (c) for which $I_{\mathrm{peak}} \approx 3.5$ GW/cm^2. For this solution, the intensity of the plasmonic part is twice higher than the peak intensity of the solitonic part. In panel (d) the plasmonic tail in the external dielectric layer is depicted. The peak intensity in this layer is at the level of $I_{\mathrm{plas}} \approx 0.45$ GW/cm^2.

5.2 No solutions in the transverse electric case

Here we present the derivation of the dispersion relation in the frame of the FBM for the four-layer structure presented in Fig. 2.1 in the case of the transverse electric (TE) polarized waves. For this light polarization the electromagnetic fields have only three nonzero components $\boldsymbol{\mathscr{E}} = [0, \mathscr{E}_y, 0]$ and $\boldsymbol{\mathscr{H}} = [\mathscr{H}_x, 0, i\mathscr{H}_z]$. Following similar method as in the TM case presented in Sec 2.1, we start the derivation from Maxwell's equations for the TE case [Eqs. (1.4.2)]. Using the field form given by Eq. (1.5.1) we obtain

$$k_0 \beta H_x - \frac{\mathrm{d}H_z}{\mathrm{d}x} = -\epsilon_0 \epsilon_y \omega E_y, \tag{5.2.1a}$$

$$H_x = -\frac{\beta}{\mu_0 c} E_y, \tag{5.2.1b}$$

$$H_z = \frac{1}{\mu_0 \omega} \frac{\mathrm{d}E_y}{\mathrm{d}x}. \tag{5.2.1c}$$

Taking the derivative with respect to x of Eq. (5.2.1c) and using Eqs. (5.2.1a) and (5.2.1b) we obtain a single nonlinear wave equation for the E_y component [compare with the nonlinear wave equation for H_y component derived in the TM case — Eq. (2.1.7a)]:

$$\frac{\mathrm{d}^2 E_y}{\mathrm{d}x^2} - k_0^2 q^2(x) E_y + k_0^2 \alpha(x) E_y^3 = 0, \tag{5.2.2}$$

where the full isotropic Kerr-type nonlinear permittivity is taken into account:

$$\epsilon_x(x) = \epsilon_y(x) = \epsilon_z(x) = \epsilon_l(x) + \alpha(x)\mathbf{E}^2(x) = \epsilon_l(x) + \alpha(x) E_y^2(x). \tag{5.2.3}$$

For TE polarized waves, only one electric field component E_y is present and the only permittivity tensor component that plays a role in Maxwell's equations is ϵ_y.

In comparison with the TM case, the derivation of the nonlinear wave equation for TE polarized light [Eq. (5.2.2)] does not require any additional assumptions. The term with the derivative of the nonlinear permittivity [see Eq. (2.1.2)] does not appear in course of the derivation. Therefore, this equation holds even for high nonlinear permittivity changes and for solution that induce permittivity profiles that vary rapidly in comparison with the wavelength.

The solution of Eq. (5.2.2) is derived in a similar manner as in Sec. 2.1.2. The electric field in each layer is given by (the y subscript of the electric field is skipped as for the TE polarization there is only one electric field component, while the subscript indicating the nonlinear layer is added, see Fig. 2.1):

$$E_1 = \sqrt{\frac{2}{\alpha_1}} \frac{q_1}{\cosh[k_0 q_1 (x - x_0)]} \qquad \text{for } x < 0, \tag{5.2.4a}$$

$$E_2 = A_+ e^{k_0 q_2 x} + A_- e^{-k_0 q_2 x} \qquad \text{for } 0 \leqslant x < L, \tag{5.2.4b}$$

$$E_3 = B_+ e^{k_0 q_3 (x-L)} + B_- e^{-k_0 q_3 (x-L)} \qquad \text{for } L \leqslant x < L + d, \tag{5.2.4c}$$

$$E_4 = C e^{-k_0 q_4 [x-(L+d)]} \qquad \text{for } x \geqslant L + d. \tag{5.2.4d}$$

Use of the boundary condition $E_y \xrightarrow{x \to \infty} 0$ in the layer 4 results in the single term in Eq. (5.2.4d).

Finally, using the continuity conditions of the E_y and H_z fields at the interfaces [H_z is calculated using Eq. (5.2.1c)], the analytical form of the nonlinear dispersion relation the TE polarized light in four-layer structures is obtained:

$$\Phi_+ \Big(q_4 + q_3 \Big) \exp(2 k_0 q_3 d) + \Phi_- \Big(q_4 - q_3 \Big) = 0, \tag{5.2.5a}$$

where

$$\Phi_\pm = \left(1 \pm \frac{q_{1,\mathrm{nl}}}{q_3} \right) + \left(\frac{q_{1,\mathrm{nl}}}{q_2} \pm \frac{q_2}{q_3} \right) \tanh(k_0 q_2 L). \tag{5.2.5b}$$

The comparison between the nonlinear dispersion relations for the TE light polarization [Eq. (5.2.5)] and the dispersion relation in the TM polarized light [Eq. (2.1.43)] shows that the former can be obtained by the following substitution in the latter:

$$\widetilde{q}_i \mapsto q_i \qquad \text{for } i \in \{2,3,4\}, \tag{5.2.6}$$

$$\widetilde{q_{1,\mathrm{nl}}}|_{x=0} \mapsto q_{1,\mathrm{nl}}. \tag{5.2.7}$$

Our studies show that for the structure parameter range studied in Chapter 4 for TM polarized light, in the TE case no solutions of the dispersion relation [Eq. (5.2.5)] exist. This results are in agreement with the linear studies of plasmons. Metallic structures do not support TE polarized waves in the linear regime [55]. We show that, in the nonlinear regime, for the materials studied in this PhD thesis, TE polarized plasmon–solitons do not exist.

Part II

Configurations with finite-size nonlinear medium — Plasmonic nonlinear slot waveguides

In Part II of this PhD manuscript, we focus on the studies of structures where a finite-size nonlinear dielectric layer is sandwiched between two semi-infinite metal layers. This type of structures will be called nonlinear slot waveguide and it is schematically presented in Fig. 6.1. There are two reasons to study the nonlinear slot waveguide structures. From the practical point of view, it is easier to fabricate high quality thin nonlinear films than bulky layers, like those needed in the configurations with semi-infinite nonlinear medium discussed in Part I (see Fig. 2.1). Moreover, the nonlinear slot waveguide configurations have more potential applications. Devices based on the nonlinear slot waveguide configuration can be used for phase matching in higher harmonic generation processes [148] and for nonlinear plasmonic couplers [93, 99]. Nonlinear switching [149] was theoretically predicted in nonlinear slot waveguide based structures that is similar to the nonlinear switching in graphene couplers [150]. Tapered nonlinear slot waveguides might be used for nanofocusing and loss compensation in order to enhance nonlinear effects [151]

Waveguides with a nonlinear dielectric core have already been studied extensively in literature for many years. The studies started in 1982, with the paper of Fedyanin and Mihalache [41] presenting TM polarized nonlinear surface waves in a layered fully dielectric structure with a nonlinear core. The structure studied there was built of a Kerr-type nonlinear dielectric core sandwiched between two linear dielectrics. A number of studies of such structures followed for both transverse electric (TE) and transverse magnetic (TM) polarizations using different techniques [38–40, 42–44]. In most of the works, the solutions of Maxwell's equations were given in terms of Jacobi elliptic functions [152]. A symmetry-breaking bifurcation of an asymmetric mode from the fundamental symmetric mode was predicted [38, 39]. Scaling rules for such nonlinear dielectric waveguides have been developed [45] that introduced reduced dimensionless parameters to describe the waveguide properties. Various methods to study waveguides with both nonlinear core and cladding were proposed [27, 28, 46–51].

In 2007, the studies of waveguides with a nonlinear core were expanded from dielectric to metal cladding. Feigenbaum and Orenstein made the first attempt to study such structures [85]. Their method describes sub-wavelength confinement of light in two-dimensional plasmon–soliton beams. Such a strong confinement is ensured by a linear plasmon profile in the transverse direction and by the self-focusing effect in the lateral direction.

In the works of Rukhlenko *et al.* [89, 90], analytical formulas for the dispersion relations of slot waveguides were presented for symmetric and antisymmetric nonlinear modes only. These dispersion relations were given in a form integral equations that have to solved numerically. Study of Davoyan *et al.* [87] showed that in slot waveguides with nonlinear dielectric core and metal cladding, symmetry-breaking bifurcation also occurs. Moreover, it was shown that plasmonic coupling and symmetry breaking phenomena can be observed in waveguides built of linear dielectric core sandwiched by nonlinear metals [99, 100].

In Chapter 6, we build two new models that have never been used before to study the nonlinear metal slot waveguide configurations. The results obtained using these models are presented in Chapter 7. In order to confirm the validity of these new models, their results are directly compared. Using our models, we confirm the existence of the already known symmetry-breaking bifurcation and show that higher-order, not known previously, nonlinear modes exist in such structures. We predict the nonlinear symmetry-breaking bifurcation for some of these higher-order modes.

Using our models, we study the influence of the size of the nonlinear core and of the permittivity contrast between the core and the metal cladding on the symmetric nonlinear slot waveguide properties. We optimize the core size and the permittivity contrast in order to obtain two kind of nonlinear effects at low power levels. Firstly, to lower the intensity threshold required to observe the symmetry-breaking bifurcation and the appearance of the nonlinear asymmetric mode. Secondly, to observe at low powers the appearance of a higher-order symmetric or antisymmetric nonlinear modes in the waveguide. Finally, we study the properties of asymmetric nonlinear slot waveguides.

Chapter 6

Theory of nonlinear slot waveguides

Contents

This chapter presents a derivation of the dispersion relations for the stationary TM polarized waves propagating in structures built of a finite-size layer of a positive Kerr-type nonlinear material sandwiched between two semi-infinite linear media which can in particular be metals (see Fig. 6.1). The structures presented in Fig. 6.1 with metal cladding are called plasmonic nonlinear slot waveguides (or shortly 'nonlinear slot waveguides').

We will propose two models for the nonlinear slot waveguides. The first model is based on the approach proposed for fully dielectric structures in [40, 41]. This approach uses the approximated treatment of the nonlinearity in the Kerr medium (only the transverse electric field component is assumed to cause the nonlinear permittivity changes) and additionally the nonlinear modification of the permittivity should remain low [81] (the assumptions on the nature of the nonlinear permittivity used here are identical to these for the FBM presented in Section 2.1). These assumptions allow us to write and to solve a single nonlinear wave equation in the finite-size nonlinear layer. Using the field continuity conditions at the core interfaces located at $x = 0$ and $x = d$ (see Fig. 6.1) the analytical formulas for the dispersion relations and for the field profiles are obtained and are expressed in terms of Jacobi elliptic functions [152]. Therefore, this model will be called Jacobi elliptic function based model (JEM).

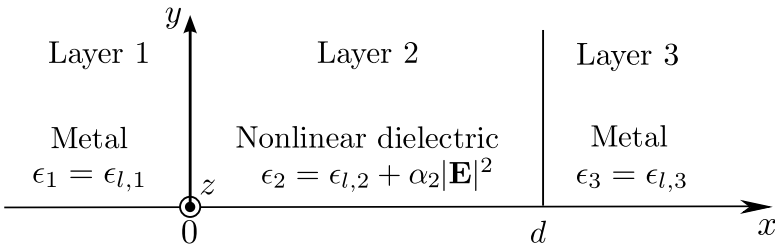

Figure 6.1: Geometry of the plasmonic nonlinear slot waveguide with the parameters of the structure.

The second model is based on the approaches from Refs. [15, 77] for a single interface between a nonlinear dielectric and a metal, and therefore it is named the interface model (IM). This model allows for obtaining separate dispersion relations on the two interfaces of the nonlinear slot waveguide in analytical forms. Comparing the dispersion equations for left interface and for the right interface, results in an analytical condition that reduces the parameter space in which the solutions of Maxwell's equations in nonlinear slot waveguides are sought. The solutions are found by the numerical integration of Maxwell's equation in the core which allows then to relate the two interfaces. Maxwell's equations in the core are solved using the shooting method [88]. If the result of integration is consistent with the previously assumed values of the field and its derivatives at the slot interfaces then the corresponding β is accepted as a genuine solution in our problem.

6.1 Jacobi elliptic function based model

We start the presentation of the models for nonlinear slot waveguides with the approach that uses strong assumptions on the form of the nonlinear Kerr term but it provides the dispersion relations and the field profiles in analytical forms. This model provides more insight and understanding of the nature of the problem of finding stationary solutions in nonlinear slot waveguides than the second, more numerical model. First, we will solve the nonlinear wave equation inside the waveguide core and find the nonlinear field profiles. Knowing the field profiles, we will be able to derive the dispersion relations for the nonlinear slot waveguide using the continuity conditions on the nonlinear core interfaces.

6.1.1 Nonlinear field profiles

In the frame of the JEM, the Kerr-type nonlinearity is not treated in an exact manner. Similar to the FBM presented in Section 2.1, we assume that the nonlinear response of the material depends only on the transverse component of the electric field E_x in the following way [compare with Eq. (2.1.5)]:

$$\epsilon_x(x, E_x) = \epsilon_z(x, E_x) = \epsilon(x, E_x) = \epsilon_l(x) + \alpha(x)E_x^2(x). \tag{6.1.1}$$

Functions $\epsilon_l(x)$ and $\alpha(x)$ are step-wise functions which take the values indicated in Table 6.1 depending on the layer (see Fig. 6.1 for layer number).

Layer	Abscissa	$\epsilon_l(x)$	$\alpha(x)$
1	$x < 0$	$\epsilon_1 = \epsilon_{l,1}$	0
2	$0 \leqslant x < L$	$\epsilon_{l,2}$	$\epsilon_0 c \epsilon_{l,2} n_2^{(2)} = \alpha_2$
3	$L \leqslant x < L + d$	$\epsilon_3 = \epsilon_{l,3}$	0

Table 6.1: Values of the functions $\epsilon_l(x)$ and $\alpha(x)$ describing the properties of the materials in different layers. The second-order nonlinear refractive index (see Page 11) in layer 2 is denoted by $n_2^{(2)}$.

The derivation of the JEM starts from Maxwell's equations [Eqs. (1.5.2)]. These equations are combined together with Eq. (6.1.1) and with the help of the approximations about small nonlinear permittivity change and using the assumption that $|E_x| \gg |E_z|$ we obtain the nonlinear wave equation [Eq. (2.1.7a)] which is recalled here:

$$\frac{\mathrm{d}^2 H_y}{\mathrm{d}x^2} - k_0^2 q^2(x) H_y + k_0^2 a(x) H_y^3 = 0. \tag{6.1.2}$$

A detailed derivation of Eq. (6.1.2) and the definitions of the functions $q(x)$ [see Eq. (2.1.7b)] and $a(x)$ [see Eq. (2.1.7c)] are presented in Section 2.1.1.

At this point, it is worth commenting on the validity of the two assumptions that were made on the nonlinear term, in order to derive Eq. (6.1.2). Even in the case of linear metal slot waveguides (linear dielectric core sandwiched between two semi-infinite linear metals), the two components of the electric

field E_x and E_z can have comparable amplitudes. The narrower the waveguide the faster the spatial (in the transverse x direction) variation of the magnetic field H_y (especially in the case of higher-order modes). Therefore the longitudinal electric field component E_z that is proportional to the derivative of the H_y [see Eqs. (1.5.2)] will have high amplitude. In the case of the semi-infinite nonlinear medium studied in Part I, the spatial variations of the magnetic field were slower than in slot waveguides, and therefore the assumption that $|E_x| \gg |E_z|$ was better fulfilled. In the case of slot waveguides, this assumption will not be satisfied by all the solutions. A more detailed analysis of the validity of this assumption will be presented in Chapter 7 (see Fig. 7.5). The second assumption states that the nonlinear permittivity change remains small compared to the linear part of the permittivity. This assumption also will not be satisfied for most of the solutions obtained in the nonlinear slot waveguides. It is known in the nonlinear optics that, interesting nonlinear effects occur when the nonlinear induced permittivity modification is comparable with the linear permittivity contrast in the structure [153]. In nonlinear slot waveguides, due to the presence of metal layers, the linear permittivity contrast is large. Therefore, as we will be able to observe later (in Chapter 7 presenting the results), most of the interesting effects in slot waveguides occur for high values of nonlinear permittivity change. Nevertheless, we will see that, although those assumptions are not fully satisfied, the JEM described in this section correctly predicts all the qualitative features of the dispersion curves.

Coming back to the derivation of the JEM, we use the first integral treatment approach and integrate Eq. (6.1.2) with respect to x. The result reads

$$\left(\frac{\mathrm{d}H_y}{\mathrm{d}x}\right)^2 - k_0^2 q(x)^2 H_y^2 + k_0^2 \frac{a(x)}{2} H_y^4 = c_0. \tag{6.1.3}$$

The left-hand side of this equation gives us a formula for a quantity that is conserved along the transverse profile of the core of our one-dimensional nonlinear waveguide. Regardless of at which x position we calculate it, the result will always be equal to the integration constant c_0. In the derivation of the FBM (see Section 2.1.2) the integration constant was set to zero, because a semi-infinite nonlinear medium was analyzed.

In semi-infinite cladding layers, we can set the integration constant $c_0 = 0$ because both the magnetic field H_y and its derivative $\mathrm{d}H_y/\mathrm{d}x$ tend to zero as $x \to \pm\infty$. Additionally, in these linear layers $a(x)$ is equal to zero. Therefore, in the cladding, Eq. (6.1.2) reduces to a standard linear wave equation whose solutions are given by:

$$H_1 = H_0 e^{k_0 q_1 x} \qquad \text{for } -\infty \leqslant x < 0, \tag{6.1.4a}$$

$$H_3 = H_d e^{-k_0 q_3 (x-d)} \qquad \text{for } d \leqslant x < +\infty, \tag{6.1.4b}$$

where the magnetic field amplitudes at the interfaces $x = 0$ and $x = d$ are denoted by H_0 and H_d, respectively and q_k denotes a constant value of the $q(x)$ function [see Eq. (2.1.7b)] in k-th layer (for $k \in \{1, 2, 3\}$).Because both of these layers are semi-infinite, only the appropriate exponential solutions that decay at minus or plus infinity are considered in layers 1 and 3. As H_y is the only component of the magnetic field, in the following derivation we omit the y subscript and instead we use a subscript that enumerates the layer in which the field profile is defined (see Fig. 6.1).

The integration constant c_0 can be expressed using the magnetic field amplitude at the core interfaces. The continuity conditions for the tangential electromagnetic field components (H_y, E_z) at $x = 0$ yield:

1. For the magnetic field:

$$H_2|_{x=0^+} = H_0, \tag{6.1.5}$$

where $H_2(x)$ denotes the magnetic field profile in the nonlinear core that is the solution of Eq. (6.1.3). This profile is yet unknown and will be found by solving Eq. (6.1.3) at the end of this section.

2. For the longitudinal component of the electric field, using Eq. (1.5.2c):

$$\left.\frac{\mathrm{d}H_2}{\mathrm{d}x}\right|_{x=0^+} = \frac{\epsilon_{l,2}}{\epsilon_1} k_0 q_1 H_0, \tag{6.1.6}$$

where, based on the assumption that the nonlinear permittivity change is small, we have substituted $\epsilon_2|_{x=0^+}$ by $\epsilon_{l,2}$ in the numerator on the right-hand side.

Using Eqs. (6.1.5) and (6.1.6), we rewrite Eq. (6.1.3) taken at the point $x = 0^+$:

$$c_0 = k_0^2 \left[\left(\frac{\epsilon_{l,2}}{\epsilon_1} \right)^2 q_1^2 - q_2^2 + \frac{a_2}{2} H_0^2 \right] H_0^2, \tag{6.1.7}$$

where a_2 denotes a constant value of $a(x)$ function in the nonlinear core (layer 2). Using continuity conditions at the right core interface $x = d$, a similar expression for c_0 can be obtained. Consequently, Eq. (6.1.3) taken at the point $x = d^-$ yields:

$$c_0 = k_0^2 \left[\left(\frac{\epsilon_{l,2}}{\epsilon_3} \right)^2 q_3^2 - q_2^2 + \frac{a_2}{2} H_d^2 \right] H_d^2. \tag{6.1.8}$$

Equations (6.1.7) and (6.1.8) together with Eq. (6.1.3) will be helpful later to find the sign of the integration constant c_0. Looking at Eq. (6.1.3) we notice that for H_y field profiles that cross zero, at the point where $H_y = 0$, the only nonzero term on the left-hand side of this equation is $(\mathrm{d}H_y/\mathrm{d}x)^2$, which is strictly positive. Therefore, for this type of solutions, c_0 can only be positive.

In Section 2.1.2, we have stated that in case of a semi-infinite nonlinear medium the integration constant in Eq. (2.1.8) should be set to zero as both the magnetic field H_y and its derivative tend to zero at infinity. Using identical argument, the integration constant c_0 in Eq. (6.1.3) must be equal to zero $c_0 = 0$ if we consider a semi-infinite nonlinear medium and therefore a single interface between a metal and a nonlinear dielectric. Using Eq. (6.1.7), we can find an approximated analytical formula for the effective indices of nonlinear waves propagating at this interface. Setting $c_0 = 0$ in Eq. (6.1.7) we obtain

$$\left(\frac{\epsilon_{l,2}}{\epsilon_1} \right)^2 q_1^2 - q_2^2 + \frac{a_2}{2} H_0^2 = 0. \tag{6.1.9}$$

Using definitions of q_k and a_2 [see Eqs. (2.1.7b) and (2.1.7c)] in Eq. (6.1.9), we find the approximated expression for the effective index of a nonlinear wave at a single interface between a metal and a nonlinear dielectric in an explicit form:

$$\beta = \sqrt{\frac{\epsilon_1 \epsilon_{l,2}(\epsilon_{l,2} - \epsilon_1)}{\epsilon_{l,2}^2 - \epsilon_1^2 + \frac{n_2^{(2)} \epsilon_1^2 H_0^2}{2\epsilon_0 c \epsilon_{l,2}}}}. \tag{6.1.10}$$

Equation (6.1.10) gives also an approximated expression for the effective index of highly asymmetric solutions in slot waveguide configurations, as it will be proven by numerical results in Section 7.1.4. Highly asymmetric solutions are strongly localized on one of the interfaces and therefore the problem can be simplified to a single-interface problem. A comparison of the approximated solution given by Eq. (6.1.10) with the exact solutions of the JEM will be given in Section 7.1.4. More details on the limiting case for a single interface between a metal and a nonlinear dielectric are presented in Section 6.1.4, where we discuss the results for the symmetric nonlinear slot waveguide configuration.

It is worth noting that using Eq. (6.1.10) in the linear case ($H_0 \to 0$ or $n_2^{(2)} \to 0$), we recover the dispersion relation for a linear surface plasmon propagating along a single interface (see Eq. (2.14) in Ref. [55])

$$\beta = \sqrt{\frac{\epsilon_1 \epsilon_{l,2}}{\epsilon_1 + \epsilon_{l,2}}}. \tag{6.1.11}$$

After this digression we come back to the derivation of the exact solution of the JEM model. We are looking for guided waves in three-layer structures. Looking at Eqs. (6.1.4), we notice that the condition for the waves to be localized at the waveguide core is satisfied when both q_1 and q_3 are real and positive quantities. In order to satisfy this condition, we will look only for the solutions with $\beta > \max\{\epsilon_1, \epsilon_3\}$ [see the definition of $q(x)$ and q_k given by Eq. (2.1.7b)]. The quantity q_2 can be either real or imaginary leading to positive or negative values of q_2^2.

In order to find the solutions of the nonlinear wave equation [Eq. (6.1.2)] in the nonlinear core, we rewrite its first integral [Eq. (6.1.3)] in the form:

$$\frac{\mathrm{d}H_2}{\sqrt{c_0 + k_0^2 q_2^2 H_2^2 - k_0^2 \frac{a_2}{2} H_2^4}} = \pm \mathrm{d}x. \tag{6.1.12}$$

We introduce the reduced parameters Q and A [compare with the definitions of the reduced parameters given by Eqs. (2.1.10) in Part I where the semi-infinite nonlinear medium was analyzed]:

$$Q = k_0^2 q_2^2, \tag{6.1.13a}$$

$$A = (k_0^2 a_2/2)^{-1}. \tag{6.1.13b}$$

Equation (6.1.12) expressed using the reduced parameters reads:

$$\frac{\mathrm{d}H_2}{\sqrt{Ac_0 + AQH_2^2 - H_2^4}} = \pm \sqrt{\frac{1}{A}}\ \mathrm{d}x. \tag{6.1.14}$$

In our studies, we deal only with the focusing Kerr-type dielectrics, therefore A is always positive. Parameter Q can be either positive or negative depending on the sign of q_2^2. In the case of negative values of q_2^2 we can use Eq. (6.1.7) to determine the sign of c_0. For $q_2^2 < 0$, Eq. (6.1.7) can be written as:

$$c_0 = k_0^2 \left[\left(\frac{\epsilon_{l,2}}{\epsilon_1} \right)^2 q_1^2 + |q_2^2| + \frac{a_2}{2} H_0^2 \right] H_0^2. \tag{6.1.15}$$

All the terms in the sum inside of a square bracket are positive or nonnegative. Therefore this sum is positive. It is multiplied by $k_0^2 H_0^2$ which takes only nonnegative values. Thus, one concludes that for $q_2^2 < 0$ and $H_0 > 0$ the integration constant c_0 is positive ($c_0 > 0$). In the opposite case ($q_2^2 > 0$), the sign of c_0 remains indeterminate and for a given structure it depends both on β and H_0.

Here we summarize the remarks about the sign of the integration constant c_0 depending on the type of solution and the sign of q_2^2. The following logical dependencies hold:

1. From Eq. (6.1.3), we notice that for solutions with nodes (for which at one or more points in the core $H_2(x) = 0$) the integration constant is positive $c_0 > 0$.

2. From Eqs. (6.1.7) and (6.1.15), we see that

$$q_2^2 < 0 \Longrightarrow c_0 > 0. \tag{6.1.16}$$

   Using the logical contraposition $[(p \Longrightarrow q) \Longleftrightarrow (\neg q \Longrightarrow \neg p)]$ of the relation given by Eq. (6.1.16), we deduce that

$$c_0 < 0 \Longrightarrow q_2^2 > 0. \tag{6.1.17}$$

3. Using the contraposition of the statement in point 1 we deduce that for the integration constant $c_0 < 0$ only node-less solutions exist.

Solutions of Eq. (6.1.14) take different forms depending on the sign of parameters c_0 and Q (and therefore q_2^2). We will solve this equation in four cases depending on the sign of q_2^2 and c_0.

I. The case $q_2^2 > 0$

First, we will consider the case where $q_2^2 > 0$. As stated above, in this case, the sign of c_0 can not be determined *a priori* using analytical expression and reasoning. Therefore we will consider two sub-cases: $c_0^2 > 0$ and $c_0^2 < 0$.

I.a The subcase $c_0 > 0$

At first, we consider the case where $c_0 > 0$ and find the solutions of the nonlinear wave equation [Eq. (6.1.3)] for this case. Equation (6.1.3) was transformed into Eq. (6.1.14) and its left-hand side can be expressed in the form of the integrand of an elliptic integral (see Ref. [154] or Appendix B):

$$\frac{\mathrm{d}H_2}{\sqrt{(\gamma^2 + H_2^2)(\delta^2 - H_2^2)}} = \pm\sqrt{\frac{1}{A}}\ \mathrm{d}x, \tag{6.1.18}$$

where the parameters γ and δ were introduced. In order to relate the newly introduced parameters with parameters A, Q, and c_0, we compare the expressions under the square-root on the left-hand sides of Eqs. (6.1.14) and (6.1.18). This comparison results in

$$\gamma^2 = \frac{\pm\sqrt{A^2Q^2 + 4Ac_0} - AQ}{2}, \tag{6.1.19a}$$

$$\delta^2 = \gamma^2 + AQ = \frac{\pm\sqrt{A^2Q^2 + 4Ac_0} + AQ}{2}. \tag{6.1.19b}$$

The proper choice for the sign in front of the square-roots is dictated by the fact that we have assumed that the magnetic field component H_y is a real quantity. Solutions of Eq. (6.1.18) are real on condition that both γ and δ are real quantities. From the fact that q_2^2 and c_0 in the subcase I.a are positive and the fact that we consider a positive Kerr effect $a_2 > 0$, we deduce that both Q and A are positive quantities. Therefore, all the quantities appearing in the definitions of γ and δ are positive. Keeping that in mind, we write bounds on the expressions for γ and δ. Using the fact that $x \leqslant \sqrt{x^2 + y^2} \leqslant x + y$ for $x, y \in R^+$, we find bonds on γ^2:

$$\frac{\pm AQ - AQ}{2} \leqslant \gamma^2 \leqslant \frac{\pm(AQ + 2\sqrt{Ac_0}) - AQ}{2}. \tag{6.1.20}$$

For γ to be real γ^2 must be positive. This is ensured by the choice of the top plus sign in front of the square-root in the definition [Eqs. (6.1.19)]. Finally, in the subcase I.a the quantities γ and δ are defined by

$$\gamma^2 = \frac{\sqrt{A^2Q^2 + 4Ac_0} - AQ}{2}, \tag{6.1.21a}$$

$$\delta^2 = \frac{\sqrt{A^2Q^2 + 4Ac_0} + AQ}{2}. \tag{6.1.21b}$$

After having determined the correct sign in expressions for γ and δ, we continue our derivation. Integrating Eq. (6.1.18), we obtain

$$\int_{H_2(0)}^{H_2(x)} \frac{\mathrm{d}H_2}{\sqrt{(\gamma^2 + H_2^2)(\delta^2 - H_2^2)}} = \pm\sqrt{\frac{1}{A}}\ x. \tag{6.1.22}$$

The integral on the left-hand side of Eq. (6.1.22) can be separated into two integrals:

$$\int_{H_2(0)}^{H_2(x)} \frac{\mathrm{d}H_2}{\sqrt{(\gamma^2 + H_2^2)(\delta^2 - H_2^2)}} = \int_{H_2(0)}^{\delta} \frac{\mathrm{d}H_2}{\sqrt{(\gamma^2 + H_2^2)(\delta^2 - H_2^2)}} - \int_{H_2(x)}^{\delta} \frac{\mathrm{d}H_2}{\sqrt{(\gamma^2 + H_2^2)(\delta^2 - H_2^2)}}. \tag{6.1.23}$$

Inserting Eq. (6.1.23) into Eq. (6.1.22), yields

$$\int_{H_2(0)}^{\delta} \frac{\mathrm{d}H_2}{\sqrt{(\gamma^2+H_2^2)(\delta^2-H_2^2)}} - \int_{H_2(x)}^{\delta} \frac{\mathrm{d}H_2}{\sqrt{(\gamma^2+H_2^2)(\delta^2-H_2^2)}} = \pm\sqrt{\frac{1}{A}}\,x. \tag{6.1.24}$$

Multiplying Eq. (6.1.24) by $\sqrt{\gamma^2+\delta^2}$ and using formula 17.4.52 from Ref. [112] (see also Appendix B), gives

$$\mathrm{cn}^{-1}\left[\frac{H_2(0)}{\delta}\middle|\frac{\delta^2}{\gamma^2+\delta^2}\right] - \mathrm{cn}^{-1}\left[\frac{H_2(x)}{\delta}\middle|\frac{\delta^2}{\gamma^2+\delta^2}\right] = \pm\sqrt{\frac{\gamma^2+\delta^2}{A}}\,x, \tag{6.1.25}$$

where $\mathrm{cn}^{-1}(u|m)$ is the inverse of the Jacobi elliptic function $\mathrm{cn}(u|m)$. Jacobi elliptic functions are defined with the argument u and the parameter m. For a review of the necessary properties of these special functions see Appendix C. Reorganizing the terms and applying the Jacobi elliptic function cn to both sides of Eq. (6.1.25), results in the expression for the magnetic field in the core of a nonlinear slot waveguide in the case where both c_0 and q_2^2 are positive:

$$H_2(x) = \delta\,\mathrm{cn}\left\{\mp\sqrt{\frac{\gamma^2+\delta^2}{A}}\,x + \mathrm{cn}^{-1}\left[\frac{H_2(0)}{\delta}\middle|\frac{\delta^2}{\gamma^2+\delta^2}\right]\middle|\frac{\delta^2}{\gamma^2+\delta^2}\right\}, \tag{6.1.26}$$

We are still left with the uncertainty about the sign in front of the square-root in the argument of the cn function in Eq. (6.1.26). From the properties of the Jacobi elliptic function cn, we conclude that $H_2(x)$ give by Eq. (6.1.22) takes values only from the interval $[-\delta,\delta]$. Knowing this and looking at Eq. (6.1.22), we notice that the expression under the square-root in the denominator of the left-hand side takes only values from the interval $[0,+\infty)$. In our case, the nonlinear core occupies the space $x\in[0,d]$ therefore we consider only $x\geqslant 0$. In the following, the argument for the case where the right interface of the core is located at $d>0$ is presented. For the opposite case ($d<0$), the reasoning is similar but the result is opposite. In order to choose the sign on the right-hand side of Eq. (6.1.22), we need to investigate the sign of $\mathrm{d}H_2$ under the integral on the left-hand side of this equation. If we consider the vicinity of the interface $x=0$ and take into account the continuity conditions for the tangential electromagnetic field components at this interface, we notice that in the case of metal cladding ($\epsilon_1<0$), the magnetic field derivative changes sign at this interface [continuity conditions for E_z electric field component given by Eq. (1.5.2c)]. In the case where the field in the left metal cladding is positive ($H_0>0$) its derivative is also positive [field described by Eq. (6.1.4a)]. Therefore, at $x=0^+$, the magnetic field derivative is negative. This means that the infinitesimal changes $\mathrm{d}H_2$ are negative. This brings us to the conclusion that for $H_0>0$, the correct choice of the sign on the right-hand side of Eq. (6.1.22) is the bottom minus sign. In the case where $H_0<0$, the derivative of the magnetic field in the core close to the left interface $(\mathrm{d}H_2/\mathrm{d}x)|_{x=0^+}$ is positive and therefore the infinitesimal changes $\mathrm{d}H_2$ are positive. In this case ($H_0<0$), the correct choice of the sign on the right-hand side of Eq. (6.1.22) is the top plus sign. The same conclusion can be drawn by looking at Eq. (6.1.51) in Section 6.1.3.

Without loss of generality of the obtained results, in the following we choose the convention that $H_0>0$. Therefore, in Eq. (6.1.26), we chose the bottom plus sign in front of the square-root. Finally, the field profile in the nonlinear core for the subcase I.a is given by

$$\boxed{H_2(x) = \delta\,\mathrm{cn}\left\{\sqrt{\frac{\gamma^2+\delta^2}{A}}\,x + \mathrm{cn}^{-1}\left[\frac{H_2(0)}{\delta}\middle|\frac{\delta^2}{\gamma^2+\delta^2}\right]\middle|\frac{\delta^2}{\gamma^2+\delta^2}\right\}.} \tag{6.1.27}$$

I.b The subcase $c_0<0$

Here we consider the case where $c_0<0$. In order to work with positive quantities only, we substitute c_0 by $-|c_0|$ in Eq. (6.1.14) and obtain

$$\frac{\mathrm{d}H_2}{\sqrt{-A|c_0|+AQH_2^2-H_2^4}} = \pm\sqrt{\frac{1}{A}}\,\mathrm{d}x. \tag{6.1.28}$$

The left-hand side of Eq. (6.1.28) is then expressed in the form of the integrand of an elliptic integral (see Ref. [154] or Appendix B):

$$\frac{\mathrm{d}H_2}{\sqrt{(\gamma^2 - H_2^2)(H_2^2 - \delta^2)}} = \pm\sqrt{\frac{1}{A}}\ \mathrm{d}x. \tag{6.1.29}$$

Comparing the expressions under the square-root on the left-hand sides of Eqs. (6.1.28) and (6.1.29) allows us to find the relations between the new parameters γ and δ and the parameters A, Q, and c_0:

$$\gamma^2 = \frac{AQ \mp \sqrt{A^2Q^2 - 4A|c_0|}}{2}, \tag{6.1.30a}$$

$$\delta^2 = AQ - \gamma^2 = \frac{AQ \pm \sqrt{A^2Q^2 - 4A|c_0|}}{2}. \tag{6.1.30b}$$

The expression that appears under the square-root in Eqs. (6.1.30) is a difference of two positive quantities. In order for γ and δ to be real, the quantity under the square-root must be positive or equal to zero. Writing expression under the square-root explicitly using the definitions of A, Q [Eqs. (6.1.13)], and c_0 [Eq. (6.1.7)] we obtain

$$A^2Q^2 + 4Ac_0 = \left(q_2^2 - a_2H_0^2\right)^2 + 2a_2H_0^2\left(\frac{\epsilon_2|_{x=0^+}}{\epsilon_1}\right)^2 q_1^2, \tag{6.1.31}$$

which is greater or equal to zero because both terms in the sum are greater or equal to zero. This proves that γ and δ are real quantities.

The choice of the signs in front of the square-roots is Eqs. (6.1.30) is arbitrary. For both the top and the bottom signs the quantities γ^2 and δ^2 are positive. If we choose the top signs, we obtain a couple denoted by (γ_- and δ_+). If we choose the bottom signs, we obtain a couple denoted by (γ_+ and δ_-). We notice that $\gamma_- = \delta_-$ and $\gamma_+ = \delta_+$. Therefore, the two couples are composed of identical values that are only denoted differently. Moreover, the left-hand side of Eq. (6.1.29) has two equivalent forms:

$$\frac{\mathrm{d}H_2}{\sqrt{(\gamma^2 - H_2^2)(H_2^2 - \delta^2)}} = \frac{\mathrm{d}H_2}{\sqrt{(\delta^2 - H_2^2)(H_2^2 - \gamma^2)}}. \tag{6.1.32}$$

Based on all the facts stated above, we conclude that it is just a matter of convention which signs to choose. Here, we decide to use the lower signs so that $\gamma > \delta$. The final expressions for γ and δ in the subcase I.b read:

$$\gamma^2 = \frac{AQ + \sqrt{A^2Q^2 - 4A|c_0|}}{2}, \tag{6.1.33a}$$

$$\delta^2 = \frac{AQ - \sqrt{A^2Q^2 - 4A|c_0|}}{2}. \tag{6.1.33b}$$

Having found the expressions for γ and δ, we proceed with the derivation process. Integrating Eq. (6.1.29) gives

$$\int_{H_2(0)}^{H_2(x)} \frac{\mathrm{d}H_2}{\sqrt{(\gamma^2 - H_2^2)(H_2^2 - \delta^2)}} = \pm\sqrt{\frac{1}{A}}\ x. \tag{6.1.34}$$

The integral on the left-hand side of Eq. (6.1.34) can be separated into two integrals:

$$\int_{H_2(0)}^{H_2(x)} \frac{\mathrm{d}H_2}{\sqrt{(\gamma^2 - H_2^2)(H_2^2 - \delta^2)}} = \int_{H_2(0)}^{\gamma} \frac{\mathrm{d}H_2}{\sqrt{(\gamma^2 - H_2^2)(H_2^2 - \delta^2)}} - \int_{H_2(x)}^{\gamma} \frac{\mathrm{d}H_2}{\sqrt{(\gamma^2 - H_2^2)(H_2^2 - \delta^2)}}. \tag{6.1.35}$$

Inserting Eq. (6.1.35) into Eq. (6.1.34), we obtain

$$\int_{H_2(0)}^{\gamma} \frac{\mathrm{d}H_2}{\sqrt{(\gamma^2 - H_2^2)(H_2^2 - \delta^2)}} - \int_{H_2(x)}^{\gamma} \frac{\mathrm{d}H_2}{\sqrt{(\gamma^2 - H_2^2)(H_2^2 - \delta^2)}} = \pm\sqrt{\frac{1}{A}}\ x. \tag{6.1.36}$$

Multiplying Eq. (6.1.36) by γ and using formula 17.4.44 from Ref. [112] (see also Appendix B) yields

$$\mathrm{dn}^{-1}\left[\frac{H_2(0)}{\gamma}\left|\frac{\gamma^2-\delta^2}{\gamma^2}\right.\right]-\mathrm{dn}^{-1}\left[\frac{H_2(x)}{\gamma}\left|\frac{\gamma^2-\delta^2}{\gamma^2}\right.\right]=\pm\sqrt{\frac{\gamma^2}{A}}\,x, \tag{6.1.37}$$

where dn^{-1} is the inverse of the Jacobi elliptic function dn (see Appendix C). Reorganizing the terms and applying the Jacobi elliptic function dn to both sides of Eq. (6.1.37) results in the expression for the magnetic field in the core of a nonlinear slot waveguide for positive q_2^2 and negative c_0:

$$H_2(x)=\gamma\,\mathrm{dn}\left\{\mp\sqrt{\frac{\gamma^2}{A}}\,x+\mathrm{dn}^{-1}\left[\frac{H_2(0)}{\gamma}\left|\frac{\gamma^2-\delta^2}{\gamma^2}\right.\right]\left|\frac{\gamma^2-\delta^2}{\gamma^2}\right.\right\}. \tag{6.1.38}$$

We are still left with the ambiguity about the sign in front of the square-root in the argument of the sd function in Eq. (6.1.38). Analyzing this equation it turns out that $H_2(x)$ takes values only from the interval $[\delta,\gamma]$. Using the same arguments as for the case $c_0>0$, we conclude that the proper choice for the sign in front of the square-root in Eqs. (6.1.34) and (6.1.36)–(6.1.38) is the bottom sign. The final expression for field profile in the nonlinear core for the subcase I.b is given by

$$\boxed{H_2(x)=\gamma\,\mathrm{dn}\left\{\sqrt{\frac{\gamma^2}{A}}\,x+\mathrm{dn}^{-1}\left[\frac{H_2(0)}{\gamma}\left|\frac{\gamma^2-\delta^2}{\gamma^2}\right.\right]\left|\frac{\gamma^2-\delta^2}{\gamma^2}\right.\right\}.} \tag{6.1.39}$$

II. The case $q_2^2<0$

Here we consider the case of $q_2^2<0$. As stated at the beginning of this section, in this case, the integration constant c_0 takes only positive values [see Eq. (6.1.16)]. In the following, we find solutions of the nonlinear wave equation [Eq. (6.1.2)] for this case.

In order to work only with positive quantities in Eq. (6.1.12), in the case of negative q_2^2, we will substitute q_2^2 by its negative absolute value $-|q_2^2|$. This substitution transforms Eq. (6.1.12) into

$$\frac{\mathrm{d}H_2}{\sqrt{c_0-k_0^2|q_2^2|H_2^2-k_0^2\frac{a_2}{2}H_2^4}}=\pm\,\mathrm{d}x. \tag{6.1.40}$$

We redefine Q given by Eq. (6.1.13a) to be positive. In the case II Q is defined by

$$Q=k_0|q_2^2| \tag{6.1.41}$$

and A is still defined by Eq. (6.1.13b). Using this definition, Eq. (6.1.40) can be written in the form:

$$\frac{\mathrm{d}H_2}{\sqrt{Ac_0-AQH_2^2-H_2^4}}=\pm\sqrt{\frac{1}{A}}\;\mathrm{d}x. \tag{6.1.42}$$

We rewrite Eq. (6.1.42) in the form of the elliptic integral:

$$\frac{\mathrm{d}H_2}{\sqrt{(\gamma^2+H_2^2)(\delta^2-H_2^2)}}=\pm\sqrt{\frac{1}{A}}\;\mathrm{d}x, \tag{6.1.43}$$

Comparing the expressions under the square-root on left-hand sides of Eqs. (6.1.42) and (6.1.43) allows us to find the relations between the new parameters γ and δ and the parameters A, Q, and c_0:

$$\delta^2=\frac{\pm\sqrt{A^2Q^2+4Ac_0}-AQ}{2} \tag{6.1.44a}$$

$$\gamma^2=\delta^2+AQ=\frac{\pm\sqrt{A^2Q^2+4Ac_0}+AQ}{2} \tag{6.1.44b}$$

The correct choice for the sign in front of the square-roots is again dictated by the fact that we have assumed that the magnetic field H_y is a real quantity. The solution of Eq. (6.1.43) is real if both γ and δ are real quantities. Using a similar reasoning as in the case I.a (see Page 82), by checking the bounding values for δ^2, we conclude that the proper choice of the sign in front of the square-root is the top plus sign. The final expressions for γ and δ in this case are:

$$\gamma^2 = \frac{\sqrt{A^2Q^2 + 4Ac_0} + AQ}{2}, \tag{6.1.45a}$$

$$\delta^2 = \frac{\sqrt{A^2Q^2 + 4Ac_0} - AQ}{2}. \tag{6.1.45b}$$

The following derivation is exactly the same as in the case I.a but we have to keep in mind that the definitions of γ and δ are reversed [compare Eqs. (6.1.21) and (6.1.45)] and that Q is defined by Eq. (6.1.41). Equation (6.1.43) is integrated and yields a formula that is identical to Eq. (6.1.22):

$$\int_{H_2(0)}^{H_2(x)} \frac{\mathrm{d}H_2}{\sqrt{(\gamma^2 + H_2^2)(\delta^2 - H_y^2)}} = \pm\sqrt{\frac{1}{A}}\, x. \tag{6.1.46}$$

By an analogy to the case presented in I.a, the final expression for the field profile in the nonlinear core for $q_2^2 < 0$ has the form:

$$\boxed{H_2(x) = \delta\,\mathrm{cn}\left\{\sqrt{\frac{\gamma^2+\delta^2}{A}}\, x + \mathrm{cn}^{-1}\left[\frac{H_2(0)}{\delta}\,\middle|\,\frac{\delta^2}{\gamma^2+\delta^2}\right]\middle|\,\frac{\delta^2}{\gamma^2+\delta^2}\right\}.} \tag{6.1.47}$$

6.1.2 Summary and unification of the expressions for field profiles in the nonlinear core

Before proceeding to the derivation of the analytical expressions for the nonlinear dispersion relations for the metal slot waveguide, we present the summary of the expressions for field profiles in the slot waveguide core in the form of a table.

The first column of Table 6.2 presents the results obtained for the subcase I.a, where q_2^2 and c_0 are greater than zero. The second column summarizes the subcase I.b, for which $q_2^2 > 0$ and $c_0 < 0$ and the third column shows the results in the case II, where $q_2^2 < 0$, in which we have shown that the only possibility is $c_0 > 0$ [see Eq. (6.1.16)]. A new quantity m was introduced that denotes the elliptic function parameter and is equal to the square of the elliptic modulus k. For more details on elliptic integrals and Jacobi elliptic functions see Appendices B and C. In Table 6.2, auxiliary parameter s and x_0 are introduced in order to simplify the notation.

During the field profile derivation, it was convenient to consider the case $c_0 > 0$ for positive and negative values of q_2^2. By distinguishing these two cases, we were able to define all the quantities that appeared during the derivation (in particular Q) in such a way that they are positive. Working with positive quantities only facilitated the choice of the plus or minus signs whenever it was ambiguous. Actually, cases I.a and II can be merged into one case using the definition $Q = k_0^2 q_2^2$. In this case, Q is no longer a strictly positive quantity and can be both positive and negative. Merging cases I.a and II together allows for reducing Table 6.2 to only two cases presented in Table 6.3.

Quantity \ Case	**I.a** $q_2^2 > 0$ and $c_0 > 0$	**I.b** $q_2^2 > 0$ and $c_0 < 0$	**II** $q_2^2 < 0$ therefore the only possibility $c_0 > 0$
c_0	$k_0^2 \left[\left(\frac{\epsilon_{l,2}}{\epsilon_1} \right)^2 q_1^2 - q_2^2 + \frac{a_2}{2} H_0^2 \right] H_0^2$		
A	$\frac{2}{k_0^2 a_2}$		
Q	$k_0^2 q_2^2$		$k_0^2 \lvert q_2^2 \rvert$
γ^2	$\frac{\sqrt{A^2Q^2+4Ac_0}-AQ}{2}$	$\frac{AQ+\sqrt{A^2Q^2-4A\lvert c_0 \rvert}}{2}$	$\frac{\sqrt{A^2Q^2+4Ac_0}+AQ}{2}$
δ^2	$\frac{\sqrt{A^2Q^2+4Ac_0}+AQ}{2}$	$\frac{AQ-\sqrt{A^2Q^2-4A\lvert c_0 \rvert}}{2}$	$\frac{\sqrt{A^2Q^2+4Ac_0}-AQ}{2}$
s	$\gamma^2 + \delta^2$	—	$\gamma^2 + \delta^2$
m	$\frac{\delta^2}{s}$	$\frac{\gamma^2-\delta^2}{\gamma^2}$	$\frac{\delta^2}{s}$
x_0	$-\sqrt{\frac{A}{s}}\,\mathrm{cn}^{-1}\left[\frac{H_2(0)}{\delta}\middle\vert m\right]$	$-\sqrt{\frac{A}{\gamma^2}}\,\mathrm{dn}^{-1}\left[\frac{H_2(0)}{\gamma}\middle\vert m\right]$	$-\sqrt{\frac{A}{s}}\,\mathrm{cn}^{-1}\left[\frac{H_2(0)}{\delta}\middle\vert m\right]$
$H_2(x)$	$\delta\,\mathrm{cn}\left[\sqrt{\frac{s}{A}}\,(x-x_0)\middle\vert m\right]$	$\gamma\,\mathrm{dn}\left[\sqrt{\frac{\gamma^2}{A}}\,(x-x_0)\middle\vert m\right]$	$\delta\,\mathrm{cn}\left[\sqrt{\frac{s}{A}}\,(x-x_0)\middle\vert m\right]$

Table 6.2: Comparison of the parameters used in the functions describing the magnetic field profile in the nonlinear core of the slot waveguide, in case of metal claddings for the three cases considered in Section 6.1.1.

Table 6.3 gives the expressions for the magnetic field profiles in the nonlinear core of the slot waveguides for $c_0 > 0$ and $c_0 < 0$. Based on these expressions and on the profiles of the Jacobi elliptic functions cn and dn shown in Appendix C, we can verify the agreement between the nature of the field profiles obtained analytically and deduced from conditions 1 and 3 on Page 81. For $c_0 > 0$, the magnetic field profile in the core is given analytically in Table 6.3 in terms of the Jacobi elliptic function cn. From Fig. C.1(a) we see that the continuous function cn, for values of the parameter $m \in [0, 1)$, takes values between -1 and 1 and therefore crosses zero. This means that the magnetic field profile for the case $c_0 > 0$ may possess nodes. This is coherent with the conclusion drawn in point 1 on Page 81. The case of $m = 1$, for which the function cn does not cross zero will be discussed in Section 6.1.4, where the limiting case of the dispersion relations obtained using the JEM for a single interface between a metal and a nonlinear dielectric is discussed.

For the case of $c_0 < 0$, the magnetic field profile in the core is given by Jacobi elliptic function dn. From Fig. C.1(b), we see that the function dn, takes values from the interval $(0, 1]$ and therefore never crosses zero. This means that the magnetic field profile for the case $c_0 < 0$ can not possess nodes. This is coherent with the conclusion drawn in point 3 on Page 81.

In Section 6.1.3, without loss of generality, we present the derivation of the dispersion relations for the nonlinear slot waveguide using in the reduced number of cases following Table 6.3.

Quantity \ Case	**I** $c_0 > 0$	**II** $c_0 < 0$
$q_2^2 = \beta^2 - \epsilon_{l,2}$	positive or negative	positive
c_0	$k_0^2 \left[\left(\frac{\epsilon_{l,2}}{\epsilon_1} \right)^2 q_1^2 - q_2^2 + \frac{a_2}{2} H_0^2 \right] H_0^2$	
A	$\frac{2}{k_0^2 a_2}$	
Q	$k_0^2 q_2^2$	
γ^2	$\frac{\sqrt{A^2Q^2+4Ac_0}-AQ}{2}$	$\frac{AQ+\sqrt{A^2Q^2-4A\lvert c_0\rvert}}{2}$
δ^2	$\frac{\sqrt{A^2Q^2+4Ac_0}+AQ}{2}$	$\frac{AQ-\sqrt{A^2Q^2-4A\lvert c_0\rvert}}{2}$
s	$\gamma^2 + \delta^2$	—
m	$\frac{\delta^2}{s}$	$\frac{\gamma^2-\delta^2}{\gamma^2}$
x_0	$-\sqrt{\frac{A}{s}}\,\mathrm{cn}^{-1}\left[\frac{H_2(0)}{\delta}\middle\vert m\right]$	$-\sqrt{\frac{A}{\gamma^2}}\,\mathrm{dn}^{-1}\left[\frac{H_2(0)}{\gamma}\middle\vert m\right]$
$H_2(x)$	$\delta\,\mathrm{cn}\left[\sqrt{\frac{s}{A}}\,(x-x_0)\middle\vert m\right]$	$\gamma\,\mathrm{dn}\left[\sqrt{\frac{\gamma^2}{A}}\,(x-x_0)\middle\vert m\right]$

Table 6.3: Simplified version of Table 6.2, where the number of cases was reduced to two. Here the distinction between cases is based on the sign of the integration constant c_0. The sign of q_2^2 in case II ($c_0 < 0$) is deduced from Eq. (6.1.17).

6.1.3 Nonlinear dispersion relations

I. The case $c_0 > 0$

At first, we derive the dispersion relation for nonlinear slot waveguides when $c_0 > 0$. Using the analytical formula for the field profile in the nonlinear core provided in Table 6.3, the field profiles in metal claddings given by Eqs. (6.1.4), and Maxwell's equations [Eqs. (1.5.2)], we write the continuity conditions for the tangential electromagnetic field components H_y and E_z at both interfaces between the nonlinear core and the metal cladding:

1. Continuity conditions at $x = 0$:

   (a) The continuity condition for the magnetic field component

   $$H_1|_{x=0^-} = H_2|_{x=0^+} \tag{6.1.48}$$

   yields

   $$H_0 = H_2(0). \tag{6.1.49}$$

   (b) The continuity condition for the tangential electric field component

   $$E_{z,1}|_{x=0^-} = E_{z,2}|_{x=0^+} \tag{6.1.50}$$

   transformed with the use of Eq. (1.5.2c) gives

   $$\frac{k_0 \epsilon_{l,2} q_1}{\epsilon_1} H_0 = \left.\frac{\mathrm{d}H_2}{\mathrm{d}x}\right|_{x=0^+}, \tag{6.1.51}$$

   where, based on the assumption that the nonlinear permittivity change is small, we substituted $\epsilon_2|_{x=0^+}$ by $\epsilon_{l,2}$ in the numerator on the left-hand side.

Equation (6.1.51) allows us to determine the sign of the magnetic field derivative inside the nonlinear core in the vicinity of its interface (at $x = 0^+$). Knowing that we look only for the solutions where $q_1 > 0$ (see Eq. (6.1.4a) and Page 81), the metal cladding permittivity is negative ($\epsilon_1 < 0$), and the core permittivity is positive ($\epsilon_{l,2} > 0$) and using the convention that H_0 is positive (see Page 83), we conclude that the sign of the derivative $(\mathrm{d}H_2/\mathrm{d}x)|_{x=0^+}$ is negative. This reasoning was used to determine the sign of the argument of the Jacobi elliptic function in Section 6.1.1 on Page 83.

Equations (6.1.48) and (6.1.51) have already been used in Section 6.1.1 in the derivation of the expression for the integration constant c_0 [see Eqs. (6.1.5) and (6.1.6)]. Therefore, we do not need to take them again into account because they do not bring any new information and do not result in a new constraint. Nevertheless, now we know the analytical expression for the magnetic field profile in the nonlinear core that is given in the first column of Table 6.3. Using this expression, the formulas for the Jacobi elliptic function derivatives, and the symmetry properties of Jacobi elliptic functions (for both derivatives and symmetry properties see Ref. [152] and Appendix C) we can express Eq. (6.1.51) explicitly:

$$\frac{k_0 q_1}{\epsilon_1} H_0 = \frac{\delta}{\epsilon_{l,2}} \sqrt{\frac{s}{A}}\, \mathrm{sn}\left[\sqrt{\frac{s}{A}} x_0 \,\middle|\, m\right] \mathrm{dn}\left[\sqrt{\frac{s}{A}} x_0 \,\middle|\, m\right], \tag{6.1.52}$$

where the parameters m, s, γ, and δ are defined in Table 6.3. We have checked numerically that this equation is an identity for all values of β which confirms the validity of our JEM formulation.

2. Continuity conditions at $x = d$:

   (a) The continuity condition for the magnetic field component

   $$H_2|_{x=d^-} = H_3|_{x=d^+} \tag{6.1.53}$$

   yields

   $$\delta \,\mathrm{cn}\left[\sqrt{\frac{s}{A}}\,(d - x_0)\,\middle|\, m\right] = H_d. \tag{6.1.54}$$

   (b) The continuity condition for the tangential electric field component

   $$E_{z,2}|_{x=d^-} = E_{z,3}|_{x=d^+} \tag{6.1.55}$$

   transformed with the use of Eq. (1.5.2c), the formulas for the Jacobi elliptic function derivatives, and the symmetry properties of Jacobi elliptic functions (see Appendix C) gives

   $$\frac{\delta\epsilon_3}{k_0 q_3 \epsilon_{l,2}}\sqrt{\frac{s}{A}}\,\mathrm{sn}\left[\sqrt{\frac{s}{A}}\,(d - x_0)\,\middle|\, m\right]\mathrm{dn}\left[\sqrt{\frac{s}{A}}\,(d - x_0)\,\middle|\, m\right] = H_d, \tag{6.1.56}$$

   where, based on the assumption that the nonlinear permittivity change is small, we substituted $\epsilon_2|_{x=0^+}$ by $\epsilon_{l,2}$ in the denominator on the left-hand side.

Comparing the two expressions for H_d given by Eqs. (6.1.54) and (6.1.56), we obtain the nonlinear dispersion relation in its final form for the case of $c_0 > 0$

$$\boxed{\mathrm{cn}\left[\sqrt{\frac{s}{A}}\,(d - x_0)\,\middle|\, m\right] = \frac{\epsilon_3}{k_0 q_3 \epsilon_{l,2}}\sqrt{\frac{s}{A}}\,\mathrm{sn}\left[\sqrt{\frac{s}{A}}\,(d - x_0)\,\middle|\, m\right]\mathrm{dn}\left[\sqrt{\frac{s}{A}}\,(d - x_0)\,\middle|\, m\right].} \tag{6.1.57}$$

In order to obtain the dispersion curves for the case $c_0 > 0$, Eqs. (6.1.57) has to be solved numerically for β for a given set of opto-geometric parameters of the structure (ϵ_1, $\epsilon_{l,2}$, $n_2^{(2)}$, ϵ_3, d) and parameters of light (λ, H_0). The values of β that satisfy this equation and the corresponding field profiles are solutions of our modal problem in the plasmonic nonlinear slot waveguide configuration.

II. The case $c_0 < 0$

Here we derive the dispersion relation for nonlinear slot waveguides when $c_0 < 0$. The method used here is exactly the same as in the previous case (for $c_0 > 0$). Using the analytical formula for the field profile in the nonlinear core provided in the second column of Table 6.3, the field profiles in metal claddings given by Eqs. (6.1.4), and Maxwell's equations [Eqs. (1.5.2)], we write the continuity conditions for the tangential electromagnetic field components H_y and E_z at both interfaces between the nonlinear core and the metal cladding:

1. Continuity conditions at $x = 0$:

   (a) The continuity condition for the magnetic field component

   $$H_1|_{x=0^-} = H_2|_{x=0^+} \tag{6.1.58}$$

   yields

   $$H_0 = H_2(0). \tag{6.1.59}$$

   (b) The continuity condition for the tangential electric field component

   $$E_{z,1}|_{x=0^-} = E_{z,2}|_{x=0^+} \tag{6.1.60}$$

   transformed with the use of Eq. (1.5.2c) gives

   $$\frac{k_0 \epsilon_{l,2} q_1}{\epsilon_1} H_0 = \left.\frac{\mathrm{d}H_2}{\mathrm{d}x}\right|_{x=0^+}, \tag{6.1.61}$$

   where, based on the assumption that the nonlinear permittivity change is small, we substituted $\epsilon_2|_{x=0^+}$ by $\epsilon_{l,2}$ in the numerator on the left-hand side.

In the general form [in the case where the $H_2(x)$ profile is not specified by any particular expression], Eqs. (6.1.58) and (6.1.61) are identical to Eqs. (6.1.48) and (6.1.51). In this general form they have already been used in Section 6.1.1 in the derivation of the expression for the integration constant c_0 [see Eqs. (6.1.5) and (6.1.6)]. Therefore, we do not need to take them again into account.

Although, if we consider Eq. (6.1.61) for the specific case of $c_0 < 0$ with the field profile given by formula Eq. (6.1.39) (corresponding to the second column of Table 6.3), then Eq. (6.1.61) is different form Eq. (6.1.51) that was written for the case $c_0 > 0$ and where the field profile H_2 is represented by Eq. (6.1.47) (corresponding to the first column of Table 6.3). We can express Eq. (6.1.61) explicitly using Eq. (6.1.39), the formulas for the Jacobi elliptic function derivatives, and the symmetry properties of Jacobi elliptic functions (see Appendix C). After these operations, Eq. (6.1.61) becomes

$$\frac{k_0 q_1}{\epsilon_1} H_0 = \frac{\gamma^2 m}{\epsilon_{l,2}} \sqrt{\frac{1}{A}}\, \mathrm{sn}\left[\sqrt{\frac{\gamma^2}{A}} x_0 \,\middle|\, m\right] \mathrm{cn}\left[\sqrt{\frac{\gamma^2}{A}} x_0 \,\middle|\, m\right]. \tag{6.1.62}$$

We have checked numerically that this equation is an identity for all values of β which confirms the validity of our JEM formulation.

2. Continuity conditions at $x = d$:

   (a) The continuity condition for the magnetic field component

   $$H_2|_{x=d^-} = H_3|_{x=d^+} \tag{6.1.63}$$

   yields

   $$\gamma\, \mathrm{dn}\left[\sqrt{\frac{\gamma^2}{A}}\,(d - x_0) \,\middle|\, m\right] = H_d. \tag{6.1.64}$$

   (b) The continuity condition for the tangential electric field component

   $$E_{z,2}|_{x=d^-} = E_{z,3}|_{x=d^+} \tag{6.1.65}$$

   transformed with the use of Eq. (1.5.2c), the formulas for the Jacobi elliptic function derivatives, and the symmetry properties of Jacobi elliptic functions (see Appendix C) gives

   $$\frac{\gamma^2 \epsilon_3 m}{k_0 q_3 \epsilon_{l,2}} \sqrt{\frac{1}{A}}\, \mathrm{sn}\left[\sqrt{\frac{\gamma^2}{A}}\,(d - x_0) \,\middle|\, m\right] \mathrm{cn}\left[\sqrt{\frac{\gamma^2}{A}}\,(d - x_0) \,\middle|\, m\right] = H_d, \tag{6.1.66}$$

   where, based on the assumption that the nonlinear permittivity change is small, we substituted $\epsilon_2|_{x=0^+}$ by $\epsilon_{l,2}$ in the denominator on the left-hand side.

Comparing the two expressions for H_d given by Eqs. (6.1.64) and (6.1.66), we obtain the nonlinear dispersion relation in its final form for the case of $c_0 < 0$

$$\boxed{\mathrm{dn}\left[\sqrt{\frac{\gamma^2}{A}}(d - x_0) \,\middle|\, m\right] = \frac{\epsilon_3 m}{k_0 q_3 \epsilon_{l,2}} \sqrt{\frac{\gamma^2}{A}}\, \mathrm{sn}\left[\sqrt{\frac{\gamma^2}{A}}\,(d - x_0) \,\middle|\, m\right] \mathrm{cn}\left[\sqrt{\frac{\gamma^2}{A}}\,(d - x_0) \,\middle|\, m\right].} \tag{6.1.67}$$

In order to obtain the dispersion relations for the case $c_0 < 0$, Eq. (6.1.67) has to be solved numerically for β for a given set of opto-geometric parameters of the structure (ϵ_1, $\epsilon_{l,2}$, n_2, ϵ_3, d) and parameters of light (λ, H_0). The values of β that satisfy this equation and the corresponding field profiles are solutions of our modal problem in the plasmonic nonlinear slot waveguide configuration. The solutions of Eq. (6.1.67) together with solutions of Eq. (6.1.57) build the full dispersion diagram for the nonlinear slot waveguide.

III. Summary of the dispersion relation results

To sum up the results of the Jacobi elliptic function based model we gather the expressions for the dispersion relations and field profiles in form of two tables. Table 6.4 presents the definitions of the auxiliary parameters used in the derivation for both cases: $c_0 > 0$ and $c_0 < 0$. Table 6.5 presents the expressions for the dispersion relations and the field profiles in these two cases.

Quantity \ Case	**I** $c_0 > 0$	**II** $c_0 < 0$
$q_2^2 = \beta^2 - \epsilon_{l,2}$	positive or negative	positive
c_0	$k_0^2 \left[\left(\frac{\epsilon_{l,2}}{\epsilon_1} \right)^2 q_1^2 - q_2^2 + \frac{a_2}{2} H_0^2 \right] H_0^2$	
A	$\frac{2}{k_0^2 a_2}$	
Q	$k_0^2 q_2^2$	
γ^2	$\frac{\sqrt{A^2Q^2+4Ac_0}-AQ}{2}$	$\frac{AQ+\sqrt{A^2Q^2-4A\lvert c_0\rvert}}{2}$
δ^2	$\frac{\sqrt{A^2Q^2+4Ac_0}+AQ}{2}$	$\frac{AQ-\sqrt{A^2Q^2-4A\lvert c_0\rvert}}{2}$
s	$\gamma^2 + \delta^2$	—
m	$\frac{\delta^2}{s}$	$\frac{\gamma^2-\delta^2}{\gamma^2}$

Table 6.4: Auxiliary parameters used in the derivation of the formulas for the magnetic field profiles and for the dispersion relations in the nonlinear slot waveguide in the frame of the JEM. The sign of q_2^2 in case II ($c_0 < 0$) is deduced from Eq. (6.1.17).

Case	c_0	$H_2(x)$ and x_0	Dispersion relation
I	$c_0 > 0$	$x_0 = -\sqrt{\frac{A}{s}}\,\mathrm{cn}^{-1}\left[\frac{H_2(0)}{\delta}\,\middle|\,m\right]$ $H_2 = \delta\,\mathrm{cn}\left[\sqrt{\frac{s}{A}}\,(x-x_0)\,\middle|\,m\right]$	$\mathrm{cn}\left[\sqrt{\frac{s}{A}}\,(d-x_0)\,\middle|\,m\right] = \frac{\epsilon_3}{k_0 q_3 \epsilon_{l,2}}\sqrt{\frac{s}{A}}\,\mathrm{sn}\left[\sqrt{\frac{s}{A}}\,(d-x_0)\,\middle|\,m\right]\mathrm{dn}\left[\sqrt{\frac{s}{A}}\,(d-x_0)\,\middle|\,m\right]$
II	$c_0 < 0$	$x_0 = -\sqrt{\frac{A}{\gamma^2}}\,\mathrm{dn}^{-1}\left[\frac{H_2(0)}{\gamma}\,\middle|\,m\right]$ $H_2 = \gamma\,\mathrm{dn}\left[\sqrt{\frac{\gamma^2}{A}}\,(x-x_0)\,\middle|\,m\right]$	$\mathrm{dn}\left[\sqrt{\frac{\gamma^2}{A}}\,(d-x_0)\,\middle|\,m\right] = \frac{\epsilon_3 m}{k_0 q_3 \epsilon_{l,2}}\sqrt{\frac{\gamma^2}{A}}\,\mathrm{sn}\left[\sqrt{\frac{\gamma^2}{A}}\,(d-x_0)\,\middle|\,m\right]\mathrm{cn}\left[\sqrt{\frac{\gamma^2}{A}}\,(d-x_0)\,\middle|\,m\right]$

Table 6.5: Formulas for the magnetic field profiles in the nonlinear core of the slot waveguide and dispersion relations obtained using JEM for the cases of positive and negative values of the integration constant c_0.

6.1.4 Single-interface limiting cases for fields and dispersion relations in Jacobi elliptic function based model

In Sections 6.1.1–6.1.3, we have developed the nonlinear dispersion relations for the plasmonic slot waveguide configuration. In course of the derivation, it was mentioned (see Page 80) that for the integration constant c_0 equal to zero, the problem of a nonlinear slot waveguide is reduced to a single interface between a metal and a semi-infinite nonlinear dielectric.

In this section, we will study the nonlinear dispersion relations given in Table 6.5 in the limiting case $c_0 = 0$ to show that they reduce to the dispersion relations of plasmon–solitons on a single interface between a metal and a nonlinear dielectric. The results obtained here for the limiting case $c_0 = 0$ will be compared with the results for the single interface between a metal and a nonlinear dielectric derived in Chapter 3.

First, we simplify the auxiliary parameters (given in Table 6.4) used in the nonlinear dispersion relations for the cases $c_0 > 0$ and $c_0 < 0$. Expressions for the parameters from Table 6.4 in the limiting case $c_0 = 0$ are presented in Table 6.6.

	Case **I**	Case **II**
Quantity	$c_0 = 0$	
$q_2^2 = \beta^2 - \epsilon_{l,2}$	positive or negative	positive
A	$\frac{2}{k_0^2 a_2}$	
Q	$k_0^2 q_2^2$	
γ^2	0	AQ
δ^2	AQ	0
s	δ^2	—
m	1	1

Table 6.6: Auxiliary parameters used in the derivation of the formulas for the magnetic field profiles and for the dispersion relations in the nonlinear slot waveguide in the frame of the JEM for the single-interface limiting case ($c_0 = 0$).

Here we will analyze the dispersion relations for the two cases ($c_0 > 0$ and $c_0 < 0$) in the limiting case $c_0 = 0$.

1. **Case I**

   We start the analysis by case I from Table 6.5. First, we will rewrite the expressions for x_0 and H_2 for $c_0 = 0$ using the parameters given in Table 6.6:

$$x_0 = -\sqrt{\frac{1}{Q}}\,\mathrm{cn}^{-1}\left[\frac{H_2(0)}{\sqrt{AQ}}\,\middle|\,1\right], \tag{6.1.68a}$$

$$H_2 = \sqrt{AQ}\,\mathrm{cn}\left[\sqrt{Q}\,(x - x_0)\,\middle|\,1\right]. \tag{6.1.68b}$$

   We see that for $c_0 = 0$ the parameter m of Jacobi elliptic functions describing the magnetic field is equal to 1. For this value of the parameter, Jacobi elliptic functions become hyperbolic functions (see Table 16.6 in Ref. [112] and Appendix C). Using Table C.1, Eqs. (6.1.68) become

$$x_0 = -\frac{1}{k_0 q_2}\,\mathrm{sech}^{-1}\left(\frac{\sqrt{a_2}H_2(0)}{\sqrt{2}q_2}\right), \tag{6.1.69a}$$

$$H_2 = \sqrt{\frac{2}{a_2}}q_2\,\mathrm{sech}\left[k_0 q_2 (x - x_0)\right], \tag{6.1.69b}$$

   where we used the physical parameters a_2, k_0, and q_2. Since for the configurations with a semi-infinite nonlinear medium we considered only $q_2^2 > 0$ (see discussion on Page 21) we substituted $\sqrt{q_2^2}$ by q_2. Equations (6.1.69), describing the magnetic field profile H_2 in the limiting case for the single interface, becomes identical to Eq. (2.1.23) which was obtained by solving the nonlinear wave equation [Eq. (2.1.7a) or (6.1.2)] for the case of a semi-infinite nonlinear medium in the frame of the FBM.

   The nonlinear dispersion relation for the case I given in Table 6.5 can be simplified in a similar manner as the expression for the magnetic field profile. Using Tables 6.6 and C.1, the nonlinear dispersion equation becomes

$$\mathrm{sech}\left[k_0 q_2 (d - x_0)\right] = \frac{\epsilon_3 q_2}{\epsilon_{l,2} q_3}\tanh\left[k_0 q_2 (d - x_0)\right]\mathrm{sech}\left[k_0 q_2 (d - x_0)\right] \tag{6.1.70}$$

   Canceling the common term with the sech function on both sides of Eq. (6.1.70) transforms this equation to

$$\tanh\left[k_0 q_2 (d - x_0)\right] = \frac{\epsilon_{l,2} q_3}{\epsilon_3 q_2} \tag{6.1.71}$$

   Equation (6.1.71) describes the nonlinear dispersion relation for plasmon–solitons on a single interface (at $x = d$) between a metal and a nonlinear dielectric. Equation (6.1.71) is equivalent to Eq. (3.1.4), which gives the dispersion relation for a single metal/nonlinear dielectric interface obtained using the FBM, taking into account that: (i) in the frame of the JEM we used the assumption that $\epsilon_2 = \epsilon_{l,2}$ in the continuity conditions used to derive the nonlinear dispersion relations (see Section 6.1.3), (ii) in the frame of the FBM the interface is located at $x = 0$.

2. **Case II**

   The derivation of the limiting case $c_0 = 0$ in the case II is very similar to the one presented for the case I. Likewise, using Tables 6.6 and C.1, the expressions for the magnetic field profile in the case II presented in Table 6.5 becomes identical to Eq. (6.1.69). Taking the limiting case of the nonlinear dispersion relation in case II presented in Table 6.5 yields and equation identical to Eq. (6.1.71).

The analysis presented in this section proves that the results of the JEM for the limiting case of a single interface between a metal and a nonlinear dielectric are compatible with the results of the FBM that was derived for structures with a semi-infinite nonlinear medium.

6.2 Interface model

In Section 6.1, we have derived the Jacobi elliptic function based model (JEM) model that treats the Kerr nonlinearity present in the core of the nonlinear slot waveguide in a simplified way. In the frame of the JEM, only the transverse electric field component contributed to the Kerr-type nonlinearity [see Eq. (6.1.1)] and the nonlinear permittivity change was assumed to be small ($\alpha E_x^2 \ll \epsilon_l$). These assumptions allowed us to obtain analytical formulas (expressed in terms of Jacobi elliptic functions) for the nonlinear dispersion relations and the field profiles of the nonlinear modes of the nonlinear slot waveguide structure (see Table 6.5).

In this section, we will present the derivation of a model that is more numerical than the JEM but treats the Kerr-type nonlinearity in a more precise way. The permittivity of the nonlinear core in the frame of the interface model (IM) is described by [compare with Eqs. (1.6.13) and (2.3.4)][1]

$$\epsilon_x(x) = \epsilon_z(x) = \epsilon_y(x) = \epsilon_2 = \epsilon_{l,2}(x) + \alpha_2 \left[E_x^2(x) + E_z^2(x)\right]. \tag{6.2.1}$$

Moreover, there is no theoretical limitation of the values of the nonlinear permittivity change.

In the IM, the solutions of Maxwell's equations are sought numerically, as explained in the following. The field profiles inside the nonlinear core are found by numerical integration of Maxwell's equations that couple the E_x and E_z field components. The novelty of our numerical method lays in the fact that, the phase space where the solutions are being sought is reduced by a constraint that is expressed in an analytical form. Below the derivation of this constraint is presented and the numerical procedure of finding the nonlinear dispersion relations using the IM is described.

6.2.1 Analytical constraint

The derivation of the IM starts with Eq. (2.3.6) derived in Section 2.3.1 during the discussion of the nonlinear medium properties in the frame of the exact model (EM). In the frame of the IM, we will study only standard cubic Kerr-type nonlinearity described by Eq. (6.2.1). Therefore, we set the parameter κ of the power-law Kerr nonlinearity considered in Section 2.3.1 to be equal to two. For $\kappa = 2$ and for the slot waveguide configuration, with the parameters given in Fig. 6.1, Eq. (2.3.6) takes the following form:

$$\left(\frac{\mathrm{d}E_z}{\mathrm{d}x}\right)^2 = (\beta k_0)^2 E_x^2 - k_0^2 \epsilon_{l,2}\left(E_x^2 + E_z^2\right) - k_0^2 \frac{\alpha_2}{2}\left(E_x^2 + E_z^2\right)^2 + C_0, \tag{6.2.2}$$

where the linear permittivity $\epsilon_{l,2}$ and the nonlinear parameter α_2 of the nonlinear core of the slot waveguide appear.

In Section 2.3.1, we considered a semi-infinite nonlinear medium for which the magnetic field H_y and its x-derivative vanish when $x \to -\infty$. We have used these boundary conditions to set the integration constant C_0 in Eq. (2.3.6) to zero. Here we deal with a problem in which the nonlinear medium is sandwiched between two linear (metal) layers, and therefore the nonlinear medium has a finite size. In this case, the integration constant can not be set automatically to zero.

Similar to Section 2.3.1, we compare the right-hand side of Eq. (6.2.2) with the square of the right-hand side of Eq. (2.3.1a). This time, the comparison gives an equation similar to Eq. (2.3.9), but with an additional term being the integration constant C_0:

$$\left(\frac{\epsilon_2^2}{\beta^2} - 2\epsilon_2\right) E_z^2 + \epsilon_{l,2}\left(E_x^2 + E_z^2\right) + \frac{\alpha_2}{2}\left(E_x^2 + E_z^2\right)^2 = C_0. \tag{6.2.3}$$

Equation (6.2.3) together with continuity conditions for the tangential components of the electromagnetic field will be helpful in finding the constraints reducing the phase space where the solutions of

[1] As in the case of the exact model described in Footnote 1 in Section 2.1.1 (Page 19), this assumption is stronger than the one required to formulate the IM. In our case, it is necessary to consider materials in which only two diagonal elements of the nonlinear permittivity tensor elements are equal $\epsilon_x = \epsilon_z = \epsilon$. The tensor component ϵ_y can have arbitrary values because it does not appear in the model derivation.

Maxwell's equations are sought, in order to find the dispersion curves for the nonlinear slot waveguide configuration.

The left-hand side of Eq. (6.2.3) represents a quantity that is conserved across the transverse (along the x direction) cross-section of the core of the nonlinear slot waveguide. Similar to Eq. (6.1.3) in the case of the JEM, the expression on the left-hand side of Eq. (6.2.3) is always equal to the integration constant C_0, regardless of the position in the nonlinear core.

We use the continuity conditions for the tangential components of the electromagnetic field in order to relate the values of the electric field components E_x and E_z at the nonlinear interfaces to the values of the total electric field amplitude, defined as $E \equiv \sqrt{E_x^2 + E_z^2}$, at these interfaces. The field distributions for the electric field components in the semi-infinite linear metal regions are found by solving linear wave equations for these components. These wave equations are derived from Maxwell's equations [Eqs. (1.5.2)] and read:

$$\frac{\mathrm{d}^2 E_x}{\mathrm{d}x^2} - k_0^2 q_k^2 E_x = 0, \tag{6.2.4a}$$

$$\frac{\mathrm{d}^2 E_z}{\mathrm{d}x^2} - k_0^2 q_k^2 E_z = 0, \tag{6.2.4b}$$

where q_k denotes a constant value of the $q(x)$ function [defined by Eq. (2.1.7b)] in k-th layer (for $k \in \{1, 3\}$). The general solution of these wave equations is a combination of decreasing and increasing exponential functions of the form $Ae^{k_0 q_k x} + Be^{-k_0 q_k x}$. The components of the electric field in the cladding metal layers are given by:

1. In the left metal region ($x < 0$ — layer 1 in Fig. 6.1):

$$E_{x,1} = A_x e^{k_0 q_1 x}, \tag{6.2.5a}$$

$$E_{z,1} = A_z e^{k_0 q_1 x} \tag{6.2.5b}$$

2. In the right metal region ($x > d$ — layer 3 in Fig. 6.1):

$$E_{x,3} = B_x e^{-k_0 q_3 (x-d)}, \tag{6.2.6a}$$

$$E_{z,3} = B_z e^{-k_0 q_3 (x-d)}. \tag{6.2.6b}$$

Only one exponential term is present in each of the expressions so that the electric field decays exponentially for $x \to \pm\infty$.

The amplitudes of the electric field components at the nonlinear medium interfaces are defined as follows:

1. At the left interface ($x = 0^+$)

$$E_x(x = 0^+) \equiv E_{x,0}, \tag{6.2.7a}$$

$$E_z(x = 0^+) \equiv E_{z,0} \tag{6.2.7b}$$

2. At the right interface ($x = d^-$)

$$E_x(x = d^-) \equiv E_{x,d}, \tag{6.2.8a}$$

$$E_z(x = d^-) \equiv E_{z,d}. \tag{6.2.8b}$$

The total electric field amplitudes on the left E_0 and right E_d interfaces are defined by

$$E_0 \equiv \sqrt{E_{x,0}^2 + E_{z,0}^2}, \tag{6.2.9a}$$

$$E_d \equiv \sqrt{E_{x,d}^2 + E_{z,d}^2}. \tag{6.2.9b}$$

We define E_0 and E_d to be positive quantities and therefore, in Eqs. (6.2.9), only the positive square-roots are considered.

Using the boundary conditions for the tangential electromagnetic field components H_y and E_z, we relate the amplitudes of the electric field components E_x and E_z on both sides of each of the interfaces.

1. At the left interface ($x = 0$):

   (a) The continuity condition for the magnetic field H_y reads

   $$H_{y,1}|_{x=0^-} = H_{y,2}|_{x=0^+}. \tag{6.2.10}$$

   Inserting Eqs. (1.5.2b), (6.2.5a), and (6.2.7a) into Eq. (6.2.10), we obtain the relation between the E_x amplitudes on both sides of the left interface:

   $$\epsilon_1 A_x = \epsilon_{2,0} E_{x,0}, \tag{6.2.11}$$

   where $\epsilon_{2,0}$ denotes the value of the nonlinear permittivity at the left interface of the core and is equal to $\epsilon_2|_{x=0^+} = \epsilon_{l,2} + \alpha_2 E_0^2$.

   (b) The continuity condition for the longitudinal electric field component E_z reads

   $$E_{z,1}|_{x=0^-} = E_{z,2}|_{x=0^+} \tag{6.2.12}$$

   Using Eqs. (6.2.5b) and (6.2.7b) in Eq. (6.2.12), we obtain the relation between the E_z amplitudes on both sides of the left interface:

   $$A_z = E_{z,0}. \tag{6.2.13}$$

2. Similar relations are obtained using the continuity conditions at the right interface ($x = d$):

   (a) From the continuity condition for the magnetic field H_y

   $$H_{y,2}|_{x=d^-} = H_{y,3}|_{x=d^+} \tag{6.2.14}$$

   using Eqs. (1.5.2b), (6.2.6a), and (6.2.8a), we obtain the relation between the E_x amplitudes on both sides of the right interface:

   $$\epsilon_3 B_x = \epsilon_{2,d} E_{x,d}, \tag{6.2.15}$$

   where $\epsilon_{2,d}$ denotes the value of the nonlinear permittivity at the right interface of the core and is equal to $\epsilon_2|_{x=d^-} = \epsilon_{l,2} + \alpha_2 E_d^2$.

   (b) From the continuity condition for longitudinal electric field component E_z

   $$E_{z,2}|_{x=d^-} = E_{z,3}|_{x=d^+} \tag{6.2.16}$$

   using Eq. (6.2.6b) and (6.2.8b) in Eq. (6.2.16) we obtain the relation between the E_z amplitudes on both sides of the right interface:

   $$B_z = E_{z,d}. \tag{6.2.17}$$

In order to relate A_x with A_z and B_x with B_z, we will use Eqs. (1.5.2b) and (1.5.2c) assuming that we deal with isotropic materials ($\epsilon_x = \epsilon_y = \epsilon_z = \epsilon$). In the linear layers, these two equations allow us to relate E_x and E_z components in the following way:

$$\frac{\mathrm{d}E_x}{\mathrm{d}x} = k_0 \beta E_z. \tag{6.2.18}$$

Using Eqs. (6.2.18), (6.2.5a), and (6.2.5b) in layer 1 (see Fig. 6.1 for layer numbers), we obtain

$$A_x = \frac{\beta}{q_1} A_z. \tag{6.2.19}$$

Inserting Eqs. (6.2.11) and (6.2.13) into Eq. (6.2.19), we obtain a relation between the amplitudes of the electric field components at the left interface of the nonlinear medium ($x = 0^+$):

$$E_{x,0} = \frac{\epsilon_1 \beta}{q_1 \epsilon_{2,0}} E_{z,0}. \tag{6.2.20}$$

Likewise, using Eqs. (6.2.18), (6.2.6a), and (6.2.6b) in layer 3, we obtain

$$B_x = -\frac{\beta}{q_3} B_z. \tag{6.2.21}$$

Inserting Eqs. (6.2.15) and (6.2.17) into Eq. (6.2.21), we obtain the relation between the amplitudes of the electric field components at the right interface of the nonlinear dielectric ($x = d^-$):

$$E_{x,d} = -\frac{\epsilon_3 \beta}{q_3 \epsilon_{2,d}} E_{z,d}. \tag{6.2.22}$$

Using Eqs. (6.2.9a) and (6.2.20), we can express the electric field components at the left interface ($E_{x,0}$, $E_{z,0}$) as a function of the total electric field amplitude at this interface E_0:[2]

$$E_{x,0}^2 = \frac{(\epsilon_1 \beta)^2}{(\epsilon_{2,0} q_1)^2 + (\epsilon_1 \beta)^2} E_0^2, \tag{6.2.24a}$$

$$E_{z,0}^2 = \frac{(\epsilon_{2,0} q_1)^2}{(\epsilon_{2,0} q_1)^2 + (\epsilon_1 \beta)^2} E_0^2. \tag{6.2.24b}$$

Similarly, using Eqs. (6.2.9b) and (6.2.22), we can express the electric field components at the right interface ($E_{x,d}$, $E_{z,d}$) as a function of a total electric field amplitude at this interface E_d:

$$E_{x,d}^2 = \frac{(\epsilon_3 \beta)^2}{(\epsilon_{2,d} q_3)^2 + (\epsilon_3 \beta)^2} E_d^2, \tag{6.2.25a}$$

$$E_{z,d}^2 = \frac{(\epsilon_{2,d} q_3)^2}{(\epsilon_{2,d} q_3)^2 + (\epsilon_3 \beta)^2} E_d^2. \tag{6.2.25b}$$

Equation (6.2.3) can now be rewritten on each interface in such a way that, it depends only on the total electric field amplitude at this interface (as a parameter), effective index β as an unknown and opto-geometric material parameters which are known and fixed for a given structure. Inserting Eqs. (6.2.24a) and (6.2.24b) into Eq. (6.2.3) taken at $x = 0^+$, we obtain the nonlinear dispersion relation at the left interface ($x = 0$):

$$\left\{ \left[\left(\frac{\epsilon_{2,0}}{\beta} \right)^2 - 2\epsilon_{2,0} \right] \frac{(\epsilon_1 \beta)^2}{(\epsilon_{2,0} q_1)^2 + (\epsilon_1 \beta)^2} + \epsilon_{l,2} + \frac{\alpha_2}{2} E_0^2 \right\} E_0^2 = C_0. \tag{6.2.26}$$

[2] Equation (6.2.24a) relates the values of $E_{x,0}$ and E_0 in the case of a single interface between a nonlinear dielectric and a metal (two-layer structure). In Section 3.2 we have derived a similar equation [Eq. (3.2.6)] for the case of a three-layer structure, where the film with the permittivity ϵ_3 and thickness d is sandwiched between a semi-infinite nonlinear cladding with permittivity ϵ_1 and a semi-infinite linear cladding with permittivity ϵ_4. Here we recall Eq. (3.2.6):

$$E_{x,0}^2 = \frac{(\beta \epsilon_3 R)^2}{(\beta \epsilon_3 R)^2 + (q_3 \epsilon_{1,0} T)^2} E_0^2,$$

where the parameters R and T are given by

$$R = q_4 \epsilon_3 \tanh(k_0 q_3 d) + q_3 \epsilon_4,$$
$$T = q_4 \epsilon_3 + q_3 \epsilon_4 \tanh(k_0 q_3 d)$$

and $\epsilon_{1,0}$ denotes the value of the nonlinear permittivity at the interface $x = 0$. Taking the limiting case $d \to 0$, one reduces the problem to a single interface between the nonlinear dielectric with permittivity ϵ_1 and the linear layer with permittivity ϵ_4. Using $d \to 0$ in expressions for R and T [$\tanh(k_0 q_3 d) \to 0$], one obtains the expression for the E_x field amplitude at the interface $x = 0$

$$E_{x,0}^2 = \frac{(\beta \epsilon_4)^2}{(\beta \epsilon_4)^2 + (q_4 \epsilon_{1,0})^2} E_0^2.$$

This expression is equivalent to Eq. (6.2.24a).

Inserting Eqs. (6.2.25a) and (6.2.25b) into Eq. (6.2.3) taken at $x = d^-$, we obtain the dispersion relation at the right interface ($x = d$):

$$\left\{\left[\left(\frac{\epsilon_{2,d}}{\beta}\right)^2 - 2\epsilon_{2,d}\right]\frac{(\epsilon_3\beta)^2}{(\epsilon_{2,d}q_3)^2 + (\epsilon_3\beta)^2} + \epsilon_{l,2} + \frac{\alpha_2}{2}E_d^2\right\}E_d^2 = C_0. \tag{6.2.27}$$

Equations (6.2.26) and (6.2.27) considered separately give the dispersion relation for a single interface between a metal and a nonlinear dielectric. In this case, the nonlinear medium is semi-infinite which means that C_0 must be set to zero (see discussion at Page 96; for semi-infinite medium both E_x and E_z components tend to zero infinitely far from the interface). Setting $C_0 = 0$ in Eq. (6.2.26) yields

$$\left\{\left[\left(\frac{\epsilon_{2,0}}{\beta}\right)^2 - 2\epsilon_{2,0}\right]\frac{(\epsilon_1\beta)^2}{(\epsilon_{2,0}q_1)^2 + (\epsilon_1\beta)^2} + \epsilon_{l,2} + \frac{\alpha_2}{2}E_0^2\right\}E_0^2 = 0. \tag{6.2.28}$$

This equation can be solved analytically for β. The solution depends on the parameters of the structure (ϵ_1, $\epsilon_{l,2}$, α_2, ϵ_3) and the electric field amplitude at the interface E_0 and is given by

$$\beta = \sqrt{\frac{\epsilon_1\epsilon_{2,0}^2(\epsilon_{l,2} - \epsilon_1 + \frac{\alpha_2}{2}E_0^2)}{(\epsilon_{2,0}^2 + \epsilon_1^2)(\epsilon_{l,2} + \frac{\alpha_2}{2}E_0^2) - 2\epsilon_1^2\epsilon_{2,0}}}. \tag{6.2.29}$$

Only the positive root is considered because we are interested here in forward propagating waves only. Equation (6.2.29) can be compared to Eq. (11) in Ref. [70] and Eq. (14) in Ref. [77] derived for the case of a single metal/nonlinear dielectric interface.[3]

The solution for a single-interface problem provides a good approximation (in terms of effective index β and the field profiles) for first-order highly asymmetric modes in the nonlinear slot waveguides whose field profiles are mostly localized on one interface of the core (see also the discussion on Page 80). These solutions are invariant with respect to the waveguide width as they interact strongly only with one of the core interfaces. More comments and illustrations of this property will be presented in Section 7.1.4, where we discuss the results for the symmetric nonlinear slot waveguide configuration.

After this digression on the single-interface case, we come back to the derivation of the constraint limiting the phase space of the solutions of Maxwell's equations in nonlinear slot waveguide structures. Comparing the dispersion relations for the single interfaces given by Eqs. (6.2.26) and (6.2.27), we eliminate the integration constant C_0 and obtain the final equation of the IM:

$$\boxed{\begin{aligned}&\left\{\left[\left(\frac{\epsilon_{2,0}}{\beta}\right)^2 - 2\epsilon_{2,0}\right]\frac{(\epsilon_1\beta)^2}{(\epsilon_{2,0}q_1)^2 + (\epsilon_1\beta)^2} + \epsilon_{l,2} + \frac{\alpha_2}{2}E_0^2\right\}E_0^2 = \\ &\qquad\left\{\left[\left(\frac{\epsilon_{2,d}}{\beta}\right)^2 - 2\epsilon_{2,d}\right]\frac{(\epsilon_3\beta)^2}{(\epsilon_{2,d}q_3)^2 + (\epsilon_3\beta)^2} + \epsilon_{l,2} + \frac{\alpha_2}{2}E_d^2\right\}E_d^2.\end{aligned}} \tag{6.2.30}$$

Equation (6.2.30) represents the constraint that will be used in the numerical algorithm computing the dispersion curves presented in Section 6.2.2, in order to reduce the dimension of the parameter space where the solutions of Maxwell's equations in nonlinear slot waveguide structures are sought.

It is worth noticing that, in Eq. (6.2.30), neither the wavelength of light λ nor the width of the waveguide core d appear. This means that the condition given by Eq. (6.2.30) is identical, regardless of the values of λ and d. This condition depends only on the material parameters (ϵ_1, $\epsilon_{l,2}$, α_2, and ϵ_3) and the field intensities at both nonlinear core interfaces (E_0 and E_d). The size of the core and the wavelength will appear in our next step — the numerical integration of Maxwell's equations leading to the field profiles in the core of the waveguide and to the dispersion curves of the plasmonic nonlinear slot waveguide.

[3] Note that in the linear limiting case ($\alpha_2 E_0^2 \to 0$ and therefore $\epsilon_{2,0} \to \epsilon_{l,2}$), Eq. (6.2.29) transforms into the dispersion relation for linear plasmons on a single metal/dielectric interface given by $\beta = \sqrt{\epsilon_1\epsilon_{l,2}/(\epsilon_1 + \epsilon_{l,2})}$ (see Eq. (2.14) in Ref. [55]).

As stated before, Eq. (6.2.30) is not a dispersion relation for the slot waveguide modes but only a constraint that limits the phase space where the solutions in the frame of the IM can be found. In order to obtain the dispersion relations in the nonlinear slot waveguide, the field profiles in the core are found by numerical integration of Maxwell's equations. Maxwell's equations are written as a set of coupled equations relating both electric field components E_x and E_z [Eqs. (2.3.1a) and (2.3.46)]. These equations are recalled here with the notation adapted for the nonlinear slot waveguide, where the quantities related to the nonlinear layer have a subscript 2:

$$\boxed{\begin{aligned}\frac{\mathrm{d}E_x}{\mathrm{d}x} &= k_0 \frac{\beta\epsilon_2 E_z - 2\alpha_2 E_z E_x^2 \left(\beta - \frac{\epsilon_2}{\beta}\right)}{\epsilon_2 + 2\alpha_2 E_x^2}, && \text{(6.2.31a)}\\ \frac{\mathrm{d}E_z}{\mathrm{d}x} &= k_0 \left(\beta - \frac{\epsilon_2}{\beta}\right) E_x. && \text{(6.2.31b)}\end{aligned}}$$

In order to prove the scaling properties of the solutions in the nonlinear slot waveguide configuration we introduce here a normalized transverse coordinate $\xi = k_0 x$. Rewriting Eqs. (6.2.31) using the normalized transverse coordinate yields:

$$\begin{aligned}\frac{\mathrm{d}E_x}{\mathrm{d}\xi} &= \frac{\beta\epsilon_2 E_z - 2\alpha_2 E_z E_x^2 \left(\beta - \frac{\epsilon_2}{\beta}\right)}{\epsilon_2 + 2\alpha_2 E_x^2}, && \text{(6.2.32a)}\\ \frac{\mathrm{d}E_z}{\mathrm{d}\xi} &= \left(\beta - \frac{\epsilon_2}{\beta}\right) E_x. && \text{(6.2.32b)}\end{aligned}$$

To find the field profiles in the core and the dispersion relations for the nonlinear slot waveguide, Eqs. (6.2.32) are integrated in the core of the waveguide:

$$\begin{aligned}\int_{E(0)}^{E(\rho)} \mathrm{d}E_x(\xi) &= \int_0^\rho \frac{\beta\epsilon_2(\xi) E_z(\xi) - 2\alpha_2 E_z(\xi) E_x^2(\xi) \left(\beta - \frac{\epsilon_2(\xi)}{\beta}\right)}{\epsilon_2(\xi) + 2\alpha_2 E_x^2(\xi)} \mathrm{d}\xi, && \text{(6.2.33a)}\\ \int_{E(0)}^{E(\rho)} \mathrm{d}E_x(\xi) &= \int_0^\rho \left(\beta - \frac{\epsilon_2(\xi)}{\beta}\right) E_x(\xi)\, \mathrm{d}\xi, && \text{(6.2.33b)}\end{aligned}$$

where the ξ dependency of all the quantities in explicitly denoted. From Eqs. (6.2.33), we notice that the field profiles (and therefore the dispersion curves, as it can be seen in Section 6.2.2) for identical values of the reduced waveguide thickness $\rho = k_0 d = 2\pi d/\lambda$ will be identical. Therefore, we conclude that the dispersion relations for a nonlinear slot waveguide with given material parameters (ϵ_1, $\epsilon_{l,2}$, α_2, and ϵ_3) will depend only on the ratio d/λ and not on the wavelength or the core thickness itself.

6.2.2 Numerical algorithm and nonlinear dispersion relations

In this section, we present the description of the numerical algorithm that is used to find the dispersion relation for the modes of a nonlinear slot waveguide in the frame of the IM. This algorithm uses the shooting method [88] to find solutions of Maxwell's equations in the waveguide core and finally the nonlinear dispersion relation for the plasmonic slot waveguide.

In a general case, the numerical procedure would be the following. First, for a given structure, we fix the parameters E_0, E_d, and β and integrate Maxwell's equations [Eqs. (6.2.31)] in the waveguide core with the values E_0 and β as initial parameters. The results of the integration are the field profiles $E_x(x)$ and $E_z(x)$ inside the nonlinear core and, in particular, the total electric field amplitude at the interface $x = d$ denoted by $E_d^{(\mathrm{num})}$. Next, we verify if the result of the numerical integration fulfills the conditions resulting from the problem formulation:

1. If $E_d^{(\mathrm{num})}$ is equal to the initially fixed value E_d?

2. If the x-derivative of the product of the permittivity and the transverse electric field $\epsilon_2 E_x$ at the interface $x = d^-$ has the correct sign? The condition for the correct sign of the product of the permittivity and the transverse electric field $\epsilon_2 E_x$ at the right nonlinear core interface ($x = d^-$) was not derived yet in course of presentation of our IM. This derivation is presented here. We start from Eq. (6.2.16):

$$E_{z,2}|_{x=d^-} = E_{z,3}|_{x=d^+}. \tag{6.2.34}$$

The longitudinal field component E_z can be expressed with the help of Eq. (2.3.1b) as

$$E_z = \frac{1}{k_0 \beta \epsilon} \frac{\mathrm{d}(\epsilon E_x)}{\mathrm{d}x}, \tag{6.2.35}$$

where we consider isotropic medium for which $\epsilon_x = \epsilon_z = \epsilon$. In the case of the uniform linear medium (as it is the case for layer 3), Eq. (6.2.35) simplifies to [compare with Eq. (6.2.18)]

$$E_z = \frac{1}{k_0 \beta} \frac{\mathrm{d}E_x}{\mathrm{d}x}. \tag{6.2.36}$$

In the nonlinear medium (layer 2) Eq. (6.2.35) is written in the form

$$E_z = \frac{1}{k_0 \beta \epsilon_2} \frac{\mathrm{d}(\epsilon_2 E_x)}{\mathrm{d}x}. \tag{6.2.37}$$

Inserting Eqs. (6.2.36) and (6.2.37) into Eq. (6.2.34) yields

$$\frac{1}{\epsilon_{2,d}} \frac{\mathrm{d}(\epsilon_2 E_x)}{\mathrm{d}x}\bigg|_{x=d^-} = \frac{\mathrm{d}E_x}{\mathrm{d}x}\bigg|_{x=d^+}. \tag{6.2.38}$$

Equation (6.2.38) is now multiplied by Eq. (6.2.15) to give

$$E_{x,d} \frac{\mathrm{d}(\epsilon_2 E_x)}{\mathrm{d}x}\bigg|_{x=d^-} = \epsilon_3 B_x \frac{\mathrm{d}E_x}{\mathrm{d}x}\bigg|_{x=d^+}. \tag{6.2.39}$$

Computing the derivative on the right-hand side of Eq. (6.2.39) using Eq. (6.2.6a) gives

$$E_{x,d} \frac{\mathrm{d}(\epsilon_2 E_x)}{\mathrm{d}x}\bigg|_{x=d^-} = -k_0 q_3 \epsilon_3 B_x^2. \tag{6.2.40}$$

The right-hand side of Eq. (6.2.40) is positive as ϵ_3 of the metal is negative and all the other quantities there are positive. Therefore, the sign of the derivative $[\mathrm{d}(\epsilon_2 E_x)/\mathrm{d}x]|_{x=d^-}$ must be identical to the sign of $E_{x,d}$. This is the condition that is checked in the numerical algorithm.

3. If the components of electric field at $x = d$ fulfill the conditions given by Eqs. (6.2.25a) and (6.2.25b)?[4]

If these three conditions are fulfilled then the triplet (E_0, E_d, and β) and the corresponding field profiles are accepted as a genuine solution of our problem.

In the general case described above, the phase space where the solutions are sought is three-dimensional and it is spanned by E_0, E_d, and β. However, we can separate the problem into two cases, where we will be able to simplify it and look for the solutions in only two dimensional spaces. The two cases are :

1. The case of symmetric ($E_{x,0} = E_{x,d}$) or antisymmetric solutions ($E_{x,0} = -E_{x,d}$) (for both symmetric and antisymmetric solutions $E_0 = E_d$) in a symmetric structure ($\epsilon_1 = \epsilon_3$). In this case, we look for the solutions of Maxwell's equations in a two-dimensional space spanned by E_0 and β for each of the cases $E_{x,0} = \pm E_{x,d}$. For $E_0 = E_d$ in symmetric structures, Eq. (6.2.30) represents an identity and it is satisfied for all values of β. Therefore, Eq. (6.2.30) will not provide any help in further reducing the parameter space where the solutions are sought.

2. The case of either the asymmetric solutions ($E_0 \neq E_d$) in a symmetric nonlinear slot waveguide structure ($\epsilon_1 = \epsilon_3$) or any solution in an asymmetric structure ($\epsilon_1 \neq \epsilon_3$). For these type of solutions, Eq. (6.2.30) is not an identity and results in a constraint on the three-dimensional space where the solutions are sought. Equation (6.2.30) is transformed to the form:

$$p_4\beta^4 + p_2\beta^2 + p_0 = 0, \tag{6.2.41}$$

where

$$p_4 = 2\epsilon_{2,d}\epsilon_3^2E_d^2(\epsilon_{2,0}^2 + \epsilon_1^2) - 2\epsilon_{2,0}\epsilon_1^2E_0^2(\epsilon_{2,d}^2 + \epsilon_3^2) + f(\epsilon_{2,0}^2 + \epsilon_1^2)(\epsilon_{2,d}^2 + \epsilon_3^2), \tag{6.2.42a}$$

$$p_2 = \epsilon_{2,0}^2\epsilon_1^2E_0^2(\epsilon_{2,d}^2 + \epsilon_3^2) - \epsilon_{2,d}^2\epsilon_3^2E_d^2(\epsilon_{2,0}^2 + \epsilon_1^2) + 2\epsilon_{2,0}\epsilon_{2,d}\epsilon_1\epsilon_3(\epsilon_{2,d}\epsilon_1E_0^2 - \epsilon_{2,0}\epsilon_3E_d^2) - f[\epsilon_{2,0}^2\epsilon_1(\epsilon_{2,d}^2 + \epsilon_3^2) + \epsilon_{2,d}^2\epsilon_3(\epsilon_{2,0}^2 + \epsilon_1^2)], \tag{6.2.42b}$$

$$p_0 = \epsilon_{2,0}^2\epsilon_{2,d}^2\epsilon_1\epsilon_3(\epsilon_3E_d^2 - \epsilon_1E_0^2 + f), \tag{6.2.42c}$$

with

$$f = \epsilon_{l,2}(E_0^2 + E_d^2) + \frac{\alpha_2}{2}(E_0^4 + E_d^4). \tag{6.2.42d}$$

This shows that Eq. (6.2.30) is satisfied only by a finite set of β values. Because we look for forward propagating nonlinear modes and material losses are neglected, the only physically meaningful solutions of Eq. (6.2.41) are the ones where β is real and positive. Therefore, the two possible roots are:

$$\beta_\pm = \sqrt{\frac{-p_2 \pm \sqrt{p_2^2 - 4p_4p_0}}{2p_4}}, \tag{6.2.43}$$

Only the real solutions among $\beta_\pm$ are used further in the process of resolution of the nonlinear problem.

Using Eq. (6.2.30), the three-dimensional space from the general case is now reduced to a two-dimensional space [one for each of the real effective indices given by Eq. (6.2.43)] spanned by E_0 and E_d. Therefore, instead of scanning a full three-dimensional space spanned by E_0 and E_d, and β we need to scan only few two-dimensional spaces spanned by E_0 and E_d corresponding to the physically meaningful β values given by Eq. (6.2.43). In other words, for a pair (E_0, E_d) we just need to check if the field integration gives good results (i.e., if conditions 1–3 on Page 102 are fulfilled) for real values among $\beta_\pm$. If all the conditions are fulfilled then the triplet (E_0, E_d, and β) and the corresponding field profiles are accepted as a genuine solution of our problem.

[4] Actually, it is necessary to verify only one of the conditions given by Eqs. (6.2.25a) and (6.2.25b) because the amplitudes $E_{x,d}$ and $E_{z,d}$ are related by Eq. (6.2.9b).

Note that here we reduce the phase space of possible solutions in terms of the effective index β. Another option would be to try to solve Eq. (6.2.30) with respect to E_0 or E_d. However, this way of proceeding would be more cumbersome. It turns out that Eq. (6.2.30) can be written as a polynomial of E_0 (or E_d) in a form $E_0^8 + r_6 E_0^6 + r_4 E_0^4 + r_0 = 0$. This equation can be reduced to a fourth-order polynomial in E_0^2, for which finding solutions is more difficult than in the case of Eq. (6.2.41) that is reducible to a second-order polynomial equation in β^2.

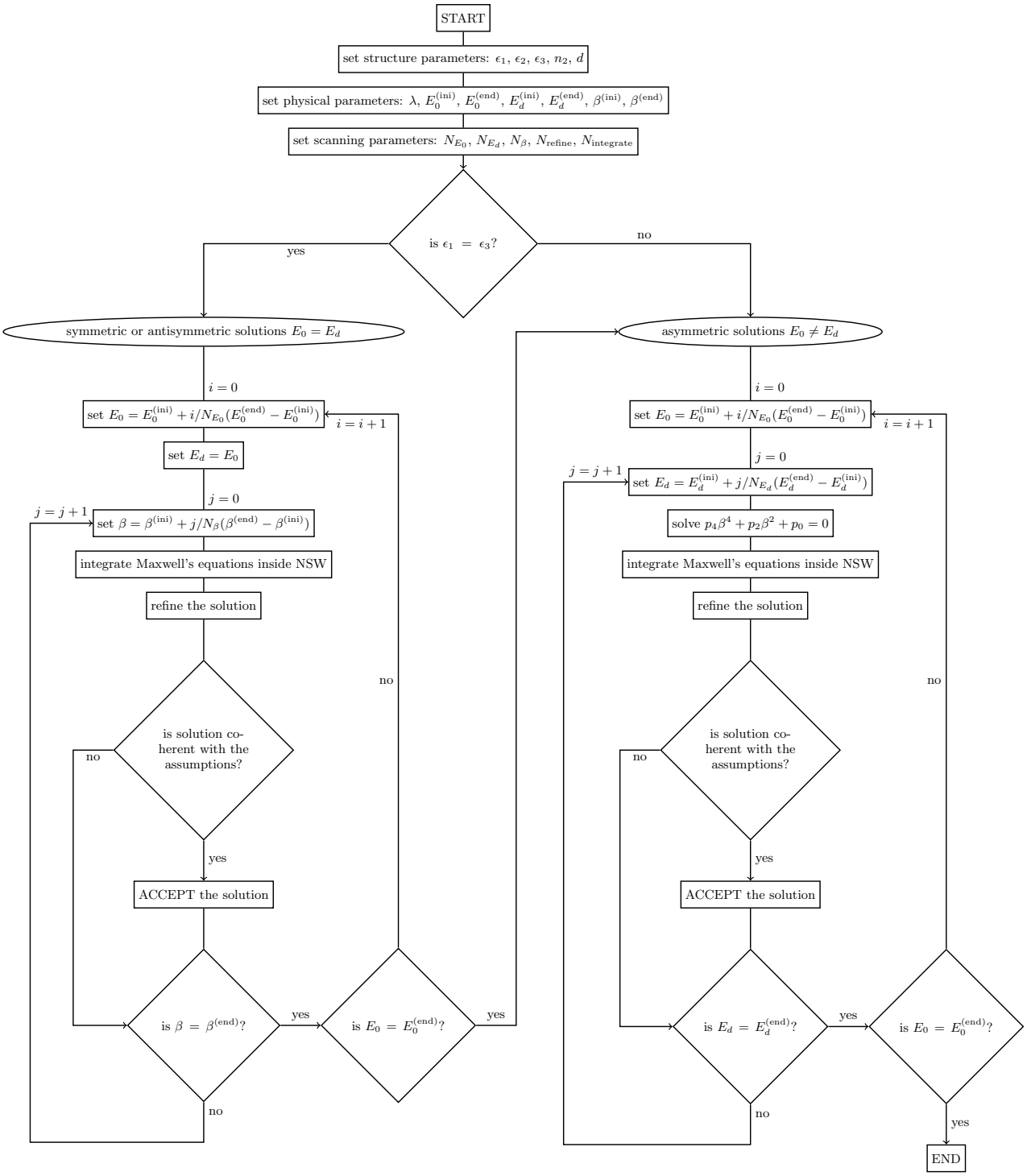

Figure 6.2: Block scheme representing the numerical procedure that finds the dispersion relations for the plasmon–solitons in the nonlinear slot waveguides (NSW) in the frame of the IM. The indices i and j denote the computational step in the scans over E_0, E_d, or β parameters.

The numerical procedure used to find the dispersion relations in the frame of the IM is presented schematically in the block scheme in Fig. 6.2. The procedure starts by setting general parameters of the structure and of the simulation (top of Fig. 6.2). The left part of Fig. 6.2 presents the details of the solution procedure described in the case 1 on Page 103 and the right part of Fig. 6.2 presents the details of the solution procedure described in the case 2 on Page 103.

First, we set the opto-geometric parameters of the structure. Then the physical parameters and the scanning intervals for E_0, E_d, and β are chosen. Solutions with values of any of these three parameters outside of the boundaries set by initial values (denoted by superscript 'ini') and the final values (denoted by the superscript 'end') will not be found by the procedure.

Next, the number of steps for the scans in E_0, E_d, and β, denoted by N_{E_0}, N_{E_d}, and N_β, respectively, is set. The numbers of steps and the scanned interval define the resolution of our algorithm. For instance, the resolution in the effective index β is given by $\Delta\beta = [\beta^{(\mathrm{end})} - \beta^{(\mathrm{ini})}]/N_\beta$. If there exist two modes that are separated by a distance smaller than $\Delta\beta$, those modes will generally not be found by the scanning procedure for the symmetric or antisymmetric modes.

There are two other parameters to be set. N_{refine} denotes the number of iterations with which the solution found by the scan is refined using the bisection method. After the solution was preliminary localized by the scanning procedure, another N_{refine} bisection steps are performed its vicinity. Therefore, the precision with witch the solutions are found, is $2^{N_{\mathrm{refine}}}$ times better than the resolution (for the effective index, the precision is given by $\Delta\beta/2^{N_{\mathrm{refine}}}$). The last parameter is $N_{\mathrm{integrate}}$, which defines the maximum number of steps that can be taken in the procedure of integration of Maxwell's equations in the nonlinear slot waveguide core. The procedure we use to integrate Eqs. (6.2.31) is the built-in ordinary differential equation solver in SCILAB called `ode` [146].

After having set all the parameters, we check if the structure is symmetric or asymmetric in terms of metal cladding permittivity. For the symmetric cladding we look first for symmetric and antisymmetric modes (the case 1 on Page 103) and then search for the asymmetric modes (the case 2 on Page 103). In the case of asymmetric cladding only the procedure to find asymmetric modes is used (the case 2 on Page 103). In the following we present the details of both procedures.

First, we will describe the procedure of finding the symmetric and antisymmetric modes presented in the left part of the scheme in Fig. 6.2:

1. We set the value of the total electric field amplitude at the left metal/nonlinear dielectric interface E_0. For the symmetric and antisymmetric modes $E_d = E_0$.

2. We set the value of the trial effective index β.

3. We integrate Maxwell's equations [Eq. (6.2.31)] and find the field profiles inside of the nonlinear slot waveguide core. The initial value of the x-component of the electric field $E_{x,0}$ is computed using Eq. (6.2.24a). The initial value of the z-component of the electric field $E_{z,0}$ is calculated using Eq. (6.2.24b) [or equivalently Eq. (6.2.9a)]. This however leaves us with the ambiguity about the choice of the sign of the initial value of the z-component of the electric field $E_{z,0} = \pm\sqrt{E_0^2 - E_{x,0}^2}$. This ambiguity is resolved by looking at the boundary condition for the tangential components of the electromagnetic field at the interface located at $x = 0$. This condition is expressed in the form of Eq. (6.2.20). The IM is formulated for positive values of β (forward propagating waves), q_1 (see discussion on Page 81), and $\epsilon_{2,0}$ (dielectric permittivity) and for negative value of ϵ_1 (metal permittivity). Having this in mind, and using Eq. (6.2.20), we conclude that the electric field components at $x = 0^+$ have opposite signs [$\mathrm{sgn}(E_{x,0}) \neq \mathrm{sgn}(E_{z,0})$].

   Therefore, if we choose positive $E_{x,0}$ then $E_{z,0}$ has to be negative and the sign in front of the square-root in the expression defining it is a minus sign. We must choose a plus, in case of a choice of negative $E_{x,0}$. Without loss of generality, in all the results presented for the IM in Chapter 7, we chose the convention $E_{x,0} > 0$.

4. We check if the solution obtained from the integration procedure is coherent with the conditions 1–3 on Page 102

To verify the Condition 1, we check if the value of the field at the right metal/nonlinear dielectric interface found in the numerical integration process $E_d^{(\mathrm{num})}$ is equal to the value assumed at the beginning E_d. This can be done only up to some numerical accuracy. Actually, in order to avoid finding minima of $\Delta E_d = |E_d^{(\mathrm{num})} - E_d|$, we compare the values of $\widetilde{\Delta E_d} = E_d^{(\mathrm{num})} - E_d$ from the present computational step (step j) and from the previous computational step (step $j-1$) (corresponding to β_j and β_{j-1}). We accept the solution only if $\widetilde{\Delta E_d}$ changes its sign. This means that the solution β_{sol} for this E_0 is located somewhere in between β_j and β_{j-1}. Having found the interval where the solution β_{sol} is located we repeat steps 2 and 3 inside of the interval $[\beta_j, \beta_{j-1}]$ using the bisection method [88] with the condition of the change of the sign of $\widetilde{\Delta E_d}$. The bisection procedure is repeated N_{refine} times.

After having refined the precision of our solution we proceed to the verification of the two physical conditions (conditions 2 and 3 on Page 102) that have to be satisfied by our solution. Condition 2 relates the sign of the electric field component at the interface $x = d^-$ ($E_{x,d}$) and the sign of the x-derivative of the product of the permittivity and the transverse electric field at this interface $[\mathrm{d}(\epsilon_2 E_x)/\mathrm{d}x]|_{x=d^-}$ and it is given by Eq. (6.2.40). It states that for negative cladding permittivity ϵ_3 (as it is for the metal cladding studied in this PhD thesis), the signs of $E_{x,d}$ and $[\mathrm{d}(\epsilon_2 E_x)/\mathrm{d}x]|_{x=d^-}$ must be identical. We check if this condition is fulfilled for the fields computed numerically. If it is not fulfilled, we discard the solution. Otherwise, we proceed to the second physical condition (condition 3).

To verify the condition 3 we check if the absolute values of the amplitudes of the field components $|E_{x,d}^{(\mathrm{num})}|$ and $|E_{z,d}^{(\mathrm{num})}|$ are coherent with the ones computed using Eqs. (6.2.25). As a matter of fact, it is enough to check the condition for only one of the components, because they are related by Eq. (6.2.9b).

5. If all the conditions from the step 4 are fulfilled we accept the solution and proceed to the next steps in the loops over β and E_0.

After finishing all the steps in E_0 and β scan in the procedure finding symmetric and antisymmetric solutions, we proceed to the second part of the code that finds asymmetric solutions. Here we will describe the details of this procedure (case 2 on Page 103) that is presented right part of the scheme in Fig. 6.2):

1. We set the value of the electric field at the left metal/nonlinear dielectric interface E_0.
2. We set the value of the electric field at the right metal/nonlinear dielectric interface E_d.
3. We solve Eq. (6.2.30) written in the form given by Eq. (6.2.41) for the possible values of the effective index β. For each of the β values found [see Eq. (6.2.43)], we integrate Maxwell's equations [Eqs. (6.2.31)] and find the field profiles inside of the nonlinear slot waveguide core. The integration procedure is identical to the one described in Step 3 for the left part of the scheme.
4. We check if the solution obtained from the integration procedure is coherent with conditions 1–3 on Page 102 (in identical way it is done in the step 4 for the left part of the scheme).
5. If all the conditions from the step 4 are fulfilled, we accept the solution and proceed to the next steps in the loops over E_0 and E_d.

Chapter 7

Numerical results

Contents

This chapter presents the results obtained using the two models we have developed for the nonlinear slot waveguide configuration described in Chapter 6. We will start by Section 7.1 that presents the results for symmetric structures, in which a nonlinear dielectric core is sandwiched between two semi-infinite metal regions with identical values of the metal permittivity on both sides. For these structures, in Section 7.1.1, we will discuss the obtained nonlinear dispersion diagrams and classify the modes according to the type of the field profile $H_y(x)$. These symmetric structures show very rich dispersion curves. Fundamental and higher-order modes can be classified according to their symmetry into: symmetric, antisymmetric and asymmetric modes. Classification can be done also using a different criterion: according to the number of nodes. We will distinguish two families: node-less modes and modes with nodes. In the node-less family, the asymmetric modes appear from the symmetric modes through the symmetry-breaking Hopf bifurcation [155]. The symmetry breaking of the lowest-order modes in nonlinear slot waveguides was reported in Ref. [87]. This type of symmetry breaking was also observed in dielectric waveguides with nonlinear cladding [24, 25, 27, 29, 30] or core [38, 39] and in plasmonic structures with metal nonlinareities [99, 100]. It is worth noting that the higher-order modes of nonlinear slot waveguides found in our work were not predicted before. The symmetry breaking for the higher-order modes of the node-less family is described in this PhD thesis for the first time. The mutual comparison between the results obtained using the two models will prove their validity.

In Sections 7.1.2 and 7.1.3, we will discuss in more detail the field profiles of the modes existing in nonlinear slot waveguides. The field profiles for the higher-order modes are presented for the first time. We will present the field transformation along the dispersion curves. We will mutually compare the

field profiles obtained using our two models and discuss the similarities and the differences between the two approaches.

In Section 7.1.4, guided by the knowledge of the field profiles and the theoretical derivation presented in Chapter 6, we will present and justify the case in which the first-order asymmetric mode dispersion curves are approximated by the results obtained using single-interface models developed in Chapter 2. In Section 7.1.5, we will show a close relationship between higher-order modes of a nonlinear waveguide that belong to the family with nodes and their linear counterparts that exist in a similar linear slot waveguide.

Section 7.1.6 will present the study of the influence of the nonlinear core width on the behavior of the dispersion curves for the symmetric nonlinear slot waveguide. The size effect on the bifurcation threshold power and mode asymmetry will also be studied. Furthermore, an interesting behavior of the dispersion curve of the first-order asymmetric mode will be observed while changing the core width. In Section 7.1.7, we will discus the influence of the permittivity contrast between the nonlinear core and the metal cladding on the dispersion curves. A precise choice of either the core width or its linear permittivity turn out to be crucial in order to be able to obtain low-power nonlinear solutions in the nonlinear slot waveguide.

Finally, in Section 7.2, the asymmetric slot waveguides will be studied where the asymmetry is introduced by sandwiching the nonlinear core between metals with different permittivities on each side of the core. No studies of asymmetric nonlinear slot waveguides have yet been presented in literature. We show that the asymmetry of the waveguide lifts the degeneracy of the asymmetric modes. We also compare the dispersion curves and the field profiles of asymmetric structures with these obtained for symmetric structures.

7.1 Symmetric structures

Here we will discuss in detail the dispersion diagrams of symmetric nonlinear slot waveguide structures. We will start by a comparison of the dispersion plots obtained using the two models that we have developed: the Jacobi elliptic function based model (JEM) and the interface model (IM). First, we present the dispersion relations in which the effective index of the mode β is plotted as a function of the nonlinear refractive index change Δn averaged over the width of the waveguide

$$\langle \Delta n \rangle = \frac{1}{d} \int_0^d \Delta n \, \mathrm{d}x = \frac{1}{d} \int_0^d n_2^{(2)} I \, \mathrm{d}x, \tag{7.1.1}$$

where the intensity I is defined by Eq. (1.7.4). Here we also present a typical field profile for each of the dispersion curves and classify the modes according to their symmetry and the number of nodes in their magnetic field profile.

Later, we will present the dispersion relations using various coordinates in order to get a better understanding of both the properties of nonlinear slot waveguides and the nature of our models.

In this section, we will focus on one particular symmetric configuration. We will study a 0.4-μm-wide hydrogenated amorphous silicon core with permittivity $\epsilon_{l,2} = 3.46^2$ and the second-order nonlinear refractive index $n_2^{(2)} = 2 \cdot 10^{-17}$ m^2/W [137–142]. This core is embedded between two semi-infinite gold layers with permittivities $\epsilon_1 = \epsilon_3 = -90$ [143–145]. The parameters of this configuration are summarized in Table 7.1. The light propagating in the structure has a free-space wavelength $\lambda = 1.55$ μm. In our modal studies, losses in metals and dielectric core are neglected. An attempt to estimate the propagation losses in nonlinear slot waveguide structures is presented in Appendix D. A study of the losses using the method presented in Section 2.1.5 adapted to nonlinear slot waveguides is presented there.

Quantity \ Layer	1	2	3
Material	gold	hydrogenated amorphous silicon	gold
Permittivity	$\epsilon_1 = -90$	$\epsilon_{l,2} = 3.46^2$	$\epsilon_3 = -90$
Second-order nonlinear refractive index	—	$n_2^{(2)} = 2 \cdot 10^{-17}$ m^2/W	—
Thickness	—	$d = 400$ nm	—

Table 7.1: Parameters of the symmetric nonlinear slot waveguide structure studied in this section.

7.1.1 Nonlinear dispersion diagrams

Jacobi elliptic function based model

Figure 7.1 presents the dispersion curves $\beta(\langle\Delta n\rangle)$ of the nonlinear slot waveguide obtained using the JEM. The horizontal axis is presented in the log scale. The dispersion curves corresponding to each mode are labeled by symbols denoting the symmetry and the order of the mode. Typical field profiles corresponding to each of the labeled modes are shown in Fig. 7.2. We will discuss the character of the dispersion curves and classify the modes using these two figures.

For small values of nonlinear index modification $\langle\Delta n\rangle$ (which is equivalent to low light intensity and low power), a symmetric mode S0 and an antisymmetric mode AN0 are supported by the nonlinear slot waveguide structure. These modes are denoted by '0' because they are the lowest-order modes for a given symmetry. Moreover, these modes are the only modes that have their low-power counterparts (similar modes exist in linear slot waveguide with identical opto-geometric parameters as the nonlinear slot waveguide studied here). Modes of nonlinear slot waveguides that exist in the low-power limit will be called the low-power modes (even if they also exist for elevated power levels). Figures 7.2(a) and (b) show the magnetic field profiles for the modes S0 and AN0, respectively. Even if the average nonlinear index modification for the profiles presented in Figs. 7.2(a) and (b) is quite elevated (≈ 0.1), they have an effective index close to their linear counterparts and the field profiles still resemble those of the linear modes. The effective index change of these modes (β-β_L, where β_L denotes the effective index of the linear counterpart of the mode) is approximately proportional to the nonlinear index modification $\langle\Delta n\rangle$. Because of that, β changes slightly for the average index modification lower then 0.2. For higher $\langle\Delta n\rangle$, the increase of the effective index is clearly visible. Together with the growth of the effective index of both S0 and AN0 modes, we observe that, with the increase of $\langle\Delta n\rangle$ these modes become closer in terms of β. The symmetric mode S0 is the mode with the highest effective index (at low powers) and do not possess nodes. Therefore, it will be called the fundamental mode.

At $\langle\Delta n\rangle \approx 0.1$ an asymmetric mode AS1 bifurcates from the symmetric mode S0.[1] This type of behavior is well known in nonlinear slot waveguides and was described in Ref. [87]. The dispersion curve corresponding to this asymmetric mode is doubly degenerate. To each point on the curve correspond two asymmetric field profile: one localized on the left metal/nonlinear dielectric interface ($x = 0$) and the second one localized at the right metal/nonlinear dielectric interface ($x = d$). Typical profiles corresponding to this dispersion curve are shown in Fig. 7.2(c). The two asymmetric field profiles are related by a mirror symmetry with respect to the center of the core ($x = d/2$). The effective index β of the asymmetric mode AS1 grows rapidly with the increase of $\langle\Delta n\rangle$ and is always above the effective index of the symmetric mode S0. For high values of effective index ($\beta > 7$) the dispersion curve of the AS1 mode is no longer smooth. Several last points of this curve are not calculated precisely with the numerical algorithm used in the JEM. This behavior is a numerical artifact and is not connected to the physical properties of the nonlinear slot waveguide studied here.

[1] This type of bifurcation is called the Hopf bifurcation [155].

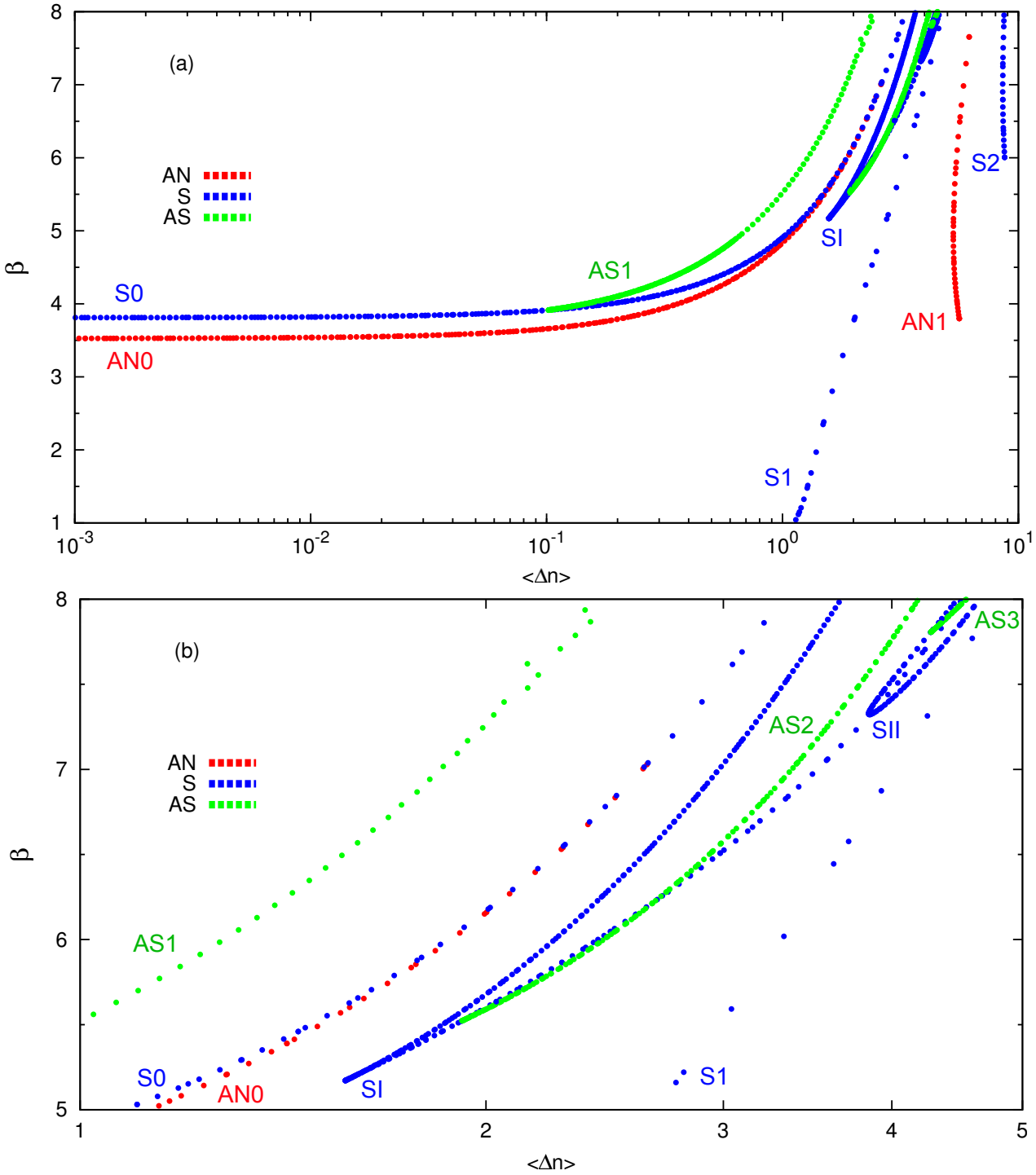

Figure 7.1: (a) Nonlinear dispersion curves of the first and the higher-order symmetric (S — blue), antisymmetric (AN — red), and asymmetric (AS — green) modes for the symmetric nonlinear slot waveguide obtained using the JEM. (b) Zoom on the region with bifurcations of the second- and the third-order asymmetric modes. Each curve is labeled with the name of the corresponding mode. Structure parameters are listed in Table 7.1.

For larger average nonlinear index modifications ($\langle \Delta n \rangle > 1$) two groups of higher-order modes appear. The modes belonging to these groups have not been reported yet in literature. Their dispersion curves and their field profiles are presented in this PhD manuscript for the first time.

The first group consists of modes that possess nodes in the magnetic field profile $H_y(x)$. The first mode of this group (S1) appears for $\langle \Delta n \rangle \gtrsim 1.1$ at the effective index $\beta = 1$. For higher $\langle \Delta n \rangle$, higher-

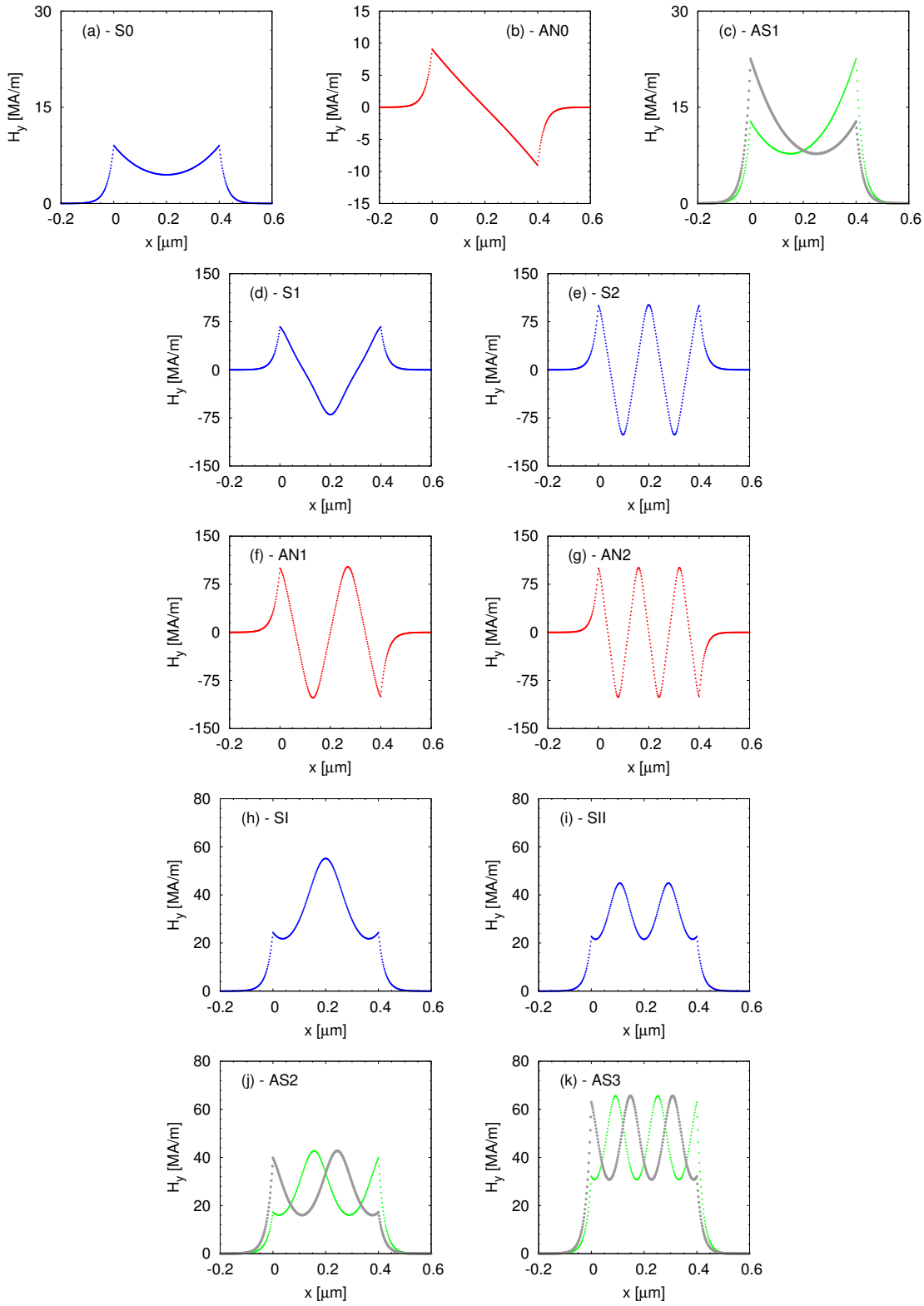

Figure 7.2: Typical magnetic field profiles $H_y(x)$, obtained using the JEM, corresponding to different dispersion curves indicated in Fig. 7.1. Abbreviations next to the subfigure labels indicate the dispersion curve to which a given profile corresponds. The color of the profile allows us to distinguish the mode symmetry: symmetric (S — blue), antisymmetric (AN — red), and asymmetric (AS — green). For asymmetric doubly degenerate modes the second profile is shown in gray.

order modes of this group appear and each of them has one node more than its predecessor. Therefore, the symmetry of these modes alternates between symmetric and antisymmetric with the increase of the order of the mode. The first mode that appears in this group of higher-order modes, is a symmetric mode S1. A typical magnetic field profile of this mode is presented in Fig. 7.2(d) and it possesses two nodes. For higher $\langle \Delta n \rangle$ an antisymmetric mode AN1 with three nodes appears. A typical magnetic field profile of this antisymmetric mode is presented in Fig. 7.2(f). With the further increase of $\langle \Delta n \rangle$, a symmetric mode S2 with four nodes and an antisymmetric mode AN2 with five nodes appear (not visible on the dispersion diagram shown in Fig. 7.1). Typical field plots for these modes are shown in Figs. 7.2(e) and (g). The higher-order nonlinear modes belonging to the family with nodes, discussed here [see Fig. 7.2(d)–(g)] are presented in this PhD manuscript for the first time in the frame of the study of nonlinear slot waveguides.

In the dispersion plots in Fig. 7.1, modes AN1 and S2 do not appear for $\beta = 1$. It is caused by the range of H_0 [field intensity at the left metal/nonlinear dielectric interface, see Eqs. (6.1.4)] scanned in order to obtain this plot. Scanning even higher values of H_0 would allow us to see that, the dispersion curves of the modes AN1 and S2 curves actually start at $\beta = 1$ (see also Fig. 7.27 for better understanding).

The number of nodes N_{node} in the magnetic field profiles of the symmetric modes SΩ and the antisymmetric modes ANΩ (here Ω denotes the order of the mode and $\Omega \in \{0, 1, 2, \dots\}$) can be calculated using the formula

$$N_{\text{node}} = 2\Omega + p, \tag{7.1.2a}$$

where p denotes the parity of the mode

$$p = \begin{cases} 0 & \text{for symmetric modes,} \\ 1 & \text{for antisymmetric modes.} \end{cases} \tag{7.1.2b}$$

The field profiles of the modes with nodes are similar to the field profiles of a linear slot waveguide with identical parameters as the nonlinear slot waveguide studied here, except for the permittivity of the core. The comparison of the dispersion curves and the field profiles obtained for the linear slot waveguide with core permittivity higher than $\epsilon_{l,2}$ is presented in Section 7.1.5.

The second group of the modes that exists only for elevated nonlinear index modifications (for $\langle \Delta n \rangle > 1$ in the example presented in Fig. 7.1), is a group consisting of the modes that do not possess any nodes in the $H_y(x)$ field profile. Moreover, the modes in this group have only very high effective indices $\beta \gtrsim 5$. Neither the dispersion curves nor the field plots of the modes of this group have already been presented in literature. We are the first to report their existence and present their dispersion curves and field profiles.

At $\langle \Delta n \rangle \approx 1.5$, a higher-order symmetric node-less mode SI[2] appears. A typical field profile of the SI mode is presented in Fig. 7.2(h). The field profile of this symmetric mode does not resemble any of the modes found in symmetric linear slot waveguides. It can be seen as a soliton propagating in the nonlinear core of the slot waveguide. The dispersion curve of the SI mode resembles a tilted letter 'V'. It starts at one extremity at low power and then two branches emerge from this extremity and continue toward higher values of $\langle \Delta n \rangle$ and β.[3]

Slightly above the appearance of the SI mode, an asymmetric node-less mode AS2 bifurcates from the symmetric SI mode. The dispersion curve of this mode starts at the bottom branch of the SI dispersion curve. For $1.9 < \langle \Delta n \rangle < 2.7$, the AS2 dispersion curve lays slightly below the bottom branch of the SI dispersion curve. For $\langle \Delta n \rangle > 2.7$ it lays between the two branches of the SI dispersion curve. A typical field profile for the AS2 mode is presented in Fig. 7.2(j). This curve, similar to AS1

[2]Notice that there is a difference in notation between modes S1 and SI. Symbol S1 (with the Arabic digit one) denotes the first-order symmetric mode that belongs to the family of the modes with nodes. Symbol SI (with the Roman digit one) denotes a first-order symmetric modes that belongs to the family of the modes without nodes. This nomenclature is used also for higher-order symmetric modes in both families.

[3]The appearance of the modes for which the dispersion curves that have parabolic shape is associated with so-called fold bifurcation [155].

curve, is doubly degenerate. The soliton peak of the green (gray) profile in Fig. 7.2(j) is located close to left (right) metal/nonlinear dielectric interface. The H_y field amplitude of the right (left) side-lobe is larger than of the left (right) side-lobe.

At $\langle \Delta n \rangle \approx 3.8$ another higher-order symmetric node-less mode appears through the fold bifurcation. It is denoted by SII and its dispersion curve resembles a tilted letter 'U'. A typical field profile for this branch is presented in Fig. 7.2(i) and can be seen as two solitons propagating in the nonlinear waveguide core. This dispersion curve, similar to the one of SI mode, starts at one extremity at low power and then two branches emerge from this extremity and continue toward higher values of $\langle \Delta n \rangle$ and β.

The asymmetric node-less mode AS3 appears through a symmetry Hopf bifurcation from the SII mode. This time, in contrast with the SI-AS2 couple, AS3 bifurcates from the top branch of SII dispersion curve. The dispersion curve of the AS3 mode lays between the two branches of the SII dispersion curve. A typical field profile for this branch is presented in Fig. 7.2(k). Similar to the case of SI-AS2 couple, the profile of the AS3 mode presented in Fig. 7.2 in green (gray) resembles the one from which it bifurcates but is shifted to the right (left) metal/nonlinear dielectric interface.

Interface model

In Fig. 7.3, the dispersion diagram for the nonlinear slot waveguide with the parameters presented in Table 7.1, obtained using the IM are presented. Typical field profiles corresponding to each of the dispersion curves labeled in Fig. 7.3 are presented in Fig. 7.4.

The analysis of the dispersion plot obtained using the IM will be done by comparison with the results discussed above for the JEM. Comparing Figs. 7.1 and 7.3, one can see that qualitatively the dispersion curves obtained using both models are very similar. The number of the modes and the character of the dispersion curves agree between the two models. The same conclusion can be drawn comparing the field plots presented in Figs. 7.2 and 7.4, corresponding to the same modes. The magnetic field profiles obtained using both models are qualitatively the same. This proves that both models correctly describe the physical phenomena occurring in the nonlinear slot waveguides. However, the quantitative description differs between the two models. These discrepancies can be explained by the fact that the JEM was built using strong assumptions about the nature and the amplitude of the nonlinear term in Maxwell's equations (see Pages 78 and 79). The differences between the JEM and the IM will be discussed in more detail in Section 7.1.3, where we compare the transformation of the magnetic and the electric field profiles along the dispersion curves obtained using the two models.

From the quantitative point of view there is several differences between the dispersion curves obtained using the JEM (Fig. 7.1) and the IM (Fig. 7.3). In the IM, the first bifurcation (appearance of the AS1 mode) occurs at $\langle \Delta n \rangle \approx 0.067$ which is slightly lower than the value predicted using the JEM. The bifurcation of the AS2 mode occurs at $\langle \Delta n \rangle \approx 3$ and $\beta \approx 7$ which is higher than in the results of the JEM (there $\langle \Delta n \rangle \approx 1.5$ and $\beta \approx 5.2$). Similarly, the AS3 mode appears in the IM for both higher $\langle \Delta n \rangle$ and β compared to the JEM. Moreover, the separation between the two branches of the dispersion curves corresponding to the symmetric node-less modes SI and SII is smaller in the case of the IM than for the JEM.

On the contrary, for the family of the modes with nodes, the situation is reversed. In the frame of the IM, all these modes appear for lower values of averaged nonlinear index modification $\langle \Delta n \rangle$. As a result, for identical range of $\langle \Delta n \rangle$, we observe more higher-order symmetric and antisymmetric modes with nodes using the IM than predicted by the JEM. In Fig. 7.4, two additional field profiles are presented for the S3 and AN3 modes. The scanning parameter range in case of the IM [in the IM the input parameters are E_0 and E_d (see Section 6.2.2); in the JEM the input parameter was H_0] allows for observing the appearance of all the modes of the family with nodes at $\beta = 1$ (unlike in the JEM where higher-order modes of this family appeared for higher β values, see Fig. 7.1).

In Fig. 7.3, the dispersion curves of the AN0 and S0 modes terminate at $\beta \approx 8$. This is the result of our numerical procedure that was no longer able to resolve the two solutions and therefore we were not capable of observing the continuation of these curves. Using the scanning algorithm with a higher

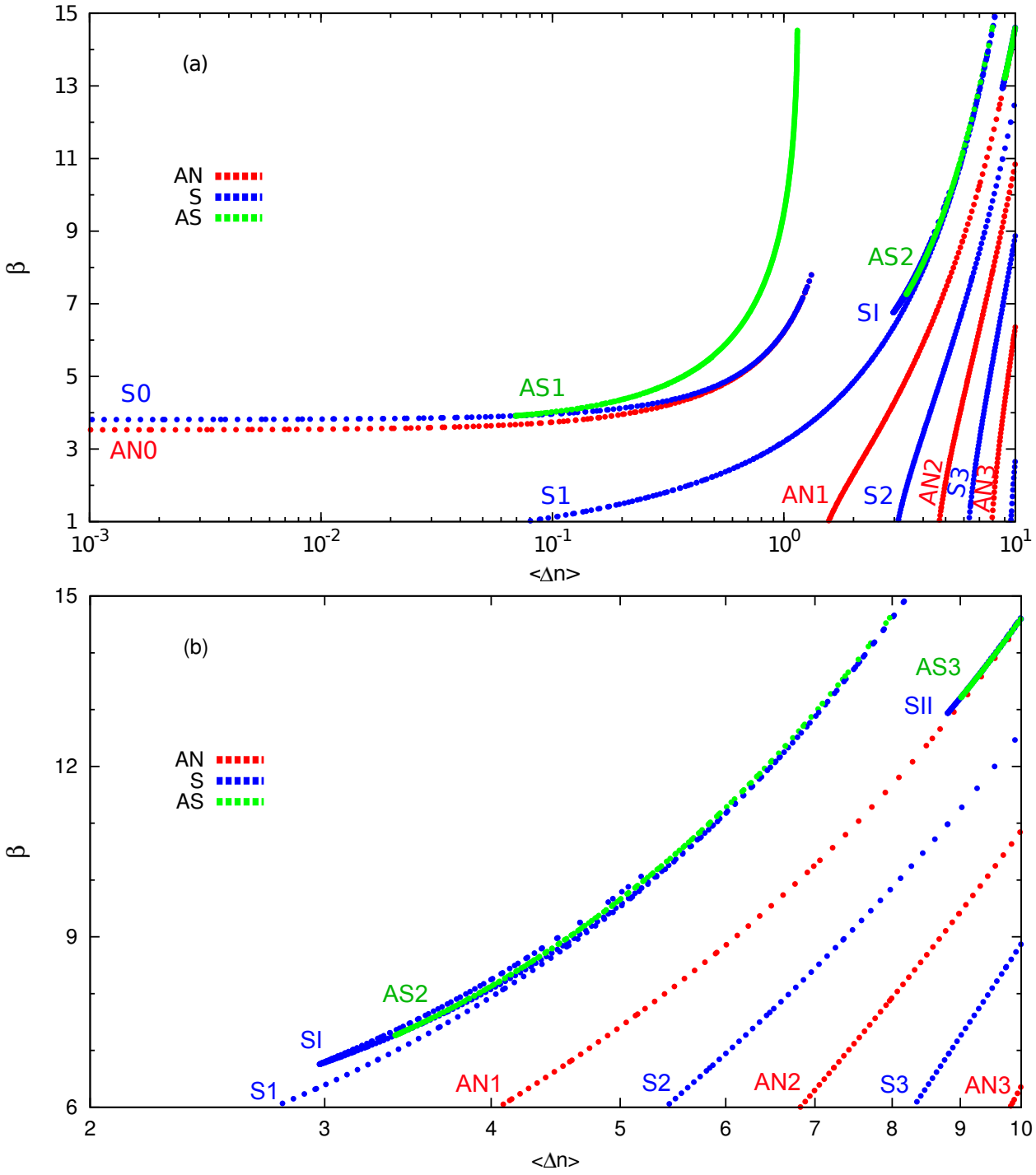

Figure 7.3: (a) Nonlinear dispersion curves of the first and the higher-order symmetric (S — blue), antisymmetric (AN — red), and asymmetric (AS — green) modes for the symmetric nonlinear slot waveguide obtained using the IM. (b) Zoom on the region with bifurcations of the second- and the third-order asymmetric modes. Each curve is labeled with the name of the corresponding mode. Structure parameters are listed in Table 7.1.

resolution (more scanning steps in β used in the numerical algorithm presented in Section 6.2.2) would allow us to compute the continuation of these two curves (see Section 6.2.2 for more details on the numerical procedure used in the IM and parameters influencing the resolution).[4]

[4]By resolution, we understand here the ability of the numerical algorithm to find two solutions that lay close to each other in terms of β. The algorithm that is able to find solutions that are separated by a smaller interval $\Delta\beta$ has higher resolution.

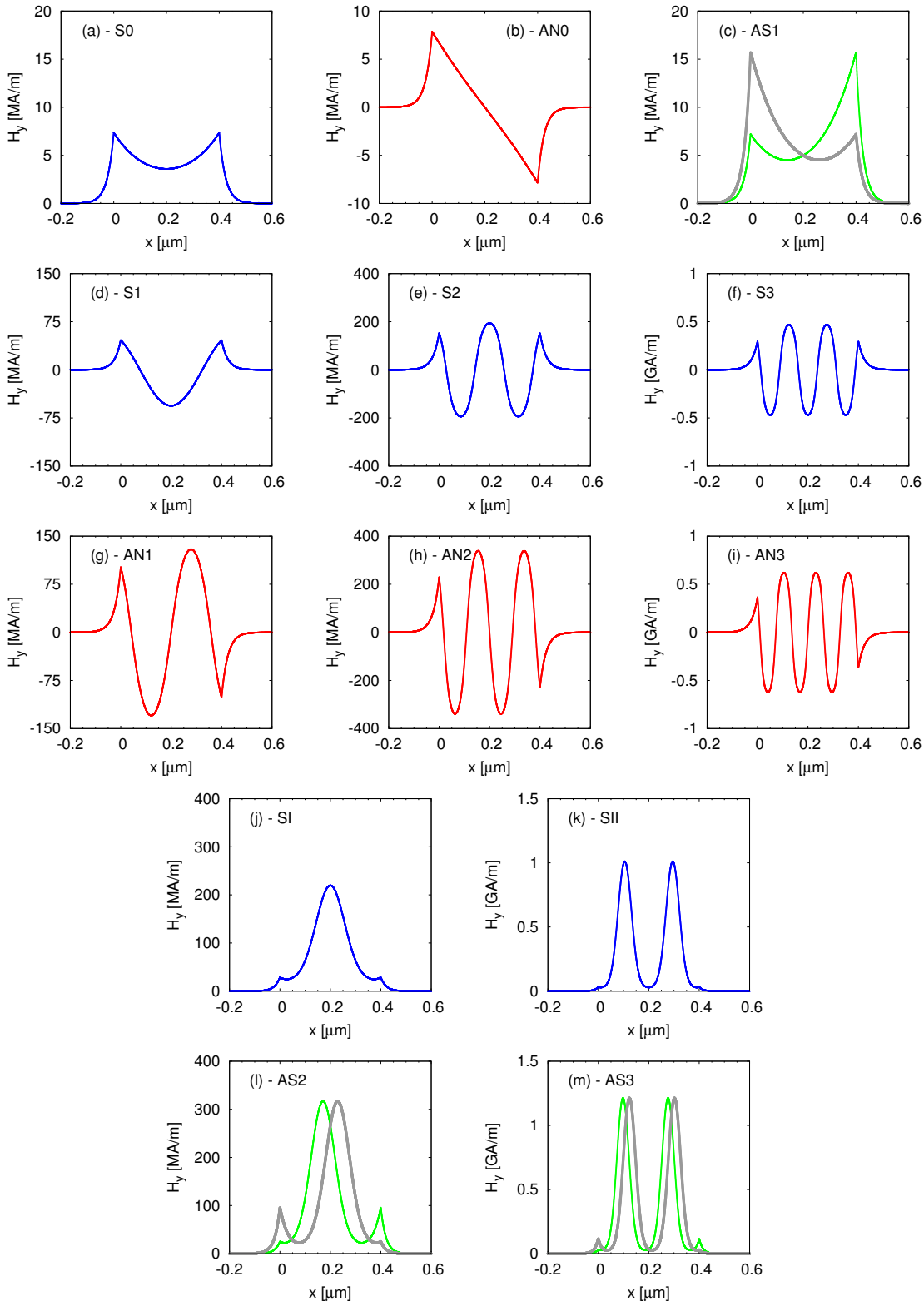

Figure 7.4: Typical magnetic field profiles $H_y(x)$, obtained using the IM, corresponding to different dispersion curves indicated in Fig. 7.3. Abbreviations next to the subfigure labels indicate the dispersion curve to which a given profile corresponds. The color of the profile allows us to distinguish the mode symmetry: symmetric (S — blue), antisymmetric (AN — red), and asymmetric (AS — green). For asymmetric doubly degenerate modes the second profile is shown in gray.

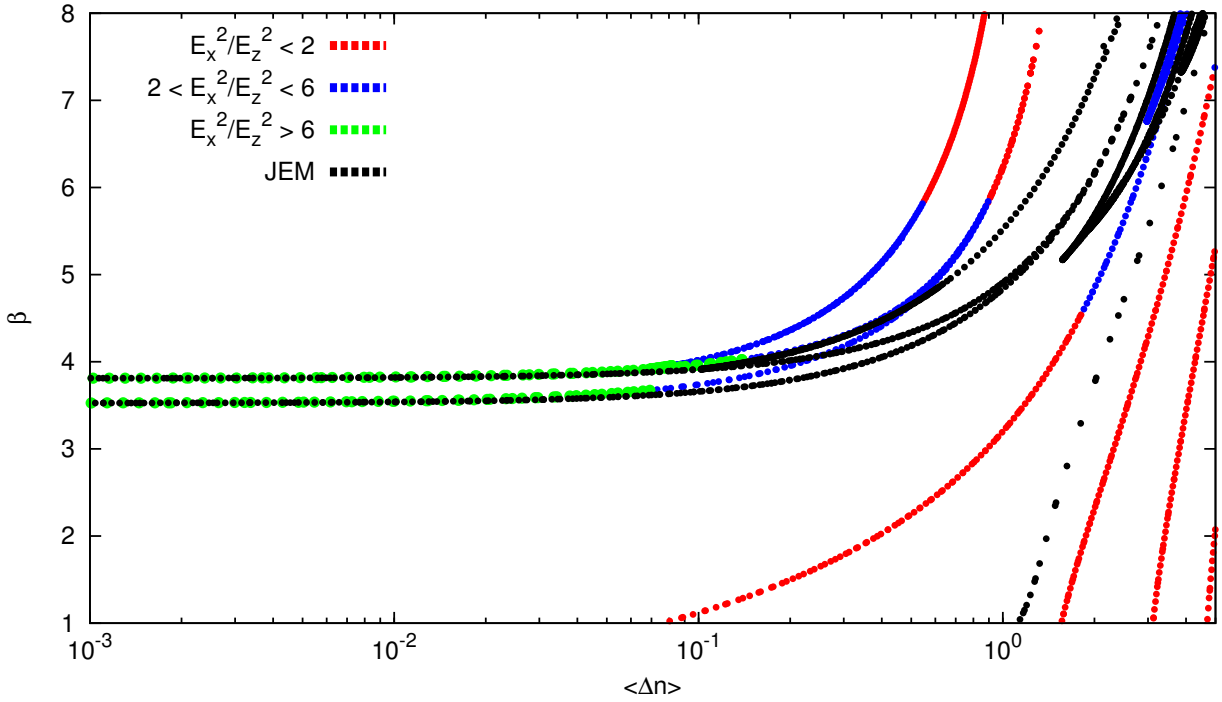

Figure 7.5: Direct comparison of the nonlinear dispersion curves obtained using the JEM (Fig. 7.1) and the IM (Fig. 7.3). For the IM the ratio of $\max\{|E_x^2|\}/\max\{|E_z^2|\}$ for the field profiles corresponding to the dispersion curves is indicated using a color code (see plot legend).

In Fig. 7.5, a direct comparison between the nonlinear dispersion curves obtained using the JEM (Fig. 7.1) and the IM (Fig. 7.3) is presented. Additionally, for the IM, the ratio of $\max\{|E_x^2|\}/\max\{|E_z^2|\}$ for the field profiles corresponding to the dispersion curves is shown. From this plot we can see that there is a good quantitative agreement between the two models in the case where $\max\{|E_x^2|\}/\max\{|E_z^2|\} > 6$. This is coherent with the assumptions that we have made while building the JEM. To derive the nonlinear wave equation used in this model [Eq. (6.1.2)], we assumed that in this model the ratio $\max\{|E_x^2|\}/\max\{|E_z^2|\} \gg 1$. Only in this case we were able to omit the E_z^2 term in the calculations of the Kerr nonlinearity. This fact helps us to understand the discrepancies between the results of our two models and shows that the approximations we made are coherent with the interpretation of the results. We notice that the assumption $\max\{|E_x^2|\}/\max\{|E_z^2|\} \gg 1$ is valid only for the two first modes (S0 and AN0) of the nonlinear slot waveguide at small nonlinear index modifications ($\langle\Delta n\rangle \lesssim 0.1$). Nevertheless, the simple JEM is able to qualitatively predict the complex behavior of the rich nonlinear dispersion relations for the nonlinear slot waveguides even for elevated values of $\langle\Delta n\rangle$.

The second assumption that we have made in the JEM was that the nonlinear index modification $\langle\Delta n\rangle$ is much lower than the linear part of the refractive index $\sqrt{\epsilon_{l,2}}$. We see that, for the range of $\langle\Delta n\rangle$ where this assumption is fulfilled ($\langle\Delta n\rangle < 0.1$), the results of our two models are in good agreement.

Nonlinear dispersion curves in various coordinates

We have thoroughly analyzed the nonlinear dispersion relations obtained using our two models in the case where the averaged nonlinear index modification $\langle\Delta n\rangle$ was used as abscissa. It is interesting to analyze the dispersion diagrams of the nonlinear slot waveguide (with the parameters listed in Table 7.1), when other quantities (such as light intensity, power or electric field amplitude at one of the interfaces between metal and nonlinear dielectric) are used as abscissa.

From the definition of $\langle \Delta n \rangle$ given by Eq. (7.1.1) we notice that this quantity is strictly proportional to the intensity density in the core (the proportionality constant is $n_2^{(2)}/d$)

$$I_c = \int_0^d I \, \mathrm{d}x. \tag{7.1.3}$$

Therefore, we will not discuss in detail the dispersion diagrams plotted as a function of I_c because they will have exactly the same character as the dispersion plots presented in Figs. 7.1 and 7.3.

Another important quantity in electrodynamics is the Poynting vector, which describes the energy flow. The power density in the core is given as the Poynting vector component parallel to the propagation direction (z component) integrated over the core cross-section:

$$P_c = \int_0^d S_z \, \mathrm{d}x, \tag{7.1.4}$$

where the Poynting vector is defined as

$$\mathbf{S} \equiv \frac{1}{2} \Re e(\mathbf{E} \times \mathbf{H}^*) \tag{7.1.5}$$

[compare with definitions given by Eqs. (2.1.53) and (2.1.54)].

The nonlinear dispersion curves obtained using both the JEM and the IM, in which the power density in the core P_c is used as abscissa, are presented in Fig. 7.6. At the first glance we notice two facts. First of all, the dispersion curves have different characters than in the dispersion diagrams presented using $\langle \Delta n \rangle$ as abscissa. Secondly, the dispersion curves obtained using both models changed their characters in identical way. Both model still provide qualitatively the same results.

The most striking difference between the dispersion diagrams plotted using $\langle \Delta n \rangle$ (Figs. 7.1 and 7.3) and P_c (Fig. 7.6) as abscissa is the change of the inclination of the dispersion curves. When $\langle \Delta n \rangle$ was used as abscissa, the increase of the effective index β was accompanied by a monotonous increase of the average nonlinear index modification and therefore the intensity density in the core for all the modes. In the case of P_c used as abscissa, the behavior is no longer monotonous and is different for different dispersion curves. For modes AN0, S0, AS1, S1, AN1, and S2, at low effective indices, the power density in the core increases with the increase of β [see Fig. 7.6(b)]. At a particular value of the effective index (different for each mode), P_c reaches its maximum and above this β value, P_c decreases with the increase of β.[5] For modes AN2, S3, and AN3 that belong to the family with nodes and for the asymmetric node-less modes AS2 and AS3, the power density in the core decreases with the increase of β in all the range of effective indices. Higher-order symmetric modes from the node-less family (SI and SII) present a more complex behavior (see Fig. 7.6).

It is also worth noting that in the dispersion diagrams where $\langle \Delta n \rangle$ was used as abscissa (Figs. 7.1 and 7.3), modes of the family with nodes were well separated in terms of $\langle \Delta n \rangle$ for all values of β. In the case where P_c is used as abscissa (Fig. 7.6) we can observe that these modes become closer to each other in terms of P_c with the increase of the effective index β.

In Fig. 7.7, a dispersion diagram obtained using the IM is shown, where the total power density P_{tot} in the slot waveguide was used as abscissa. The total power density is defined as

$$P_{\mathrm{tot}} \equiv \int_{-\infty}^{+\infty} S_z \, \mathrm{d}x, \tag{7.1.6}$$

and can be seen as a sum of the power density in the core and in the two metal regions

$$P_{\mathrm{tot}} = P_c + P_1 + P_3 \tag{7.1.7}$$

[5] Similar behavior is observed for the dispersion diagram where the total power P_{tot} (see Fig. 7.7) or the total intensity I_{tot} (see Fig. 8.2) of the mode is used as abscissa. The change of inclination of the $\beta(I_{\mathrm{tot}})$ curves may influence the stability of the mode (see Chapter 8).

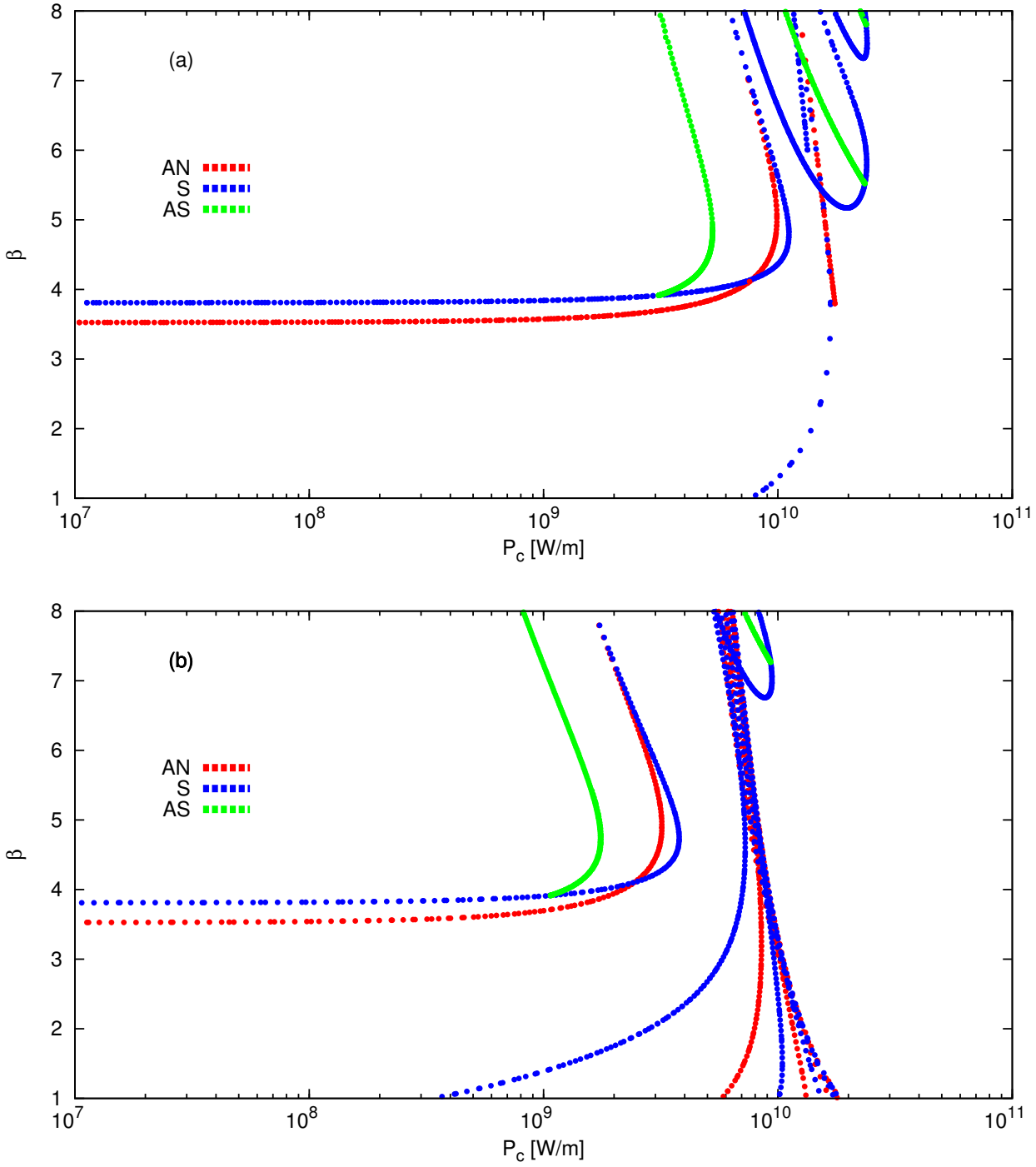

Figure 7.6: Dispersion curves for the symmetric nonlinear slot waveguide presenting the effective index β as a function of the power density in the core P_c obtained using (a) the JEM and (b) the IM. For clarity of the plots and to facilitate mutual comparison the case of the IM the range of the effective indices shown was reduced and is now identical to these in the case of JEM ($\beta \in [1, 8]$). Structure parameters are listed in Table 7.1.

[compare with definition given by Eq. (2.1.56)]. Here P_1 and P_3 denote the power density in left and right semi-infinite cladding metal layers, respectively (see Fig. 6.1) and can be calculated using formulas similar to Eq. (7.1.4). As it can be seen from the definition given by Eq. (2.1.55), the power density in metal layers is negative due to the negative value of the metal permittivity. Therefore, the total power density P_{tot} is lower than the power density in the core P_c. However, this difference is small

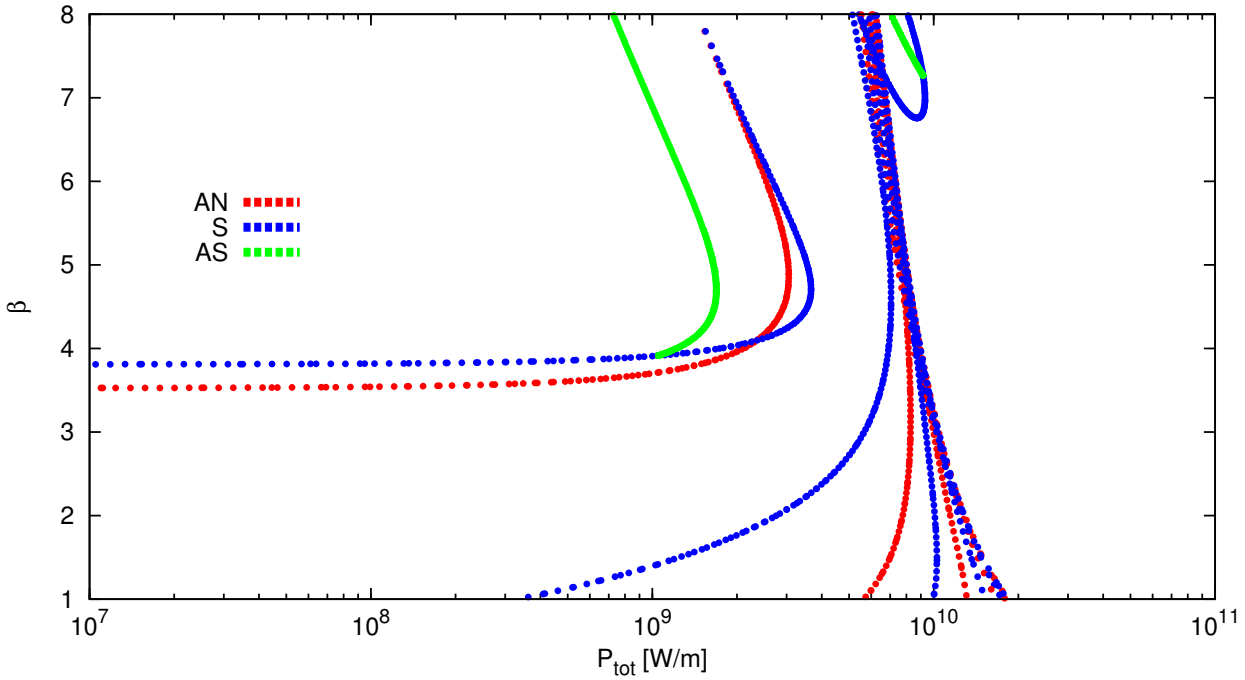

Figure 7.7: Dispersion curves for the symmetric nonlinear slot waveguide obtained using the IM. Dependency of effective index β presented as a function of the total power density P_{tot}. Structure parameters are listed in Table 7.1.

for two reasons. Firstly, the field in the metal decays exponentially very quickly, with a penetration depth of the order of 0.05 μm. Secondly, even for identical magnetic field amplitude in the metal and in the dielectric, the absolute value of the power density in the metal is $|\epsilon_{\text{metal}}|/\epsilon_{\text{dielectric}}$ times lower (in our case $|\epsilon_3|/\epsilon_{l,2} \approx 90/12 = 7.5$). These theoretical considerations are confirmed, if we compare the plots in Figs. 7.6(b) and 7.7. These two plots are practically identical and it is difficult to spot a difference between them. The only visible change occurs for the first-order asymmetric curve AS1, for very high effective indices. For $\beta = 8$, the total power density of this mode is $P_{\text{tot}} \approx 7 \cdot 10^8$ W/m and the power density in the core is $P_c \approx 8 \cdot 10^8$ W/m, which accounts to about 15 % difference between the two powers densities. A detailed analysis shows that for low β region the ratio P_c/P_{tot} is less that 1.05. For modes S0, AN0, and AS1 this ratio reaches 1.3 for very high values of mode effective indices. For the rest of the modes it stays at the level 1.05 for all the range of effective indices β.

The situation is similar if we compare the dispersion curves plotted in the coordinates of the intensity density in the core I_c and the total intensity density I_{tot} in the waveguide.[6] The comparison of these two dispersion diagrams is presented in Fig. 7.8. Here, the total intensity density I_{tot} is slightly higher than the intensity density in the core I_c due to the fact that we have defined the light intensity to be positive regardless of the sign of the material permittivity [see Eq. (1.7.4)]. The ratio I_{tot}/I_c is below 1.05 for the region of low β values. For the S0, AN0, and AS1 modes, this ratio increases to 1.5 for high values of β. For all the other modes, it decreases toward 1 with the increase of β.

To conclude this part, we can observe that for the opto-geometric parameters we use in Figs. 7.6(b) and 7.7, there is no qualitative difference between the dispersion curves plotted in the coordinates of the total power density P_{tot} and the power density in the core P_c. Similarly, there is no qualitative difference between the dispersion diagrams plotted in the coordinates of the intensity density in the

[6]The total intensity density in the nonlinear slot waveguide is defined by

$$I_{\text{tot}} \equiv \int_{-\infty}^{+\infty} I \, \mathrm{d}x,$$

in a similar manner to the total power density [see Eq. (7.1.6)].

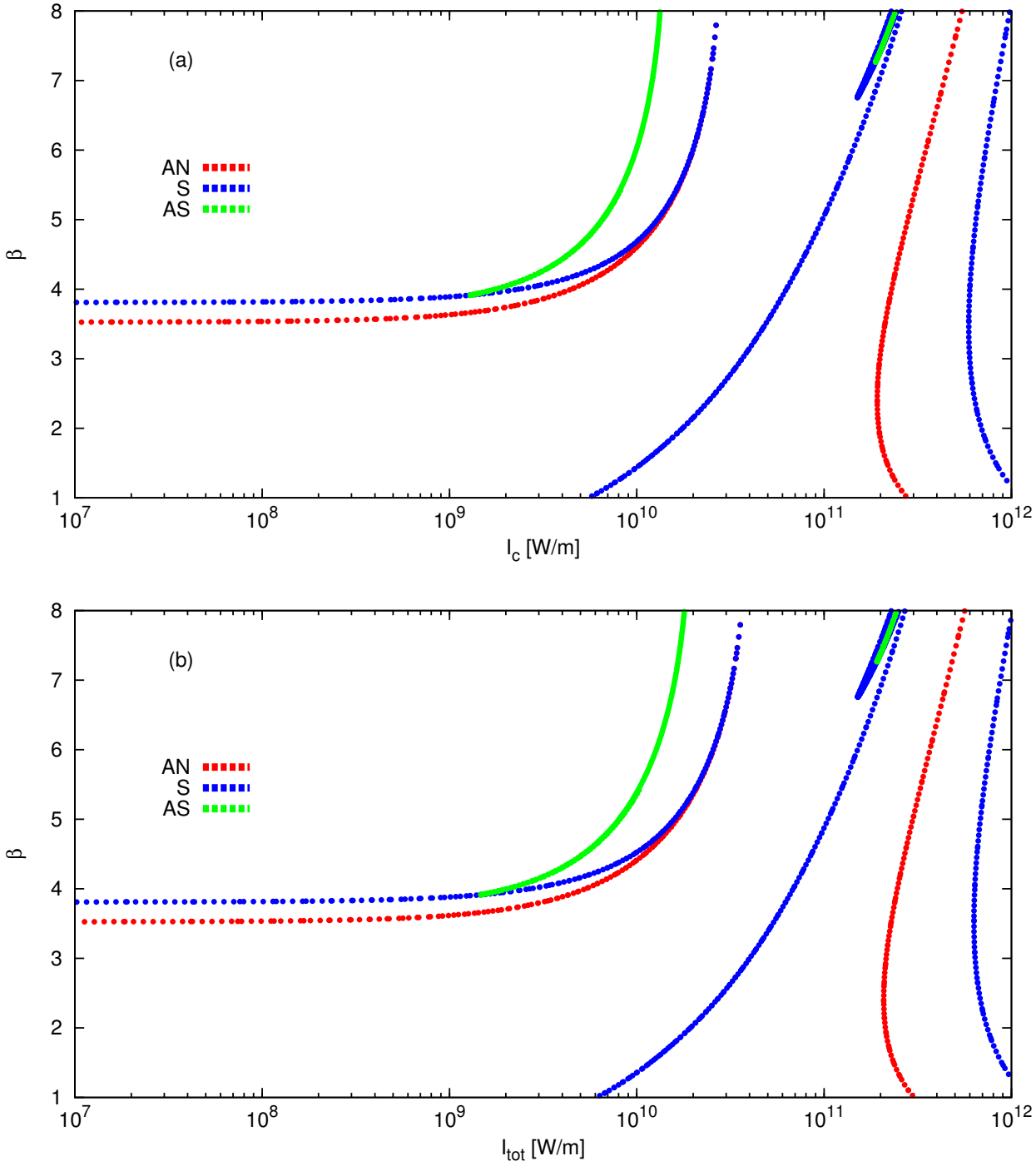

Figure 7.8: Dispersion curves for the symmetric nonlinear slot waveguide obtained using the IM. Dependency of effective index β presented as a function of (a) the intensity density in the core I_c and (b) the total intensity density in the waveguides I_{tot}. Structure parameters are listed in Table 7.1.

core I_c [Fig. 7.8(a)] and the total intensity density I_{tot} [Fig. 7.8(b)]. For the configurations where the core width is much smaller than in our case and it is comparable with the field penetration depth in the metal, the differences between such plots are more pronounced [87].

It is equally interesting to look at the dispersion diagrams where the effective index β is presented as a function of the total electric field amplitude at one of the interfaces between the metal and the nonlinear dielectric core. Figure 7.9 shows such plots obtained using both the JEM and the IM. This time, the quantity used as abscissa is not a global quantity as in the cases of $\langle \Delta n \rangle$, or power

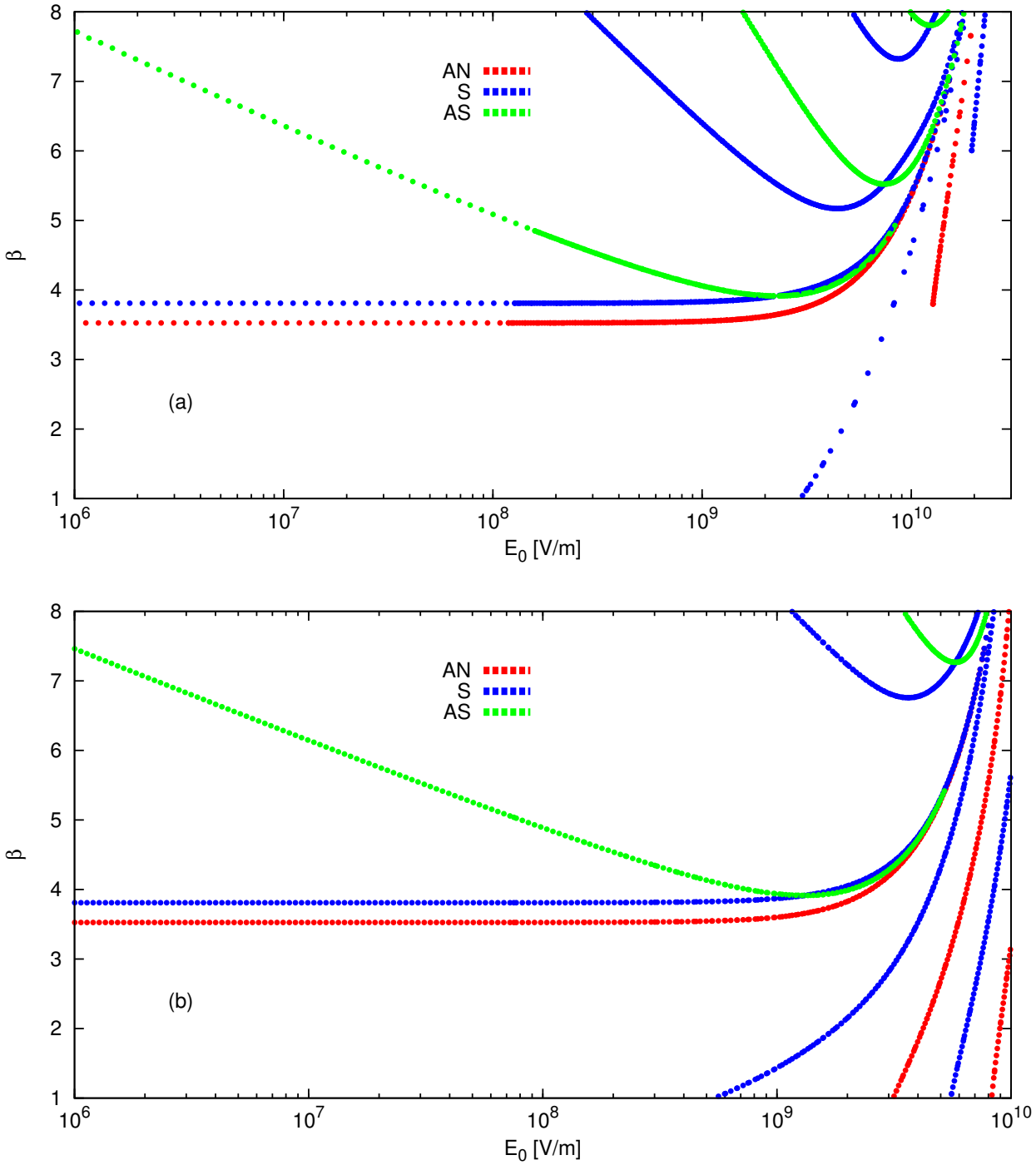

Figure 7.9: Dispersion curves for the symmetric nonlinear slot waveguide presented as the dependency of the effective index β on the total electric field amplitude on the left interface between metal and nonlinear dielectric E_0. Results obtained using (a) the JEM and (b) the IM. Structure parameters are listed in Table 7.1.

and intensity densities. Here we use a local quantity E_0 [defined by Eq. (6.2.9a)], which denotes the total electric field amplitude at the left metal/nonlinear dielectric interface. The dispersion diagrams plotted using a local quantity as abscissa look drastically different from the dispersion curves presented using global quantities as abscissa. The most interesting is the fact that, the asymmetric dispersion curves are no longer degenerate in this coordinate frame. The pairs of asymmetric field profiles with identical β value that corresponded to one point in the dispersion curves drawn in the coordinates

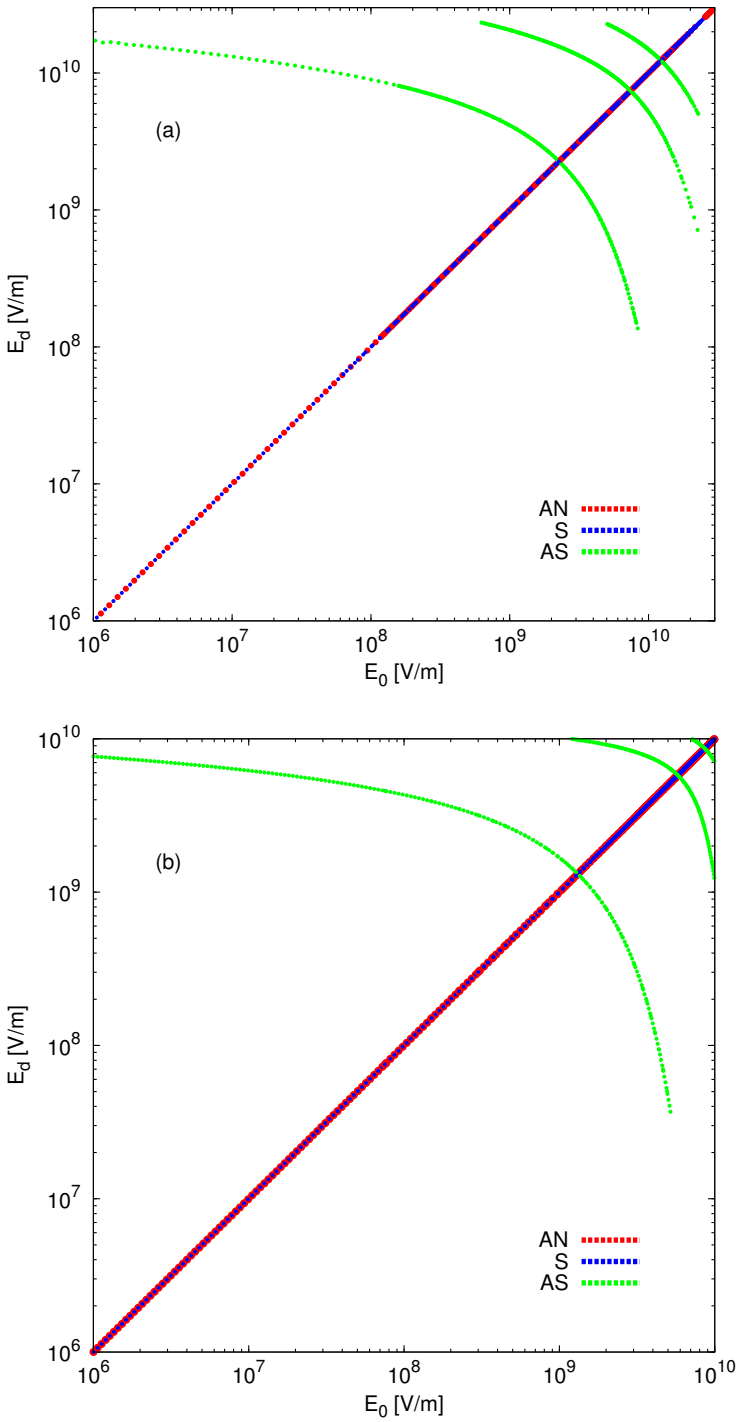

Figure 7.10: Dependency of E_d on E_0 for the symmetric nonlinear slot waveguide, with parameters are listed in Table 7.1, obtained using (a) the JEM and (b) the IM.

of a global quantity [green and gray field profiles in Figs. 7.2(c), (j), (k) and Figs. 7.4(c), (l), (m)], are now represented by different points on the dispersion diagrams. The field profile localized at the left core interface ($E_0 > E_d$ — gray profile) corresponds to a point located at the right branch (high E_0) of the dispersion curves of asymmetric modes in Fig. 7.9. The profile localized at the right core interface ($E_0 < E_d$ — green profile) corresponds to a point located at the left branch (low E_0) of these dispersion curves for identical β value.

At the end of this section, we analyze the plots presenting the dependency of the total electric field amplitude at the right metal/dielectric interface E_d [defined by Eq. (6.2.9b)] as a function of the total electric field amplitude at the left interface E_0. These plots, obtained using the JEM and the IM, are presented in Fig. 7.10. They resemble Fig. 3 in Ref. [38] presenting the nonlinear permittivity modification on the left and right interface of the nonlinear core in a fully dielectric waveguide with the nonlinear core. These plots show that in both our models the assumption about the symmetry of the modes is well satisfied. As expected, for the symmetric and antisymmetric field profiles the values of the electric field amplitudes on both core interfaces are identical ($E_d = E_0$). For asymmetric profiles, the green curves in Fig. 7.10 are symmetric with respect to the line $E_d = E_0$, which reflects the mirror symmetry of the green and gray field plots of asymmetric modes [see Figs. 7.2(c), (j), (k) and Figs. 7.4(c), (l), (m)]. Parts of the asymmetric curves for low values of E_d and high values of E_0 (bottom right corner) are missing due to the asymmetric scanning range used in our simulations.

7.1.2 Field profiles obtained using the interface model

In Section 7.1.1, we have described in detail the nonlinear dispersion relations obtained using the JEM and the IM for the symmetric nonlinear slot waveguide with the parameters shown in Table 7.1. We have shown that there is a very good qualitative agreement between the dispersion diagrams and the magnetic field profiles of the modes obtained using the two models. We have also presented a typical magnetic field profiles for each of the mode in the dispersion plots. This helped us to classify the modes according to their symmetry and the number of nodes.

In this section and in Section 7.1.3, we will study the field profiles in more detail. We will present not only magnetic field, but also electric field components, intensity, power (z component of the Poynting vector), and distribution of the nonlinear index modification in the core of the nonlinear slot waveguide. Furthermore, we will analyze the transformation of the field profiles along all the dispersion curves. This study will help us to get a better understanding of the behavior of the nonlinear dispersion curves. It will also help us to further understand the differences and discrepancies between the JEM and the IM.

As we have discussed on Page 116, the theoretical assumptions used to derive the JEM are not fulfilled by my most of the solutions found in the nonlinear slot waveguide structure. Therefore, we will present first the field profiles obtained using the IM, as this model is more suited for nonlinear slot waveguide studies. Because the IM does not use any limiting assumptions, we use its results as a reference. In Section 7.1.3 the field profiles obtained using the JEM will be discussed and the comparison between the results of the two models will be presented.

In Figs. 7.11 and 7.12, the dispersion curves $\beta(E_0)$ obtained using the IM are presented. These dispersion diagrams show the same dispersion plots as Fig. 7.9(b) but are more detailed. On the dispersion curves presented in Figs. 7.11 and 7.12 points were marked and labeled. The field profiles corresponding to these points are presented in the following and will help us to understand the mode transformation along the dispersion curves.

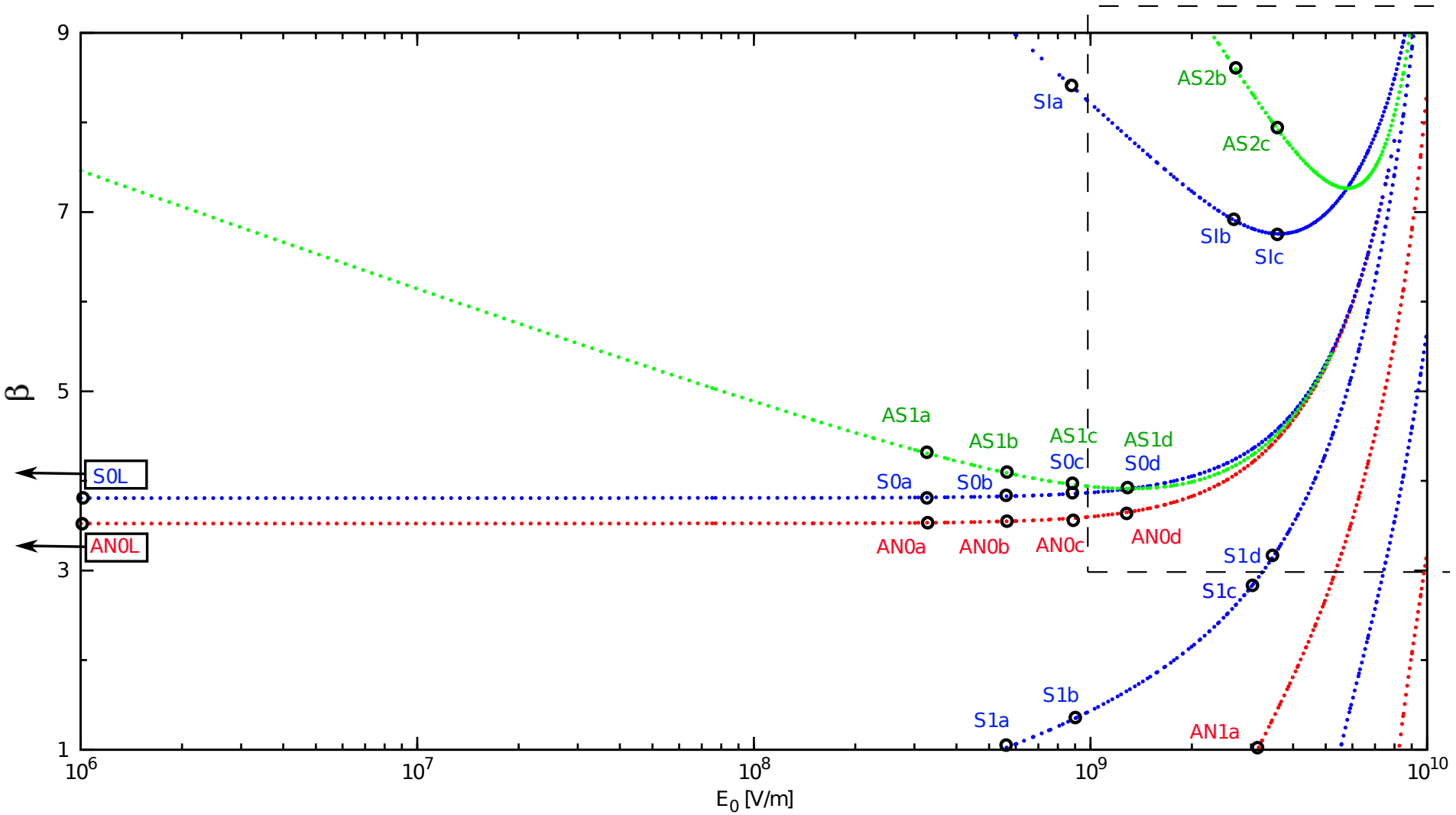

Figure 7.11: Nonlinear dispersion curves $\beta(E_0)$ obtained using the IM for the structure with parameters listed in Table 7.1. Labeled points on each of the dispersion curves are used in the following to analyze mode transformation along the dispersion curves. The zoom of the part enclosed in a rectangle marked by a dashed line is presented in Fig. 7.12.

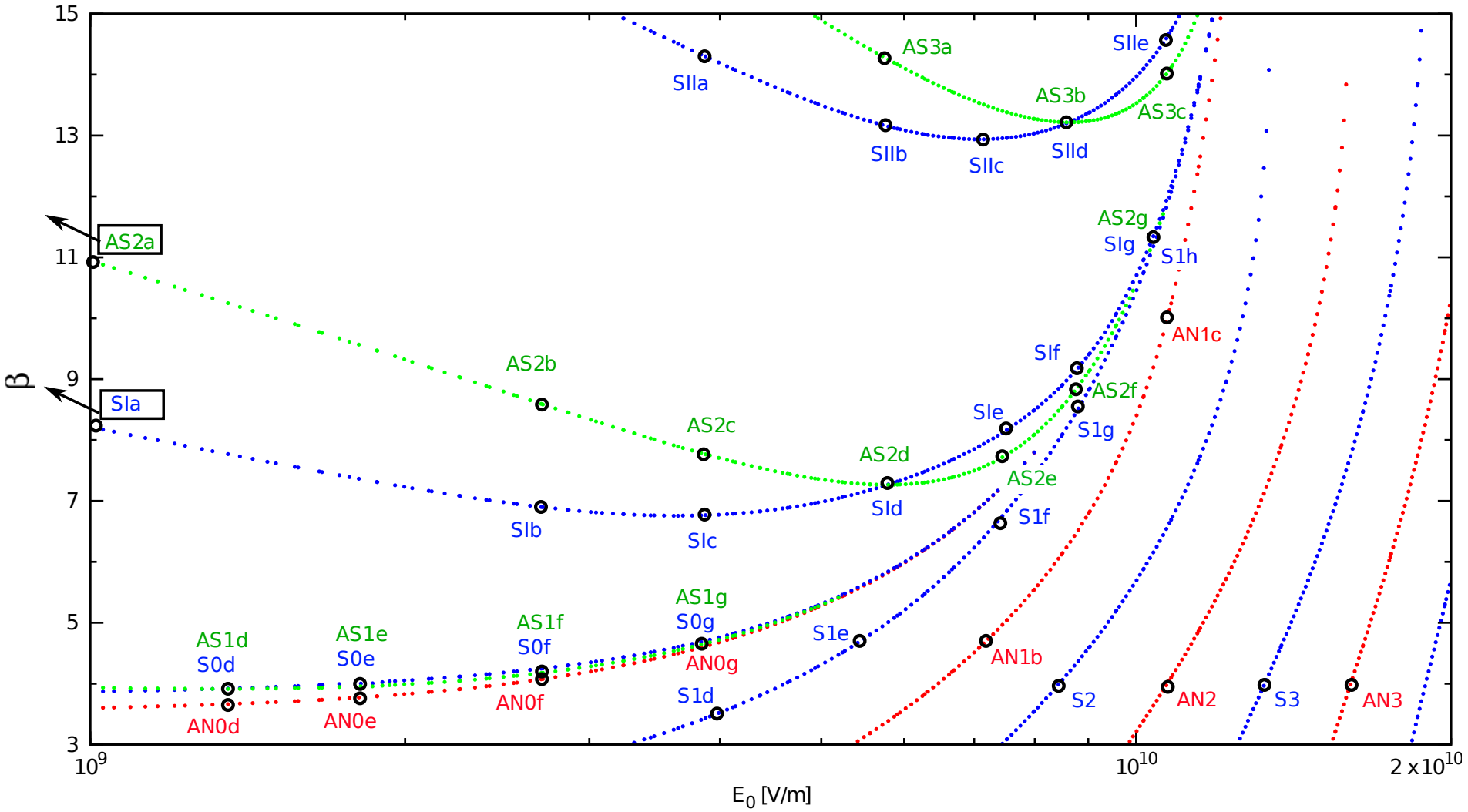

Figure 7.12: Zoom on the high E_0 part of the nonlinear dispersion curves $\beta(E_0)$ obtained using the IM and presented in Fig. 7.11. Labeled points on each of the dispersion curves are used in the following to analyze mode transformation along the dispersion curves

Modes with linear counterparts (low-power modes)

We start by discussing the transformation of the field profiles along the nonlinear dispersion curves corresponding to the first symmetric mode S0 and the first antisymmetric mode AN0 that originate for low powers and resemble the linear modes of the slot waveguide. These modes are called the low-power modes even if they exist also in the high power regime. Figure 7.13 presents the magnetic and electric field components, total electric field amplitude, intensity and power distribution in the nonlinear slot waveguide with the parameters given in Table 7.1 for the limiting case $n_2^{(2)} = 0$. In this limiting case two modes are supported by the studied structure: a symmetric mode S0L and and antisymmetric mode AN0L (see Figs. 7.11 and 7.12 for the point labels).

The profiles presented in Fig. 7.13 and all the following plots in this section are computed using the following scheme. In the frame of the IM, the quantities that are obtained directly at the output of the numerical procedure are E_x and E_z field components (see Section 6.2.2). Based on these quantities the magnetic field is calculated using Eq. (1.5.2b), where the full nonlinear expression for the refractive index given by Eq. (6.2.1) is used. The total electric field amplitude is simply $E = \sqrt{E_x^2 + E_z^2}$ (as defined on Page 97). The intensity distribution[7] I is calculated using Eq. (1.7.4) and the power distribution P (equivqlent to the longitudinal component of the Poynting vector S_z) is computed using Eq. (7.1.5).

In Fig. 7.14, the transformation of the modes S0 and AN0 along their respective dispersion curves is presented. In the first two columns, the effect of the increase of E_0 (and therefore the total intensity density defined in Footnote 6 on Page 119) on the S0 mode is presented and in the last two columns the same effect is presented for the AN0 mode. In addition to the profiles presented in Fig. 7.13, the distribution of the nonlinear index modification is presented in the last row of Fig. 7.14. The nonlinear index modification in the nonlinear dielectric is calculated using the following formula:

$$\Delta n = n_2^{(2)} I - n_0, \tag{7.1.8}$$

where n_0 denotes the linear part of the refractive index and in our case is equal to $\sqrt{\epsilon_{l,2}}$. In the linear materials (metal cladding) $\Delta n = 0$.

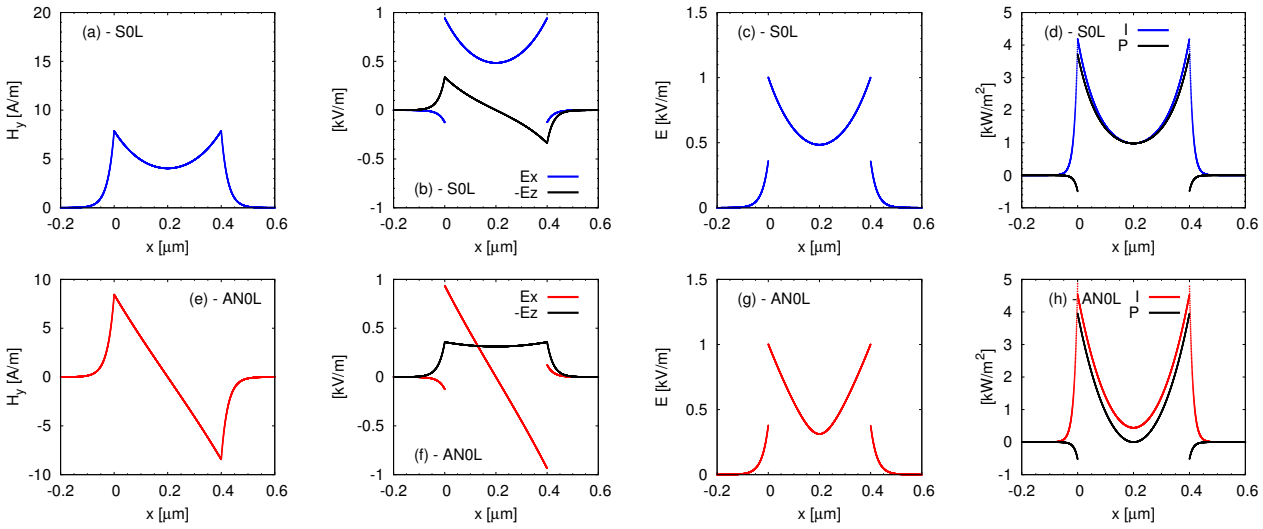

Figure 7.13: Profiles of (a), (e) magnetic field component H_y; (b), (f) electric field components E_x (red or blue) and $-E_z$ (black); (c), (g) total electric field amplitude E; (d), (h) intensity I (red or blue) and power P (black). Plots in the top row corresponds to for the linear fundamental symmetric mode of the slot waveguide (S0L) and in the bottom row to the linear antisymmetric mode of the slot waveguide (AN0L) (see Figs. 7.11 and 7.12 for the point labels).

[7] Here we stress on the fact that, the discontinuity that is observed in the intensity distribution at the metal/nonlinear dielectric interfaces in plots presented in this section, is a physical effect and not a numerical artifact.

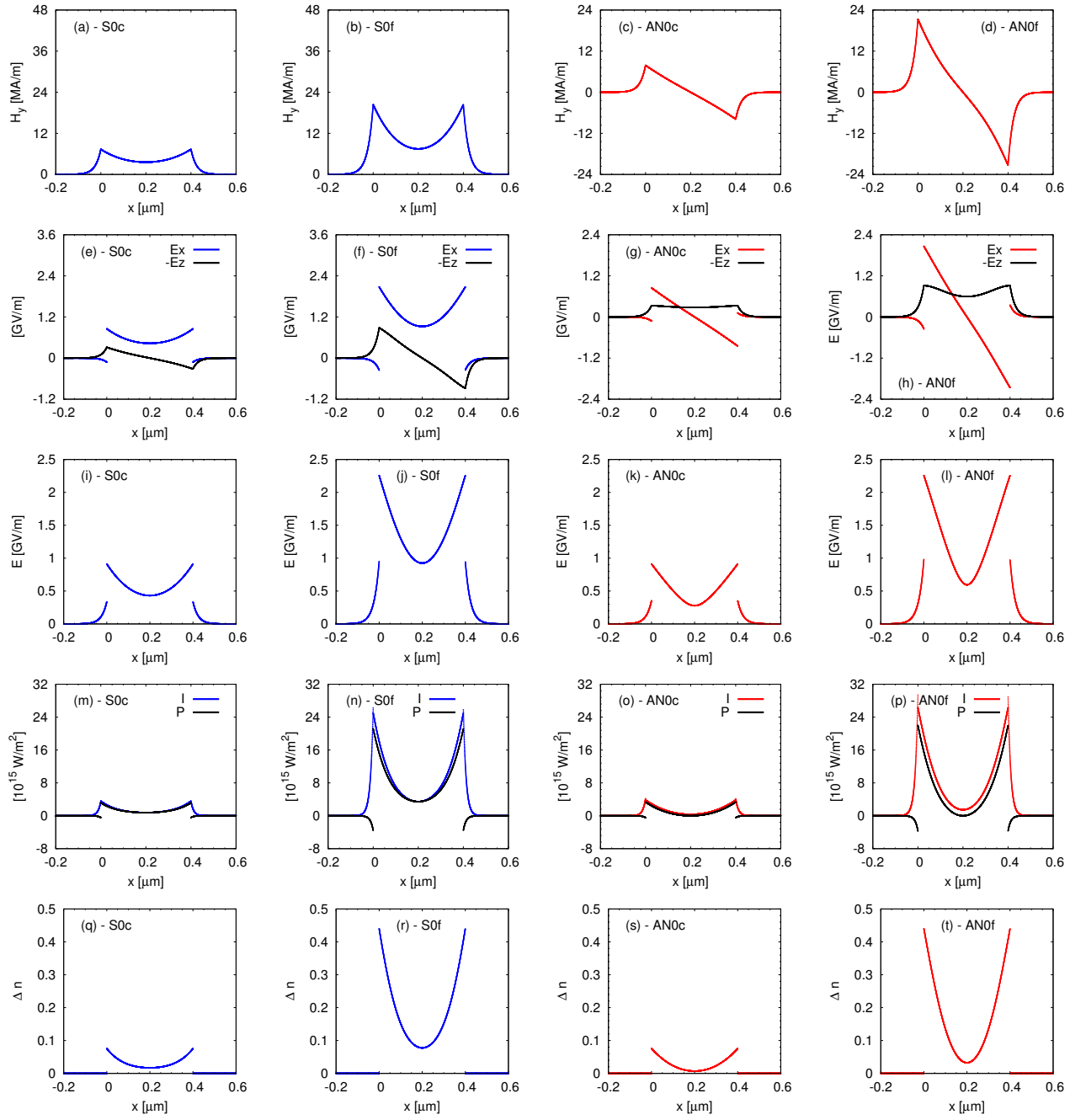

Figure 7.14: Profiles of (a)–(d) magnetic field component H_y, (e)–(h) electric field components E_x (red or blue) and $-E_z$ (black), (i)–(l) total electric field amplitude E, (m)–(p) intensity I (red or blue) and power P (black), (q)–(t) and nonlinear index modification Δn corresponding to points (first column) S0c, (second column) S0f, (third column) AN0c, and (fourth column) AN0f in Figs. 7.11 and 7.12.

We can see from Fig. 7.14 that, with the increase of the total intensity density, the amplitudes of the magnetic field, electric field components and the related quantities that are presented increase. However, there is no qualitative change in the field profiles and all the profiles (except for the nonlinear index modification) resemble their linear counterparts presented in Fig. 7.13.

Modes without nodes (node-less modes)

In Fig. 7.15, the transformation of the nonlinear first-order asymmetric node-less mode AS1 along its dispersion curve is presented, in a way similar to modes S0 and AN0 shown Fig. 7.14. The total intensity density increases from column one to column three. It is interesting to observe that the field profiles become more and more asymmetric with the increase of the total intensity density. In the first column, the ratio between the total electric field amplitude on the two interfaces E_d/E_0 is approximately equal to 2. With the increase of the mode energy, the intensity on one interface decreases and on the other one increases. Therefore, the E_d/E_0 ratio increases to ≈ 4 in the second column and ≈ 10 in the third column. As a result of the increased asymmetry of the field distribution, the mode tends to be located at one of the interfaces only. Because the light intensity at the other interface is very weak [see Fig. 7.15(o)], it is justified to assume that strongly asymmetric modes interact mainly with only one interface. This fact is used in Section 7.1.4 to approximate the dispersion relation of the AS1 mode by the dispersion relation for a single metal/nonlinear dielectric interface. This approximation is practical, because the dispersion relations for single-interface problems are given in an analytical way.

It is interesting to compare the field profiles of the three nonlinear modes AN0, S0, and AS1 for points at which the total electric field amplitude at the left metal/nonlinear dielectric interface E_0 is identical for all three modes (see Figs. 7.11 and 7.12). This comparison is presented in Fig. 7.16. We observe that for the bifurcation point, to which corresponds Fig. 7.16(d), the field profiles of the symmetric and asymmetric modes are identical. Moving away from the bifurcation point causes the increase of the asymmetric field profile asymmetry. At the bifurcation point, the ratio E_d/E_0 for the AS1 mode is equal to 1. Moving toward lower values of E_0, this ratio increases and is approximately equal to 2 for subplot (c), 4 for subplot (b), and 10 for subplot (a). On the contrary, moving to the higher values of E_0, this ratio decreases and is approximately equal to 1/2 for subplot (e), 1/4 for subplot (f), 1/20 for subplot (g). Both effects evidence the increase of the AS1 mode asymmetry.

Then we analyze the transformation of the light intensity profiles $I(x)$ for the three nonlinear modes (AN0, S0, and AS1) along their dispersion curves. The intensity profiles, corresponding to the magnetic field profiles presented in Fig. 7.16, are shown in Fig. 7.17. Here we can observe that for low E_0 values [see Figs. 7.17(a)–(c)] the total intensity density of the mode is much lower for the symmetric and antisymmetric modes than for the asymmetric mode. At the value of E_0 where the bifurcation occurs, the total intensity density of the three modes is comparable [see Fig. 7.17(d)]. With further increase of E_0, the total intensity density of the symmetric and antisymmetric modes becomes larger than the total intensity density of the asymmetric mode [see Figs. 7.17(e)–(g)]. In Fig. 7.17(g), the total intensity density of the symmetric or antisymmetric mode is twice larger than the one of the asymmetric mode. This can be also seen from the dispersion diagrams presented in Section 7.1.1. For high values of β in the dispersion plot $\beta(I_{\text{tot}})$ [see Fig. 7.8(b)], the symmetric S0 mode and antisymmetric AN0 mode have total intensity density that is two times larger than the total intensity density of the asymmetric AS1 mode with identical value of effective index. Similar observation can be made for the dispersion curves $\beta(\langle\Delta n\rangle)$ or $\beta(P_{\text{tot}})$ (see Figs. 7.5 and 7.7).

From Fig. 7.17 it can also be seen that the intensity distributions of the symmetric S0 and antisymmetric AN0 modes become more similar with the increase of E_0 (and therefore with the increase of the total intensity density) accompanied by the increase of the effective index β. This explains the fact that in the dispersion diagrams presented in Section 7.1.1, the dispersion curves of the S0 and AN0 modes become close to each other for high values of β.

The three modes described above (AN0 that belongs to the family with nodes and S0 and AS0 belonging to the node-less family) have been already reported in nonlinear slot waveguide structures [87]. However, no exhaustive study of their properties has been presented yet. The analysis presented above is the first that describes in detail the mode transformations along the dispersion curves.

Below we present a detailed description of the higher-order modes from the node-less family. The existence of these modes has not been reported previously in literature. The analysis presented in the following provides the first description of the properties of these modes.

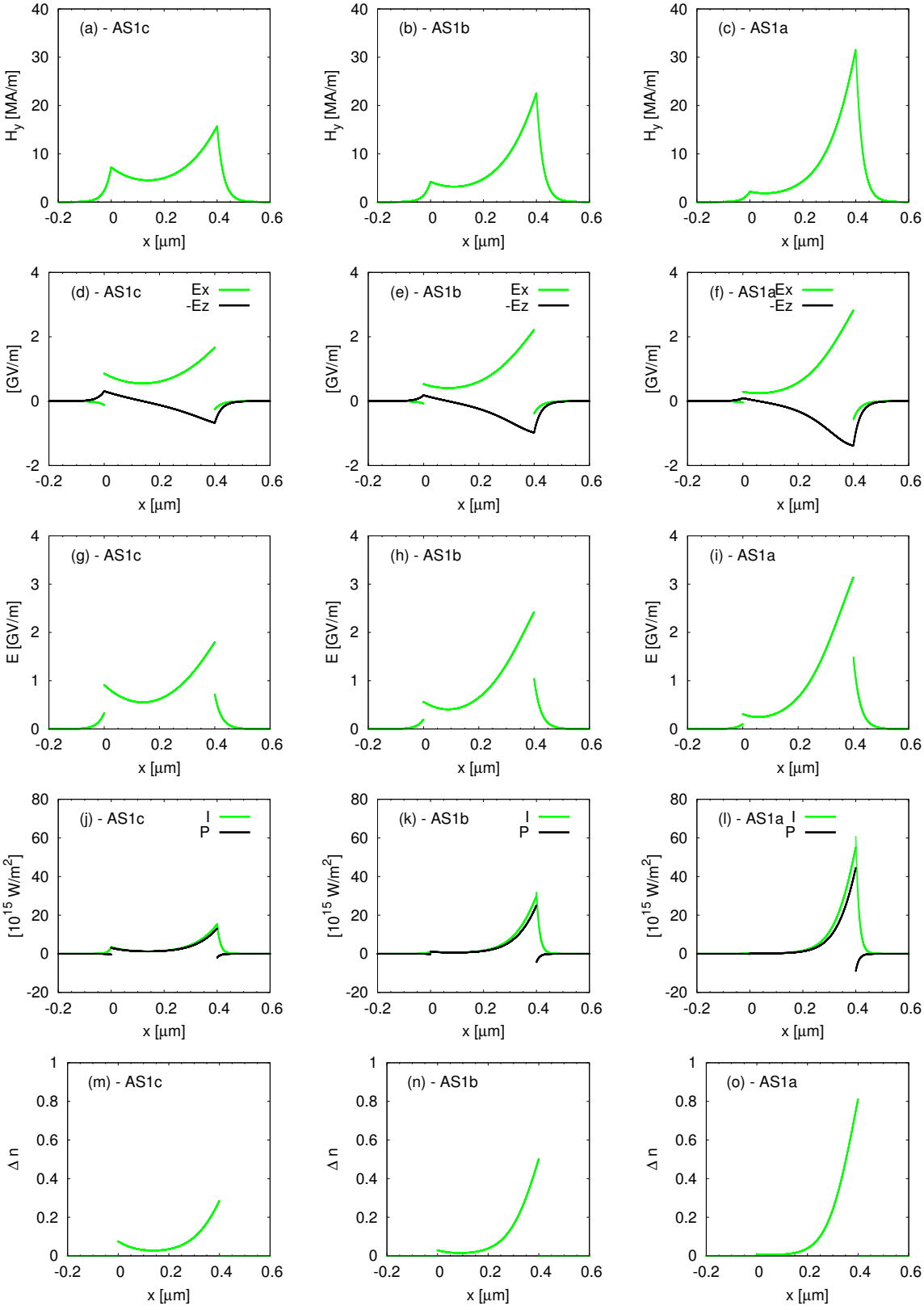

Figure 7.15: Profiles of (a)–(c) magnetic field component H_y, (d)–(f) electric field components E_x (red or blue) and $-E_z$ (black), (g)–(i) total electric field amplitude E, (j)–(l) intensity I (red or blue) and power P (black), (m)–(o) and nonlinear index modification Δn corresponding to points (first column) AS1c, (second column) AS1b, and (third column) AS1a in Figs. 7.11 and 7.12.

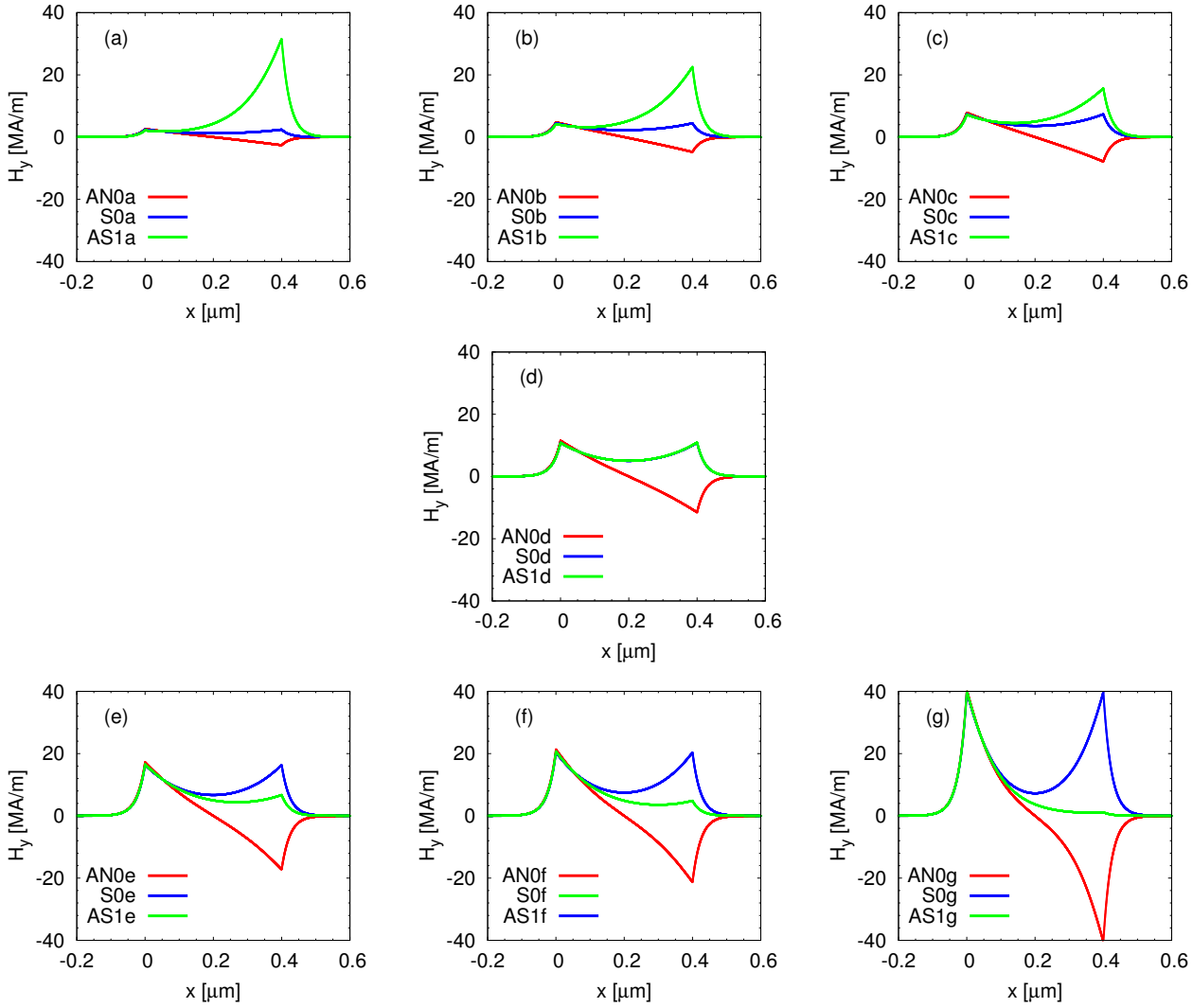

Figure 7.16: Profiles of magnetic field H_y for the symmetric S0 mode (blue), antisymmetric AN0 mode (red), and the first-order asymmetric AS1 mode (green). The subplots present the transformation of the field profiles at the points labeled by a, b, c, d, e, f, and g indicated in Figs. 7.11 and 7.12. In all the subplots, the scale was kept identical to see the relative change of the magnetic field amplitude between the points. In each of the subplots, the total electric field amplitude at the left metal/nonlinear dielectric interface (E_0) is identical for all three modes.

In Fig. 7.18, the transformation of the field profiles of the higher-order symmetric node-less mode SI along its dispersion curve is presented. Columns are ordered by increasing values of total intensity density of the mode, which correspond to the decrease of E_0. The field profile of the SI mode resembles a soliton trapped inside of the core of the nonlinear slot waveguide. With the increase of the total intensity density, we first observe a slight decrease of the peak amplitude in the center of the waveguide (columns one to two) and then the increase of that amplitude (columns two to four). Moreover, we notice that with the increase of the total mode intensity density the amplitudes close to both metal interfaces decrease and therefore the side-lobes of the mode become less pronounced. The mode presented in the second column is the one with the lowest values of β and the lowest total intensity; it corresponds to the point SIc in Figs. 7.11 and 7.12.

In Fig. 7.19, the transformation of the field profiles of the second-order asymmetric node-less mode AS2 along its dispersion curve is presented. The mode profile resembles a soliton propagating in the core of the nonlinear waveguide, similar to the SI mode. The soliton peak of the AS2 mode is not located at the center of the waveguide, but is shifted to one side of the waveguide. Columns in Fig. 7.19

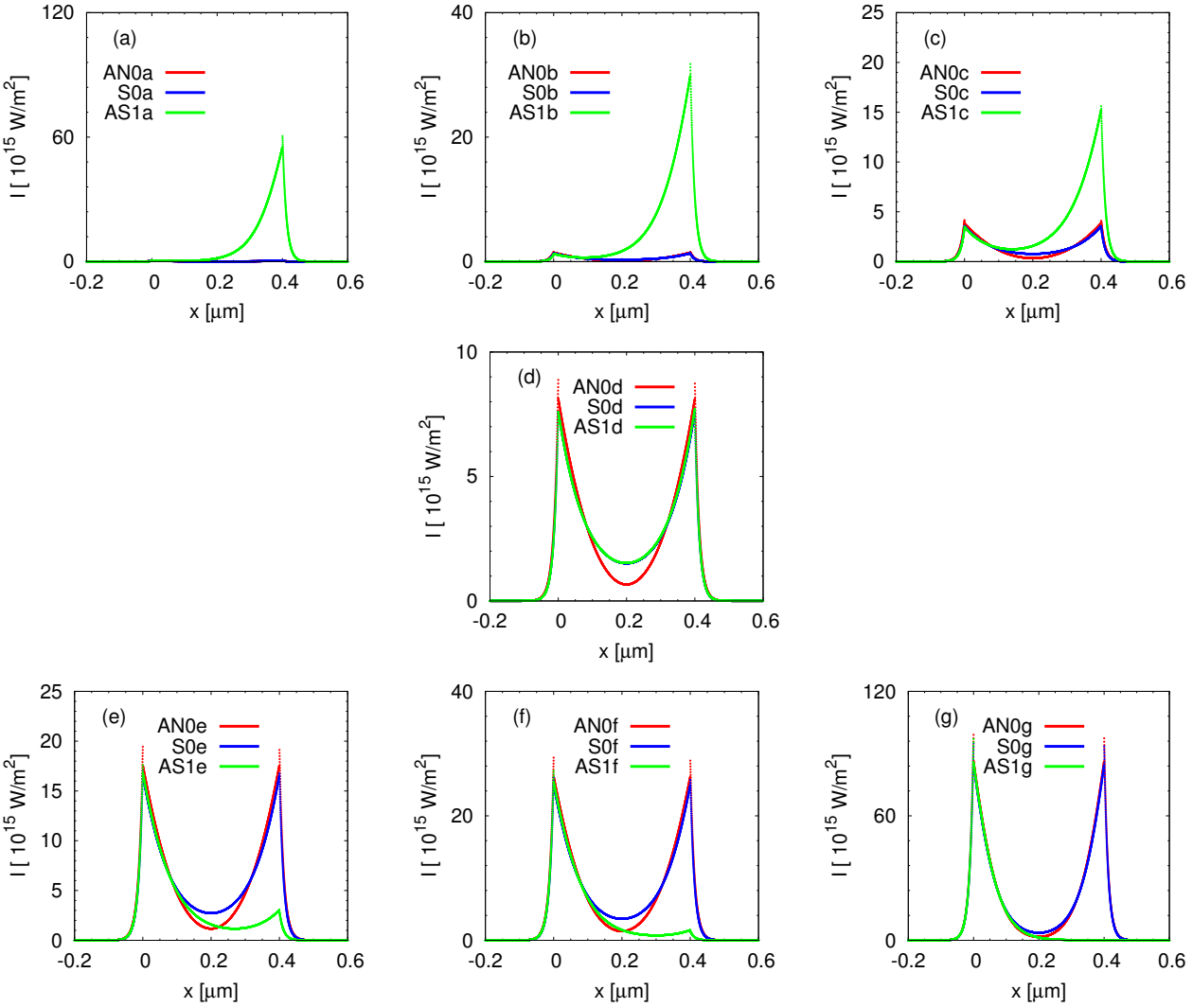

Figure 7.17: Profiles of light intensity I for the symmetric S0 mode (blue), antisymmetric AN0 mode (red), and the first-order asymmetric AS1 mode (green). Each subplot corresponds to the respective subplot in Fig. 7.16. The scale on the vertical axis is not kept identical in all the subplots in order to be able to observe the features of the intensity profiles.

are ordered by increasing values of the total intensity density of the mode, which correspond to the decrease of E_0 and the increase of E_d. The ratio between the total electric field amplitudes E_d/E_0 is approximately equal to 2 in the first column, 4 in the second column, and 10 in the third column. This means that the asymmetry of the mode increases with the increase of its total intensity density. The increase of the asymmetry is also accompanied by the change of the position of the soliton peak. The higher the mode asymmetry, the more off-center the soliton peak is located.

The effect of the soliton peak location shift is better visible in Fig. 7.20, where a comparison of the magnetic field profiles of the symmetric SI mode and the asymmetric AS2 mode is presented. In each subplot magnetic field profiles are compared for the modes with identical value of E_0 (see Figs. 7.11 and 7.12). In Fig. 7.20, the shift of the soliton peak is clearly visible, because its position can be directly compared with the position of the soliton peak of the symmetric mode, which is always located in the center of the waveguide. Figure 7.20(d) corresponds to the bifurcation point of the asymmetric AS2 mode. At this point, the total intensity density of the AS2 mode is the lowest and it is identical to the total intensity density of the symmetric SI mode. Additionally, the E_d/E_0 ratio is equal to 1. With the decrease of the E_0 values [moving from the subplot (d) toward the subplot (a)], the soliton peak of the AS2 mode shifts toward the left metal/nonlinear dielectric interface. At the

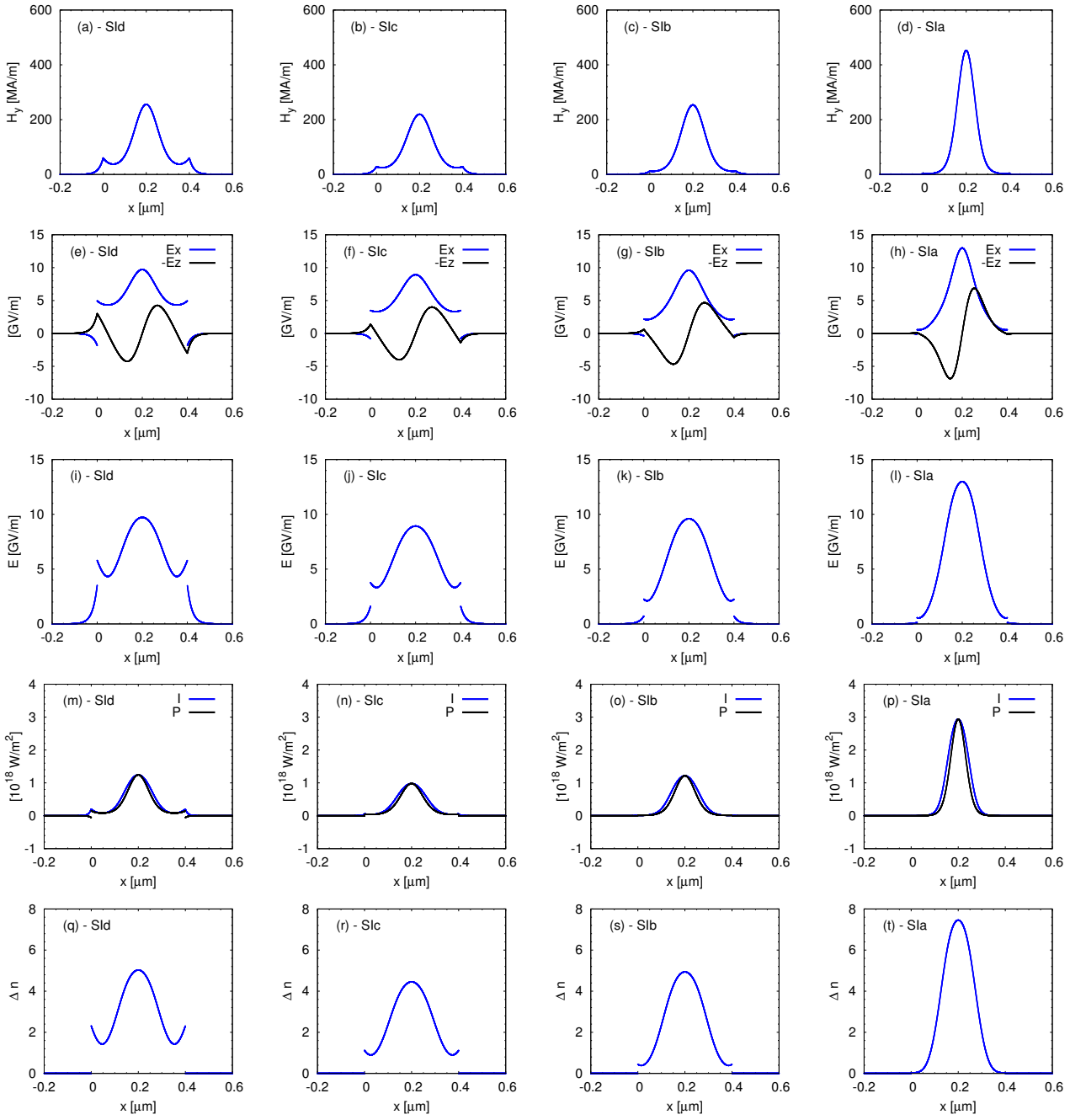

Figure 7.18: Profiles of (a)–(d) magnetic field component H_y, (e)–(h) electric field components E_x (red or blue) and $-E_z$ (black), (i)–(l) total electric field amplitude E, (m)–(p) intensity I (red or blue) and power P (black), and (s)–(t) nonlinear index modification Δn corresponding to points (first column) SId, (second column) SIc, (third column) SIb, (fourth column) and SIa in Figs. 7.11 and 7.12.

same time, the total electric field amplitude at the right interface E_d increases. The E_d/E_0 ratio is approximately equal to 20 in for the subplot (a), 4 for the subplot (b), and 2 for the subplot (c). On the contrary, increasing the E_0 values [moving from the subplot (d) toward the subplot (g)], causes the shift of the soliton peak of the AS2 mode toward the right metal/nonlinear dielectric interface. We conclude that the soliton peak always shifts toward the interface at which the total electric field amplitude is lower. The E_d/E_0 ratio is approximately equal to 1/2 in for the subplot (e), 1/4 for the subplot (f), and 1/25 for the subplot (g).

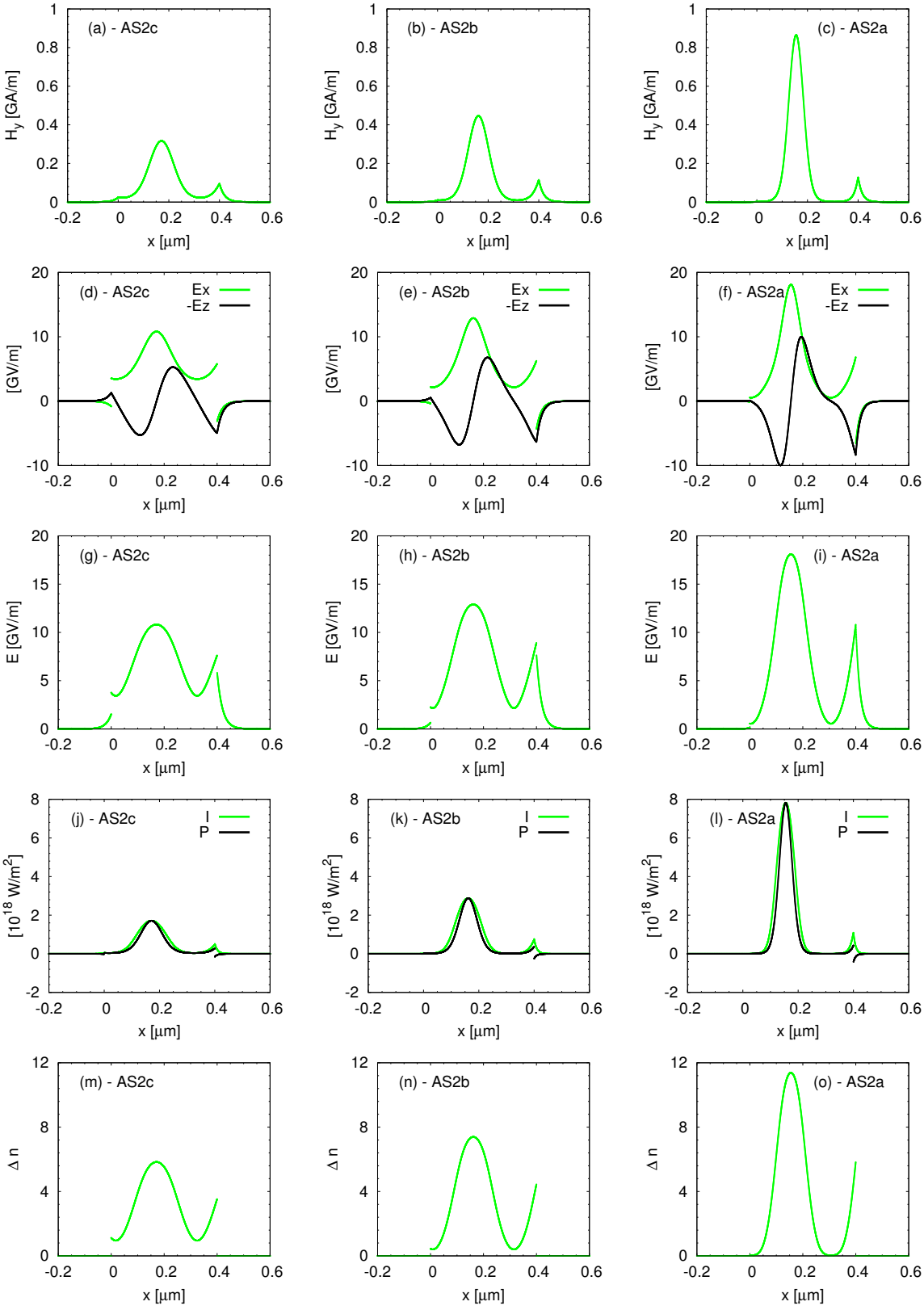

Figure 7.19: Profiles of (a)–(c) magnetic field component H_y, (d)–(f) electric field components E_x (red or blue) and $-E_z$ (black), (g)–(i) total electric field amplitude E, (j)–(l) intensity I (red or blue) and power P (black), and (m)–(o) nonlinear index modification Δn corresponding to points (first column) AS2c, (second column) AS2b, and (third column) AS2a in Figs. 7.11 and 7.12.

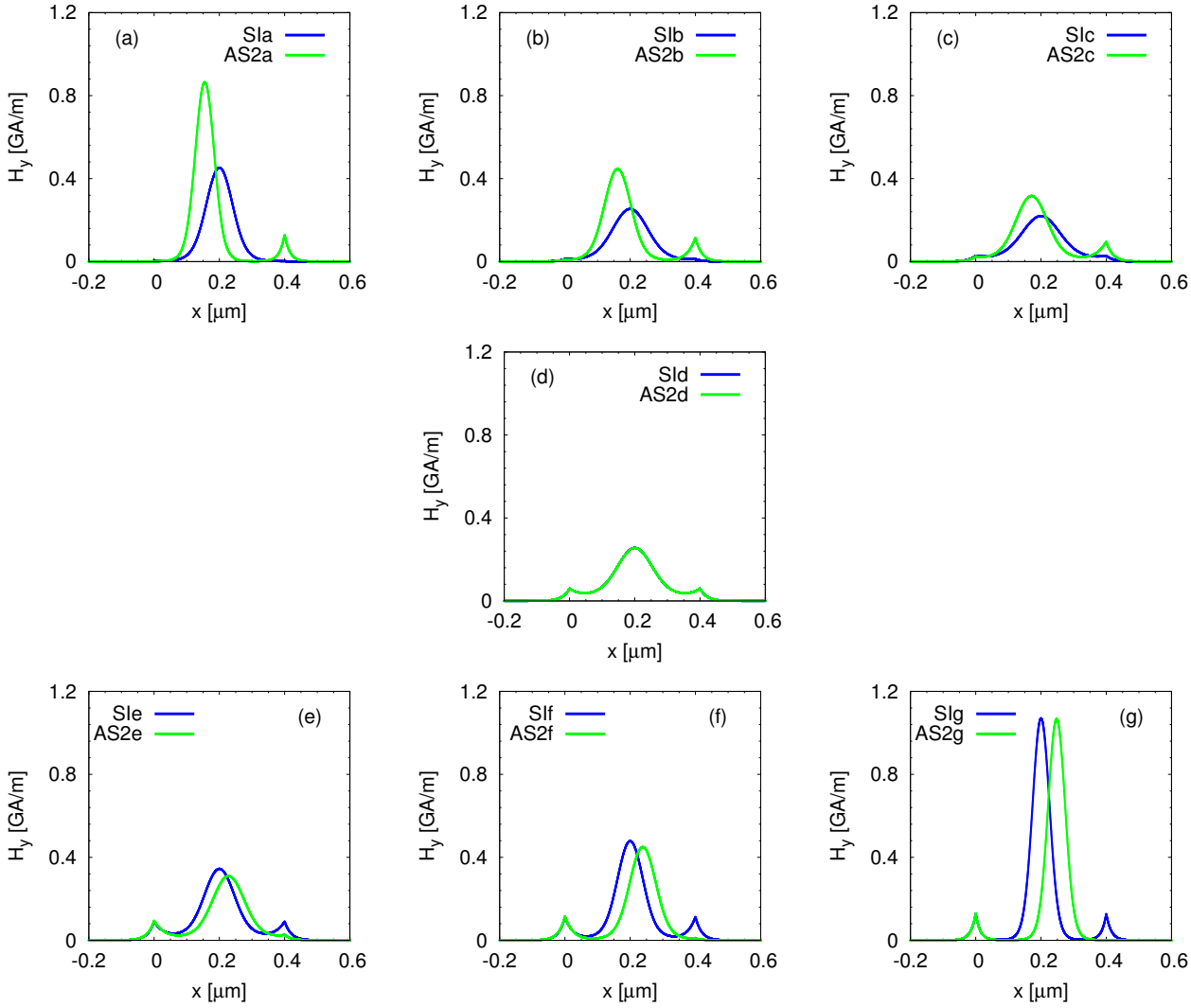

Figure 7.20: Profiles of magnetic field H_y for the symmetric SI mode (blue) and the second-order asymmetric AS2 mode (green). The subplots present the transformation of the field profiles at the points labeled a, b, c, d, e, f, and g indicated in Figs. 7.11 and 7.12. In all the subplots the scale is kept identical to see the relative change of the magnetic field amplitude between the points. In each subplot the value of E_0 is identical for both modes.

In Fig. 7.21, the transformation of the intensity profiles of the symmetric mode SI, asymmetric mode AS2 and the symmetric mode S1[8] along their respective dispersion curves are presented. The subplots are ordered by increasing values of E_0. In each of the subplots the value of E_0 for all the three modes is identical. From the intensity profiles presented in Fig. 7.21, we can observe that the intensity distributions of the symmetric modes SI and S1 become more similar with the increase of E_0. Additionally, the intensity profile of the asymmetric mode AS2 for high values of E_0 also resembles the intensity profiles of the symmetric modes [see Fig. 7.21(g)]. The AS2 profile has exactly the same main peak of the soliton as the SI mode, but it has only one instead of two side-lobes at the metal/nonlinear dielectric interfaces. This explains why the three dispersion curves (SI, AS2 and S1) become very close to each other for high values of E_0 in the dispersion plot presented in Figs. 7.11 and 7.12. Because the three field profiles corresponding to the points SIg, AS2g, and S1h have very similar values of the total intensity density [see Fig. 7.21(g)], the dispersion curves of these modes lay close to each other

[8]We remind the reader that the symmetric mode SI belongs to the node-less family, whereas the symmetric mode S1 belongs to the family with nodes (see Footnote 2 on Page 112).

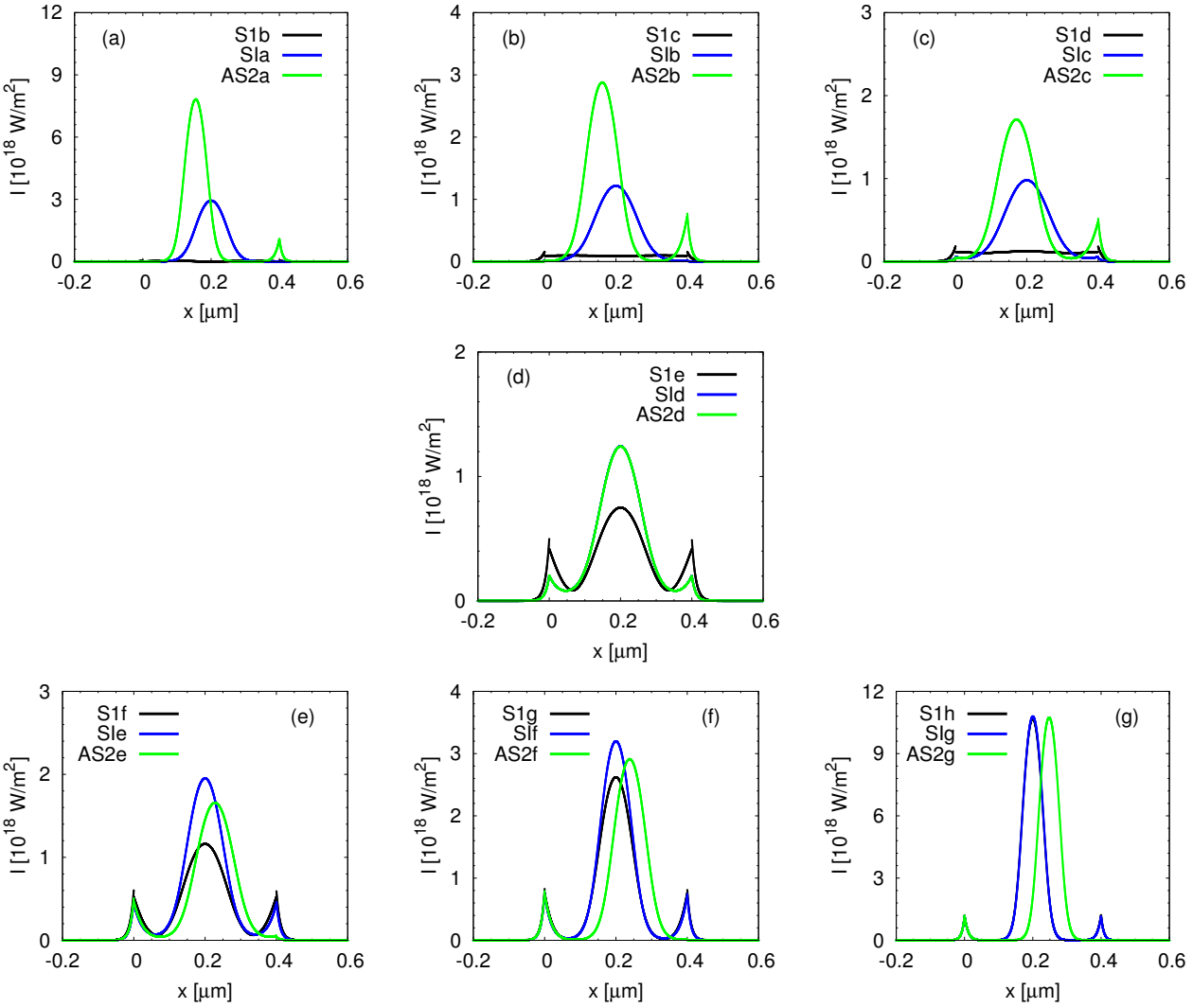

Figure 7.21: Profiles of light intensity I for the symmetric SI mode (blue), the second-order asymmetric AS2 mode (green), and the higher-order symmetric S1 mode with nodes (black). Each subplot corresponds to the respective subplot in Fig. 7.20 where the H_y profiles for the node-less modes are presented. The additional plots for the S1 mode presented in the subplots (a)–(g) correspond to the points on the S1 nonlinear dispersion curve with identical value of E_0 as for the respective SI and AS2 modes. For the S1 mode the field profiles corresponding to the points labeled b, c, d, e, f, g, and h in Figs. 7.11 and 7.12 are shown. The scale on the vertical axis is not kept identical in all the subplots in order to be able to observe more easily the features of the intensity profiles. In subplot (d) the intensity profiles of the SI and AS2 modes are identical. In subplot (g) the intensity profiles of the SI and S1 modes overlap.

also on the dispersion diagrams where $\langle \Delta n \rangle$ or I_{tot} is used as abscissa (see high β regions of Figs. 7.3 and 7.8).

In Fig. 7.22, the transformation of the symmetric node-less mode SII along its dispersion curve is presented. The field profile of this mode resembles two solitons trapped in the core of the nonlinear slot waveguide. The columns are ordered by the increase of the total electric field amplitude at the left core interface E_0. With the increase of E_0, the total intensity density of this mode first decreases (column one to three). In the third column, the mode profiles at the lowest point of the SII dispersion curve (lowest β and I_{tot} for the SII mode — see point SIIc in Fig 7.12) are presented. With further increase of E_0, the total intensity density of the SII mode starts to grow again (column three to four in Fig. 7.22).

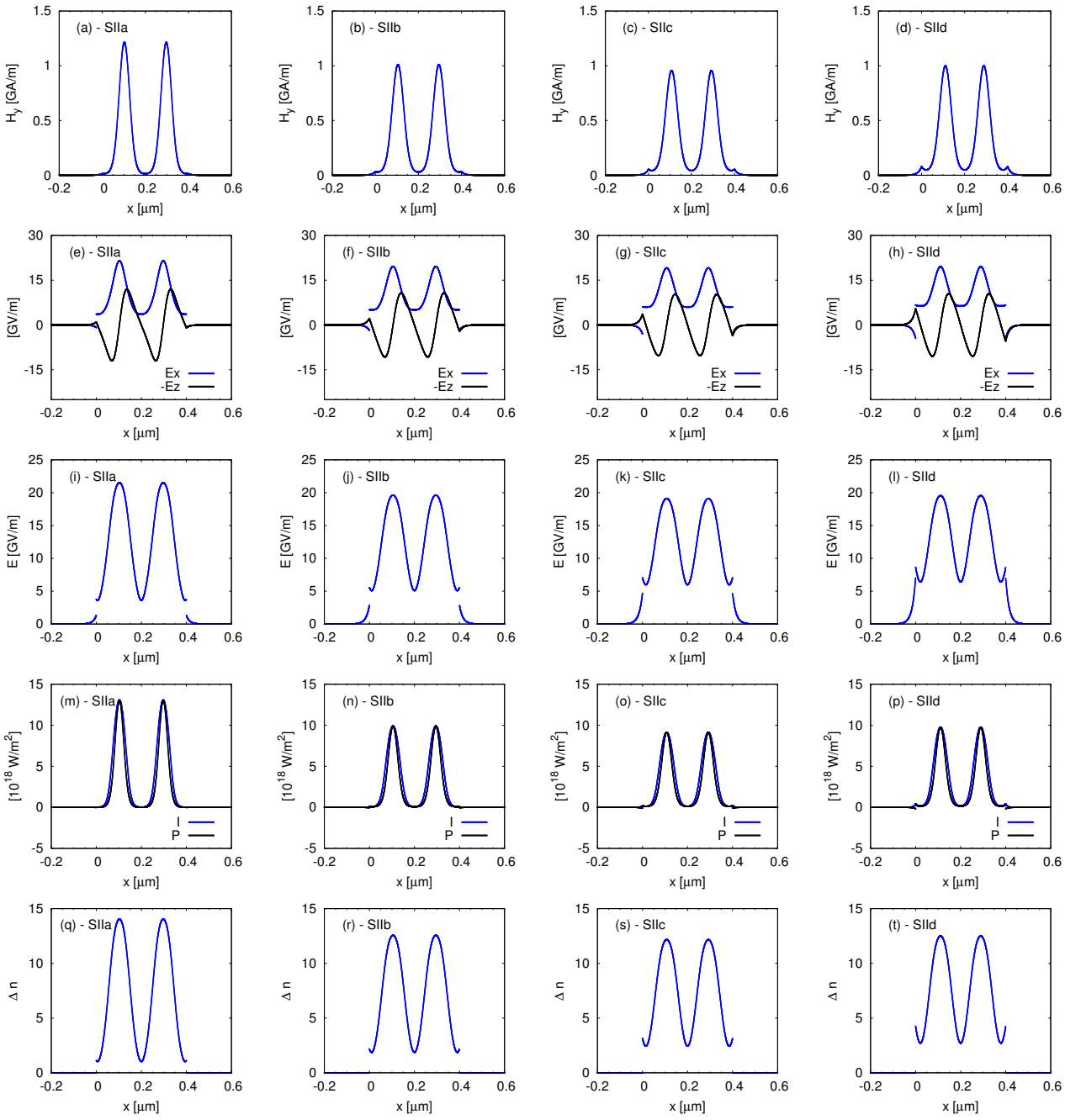

Figure 7.22: Profiles of (a)–(d) magnetic field component H_y, (e)–(h) electric field components E_x (red or blue) and $-E_z$ (black), (i)–(l) total electric field amplitude E, (m)–(p) intensity I (red or blue) and power P (black), and (s)–(t) nonlinear index modification Δn corresponding to points (first column) SIIa, (second column) SIIb, (third column) SIIc, and (fourth column) SIId in Figs. 7.11 and 7.12.

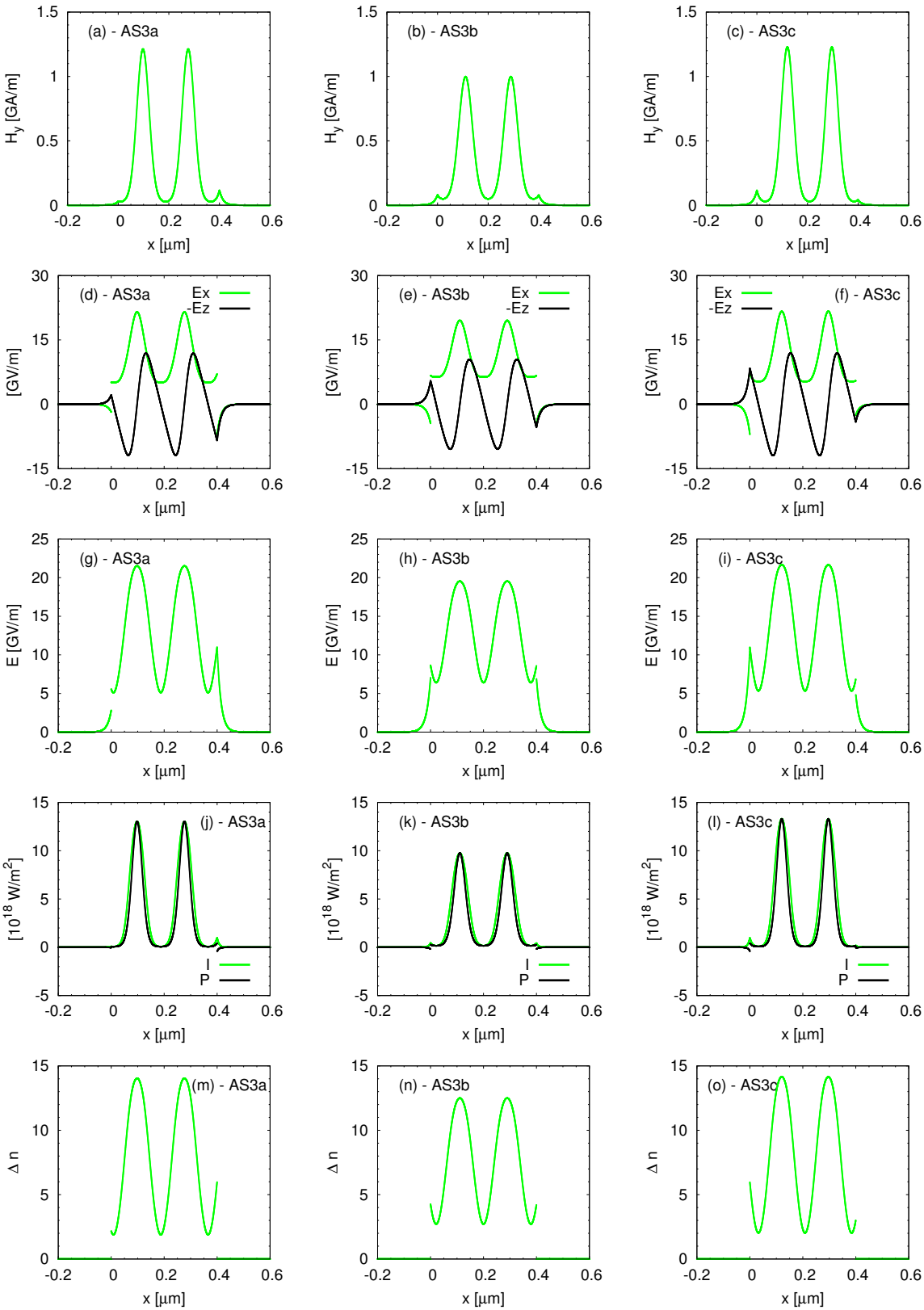

Figure 7.23: Profiles of (a)–(c) magnetic field component H_y, (d)–(f) electric field components E_x (red or blue) and $-E_z$ (black), (g)–(i) total electric field amplitude E, (j)–(l) intensity I (red or blue) and power P (black), and (m)–(o) nonlinear index modification Δn corresponding to points (first column) AS3a, (second column) AS3b, and (third column) AS3c in Figs. 7.11 and 7.12.

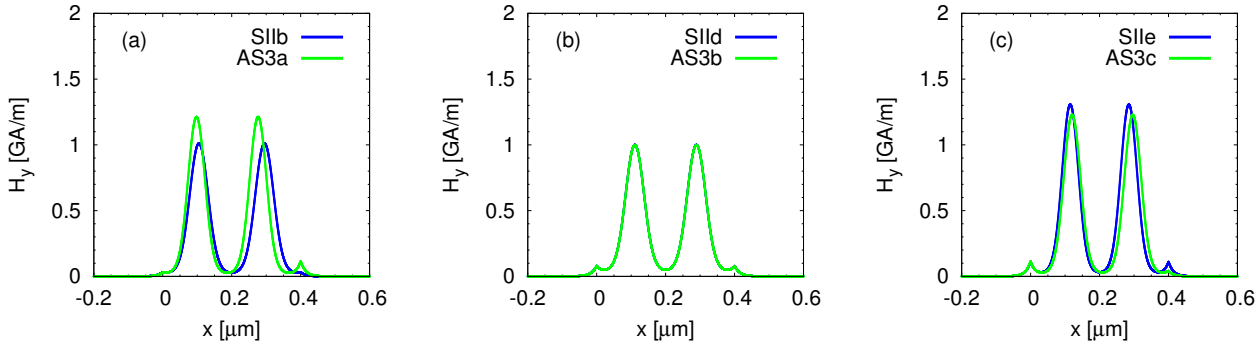

Figure 7.24: Profiles of magnetic field component H_y for the symmetric mode SII (blue) and the third-order asymmetric mode AS3 (green). The subplots present the transformation of the field profiles corresponding to the points indicated on the dispersion curve in Figs. 7.11 and 7.12. The labels of the points are given in the subplot legends.

In Fig. 7.23, the transformation of the third-order asymmetric node-less mode AS3 along its dispersion curve is presented. The field profile of this mode resembles two solitons propagating in the core of the nonlinear slot waveguide, similar to the SII mode. The field profiles of the AS3 mode are not symmetric and the solitons are shifted toward one of the core interfaces. The columns in Fig. 7.23 are ordered by increasing values of E_0. The second column shows the field profiles at the bifurcation point, at which the mode is symmetric and the total electric field amplitude ratio E_d/E_0 is equal to 1. In the first column the asymmetric mode AS3 is shown for which $E_d/E_0 \approx 2$. In this case, the peaks of the two solitons present in the core are shifted toward the left interface. In the third column, a mode that is a mirror image (symmetry with respect to $x = d/2$) of the mode shown if the first column is presented. Here, similar to the case of the asymmetric mode AS2, we conclude that the soliton peaks shift toward the interface where the total electric field amplitude is lower (both soliton peaks shift in the same direction). It is worth noting that, the asymmetry of the field profiles is introduced only by the shift of the positions of the two solitons. There is no visible asymmetry in the amplitude or the width of the two solitons.

Figure 7.24 shows the comparison of the magnetic field profiles of the symmetric SII mode and the asymmetric AS3 mode. In each subplot, the value of E_0 for both modes is identical. Subplot (b) corresponds to the bifurcation point at which the two mode profiles are identical. With the increase [subplot (c)] or the decrease [subplot (a)] of E_0 it is clearly visible that the soliton peaks of the asymmetric mode shift with respect to their positions in the profile obtained at the bifurcation point [Fig. 7.24(b)].

All the modes described above (except for the antisymmetric low-power mode AN0) belonged to the node-less family. The analysis of the higher-order modes of this family (SI, AS2, SII, and AS3) was presented here for the first time. In the next section we will discuss the properties of the modes that possess nodes in their magnetic field profile $H_y(x)$.

Modes with nodes

Above we have presented a first detailed description of the higher-order node-less modes. Here we will proceed to the description of the modes belonging to the family with nodes. The modes of this family (except for the lowest-order AN0 mode [87]) have not been reported before in nonlinear slot waveguides. We present here the first detailed analysis of their properties and transformation along their dispersion curves.

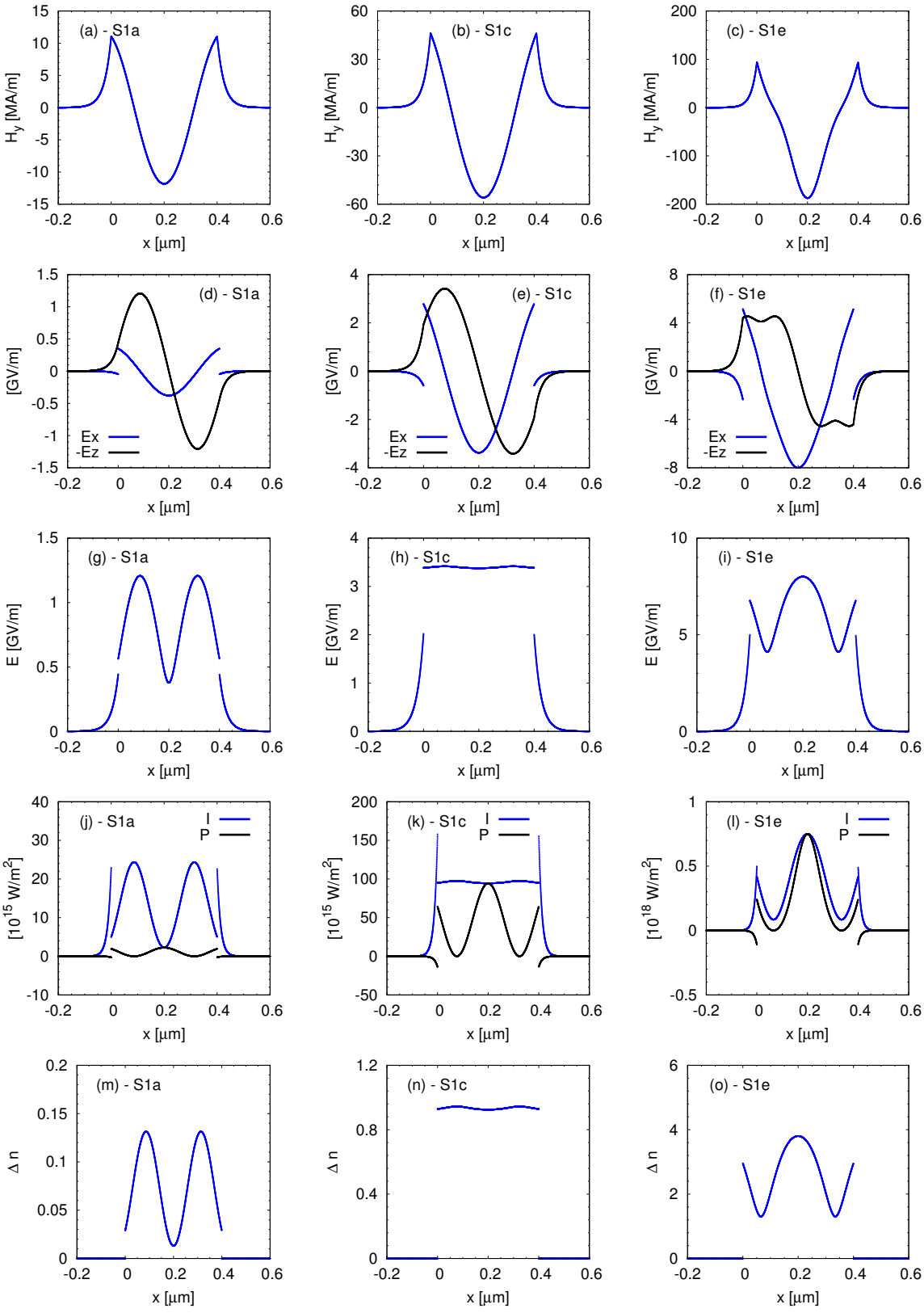

Figure 7.25: Profiles of (a)–(c) magnetic field component H_y, (d)–(f) electric field components E_x (red or blue) and $-E_z$ (black), (g)–(i) total electric field amplitude E, (j)–(l) intensity I (red or blue) and power P (black), and (m)–(o) nonlinear index modification Δn corresponding to points (first column) S1a, (second column) S1c, and (third column) S1e in Figs. 7.11 and 7.12. The scale in the subplots presenting the same quantity is not kept identical for different points in order to improve the visibility of profile features.

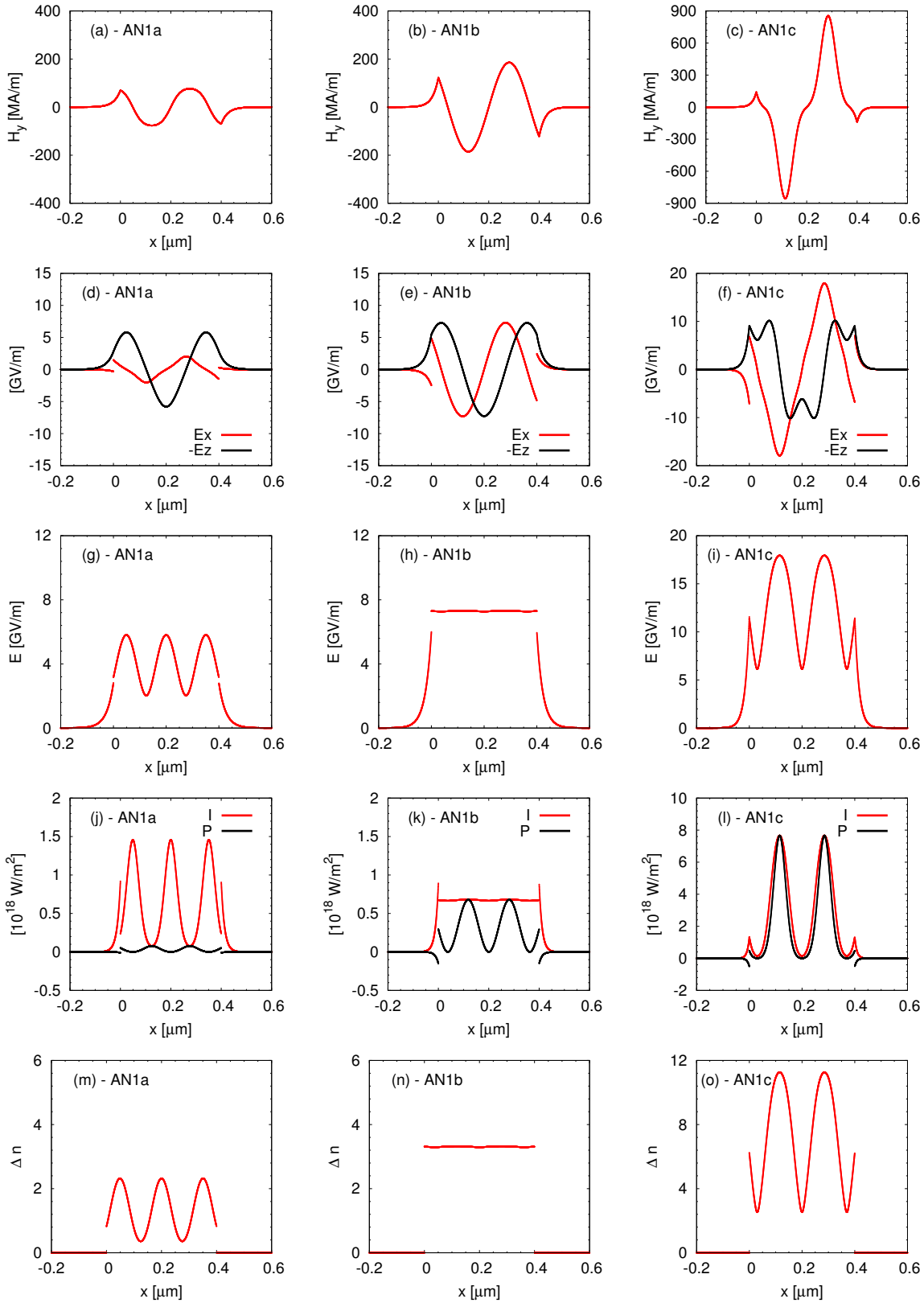

Figure 7.26: Profiles of (a)–(c) magnetic field component H_y, (d)–(f) electric field components E_x (red or blue) and $-E_z$ (black), (g)–(i) total electric field amplitude E, (j)–(l) intensity I (red or blue) and power P (black), and (m)–(o) nonlinear index modification Δn corresponding to points (first column) AN1a, (second column) AN1b, and (third column) AN1c in Figs. 7.11 and 7.12. The scale in the subplots presenting the same quantity is not kept identical for different points in order to improve the visibility of profile features.

At first, we discuss the symmetric mode that possesses two nodes in the magnetic field profile and is denoted by S1. The transformation of the field profiles of this mode along its dispersion curve is presented in Fig. 7.25. Columns are ordered by increasing values of E_0 and at the same time with the increasing total intensity density of the mode. The magnetic field profile of this mode resembles the magnetic field profile of a higher-order linear mode of a linear slot waveguide with identical parameters as the nonlinear slot waveguide considered here but with higher core refractive index. The connection between these two modes (and also between the antisymmetric higher-order modes described later in this section) will be discussed in Section 7.1.5.

For all the modes of the node-less family, the transverse electric field component E_x had a higher amplitude than the longitudinal component E_z (see second rows of Figs. 7.15, 7.18, 7.19, 7.22, and 7.23). Therefore, the profile of the total electric field amplitude E resembled the field profile of the $|E_x|$ component. Because E_x is proportional to H_y [see Eq. (1.5.2b)], for the node-less modes the profiles of $|H_y|$ and E were similar. For the modes with nodes [S1 (see Fig. 7.25), AN1 (see Fig. 7.26), and higher-order modes with nodes (data not shown)] at low power, the longitudinal component of the electric field E_z has higher amplitude than the transverse component E_x [see Figs. 7.25(d) and 7.26(d)], contrary to the node-less modes. This implies that the total electric field amplitude E has a profile that is closer to the $|E_z|$ profile than to the $|H_y|$ profile. For higher powers [see subplots (e) and (f) in Figs. 7.25 and 7.26] the amplitudes of the two electric field components become close to each other (for graphical illustration of the E_x/E_z ratio see also Fig. 7.5).

It is interesting to notice that, for the S1 mode for high intensities (the third column in Fig. 7.25), the profile of the electric field component E_z changes its character. A single maximum or minimum in the field profile splits for high E_0 into two maxima or minima, respectively.

Connected to the ratio of E_x and E_z, and equally interesting, is the behavior of the $E(x)$, $I(x)$, $P(x)$, and $\Delta n(x)$ profiles. For low intensities (corresponding to point S1a in Fig. 7.11 — first column in Fig. 7.25), the $E(x)$ profile has a shape that is close to the absolute value of the transverse component of the electric $|E_z|$, because the amplitude of the longitudinal E_z component is higher than the amplitude of the transverse component E_x. With the increase of the light intensity, the ratio between the two components becomes closer to one, and at a certain point (S1c — second column in Fig. 7.25) these component have equal amplitudes. In this case [as it can be seen from Fig. 7.25(h)], the total electric field amplitude E, the light intensity I, and the nonlinear refractive index modification Δn have flat profiles. This explains a close relation between these field profiles and those of the linear slot waveguide with identical parameters as the nonlinear slot waveguide considered here, but with higher core refractive index.[9] Increasing E_0 (and therefore the total intensity density) even more, we observe a change of shape of the total electric field amplitude profile and the related quantities (intensity and nonlinear index modification). In the place where for low intensities there was a maximum in the profile, now a minimum appears (compare columns one and three in Fig. 7.25). In other words, the positions of minima and maxima switch.

Only the power profile of the symmetric S1 mode does not change qualitatively with the increase of the light intensity. It always has a maximum in the center of the waveguide and side-lobes at the metal/nonlinear dielectric interfaces (see the fourth row in Fig. 7.25). Comparing the intensity profile with the power profile we may say that the intensity profile for low E_0 values is 'out of phase' with respect to power profile [see Fig. 7.25(j)] and becomes 'in phase' for high E_0 values [see Fig. 7.25(l)].

Figure 7.26 presents the field profiles corresponding to three different points on the nonlinear dispersion curve of the antisymmetric AN1 mode (see Figs. 7.11 and 7.12 for the location of these points). Columns in Fig. 7.26 are ordered by increasing values of E_0 and at the same time with the increasing total intensity density of the mode. Because this mode belongs to the same nonlinear family (modes with nodes) as the S1 mode, their behaviors are very similar. As in the case of the S1 mode, in the profile of the electric field component E_z of the AN1 mode, the maxima and minima split into

[9] For more detailed analysis of this problem refer to Section 7.1.5. The fact that the mode with a flat Δn profile is similar to the mode of a linear waveguide with a higher refractive index of the core is not surprising and can be explained using the self-coherent definition of the nonlinear modes [4]. According to this definition, the nonlinear mode is a linear mode of a linear (graded refractive index) waveguide that is induced by the light distribution of this mode.

two peaks for high light intensities [see Fig. 7.26(f)]. With the increase of E_0 we also observe flattening of the profile of the total electric field amplitude E (and related quantities) (see rows three to five in Fig. 7.26). The flattening occurs at higher value of E_0 and $\langle \Delta n \rangle$ than in the case of the S1 mode. For very high E_0 positions of minima and maxima in the E profile switch [compare Figs. 7.26(g) and (i)]. The intensity I is 'out of phase' with the power P for low E_0 values [see Fig. 7.26(j)] and 'in phase' for high E_0 values [see Fig. 7.26(l)], similar to the case of the S1 mode.

The magnetic field profiles of higher-order modes of the family with nodes (S2, AS2, S3, AS3) are presented in Figs. 7.4(e), (f), (h), and (i). All the modes are presented for the values of E_0 at which their respective effective indices $\beta \approx 4$. We observe that the increase of the mode order causes an increase of the number of nodes in the magnetic field profile, according to Eq. (7.1.2). The symmetric and antisymmetric modes appear in the alternating order with the increase of E_0. The behavior of these modes with the increase of E_0 value is similar to the behavior observed for the S1 and AN1 modes in Figs. 7.25 and 7.26. Therefore, these modes will not be described in detail in this PhD manuscript.

7.1.3 Field profiles obtained using the Jacobi elliptic function based model

In Section 7.1.2, we have discussed in detail the field profiles obtained using the IM for all the modes supported by the nonlinear slot waveguide structure with parameters indicated in Table 7.1. In this section, we present the field profiles obtained using the JEM. We will not describe them as thoughtfully as it was done in the case of the IM to avoid repetitions. The study will be done in a comparative way. The similarities and differences between the field profiles obtained using the JEM and using the IM will be described and explained, in order to get a better understanding of the nature of our models.

For all the modes in this section, only the field profiles of the magnetic field $H_y(x)$, electric field components $E_x(x)$ and $E_z(x)$ and the total electric field amplitude $E(x)$ are shown. We do not present the profiles that are functions of these basic quantities. The light intensity is proportional to E^2, the power is proportional to H_y^2 and the nonlinear index modification in the frame of the JEM is proportional to E_x^2 [see Eq. (6.1.1)].

The field profiles presented in this section correspond to the labeled points indicated on the nonlinear dispersion curves $\beta(H_0)$ shown in Fig. 7.27, where the magnetic field amplitude at the left metal/nonlinear dielectric interface ($x = 0$, see Fig. 6.1) H_0, defined by Eq. (6.1.4a), is used as abscissa. The dispersion diagram $\beta(H_0)$ shown in Fig. 7.27 has a similar character to the dispersion diagram $\beta(E_0)$ that is presented in Fig. 7.9(a). We choose here to use H_0 as abscissa because in the JEM, it is a free parameter that is varied in order to obtain the nonlinear dispersion curves.

Looking at the dispersion relation presented in Fig. 7.27, we notice that if H_0 is used as abscissa, then the dispersion curves AN1, S2 and of the higher-order modes from the family with nodes have negative slope: β deceases with the increase of H_0. Because in the scanning procedure we did not look for solutions with H_0 higher than 10^8 A/m, parts of the dispersion curves AN1 and S2 with low values of β were not found. This explains why, in other coordinates, it seems that these dispersion curves do not start from $\beta = 1$ [compare with Figs. 7.1(a), 7.6(a), and 7.9(a)]. Increasing the scanning range of H_0 would allow us to find the missing parts of these curves. After this digression, we come back to the discussion of the field profiles obtained using the JEM.

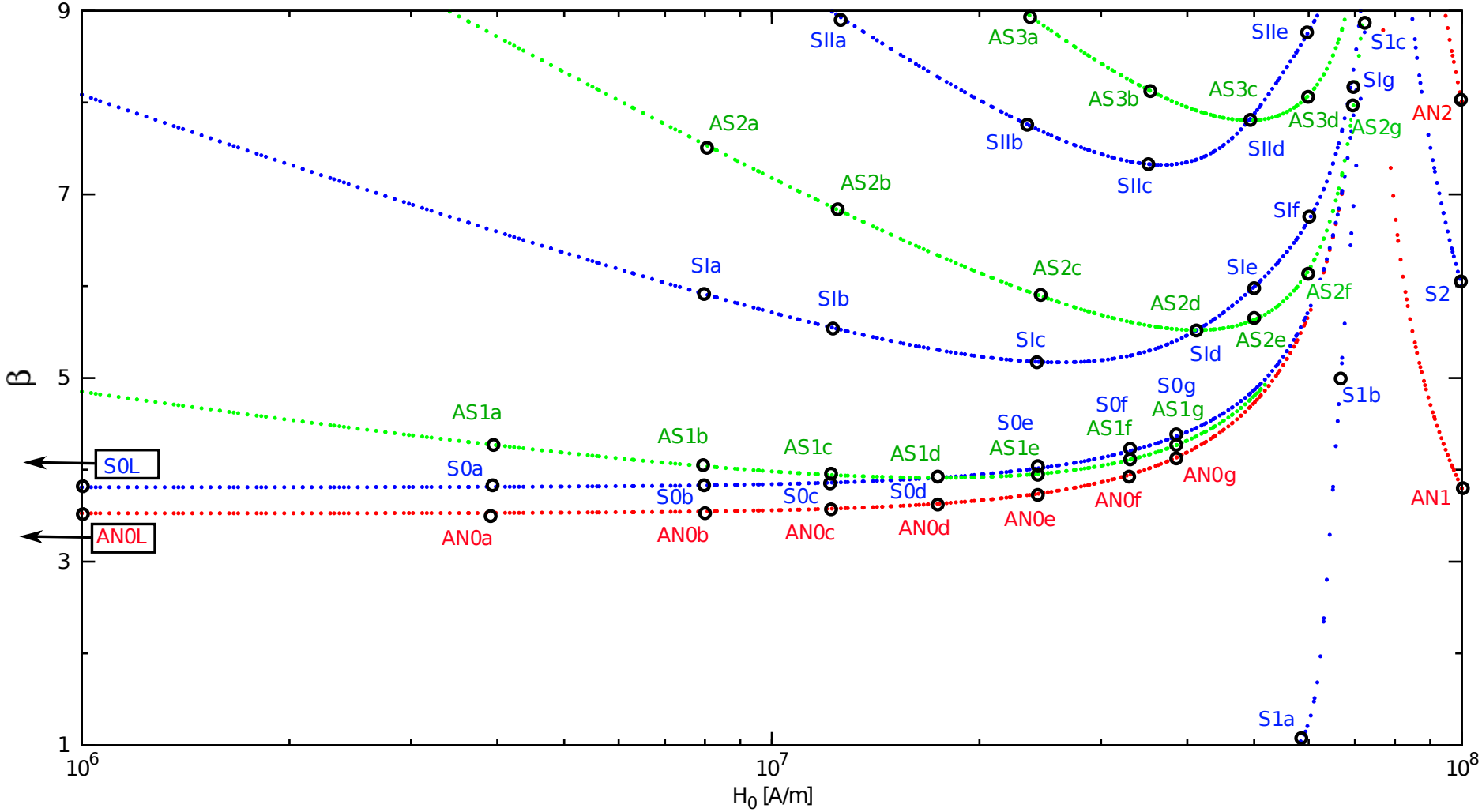

Figure 7.27: Nonlinear dispersion curves $\beta(H_0)$ obtained using the JEM for the structure with parameters listed in Table 7.1. Labeled points on each of the dispersion curves are used in the following to analyze mode transformation along the dispersion curves.

Modes with linear counterparts (low-power modes)

In Fig. 7.28, the profiles of the linear symmetric mode S0L and the linear antisymmetric mode AN0L are shown in the limiting linear case. These profiles are identical to the corresponding profiles obtained using the IM presented in Fig. 7.13.

In Fig. 7.29, the field plots of the symmetric mode S0 and the antisymmetric mode AN0 are shown for higher values of the magnetic field on the left interface H_0 and therefore higher total intensity densities. For moderate values of H_0, the profiles are presented in the first and the third column in Fig. 7.29 and they resemble well the corresponding profiles obtained using the IM shown in the first and the third columns of Fig. 7.14. On the contrary, for very high H_0 values (the second and the fourth column in Fig. 7.29) the field profiles obtained using the JEM differ qualitatively from the profiles obtained using the IM. We observe that the profiles of both components of the electric field close to the metal/nonlinear dielectric interfaces, where the magnetic field is high, become less steep than the corresponding profiles obtained using the IM. The x-derivative of the E_z component in the nonlinear core, close to the metal/nonlinear dielectric interfaces changes its sign with the increase of H_0. For low values of H_0, it has opposite sign to the x-derivative of E_z in the metal cladding. On the contrary, for high values of H_0, the signs of the x-derivative of E_z on both sides of the metal/nonlinear dielectric interfaces are identical [compare for example Figs. 7.28(e) and 7.29(h)].

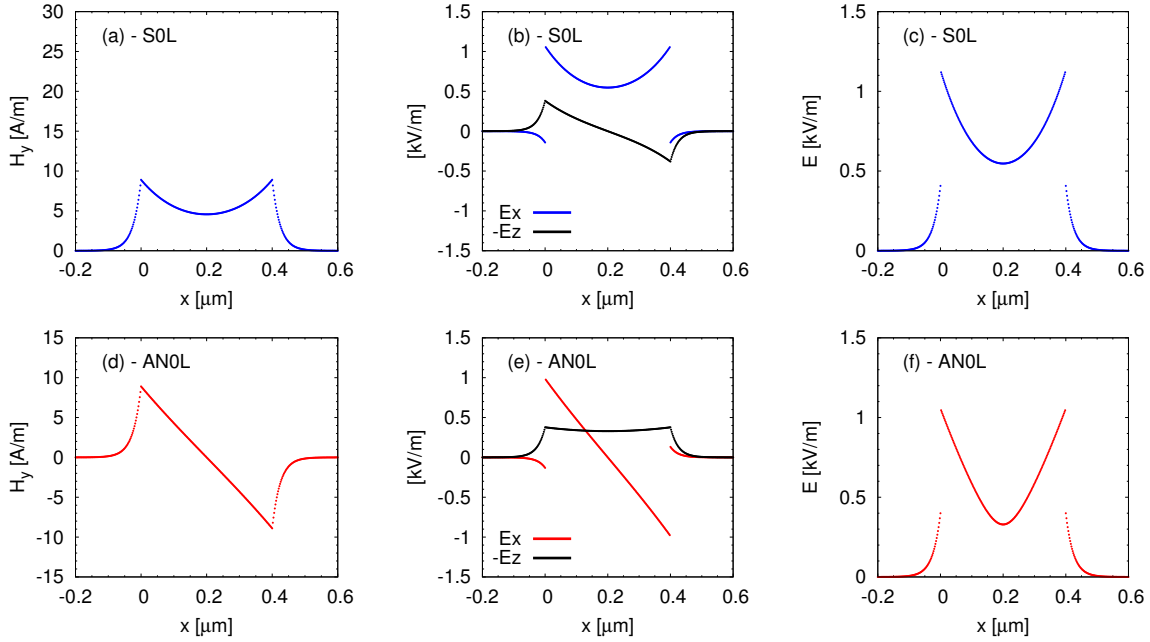

Figure 7.28: Profiles of (a), (d) magnetic field component H_y; (b), (e) electric field components E_x (red or blue) and $-E_z$ (black); and (c), (f) total electric field amplitude E. Plots in the top row corresponds to the linear symmetric mode of the slot waveguide (S0L) and in the bottom row to the linear antisymmetric mode of the slot waveguide (AN0L) (see Fig. 7.27 for the point labels).

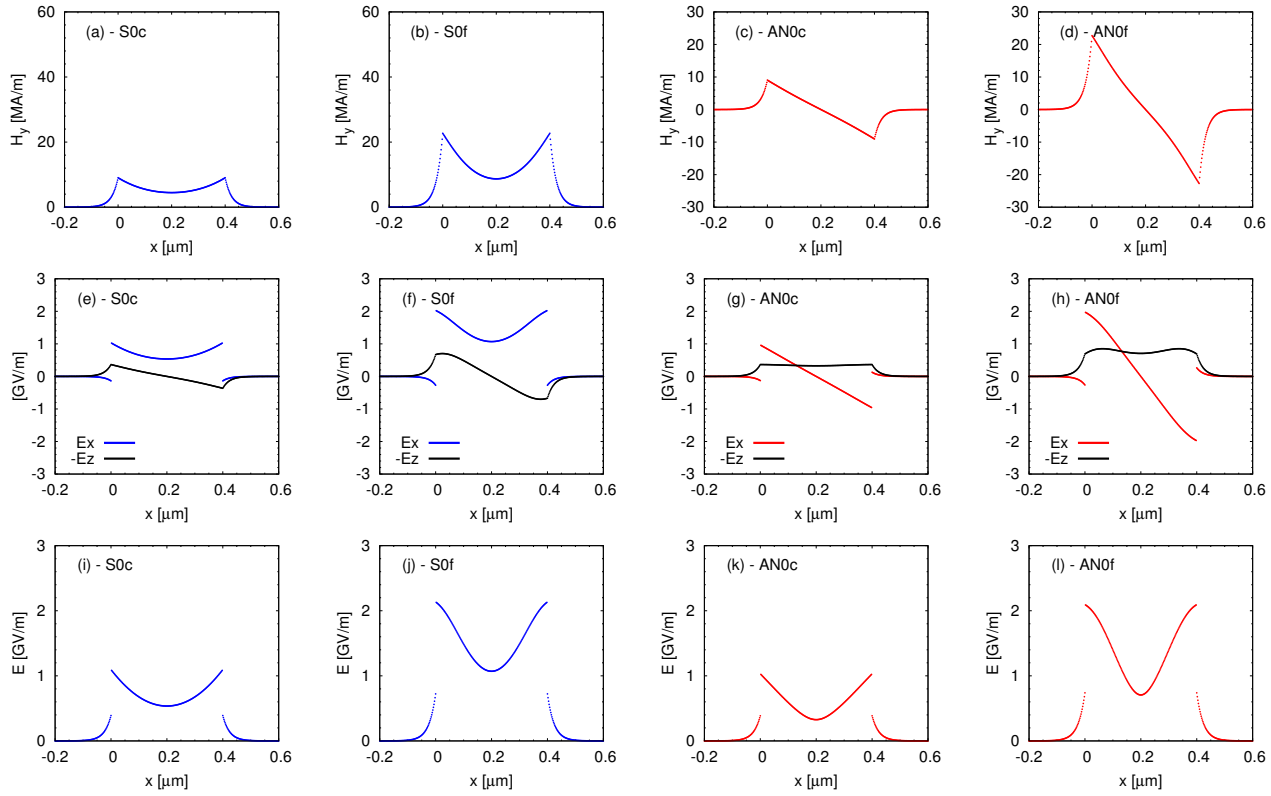

Figure 7.29: Profiles of (a)–(d) magnetic field component H_y, (e)–(h) electric field components E_x (red or blue) and $-E_z$ (black), and (i)–(l) total electric field amplitude E corresponding to points (first column) S0c, (second column) S0f, (third column) AN0c, and (fourth column) AN0f in Fig. 7.27.

Modes without nodes (node-less modes)

The transformation of the profiles of the asymmetric AS1 mode is shown in Fig. 7.30. The comparison between the results of the JEM and the IM (Fig. 7.15) for this mode results in conclusions similar to these drawn in for the low-power modes. Close to the bifurcation point (solution at low power level shown in the first column in Fig. 7.30), the field profiles resemble those obtained using the IM and shown in the first column in Fig. 7.15. For higher values of the mode energy (the second and the third column in Fig. 7.30) the magnetic field behaves in the same way as for the IM but the electric fields in the regions with high magnetic field intensity have lower amplitudes than for the corresponding profiles in Fig. 7.15. Additionally, the sign of the x-derivative of E_z close to the metal/nonlinear dielectric interfaces inside of the nonlinear core changes with the increase of H_0 [compare Figs. 7.30(d) and 7.30(f)].

There are two reasons for the different behavior of the electric field predicted by our two models. The fundamental reason is the fact that, in the formulation of the models we did not use the same expressions for the Kerr nonlinear term. The full Kerr-type nonlinearity used in the IM [see Eq. (6.2.1)] was approximated by the Eq. (6.1.1) in the JEM. Additionally, in order to derive the JEM, we have assumed that the nonlinear permittivity change is small compared to the linear permittivity. These two assumptions are not fulfilled for the modes presented here, for which E_z is comparable with E_x and the nonlinear permittivity change is high.

The second reason for the discrepancies between the IM and the JEM is the fact that the field profiles and the related quantities are computed in a different way. In the IM, the main parameter in the dispersion relations is the total electric field intensity at one of the metal/nonlinear dielectric interfaces and at the output of the dispersion procedure, we obtain the profiles of both electric field components E_x and E_z (see Section 6.2.2). Then, employing Eq. (1.5.2b), the magnetic field in the

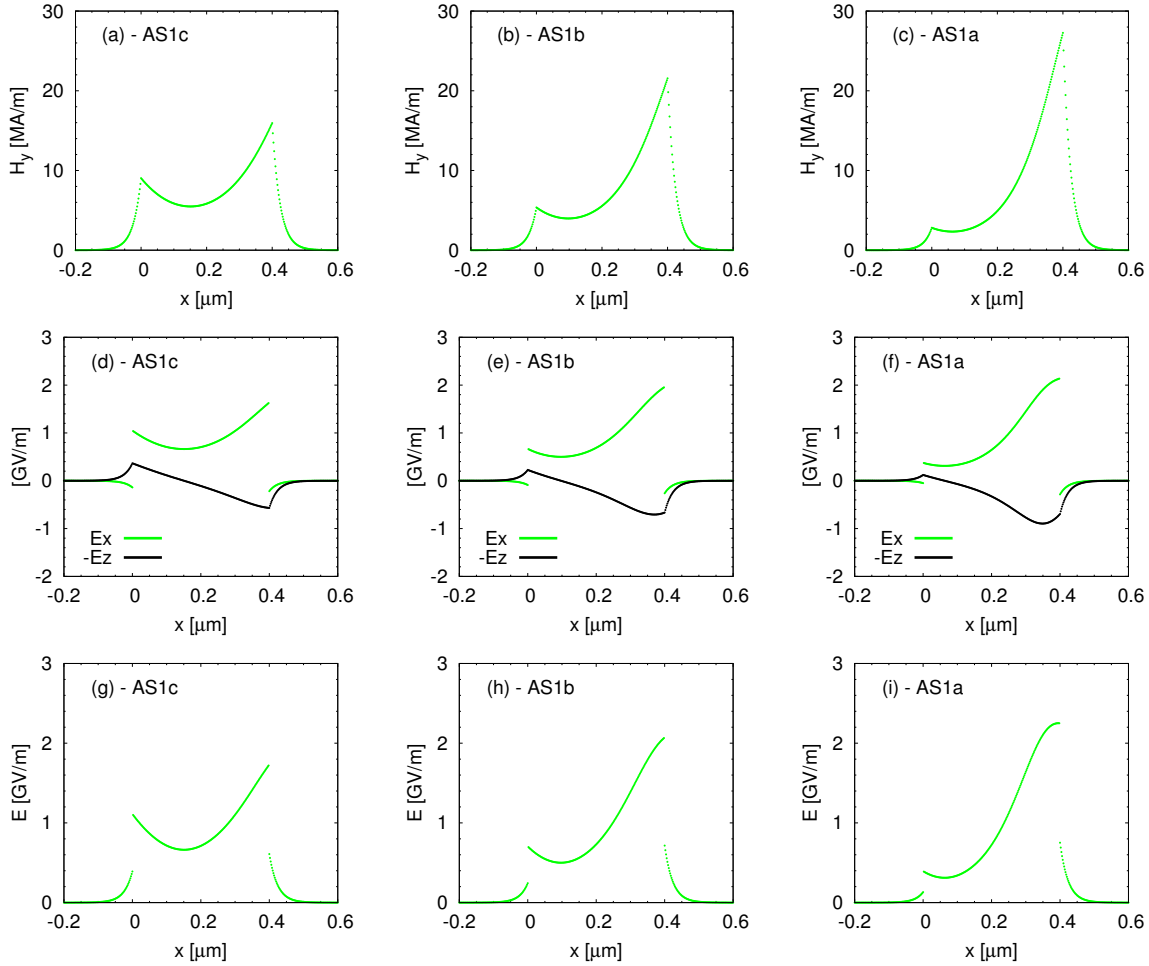

Figure 7.30: Profiles of (a)–(c) magnetic field component H_y, (d)–(f) electric field components E_x (green) and $-E_z$ (black), and (g)–(i) total electric field amplitude E corresponding to points (first column) AS1c, (second column) AS1b, (third column) AS1a in Fig. 7.27. The total electric amplitude ratio E_d/E_0 is approximately equal to 2 for ASc, 4 for ASb and 10 for ASa.

waveguide core is calculated using the formula:

$$H_y = \frac{\epsilon_0 \epsilon_2 c}{\beta} E_x = \frac{\epsilon_0 \left[\epsilon_{l,2} + \alpha_2 \left(E_x^2 + E_z^2\right)\right] c}{\beta} E_x. \tag{7.1.9}$$

In the nonlinear case, the magnetic field is not a linear function of E_x but depends also on the nonlinear permittivity. For very high nonlinear permittivity modification, with which we deal in this work, the magnetic field profile will be strongly affected by the nonlinear term. In regions where the nonlinear permittivity modification is high compared to the linear part, the magnetic field profile amplitude will be larger than in the case of the linear $H_y(E_x)$ dependency.

In the JEM, we proceed in the reverse way. In the formulation of JEM, the only field component present in the final formulation of the model is the magnetic field component H_y. Therefore, the quantity that is a direct output of the JEM numerical procedure is the magnetic field profile $H_y(x)$. Based on the magnetic field profile, the electric field components are calculated using Eqs. (1.5.2b) and (1.5.2c) and the simplified treatment of the Kerr nonlinear term [Eq. (6.1.1)]. The resulting expressions

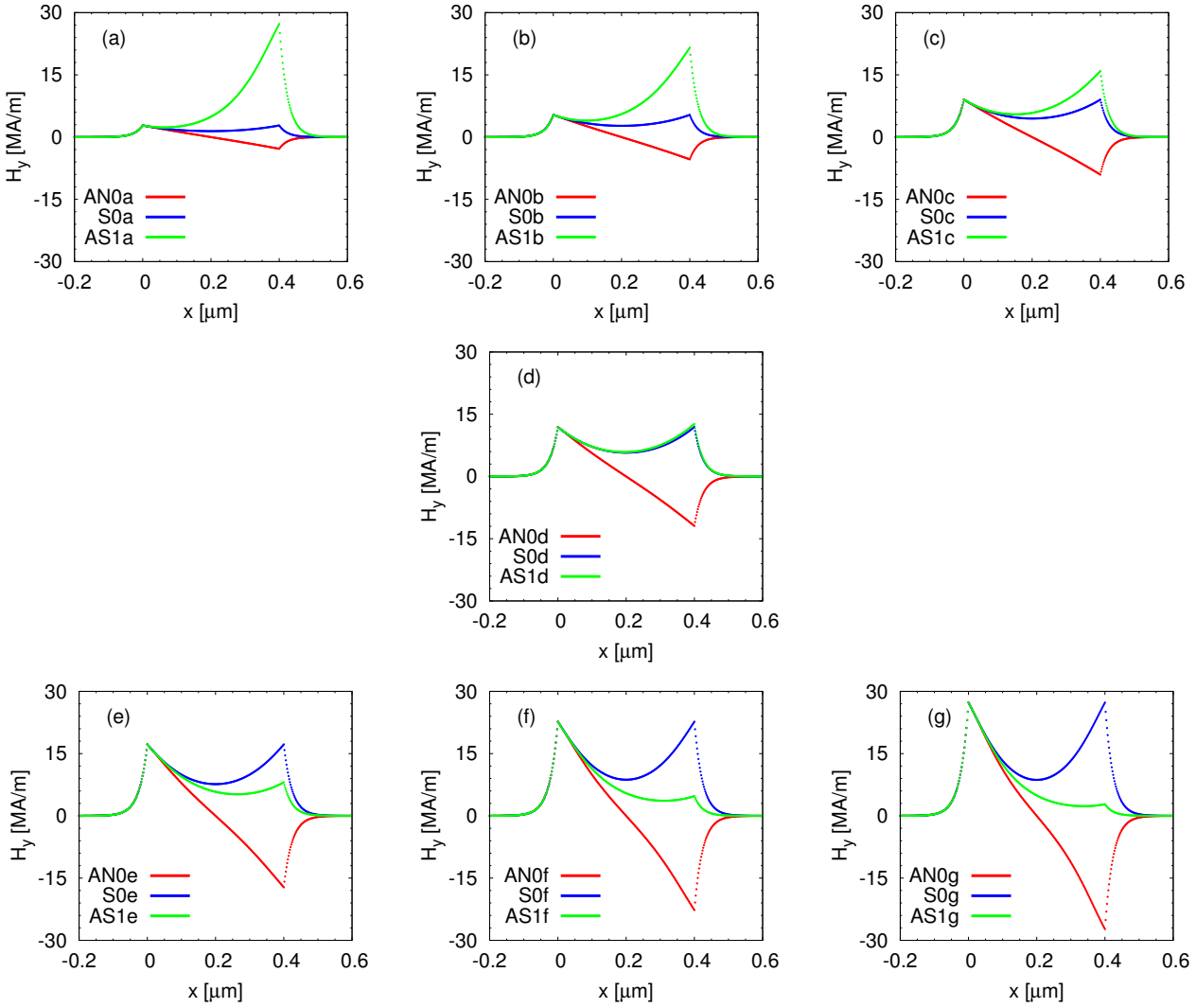

Figure 7.31: Profiles of the magnetic field component H_y for the symmetric S0 mode (blue), antisymmetric AN0 mode (red), and the first-order asymmetric AS1 mode (green). The subplots present the transformation of the field profiles at the points a, b, c, d, e, f, and g indicated in Fig. 7.27. In all the subplots, the scale was kept identical to see the relative change of the magnetic field amplitude between the points. In each of the subplots, the magnetic field amplitude at the left metal/nonlinear dielectric interface (H_0) is identical for all three modes.

for the electric field components are:

$$E_x = \frac{\beta}{\epsilon_0 \left(\epsilon_{l,2} + a_2 H_y^2\right) c} H_y, \tag{7.1.10a}$$

$$E_z = \frac{1}{\epsilon_0 \left(\epsilon_{l,2} + a_2 H_y^2\right) \omega} \frac{\mathrm{d}H_y}{\mathrm{d}x}. \tag{7.1.10b}$$

In this case, due to the presence of the nonlinear permittivity in the denominator, in the regions of high nonlinear permittivity change, the electric field component amplitudes are lower than in the case of a linear dependency of E_x and E_z on H_y. This is one of the reasons why the magnetic fields obtained using both models are qualitatively the same, while there are qualitative differences in the behavior of the electric field components. This effect will be even more visible for higher-order modes, where the nonlinear permittivity change is of the same order of magnitude as the linear part of the nonlinear dielectric permittivity.

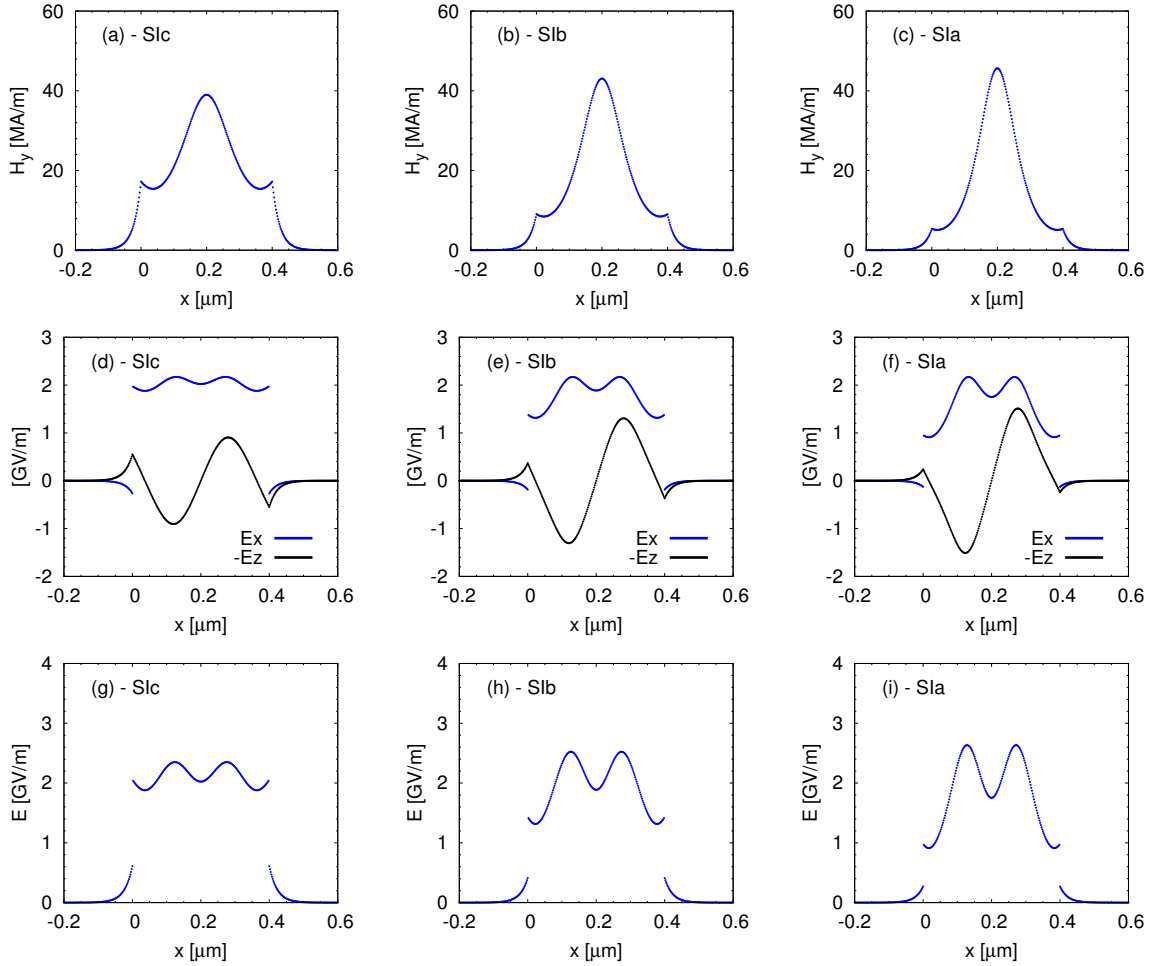

Figure 7.32: Profiles of (a)–(c) magnetic field component H_y, (d)–(f) electric field components E_x (blue) and $-E_z$ (black), and (g)–(i) total electric field amplitude E corresponding to points (first column) SIc, (second column) SIb, and (third column) SIa in Fig. 7.27.

In Fig. 7.31, a direct comparison of the magnetic field plots is presented for the three modes S0, AN0, and AS1. In each of the subplots in Fig. 7.31, the values of H_0 for all the modes are identical. The subplots are ordered by increasing values of H_0. The transformation of the magnetic field profiles connected with the increase of H_0 that is illustrated in Fig. 7.31, is the same as in the case of the IM shown in Fig. 7.16, where the field transformation connected with the increase of E_0 was presented.

Figure 7.32 presents the transformation of the higher-order symmetric node-less SI mode associated with the increase of the mode energy. The field intensity H_0 decreases in columns from left to right, whereas the total intensity density increases. The magnetic field profiles predicted by the JEM are in qualitative agreement with those of the IM presented in Fig. 7.18. However, there is a quantitative difference between the ratio of the soliton peak H_{peak} and the magnetic field intensity at the metal/nonlinear dielectric interfaces ($H_0 = H_d$) obtained using two models. In the magnetic field profiles obtained using the JEM, the ratio H_0/H_{peak} is higher than in case of the IM. The profiles of the E_z field component are also in good agreement with the results of the IM. The agreement between the E_z profiles for the higher-order node-less modes, obtained using our two modes results from the fact that in the region where the nonlinear permittivity change (proportional to H_y^2) is the largest (in the center of the waveguide core), the E_z component has its minimum. Therefore, in the case of the E_z profile the limitation of the JEM discussed on Page 147 is not visible. On the contrary, the E_x component computed using the IM has a maximum in the center of the core, just like the magnetic field (see Fig. 7.18). In the frame of the JEM, due to the way of computing the values of E_x [see Eq. (7.1.10a)] the transverse electric field component E_x has a minimum in the center of the waveg-

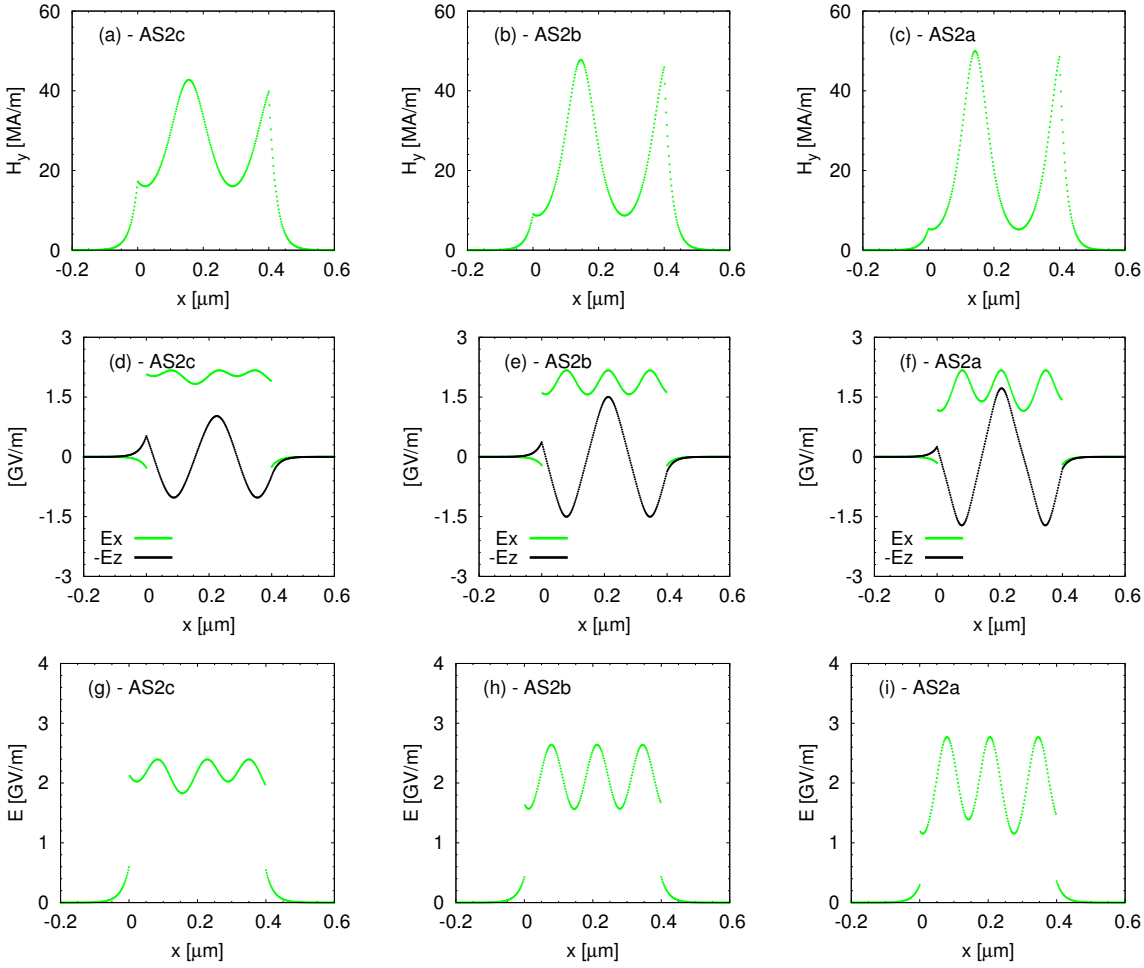

Figure 7.33: Profiles of (a)–(c) magnetic field component H_y, (d)–(f) electric field components E_x (green) and $-E_z$ (black), and (g)–(i) total electric field amplitude E corresponding to points (first column) AS2c, (second column) AS2b, and (third column) AS2a in Fig. 7.27.

uide core [see Figs. 7.32(d)–(f)]. The E_x and E profiles obtained using the JEM, instead of a single maximum in the center of the waveguide, as predicted by the IM, have two maxima and separated by a local minimum in the core center.

In Fig. 7.33, the transformation of the second-order asymmetric node-less mode AS2 along its dispersion curve is presented. The columns are ordered from left to right by increasing total intensity density (decrease of H_0 but increase of H_d). In case of the AS2 mode, we see a qualitative difference of all the field profiles between the results of the JEM (Fig. 7.33) and the IM presented in Fig. 7.19. The magnetic field profiles obtained with both models can be interpreted as a soliton trapped in the core of the nonlinear slot waveguide and shifted toward one of the interfaces. The intensity on the other interface is high due to the presence of a side-lobe. Comparing the result of the JEM and the IM, we notice that in case of the JEM, the magnetic field amplitude of the right side-lobe H_d is almost equal to the peak amplitude of the soliton H_{peak}. On the contrary, in case of the IM, the value of H_d was much lower than H_{peak}. The electric field component E_x in case of the JEM has a complex behavior resulting from Eq. (7.1.10a) and is drastically different than in case of the IM. Also the E_z component of the electric field changes its behavior. The x-derivative of this component at the right core interface has different signs between the JEM and the IM (compare the second row in Figs. 7.33 and 7.19). Consequently, the profiles of the total electric field amplitude also differ between the two models.

To finish the description of the profiles of the modes belonging to the node-less family, in Fig. 7.34 we present a direct comparison of the transformation of the symmetric SI mode and the asymmetric AS2 mode. The subplots are ordered by increasing values of H_0. In each of the subplots, both modes

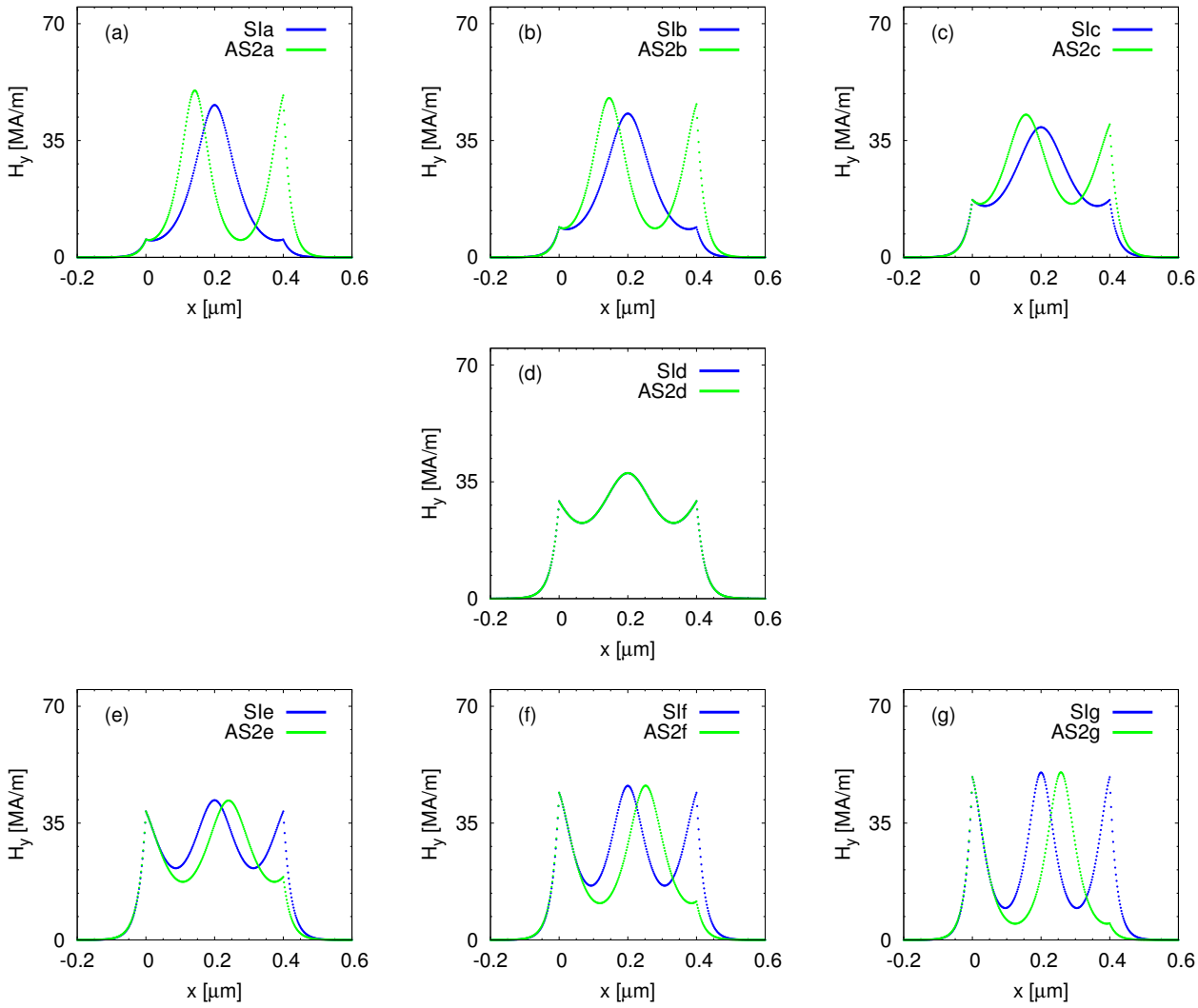

Figure 7.34: Profiles of the magnetic field H_y for the symmetric SI mode (blue) and the second-order asymmetric AS2 mode (green). The subplots present the transformation of the field profiles at the points a, b, c, d, e, f, and g indicated in Fig. 7.27. In all the subplots the scale was kept identical to see the relative change of the magnetic field amplitude between the points.

have identical values of H_0. Generally speaking, the transformation has the same character as in case of the IM model (see Fig. 7.20), where the field transformation connected with the increase of E_0 was presented. At the bifurcation point [Fig. 7.34(d)], the modes SI and AS2 are identical. With the decrease of the magnetic field amplitude at the left interface H_0, the soliton of the asymmetric mode becomes more localized at the left interface [subplots (a), (b), and (c)]. Increase of H_0 causes the shift of the soliton peak position toward the right interface [subplots (e), (f), and (g)]. The difference between the two models is visible looking at the ratio of the peak amplitude of the soliton H_{peak} and the higher of the two amplitudes at the core interfaces $\max(H_0, H_d)$. In the JEM, this ratio is very close to one for all the asymmetric profiles and also for the symmetric profiles with H_0 above the bifurcation point. In case of the IM, ratio $H_{\text{peak}}/\max(H_0, H_d)$ is always much higher than one.

The description of the node-less modes obtained using the JEM ends here. For the IM, we have described also higher-order node-less modes. The comparison between the two models for this profiles gives the same conclusions as these drawn above. Nevertheless, to present a complete study, the profiles of the higher-order modes from the node-less family obtained using the JEM are presented and compared with the results of the IM in Appendix E.

Modes with nodes

The comparison of the field profiles that belong to the family with nodes will be done only on one example of the symmetric S1 mode. The transformation of this mode along its dispersion curve is presented in Fig. 7.35. The comparison of the results of the JEM with the corresponding field profiles obtained using the IM (presented in Fig. 7.25) shows that for low mode energy (the first column in Fig. 7.35) all the field profiles are in good agreement. With the increase of the mode energy the agreement of the field profiles deteriorates. First, we observe that in the profile of the electric field component E_x, the single minimum in the center of the waveguide splits into two minima separated by a local maximum [see Fig. 7.35(e)]. The profile of the total intensity is also different than in the case of the IM and does not become flat [see Fig. 7.25(h) for the results obtained with the IM]. For very high total intensity density I_{tot} and effective index β (the third column in Fig. 7.35) all the field profiles (except for the E_z) are qualitatively different. For the magnetic field profile, the ratio $|H_{\mathrm{peak}}|/H_0$ is much closer to one in case of the JEM than for the IM. In case of the JEM, the maxima and minima of E_x profiles split into two. In the profile of the total electric field amplitude, each of the two maxima also splits into two with the increase of H_0. The maxima and minima of the E_z profile presented in Fig. 7.35(f) split into two. This behavior is the same as observed in the corresponding figure obtained using the IM [Fig. 7.25(f)].

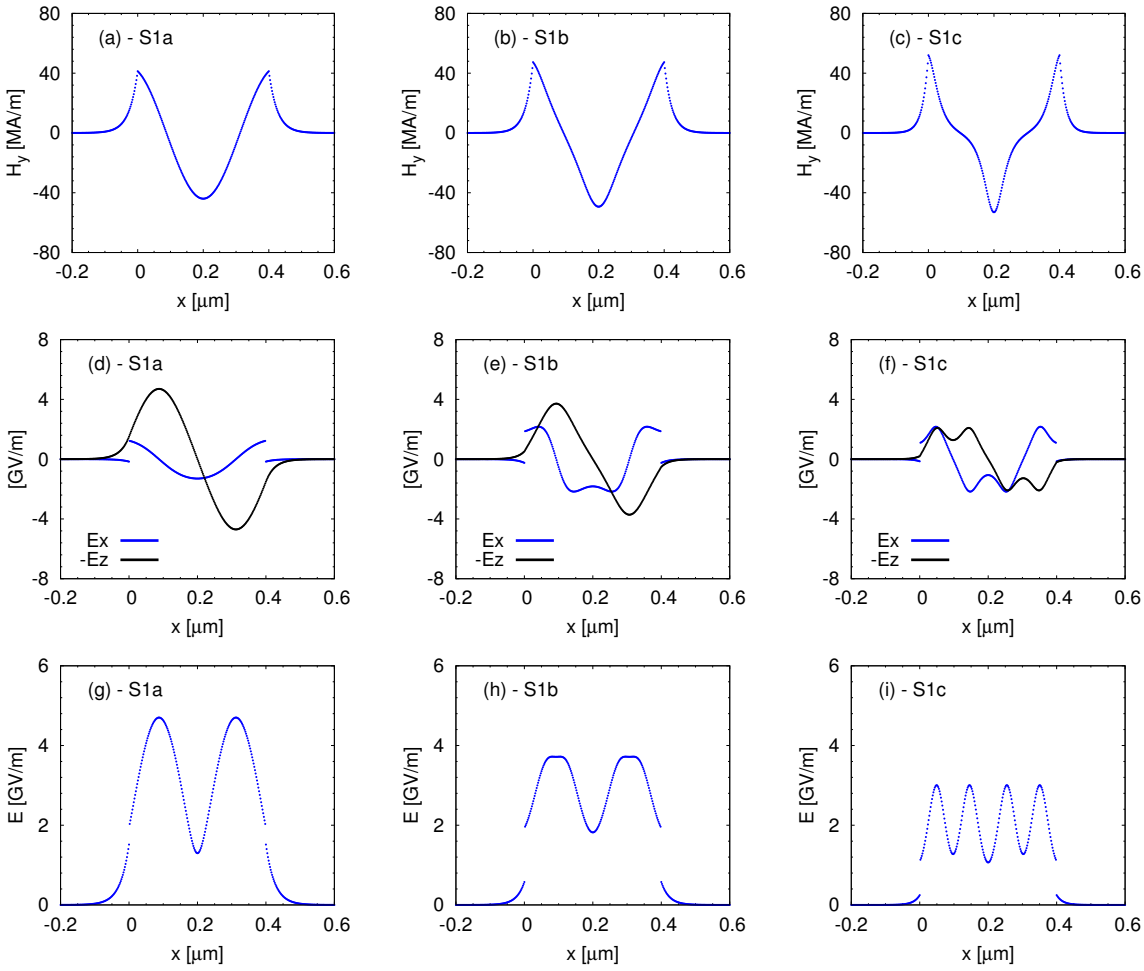

Figure 7.35: Profiles of (a)–(c) magnetic field component H_y, (d)–(f) electric field components E_x (blue) and $-E_z$ (black), and (g)–(i) total electric field amplitude E corresponding to points (first column) AS2c, (second column) AS2b, and (third column) AS2a in Fig. 7.27.

The behavior of the higher-order modes of the family with nodes is similar to the S1 mode and will not be discussed in detail. The magnetic field plots for the AN1, S2, and AN2 modes are presented in Figs. 7.2(e), (f), and (g).

Summary

Summarizing the results of this section, we observe that the general features of the magnetic field profiles obtained using the IM and the JEM are similar and lead to the same conclusions about the nature of the modes of the nonlinear slot waveguide. A closer examination of the electric field profiles reveals qualitative differences between the the two models. They do not have any impact on the dispersion plots, because in the frame of the JEM the dispersion relations depend only on the magnetic field. These differences reflect the fact that the JEM was built using assumption about the weak nonlinearity and the weak longitudinal electric field component compared to the transverse one. Therefore, it could be expected that, in the highly nonlinear regime and for the slot waveguide modes for which both electric field components have comparable amplitudes, the simpler Jacobi elliptic function based model fails to correctly predict profiles of all the field components. Because of that in Sections 7.1.5–7.2 we will use only the results of the interface model that describes the physics of nonlinear slot waveguides more accurately.

7.1.4 Single-interface limit

In Chapter 6, describing the theoretical derivation of the models for nonlinear plasmonic slot waveguides, we mentioned that in the limiting case, where the integration constants c_0 in Eqs. (6.1.3) and (6.1.7) or C_0 in Eqs. (6.2.2) and (6.2.26) are equal to zero, we recover the case of a single interface between a metal and a nonlinear dielectric. Looking at the field profiles of highly asymmetric modes AS1 (see Fig. 7.15), we see that this mode is mostly localized at one interface only. Therefore, it can be well approximated by a solution of the single-interface problem.

In Fig. 7.36, we present the dispersion curves $\beta(P_c)$ for the nonlinear slot waveguide obtained using the JEM and the IM (compare with Fig. 7.6). Additionally to the antisymmetric (red), symmetric (blue), and asymmetric (green) dispersion curves, black dispersion curves obtained using single-interface models are presented. In the case of the JEM, the single-interface approximation was obtained using the FBM for configurations with semi-infinite nonlinear medium described in Section 2.1. Effectively, Eq. (3.1.4) for a single interface between a metal and a nonlinear dielectric was solved using the parameters of our nonlinear slot waveguide (see Table 7.1). In case of the IM, the corresponding single-interface approximation was obtained using the EM for configurations with semi-infinite nonlinear medium described in Section 2.3. The dispersion relation in this case is given by Eq. (6.2.29).

In both cases presented in Fig. 7.36, we see that the single-interface dispersion curves for low effective indices and low values of P_c are located between the antisymmetric AN0 and symmetric S0 dispersion curves. They intersect with the S0 curves slightly below the bifurcation points of asymmetric modes AS1. For the values of β above the bifurcation points, the curves obtained using single-interface models follow the AS1 asymmetric dispersion curves. The fact that the black curves overlap with the green AS1 curves confirms that the highly asymmetric AS1 modes (for high effective index β) are well approximated using the single-interface approach.

In Fig. 7.37, the dispersion curves $\beta(E_0)$ obtained using the JEM and the IM are presented (compare with Fig. 7.9). Additionally, dispersion curves for the single-interface configuration calculated using the FBM (in case of the JEM) and the EM (in case of the IM) are depicted in black. In these coordinates, both for the JEM and for the IM, the single-interface dispersion curve always lays between the antisymmetric AN0 curve and the symmetric S0 curve. For high values of E_0, the asymmetric AS1 curve becomes very close to the black curve, but remains slightly above it.

Looking at Fig. 7.37(a), we observe that indeed, as predicted in Section 6.1 (see Page 88), the black curve corresponding to the integration constant c_0 equal to zero (single-interface dispersion curve) separates the dispersion plot in two parts. Above the $c_0 = 0$ curve, only node-less solutions exist (for negative values of the integration constant c_0). Below this curve, only solutions with nodes

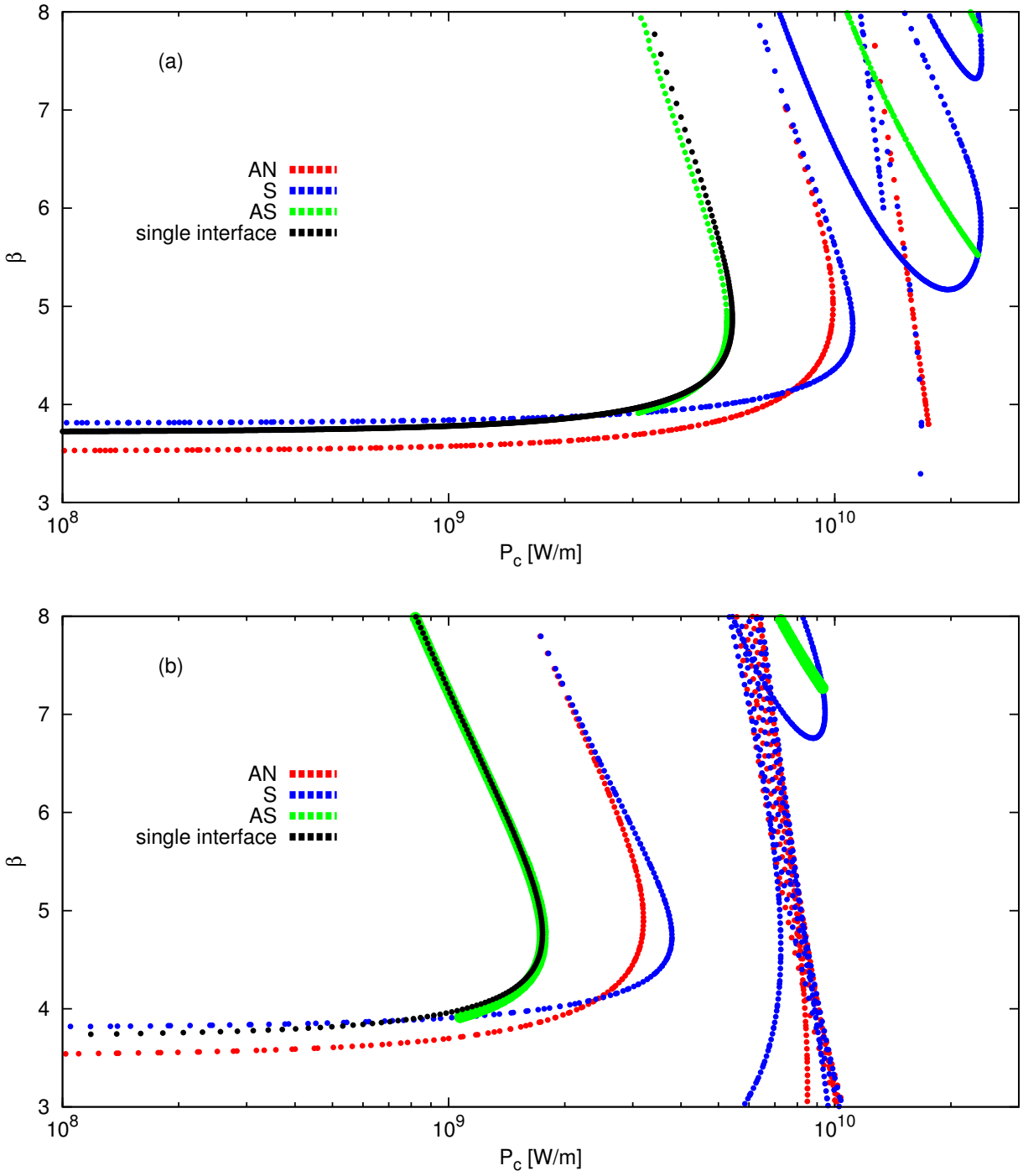

Figure 7.36: Dispersion diagram for the nonlinear slot waveguide presenting the effective index β as a function of the power density in the core P_c [defined by Eq. (7.1.4)] obtained using (a) the JEM and (b) the IM. On both plots dispersion curves presenting single-interface approximations (computed using the FBM and the EM) are shown in black. For clarity of the plots, the range of the effective indices shown was reduced to $\beta \in [3, 8]$.

appear (for positive values of c_0). The same conclusion can be drawn looking at Fig. 7.37(b). In case of the IM, the numerical results also show that the dispersion curves are divided in two families: with nodes and node-less. The regions of the dispersion diagram corresponding to these two families are separated by the curve described by the equation $C_0 = 0$ (black curve for the single-interface problem).

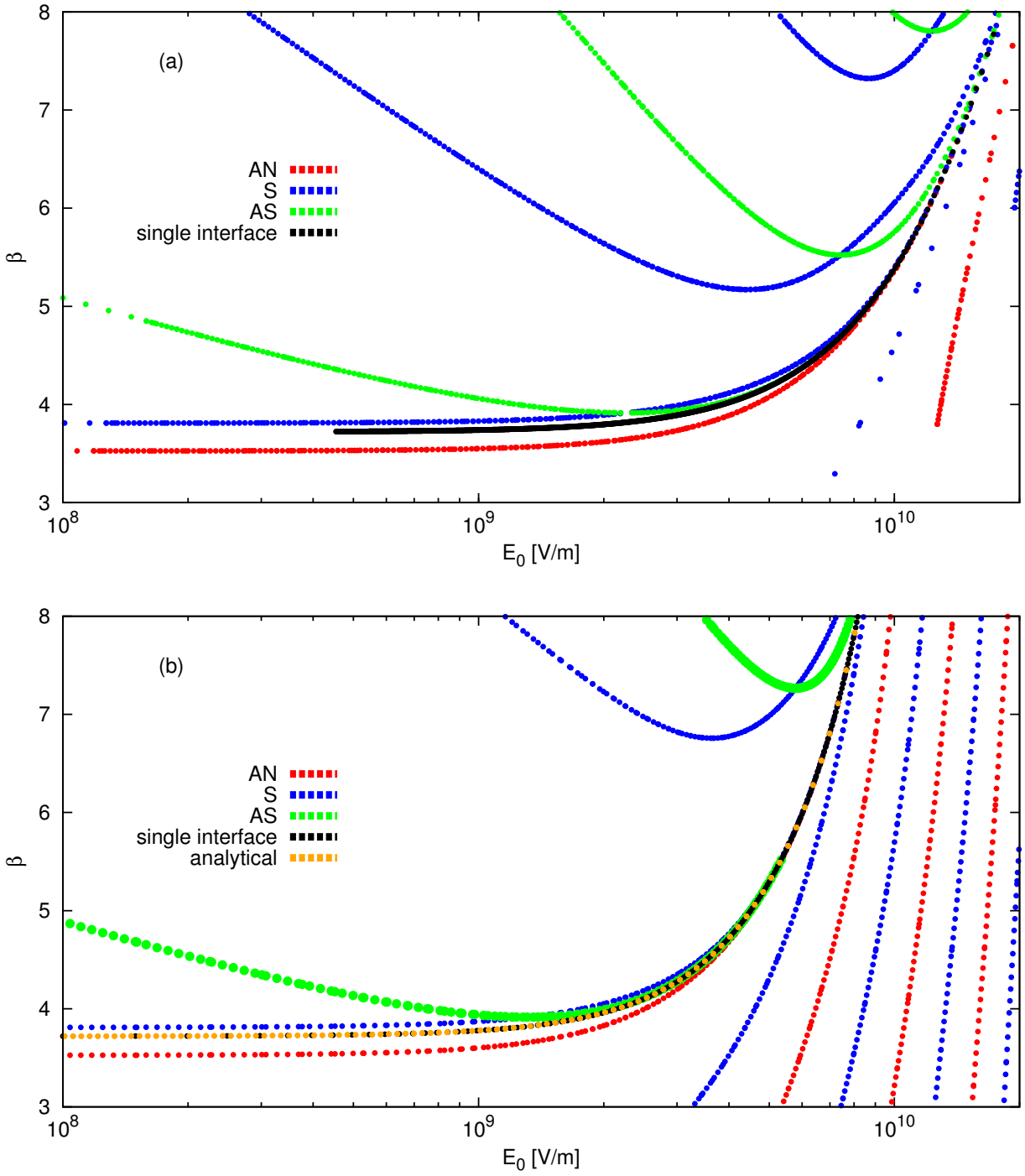

Figure 7.37: Dispersion diagram for the nonlinear slot waveguide presenting the effective index β as a function of the total electric field amplitude on the left interface between the metal and the nonlinear dielectric E_0. Results obtained using (a) the JEM and (b) the IM. In both plots, dispersion curves presenting single-interface approximation (computed using the FBM and the EM) are shown in black. Additionally, in the figure presenting the dispersion relation for the IM, the curve corresponding to the analytical expression for the single-interface dispersion relation [Eq. (6.2.29)] is shown in yellow.

In the frame of the IM, we could not prove this property analytically because the field plots in the IM are calculated numerically.

Finally, instead of using the models for configurations with a semi-infinite nonlinear medium developed in Section 2.1 (the FBM) and Section 2.3 (the EM), we will use the formulas found in Sections 6.1

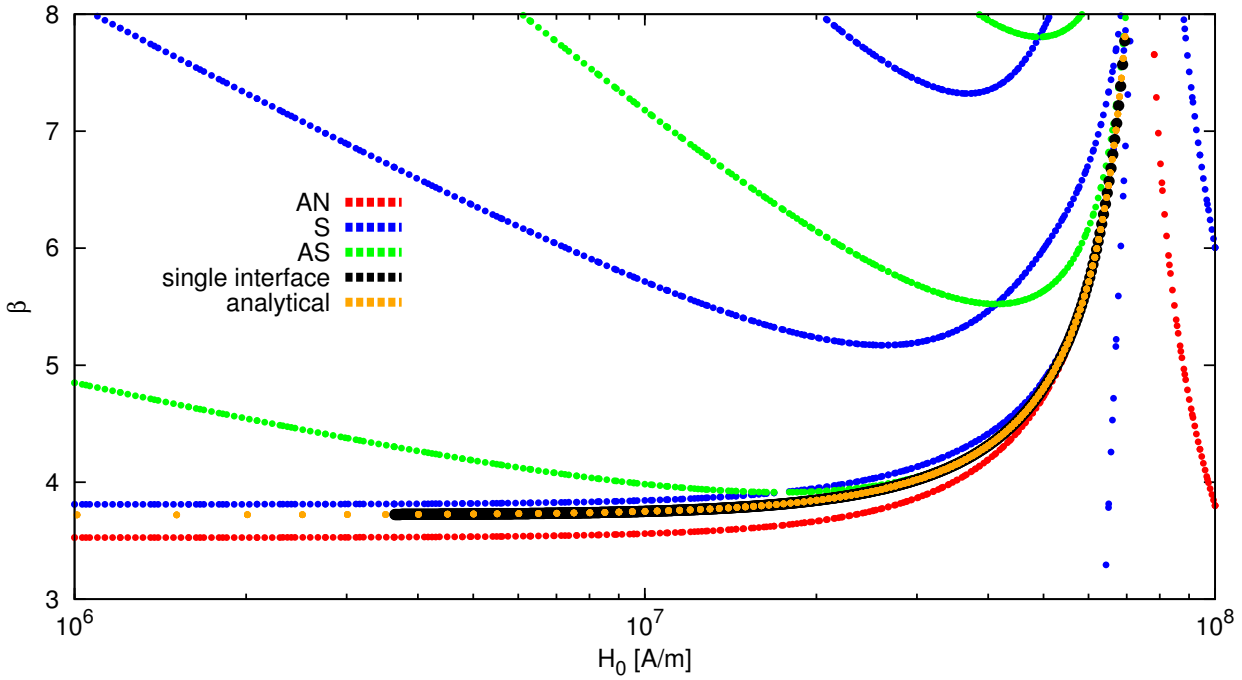

Figure 7.38: Dispersion diagram obtained using the JEM for the nonlinear slot waveguide presenting the effective index β as a function of the magnetic field amplitude on the left interface between the metal and the nonlinear dielectric H_0. Dispersion curves presenting single-interface approximation obtained using FBM are shown in black. Additionally, the curve corresponding to the analytical expression for the single-interface dispersion relation [Eq. (6.1.10)] is shown in yellow.

and 6.2 that give us the dispersion relations for the single-interface problem. In case of the IM, the analytical formula for the dispersion relation for the single-interface problem is given by Eq. (6.2.29). The effective index of the mode expressed as a function of the material parameters of the structure and the total electric field intensity at the interface E_0. The curve described by Eq. (6.2.29) is plotted in yellow in Fig. 7.37(b) and it overlaps well with the black curve obtained using the EM.

In the case of the JEM, the analytical formula for the dispersion relation of a single metal/nonlinear dielectric interface problem is given by Eq. (6.1.10). In this equation, as in the entire formulation of the JEM, the primary parameter is the magnetic field amplitude at the interface H_0. Therefore, to be able to show the dependency described by Eq. (6.1.10), we need to use the coordinates where the effective index is presented as a function of the magnetic field amplitude at the interface H_0. This plot is presented in Fig. 7.38 (compare with Fig. 7.27). We observe that in these coordinates the dispersion relations calculated using the FBM (balck curve) and the yellow curve described by Eq. (6.1.10) overlap perfectly. The single-interface dispersion curve, which corresponds to the limiting case $c_0 = 0$ divides the dispersion plot $\beta(H_0)$ into the regions corresponding to the node-less family and the family with nodes.

In all the plots presented in this section, in the region of high effective indices, the dispersion curves of the AS1 mode overlap with the curves obtained using single-interface approximations. This confirms our hypothesis (formulated on Pages 80 and 100) that highly asymmetric modes AS1 can be approximated by solutions obtained using the corresponding single-interface models.

7.1.5 Relation between nonlinear modes with nodes and their linear counterparts

In Section 7.1.2, while discussing the field profiles of the modes belonging to the family with nodes, we noticed that they resemble higher-order modes of linear slot waveguides with parameters similar

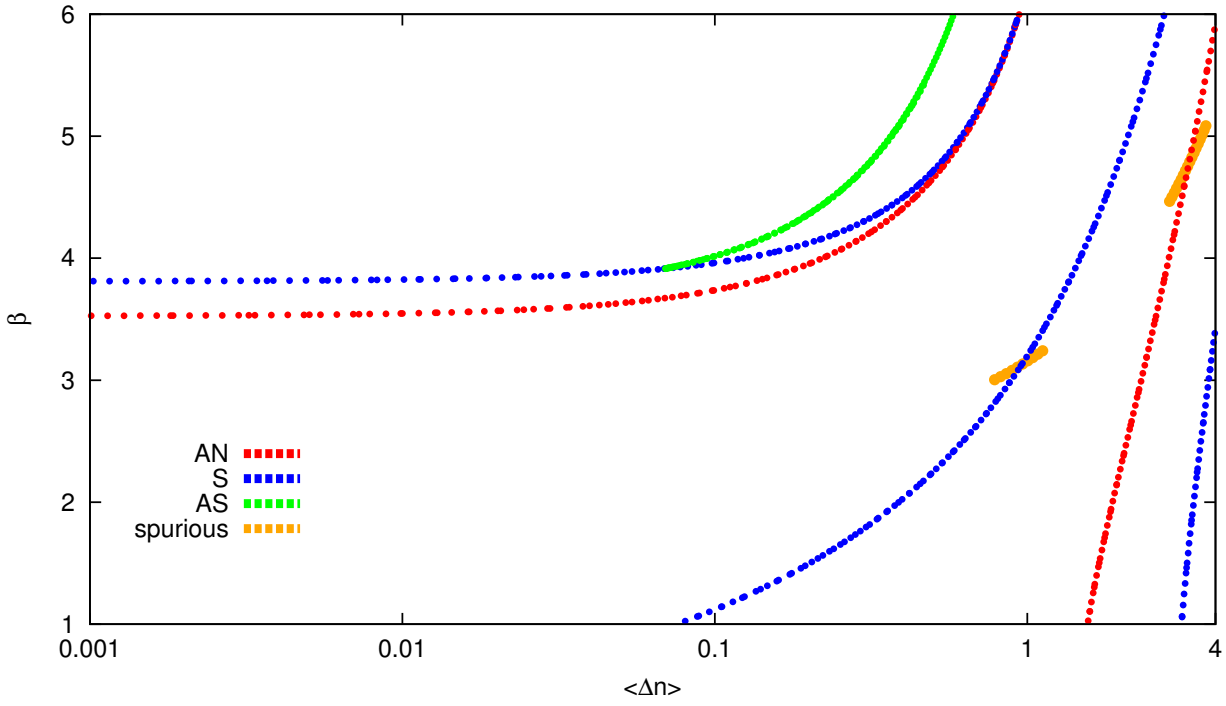

Figure 7.39: Nonlinear dispersion diagram for the symmetric nonlinear slot waveguide showing the effective index of the mode β as a function of the averaged nonlinear refractive index modification $\langle \Delta n \rangle$ defined by Eq. (7.1.1). Small portions of dispersion curves of spurious modes are shown in yellow and help to locate the point at which modes with nodes induce a flat refractive index distribution.

to the nonlinear slot waveguide studied in Section 7.1.2. In this section, we will explain the origin of the similarities between these nonlinear and linear modes.

In Fig. 7.39, we remind the nonlinear dispersion curves obtained using the IM for our nonlinear slot waveguide with the following parameters: core thickness $d = 0.4$ μm, core permittivity $\epsilon_{l,2} = 3.46^2$, second-order nonlinear refractive index $n_2^{(2)} = 2 \cdot 10^{-17}$ m^2/W, metal permittivities $\epsilon_1 = \epsilon_3 = -90$ at a free-space wavelength $\lambda = 1.55$ μm (parameters identical to these used in Sections 7.1.1 and 7.1.2 and presented in Table 7.1). This plot is a part of a previously presented plot in Fig. 7.3.

From the analysis of the dispersion curves of the symmetric mode S1 and the antisymmetric mode AN1 belonging to the family with nodes presented in Section 7.1.2 at Page 141, we know that there is one point on each of these curves where the nonlinear index modification profiles induced by these modes are flat [see Figs. 7.25(h) and 7.26(h) obtained using the IM]. These points can be easily found using the numerical procedure to obtain the dispersion curves in the frame of the IM, which is described in Section 6.2.2. If we relax the physical condition that requires the amplitudes of the electric field component obtained by the numerical integration of Maxwell's equations $E_{x,d}^{\text{num}}$ and $E_{z,d}^{\text{num}}$ to be in agreement with the values given by Eqs. (6.2.25) (see condition 3 on Page 103), then spurious modes are found by the numerical procedure (unphysical modes, not fulfilling all the assumptions). These spurious modes have flat nonlinear index modification distributions all along their dispersion curves and they intersect with the modes of the family with nodes in the points where the index distribution corresponding to the genuine nonlinear modes is flat (this property is found empirically). Small portions of the dispersion curves of these spurious modes are shown in Fig. 7.39 (yellow curves) in order to locate the points corresponding to the genuine nonlinear modes that induce a flat nonlinear index distribution. At these points, we expect the field profiles of the modes of the nonlinear slot waveguide to be the most similar to the profiles of the modes of the linear slot waveguide with identical parameters but higher core refractive index. We base this expectation on the self-coherent definition of nonlinear modes. This definition was introduced by Townes and co-workers in Ref. [4] and was used later in other works (e.g., Ref [153]). It defines a nonlinear mode as

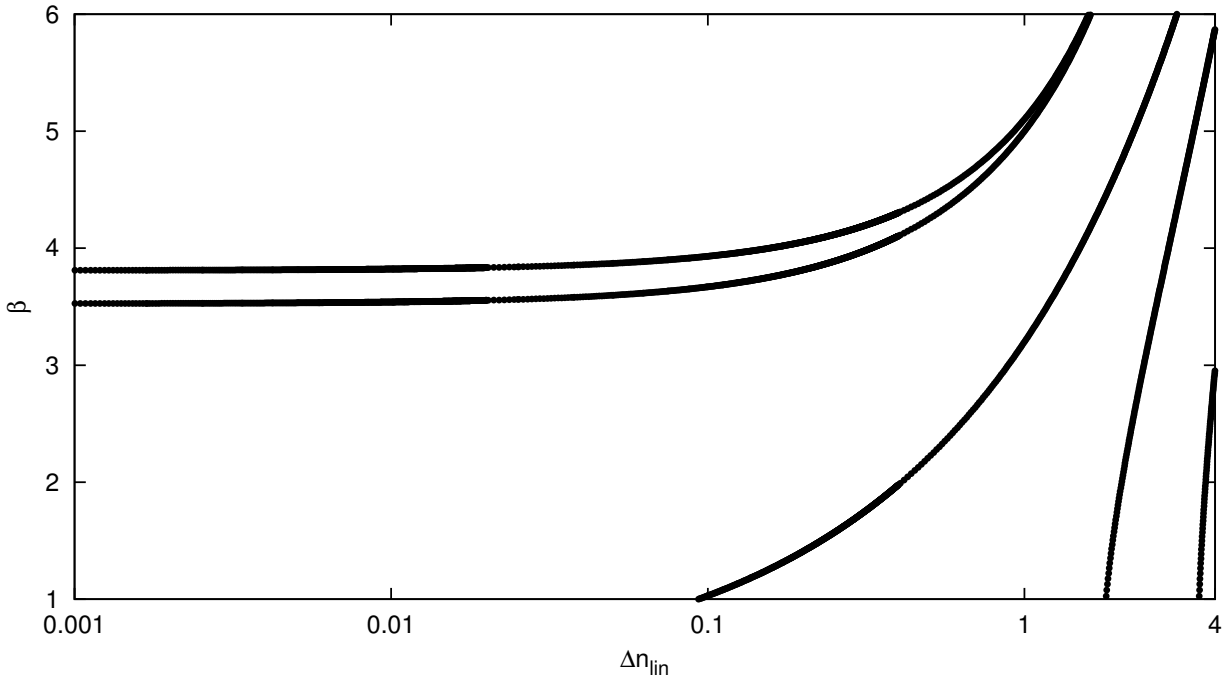

Figure 7.40: Dispersion curves for the linear slot waveguide with identical parameters as our nonlinear slot waveguide showing the effective index of the mode as a function of the linear refractive index increase Δn_{lin}. See the text for more details.

a linear mode of a linear (graded refractive index) waveguide that is induced by the light distribution of this mode. According to this definition, there is no difference between the nonlinear modes of the nonlinear slot waveguide for which the nonlinear index modification has a flat distribution and the linear modes of the waveguide with higher refractive index of the linear core. In the following, we will verify the validity of this definition for modes of the nonlinear slot waveguide.

To this end, we analyze another type of dispersion relations. Consider a linear slot waveguide: a linear dielectric core sandwiched between two metal regions. The parameters of this waveguide are given by: metal permittivities $\epsilon_1 = \epsilon_3 = -90$ and the core refractive index is given by $n = n_0 + \Delta n_{\text{lin}} = 3.46 + \Delta n_{\text{lin}}$ and the core thickness $d = 0.4$ μm. The parameters ϵ_1, ϵ_3 and $n_0 = \sqrt{\epsilon_{l,2}}$ are identical to these in the case of the nonlinear waveguide studied here (see Table 7.1). Figure 7.40 presents the dispersion diagram of the linear slot waveguide with core index $n = n_0 + \Delta n_{\text{lin}}$ where the effective index β is plotted as a function of Δn_{lin}. We notice that this linear dispersion diagram is similar to the dispersion plot of the nonlinear slot waveguide shown in Fig. 7.39. For the core with index $n = n_0$ only two modes are present and they are the linear counterparts of the modes S0 and AN0. With the increase of the core index n, the effective index of these modes increases and they become closer to each other. At $\Delta n_{\text{lin}} \approx 0.1$, a higher-order linear mode appears that is a counterpart of the S1 mode. For $\Delta n_{\text{lin}} \approx 2$ and $\Delta n_{\text{lin}} \approx 3.5$, another two higher-order modes appear. They are the linear counterparts of the AN1 and S2 modes. The effective index of these modes increases rapidly with the increase of Δn_{lin}. The only modes not present in the linear dispersion curves are the asymmetric modes AS1, AS2, ... and the symmetric node-less modes SI, SII, etc. The asymmetric modes can not be observed in the linear case because nothing breaks the symmetry in the symmetric linear slot waveguide. The node-less symmetric modes are not supported by the linear slot waveguide because they have purely nonlinear solitonic character (see Figs. 7.18 and 7.22 in Section 7.1.2).

A direct comparison between the nonlinear and the linear dispersion diagrams presented in Figs. 7.39 and 7.40, respectively, is shown in Fig. 7.41. The dispersion curves of the nonlinear modes AN0 and S0 overlap with the corresponding linear dispersion curves only for small $\langle \Delta n \rangle$ values. The nonlinear modes increase their effective indices β faster than the linear modes. In case of higher-order modes S1,

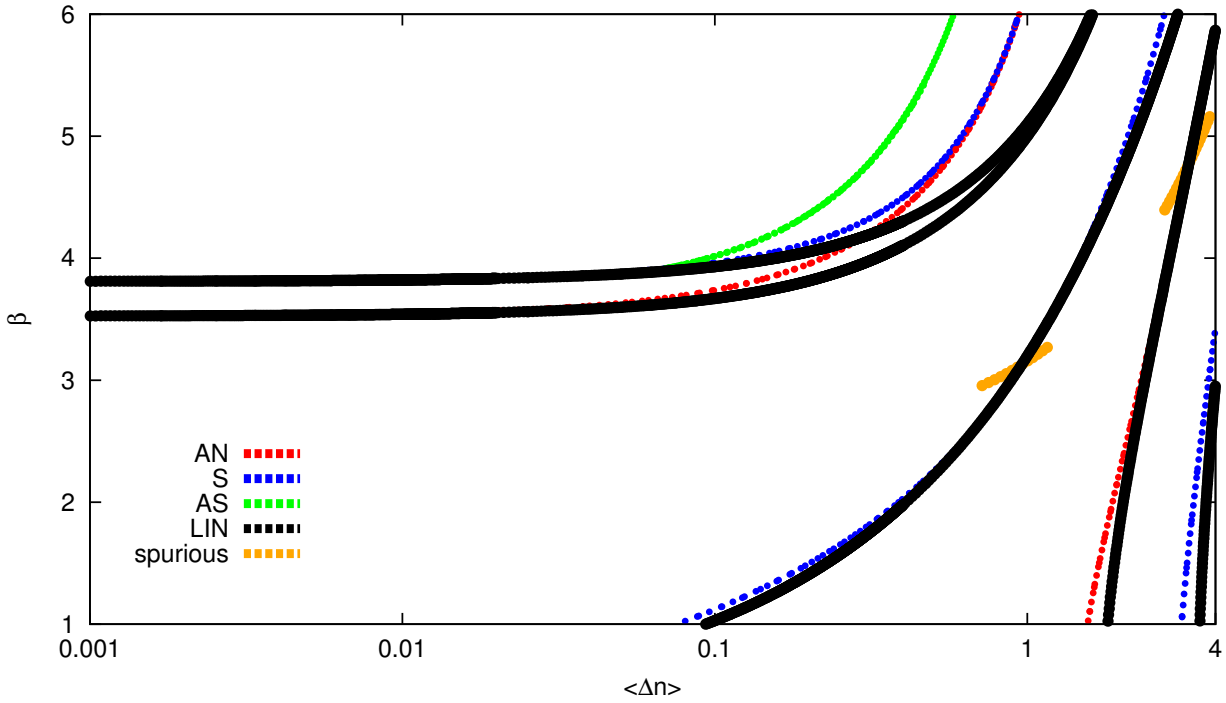

Figure 7.41: A comparison of the nonlinear (red, blue and green curves) and the linear dispersion plots (black curves) of the symmetric slot waveguides from Figs. 7.39 and 7.40. In case of the linear waveguide $\langle \Delta n \rangle$ is equivalent to Δn_{lin}. Small portions of dispersion curves of spurious modes are shown in yellow and help to locate the point at which modes with nodes generate flat refractive index distribution. See the text for more details.

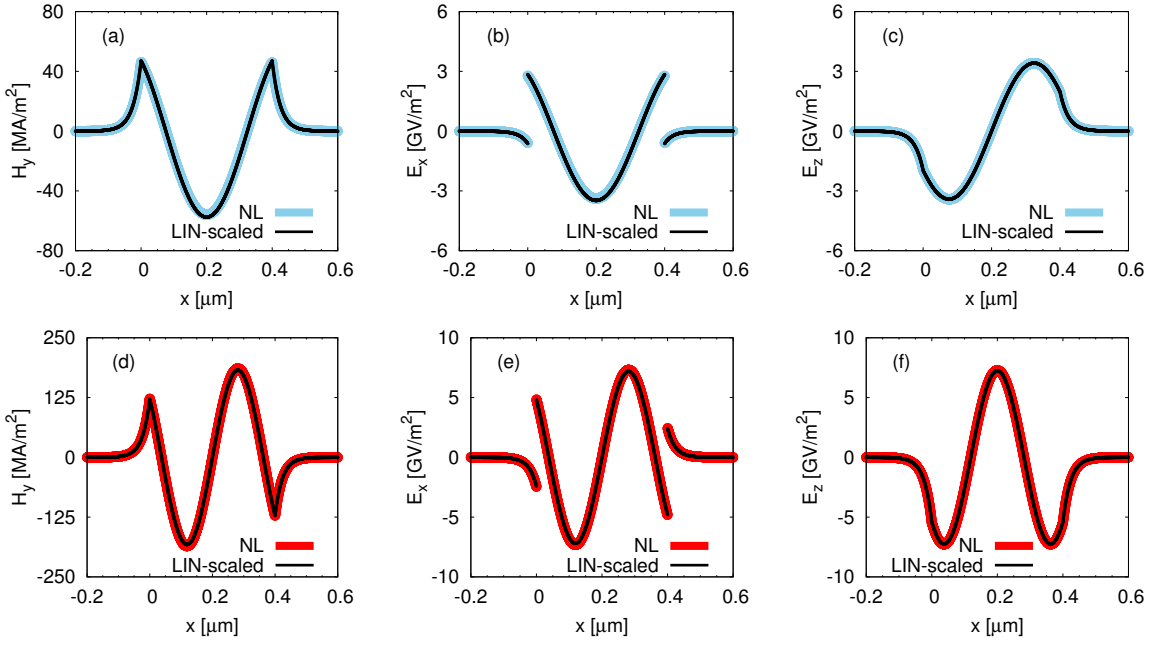

Figure 7.42: A comparison of (a), (d) $H_y(x)$; (b), (e) $E_x(x)$; and (c), (f) $E_z(x)$ for the nonlinear modes S1 (blue curve) (first row) and AN1 (red curve) (second row) at the points where the refractive index distribution is flat (intersection of yellow and blue or red dispersion curves in Figs. 7.39 and 7.41) and the normalized profiles of their linear counterparts (black curves).

AN1 and S2, the dispersion curves of the linear modes lay below the corresponding nonlinear modes. There is only one common point between these curves and it is, as expected, the point where the index distribution in the nonlinear core is flat.

The comparison of the field profiles $H_y(x)$, $E_x(x)$, and $E_z(x)$ for nonlinear S1 and AN1 modes at the point where the nonlinear index distribution is flat (intersection of yellow and blue or red dispersion curves in Figs. 7.39 and 7.41) and the corresponding linear modes (for identical β value) is presented in Fig. 7.42. We observe that the nonlinear profiles overlap perfectly with the profiles of the linear modes normalized to the same amplitude as the nonlinear modes.

The results presented in this section prove that the modes with nodes found in the nonlinear slot waveguides are close to the modes of the linear slot waveguide with similar opto-geometric parameters. We have explained the similarities between these nonlinear and linear modes using the self-coherent definition of nonlinear modes introduced in Ref. [4].

7.1.6 Core width study

In this section, we study the influence of the core width on the behavior of the dispersion curves of the nonlinear slot waveguides. The material parameters used here will be identical to these in the previous section: core permittivity $\epsilon_{l,2} = 3.46^2$, second-order nonlinear refractive index $n_2^{(2)} = 2 \cdot 10^{-17}$ m^2/W, metal permittivities $\epsilon_1 = \epsilon_3 = -90$ at a free-space wavelength $\lambda = 1.55$ μm (see also Table 7.1). The core width will be varied here.

In Figs. 7.43–7.46, we present the nonlinear dispersion diagrams for the nonlinear slot waveguide with the core widths d equal to 100 nm, 200 nm, 400 nm, and 800 nm obtained using the IM. The comparison of these curves illustrates the influence of the core width on the dispersion curves of all the modes. In order to facilitate the mutual comparison of the dispersion curves, all the plots were drawn using identical $\langle \Delta n \rangle$ range and β range (except for Fig. 7.46 where the range of β is reduced).

At first, we analyze the low-power modes of the nonlinear waveguides (modes which start from the limiting linear case for very low levels of $\langle \Delta n \rangle$). For $d = 100$ nm (Fig. 7.43), there is only one such mode. It is the fundamental symmetric node-less mode that exists in metal slot waveguides regardless of the core thickness. With the increase of the thickness to 200 nm (Fig. 7.44), a second low-power

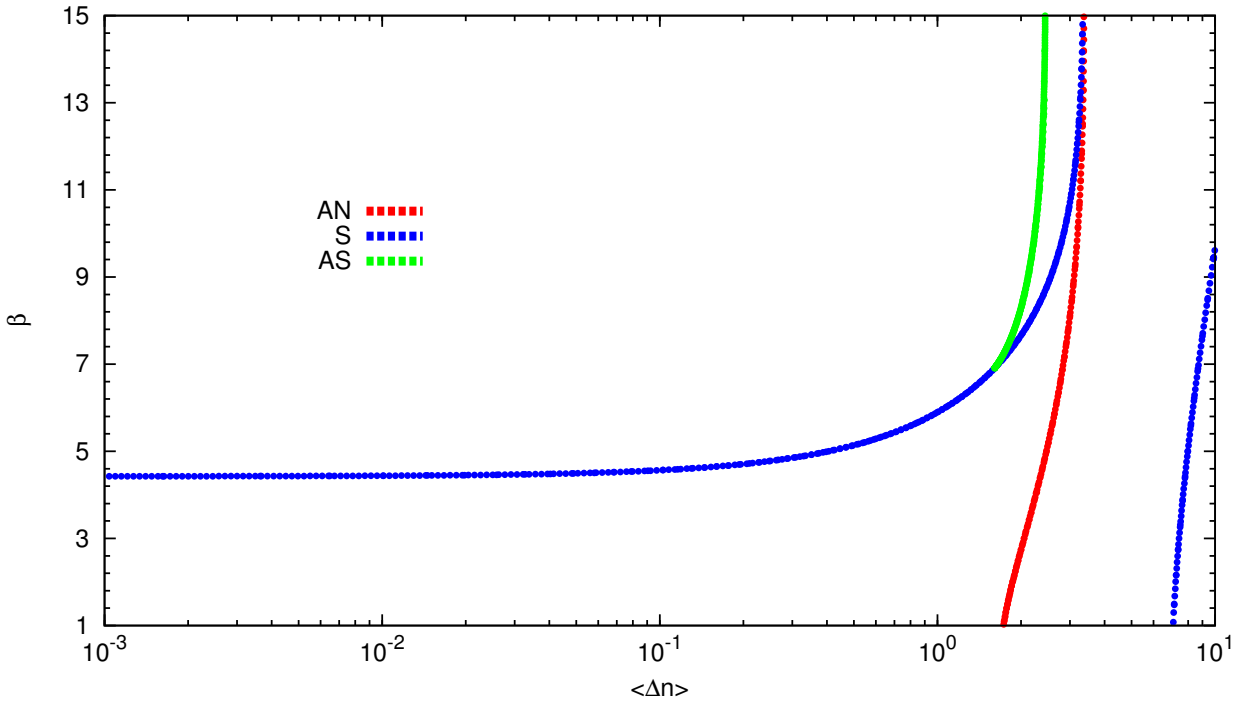

Figure 7.43: Dispersion relations for the nonlinear slot waveguide with the core thickness $d = 100$ nm.

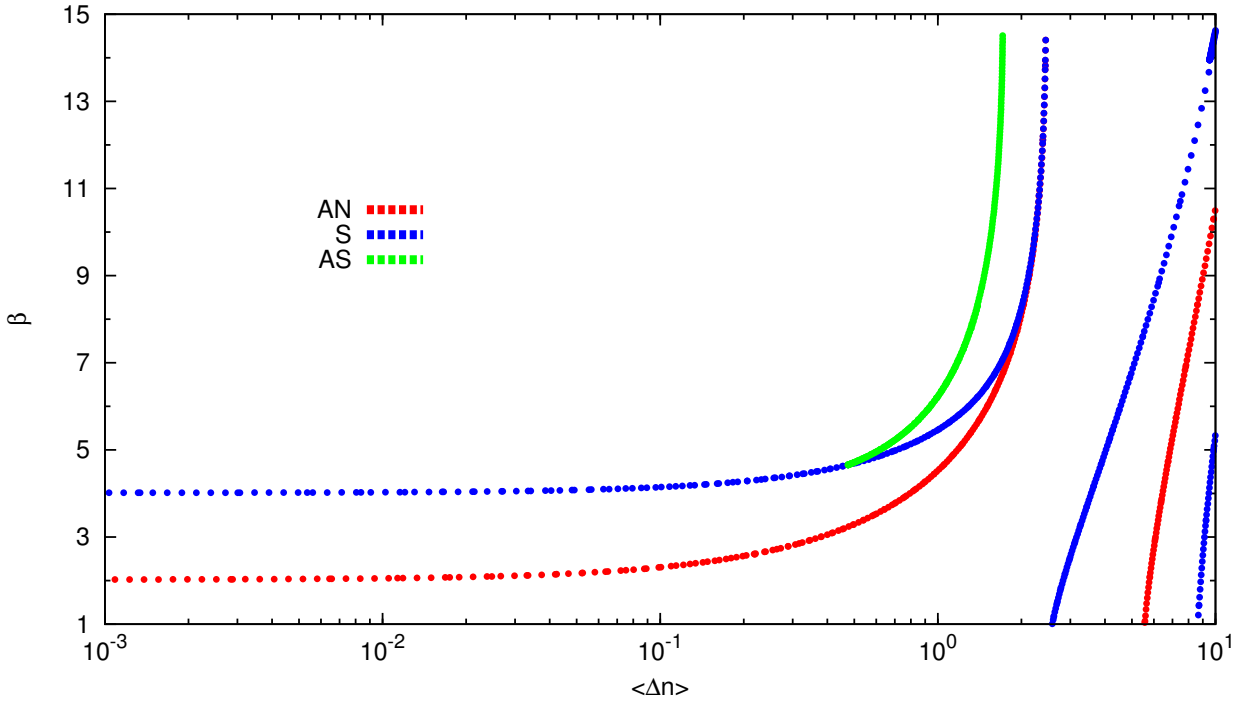

Figure 7.44: Dispersion relations for the nonlinear slot waveguide with the core thickness $d = 200$ nm.

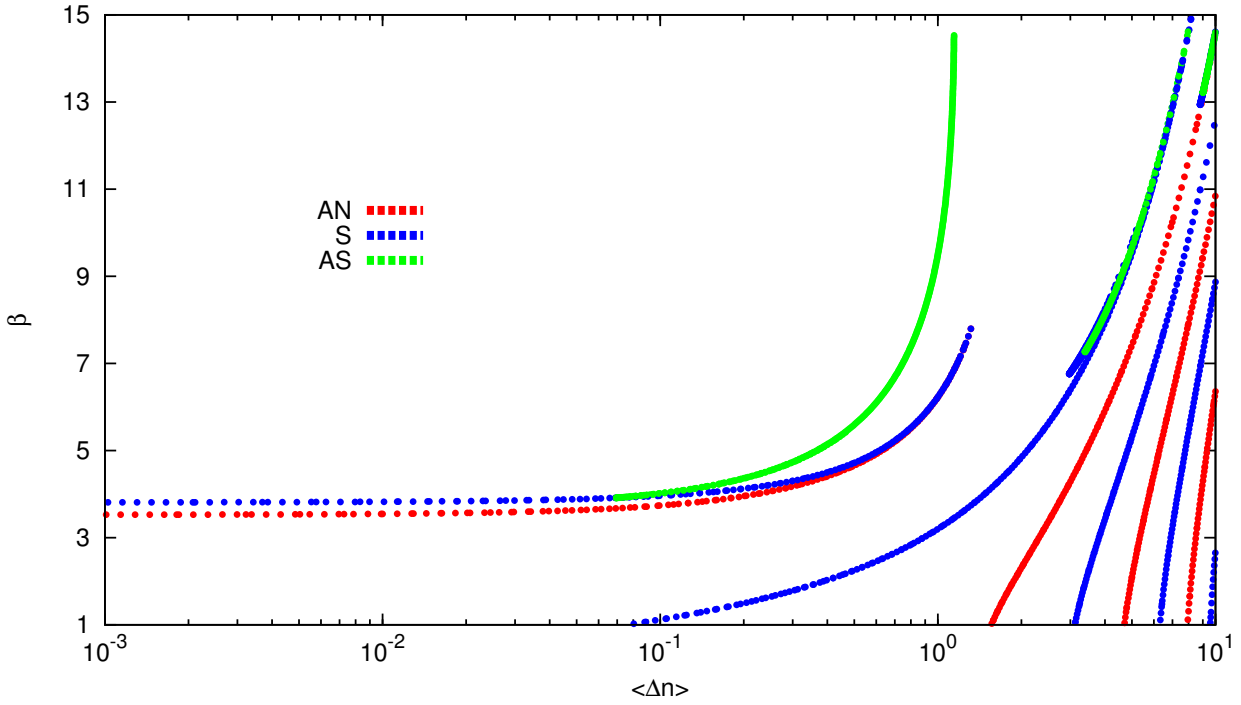

Figure 7.45: Dispersion relations for the nonlinear slot waveguide with the core thickness $d = 400$ nm.

mode appears. It is the antisymmetric mode with one node in the H_y profile. It is interesting to notice that in the case of $d = 100$ nm, the first nonlinear mode of the family with nodes was the antisymmetric mode with one node. In the case of $d = 200$ nm, the first mode of this nonlinear family is the symmetric mode with two nodes. We observe that with the increase of the waveguide thickness, the nonlinear modes of the waveguide with a thin core become low-power modes that start in the linear limit for the waveguides with thicker cores.

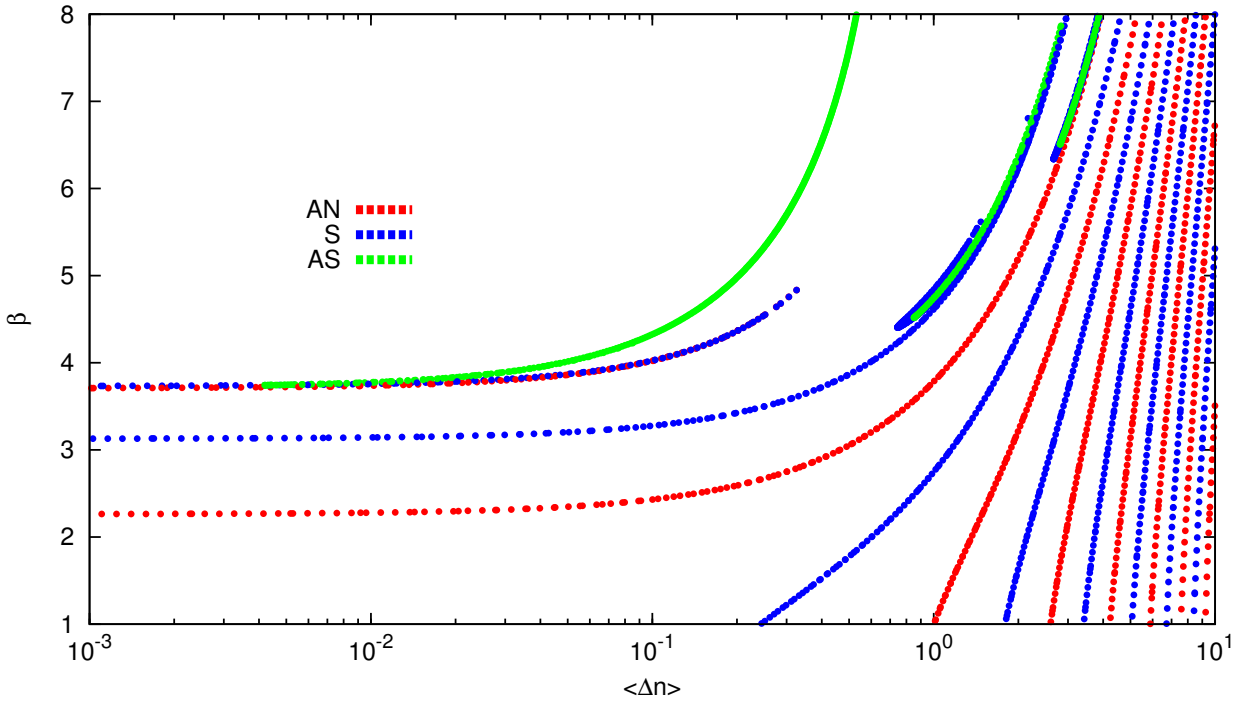

Figure 7.46: Dispersion relations for the nonlinear slot waveguide with the core thickness $d = 800$ nm. The range of β presented here is smaller than in the previous plots in this section in order to present the results more clearly.

With further increase of the thickness (to 400 nm, see Fig. 7.45), we notice that the two low-power modes of the nonlinear slot waveguide become much closer in terms of the effective index β. Additionally we observe that the $\langle \Delta n \rangle$ threshold for the appearance of the first and higher-order nonlinear modes with nodes becomes lower. For instance, the symmetric mode with two nodes appears for $\langle \Delta n \rangle \approx 2.5$ for the nonlinear slot waveguide with 200-nm-thick core and at $\langle \Delta n \rangle \approx 0.08$ for the waveguide with 400-nm-thick core.

The nonlinear slot waveguide with an 800-nm-thick core supports 4 modes present at low levels of $\langle \Delta n \rangle$ (see Fig. 7.46). Two of them (symmetric node-less mode and antisymmetric mode with one node) are located very close to each other in terms of β (in the vicinity of $\beta \approx 3.75$). A low-power symmetric mode with two nodes and a low-power antisymmetric mode with three nodes also exist. The first nonlinear mode of the family with nodes is the symmetric mode with four nodes. Because the appearance of the modes of the family with nodes occurs at lower values of $\langle \Delta n \rangle$ with the increase of the core thickness, the waveguide with the 800-nm-thick core supports many of these modes for high values of $\langle \Delta n \rangle$.

Moreover, we notice that the first fundamental node-less symmetric mode has quite elevated effective index in the waveguides with a thin core [for $d = 100$ nm (see Fig. 7.43) its effective index is $\beta \approx 4.4$]. With the increase of the core thickness, the effective index of this fundamental mode decreases [for $d = 800$ nm (see Fig. 7.46) its effective index is $\beta \approx 3.76$] and converges for high thicknesses to the value of the effective index of a plasmon on a single metal/dielectric interface. On the contrary, the first antisymmetric mode with one node appears for very low values of β for waveguides with a thin core ($d = 200$ nm, see Fig. 7.44) and its effective index increases with the increase of the core thickness to reach the single-interface limit in the waveguides with a very thick core [for $d = 800$ nm (see Fig. 7.46) its effective index is $\beta \approx 3.75$] (these observations are confirmed later in this section; see Fig. 7.50).

Here we will discuss the influence of the core thickness on the modes of the node-less family. For these modes with the increase of the waveguide thickness we also observe the decrease of the $\langle \Delta n \rangle$ threshold values for their appearance. The decrease of the threshold values can be very large for these

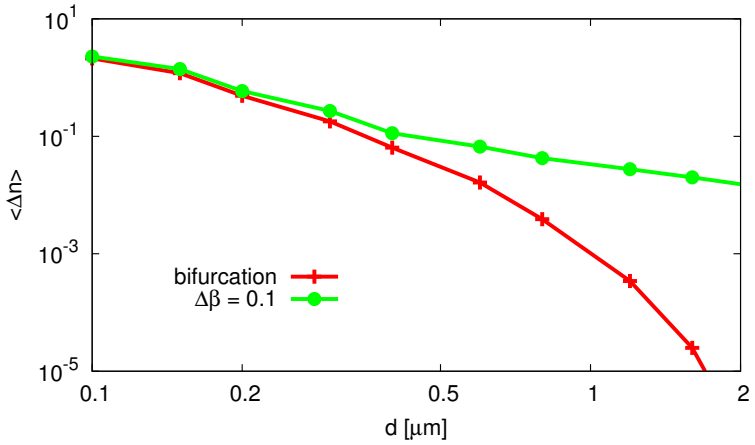

Figure 7.47: Average nonlinear index change $\langle \Delta n \rangle$ at the appearance of the asymmetric modes AS1 (bifurcation) (red +) and for $\Delta\beta = 0.1$ (green •) as a function of the core width d. All the other parameters of the nonlinear slot waveguides are identical to these in Table 7.1.

modes. The first asymmetric AS1 mode bifurcates at $\langle \Delta n \rangle \approx 1.5$ for the waveguide with $d = 100$ nm and at $\langle \Delta n \rangle \approx 0.004$ for the case of $d = 800$ nm. Similarly, the appearance of the higher-order modes SI and AS2 occurs for very high values of $\langle \Delta n \rangle$ and β for thin waveguides (not in the range of Fig. 7.43). Mode SI appears at $\beta \approx 14$ and $\langle \Delta n \rangle \approx 9$ for the waveguide with a 200-nm-thick core (top right corner in Fig. 7.44). In the case of $d = 800$ nm, modes SI and AS2 appear at $\langle \Delta n \rangle \approx 0.8$ which approximately ten times lower than for the waveguides with a core thickness $d = 200$ nm.

In order to sum up the observations made on the bifurcation threshold of the first asymmetric AS1 nonlinear mode, we present Fig. 7.47 that shows the dependency of the nonlinear index change $\langle \Delta n \rangle$ at which the first bifurcation occurs (red curve) on the width of the nonlinear slot waveguide core d. We notice that the thicker the core the lower the value of $\langle \Delta n \rangle$ where the bifurcation occurs. For $d \approx 1$ μm the bifurcation occurs at $\langle \Delta n \rangle \approx 10^{-3}$. For even thicker cores, the bifurcation occurs at $\langle \Delta n \rangle$ values as low as 10^{-5} which are realistic values for hydrogenated silicon [139]. The proper choice of the core thickness is important in order to obtain asymmetric solutions at low $\langle \Delta n \rangle$ values. Modifying the core thickness is a very effective way to lower the bifurcation threshold. In the structure studied here, the increase of the core thickness by a factor 20 allows us to reduce the bifurcation threshold by 5 orders of magnitude.

From the experimental point of view, it is also important to control the number of modes supported by the waveguide. In waveguides supporting a low number of modes the interpretation of the results may be simpler than in multi-mode waveguides. With the increase of the nonlinear core thickness, the number of modes supported be the nonlinear slot waveguides presented in Figs. 7.43–7.46 increases. Therefore, it is important to find a thickness that results in a good balance between the bifurcation threshold and the number of modes supported by the waveguide. These two parameters can be also tuned changing the permittivities of the core and the cladding (see Section. 7.1.7).

In experiments, it is important to be able to distinguish between the symmetric and asymmetric modes. The higher the asymmetry of the mode the easier it is to distinguish it from the symmetric one. Therefore, we look for the values of $\langle \Delta n \rangle$ for which the asymmetric modes becomes strongly asymmetric (here we assume that the mode is strongly asymmetric when the light intensity at one metal/dielectric interface is five times larger than at the second interface). Our study shows that it happens for $\langle \Delta n \rangle$ values approximately two times higher than the bifurcation threshold.

In Fig. 7.47, the value of $\langle \Delta n \rangle$ at which the difference between the propagation constants of the asymmetric AS1 mode and the symmetric S0 mode ($\Delta\beta = \beta_{\mathrm{AS1}} - \beta_{\mathrm{S0}}$) is equal to 0.1 is shown in green. This curve for low core thickness values follows the red curve for bifurcation point but for high thickness values decreases more slowly than the red curve.

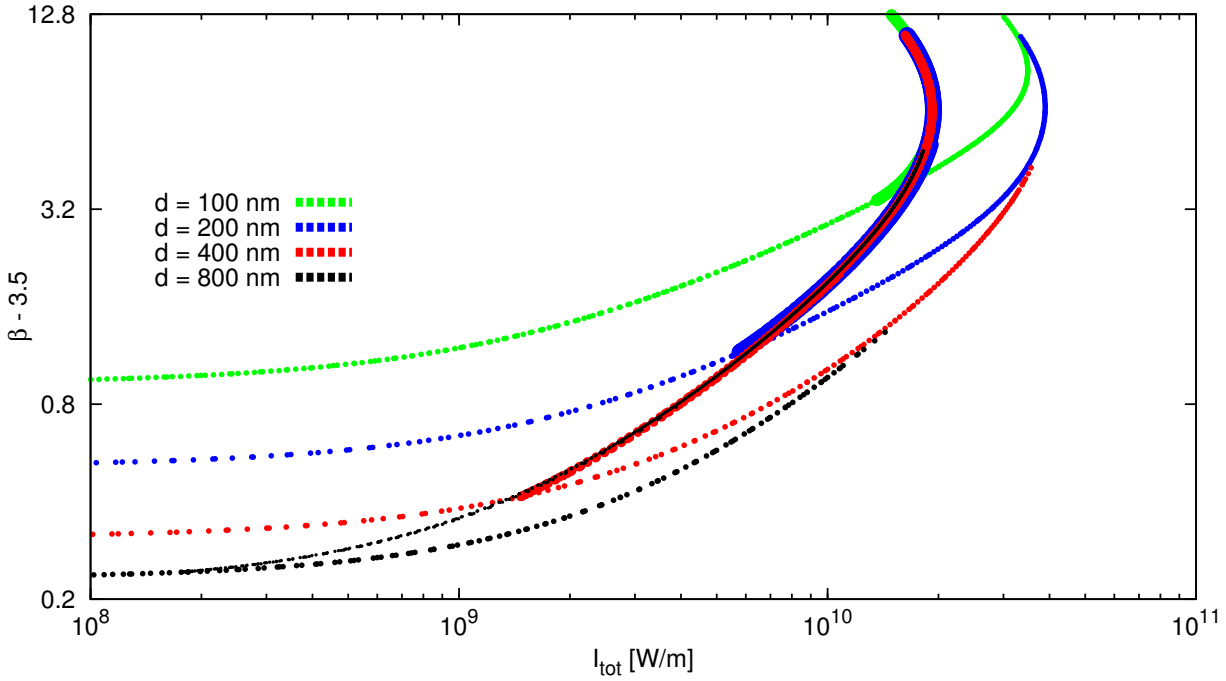

Figure 7.48: Locus of the asymmetric mode dispersion curves for various core widths d using the total intensity density [defined in Footnote 6 on Page 119] as abscissa. Only the first symmetric (thin curve) and asymmetric modes (thick curves, except for the case of $d = 800$ nm) are shown using one color per width. Both axes are in log scale.

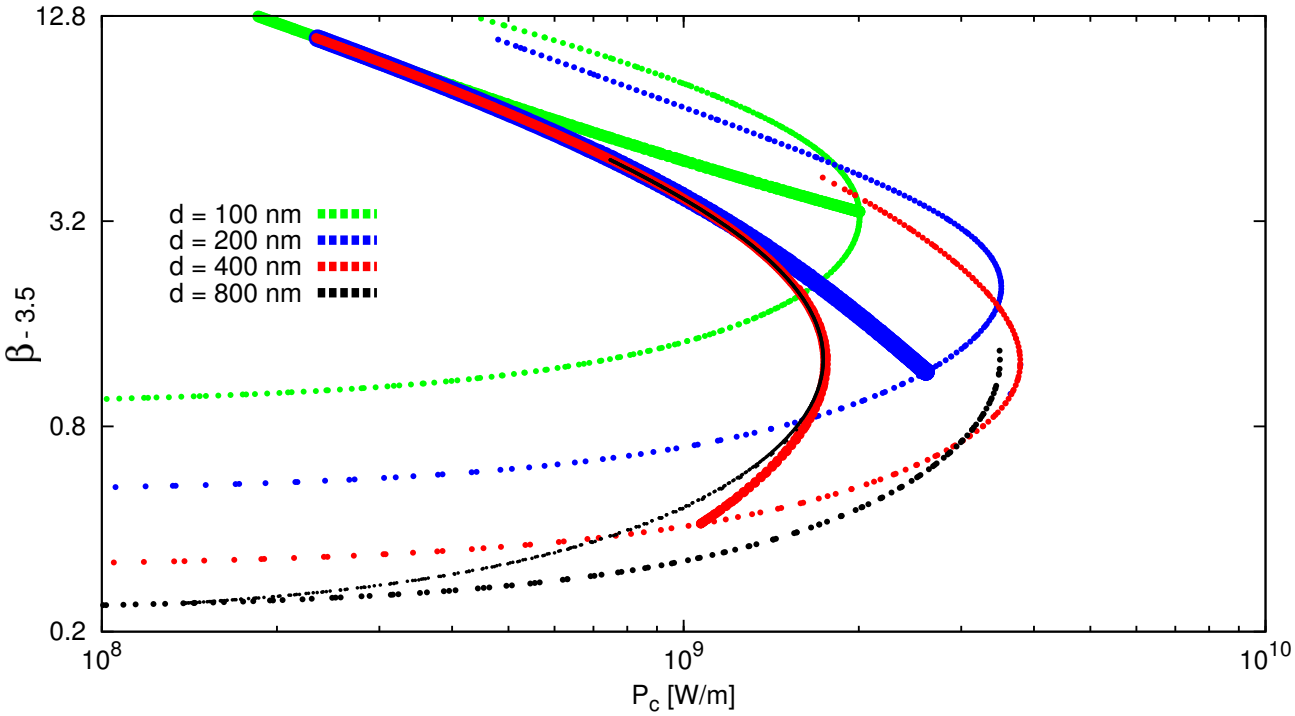

Figure 7.49: Locus of the asymmetric mode dispersion curves for various core widths d using the power density in the core [defined by Eq. (7.1.4)] as abscissa. Only the first symmetric (thin curve) and asymmetric modes (thick curves, except for the case of $d = 800$ nm) are shown using one color per width. Both axes are in log scale.

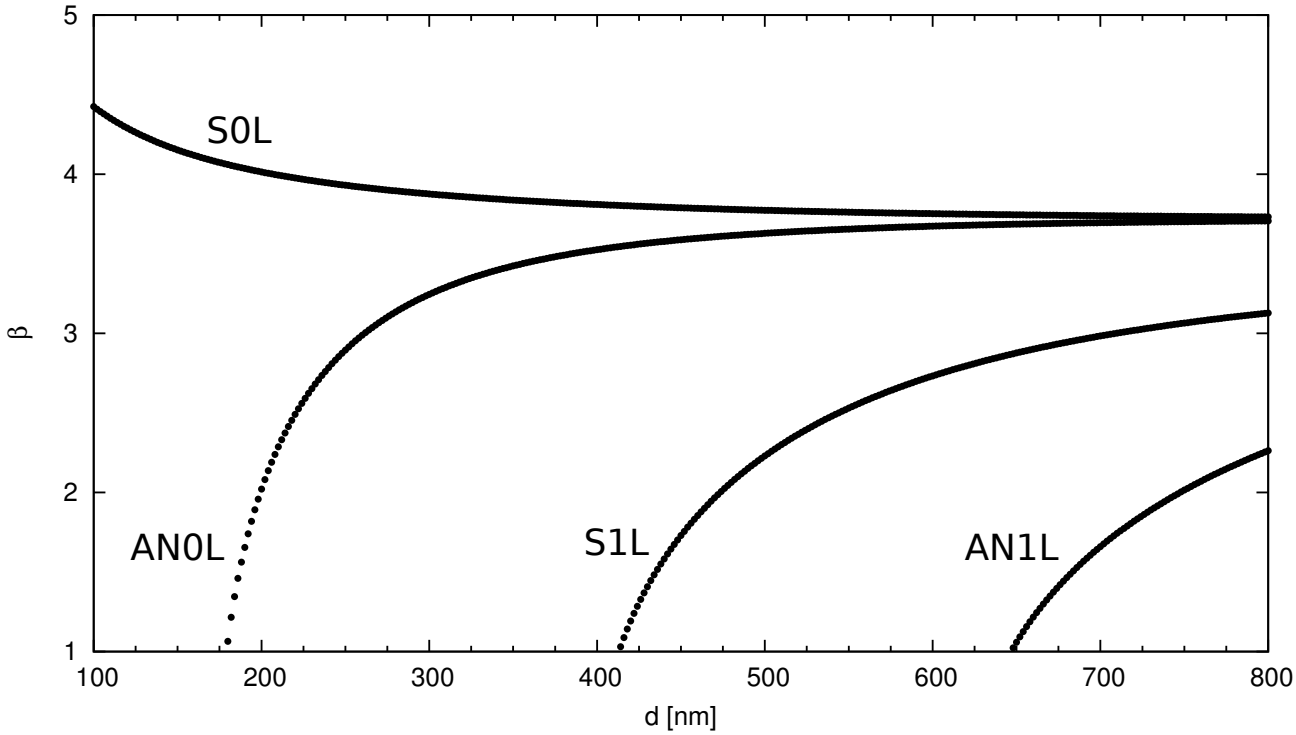

Figure 7.50: Dispersion diagram for the linear slot waveguide with identical parameters as our nonlinear slot waveguide showing the effective index of the mode as a function of the core thickness.

In Figs. 7.48 and 7.49, a direct comparison between the dispersion curves of the nonlinear slot waveguides with core thickness values 100 nm, 200 nm, 400 nm, and 800 nm is presented. Only the curves corresponding to the fundamental symmetric S0 mode and the first antisymmetric AS1 mode are shown. In Fig. 7.48, the total intensity density is used as abscissa and in Fig. 7.49, the power density in the core is used as abscissa. In both coordinates, we observe that for high values of the effective index of the asymmetric mode AS1, the dispersion curves of this mode in waveguides with different core thickness overlap. This is a consequence of the fact discussed in Section 7.1.4. For high values of the effective index β, the asymmetric modes AS1 are strongly localized on one of the core interfaces (see the third column in Fig. 7.15). Therefore, they resemble the modes obtained on a single metal/nonlinear dielectric interface and their dispersion relations can be approximated by the curve corresponding to the single-interface problem. As a result, the waveguide thickness does not have a strong influence on the dispersion curves of highly asymmetric modes. For all the values of the core thickness d, the dispersion curves of the asymmetric AS1 mode follow the dispersion curve for the single-interface case in the limit of high β values. For this reason the dispersion curves of the asymmetric AS1 modes in waveguides with different widths have a single locus for high β values.

In Figs. 7.43–7.46, the evolution of the nonlinear slot waveguide dispersion curves with the increase of the core thickness from 100 nm to 800 nm was shown. We observed that with the increase of the core thickness, the number of low-power modes (modes that exist in the low $\langle \Delta n \rangle$ limit) increases. The number of the low-power modes can be inferred from the linear studies of the metal slot waveguides. We consider a linear metal slot waveguide with the following parameters: metal permittivities $\epsilon_1 = \epsilon_3 = -90$ and the core refractive index is given by $n = n_0 = 3.46$ (compare with the parameters used for the nonlinear sot waveguides studied here presented in Table. 7.1 on Page 109). In Fig. 7.50, the dispersion relation for this waveguide is presented. The effective index of the modes β is shown as a function of the core thickness d. For low values of the core thickness, only the fundamental symmetric node-less linear mode of the slot waveguide exists. With the increase of the core thickness (around $d = 160$ nm), a second mode appears (antisymmetric mode with one node). Further increase of the thickness causes higher-order linear modes to appear with alternating symmetry and increased by one number of nodes.

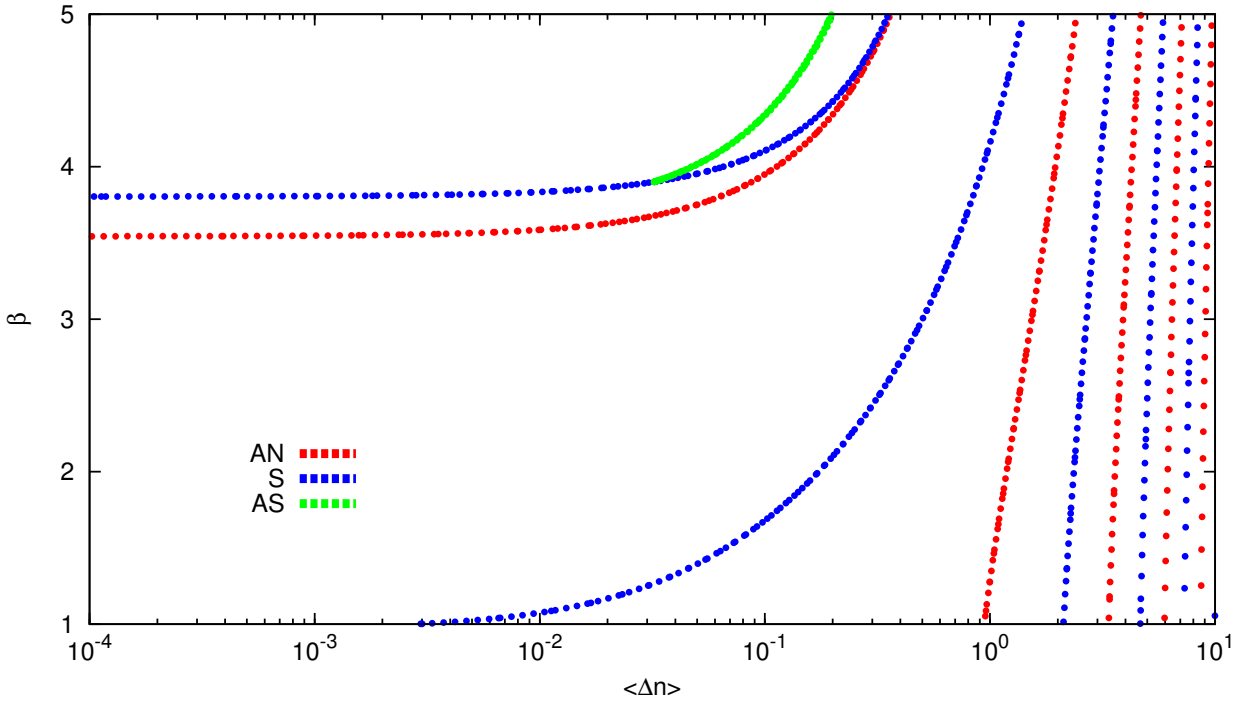

Figure 7.51: Dispersion diagram for the nonlinear slot waveguide with the core thickness $d = 412$ nm.

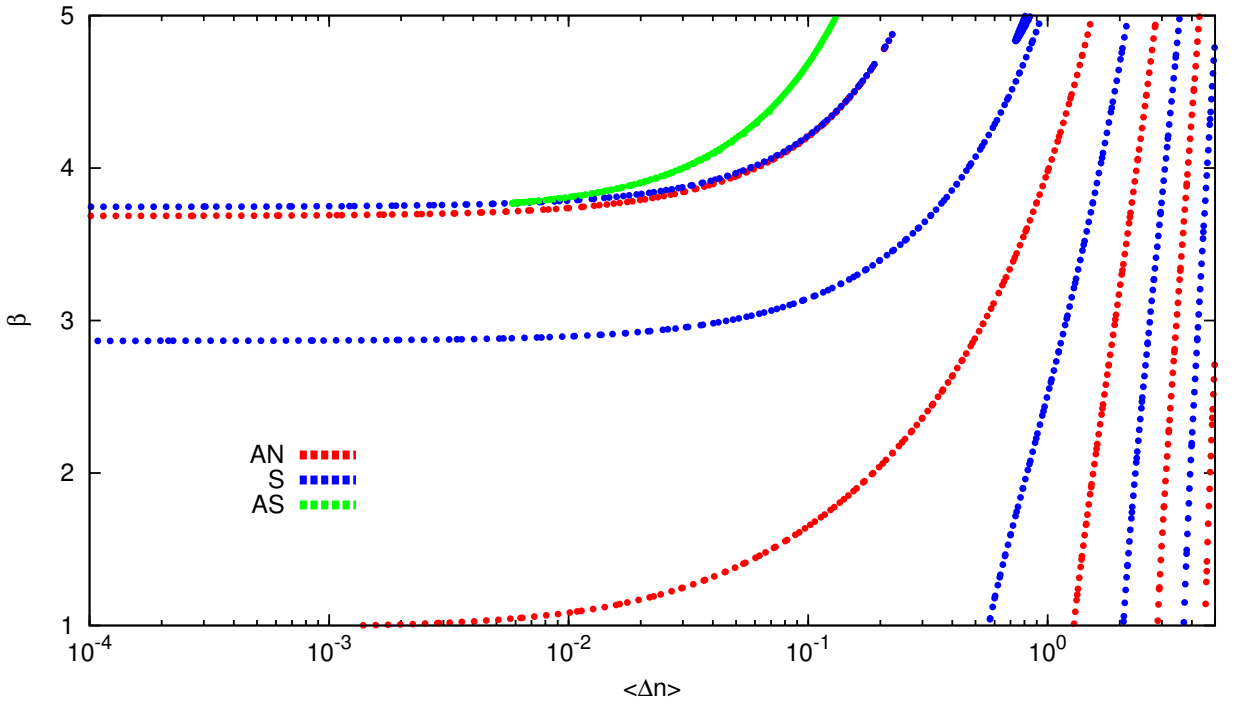

Figure 7.52: Dispersion diagram for the nonlinear slot waveguide with the core thickness $d = 646$ nm.

With the increase of the thickness, the two first modes become closer in terms of the effective index and converge to the effective index of a linear plasmon on a single metal/dielectric interface. From this plot, we can easily read how many low-power modes will the nonlinear slot waveguide support for a given thickness and what will be their effective index in the low $\langle \Delta n \rangle$ limit.

In Figs. 7.43–7.46, we have seen that with the increase of the waveguide thickness, the nonlinear modes of the nonlinear family with nodes were appearing at lower $\langle \Delta n \rangle$ and finally became low-power

modes, if the core thickness was large enough. Using this effect, we can tune the core thickness in such a way that a nonlinear mode with nodes will appear for very low $\langle \Delta n \rangle$ values. If we choose the thickness of the nonlinear core slightly below the cut-off of the third mode ($d_{\text{cut-off}} = 413$ nm) in the linear case, this mode will appear for low value of $\langle \Delta n \rangle$ in the nonlinear slot waveguide. The dispersion relation for the nonlinear slot waveguide with the core thickness $d = 412$ nm is presented in Fig. 7.51. In this case, the nonlinear symmetric mode with two nodes appears for $\langle \Delta n \rangle \approx 0.003$ which is approximately twenty times lower than in the case of the core thickness $d = 400$ nm (see Fig. 7.45)

Figure 7.52 presents the dispersion curves obtained for the nonlinear slot waveguide with the thickness of 646 nm which is sightly below the cut-off thickness for the linear antisymmetric mode with three nodes (the fourth mode in Fig. 7.50). In this case the nonlinear antisymmetric mode with three nodes appear for $\langle \Delta n \rangle \approx 0.0015$.

Summarizing this section, we have observed that the core thickness is one of the parameters of the nonlinear slot waveguide that can be tuned to obtain low-power nonlinear solutions. Figure 7.47 shows that the bifurcation threshold for the node-less symmetric mode AS1 can be efficiently reduced by a proper choice of the core thickness. The results presented in Figs. 7.51 and 7.52 prove that fine tuning of the core thickness allows us to observe the genuine nonlinear modes of the family with nodes at low $\langle \Delta n \rangle$ levels ($\langle \Delta n \rangle < 0.005$).

7.1.7 Permittivity contrast study

In Section 7.1.6, we have studied the influence of the width of the nonlinear slot waveguide core on the dispersion for this this structure. Here we will discuss the influence of the permittivity contrast between the dielectric core and the metal cladding on the nonlinear dispersion diagrams of symmetric nonlinear slot waveguides.

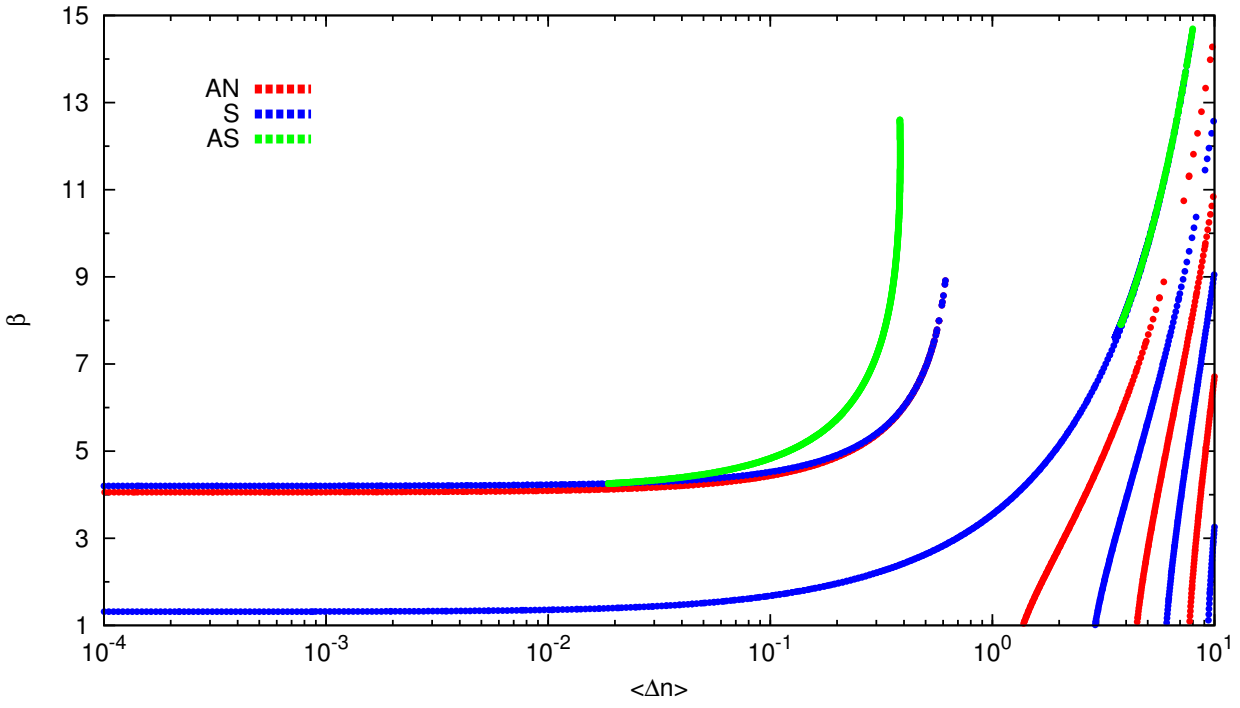

Figure 7.53: Dispersion diagram for the nonlinear slot waveguide with the metal cladding permittivities $\epsilon_1 = \epsilon_3 = -40$. All the other parameters are identical to these in Table 7.1.

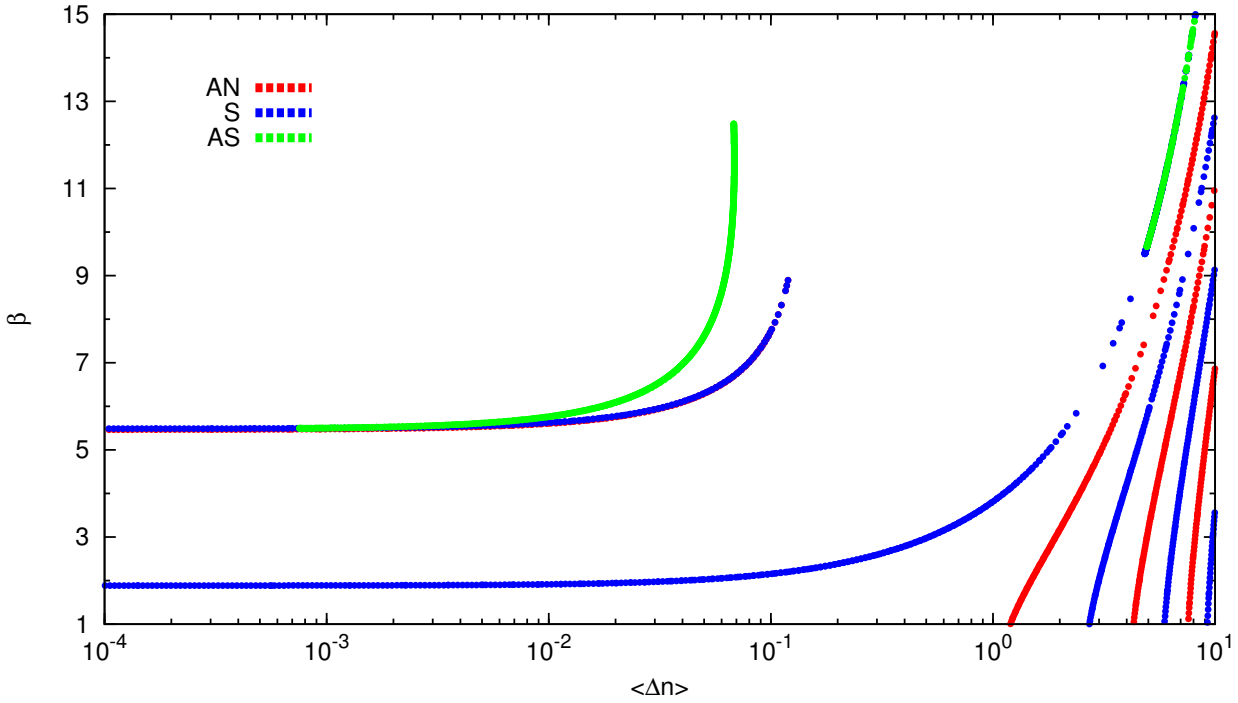

Figure 7.54: Dispersion relations for the nonlinear slot waveguide with the metal cladding permittivities $\epsilon_1 = \epsilon_3 = -20$. All the other parameters are identical to these in Table 7.1. The dispersion curve of the low-power AN0 mode (red curve for low $\langle \Delta n \rangle$) lays slightly below the curve corresponding to the low-power S0 mode (top blue curve starting at low $\langle \Delta n \rangle$).

Influence of the cladding permittivity

First, we will discuss the influence of the metal cladding permittivity on the nonlinear dispersion diagrams of nonlinear slot waveguides. The dispersion plots for the nonlinear slot waveguides with identical parameters as these used in Section 7.1.1 (see Table 7.1) but with increased values of the metal cladding permittivity will be studied. Figures 7.53 and 7.54 show the dispersion relations obtained using the IM for the waveguides with metal cladding permittivity $\epsilon_1 = \epsilon_3$ equal to -40 and -20, respectively (for comparison with the case of $\epsilon_1 = \epsilon_3 = -90$ studied in Section 7.1.1 see Fig. 7.3). In the dispersion curves for both configurations presented in Figs. 7.53 and 7.54, we observe three low-power modes, whereas the configuration with $\epsilon_1 = \epsilon_3 = -90$ supported only two low-power modes. The separation between the two first (with highest β values) low-power modes decreases with the increase of the metal cladding permittivity values.

Moreover, we observe that the cladding with higher permittivity allows us to reduce the $\langle \Delta n \rangle$ threshold values where the bifurcation of the AS1 mode occurs. For metals with permittivity equal to -40, the bifurcation occurs at $\langle \Delta n \rangle \approx 0.02$, which is 4 times lower than in the case of $\epsilon_1 = \epsilon_3 = -90$. For metals with permittivity equal to -20, the bifurcation occurs at $\langle \Delta n \rangle \approx 8 \cdot 10^{-4}$, which corresponds to the reduction of the bifurcation threshold by two orders of magnitude with respect to the configuration with $\epsilon_1 = \epsilon_3 = -90$. The dependency of the AS1 mode bifurcation threshold $\langle \Delta n \rangle_{\text{th}}$ on the metal cladding permittivity is illustrated in Fig. 7.55. Looking at this plot, we conclude that with the increase of the metal cladding permittivity (decrease of its absolute value) the bifurcation threshold of the AS1 mode decreases. This decrease is slow in the range of high index contrast between the metal and the nonlinear dielectric permittivity. Although, for $|\epsilon_1| = |\epsilon_3|$ close to $\epsilon_{l,2}$ the decrease of the bifurcation threshold is more rapid. Changing the metal permittivity from -20 to -15 allows us to decrease the bifurcation threshold by almost two order of magnitudes. For the metal cladding permittivity $\epsilon_1 = \epsilon_3 = -15$ the bifurcation threshold is at the level of $\langle \Delta n \rangle \approx 10^{-5}$. This is four orders of magnitude lower than for the $\epsilon_1 = \epsilon_3$ from the range $[-400, -90]$, for which the bifurcation occurs

at $\langle \Delta n \rangle \approx 0.1$. For telecommunication wavelengths, it is difficult to find a metal with a permittivity equal to -15. Such high permittivity values might be obtain with hybrid metal/dielectric materials.

Influence of the core refractive index

Next, we will study the influence of the change of the core refractive index on the dispersion diagram of the symmetric nonlinear slot waveguide. From the analysis presented in Section 7.1.5, we have seen that there is a direct link between the nonlinear modes from the family with nodes and the linear modes of the waveguides with higher refractive indices of the core. For the nonlinear waveguide with parameters presented in Table 7.1, the first nonlinear mode from this family (S1) appeared for the nonlinear index modification $\langle \Delta n \rangle \approx 0.08$ [see Figs. 7.3(a) or 7.39]. Moreover, from the analysis of

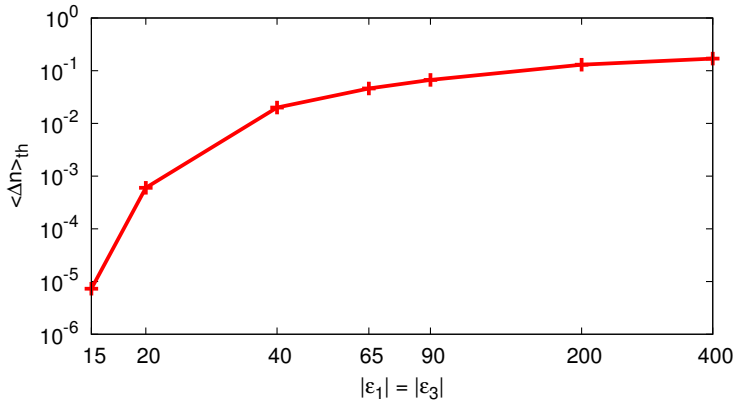

Figure 7.55: Average nonlinear index change at the appearance of the asymmetric AS1 modes $\langle \Delta n \rangle_{\mathrm{th}}$ as a function of the absolute value of the metal cladding permittivity of the symmetric waveguide $|\epsilon_1| = |\epsilon_3|$. All the other parameters of the nonlinear slot waveguide are identical to these in Table 7.1.

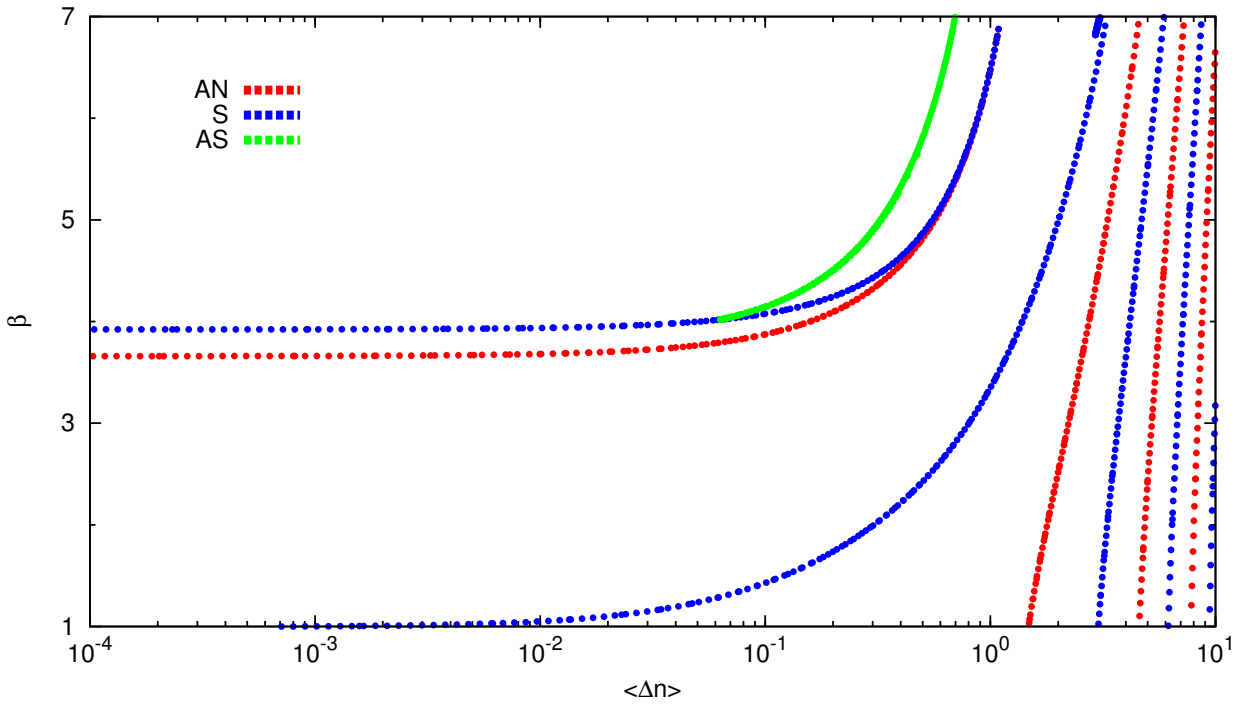

Figure 7.56: Dispersion relations for the nonlinear slot waveguide with the core linear refractive index $\sqrt{\epsilon_{l,2}} = 3.556$. All the other parameters are identical to these in Fig. 7.39.

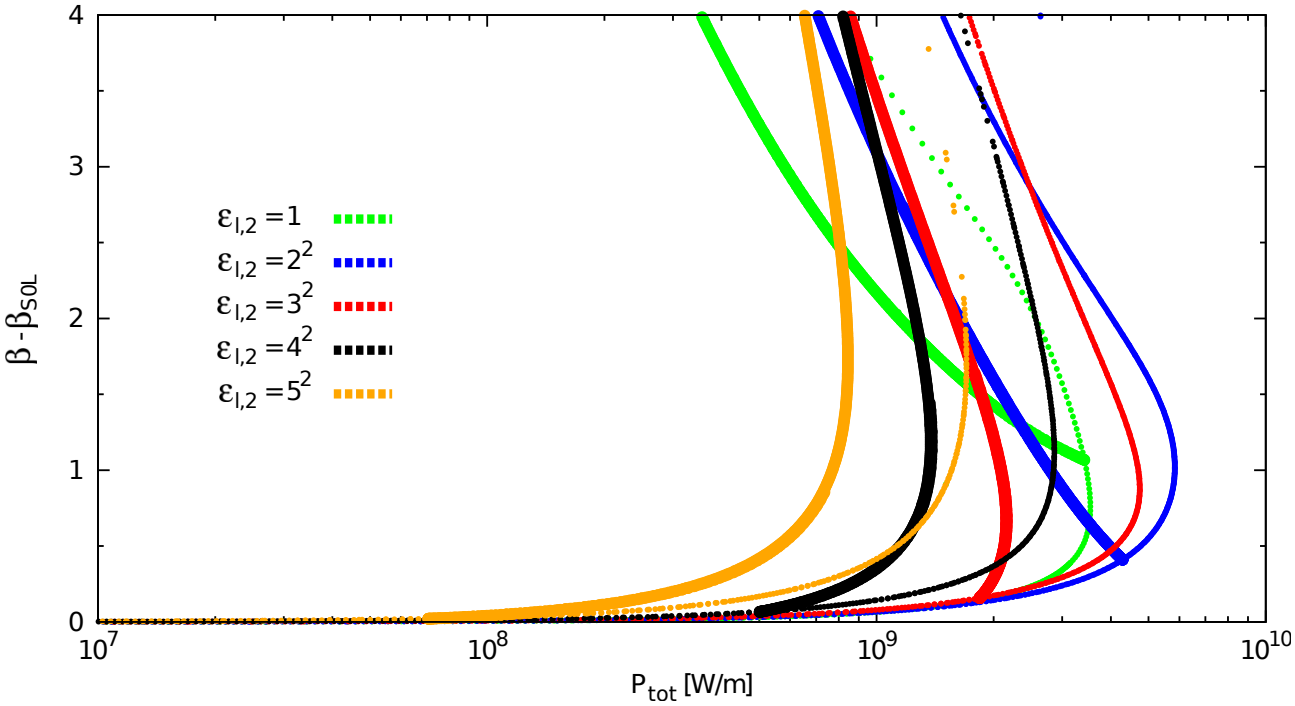

Figure 7.57: Dispersion curves of the fundamental symmetric node-less mode S0 (thin curve) and the first-order asymmetric node-less mode AS1 (thick curves) for symmetric nonlinear slot waveguides with parameters presented in Table 7.1, but varied linear part of the permittivity of the nonlinear core $\sqrt{\epsilon_{l,2}}$. The effective indices normalized with the effective index of the linear fundamental mode S0L ($\beta - \beta_{\mathrm{S0L}}$) are presented as a function of total power density P_{tot} [defined by Eq. (7.1.6)].

the linear structure, we have seen that the linear counterpart of the S1 mode appears at the value of $\Delta n_{\mathrm{lin}} \approx 0.097$ (see Fig. 7.40). Here we will study a nonlinear slot waveguide with the linear part of the refractive index of the core $\sqrt{\epsilon_{l,2}} = 3.556$. This value of the linear part of the refractive index of the nonlinear core is 0.096 higher than linear part of the core refractive index of the nonlinear waveguide studied in Sections 7.1.1–7.1.5. This value is chosen in such a way that in the linear regime (low intensity and low $\langle \Delta n \rangle$) only two low-power modes are supported by the nonlinear slot waveguide. This means that we still operate below the cut-off refractive index at which the symmetric mode with two nodes appears in the linear waveguide (see Fig. 7.40).

The dispersion diagram for the nonlinear slot waveguide with $\sqrt{\epsilon_{l,2}} = 3.556$ is presented in Fig. 7.56. We see that now the first nonlinear mode of the family with nodes (S1) appears at a very low value of the nonlinear index modification ($\langle \Delta n \rangle \approx 7 \cdot 10^4$). This result shows that a precise choice of the nonlinear core refractive index allows us to obtain nonlinear effects in nonlinear slot waveguides at low power levels. In Fig. 7.56, we observe also a slight decrease of the bifurcation threshold of the first asymmetric mode AS1. The AS1 mode bifurcates here at $\langle \Delta n \rangle \approx 0.061$, whereas for waveguides with the core index $\sqrt{\epsilon_{l,2}} = 3.46$ [see Figs. 7.3(a) or 7.39] this bifurcation occurs at $\langle \Delta n \rangle \approx 0.067$.

It is interesting to remind that, in the case of changing the permittivity contrast by varying the metal cladding permittivity, we observed a decrease of the bifurcation threshold for the AS1 mode with the decrease of the permittivity contrast between the cladding and the core permittivity (see Fig. 7.55). The example presented in Fig. 7.56 illustrates a different type of behavior. Here, with the increase of the permittivity contrast between the cladding and the core, the bifurcation threshold of the AS1 mode decreased. This type of behavior is studied in more detail in Fig. 7.57. In this figure, the plots of the dispersion curves for the nonlinear slot waveguides with different linear parts of the core refractive index $\sqrt{\epsilon_{l,2}}$ are presented. All the other parameters are identical to these in Table 7.1. The dispersion diagrams presented in Fig. 7.57 show only the two modes of interest: the fundamental symmetric mode S0 and the first-order asymmetric mode AS1. The effective index of the modes in

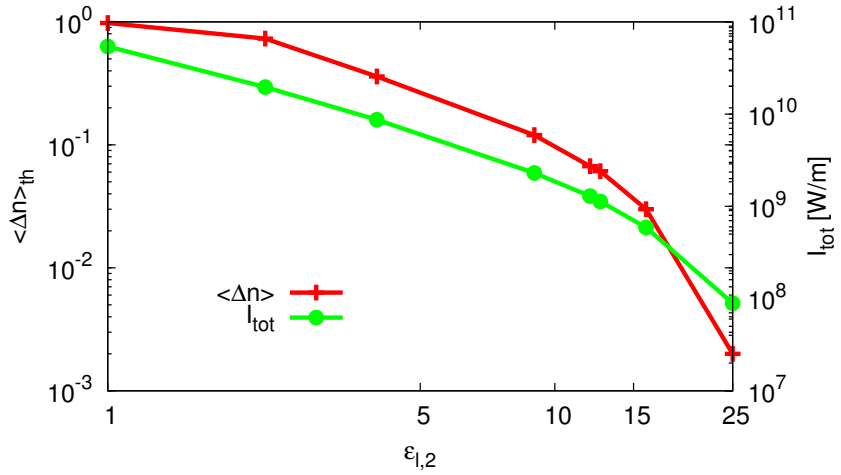

Figure 7.58: Bifurcation threshold for the AS1 mode expressed as the average nonlinear index change $\langle \Delta n \rangle_{\mathrm{th}}$ (red curve, left vertical axis) and as the total intensity density I_{tot} (green curve, right vertical axis), both shown as a function of the linear part of the nonlinear core permittivity $\epsilon_{l,2}$. All the other parameters of the symmetric nonlinear slot waveguide are identical to these in Table 7.1.

each of the waveguides is normalized in the following way. The value of the effective index of the fundamental linear symmetric mode S0L is subtracted from the effective indices of the nonlinear modes. This normalization causes all the flat low-power parts of the dispersion curves to overlap at $\beta - \beta_{\mathrm{S0L}} \approx 0$. In Fig. 7.57, the total power density of the mode P_{tot} [defined by Eq. (7.1.6)] is used as abscissa.

From Fig. 7.57 we obtain the total power density P_{tot} at which the bifurcation of the asymmetric mode AS1 occurs. For core indices $\sqrt{\epsilon_{l,2}}$ between 1 and 2, the bifurcation threshold (expressed as the total power density) increases with the increase of $\sqrt{\epsilon_{l,2}}$.[10] For higher values of $\sqrt{\epsilon_{l,2}}$ (from 2 to 5) the bifurcation threshold decreases with the increase of $\sqrt{\epsilon_{l,2}}$. The behavior of the bifurcation threshold expressed as the averaged nonlinear index modification $\langle \Delta n \rangle$ and as the total intensity density I_{tot} is presented in Fig. 7.58. In these coordinates the increase of the linear part of the core permittivity $\epsilon_{l,2}$ (and therefore the linear part of the core index $\sqrt{\epsilon_{l,2}}$) is accompanied by a monotonous decrease of the bifurcation threshold.

From Fig. 7.58 we notice that the increase of $\epsilon_{l,2}$ from 1 to 25 results in the decrease of the bifurcation threshold by approximately three orders of magnitude (both when the bifurcation threshold is expressed as $\langle \Delta n \rangle$ and I_{tot}).[11] From Fig. 7.57, we notice that the same change of $\epsilon_{l,2}$ results in the decrease of the bifurcation threshold expressed as P_{tot} by less than two orders of magnitude. This is connected with the non-monotonous behavior of the bifurcation threshold in the $\beta(P_{\mathrm{tot}})$ dispersion diagram.

We conclude that changing the permittivity contrast by varying the linear part of the nonlinear core permittivity, has opposite effect than changing the permittivity contrast by varying the metal cladding permittivity. In the former case, the bifurcation threshold decreases with the increase of the permittivity contrast (see Fig. 7.58). In the latter case, as seen in Fig. 7.55, the bifurcation threshold increases with the increase of the permittivity contrast.

It is interesting to discuss the relative positions of the bifurcation points visible in Fig. 7.57. In the previous considerations we were mainly interested in the bifurcation points associated with the birth of

[10] This conclusion is confirmed by the study of the nonlinear waveguide with $\sqrt{\epsilon_{l,2}} = 1.5$ (data not shown in Fig. 7.57 for the clarity of the plot). The total power density threshold increases form ≈ 3.5 GW/m for $\sqrt{\epsilon_{l,2}} = 1$ to ≈ 4.8 GW/m for $\sqrt{\epsilon_{l,2}} = 1.5$. The points corresponding to this configuration are shown in Fig. 7.58.

[11] The intensity threshold for the appearance of higher-order node-less modes (modes SI and AS2) also decreases with the increase of the linear part of the nonlinear core permittivity $\epsilon_{l,2}$ (data not shown). The decrease in this case is slower. The bifurcation threshold for the SI and AS2 modes decreases from $\langle \Delta n \rangle \approx 5$ for $\epsilon_{l,2} = 1$ to $\langle \Delta n \rangle = 1.5$ for $\epsilon_{l,2} = 5^2$.

the asymmetric AS1 modes. This type of bifurcation (where a new doubly degenerate branch appears) is called Hopf bifurcation [155]. Another type of bifurcation occurs at the points on the dispersion curves corresponding to a local maximum or minimum of the total power density of the modes (for example at point $\beta = 1$ and $P_{\text{tot}} \approx 6$ GW/m in Fig. 7.57). In the vicinity of such bifurcation points dispersion curves have parabolic shape. This type of bifurcation is called fold bifurcation [155]. In Fig. 7.57 we observe that for $\epsilon_{l,2} = 1$ (green curves) the Hopf bifurcation lays above (in terms of β) the fold bifurcation. For higher values of $\epsilon_{l,2}$, the Hopf bifurcation point is located below the fold bifurcation. The change of the order of bifurcations may influence the mode stability, as it is discussed in Chapter 8.

7.2 Asymmetric structures

In Section 7.1, we have comprehensively discussed dispersion diagrams and mode profiles in symmetric nonlinear slot waveguide structures. In this section, we will discuss the influence of the nonlinear slot waveguide asymmetry on the dispersion curves. The asymmetry is introduced by sandwiching the nonlinear core by metals with different values of the permittivity on both sides. Asymmetric nonlinear slot waveguide structures have not been studied before in literature. Here we present the analysis of these structures for the first time.

7.2.1 Dispersion diagrams

Figure 7.59 presents the nonlinear dispersion diagram obtained using the IM for the structure with the following parameters: core permittivity $\epsilon_{l,2} = 3.46^2$, the second-order nonlinear refractive index (see Page 11 for its definition) $n_2^{(2)} = 2 \cdot 10^{-17}$ m^2/W, core with $d = 400$ nm, metal permittivities $\epsilon_1 = -110$, $\epsilon_3 = -90$ at a free-space wavelength $\lambda = 1.55$ μm. These parameters are identical to these for the structure studied in Section 7.1 except for the metal permittivities (compare with Table 7.1). Here the permittivity of the left metal layer is decreased to -110 making the structure asymmetric.

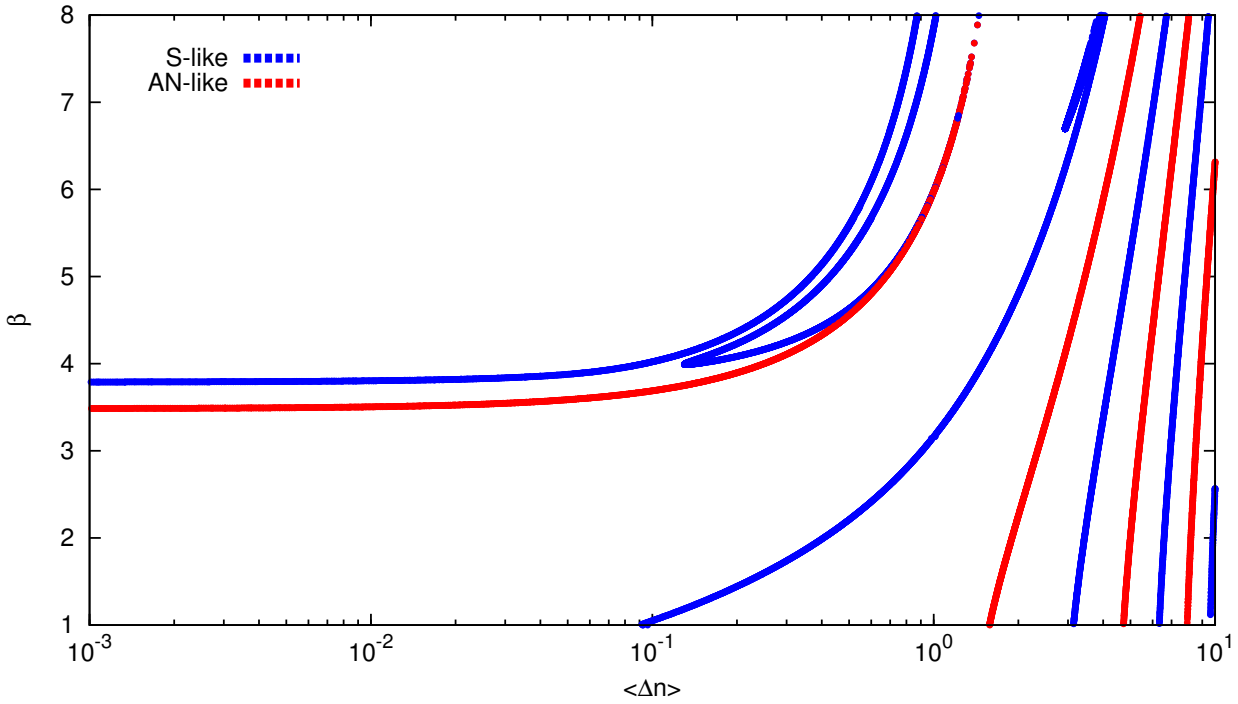

Figure 7.59: Dispersion diagram $\beta(\langle \Delta n \rangle)$ obtained using the IM for the asymmetric structure with $\epsilon_1 = -110$ and $\epsilon_3 = -90$ (for the scheme of the structure see Fig. 6.1). Blue curves correspond to the modes for which $\text{sgn}[E_0] = \text{sgn}[E_d]$ and red curves correspond to the modes for which $\text{sgn}[E_0] \neq \text{sgn}[E_d]$. Compare this dispersion diagram for the asymmetric structure with the dispersion diagram for the symmetric structure presented in Fig. 7.3.

In the asymmetric structure only asymmetric modes are present. However, in the dispersion diagram shown in Fig. 7.59, we divide the modes in two groups: modes that resemble the antisymmetric modes of the symmetric structure for which $\mathrm{sgn}[E_0] \neq \mathrm{sgn}[E_d]$ (red curve labeled AN-like) and modes that resemble the symmetric or asymmetric modes of the symmetric structure for which $\mathrm{sgn}[E_0] = \mathrm{sgn}[E_d]$ (blue curve labeled S-like).

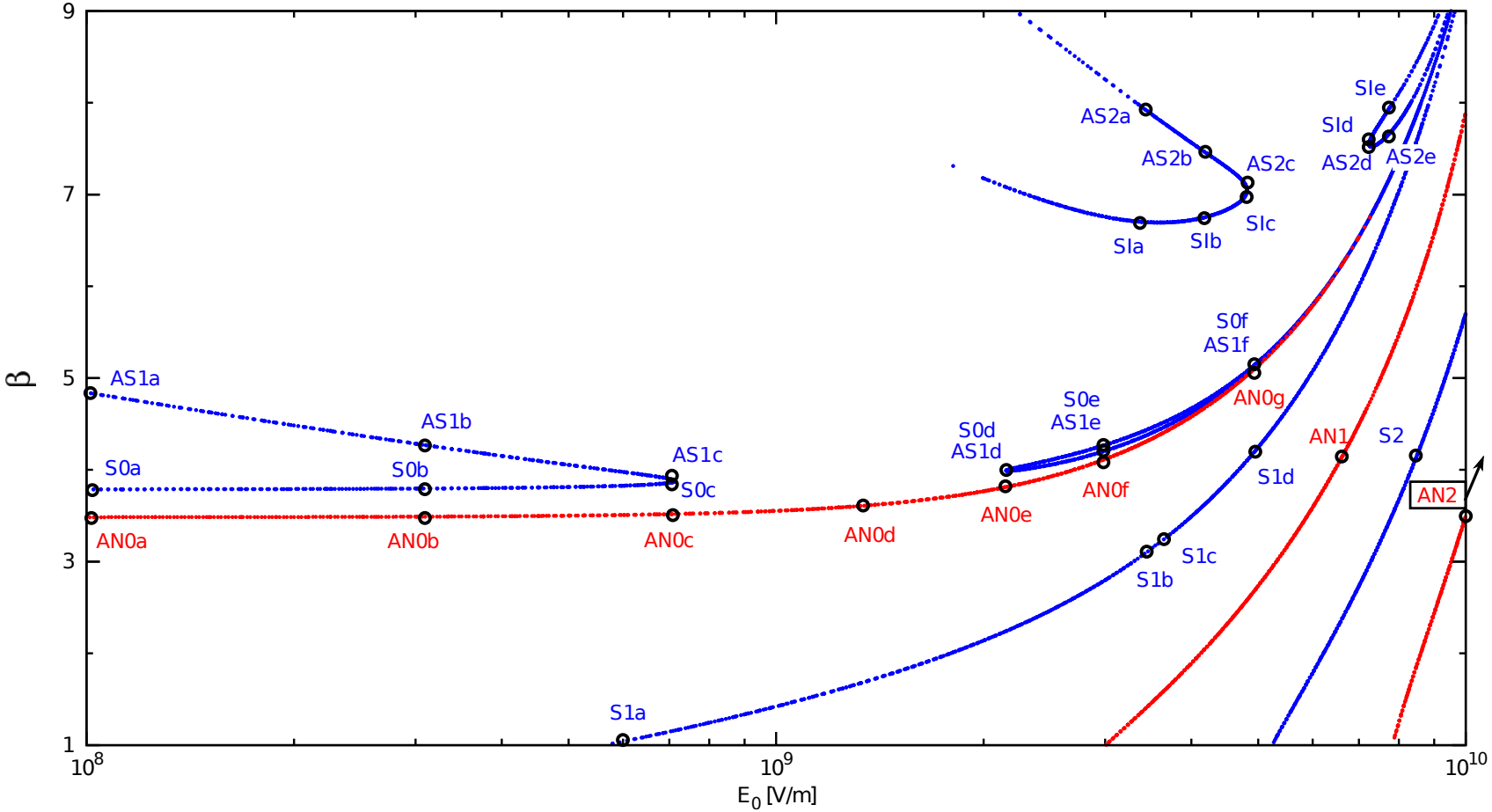

Figure 7.60: Dispersion curves $\beta(E_0)$ for the asymmetric structure with $\epsilon_1 = -110$ and $\epsilon_3 = -90$. Labeled points on each of the dispersion curves are used in the following to analyze mode transformation along the dispersion curves. Compare this dispersion diagram for the asymmetric structure with the dispersion diagram for the symmetric structure presented in Figs. 7.11 and 7.12.

We compare the nonlinear dispersion curves for the asymmetric structure presented in Fig. 7.59 with the dispersion curves obtained for the symmetric structure shown in Fig. 7.3. We notice that the dispersion curves for the symmetric and antisymmetric modes from the family with nodes did not change much. The number of modes and the character of their dispersion curves is conserved. The main difference between the dispersion curves of the asymmetric and symmetric structures can be observed for the symmetric and asymmetric modes of the node-less family. The asymmetry of the structure lifts the double degeneracy of the asymmetric branch AS1 (see green curve in in Fig. 7.3). This branch splits into two branches (see Fig. 7.59). One of them (the branch with higher effective indices β) is a continuation of the symmetric-like fundamental mode (blue curve) that starts for small averaged nonlinear index modification $\langle \Delta n \rangle$ levels. The second branch lays along the first one but has slightly higher power levels (branch with lower β values). The degeneracy of the higher-order asymmetric modes is also lifted by the asymmetry of the structure. These branches also split into two separate branches, similar to the case the AS1 mode. It is difficult to observe this effect in Fig. 7.59, where the averaged nonlinear index modification is used as abscissa (even enlarging the region of interest), because the two dispersion curves into which dispersion curves of the higher-order asymmetric mode split lay very close to each other. The degeneracy lift of the AS2 mode can be however observed from the dispersion curve $\beta(E_0)$ presented in Fig. 7.60, where the effective index is shown as a function of the field intensity at the left core interface. As discussed later in this section, in these coordinates the separation of the SI and AS2 curves reflects the degeneracy lift of the AS2 mode.

In Fig. 7.60, the nonlinear dispersion curves $\beta(E_0)$ for the asymmetric structure are shown [for comparison with the dispersion curve of the symmetric nonlinear slot waveguide see Fig. 7.9(b) or Figs. 7.11 and 7.12]. The points indicated on these curves correspond to the field plots presented in Figs. 7.61 and 7.63–7.65. The points are labeled with analogy to the names of the modes of the symmetric structure. For example, point S0e in Fig. 7.60 lays on the dispersion curve that corresponds to the curve named S0 in the case of the symmetric structure (see Figs. 7.11 and 7.12). It does not mean that the S0 mode of the asymmetric structure is symmetric (it is asymmetric). This asymmetric mode is denoted by S0, because its field profiles and their transformation along the dispersion curve are similar to the S0 mode of the symmetric structure.

7.2.2 Field profiles

At first, we discuss the transformation of the field profiles along the nonlinear dispersion curves labeled AN0, S0 and AS1 in Fig. 7.60. The magnetic field profiles corresponding to the points with these labels are presented in Fig. 7.61. The field profiles are ordered by increasing E_0 values and in each subplot, the value of E_0 is identical for all the three modes [except in subplot (d) where only one mode exists]. The AN0 branch is continuous and we find points of this branch for every used value of E_0. The S0 and AS1 dispersion curves are discontinuous. There is a gap separating the two branches of each of these curves. For the E_0 values inside this gap, the modes S0 and AS1 do not exist. Moreover, this gap becomes broader with the increase of the metal permittivity contrast $|\epsilon_1 - \epsilon_3|$. This gap is visible only in the dispersion curves where the effective index of the modes is plotted as a function of the total electric field intensity on the interface with the lower permittivity [here E_0 is taken at the interface between the nonlinear core and the metal with lower permittivity (equal to -110)]. For comparison, the dispersion diagram $\beta(E_d)$ for this structure is presented in Fig 7.62. In dispersion diagrams where the total electric field amplitude at the interface between the core and the metal with higher permittivity [here E_d is taken at the interface with the metal with $\epsilon_3 = -90$, which is higher than $\epsilon_1 = -110$], there is no gap in the S0 and AS1 dispersion curves. In the dispersion plot $\beta(E_d)$ presented in Fig. 7.62, we can observe that in these coordinates, the dispersion curves of the two symmetric-like modes (blue curves) starting at low values of E_d do not intersect. The corresponding curves in the symmetric structure (S0 and AS1 curves) shown in Figs. 7.9(b) or 7.11 intersect at the bifurcation point of the AS1 mode. In Fig. 7.62, the fact that these two curves do not intersect indicates that the degeneracy of the AS1 mode is lifted.

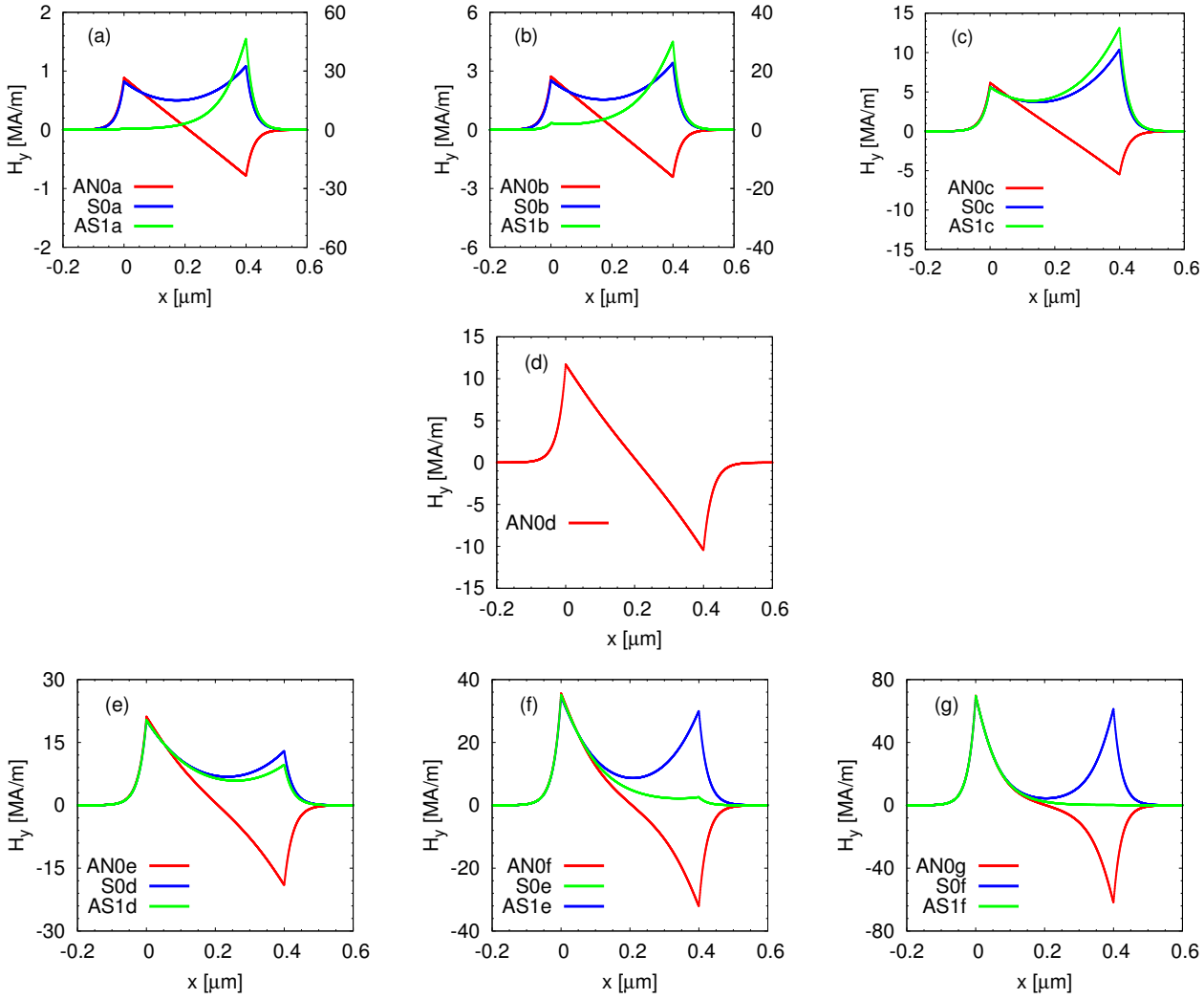

Figure 7.61: Profiles of magnetic field component H_y for the symmetric-like modes S0 (blue) and AS1 (green) and the antisymmetric-like AN0 (red) mode. The subplots present the transformation of the field profiles with the increase of the E_0 values. The label of the point corresponding to each profile is indicated in the subplot legend. The labeled points are indicated in Fig. 7.60. The scale in all the subplots is not kept identical in order to facilitate the observation of the field profile changes. In subplots (a) and (b) the AS1 mode is plotted using a second y axis (the right one). The E_0 value of all the modes in each of the subplots is identical.

Due to the presence of the gap in the dispersion curves S0 and AS1 presented in Fig. 7.60, both the S0 and AS1 dispersion curves are separated into two branches. At low values of E_0, the low β branch (S0) with the increase of the E_0 value becomes closer (in terms of β) to the high β branch (AS1). These branches finally merge into one point and vanish (directly above the points S0c and AS1c). The second branches of S0 and AS1 dispersion curves reappear for higher values of E_0. These branches start at one point (directly below the points S0d and AS1d), and with the increase of E_0, they first separate and then become close again for very high values of E_0. In the high E_0 range (above the gap), the dispersion curve S0 mode lays above the curve corresponding to the AS1 mode.

In Fig. 7.61(a)–(c), the transformation of the AN0, S0, and AS1 modes is presented for the branches laying below the gap. For low E_0 values, the AS1 mode is highly asymmetric and localized mainly on the right interface (between the core and the metal with higher permittivity $\epsilon_3 = -90$). The S0 mode is slightly asymmetric and localized more on the same interface as the AS1 mode. The AN0 mode is also slightly asymmetric but its asymmetry is so small that it is difficult to notice in the plot. With

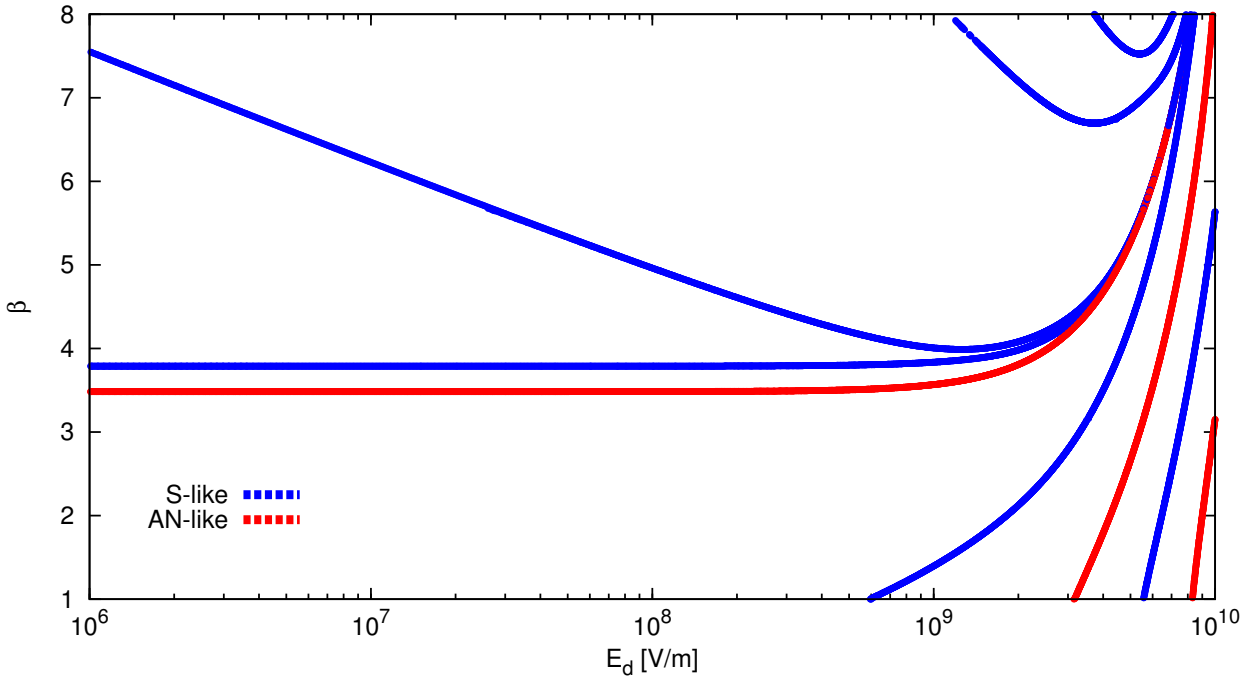

Figure 7.62: Dispersion curves $\beta(E_d)$ for the asymmetric structure with $\epsilon_1 = -110$ and $\epsilon_3 = -90$.

the increase of E_0 the AS1 mode becomes more symmetric. On the contrary, the asymmetry of the S0 mode increases with the increase of E_0. In Fig. 7.61(c), the profiles of these modes are shown for the value of E_0, where two branches almost merged to one point. We observe that for this value of E_0, the magnetic field profiles of S0 and AS1 modes are very similar.

In the gap only, the AN0 mode exists and its magnetic field profile is shown in Fig. 7.61(d). At the beginning of the high E_0 branches, the profiles of S0 and AS1 modes are similar again. They are asymmetric and localized on the left interface (between the core and the metal with the lower permittivity $\epsilon_1 = -110$). For the region above the gap, with the increase of the E_0 values, the AS1 field profile becomes more asymmetric and the S0 mode becomes more symmetric. The AN0 mode transforms its field profile slightly with the increase of E_0 but does not change its asymmetry. For AN0 mode, the total electric field amplitude at the interface with the metal with lower permittivity E_0 is always slightly higher than E_d. For very high E_0 values, the profiles of AN0, S0, and AN1 modes in the left half of the waveguide become very similar [see Fig. 7.61(g)]. The intensity profiles (data not shown) of AN0 and S0 mode also become very similar. These two facts explain why the dispersion curves of these three modes become close to each other for high values of E_0 (see Fig. 7.60).

Here we discuss the dispersion curves of the symmetric-like modes SI and AS2. From the dispersion diagram $\beta(E_0)$ presented in Fig. 7.60, we notice that here there is a gap separating left and right parts of these curves. For the values of E_0 below the gap ($E_0 < 5 \cdot 10^9$ V/m), the SI curve lays below the AS2 curve. With the increase of E_0, the separation between these two curves decreases and directly above points SIc and AS2c these curves merge into one point and vanish. Above the gap ($E_0 > 7 \cdot 10^9$ V/m), the SI dispersion curve lays above the AS2 curve.

The appearance of the gap between the SI and AS2 dispersion curves [on the plots where effective index β is plotted as a function of the total electric field amplitude at the interface between the core and the metal with lower permittivity (in our case E_0)] is the indication of the degeneracy lift of the asymmetric AS2 mode. In symmetric structures (where the dispersion curves of the asymmetric mode AS2 are doubly degenerate, see Figs. 7.11 and 7.12) the AS2 and SI curves intersect at the point of the bifurcation of the AS2 mode.

The magnetic field profiles corresponding to the transformation of the SI and AS2 modes along their nonlinear dispersion curves are presented in Fig. 7.63. The subplots are ordered by increasing

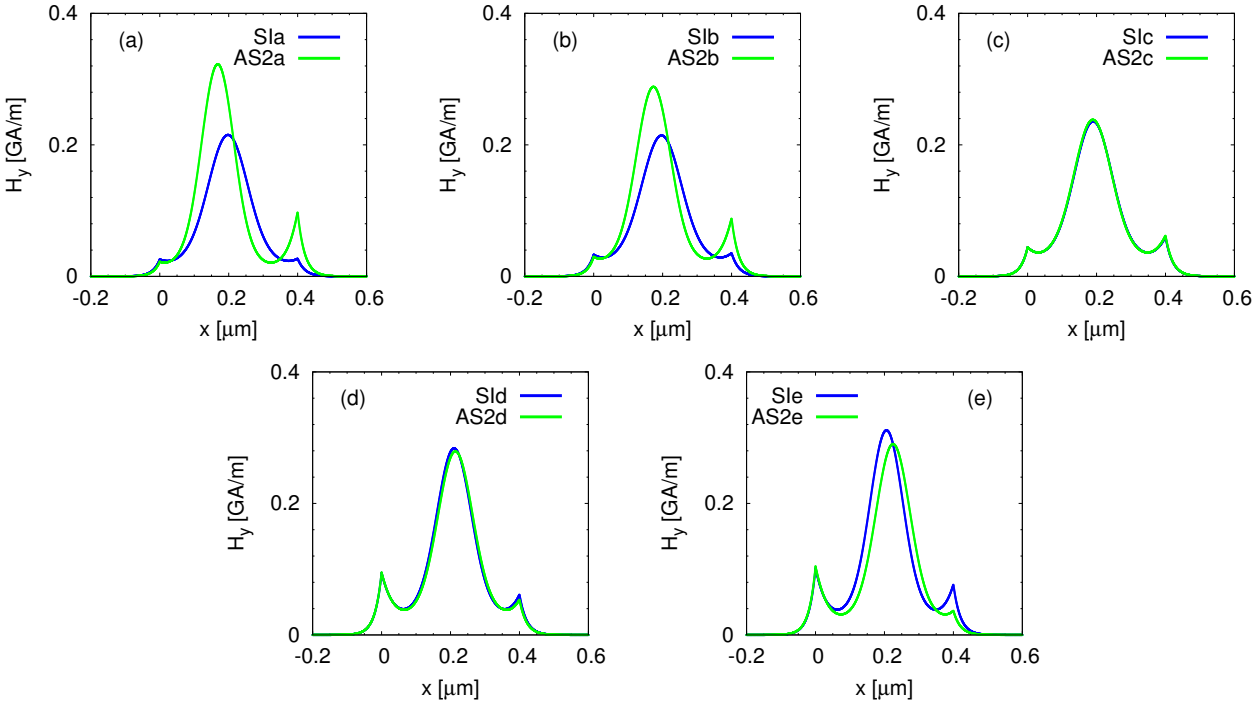

Figure 7.63: Profiles of magnetic field component H_y for the symmetric-like SI (blue) and AS2 (green) modes. The subplots present the transformation of the field profiles with the increase of the E_0 values. The labels of points corresponding to each profile is indicated in subplots legends. The labeled points are indicated in Fig. 7.60. The scale in all the subplots is kept identical. The E_0 value of all the modes in each of the subplots is identical.

values of E_0 and in each of the subplots, the value of E_0 for both modes is identical. The field profiles corresponding to the points laying on the left branch of the SI dispersion curve (the first row in Fig. 7.63) are only slightly asymmetric and the field is slightly higher on the right core interface than on the left one. The asymmetry of the SI mode increases with the increase of E_0 value. On the contrary, the asymmetry of the AS2 modes laying on the left branch of the AS2 dispersion curve decreases with the increase of E_0. In subplot (c), the field profiles corresponding to points SIc and AS2c are shown. These points lay close to the place where the two dispersion curves merge into to one point and disappear. At this point, the field profiles of the SI and AS2 modes are identical. On the right branches of the SI and AS2 dispersion curves, the asymmetry of the SI mode decreases with the increase of E_0 and the asymmetry of the AS2 mode increases (see the second row in Fig. 7.63). The left side-lobe of these modes has higher amplitude than the right one. Figure 7.63(d) shows the field profiles corresponding to the points SId and AS2d. These points lay close to the point there the right branches of the SI and AS2 curves appear. The field profiles corresponding to the SId and AS2d points are very similar.

From the transformation presented in Fig. 7.63, we observe that the soliton peak of the SI mode is located very close to the core center in all the subplots. The soliton peak of the AS2 mode shifts from left interface [between the core and the metal with lower permittivity ($\epsilon_1 = -110$)] to right interface [between the core and the metal with higher permittivity ($\epsilon_3 = -90$)] with the increase of the E_0.

In Fig. 7.62, where the effective index β is plotted as a function of the total electric field amplitude at the interface between the core and the metal with higher permittivity (in our case E_d), the dispersion curves of the SI and AS2 modes do not intersect at any point (see top right corner of Fig. 7.62). In these coordinates, this is the indication of the degeneracy lift of the AS2 mode [compare with the degenerate symmetric case where the SI and AS2 dispersion curves intersect (Figs. 7.11 and 7.12)].

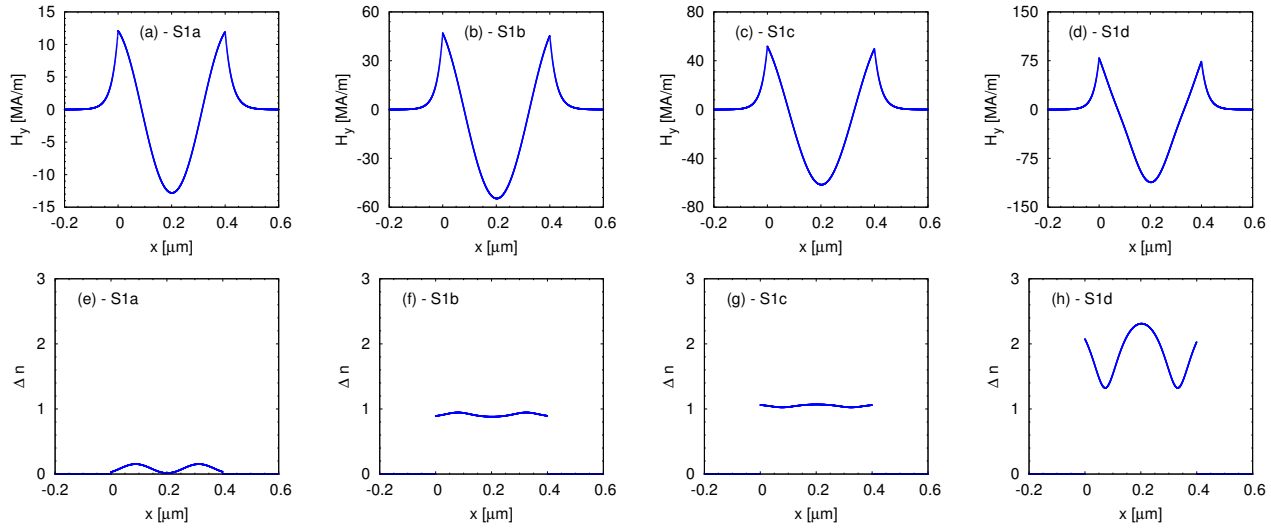

Figure 7.64: Profiles of (a)–(d) magnetic field component H_y and (e)–(h) nonlinear index modification for the symmetric-like S1 mode. The subplots present the transformation of the field profiles with the increase of the E_0 values. The labels of points corresponding to each profile is indicated in subplots legends. The labeled points are indicated in Fig. 7.60. The scale in each of the subplots presenting the magnetic field is different. In all the subplots presenting the nonlinear index modification the scale is kept identical.

In Fig. 7.64, the transformation of the S1 mode[12] along its dispersion curve is presented. The columns are ordered by increasing E_0 values. We observe that the field profile of the S1 mode is almost symmetric even if the structure is asymmetric. The magnetic field profile does not change much except for the increase of the amplitude. However, even these small changes in the magnetic field profile induce qualitative changes in profiles of the electric field components (data not shown) and in the nonlinear index modification profiles. The minima and maxima of the nonlinear index modification profiles switch positions with the increase of E_0, similar to the case of the S1 mode in symmetric nonlinear slot waveguides (see Fig. 7.25). In the second and the third column in Fig. 7.64, the field plots corresponding to the points located below and above the point where the nonlinear index modification has a flat profile. Below this point, there are two local maxima in the profile of Δn. Above this point these maxima transform into local minima.

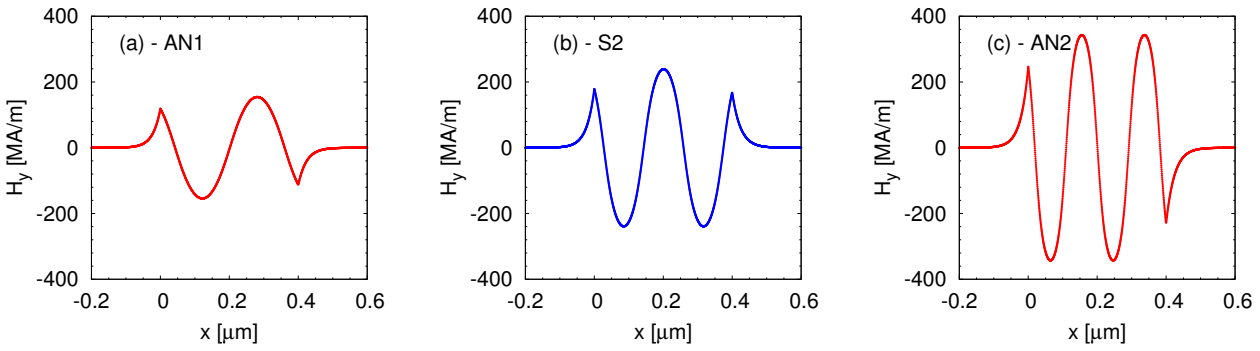

Figure 7.65: Profiles of magnetic field component H_y corresponding to points (a) AN1, (b) S2, and (c) AN2 in Fig. 7.60.

[12] We remind the reader that the S1 mode belongs to the family with nodes, whereas SI modes belongs to the node-less family.

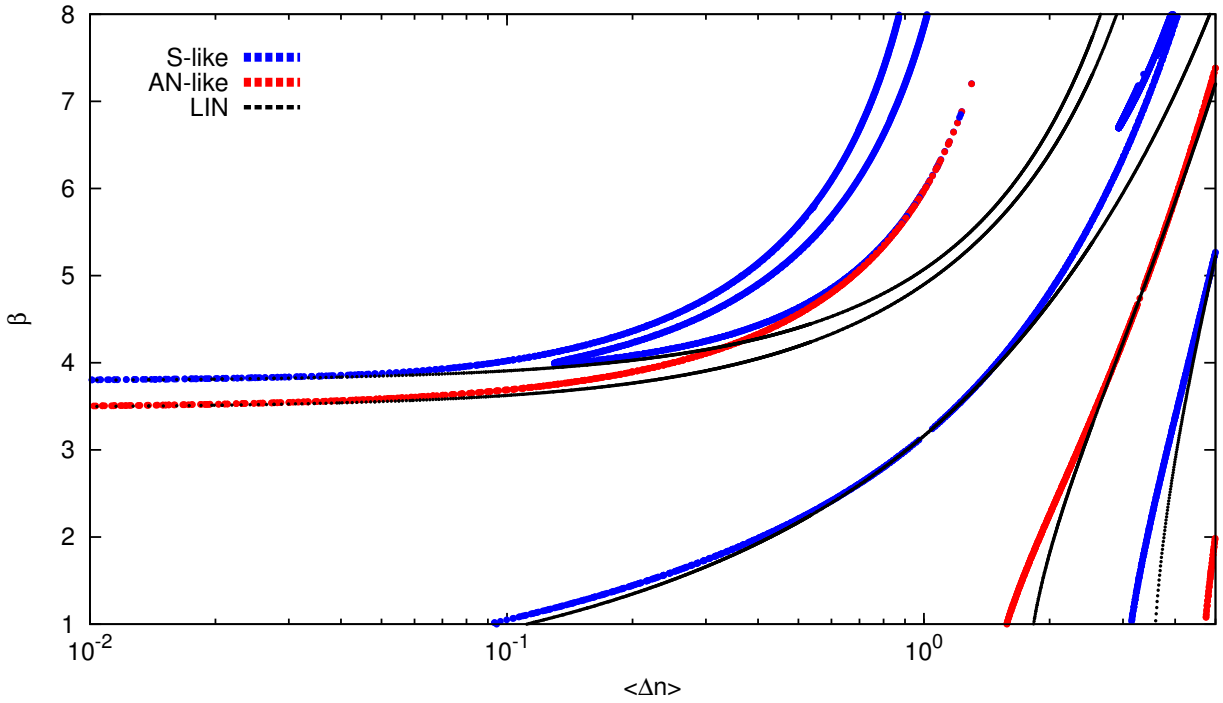

Figure 7.66: Comparison of the dispersion diagrams for the asymmetric nonlinear slot waveguide (with identical parameters as in Fig. 7.59 — blue and red curves) and the asymmetric linear slot waveguide (black curves). Both waveguides have cladding metals with $\epsilon_1 = -110$ and $\epsilon_3 = -90$. The value used as abscissa ($\langle \Delta n \rangle$) represents the averaged nonlinear index modification for the nonlinear slot waveguide and Δn_{lin} for the linear slot waveguide.

Figure 7.65 presents typical field profiles of the AN1, S2, and AN2 modes. We see that these modes resemble the respective modes in the symmetric structures discussed at the end of Section 7.1.2. Even if the structure discussed here is asymmetric, the asymmetry of these modes is very small and difficult to notice from the field plots. The transformation of the AN1, S2, and AN2 modes of the asymmetric nonlinear slot waveguide is very similar to the transformation of the corresponding modes in symmetric structures and therefore will not be described in this PhD manuscript.

Figure 7.66 presents a direct comparison of the dispersion curves of the asymmetric nonlinear slot waveguide (with identical parameters as in Fig. 7.59 — blue and red curves) and a corresponding linear asymmetric slot waveguide (black curves). The linear slot waveguide has the following parameters: $\epsilon_1 = -110$, $\epsilon_3 = -90$, and the linear core permittivity $\sqrt{\epsilon_{l,2}} = 3.46 + \Delta n_{\text{lin}}$. Figure 7.66 can be compared with Fig. 7.41, presenting a similar comparison for the symmetric nonlinear slot waveguide.

The comparison between the nonlinear and linear asymmetric slot waveguides presented in Fig. 7.66, shows that the nonlinear and linear dispersion curves of the higher-order modes from the family with nodes are alike. For asymmetric nonlinear slot waveguides, similar to the case of symmetric structures, there is one common point between the linear and the nonlinear dispersion curves for each of these modes. This point corresponds to the nonlinear mode with a flat nonlinear index modification distribution. All the nonlinear dispersion curves lay above their linear counterparts. Purely nonlinear modes of the node-less family (AS1, SI, and AS2) are not supported by the linear slot waveguide.

7.2.3 Permittivity contrast study

To finish our discussion of the asymmetric nonlinear slot waveguide properties, we compare the dispersion diagrams $\beta(\langle \Delta n \rangle)$ of the symmetric structure with these of the asymmetric structures. In Fig. 7.67, the dispersion plot of the symmetric structure ($\epsilon_1 = \epsilon_3 = -90$, see Fig. 7.3) is directly compared with the dispersion plot for the asymmetric structure ($\epsilon_1 = -110, \epsilon_3 = -90$, see Fig. 7.59).

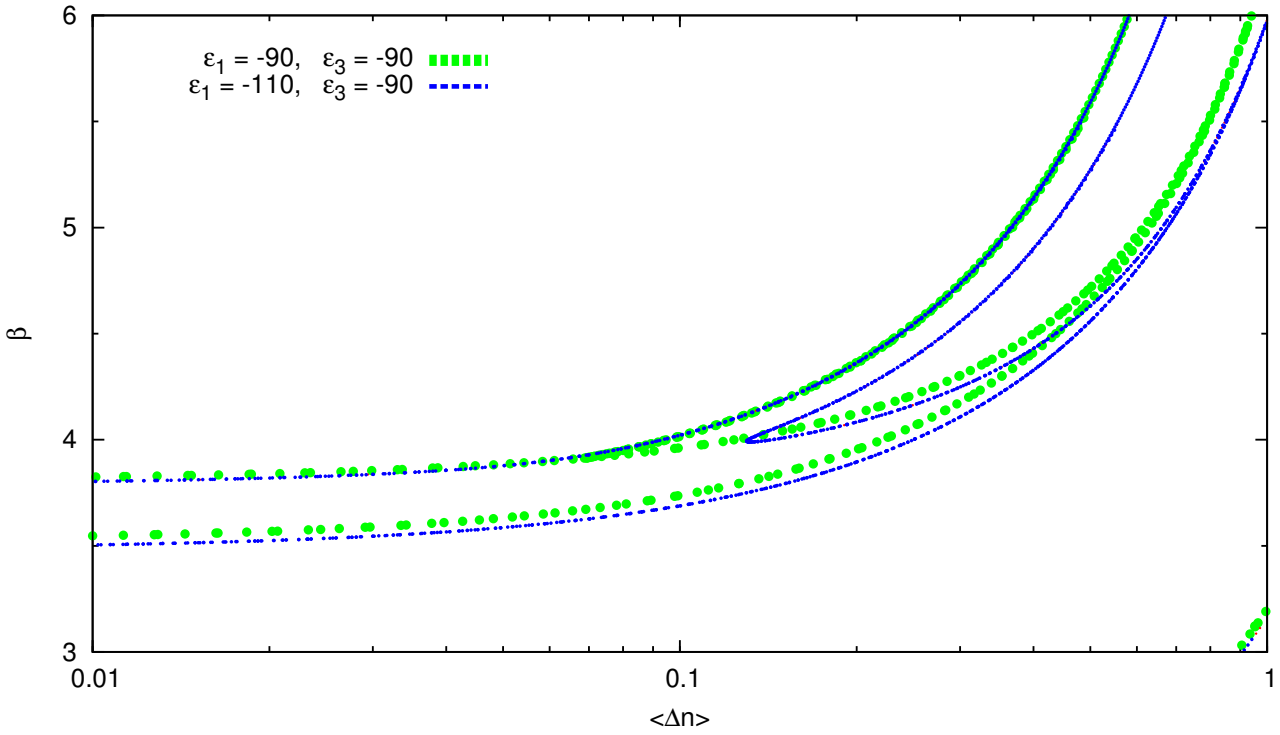

Figure 7.67: Dispersion curves of the asymmetric nonlinear slot waveguide with $\epsilon_1 = -110, \epsilon_3 = -90$ (blue curve) and the symmetric structure $\epsilon_1 = \epsilon_3 = -90$ (green curve).

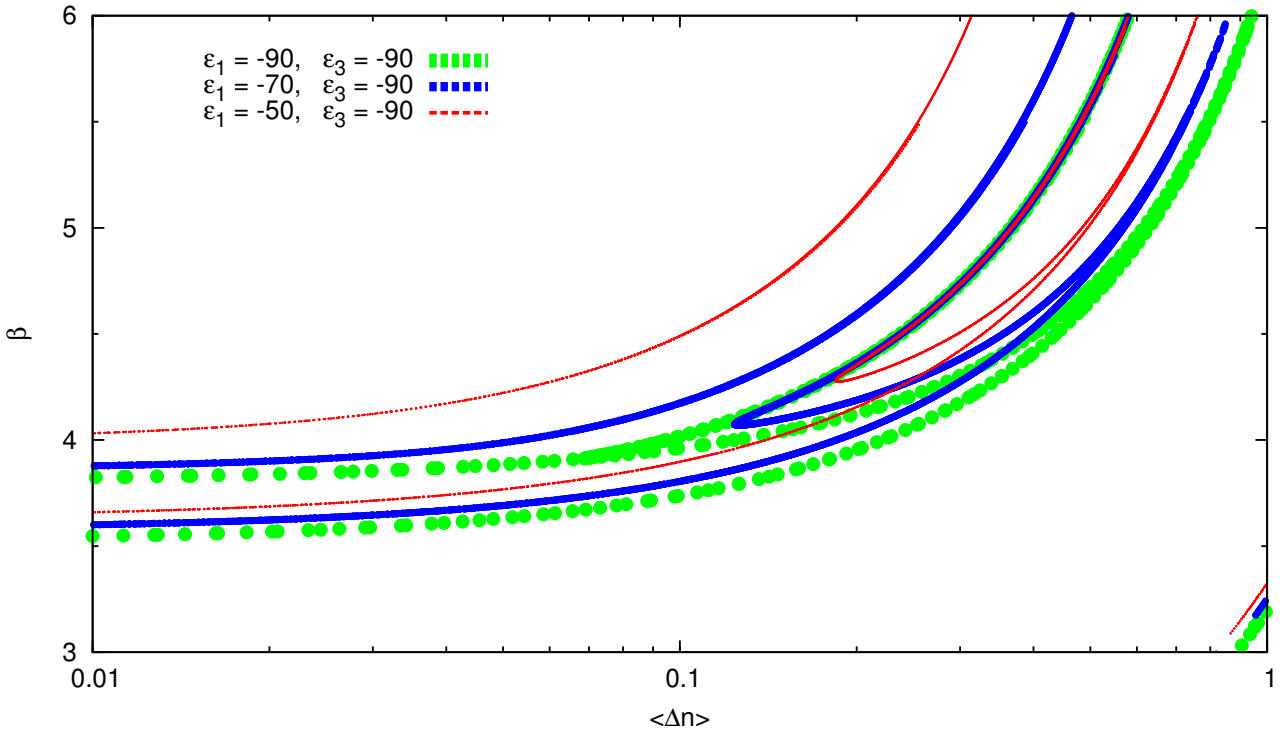

Figure 7.68: Dispersion curves of the asymmetric nonlinear slot waveguides with $\epsilon_1 = -70$ and $\epsilon_3 = -90$ (blue curve), $\epsilon_1 = -50$ and $\epsilon_3 = -90$ (red curve), and the symmetric structure $\epsilon_1 = \epsilon_3 = -90$ (green curve).

Only a vicinity of the bifurcation point of the AS1 mode is presented. We observe that for small averaged index modifications the dispersion curves of the two low-power modes are slightly modified due to the waveguide asymmetry. For higher values of $\langle \Delta n \rangle$, the dispersion curve of the fundamental mode (upper blue curve) exactly overlaps with the dispersion curve of the asymmetric mode of the symmetric structure. This is a consequence of the fact that, on this upper blue curve the field profiles are strongly localized on the interface with the metal with higher value of the permittivity [in this case $\epsilon_3 = -90$, see Figs. 7.61(a) and (b) for the field profiles]. These profiles resemble the profiles of the highly asymmetric modes of the symmetric structure [see Figs. 7.16(a) and (b)]. Therefore, we are not surprised that these two dispersion curves overlap. The second curve that results from the degeneracy lift of the asymmetric mode lays below (in terms of β) the dispersion curve (green curve) of the asymmetric mode AS1.

In Fig. 7.68, we present a comparison of the dispersion curves of the symmetric structure ($\epsilon_1 = \epsilon_3 = -90$, see Fig. 7.3) and the asymmetric structures, where one of the metal permittivity values is higher than in the case of the symmetric structure. The dispersion curves of the symmetric structure (green curves) are compared with these of the asymmetric structures with $\epsilon_1 = -70$, $\epsilon_3 = -90$ (blue curves), and $\epsilon_1 = -50$, $\epsilon_3 = -90$ (red curves).

In the case illustrated in Fig. 7.68, contrary to the one presented in Fig. 7.67, it is the lower (in terms of β) of the two curves that result from the lift of the degeneracy that overlap with the dispersion curve of the asymmetric modes of the symmetric structure. This lower curve corresponds to the modes that are localized on the interface between the core and the metal with permittivity equal to -90. For the structures studied in Fig. 7.68, $\epsilon = -90$ is the lowest cladding permittivity. For that reason, the dispersion curves corresponding to the mode localized on the interface with metal with lower permittivity, overlap with the dispersion curves of the symmetric structure.

Another effect that can be observed in Fig. 7.68, is that with the increase of the structure asymmetry $|\epsilon_1 - \epsilon_3|$ the separation of the two curves that appear as a result of the degeneracy lift, increases, as expected. In the limiting case $\epsilon_1 \to \epsilon_3$, these two curves merge into one doubly degenerate curve.

Chapter 8

Stability analysis

In Chapters 2 and 6, we have studied plasmon–soliton waves using different modal approaches. From both theoretical and practical points of view, the issue of the stability of these waves arises. In several works, the general problem of the stability of nonlinear waves was studied [6, 156, 157]. Despite an enormous interest in the stability properties of nonlinear waves over the last decades, there in no universal condition on the stability of nonlinear waves [153]. In most of the cases, the stability is studied numerically for each of the cases separately. Stability of nonlinear guided waves in fully dielectric structures was studied numerically in Refs. [26, 28, 35–37, 50, 158–160].

In structures made of metals and nonlinear dielectrics, due to the presence of media with negative permittivity, the problem of stability of plasmon–solitons is difficult to study even numerically. Only in Refs. [72, 82] the stability of plasmon–solitons at a single metal/nonlinear dielectric interface was analyzed, using numerical algorithms (like finite-difference time-domain — FDTD [161, 162]). The propagation of light in plasmonic couplers was studied using Fourier methods based on mode decomposition in linear [163] and nonlinear [164] regimes.

In this chapter, we make a first attempt to estimate the stability of the plasmon–soliton waves described in Chapters 2 and 6. In Section 8.1, we use the topological criterion presented in Ref. [153] that is based on the linear stability analysis [165] and the Vakhitov–Kolokolov criterion [166]. In Section 8.2, the stability properties of the fundamental symmetric mode and the first asymmetric mode of the nonlinear slot waveguide predicted theoretically will be confirmed by vector nonlinear propagation simulations from two different methods.

8.1 Theoretical arguments

The stability criterion presented in Ref. [153], is based only on the topology of the dispersion curves and the stability of the modes can be read by analyzing $\beta(I_{\mathrm{tot}})$ diagrams (where I_{tot} is the total intensity of the light in the waveguide defined in Footnote 6 on Page 119). This approach was confirmed in multiple settings dealing with purely dielectric structures, and there is a strong indication that it should be also effective in systems including metallic layers due to similar behavior of soliton families and similar structure of I_{tot} diagrams. First, we will recall the principle used to estimate the stability of nonlinear modes using the criterion from Ref. [153]. Then we will use this criterion to analyze the stability of the plasmon–solitons found in nonlinear slot waveguides.

The stability criterion derived in Ref. [153] uses several assumptions. It provides stability for the fundamental nonlinear modes[1] in structures composed of arbitrary nonlinear material distributed nonuniformly in the transverse direction. The derivation of the stability criterion from Ref. [153] is

[1] A nonlinear mode is defined as a linear mode of a linear (graded refractive index) waveguide that is induced by the light distribution of this mode. This self-coherent definition of nonlinear modes was first introduced in Ref. [4]. The fundamental mode of a linear waveguide is the one with the largest propagation constant and fields profiles that are nonzero at any finite distance (node-less mode).

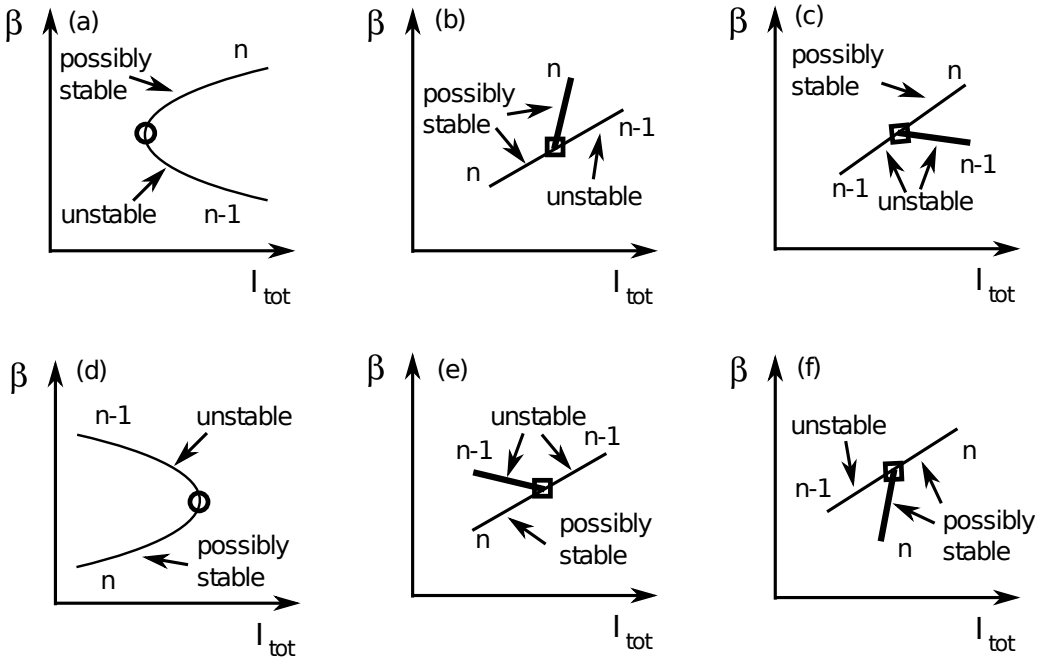

Figure 8.1: Rules of assigning the stability of the modes for (a), (d) the fold bifurcations (open circles) and (b), (c), (e), and (f) the Hopf bifurcations (open squares). Thick lines indicate a doubly degenerate branch (existence of two modes), whereas thin lines indicate non-degenerate dispersion curves.

conducted for scalar waves in the weak guiding approximation[2] for which the electric field satisfies the scalar wave equation. In our case, for the TM polarized waves, we will consider the approximation in which it is the magnetic field component that satisfies the scalar wave equation [Eq. (2.1.7a)]. We are fully aware of the fact that the metal/nonlinear dielectric structures studied here, in which plasmon–soliton waves propagate, do not fulfill the weak guiding approximation due to high permittivity contrast between the metal and the nonlinear dielectric. This means that the interesting nonlinear effect will occur for quite high nonlinear permittivity modifications. Despite that fact, we use here the criterion from Ref. [153], because the dispersion diagrams obtained for our structures have similar character to the dispersion plots of the fully dielectric structures where the criterion is applicable.

In Fig. 8.1, the rules to determine the stability of the modes derived in Ref. [153] are schematically shown. Consider an exemplary dispersion relation presented in Fig. 8.2. The stability of modes changes only at the bifurcation points [153]. To determine the stability, first we have to identify all the bifurcation points on the dispersion diagram $\beta(I_{\mathrm{tot}})$. In Fig. 8.2, the bifurcation points are located at the points where power has its local minima or maxima (points indicated by open circles — so-called fold bifurcation [155]) or where another branch appears [point indicated by an open square — so-called Hopf bifurcation associated with the birth of a doubly degenerate branch (to a single point on this branch correspond two asymmetric field profiles)]. Modes appear from or disappear at the points of bifurcation. The next step is to label the sections between the bifurcation points with numbers. The numbers are assigned in the following way. At first, we arbitrarily choose one section and label it with any number (in Fig. 8.2 we labeled the most bottom section with a number 0). The numbers of all the other sections of dispersion curves are assigned using the geometric rules given in Fig. 8.1. For the smooth parts of the dispersion curves (characterized by fold bifurcations, also called generic bifurcations) which are locally parabolic we use the rules presented in Figs. 8.1(a) and (d). For the parts of the dispersion curves that are not smooth (characterized by Hopf bifurcation, which is degenerate), where new modes are born, we use rules presented in Figs. 8.1(b), (c), (e), and (f).

[2]In the weak guiding approximation the refractive index contrast of the waveguiding structure is assumed to be low [$\max(n) \approx \min(n)$] and therefore interesting nonlinear effects can occur when the magnitude of the nonlinear induced refractive index change is comparable with the linear index contrast of the structure [153].

Finally, after having numbered all the sections of the dispersion curves, we can read the stability of the modes directly from the $\beta(I_{\text{tot}})$ dispersion curves. The topological stability criterion presented in Ref. [153] tells us that the modes corresponding to the parts of the curves with the largest number are possibly stable. In Fig. 8.1, only the modes labeled by 1 are possibly stable. All the other modes are unstable. The stability of all the possibly stable modes can be specified at once, as soon as the stability of one of them is determined. The stability can be determined either using numerical methods or using the physical intuition and theoretical arguments. For example, if a nonlinear mode has its counterpart in the linear limit, then we know that this nonlinear mode is stable in the limit $I_{\text{tot}} \to 0$.

Here we will analyze the stability of some of the plasmon–soliton waves described in Chapters 2 and 6 using the stability criterion described above. As it was mentioned at the beginning of this section, the stability criterion presented in Ref. [153] can be used only for the fundamental modes of the structure. The fundamental mode of the structure is the one with the highest effective index and a node-less field profile (in our case magnetic field profile) [153]. Therefore, we can only analyze the stability of such modes among all the types of solutions found in Chapters 2 and 6. In this PhD manuscript we have found such solutions only in nonlinear slot waveguide configurations presented in Chapter 6, for which the permittivity of the core is higher than the cladding metal permittivity. In the structures with a semi-infinity nonlinear medium studied in Chapter 2, where the low-permittivity metal film is sandwiched between high-permittivity dielectrics, we find node-less modes, but they do not possess the highest effective index. The modes with the highest effective index possess nodes in their magnetic field profiles. Therefore, none of these modes fulfill the definition of the fundamental mode given here and the stability criterion can not be applied to the solutions found in Chapter 2

We will analyze the stability of the plasmon–solitons in the nonlinear slot waveguide configuration presented in Chapter 6. We consider here the configuration discussed in Section 7.1. At first, the stability of the modes in the vicinity of the bifurcation that gives birth to a first-order asymmetric mode is studied. The dispersion curves of interest are presented in Fig. 8.3 (for the corresponding field plots see Fig. 7.16). The bifurcation points divide these dispersion curves into four sections. We arbitrarily choose the low-power section and label it with number 0. The numbers for the two sections above the Hopf bifurcation point (open square) are assigned according to the rule presented in Fig. 8.1(b). On the asymmetric branch (at $\beta \approx 10$) another bifurcation occurs (fold type bifurcation indicated by an open circle). The number for the section above this bifurcation point is assigned using the rule presented in Fig. 8.1(d). After assigning numbers to all the sections, we can determine the stability of the solutions corresponding to each of the sections. The sections with the highest number (0) correspond to possibly stable (ps) solutions and all the other sections correspond to unstable (u)

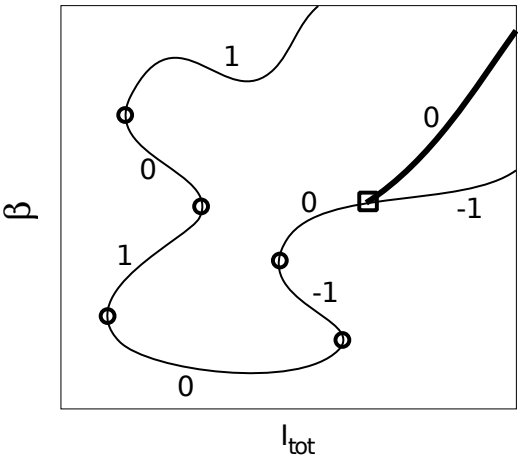

Figure 8.2: Exemplary dispersion curve illustrating the use of the rules presented in Fig. 8.1. The thick line indicates a doubly degenerate branch. Bifurcation points are indicated by open circles (fold bifurcation) or open square (Hopf bifurcation) and the numbers of the dispersion curves sections are assigned using the rules presented in Fig. 8.1. For a detailed description see text below.

modes. The stability of the sections indexed by number 0 can be inferred from the linear limiting case. The low-power section of the symmetric branch in the linear limit corresponds to a linear plasmon in metal/insulator/metal (MIM) configurations, which is stable. Therefore, the solutions corresponding to this section of the nonlinear dispersion curves are stable. Because the stability of the sections with the same number is the same, we conclude that also the section of the asymmetric branch indexed by number 0 corresponds to stable modes. The high power (and high effective index) sections of the symmetric and asymmetric branches (above the Hopf and the fold bifurcation points, respectively), labeled with -1, are unstable.

In Fig. 8.4, the stability of the higher-order node-less modes of the structure discussed in Section 7.1 is analyzed (see Fig. 7.20 for the field plots of interest). There are two bifurcation points on the dispersion curves for the higher-order symmetric mode SI and the second-order asymmetric mode AS2. These points divide the dispersion curves into four sections. We start by assigning number 0 to the upper section of the symmetric branch. Then, using the rule presented in Fig. 8.1(a), number -1 is assigned to the section between the two bifurcation points. The numbers for the sections above the Hopf bifurcation point (indicated by an open square) are assigned using the rule presented in Fig. 8.1(b). According to the stability criterion from Ref. [153], only the section with the highest number corresponds to possibly stable nonlinear modes. In the case presented in Fig. 8.4, it is the upper section of the symmetric dispersion curve. All the other modes are unstable. According to Ref. [153], the stability of the upper section of the symmetric branch can be deduced from the high-intensity limit ($I_{\mathrm{tot}} \to \infty$). As it can be seen from Fig. 7.18 in Section 7.1, with the increase of the total intensity, the higher-order solution (SI) becomes narrower and interacts weaker with the metal cladding. In the limit $I_{\mathrm{tot}} \to \infty$, the soliton in the nonlinear core becomes very narrow and does not interact with the cladding at all. Therefore, it can be regarded as a one-dimensional soliton in an infinite Kerr-type dielectric. Such solitons are stable for any intensity (see the beginning of Section 5 in Ref. [153] and Refs. [5, 21] therein). Hence, we expect the upper section of the symmetric branch to

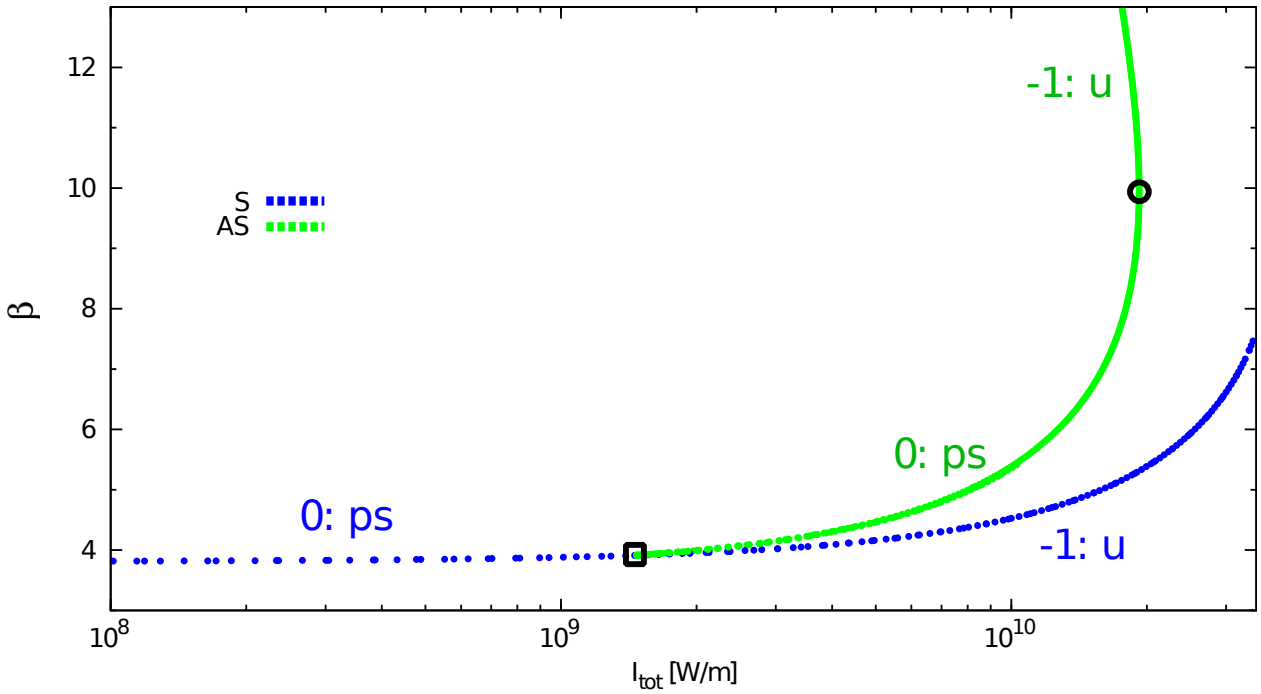

Figure 8.3: Zoom on the region with the birth of the first-order asymmetric mode of the dispersion curves of the symmetric slot waveguide presented in Fig. 7.8(b). Bifurcation points are marked with open circle (fold bifurcation) and open square (Hopf bifurcation). The numbers facilitating the stability analysis are assigned to the sections of the dispersion curves according to the rules presented in Fig. 8.1. Labels ps and u denote possibly stable and unstable modes, respectively.

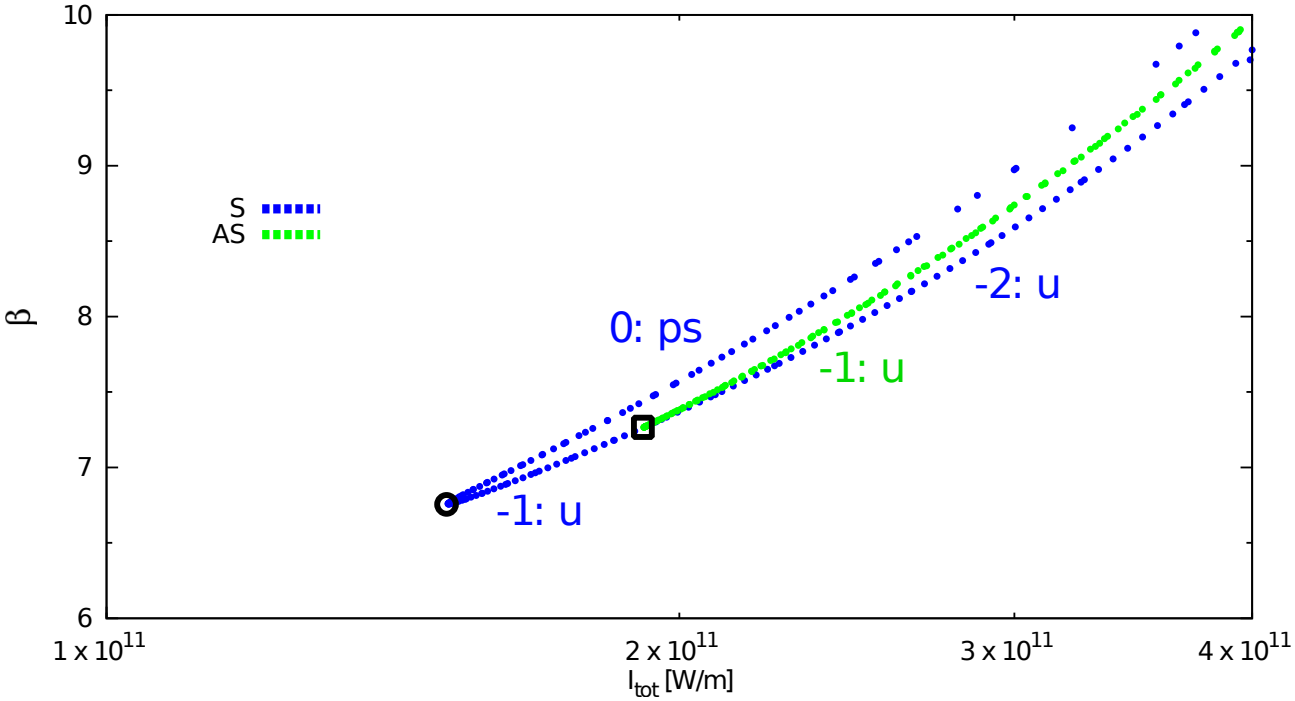

Figure 8.4: Zoom on the region with the birth of higher-order node-less symmetric and asymmetric modes of the dispersion curves of the symmetric slot waveguide presented in Fig. 7.8(b). The bifurcation points are marked with open circle (fold bifurcation) and open square (Hopf bifurcation). The numbers facilitating the stability analysis are assigned to the sections of the dispersion curves according to the rules presented in Fig. 8.1. Labels ps and u denote possibly stable and unstable modes, respectively.

correspond to stable solutions. The asymmetric mode AS2 and the modes corresponding to the lower part of the symmetric curve (labeled with -1 and -2) are unstable.

In this section, we have presented the first attempt to determine the stability of the plasmon–soliton waves that were described in this PhD thesis. We used the stability criterion proposed in Ref. [153] which was proposed for the fundamental modes of the structures in the weak guiding approximation. We use this criterion here being fully aware of its limited applicability for the configurations with metal layers, where the permittivity contrast is high. The criterion from Ref. [153] is easy to use, because it allows us to read the stability directly from the dispersion curves $\beta(I_{\mathrm{tot}})$, and it is general (can be applied to various structures). Another approach to determine the stability of plasmon–solitons waves is to use numerical methods. In this case, the study has to be done case by case for each of the studied configurations and modes. Our first attempts to study the stability of plasmon–solitons in the structures build of metal and nonlinear dielectrics, using numerical methods, are described below.

8.2 Numerical simulations of nonlinear propagations

In the previous section we have found the stability of the plasmon–solitons of the low orders using the topological criterion derived in Ref. [153]. In the slot waveguides studied here the weak guiding approximation, used in the derivation of this topological criterion, is not fulfilled. This fact makes the conclusions drawn using the criterion not definitive. For this reason we verify the predicted stability using two different vector numerical propagation methods.

At first, the stability of plasmon–solitons in nonlinear slot waveguides is verified using the nonlinear propagation scheme implemented in COMSOL [167]. This approach, developed and implemented in the group of Fangwei Ye, was successfully used to study the stability of solitons in nonlinear metallic structures [168–170]. The numerical simulations in COMSOL were performed for the sym-

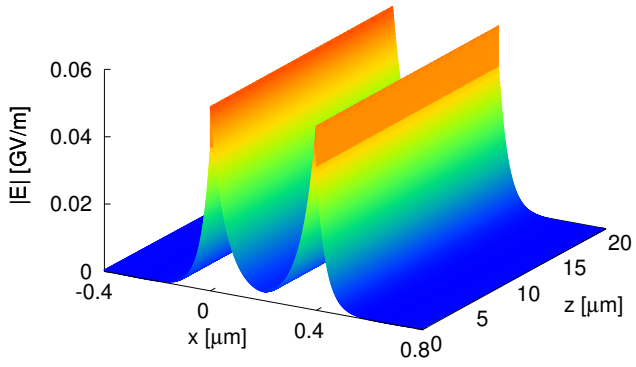

Figure 8.5: Evolution of the electric field norm during the propagation of the symmetric mode located below the Hopf bifurcation threshold. The average nonlinear index change in the core induced by this mode is equal to $\langle \Delta n \rangle = 10^{-4}$ and the propagation distance is approximately 13 free-space wavelengths.

metric nonlinear slot waveguide structure with the following parameters: $\epsilon_1 = \epsilon_3 = -20$, $\epsilon_{l,2} = 3.46^2$, $n_2^{(2)} = 2 \cdot 10^{-17}$ m^2/W, and $d = 400$ nm at $\lambda = 1.55$ μm. This configuration has different metal permittivity value compared to the structure studied in Section 8.1 (see parameters in Table. 7.1). The choice of the configuration with a higher metal permittivity is dictated by the fact that, in this new structure the threshold of the first bifurcation is lower (see Fig. 7.55). Low bifurcation threshold is required for numerical simulation because the numerical algorithms might have troubles dealing with the high nonlinear index modifications (see the study of highly nonlinear regime presented in Appendix F). The bifurcation threshold of the AS1 mode in the configuration studied here is equal to $\langle \Delta n \rangle_{\text{th}} = 7 \cdot 10^{-4}$. Even though the structure studied here differs from the configuration investigated in Section 8.1, the qualitative stability properties of the nonlinear modes in both structures are the same.

Firstly, we confirm the stability of the symmetric nonlinear mode corresponding to the low-power section (below the Hopf bifurcation point) of the blue dispersion curve labeled '0: ps' in Fig. 8.3. Figure 8.5 presents the evolution of the electric field norm over 13 free-space wavelengths of propagation for the symmetric mode below the bifurcation point in the structure with metal cladding permittivity $\epsilon_1 = \epsilon_3 = -20$. The average nonlinear index modification in the core for this mode is equal to $\langle \Delta n \rangle = 10^{-4}$, that is below the computed bifurcation threshold $\langle \Delta n \rangle_{\text{th}}$. We observe no change of the filed profiles during the propagation. Therefore, the stability of this mode predicted by the topological criterion is confirmed by the field evolution presented in Fig. 8.5.

Secondly, we confirm the stability of the asymmetric nonlinear modes laying on the section of the green dispersion curve labeled '0: ps' (between the Hopf and the fold bifurcation points) in Fig. 8.3. In Fig. 8.6, we present the evolution of the electric field norm of three different asymmetric modes laying between the two bifurcation points on the dispersion diagram of the structure with metal cladding permittivity $\epsilon_1 = \epsilon_3 = -20$. All these modes are stable during the propagation, which confirms the conclusion drawn from the topological criterion.

Figure 8.7 shows the transverse field profiles of symmetric and asymmetric plasmon–solitons in the nonlinear slot waveguides. For each symmetry, the comparison between the profiles obtained using the IM (see Section 6.2, that are the input profiles for the COMSOL based propagation simulations) and the cuts of the evolution profiles presented in Figs. 8.5 and 8.6(b). We observe that the profiles obtained after 6 and 12 free-space wavelengths of propagation are in a very good agreement with the input field profiles.

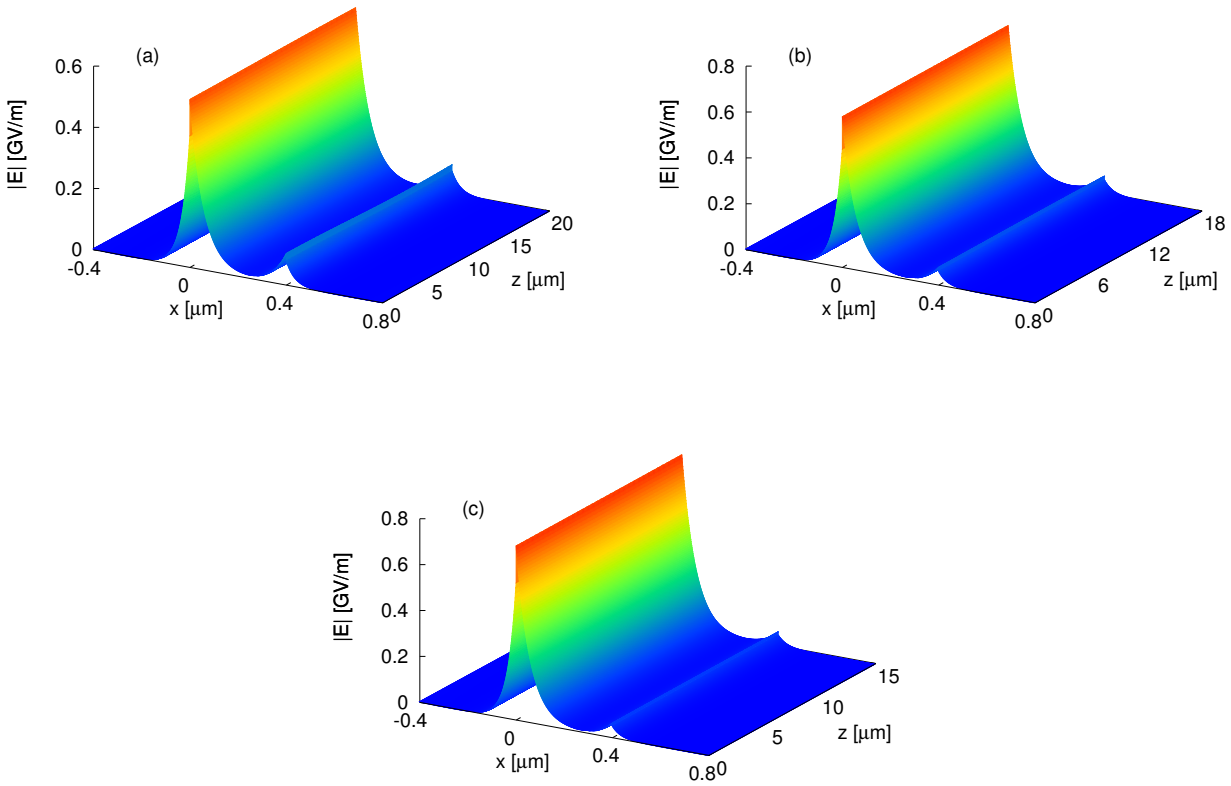

Figure 8.6: Evolution of the electric field norm during the propagation of asymmetric modes located between the Hopf bifurcation and the fold bifurcation. The average nonlinear index change in the core $\langle \Delta n \rangle$ induced by these modes is equal to (a) $2 \cdot 10^{-3}$, (b) $3 \cdot 10^{-3}$, and (c) $4 \cdot 10^{-3}$. The propagation distance is approximately 12 wavelengths.

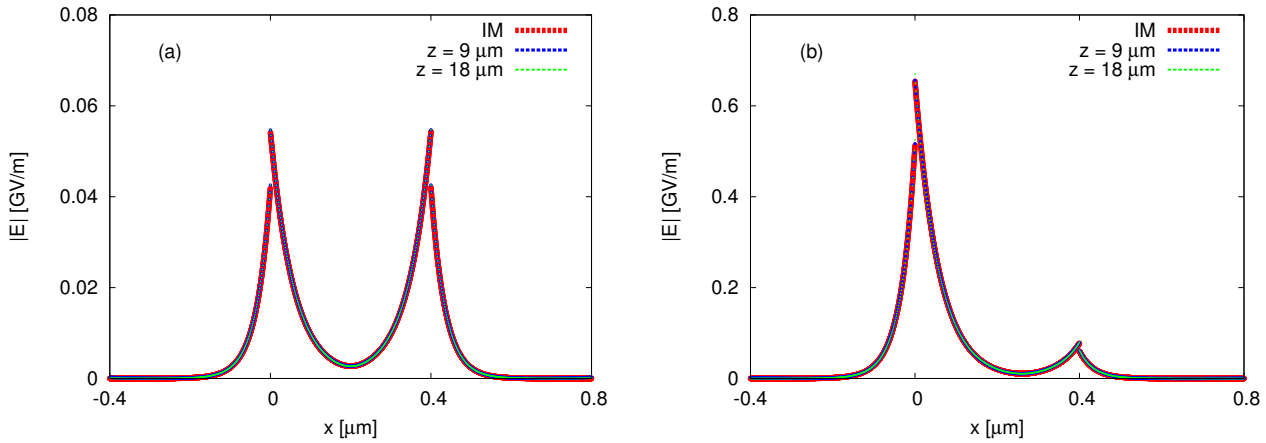

Figure 8.7: Comparison of the $|\mathbf{E}|$ profiles obtained using the IM (the input profiles in the COMSOL based simulations) and cuts of the field evolution in the middle of the propagation range ($z = 9$ μm — 6 free-space wavelengths) and at the end of the propagation ($z = 18$ μm — 12 free-space wavelengths) for (a) the symmetric nonlinear plasmon–soliton (see Fig. 8.5) and (b) the asymmetric nonlinear plasmon–soliton [see Fig. 8.6(b)].

Figure 8.8 presents the evolution of the transverse component of the electric field E_x corresponding to the solution presented in Fig. 8.6(b). The evolution is presented only on the distance of 9 μm

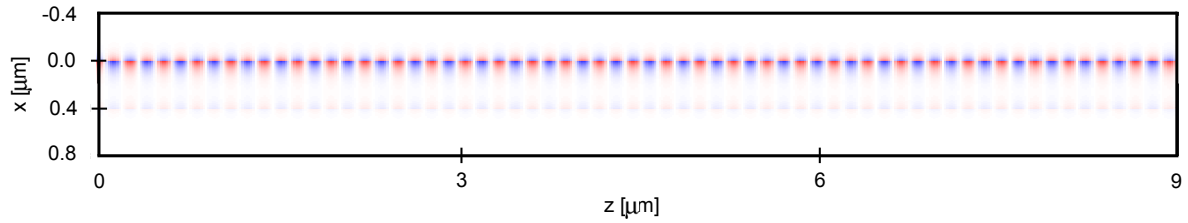

Figure 8.8: Evolution of the E_x field profile during the propagation of the solution presented in Fig. 8.6(b).

for better visibility of the changes in the field profile at the wavelength scale. In the plot of a single component of the electric field, contrary to the norm of the electric field, we see the sinusoidal harmonics evolution. Nevertheless, the envelope of the field profile does not change, which indicates the stability of the solution.

We have studied the stability of nonlinear asymmetric plasmon–solitons using a second numerical method. To this end we have used the nonlinear capabilities of the FDTD method implemented in MEEP software [171]. A short description of the FDTD method, the MEEP software, and the preliminary simulations on plasmons and solitons is presented in Appendix. F. It is important to point out that this method is fully different from the one used by COMSOL. In this study we simulated the light propagation in symmetric nonlinear slot waveguide structure with the following parameters: $\epsilon_1 = \epsilon_3 = -6$, $\epsilon_{l,2} = 3.8$, $n_2^{(2)} = 2 \cdot 10^{-17}$ m^2/W, and $d = 500$ nm at $\lambda = 2$ μm.

The evolution of transverse component of the electric field E_x during the propagation is presented in Fig. 8.9 for the asymmetric nonlinear plasmon–soliton above the Hopf bifurcation threshold (for which $E_0/E_d = 6$). Here, similar to the evolution presented in Fig. 8.8, we see the harmonic oscillation of the field, but the shape of the envelope remind the same during the propagation, which indicates the stability of the mode.

In Fig. 8.10, we present the comparison of the field profile of the asymmetric mode obtained using the IM and the FDTD simulations. The FDTD profiles are obtained by taking cuts of the color map presented in Fig. 8.9 in the middle and close to the end of the observation window. The comparison presented in Fig. 8.10 reveals small changes of the envelope during the propagation in the FDTD simulations. Such changes were not present in the simulations performed in COMSOL (see Fig. 8.7). The different behavior of the two simulation methods is probably caused by different way of exciting of the input field profile. In the COMSOL based simulations, the input field profile corresponds exactly

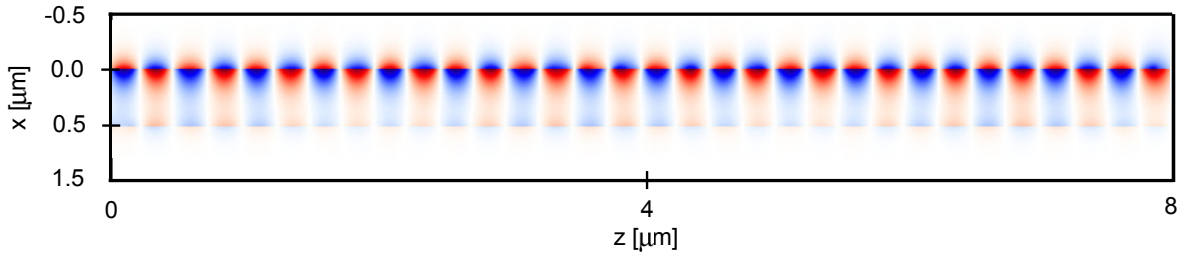

Figure 8.9: Evolution of the E_x field profile during the propagation of the asymmetric plasmon–soliton simulated using the FDTD method implemented in the MEEP software.

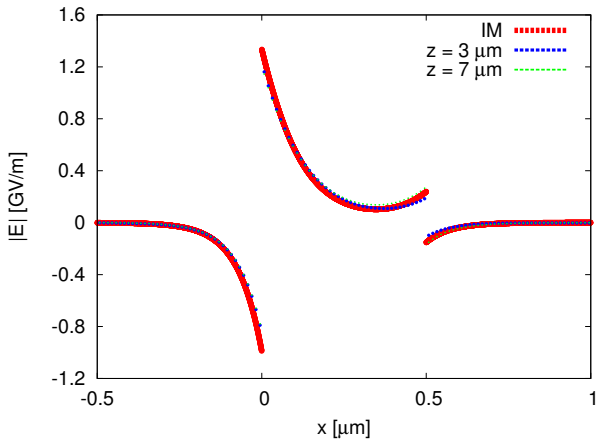

Figure 8.10: Comparison of the E_x profiles obtained using the IM and cuts of the field evolution in the middle of the propagation range ($z = 3$ μm) and at the end of the propagation ($z = 7$ μm) for the asymmetric nonlinear plasmon–soliton [see Fig. 8.9].

to the stationary solution found using the IM. In the simulations performed in MEEP, the input field is generated by a current source (see Appendix F). This source generates a field profile similar to the one of the IM but differs from it. This difference in the input profile might be the reason for small changes of the envelope of the field during the propagation.

To sum up, we have studied the stability of the nonlinear plasmon–soliton waves in nonlinear slot waveguides using three independent methods. The theoretical predictions based on the topological criterion were confirmed by the propagation simulations obtained using two numerical methods. Therefore, the stability of the low-order asymmetric solutions in nonlinear slot waveguides was confirmed.

Chapter 9

Conclusions and perspectives

9.1 General conclusion

The theoretical studies of nonlinear surface waves on interfaces between metals and nonlinear dielectrics, referred here as plasmon–solitons, represent an important but not fully explored branch of nonlinear optics. Plasmon–solitons merge the properties of spatial optical solitons and surface plasmons in a single nonlinear wave. Even though this type of nonlinear waves has been studied for more than thirty years, there are still no experimental results confirming their existence. In this PhD thesis, we have developed new and efficient models to study the properties of plasmon–solitons and we have provided results that may facilitate the experimental observation of these nonlinear states.

In the first part of this manuscript, we have studied configurations where a semi-infinite Kerr-type nonlinear medium was in contact with metal or linear dielectric layers. For this type of structures, we have developed two independent models based on Maxwell's equations that allow us to find nonlinear stationary transverse magnetic polarized states in these structures. The models we have developed are semi-analytical and they provide closed expressions for the dispersion relations and for the field profiles of the modes. This fact allows us to rapidly scan multi-dimensional space of opto-geometric parameters of studied structures, which is essential in the process of structure optimization and allows us to efficiently find the configuration with desired physical properties (for example configurations supporting low-power plasmon–solitons).

The validity of the two models that we have developed, has been confirmed analytically and numerically. The analytical validation is based on the fact that, in the limiting cases (for simpler structures with lower number of layers or linear structures) our models reproduce the results that are already known from literature. The numerical validation of our models has been done in three stages. The results obtained using our models have been: (i) compared with the results published in other works for the same type of structures, (ii) mutually compared with each other, (iii) compared with the results of a home-made finite element method that uses a fixed power algorithm to find self-coherent solutions in the metal/nonlinear dielectric planar structures. In all the three cases, the results are in accord.

After having confirmed the validity of our models, we have presented the results for the dispersion diagrams and the mode profiles in various multilayer configurations with a semi-infinite nonlinear medium and a metal layer. We started with the simplest configuration: a single interface between a metal and a nonlinear dielectric. We have proven analytically that in such structures, only plasmonic-type nonlinear surface waves exist (waves whose field profile resembles that of a linear plasmon, but is slightly modified due to the presence of the nonlinearity). In case of a more complicated structure that is composed of a thin metal film sandwiched between a nonlinear and a linear medium (NML structure), another type of solutions is found. At first, we studied a symmetric NML configuration in which the linear parts of the permittivity of the dielectric claddings are equal on both sides. Based on this example, we introduced a general classification of nonlinear surface waves in structures with a nonlinear dielectric layer, a metal layer and linear dielectric layers. There exist two types of plasmon–solitons: the plasmonic type and the solitonic type. In the field profiles of the solitonic-type

plasmon–solitons, a soliton peak is visible in the nonlinear medium and a plasmon peak is visible at one of the metal interfaces. Studying the asymmetric NML structures, we have demonstrated that there exists a range of precisely chosen parameters, for which solitonic-type plasmon–solitons can be observed at realistic intensity levels. Thus, we can conclude that, for asymmetric NML structures the permittivity of the linear material has to be fine-tuned in order to find low-power solutions in the structure. In the configuration that we have studied, for a fixed geometry, the change in the linear refractive index by 0.01 resulted in the change of plasmon–soliton peak power from 1 to 30 GW/cm^2.

Studies of low-power plasmon–solitons are crucial from a practical point of view. The absence of experimental confirmation of the existence of plasmon–soliton waves results from the fact that, all the nonlinear surface waves of this type predicted before require extremely high refractive index change, which is equivalent to the high power levels that exceed the damage threshold of the conventional materials used in integrated optics. The discovery of the low-power solitonic-type plasmon–solitons indicates the direction toward which the experimental investigations should be focused. Low-power solitonic-type plasmon–solitons can be easily excited in structures proposed by us with a Gaussian laser beam and could be unmistakably distinguished from any linear modes propagating in the structure.

Subsequently, the four-layer structures were also studied, in which an additional low-refractive index dielectric layer was introduced between the nonlinear dielectric and the metal film. We have found the dispersion diagrams for such four-layer structures for first time. Depending on the choice of the structure's opto-geometric parameters, we obtained rich or simple dispersion diagrams. We have demonstrated that, the introduction of an additional dielectric layer can greatly enlarge the region of parameters in which low-power solitonic-type plasmon–solitons exist (e.g., the refractive index interval in which solutions with peak intensity below 30 GW/cm^2 exist is enlarged from 0.01 in the case of a three-layer structure to 1.7 in a four-layer structure with similar opto-geometric parameters). Using this fact, we have optimized the four-layer structure in order to facilitate the experimental observation of such nonlinear waves. We have found configurations that support plasmon–solitons with the peak intensity around 1 GW/cm^2. This level of light intensity was already used experimentally in 2009 to generate spatial solitons in fully dielectric waveguides with a chalcogenide core.

Nonlinear plasmon–solitons in structures with a semi-infinite nonlinear medium may find potential applications in sensing (for example in surface plasmon resonance based detectors), because they offer an additional free parameter (the light intensity) that influences the resonance condition and can be tuned by adjusting the power level of the incident light. However, in structures with a semi-infinite nonlinear medium that support low-power plasmon–solitons, the solitonic part is weakly localized. Typical full width at half maximum, of a plasmon–soliton with 1 GW/cm^2 peak intensity, is of the order of few tens of microns. This creates the need for thick nonlinear layers. From the fabrication point of view, it is problematic to obtain uniform, high quality, nonlinear layers of such thickness.

In the second part of this PhD manuscript, we have studied nonlinear plasmonic slot waveguide configurations in which the nonlinear Kerr-type dielectric film is sandwiched between two semi-infinite metal cladding layers. This configuration has some advantages over the structures with semi-infinite nonlinear media. Stationary solutions in nonlinear slot waveguides are strongly confined, primarily due to the high permittivity contrast between the nonlinear dielectric core and the metal cladding and secondarily due to the self-focusing nonlinear effect. Moreover, as stated above, from the practical point of view it is easier to fabricate high quality thin films of nonlinear materials than bulky samples.

For nonlinear plasmonic slot waveguides, we have developed two models based on Maxwell's equations for the transverse magnetic polarized light. One of them is semi-analytical and provides closed formulas for the dispersion relations and the field profiles of the modes in terms of special Jacobi elliptic functions. The limitation of this model is the fact that it uses a simplified treatment of the Kerr-type nonlinearity. The second model, that accounts for the full nonlinear Kerr term, is based on the shooting method, which is a common numerical way to solve Maxwell's equations in nonlinear structures. The novelty of the second model lays in the fact that we have found an analytical condition that allows us to reduce the dimension of the parameter space in which nonlinear solutions of Maxwell's equations are sought. The validity of both our models has been validated by a mutual comparison of their results. Because interesting nonlinear effects occur for the nonlinear permittiv-

ity contrast comparable to the built-in permittivity contrast in the structure, in the nonlinear slot waveguide configuration, built of metals and dielectrics, interesting nonlinear effects occur for elevated nonlinear permittivity changes. Some of these effects occur outside of the validity range of the first model, which treats the Kerr-type nonlinearity in a simplified and approximated way. For this reason, the two models agree quantitatively only for low intensity levels. Nevertheless, the results of both our models are in excellent qualitative agreement for the whole range of intensities.

Using these two models that we developed, we have studied the dispersion relations and mode profiles of nonlinear plasmonic slot waveguides. First, we have analyzed very rich dispersion diagrams for the symmetric nonlinear slot waveguides (in which the permittivities of the two metal claddings are equal). We have found the zero-order modes (symmetric and antisymmetric modes that exist in the linear limit) and the first-order asymmetric nonlinear mode that have already been studied in literature. The asymmetric mode appears from the symmetric one in the nonlinear regime through a symmetry-breaking Hopf bifurcation. Apart from these modes, due to the completeness of our models, we have found new symmetric, antisymmetric and asymmetric higher-order modes in nonlinear slot waveguides. Among these higher-order modes, the asymmetric modes bifurcate from the symmetric ones. All the dispersion curves of the asymmetric modes in the symmetric nonlinear slot waveguide are doubly degenerate.

We have classified all the modes of the nonlinear slot waveguide according to the symmetry of the magnetic field profile and to the presence of the nodes in the magnetic field profile. The nonlinear dispersion diagrams can be divided into two parts: one containing only dispersion curves of the modes with nodes and the second one containing the dispersion curves corresponding to the node-less modes. The limit between the two regions is given by the dispersion curve corresponding to a single interface between the metal and the nonlinear dielectric. We have found the analytical expressions for this curve using the formulation of each of our models. The family of the modes with nodes has been studied in more detail. We have shown that at a certain point (one for each of the higher-order modes with nodes), the nonlinear refractive index distribution induced by this mode is flat. This fact allowed us to find a direct relationship between these modes and their linear counterparts that exist in linear slot waveguides.

For the symmetric nonlinear slot waveguide structure, we have studied the influence of the width of the core on the dispersion curves. We concluded that the increase of the waveguide core width allows for a drastic decrease of the intensity threshold at which the birth of new nonlinear modes is observed. We have reported that the increase of the waveguide thickness by a factor of 20 allows us to decrease the intensity required to observe the first asymmetric mode bifurcation by 5 orders of magnitude. Moreover, studying waveguides with different core widths, we observed that a part of the dispersion curve of the first asymmetric mode for high effective index values is invariant with respect to the waveguide core width. For high effective index values, the dispersion curves of the first asymmetric mode in waveguides with different thickness overlap. This behavior is explained by the fact that the high-effective index asymmetric solutions are strongly localized at one of the nonlinear slot waveguide interfaces and interact very weakly with the second interface. Therefore, the problem can be simplified to a single-interface situation, where the thickness of the waveguide does not play any role.

Furthermore, the influence of the permittivity index contrast between the dielectric core and the metal cladding on the dispersion curves has been studied. We have noticed two types of behavior. Decreasing the permittivity contrast by changing the permittivity of the metal cladding allows us to decrease the intensity threshold for the bifurcation points for the asymmetric modes. In the studied structure, we have managed to reduce the intensity threshold for the first bifurcation by four orders of magnitude by changing the metal cladding permittivity from -200 to -15 while the linear part of the core permittivity was kept equal to 3.46^2. On the contrary, increasing the permittivity contrast by changing the permittivity of the core allows us to decrease the intensity threshold for the first bifurcation. We have reduced the intensity threshold by three orders of magnitude by changing the core permittivity from 1 to 25 while the cladding permittivity was kept equal to -90.

Moreover, the properties of asymmetric nonlinear slot waveguides were studied. We have shown that, in agreement with the group theory, the double degeneracy of the dispersion curves corresponding

to the asymmetric modes is lifted when the asymmetry of the structure is introduced (different metal permittivity values for the two cladding regions). Additionally, we have observed that the separation between the two branches into which the doubly degenerate branch splits, grows with the increase of the structure asymmetry, as expected. For high effective indices, one of these branches overlaps with the dispersion curve of the asymmetric mode in the symmetric structure. This behavior was explained using the fact that for highly asymmetric modes that are strongly localized at one interface, the problem can be reduced to a single-interface situation.

Last but not least, the stability of the nonlinear plasmon-solitons in nonlinear slot waveguides was studied. We have confirmed the stability of the low-order asymmetric modes using three different methods. The conclusions about the stability drawn using the general topological criterion for nonlinear structures were confirmed using two independent numerical methods.

Nonlinear plasmonic slot waveguides may find potential applications in integrated optics, as they offer the possibility of extreme light confinement required to miniaturize devices and reduce the cross-talk between separate channels. Applications in nonlinear plasmonic couplers have already been proposed in literature.

9.2 Perspectives

9.2.1 Theoretical studies

Even though plasmon–solitons in metal/nonlinear dielectric structures have been studied for more than thirty years, there are still a lot of questions that remain unanswered. One of the most important issues is the stability of these waves. The stability of low-order plasmon–solitons in nonlinear slot waveguide configurations has been demonstrated in Chapter 8. However, the theoretical method used there was not fully suited for the structures with high refractive index contrast as the ones studied in this PhD manuscript. It has not been rigorously proven that the framework we used, developed in Ref. [153], is applicable to the structures studied in our study. It is desirable to find an analytical criterion for plasmon–soliton stability, similar to the one presented in Ref. [153] for weak contrast dielectric waveguides. Since this might be a difficult task, in the short term it might be more efficient to study the stability of nonlinear surface waves using numerical tools. Methods such as split-step Fourier or finite-difference time-domain (FDTD) can be used to study the propagation and stability of plasmon–solitons. Some results connected with our FDTD studies of plasmon–soliton propagation are shown in Section. 8.2 and in Appendix F. Numerical FDTD method seems to fail in the case of high nonlinear refractive index modifications (comparable with the linear refractive index). Therefore, it is important to improve the numerical methods and to develop new algorithms that will be able to tackle this difficulty. This would enable us to study numerically the stability of higher order modes in nonlinear slot waveguides, that require high nonlinear index modifications.

Apart from the stability issue, more complicated structures in which plasmon–solitons can propagate should be considered in the future. The models presented in this work can be extended to treat structures with higher number of layers. Combining the results from Sections 2.3 and 6.2, allows us to readily analyze nonlinear waveguides with multiple cladding layers. As an extension of this idea, periodic structures with metal and nonlinear dielectric layers may be studied. Moreover, analysis of more realistic two-dimensional solutions in both one- and two-dimensional waveguide geometries should be continued. The two-dimensional nonlinear dielectric waveguides embedded in metal/dielectric structures may offer further flexibility in the structure design and plasmon-soliton properties control. Additionally, the waveguides in which the interface between a nonlinear dielectric and a metal is structured may result in new properties of plasmon–soliton waves.

9.2.2 Experiment

In this PhD thesis, we have presented several results that should facilitate experimental observation of plasmon–soliton waves. We have designed realistic structures (both for the configuration with semi-infinite nonlinear medium and for the nonlinear slot waveguide configuration) in which purely nonlinear

states can be observed at the level of induced nonlinear permittivity change reachable in materials used for integrated optics. We have used realistic parameters of the materials at the telecommunication wavelength and optimized the structures in order to observe nonlinear effect at the levels of intensity that can be provided by modern high power lasers and that do not destroy the material. These designs have been made in close collaboration with groups working on the experimental observation of plasmon–solitons. There are still a lot of difficulties that have to be overcome from the fabrication point of view. Proper materials have to be chosen in order to maximize their nonlinear response and minimize parasitic effects, such as linear losses, three-photon absorption or permanent material degradation upon long exposure to high-intensity laser light.

Appendices

Appendix A

Intensity dependent refractive index

In literature, we can find various definitions of the intensity dependent (Kerr) refractive index. Here we present in detail the relations between various nonlinear parameters.

In the case of many materials the refractive index can be described by the relation [172]:

$$n = n_0 + \overline{n}_2 \langle \widetilde{\mathscr{E}}^2(t) \rangle_t, \tag{A.1}$$

where n_0 represents the usual, weak-field refractive index and $\overline{n}_2$ is the constant describing the rate of index change with the increase of the time averaged electric field $\langle \widetilde{\mathscr{E}}^2(t) \rangle_t$. We put a bar over this coefficient to avoid confusion with the second-order nonlinear refractive index n_2 introduced in Section 1.7. The time dependent electric field is defined by Eq. (1.6.1a) as:

$$\widetilde{\mathscr{E}}(t) = \mathbf{E}(\omega) e^{-i\omega t} + c.c. \tag{A.2}$$

The time average of $\widetilde{\mathscr{E}}^2(t)$ can be written as

$$\langle \widetilde{\mathscr{E}}^2(t) \rangle_t = \langle \mathbf{E}(\omega) e^{-i\omega t} + 2\mathbf{E}(\omega)\mathbf{E}^*(\omega) + \mathbf{E}^*(\omega) e^{i\omega t} \rangle_t. \tag{A.3}$$

The averaging of the oscillating terms gives zero and Eq. (A.3) reads:

$$\langle \widetilde{\mathscr{E}}^2(t) \rangle_t = 2|\mathbf{E}(\omega)|^2. \tag{A.4}$$

Using this result we can rewrite Eq. (A.1) to obtain the dependency of refractive index on the field amplitude:

$$n = n_0 + 2\overline{n}_2 |\mathbf{E}|^2. \tag{A.5}$$

An alternative, more common way of defining the Kerr-type refractive index is to connect the index changes with the light intensity [see Eq. (1.7.1)]:

$$n = n_0 + n_2 I. \tag{A.6}$$

Comparing Eqs. (A.5) and (A.6) and using the definition of the light intensity given by Eq. (1.7.4), we relate the two nonlinear coefficients:

$$n_2 = \frac{4\beta \overline{n}_2}{\epsilon_0 |\epsilon| c}. \tag{A.7}$$

In Section 1.7, we have obtained a simplified relation between the nonlinear coefficient α (appearing in the definition $\epsilon = \epsilon_l + \alpha|\mathbf{E}|^2$) using several assumptions. We assumed there that the nonlinear modification of the permittivity is much lower than the linear part of permittivity ($\alpha|\mathbf{E}|^2 \ll \epsilon_l$) and that the effective index of the modes can be approximated by the value of the linear refractive index

($\beta \approx n_0$, which is true for low-power solitonic waves). Using the same assumptions in Eq. (A.7), we rewrite it in the form:

$$n_2 = \frac{4\overline{n}_2}{\epsilon_0 n_0 c}. \tag{A.8}$$

Equation (A.8) differs by a factor 4 from Eq. (4.1.18) in Ref. [2] due to a different definition of the light intensity used {compare Eq. (1.7.4) in this manuscript and Eq. (4.1.16) in Ref. [2]}.

Here we recall the simplified relation between n_2 and α given by Eq. (1.7.7):

$$\alpha = \epsilon_0 n_0^2 c n_2, \tag{A.9}$$

where we used the identity $|\epsilon_l| = n_0^2$. Using the fact that $\chi^{(3)} = \alpha/3$ [see Eq. (1.6.10)] we relate n_2 with $\chi^{(3)}$:

$$n_2 = \frac{3\chi^{(3)}}{\epsilon_0 n_0^2 c}. \tag{A.10}$$

Equation (A.10) can be numerically expressed as:

$$n_2\left[\frac{\mathrm{m}^2}{\mathrm{W}}\right] = \frac{1128}{n_0^2}\chi^{(3)}\left[\frac{\mathrm{m}^2}{\mathrm{V}^2}\right], \tag{A.11}$$

where again the difference by factor 4 with Eq. (4.1.20) in Ref. [2] is due to different definitions of the light intensity used here and in Ref. [2]. In some older works, the third-order nonlinear susceptibility values are given in the Gaussian system. In this case, the conversion procedure is the following:

$$n_2\left[\frac{\mathrm{m}^2}{\mathrm{W}}\right] = \frac{1.56 \cdot 10^{-5}}{n_0^2}\chi^{(3)}\big[\mathrm{esu}\big]. \tag{A.12}$$

Appendix B

Elliptic integrals

During the derivation of the expressions for the field profiles in the frame of the Jacobi elliptic function based model in Section 6.1.1, we have encountered the elliptic integrals. By definition, an integral of the type

$$\int R(x, y)\, \mathrm{d}x, \tag{B.1}$$

where $R(x, y)$ is a rational function of x and y, y^2 is equal to a cubic or quartic polynomial in x, $R(x, y)$ contains at least one odd power of y, and y^2 has no repeated factors is called an elliptic integral. More details on the elliptic integrals can be found in Ref. [154].

Table B.1 presents the formulas used to integrate the elliptic integrals that were used in Section 6.1.1. The results of the integrations of the elliptic integrals are expressed as the inverse Jacobi elliptic functions. The Jacobi elliptic functions are discussed in Ref. [152] and in Appendix C.

Condition	Formula number in Ref. [112]	Elliptic integral	Equivalent inverse Jacobi elliptic function
$\gamma > \delta$	17.4.43	$\gamma \int_{\delta}^{x} \frac{\mathrm{d}t}{\sqrt{(\gamma^2-t^2)(t^2-\delta^2)}}$	$\mathrm{nd}^{-1}\left(\frac{x}{\delta}\middle\vert \frac{\gamma^2-\delta^2}{\gamma^2}\right)$
$\gamma > \delta$	17.4.44	$\gamma \int_{x}^{\gamma} \frac{\mathrm{d}t}{\sqrt{(\gamma^2-t^2)(t^2-\delta^2)}}$	$\mathrm{dn}^{-1}\left(\frac{x}{\gamma}\middle\vert \frac{\gamma^2-\delta^2}{\gamma^2}\right)$
—	17.4.51	$\sqrt{\gamma^2+\delta^2} \int_{0}^{x} \frac{\mathrm{d}t}{\sqrt{(t^2+\gamma^2)(\delta^2-t^2)}}$	$\mathrm{sd}^{-1}\left(\frac{x\sqrt{\gamma^2+\delta^2}}{\gamma\delta}\middle\vert \frac{\delta^2}{\gamma^2+\delta^2}\right)$
—	17.4.52	$\sqrt{\gamma^2+\delta^2} \int_{x}^{\delta} \frac{\mathrm{d}t}{\sqrt{(t^2+\gamma^2)(\delta^2-t^2)}}$	$\mathrm{cn}^{-1}\left(\frac{x}{\delta}\middle\vert \frac{\delta^2}{\gamma^2+\delta^2}\right)$

Table B.1: Elliptic integrals and the equivalent inverse Jacobi elliptic functions. This table is part of the table presented on Page 596 in Ref. [112].

Appendix C

Jacobi elliptic functions

The field profiles and the dispersion relations in the frame of the Jacobi elliptic function based model derived in Section 6.1 are expressed in terms of Jacobi elliptic functions. This appendix presents the necessary informations about these functions and their basic properties. More details on the Jacobi elliptic functions can be found in Ref. [152].

C.1 Definitions and plots

The Jacobi elliptic functions can be defined with respect to some integrals. Consider an integral

$$u = \int_0^{\varphi} \frac{\mathrm{d}\theta}{\sqrt{1 - m\sin^2\theta}}, \tag{C.1}$$

where the angle φ is called the amplitude.

$$\varphi = \mathrm{am}(u|m) \tag{C.2}$$

and m is called the parameter. The parameter m takes values from the interval $[0, 1]$, We define the three first Jacobi elliptic functions as

$$\mathrm{cn}(u|m) = \cos\varphi, \tag{C.3a}$$

$$\mathrm{dn}(u|m) = \sqrt{1 - m\sin^2\varphi}, \tag{C.3b}$$

$$\mathrm{sn}(u|m) = \sin\varphi, \tag{C.3c}$$

The remaining nine Jacobi elliptic functions can be expressed using the three functions given by Eqs. (C.3) using the following rules. For p, q, and r being any of the four letters s, c, d, and n the following relations hold:

$$\mathrm{pq}(u|m) = \frac{1}{\mathrm{qp}(u|m)}, \tag{C.4}$$

$$\mathrm{pq}(u|m) = \frac{\mathrm{pr}(u|m)}{\mathrm{qr}(u|m)}. \tag{C.5}$$

Two equivalent notations are used for the Jacobi elliptic functions. In this PhD manuscript, we use the notation with the parameter m, as it is done for instance in Ref. [112] and in the computer algebra software Maxima [173] that was used for a part of the numerical implementation of the Jacobi elliptic function based model. The second notation for the Jacobi elliptic functions uses the modulus $k^2 = m$ instead of the parameter m. This notation is used for example in Ref. [111] and in the computer

algebra software MAPLE [174], in which the main code of the Jacobi elliptic function based model was written. These two notations are equivalent in the sense

$$\widetilde{\mathrm{pq}}(u|k) \equiv \mathrm{pq}(u|m), \tag{C.6}$$

where the Jacobi elliptic function denoted by $\widetilde{\mathrm{pq}}$ uses the second notation.

In Figs. C.1 and C.2, we present plots of the six Jacobi elliptic functions used in Section 6.1. The plots illustrate the behavior of these Jacobi elliptic functions for different values of the parameter m.

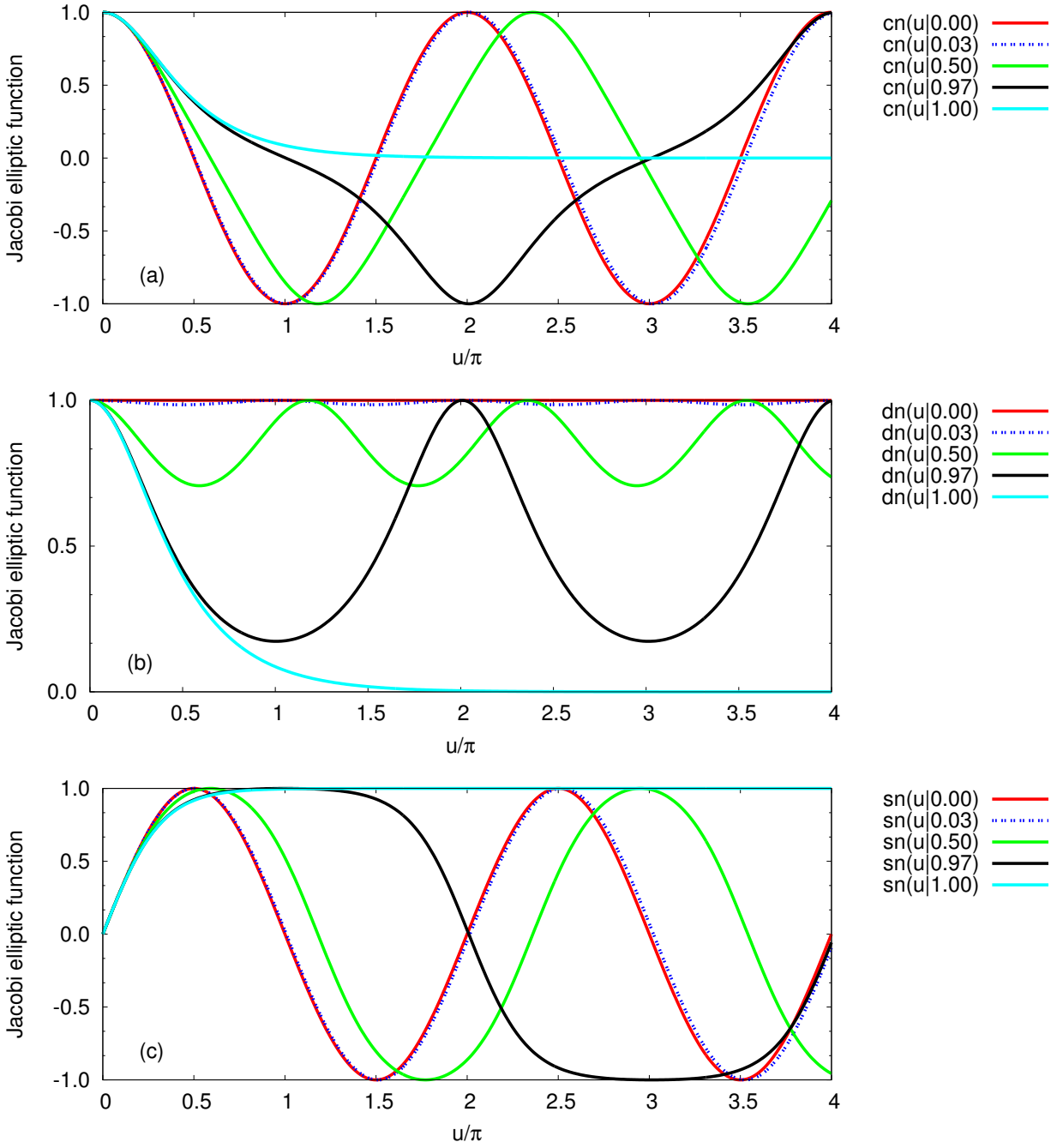

Figure C.1: Jacobi elliptic functions (a) $\mathrm{cn}(u|m)$, (b) $\mathrm{dn}(u|m)$, and (c) $\mathrm{sn}(u|m)$ for five different values of the parameter m.

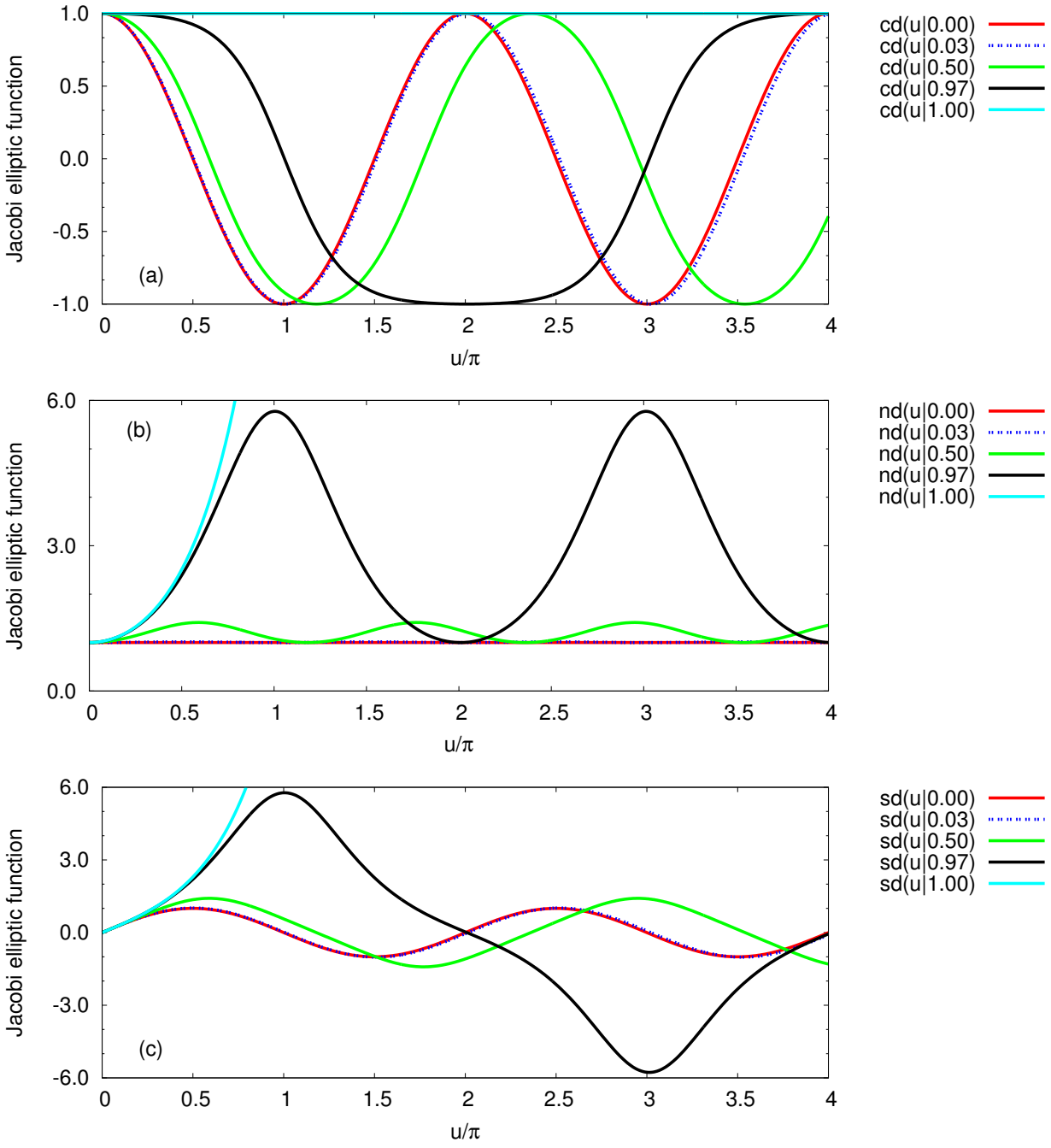

Figure C.2: Jacobi elliptic functions (a) $\mathrm{cd}(u|m)$, (b) $\mathrm{nd}(u|m)$, and (c) $\mathrm{sd}(u|m)$ for five different values of the parameter m.

C.2 Properties

Here we present some of the basic properties of the six Jacobi elliptic functions that were used in Section 6.1.

Limiting cases

The expressions for the Jacobi elliptic functions in the limiting case $m = 1$ are used in Section 6.1.4, where the derivation of the field profiles and the nonlinear dispersion relations for the limiting case of a single interface between a metal and a nonlinear dielectric is presented. Table C.1 presents the expression for the Jacobi elliptic functions for the limiting cases of the parameter $m = 0$ and $m = 1$.

Function \ Case	$m = 0$	$m = 1$
$\mathrm{cn}(u\|m)$	$\cos u$	$\operatorname{sech} u$
$\mathrm{dn}(u\|m)$	1	$\operatorname{sech} u$
$\mathrm{sn}(u\|m)$	$\sin u$	$\tanh u$
$\mathrm{cd}(u\|m)$	$\cos u$	1
$\mathrm{nd}(u\|m)$	1	$\cosh u$
$\mathrm{sd}(u\|m)$	$\sin u$	$\sinh u$

Table C.1: Expression for the Jacobi elliptic functions for the limiting values of the parameter $m = 0$ or $m = 1$. This table is part of Table 16.6 presented on Page 571 in Ref. [112].

Symmetry

The symmetry properties of the Jacobi elliptic functions were used in Section 6.1 to simplify the expressions for the field profiles and the nonlinear dispersion relations. Table C.2 presents the symmetry properties of the Jacobi elliptic functions.

Function \ Argument	u	$-u$
cn	$\mathrm{cn}(u\|m)$	$\mathrm{cn}(u\|m)$
dn	$\mathrm{dn}(u\|m)$	$\mathrm{dn}(u\|m)$
sn	$\mathrm{sn}(u\|m)$	$-\mathrm{sn}(u\|m)$
cd	$\mathrm{cd}(u\|m)$	$\mathrm{cd}(u\|m)$
nd	$\mathrm{nd}(u\|m)$	$\mathrm{nd}(u\|m)$
sd	$\mathrm{sd}(u\|m)$	$-\mathrm{sd}(u\|m)$

Table C.2: The symmetry properties of the Jacobi elliptic functions. This table is part of Table 16.8 presented on Page 572 in Ref. [112] that presents more general relations between Jacobi elliptic functions upon the change of the argument.

Derivatives

The expressions for the Jacobi elliptic function derivatives were used in Section 6.1 to obtain the formulas for the field profiles and the nonlinear dispersion relations. Table C.3 present expressions for the derivatives of the Jacobi elliptic functions used in Section 6.1.

Function	Derivative
$\mathrm{sn}(u\|m)$	$\mathrm{cn}(u\|m)\,\mathrm{dn}(u\|m)$
$\mathrm{cn}(u\|m)$	$-\mathrm{sn}(u\|m)\,\mathrm{dn}(u\|m)$
$\mathrm{dn}(u\|m)$	$-m\,\mathrm{sn}(u\|m)\,\mathrm{cn}(u\|m)$
$\mathrm{sd}(u\|m)$	$\mathrm{cd}(u\|m)\,\mathrm{nd}(u\|m)$
$\mathrm{cd}(u\|m)$	$(m-1)\,\mathrm{sd}(u\|m)\,\mathrm{nd}(u\|m)$
$\mathrm{nd}(u\|m)$	$m\,\mathrm{sd}(u\|m)\,\mathrm{cd}(u\|m)$

Table C.3: Expressions for the derivatives with respect to the argument u of the Jacobi elliptic functions. This table is part of Table 16.16 presented on Page 574 in Ref. [112].

Appendix D

Study of the losses in nonlinear slot waveguide structures

In this appendix we present an estimation of the propagation losses for the modes of a nonlinear slot waveguide. The losses will be evaluated using the method proposed in Section 2.1.5. The imaginary part of the effective index is calculated using the expression [compare with Eq. (2.1.73)]:

$$\beta'' = \frac{\epsilon_0 c}{4} \frac{\int_T \epsilon''(x) |\mathbf{E}(x)|^2 \, \mathrm{d}x}{P_{\mathrm{tot}}}, \tag{D.1}$$

where P_{tot} denotes the total power density of the mode [defined by Eq. (7.1.6)], $\epsilon''(x)$ denotes distribution of the imaginary part of the permittivity, and T is the transverse cross-section of the waveguide.

The waveguides studied here have parameters similar to these given in Table 7.1, but now the imaginary part of the permittivity of the materials is nonzero. In this appendix, waveguides with two thicknesses of the core are studied: 400 nm and 800 nm.

Quantity \ Layer	1	2	3
Material	gold	hydrogenated amorphous silicon	gold
Permittivity	$\epsilon_1 = -90 + 10i$	$\epsilon_{l,2} = 3.46^2 + 10^{-4}i$	$\epsilon_3 = -90 + 10i$
$n_2^{(2)}$	—	$2 \cdot 10^{-17}$ m^2/W	—

Table D.1: Parameters of the symmetric nonlinear slot waveguide structures with losses studied in this section.

Figure D.1 presents the dispersion diagram for the nonlinear slot waveguide with a 400-nm-thick core obtained using the interface model. The real and the imaginary parts of the effective index are plotted as a function of the averaged nonlinear index modification in the core $\langle \Delta n \rangle$ defined by Eq. (7.1.1). In the description of the dispersion curves, the names of the modes introduced in Section 7.1.1 are used. Figure D.1(a) shows the real part of the dispersion curves $\beta(\langle \Delta n \rangle)$ (it is a part of Fig. 7.3). The behavior of these dispersion curves is discussed in Section. 7.1.1. Here we will focus on the description of Fig. D.1(b) that presents the dispersion curves for the imaginary part of the effective index $\beta''(\langle \Delta n \rangle)$.

Form Fig. D.1(b), we notice that the imaginary part of the effective index of the fundamental symmetric mode S0 (blue curve that starts at low $\langle \Delta n \rangle$ values) are lower than β'' for the low-power antisymmetric AN0 mode (red curve starting at low $\langle \Delta n \rangle$). The lowest value of the imaginary part of the effective index for the S0 mode is $\beta'' \approx 3 \cdot 10^{-2}$ and for the AN0 mode $\beta'' \approx 5 \cdot 10^{-2}$. These values are equal to the imaginary part of the effective indices of the first symmetric and antisymmetric modes

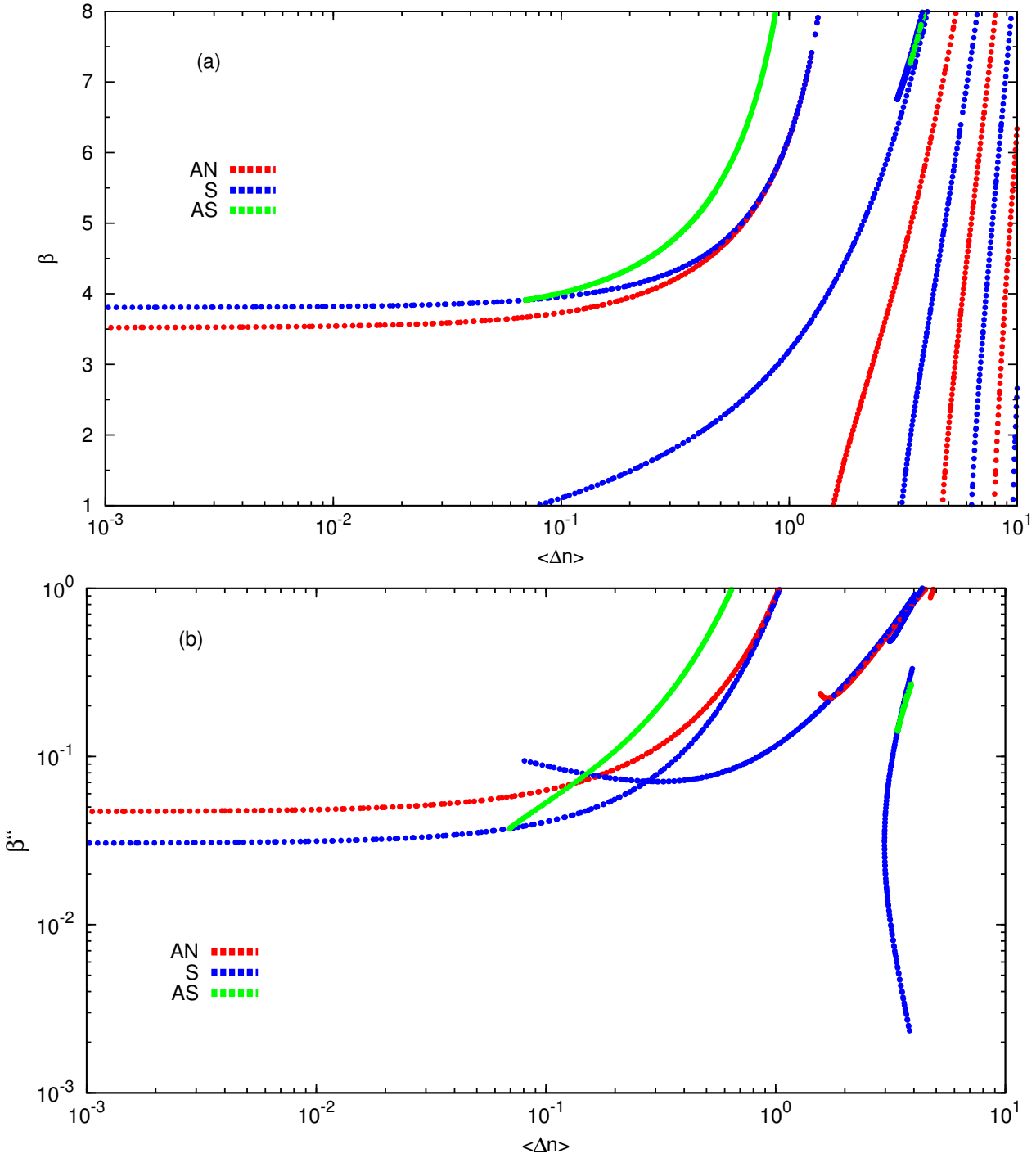

Figure D.1: Nonlinear dispersion diagrams for (a) the real part and (b) for the imaginary part of the effective index as a function of the averaged nonlinear index modification in the nonlinear slot waveguide with the parameters indicated in Table D.1 and a 400-nm-thick core.

of the corresponding linear slot waveguide. The imaginary part of the effective index of the S0 and AN1 modes increases with the increase of $\langle \Delta n \rangle$. Similarly, the imaginary part of the effective index of the AS1 mode increases with the increase of $\langle \Delta n \rangle$.

The lowest values of β'' for the low-power modes of the slot waveguide correspond to the attenuation of the mode $\mathfrak{L} \approx 1$ dB/μm [the relation between the imaginary part of the effective index and the attenuation is given by Eq. (2.1.74)].

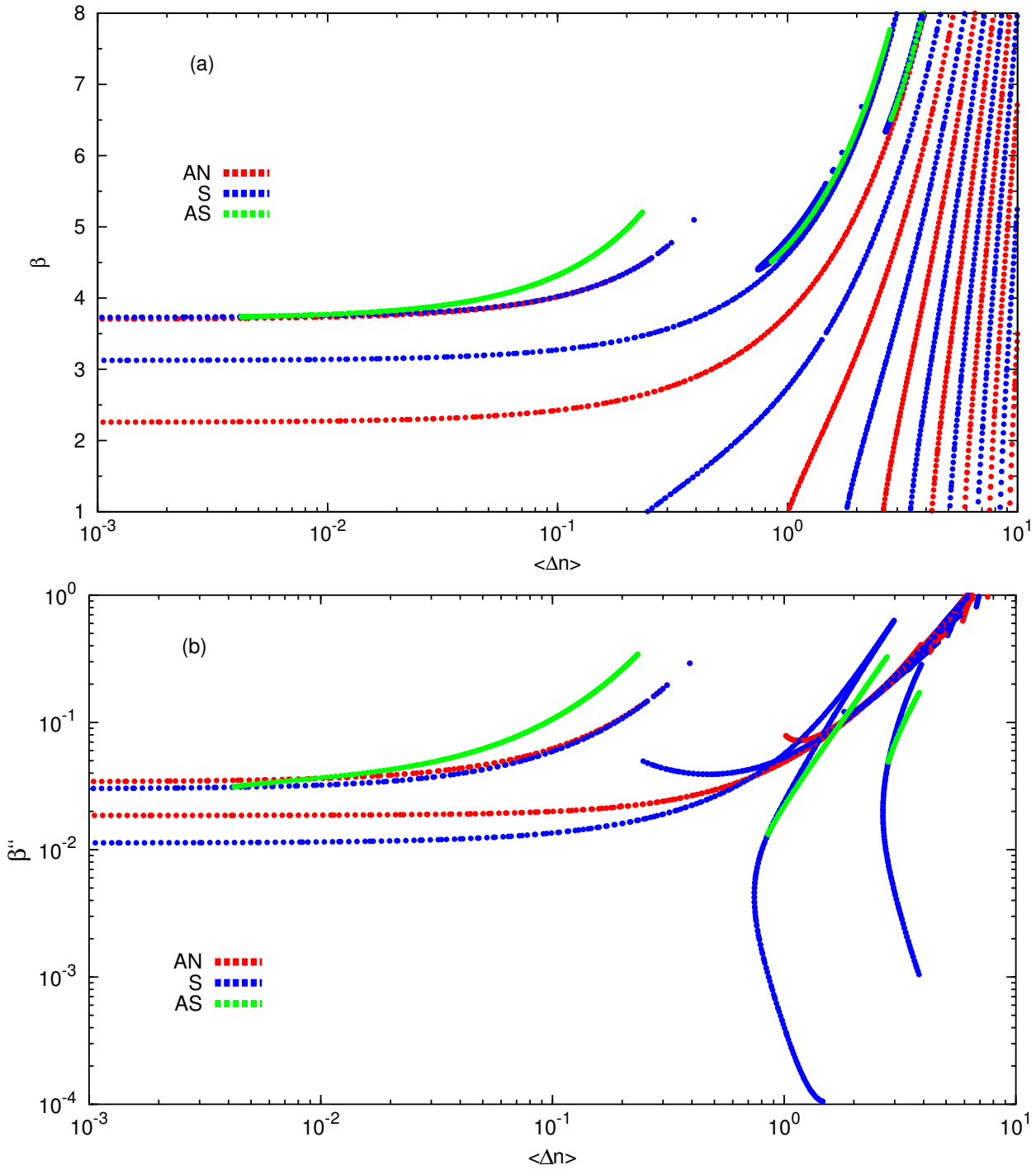

Figure D.2: Nonlinear dispersion diagrams for (a) the real part and (b) for the imaginary part of the effective index as a function of the averaged nonlinear index modification in the nonlinear slot waveguide with the parameters indicated in Table D.1 and an 800-nm-thick core.

The nonlinear dispersion curves for β'' of the higher-order modes from the family with nodes (modes S1 and AN1) have a parabolic shape. These curves start at a certain level of losses corresponding to the appearance of the mode at $\beta = 1$. With the increase of $\langle \Delta n \rangle$, the imaginary part of the effective index first decreases and then increases rapidly. With the increase of the order of the mode, the values of β'' at the beginning of the curve and at the minimum increase.

The most interesting is the behavior of the $\beta''(\langle \Delta n \rangle)$ curve for the higher-order node-less symmetric mode SI. This mode appears through a fold bifurcation [155] at $\langle \Delta n \rangle \approx 3$. At the bifurcation point,

two branches are born and their effective index β increases with the increase of $\langle\Delta n\rangle$ [see Figs. D.1(a) and 7.3(b)]. The imaginary part of the effective index for one of these branches increases with the increase of $\langle\Delta n\rangle$. On the contrary, for the second branch, the values of β'' decrease with the increase of $\langle\Delta n\rangle$. This behavior can be understood looking at the field profiles of the SI mode presented in Fig. 7.18. There, we observe that the field profiles laying on the upper SI branch have large side-lobes [see Fig. 7.18(a) and (b)] and therefore they interact strongly with the metal cladding. The field profiles corresponding to the lower branch have low side-lobes [see Fig. 7.18(c) and(d)] and therefore they interact weakly with the metal cladding.

The interaction with the metal cladding is crucial in the studies of losses, because the imaginary part of the metal permittivity is orders of magnitude higher than ϵ'' of the dielectric core (in terms of absolute value — see Table D.1). Looking at Eq. (D.1) we see that, the higher the fraction of the field localized in the metal layers, the higher is the value of β''. Consequently, solutions that interact with the metal cladding weakly (that are mainly localized in the dielectric core) have low β'' values. The lowest value of β'' of the SI mode that we compute is $\beta'' \approx 2 \cdot 10^{-3}$. It corresponds to the attenuation of $\mathfrak{L} \approx 0.07$ dB/μm. Unfortunately, this low vale of losses occurs for extremely large nonlinear index modifications $\langle\Delta n\rangle \approx 4$.

The imaginary part of the effective index of the asymmetric mode AS2 grows with the increase of $\langle\Delta n\rangle$. This is caused be the fact that, with the increase of $\langle\Delta n\rangle$, the asymmetry of this mode increases. With the increase of the asymmetry, the amplitude of one of the side-lobes grows and the amplitude of the other one decreases. However, the net effect gives the increase of the fraction of the light that is confined in the metal cladding.

In Fig. D.2 the dispersion diagram for a nonlinear slot waveguide with the parameters shown in Table D.1 and the core thickness $d = 800$ nm is shown. Figure D.2(a) shows the real part of the dispersion curves $\beta(\langle\Delta n\rangle)$ (the same plot is shown inf Fig. 7.46). The behavior of these dispersion curves is discussed in Section. 7.1.1. Here we will focus on the comparison between Fig. D.2(b) that presents the dispersion curves for the imaginary part of the effective index $\beta''(\langle\Delta n\rangle)$ for the waveguide with an 800-nm-thick core, and Fig. D.1(b) showing the same dependency for the waveguide with a 400-nm-thick core.

Qualitatively, the behavior of the nonlinear dispersion curves $\beta''(\langle\Delta n\rangle)$ of the corresponding modes of the waveguides with a thin core and with a thick core is the same. However, here are some qualitative differences. In Fig. D.2(b), we see four low-power modes. The imaginary part of the effective index for the fundamental symmetric mode (blue curve form which the asymmetric AS1 mode bifurcates) is at the same level as for the waveguide with the thin core ($\beta'' \approx 3 \cdot 10^{-2}$). However, for the waveguide with the thick core, two additional higher-order low-power modes with nodes exist, for which β'' can be as low as 10^{-2}.

The lowest value of the imaginary part of the effective index is obtained for the higher-order symmetric node-less modes. One branch of the SI dispersion curve corresponds to $\beta'' \approx 10^{-4}$. The lowest β'' for the SII mode is at the level of 10^{-3}. Comparing Figs. D.1 and D.2, we notice that with the increase of the core thickness, the lowest value of β'' for the SI mode decreases (from $2 \cdot 10^{-3}$ to 10^{-4}) and that it occurs for lower value of the nonlinear index modification $\langle\Delta n\rangle$. For the waveguide with the thick core it occurs at $\langle\Delta n\rangle \approx 1.5$ which is two times lower than for the waveguide with the thin core.

The lowest attenuation obtained for the SI mode in the nonlinear slot waveguide with the 800-nm-thick core is $\mathfrak{L} \approx 3.5$ dB/mm. We notice that by changing the nonlinear core thickness, we are able to lower the level of the losses of the modes propagating in the nonlinear slot waveguide.

Appendix E

Field profiles of higher-order node-less modes obtained using the Jacobi elliptic function based model

In this appendix, field profiles of higher-order node-less modes obtained using the Jacobi elliptic function based model (JEM) are presented. These profiles have similar features to the profiles of the node-less modes discussed in Section 7.1.3 and their analysis does not bring any new information about the nature of the JEM. Nevertheless, we present these profiles here to prove that the JEM is able to find the corresponding higher-order modes, to point out similarities and differences between the results of the JEM and the interface model (IM), and to complete the study presented in Section 7.1.3.

Figure E.1 presents the transformation of the field profiles of the magnetic field H_y, electric field components E_x and E_z and the total electric field amplitude E for the second-order symmetric node-less mode SII along its dispersion curve (see Fig. 7.27). The columns are ordered by increasing values of the magnetic field amplitude on the left metal/nonlinear dielectric interface H_0. The differences between the field profiles for SII mode obtained using the JEM (Fig. E.1) and the IM (presented in Fig. 7.22) are the same as for the SI mode (discussed on Page 148). The qualitative agreement between the magnetic field profiles obtained using the two models is good. Quantitatively, the ratio between the magnetic field intensity at the metal/nonlinear dielectric interface and the soliton peak (H_0/H_{peak}) is much higher for the JEM than for the IM. The profiles of the electric field component E_z obtained using the two models are very similar. On the contrary, the electric field component E_x differ drastically between the results of two models. In the IM, the E_x profile has the shape similar to the magnetic field profile H_y (positions of minima and maxima are identical for E_x and H_y in Fig. 7.22). In the case of the JEM, in Fig. E.1(a) we see that the positions of minima and maxima are switched in the E_x profile. At the positions of the two solitonic peaks in the H_y profile, there are two minima in the E_x profile. The E_x profiles presented in Fig. E.1(d) possesses three maxima (one in the center of the nonlinear core and two close to the core interfaces). For higher total intensity densities of the mode [Figs. E.1(e) and (f)], the maximum in the center splits into two maxima, and the maxima close to the core interfaces change their shape. The profiles of the total electric field amplitude [Figs. E.1(g)–(i)] have complicated shapes and do not resemble the profiles obtained using the IM [Figs. 7.22(i)–(l)], which resemble two solitons trapped in the waveguide core.

Figure E.2 presents the transformation of field profiles of the third-order asymmetric node-less mode AS3 along its dispersion curve (see Fig. 7.27). The columns are ordered by increasing values of H_0. Comparison of the field profiles obtained using the JEM and the field profiles of the AS3 mode obtained using the IM (see Fig. 7.23) leads to similar conclusions as for the SII mode. Here also, the H_y and E_z profiles agree relatively well between the two models. The comparison of the E_x and E profiles reveals big differences between the two models.

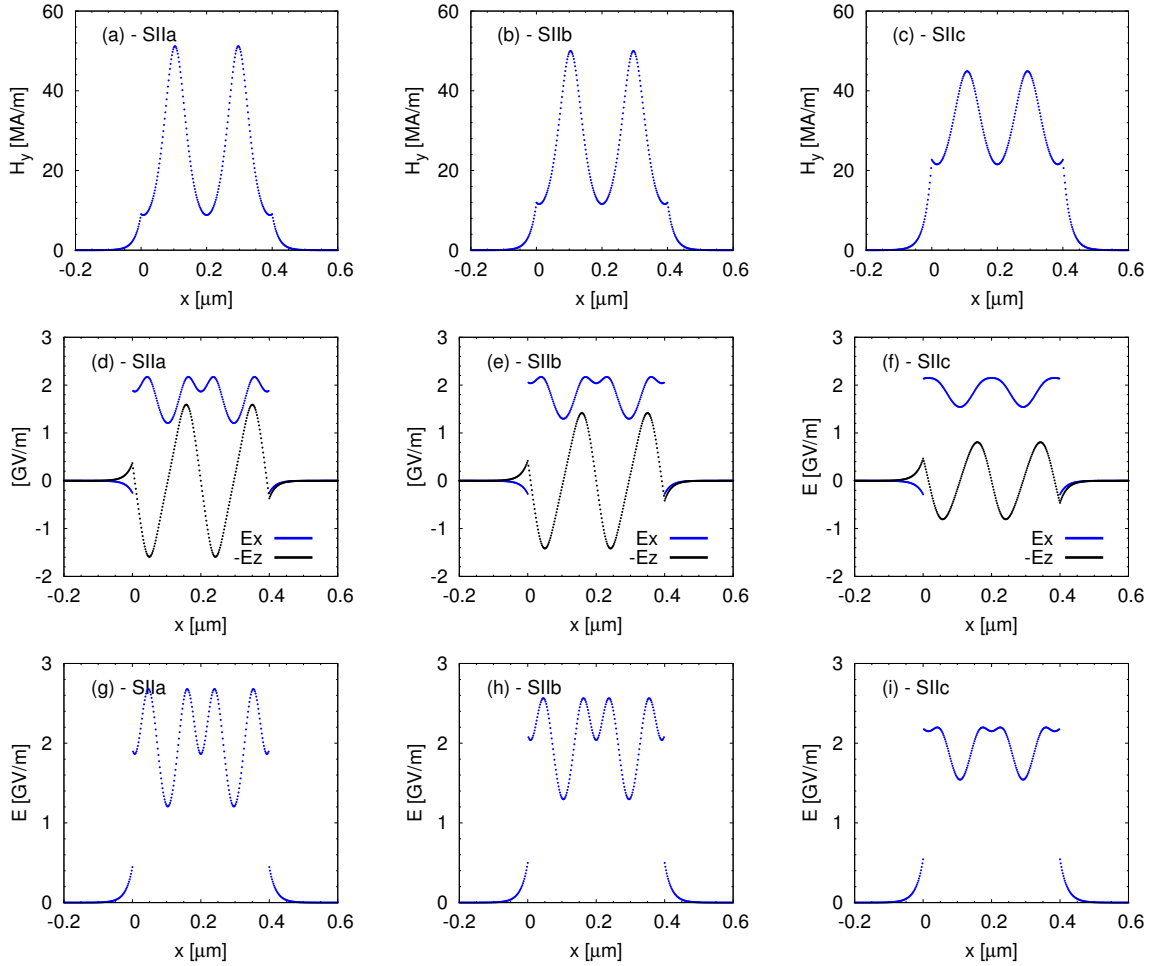

Figure E.1: Profiles of (a)–(c) magnetic field component H_y, (d)–(f) electric field components E_x (blue) and $-E_z$ (black), and (g)–(i) total electric field amplitude E corresponding to points (first column) SIIa, (second column) SIIb, and (third column) SIIc in Fig. 7.27.

Figure E.3 presents a direct comparison of the transformation of the SII and AS3 modes along their respective dispersion curves (see Fig. 7.27) with the increase of the magnetic field at the left metal/nonlinear dielectric H_0. This transformation has a similar character to the transformation observed in the frame of the IM (see Fig. 7.24). We observe that the two soliton peaks of the asymmetric mode shift toward the interface with lower value of H_0 [to the left in Fig. E.3(a) and to the right in Fig. E.3(b)].

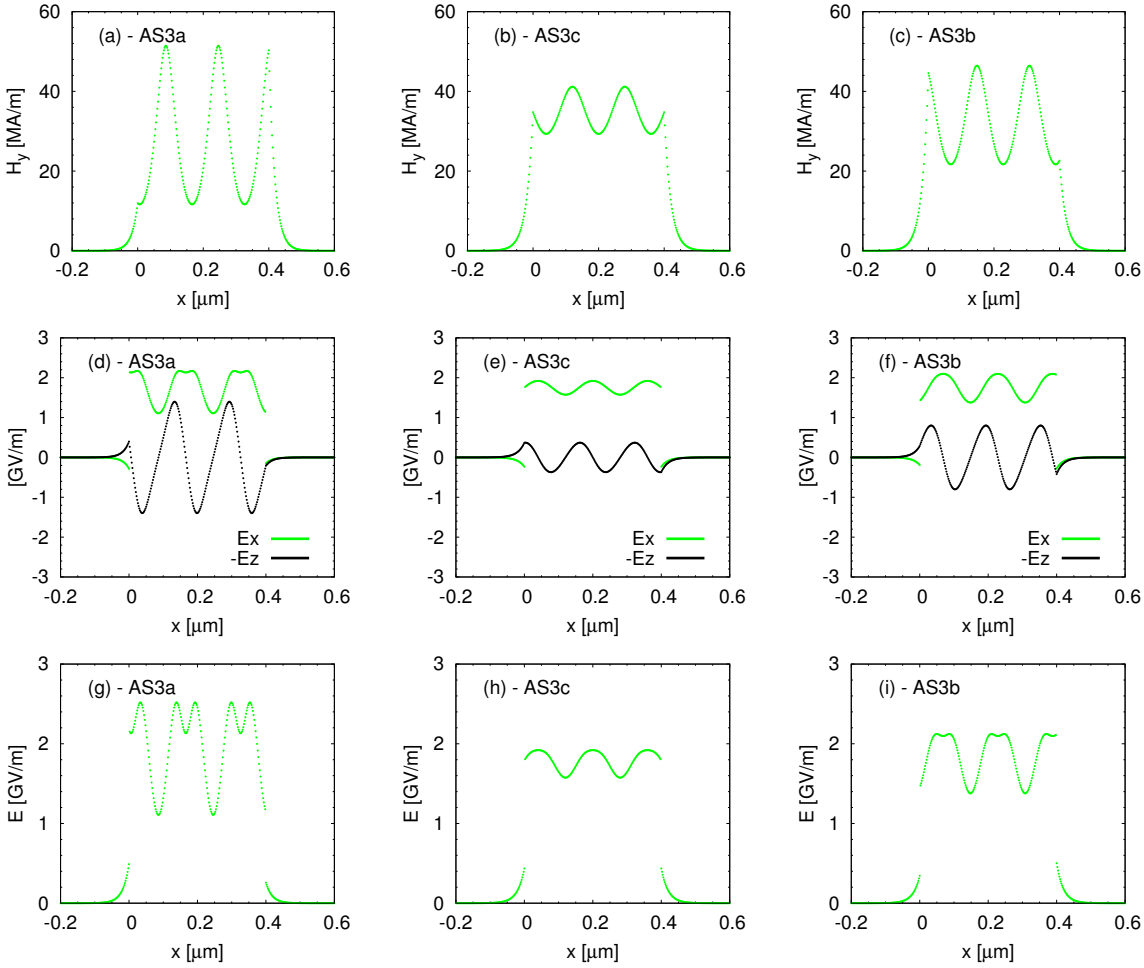

Figure E.2: Profiles of (a)–(c) magnetic field component H_y, (d)–(f) electric field components E_x (green) and $-E_z$ (black), and (g)–(i) total electric field amplitude E corresponding to points (first column) AS3a, (second column) AS3c, and (third column) AS3d in Fig. 7.27.

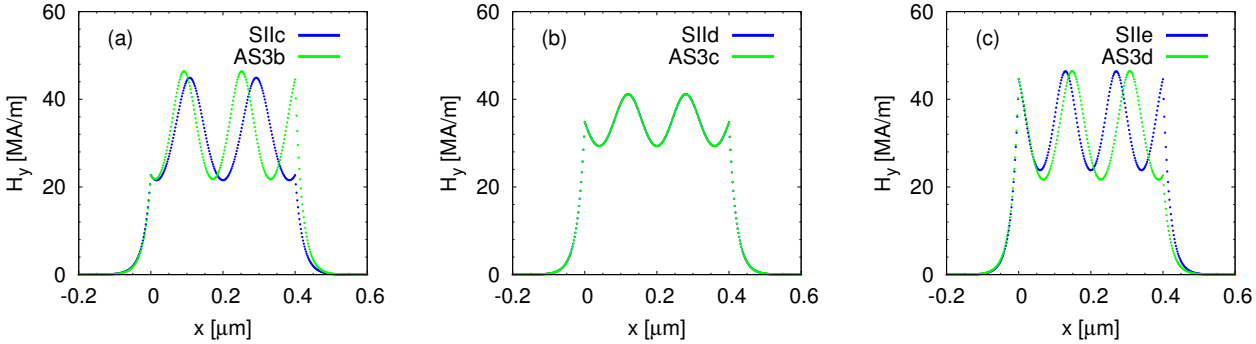

Figure E.3: Profiles of the magnetic field H_y for the symmetric SII mode (blue) and the second-order asymmetric AS3 mode (green). The subplots present the transformation of the field profiles corresponding to the points indicated on the dispersion curve in Fig. 7.27. The labels of the points are given in the subplot legends.

Appendix F

Finite-difference time-domain studies

Studies of the temporal evolution of plasmon–solitons provide a way to confirm the results obtained using modal methods and are crucial in the studies of the stability of these waves. This appendix presents our first and preliminary results on the propagation of plasmon and soliton waves. These results show the capabilities and limitations of the finite-difference time-domain (FDTD) methods to study strongly confined fields in nonlinear structures.

Firstly, we shortly describe the FDTD method and the software package used for the simulations. Next, we present results obtained for the propagation of linear plasmons in slot waveguide configurations. Finally, we discuss the soliton formation in uniform bulk media: in vacuum and in a high refractive index medium (e.g., chalcogenide glass). The studies of the plasmon and soliton propagation reveal the difficulties that can be encountered during the FDTD simulations, in particular for the waves generating high nonlinear index modifications.

F.1 Finite-difference time-domain method

The FDTD method [161, 162] is a numerical technique used for the modeling of electrodynamic phenomena. This method allows one to numerically solve Maxwell's equations [system of six coupled partial differential equations given by Eqs. (1.3.8a) and (1.3.8b)]. Because the FDTD method is a time-domain method, it enables us to find solutions in a wide frequency range in a single simulation run. Moreover, this method allows for the treatment of some nonlinearities. The FDTD method offers an alternative and complementary approach to the modal methods. It allows us to obtain results that illustrate the situation more similar to the experimental conditions (e.g., launching and propagation of picosecond pulses).

The FDTD method is a grid-based method. The values of the electric and magnetic field components are found at the nodes of a uniform grid. In Fig. F.1, we present a simple Yee grid [for a one-dimensional problem where only two electromagnetic field components are nonzero (E_z and H_y)] and indicate the points at which the electromagnetic field amplitudes are evaluated. In order to solve the system of coupled differential equations [Eqs. (1.3.8a) and (1.3.8b)], the FDTD method uses the central difference scheme which results in a leapfrog algorithm. The electric and magnetic fields are computed at different space and time coordinates. In the example shown in Fig. F.1, the electric field is calculated for integer values of the space and time steps, and the magnetic field is calculated at the half-integer space and time steps.

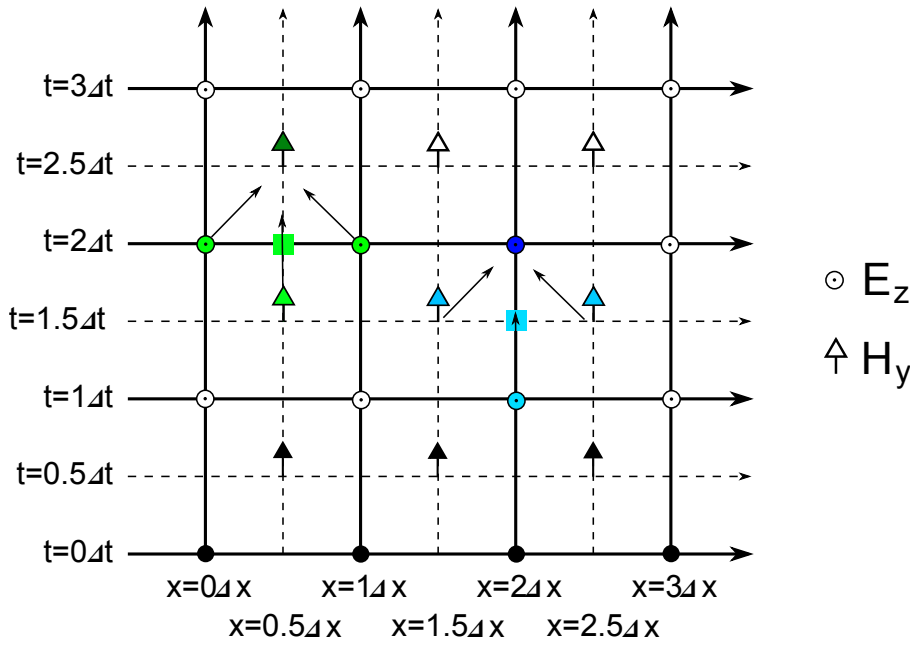

Figure F.1: Schematic representation of the Yee lattice in a one-dimensional problem. The lattice sites in which the electric (open points) and magnetic (arrows) field components are calculated in various instances of time are marked. The symbols filled with black denote the initial conditions. The color squares denote the points at which the derivatives are written using the central difference scheme. The field values indicated by light green (blue) symbols used to calculate the new (in the next time step) value of the electric (magnetic) field at the point marked by the dark color.

F.2 Finite-difference time-domain simulation software package MEEP

In our FDTD studies we have used the MEEP software package [171, 175] that was developed at Massachusetts Institute of Technology. This is a free software distributed on the GNU General Public License. The capabilities of the software are listed in Refs. [171, 175]. Among the most important feature we can cite:

- Simulations of one-, two-, and three-dimensional problems in Cartesian and cylindrical coordinates.
- Anisotropic, dispersive and nonlinear material. The dispersion of the material is described by the Drude-Lorentz model of N different oscillators:

$$\epsilon_l = \left(1 + \frac{i\sigma_D}{2\pi f}\right)\left[\epsilon_\infty + \sum_n^N \frac{\sigma_n f_n^2}{f_n^2 - f^2 - i\frac{\gamma_n f}{2\pi}}\right], \tag{F.1}$$

  where ϵ_∞ denotes the infinite frequency permittivity (instantaneous dielectric function), σ_D denotes the dielectric conductivity, σ_n denotes the strength on the n-th resonance, and f_n denotes the central frequency of this resonance. The parameter γ_n is responsible for the losses associated with the n-th resonance.

  The nonlinearity is described by:

$$\epsilon = \epsilon_l + \chi^{(3)}|\mathbf{E}|^2. \tag{F.2}$$

  The comparison of Eqs. (F.2) and (1.6.13) reveals that, in the notation used in MEEP $\chi^{(3)}$ is identical to the parameter α used in our modal approaches developed in Chapters 2 and 6.
- Various types of boundary conditions including the Perfectly Matched Layers (PML).
- Reduction of the computational domain taking into account the symmetries of the problem.

- Study of an arbitrary material distribution.
- Parallel computations.

It is important to mention that, MEEP uses dimensionless units to express all the quantities that appear in the simulations. In all our simulations, the speed of light is set to be dimensionless: $c = 1$. Therefore the free-space wavelength is defined as the inverse of the light frequency f:

$$\lambda_0 = \frac{c}{f} = \frac{1}{f}, \tag{F.3}$$

The wavelength is expressed in a dimensionless MEEP unit of length [L]. Therefore, the frequency is expressed in the [1/L]. Because Maxwell's equations are scale invariant, the unit of wavelength can be chosen arbitrarily. We can assume that the vacuum wavelength $\lambda_0 = 1$ corresponds to 1 μm in order to simulate infrared light propagation. However, the same simulation can be interpreted as a study of microwaves, if we assume that $\lambda_0 = 1$ corresponds to 1 mm. All the physical dimensions have to be scaled accordingly. In the following, all the quantities will be expressed in the dimensionless MEEP units.

Using MEEP for nonlinear studies requires special care concerning the units. Here we discuss the way of the physical interpretation of the MEEP results on an example of the third-order nonlinear Kerr effect. The Kerr effect is described by Eq. (1.7.1) (see Sec. 1.7) which is recalled here:

$$n = n_0 + n_2 I. \tag{F.4}$$

For the nonlinear effects, the only significant quantity is the product $n_2 I$ and not the second-order nonlinear refractive index n_2 or the intensity density I separately. Therefore, the important thing is to recover numerically the correct value of this product. In MEEP, the second-order nonlinear refractive index n_2 is defined through the third-order susceptibility $\chi^{(3)}$ in the following way:

$$n_2 = \frac{3\chi^{(3)}}{4n_0^2}. \tag{F.5}$$

The unit of the second-order nonlinear refractive index n_2 [NL] is expressed as a unit of length square $[\mathrm{L}]^2$ divided by a unit of intensity [P]: $[\mathrm{NL}] = [\mathrm{L}]^2/[\mathrm{P}]$. Only two of these units can be chosen independently. The remaining one is fixed be the choice of the other two. For example, if we choose a unit of length [L] to be a μm and the unit of intensity to be W, then the unit of the second-order nonlinear refractive index n_2 is fixed to be $\mu\mathrm{m}^2/\mathrm{W}$.

In MEEP simulations, it is impossible to fix the power density or the total power transmitted by the studied structure as an input parameter in the code. In order to obtain the right value of the product $n_2 I$, we have to fix the n_2 value and then monitor the power inside the waveguide (see Ref. [176]). We need to obtain the power that results in the desired value of the product $n_2 I$. The power in the waveguide can be controlled by adjusting the amplitude of the current sources that generate the wave.

F.3 Linear plasmons is slot waveguide configuration

The first simulations performed using the FDTD method was a study of linear plasmons propagating in the slot waveguide. During this simple linear study we encountered several problems connected with the FDTD simulations (such as the choice of an optimal spatial resolution, a proper configuration of the sources or the behavior of the field on the metal interfaces in the PMLs).

To study the evolution of plasmons in the linear slot waveguide we choose the following configuration. A linear dielectric of thickness 0.5 and refractive index $n = \sqrt{\epsilon_{l,2}} = 2$ is sandwiched between two identical metal layers of thickness 2 and permittivity $\epsilon_m = -80 + 0.03i$.[1] The center of the structure

[1] In order to obtain negative values of permittivity in MEEP, we need to use the Drude-Lorentz model for the permittivity described by Eq. (F.1) with the appropriate parameters. The parameters used here were $\sigma_D = 0$, $\epsilon_\infty = 5$, $N = 1$, $\sigma_1 = 2000$, $f_1 = 0.1$, and $\gamma_1 = 0.001$.

is located at the point (0,0) in the MEEP coordinate frame. The structure length in the propagation (z) direction is equal to $L = 40$. In both x and z directions, a layer of thickness 1 at the extremities of the computational region is used to create the PMLs. The scheme of the computation cell is presented in Fig. F.2. The light frequency $f = 0.5$ is used for the simulations. The spatial resolution[2] used here is $R = 80$.

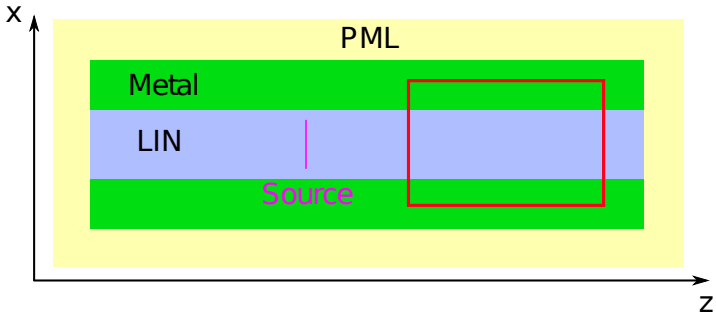

Figure F.2: Scheme of the computational domain where the linear plasmon propagation in the slot waveguide configuration was studied using the FDTD method. The blue region depicts the linear dielectric core, the green region represents the metal cladding. The PML layers, depicted in yellow, surround the slot waveguide structure. The location of the line source is depicted by the pink line and the domain in which the results are output is enclosed in the red rectangle.

In the FDTD method, the light is generated using electric and magnetic current sources. In our case, in order to generate TM polarized light, we use an electric current source polarized along the x direction in order to excite transverse magnetic waves.[3] We have tested several configurations of the current sources. We have started by point sources localized in the dielectric core close to the metal interfaces. The relative phase difference between the two point sources allowed us to excite symmetric plasmons (for the phase difference equal to 0) and antisymmetric plasmons (for the phase difference equal to π). The plasmon profiles obtained using point sources were in good agreement with the profiles found analytically. However, the point sources generate spherical waves that cause an important reflection from the metal surfaces close to the source location.

Another source current used by us was a line source in the full cross-section of the slot waveguide core. Because the field profiles inside of the waveguide core of the plasmons resemble simple analytical functions, plasmons can be excited using simple expressions for the line current distribution {flat profile $H_y = const$ for the symmetric plasmon and linear function $H_y = -x$ for the antisymmetric plasmon [see Figs. 7.13(a), (e), and Fig. F.4(a)]}. For the antisymmetric plasmon, the agreement between the $H_y = -x$ function and the field profile is very good. For the case of the symmetric plasmon, the field profile differs slightly from the flat function $H_y = const$. To check if this approximation is sufficient, we have tested the current source that had a profiled closer to the symmetric plasmon profile (a sum of two exponential functions or a parabolic function). The final field profiles (after the propagation) obtained using all these forms of the current source gave similar results. For the sake of the simplicity we decided to use a flat profile to excite symmetric plasmons. This allows us to use one simple form of the excitation regardless of the waveguide parameters and the expected plasmon profile (found analytically). There is no need of fitting the parabolic function parameters to overlap with the expected symmetric plasmon field profile for a given configuration. Our studies show that, the field profile generated by the flat current source reaches the expected profile after approximately one wavelength of propagation (one oscillation period).

[2]The spatial resolution of the FDTD method is defined by the number of computational points (pixels) in which a unit of length is divided. The field values are computed at these points.

[3]In our simulations we study two dimensional problems where the materials are isotropic (except in th PMLs). In this case we observe that, the FDTD method does not mix the polarizations excited by the source. The electric current source polarized along the x direction (E_x) excites the waves that have only three nonzero electromagnetic field components (E_x, E_z, and H_y). This polarization is maintained throughout the simulation. Other components of the electromagnetic field remain zero in the whole simulation domain at every instant of the simulation.

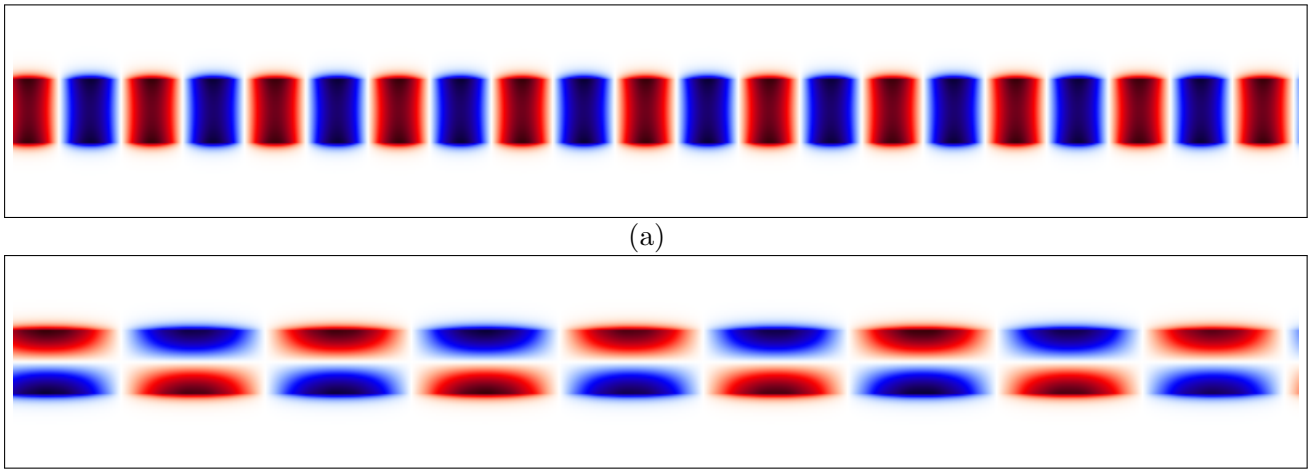

(a)

(b)

Figure F.3: Color maps of the magnetic field component $H_y(x, z)$ for the (a) symmetric and (b) antisymmetric linear plasmons in the slot waveguide for the simulation time step 200. See the text for the configuration parameters.

Another critical issue concerns the distance between the current source and the metal surface. If the line source occupies the full width of the core and therefore is in contact with the metal surface, spurious waves are generated on the surface of the metal. In order to avoid the appearance of these parasitic waves, we have used line sources with the width slightly smaller than the core width. Our analysis shows that, in order to avoid the spurious wave generation it is sufficient to use sources that are 8 pixels smaller than the core width (distance of 4 pixels from the metal layer on each side; see the pink line in Fig. F.2).

In Fig. F.3, we present the distribution of the magnetic field component $H_y(x, z)$ in a part of the computational domain for symmetric and antisymmetric plasmons in the linear slot waveguide (see the red rectangle in Fig. F.2). The size of the computational domain shown is 10×1.5 and is located far (10λ, where $\lambda = 1/(fn)$ denotes the wavelength in the medium) from the source. The choice of the part of the computational domain in which the results are output was dictated by the fact that, we have encountered difficulties with the behavior of the field at the metal interface in the PMLs. When the wave front reaches the PML, a standing wave localized at the metal interface is generated inside the PMLs. The amplitude of this wave grows rapidly. In the normalized color maps, this high intensity artifact was overshadowing the light propagating in the rest of the computational domain. We have found two partial solutions for this problem:

- We output the fields only in the small region that does not contain the PML's (see the red rectangle in Fig. F.2). This does not solve the problem of the generation of the standing wave in the PMLs, but allows us to observe the solution in the region that is not affected by this artifact.
- We locate the current source in the middle of the computational domain and study the propagation until the wave front reaches the PMLs. This prevents the generation of the standing wave in the PMLs. The drawback of this solutions is the fact that, we need to study large computational domains in order to be able to study long time of propagation. Long propagation times are required for the stabilization of some of the plasmon modes.

From Fig. F.3, we observe that both symmetric and antisymmetric plasmons are stable during the propagation and possess the desired symmetry.[4] These observations based on the color maps are confirmed using the cuts of the field profiles. We analyzed the profiles of the magnetic field component

[4]The symmetry of the solutions depends on the symmetry of the structure and sources. In the symmetric structures studied here, we obtained symmetric and antisymmetric solutions depending on the symmetry of the source. The symmetry of the solution was conserved during the propagation. The results were confirmed forcing the symmetry of the solution (simulations performed only in one half of the computational domain with the appropriate boundary conditions).

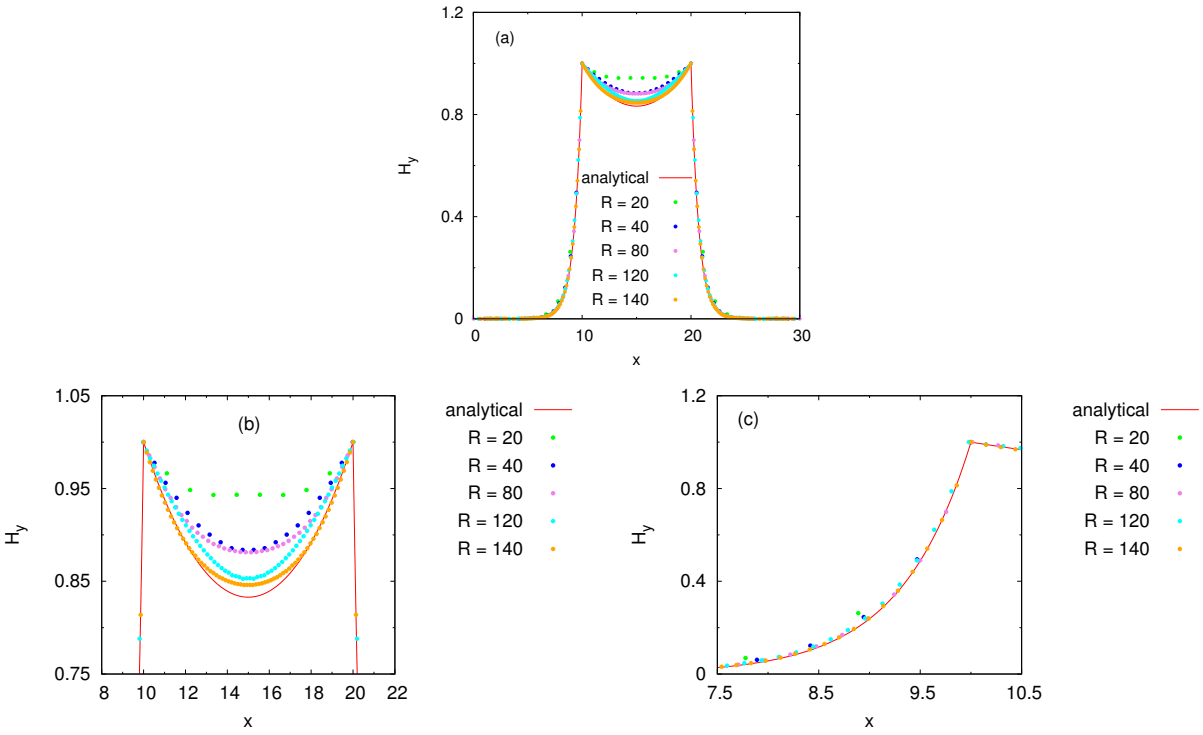

Figure F.4: Magnetic field profiles obtained by cuts of the field maps computed for different resolutions. (a) The full field profile, (b) the zoom of the region inside the dielectric core, and (c) zoom of the left cladding region. The cut is realized at the z coordinate corresponding to one of the maxima of the field intensity in the propagation direction.

along the waveguide cross-section for a few values of z. The profile of the antisymmetric plasmon is in a full agreement with the result of the analytical solution for the same structure (data not shown). The symmetric field profile obtained at the resolution $R = 80$ is quite different form the profile obtained using the analytical method [see the pink dots (for FDTD) and the red curve (for analytical solution) in Fig. F.4].

In order to improve the agreement between the analytically computed field profile and the results of the FDTD, we have increased the resolution of our simulations. It is important to notice that, the increase of the spatial resolution is accompanied by a rapid increase of the computational time and memory requirements. For the simulations in D spatial dimensions, the memory required scales like R^D and the computational time scales like R^{D+1} because the time step has to be reduced together with the space step in order for the FDTD method to be stable (non-diverging fields). In our two-dimensional problem, doubling the resolution results in the increase of the time simulation by a factor eight. The comparison of the results obtained using different resolutions is presented in Fig. F.4. From this figure, we notice that, the increase of the resolution improves the resemblance between the analytical and the FDTD results. For low resolution, the field profile in the waveguide core is much flatter than the analytical solution. Increasing the resolution, the curvature of the field profile obtained numerically becomes more similar to the curvature of the analytical solution.

To illustrate the effect of the field propagation, in Fig. F.5 we present the cut of the color map presenting the field profile of the symmetric plasmon at the z coordinate different from the one in Fig. F.4. We observe that the general character of the field profiles did not change. The field profiles obtained for high resolution resemble the analytical profile better than the field profiles obtained at low resolution. However this time, contrary to the situation presented in Fig. F.4, the profile obtained for the resolution 120 is closer to the analytical solution than the field profile computed with resolution 140. This shows that, even for high resolution, the field profiles evolve during the propagation.

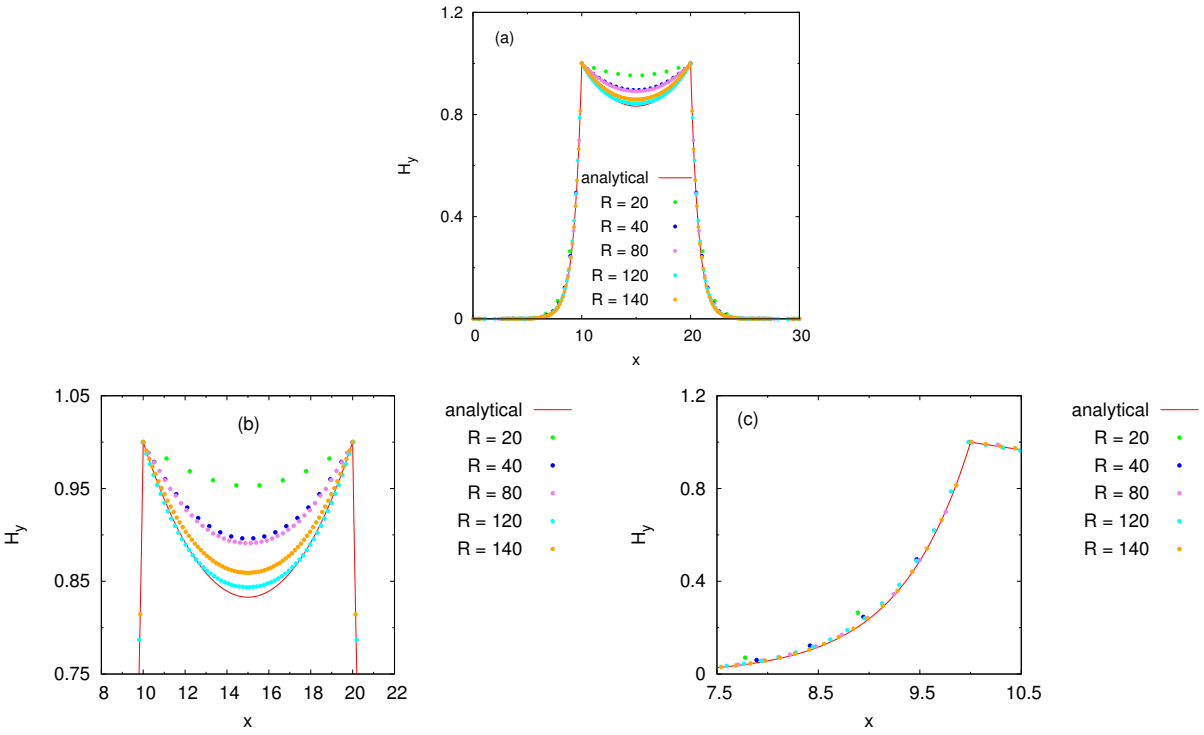

Figure F.5: Cuts of the magnetic field maps resulting in field profiles for different resolutions obtained using FDTD method. Cut taken at different position than in Fig. F.4. (a) Thee full field profile, (b) the zoom on the region inside the dielectric core, and (c) the zoom on field in the left cladding regions. The cut is realized at the z coordinate corresponding to one of the maxima of the field intensity in the propagation direction.

In order to confirm the improvement of the quality of the numerical solution with the increase of the resolution, we analyze the effective index β of the symmetric plasmon as a function of resolution.

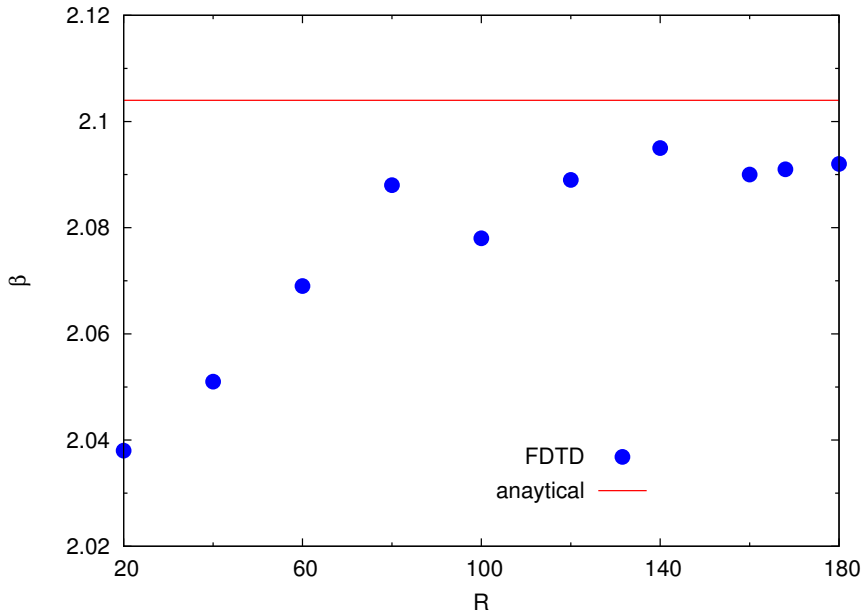

Figure F.6: Effective index of the symmetric plasmon in the linear slot waveguide as a function of the resolution of the FDTD method. The red line represents the effective index value obtained using the analytical model.

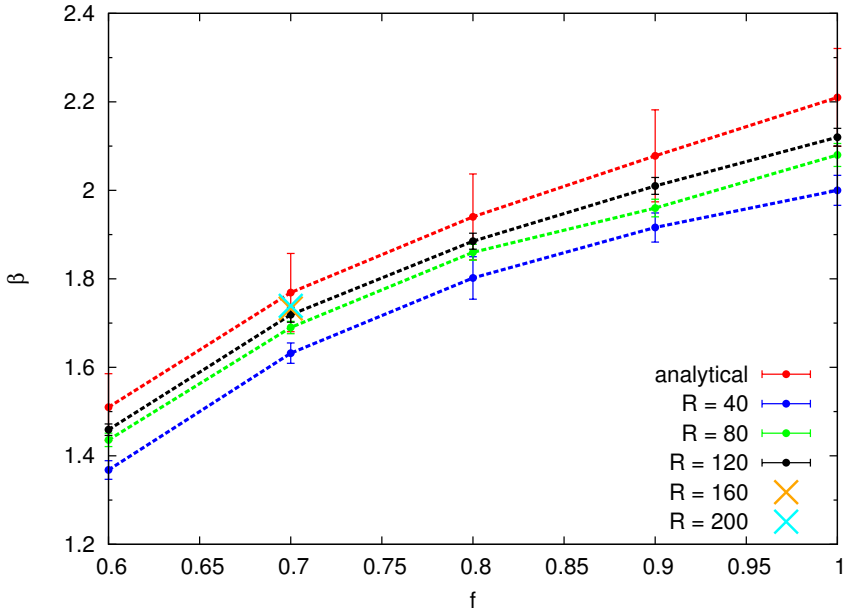

Figure F.7: Dispersion curves presenting the dependency of the effective index β of the antisymmetric linear plasmon as a function of the light frequency f. The red curve represents the analytic solution with the $\pm 5\%$ error bars. Blue, green, and black curves represent the FDTD solutions obtained using resolutions of 40, 80, and 120, respectively. The error bars denote the standard deviation of the effective index obtained numerically. Two points indicate the effective index obtained for resolutions 160 and 200 for the light frequency $f = 0.7$.

The effective index is calculated in the following way. We study the cut $H(x_c, z)$ of the color map $H(x, z)$ presented in Fig. F.3 along the z direction (at a constant x value). The position of the cut is chosen in such a way that the field amplitude along the cut is high. We choose $x_c = 0.45d$, so that the field amplitude for the cut is high both for symmetric and antisymmetric plasmons.[5] This cut represents a sinusoidal evolution of the wave during the propagation. We locate the position of all the zeros in this profile $z_0^{(n)}$, where n denotes the number of the zero found. The differences of the zero positions are calculated $\Lambda_n = z_0^{(n+1)} - z_0^{(n)}$. These differences are then averaged in order to give the average period of the wave $\Lambda = 1/N \sum_1^N \Lambda_n$. The ratio between the free-space wavelength and the average period gives us the effective index $\beta = \lambda_0/\Lambda$.

Figure F.6 presents the dependency of the effective index of the symmetric plasmon as a function of the resolution. We notice that with the increase of the resolution, the effective index values obtained using the FDTD become closer to the analytical value of the effective index for the symmetric plasmon in the studied structure. Even if the convergence is not monotonous, it confirms the conclusion drawn by analyzing the field profiles.

To verify if we correctly define the metal permittivity using the Drude-Lorentz permittivity dispersion given by Eq. (F.1) we perform two supplementary studies. We study the dispersion of the linear antisymmetric plasmons for different frequencies of the light. The dispersion curve obtained using the analytical model is compared with the numerical results in Fig. F.7. The parameters used for the Drude-Lorentz model are listed in Footnote 1 on Page 219 and correspond to the change in the real part of the metal permittivity from -55 at $f = 0.6$ to -15 at $f = 1$.

[5] For the symmetric plasmons we could choose the position close to the center of the waveguide as the field amplitude there is nonzero. However, for the antisymmetric plasmons, the amplitude in the center of the waveguide is equal to zero. Therefore the choice $x_c = 0.45d$ is more universal and can be used for studies of the propagation constant of both symmetric and antisymmetric plasmons. We also do not choose $x_c = 0.5d$, because the value of the derivative of the magnetic field at this point is not continuous.

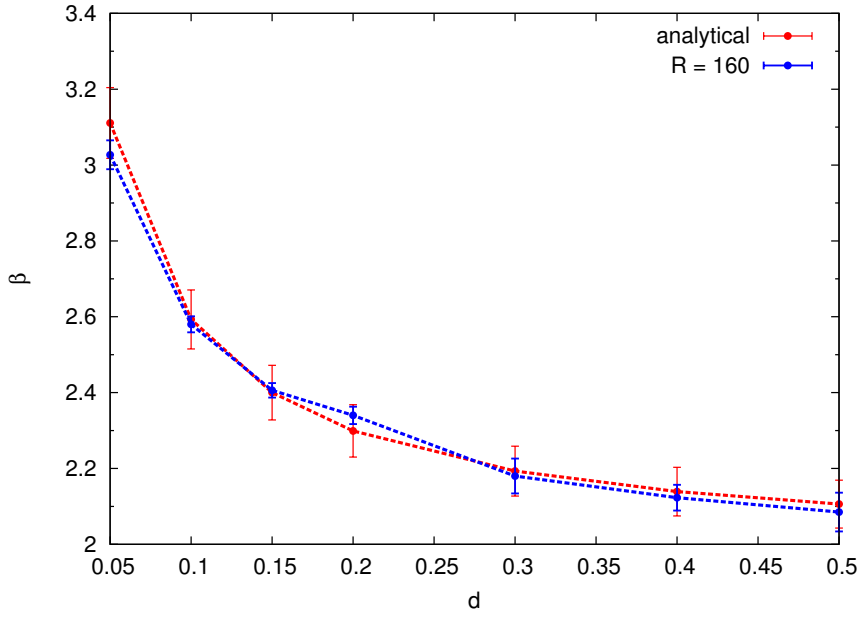

Figure F.8: Dispersion curves presenting the effective index β of the antisymmetric linear plasmon as a function of the slot waveguide core thickness d. The analytical results are show by the red curve with the $\pm 3\%$ error bars. The blue curve represents the FDTD results obtained at the resolution $R = 160$. The blue error bars denote the standard deviation of the effective index obtained numerically.

We see that even for the lowest resolution used ($R = 40$) the dispersion curve follows the analytical curve but is located below this curve. Increasing the resolution brings the numerical curve closer to the analytical one. The relative difference of the dispersion curves obtained at $R = 120$ and the one obtained analytically is less than 5% (the red error bars denote the 5% deviation from the analytical value). The resolutions above 120 were studied only for a single frequency $f = 0.7$. The increase of the resolution monotonously improves the quality of the numerical solution but it still remains below the analytical curve.

Moreover, we have studied the dependency of the effective index of the symmetric plasmon in the linear slot waveguide for different values of the thickness of the core. The comparison of the analytical and numerical results obtained for the resolution $R = 160$ is shown in Fig. F.8. We notice that the result obtained using the two methods are in agreement. The results obtained numerically using the FDTD method do not differ more than 3% from the analytical values (red error bars).

In conclusions, it is possible to study linear plasmons in the slot waveguide configurations using the FDTD method. However, one has to pay attention to several factors: (i) a proper choice of the source in order to avoid spurious excitations on the metal surfaces, (ii) careful choice of the output region, to avoid observation of the standing waves (whose amplitude grows exponentially in time) in the PML regions containing interfaces between metal and the nonlinear dielectric core, (iii) the choice of the spatial resolution that allows to reproduce plasmon features with sufficient accuracy, keeping the simulation time reasonably short.

F.4 Vacuum solitons

The second study that we have performed using the FDTD method is the analysis of the soliton propagation in a uniform bulk media with the refractive index $n = \sqrt{\epsilon_l} = 1$ (vacuum solitons). The aim of this study is to verify if the known relation between the soliton amplitude and its width is fulfilled in the numerical FDTD studies. The relation between the soliton amplitude and its width can be obtained from Eq. (2.1.23) [compare with Eqs. (23) and (24) from Ref. [5], Eq. (1.2.21) from Ref. [6], and Eq. (2.4) from Ref. [7] which give the expressions for a solitonic solution of a general

nonlinear Schrödinger equation]. Here we recall Eq. (2.1.23):

$$H_y = \sqrt{\frac{2}{a}} \frac{q}{\cosh[k_0 q(x - x_0)]}. \tag{F.1}$$

Equation (F.1) and be rewritten in the form:

$$\sqrt{a} H_y = \sqrt{2} q \operatorname{sech}[x/\sigma], \tag{F.2}$$

where x_0 was set to zero (the center of the beam can be chosen arbitrary in bulk medium) and k_0 was set to one, as in MEEP we work with dimensionless units that can be scaled arbitrarily. Here $\sigma = 1/q$ denotes the width of the beam. From Eq. (F.2), we observe that the normalized amplitude of the bulk solitons $\sqrt{a} H_y$ is proportional to q and therefore inversely proportional to the beam width σ:

$$\sqrt{a} H_y \propto \frac{1}{\sigma}. \tag{F.3}$$

Similar equation can be obtained for the electric field amplitude:

$$\sqrt{\chi^{(3)}} |\mathbf{E}| \propto \frac{1}{\sigma}. \tag{F.4}$$

We want to verify if the law described by Eq. (F.4) is fulfilled by the bulk solitons obtained using the FDTD method. To this end we study a bulk nonlinear dielectric with permittivity $\epsilon + \chi^{(3)} |\mathbf{E}|^2$.[6] To study vacuum solitons we set $\epsilon = n^2 = 1$. We consider a system of the dimension 50×150. The frequency of the source used is $f = 1$, which corresponds to the free-space wavelength $\lambda_0 = 1$. The PMLs are set around the whole simulation domain. The scheme of the simulation domain is presented in Fig. F.9. In the simulations of this fully dielectric system we did not encounter problems with the behavior of the fields in the PML layers.

The source is placed close to the left extremity of the simulation domain. The current source is a line source with the Gaussian profile. We use Gaussian excitation profile because it resembles the expected secant hyperbolic profile of the soliton. In the case of the dielectric with the refractive index $n = 1$, the wavelength in the material $\lambda = \lambda_0/n$ is equal to the free-space wavelength.

Figure F.10 presents the results of the propagation of the beam with the initial (input) width $\sigma = 1.5\lambda$ in the nonlinear medium for different values of the nonlinear parameter $\chi^{(3)}$. In panel (a),

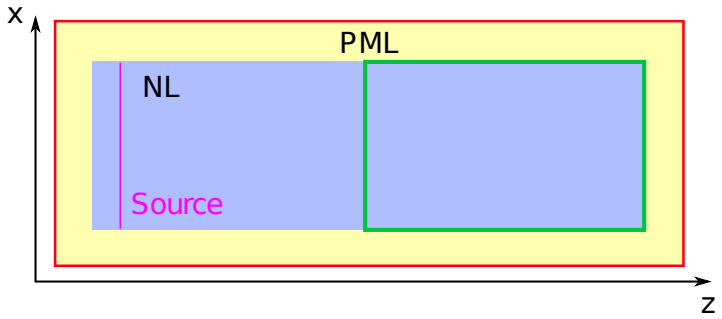

Figure F.9: Scheme of the computational domain where bulk solitons were studied using the FDTD method. The blue region depicts the nonlinear dielectric and the yellow region represents the PML layers. The location of the Gaussian current source is depicted by the pink line and the domain in which the results are output is enclosed in the red rectangle. The green rectangle encloses the region in which the fields are analyzed in order to calculate average width of the beam and the standard deviation of the width.

[6] In order to avoid the third harmonic generation in the Kerr medium studied numerically, we introduce a strong dispersion $\epsilon(f)$ in the nonlinear dielectric [using the Drude-Lorentz model described by Eq. (F.1)]. The parameters used here are $\sigma_D = 0$, $\epsilon_\infty = 0.8$, $N = 1$, $\sigma_1 = 0.2$, $f_1 = 4$, and $\gamma_1 = 0.005$. The losses were kept on a low level $\Im m(\epsilon) = 10^{-5}$.

we present the propagation of the Gaussian beam in the medium for which the nonlinearity is not strong enough to be able to preserve the initial width of the beam ($\chi^{(3)} = 0.1$). We observe that at the beginning of the propagation (left part of the color map), the beam diffracts. After the propagation distance approximately equal to 50 (1/3 of the simulation domain length), the beam width is stabilized at a value greater than the initial beam width.

In Fig. F.10(b), the propagation of the beam in the medium with $\chi^{(3)} = 0.2$ is shown. This value of the nonlinear parameter is optimal to balance the diffraction of the beam. In this figure we notice that, the beam width does not change during the propagation. This means that the value of the parameter $\chi^{(3)} = 0.2$ is appropriate to generate solitons with the beam width $\sigma = 1.5\lambda$.

In Fig. F.10(c), the propagation of the beam in the medium with $\chi^{(3)} = 0.3$ is shown. This value of the nonlinearity allows to focus the input beam below its initial beam width. The resulting soliton has lower beam width than the initial Gaussian beam.

Based on the methodology described in the example of Fig. F.10 for the beam width $\sigma = 1.5\lambda$, we analyze the formation of the solitons with various widths. The values of the nonlinear parameter $\chi^{(3)}$ required to find solitons of different widths is found analyzing the maps presenting the propagation. As we have seen in Fig. F.10, the optimal value of $\chi^{(3)}$ corresponds to the smallest variation in the beam width during the propagation. Therefore, the color maps $E_y(x, z)$ are analyzed numerically in the following way. First, we study the cut of the color map at $x = 0$. This results in a sinusoidal profile of the propagation along the z direction $E_y(x = 0, z)$. We find the positions of the maxima of this profile $z^{(n)}_{\max}$. At the position of each of the maxima we take a cut along the x direction, which gives us the transverse profile of the soliton $E_y(x, z = z^{(n)}_{\max})$ (the transverse profile resembles the well known secant hyperbolic field profile of the soliton). At each position, we measure the width σ_n (full width at half maximum - FWHM) of the soliton beam. The widths σ_n are then averaged and the standard deviation is calculated. This process is repeated for each value of the $\chi^{(3)}$ parameter studied. The $\chi^{(3)}$ for which the standard deviation of the width is the smallest is selected to be the optimum $\chi^{(3)}$ for the propagation of the soliton with a given width (equal to the initial width of the Gaussian beam).

The results of this analysis are presented in Fig. F.11. From this figure we notice that, the dependency given by Eq. (F.4) is well fulfilled by the simulation points obtained using the FDTD method. The data points were fit with a linear function $\sqrt{\chi^{(3)}} = b/\sigma$ which has the same form as Eq. (F.4) for a constant $|\mathbf{E}|$ value. The largest beam width that is studied is equal to 3.5λ. It is difficult to study wider beams because they diffract weakly. Study of wider beams requires large computational domains (both in the x direction due to the large beam width and in the z direction due to the slow diffraction) and long propagation times, that results in time and memory consuming simulations. The narrowest vacuum solitons studied here were 1.5λ wide. For this beam width the dependency given by Eq. (F.4) is well fulfilled. Narrower beams are studied in the next section, where the behavior of highly confined solitons is discussed.

F.5 Solitons in media

In this section, we present a study of the soliton formation in dielectric media, similar to the study of the vacuum solitons presented in Section F.4. Additionally to wide soliton beams, we analyze solitons confined to sub-wavelength widths. A nonlinear dielectric medium with the permittivity $\epsilon = n^2 = 4$ is considered.[7] The current source is generating waves at the frequency $f = 0.3$. The wavelength in the medium is $\lambda = 1/(fn) = 1.67$. The simulation domain has dimension 40×100.

Figure F.12 presents the propagation of the beam with the input width $\sigma = \lambda$ for different values of the nonlinear parameter $\chi^{(3)}$. Panel (a) shows the propagation of the Gaussian beam in the linear case ($\chi^{(3)} = 0$), where we can observe a strong diffraction of the beam. Panel (b) presents the propagation

[7] In order to avoid the third harmonic generation in the Kerr medium, we introduce a strong dispersion $\epsilon(f)$ in the nonlinear dielectric [using the Drude-Lorentz model described by Eq. (F.1)], similar to the case of vacuum solitons. The parameters used here are $\sigma_D = 0$, $\epsilon_\infty = 1.35$, $N = 1$, $\sigma_1 = 2.59$, $f_1 = 2$, and $\gamma_1 = 0.001$. The losses were at the level $\Im m(\epsilon) = 3 \cdot 10^{-5}$.

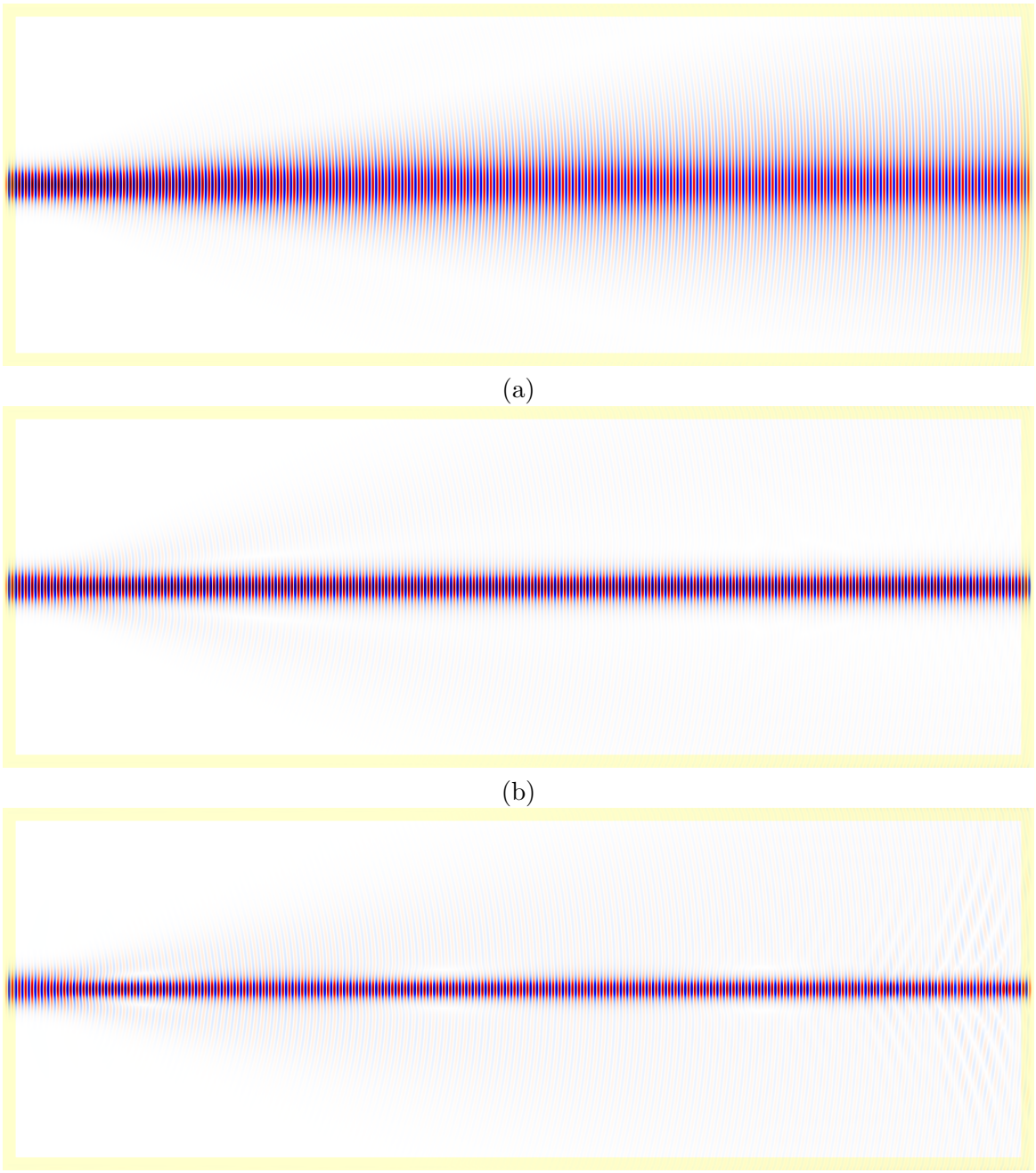

(a)

(b)

(c)

Figure F.10: Map of the electric field component $E_y(x, z)$ for the vacuum soliton propagation. The input beam width is $\sigma = 1.5\lambda$ and the snapshot is taken at the time step 200. The yellow borders at the extremities of the computational borders show the location of the PML layers. The nonlinear parameter $\chi^{(3)}$ is equal to (a) 0.1, (b) 0.2, and (c) 0.3. The peak amplitude is equal in each subplot. The output domain is marked in red in the scheme presented in Fig. F.9.

of the stationary soliton with the width equal to the initial width of the Gaussian beam. The stationary soliton is obtained for $\chi^{(3)} = 9$. In Fig. F.12(c), the nonlinear parameter is twice higher than for the stationary soliton with the width $\sigma = \lambda$ ($\chi^{(3)} = 20$). In this subfigure we observe that the input Gaussian beam is focused slightly stronger and the resulting soliton has the width smaller than λ. Figure F.12(d) shows the propagation of the beam for the nonlinear parameter five times higher than in panel (c) ($\chi^{(3)} = 100$). Surprisingly, we do not observe further focusing of the beam. The width of the

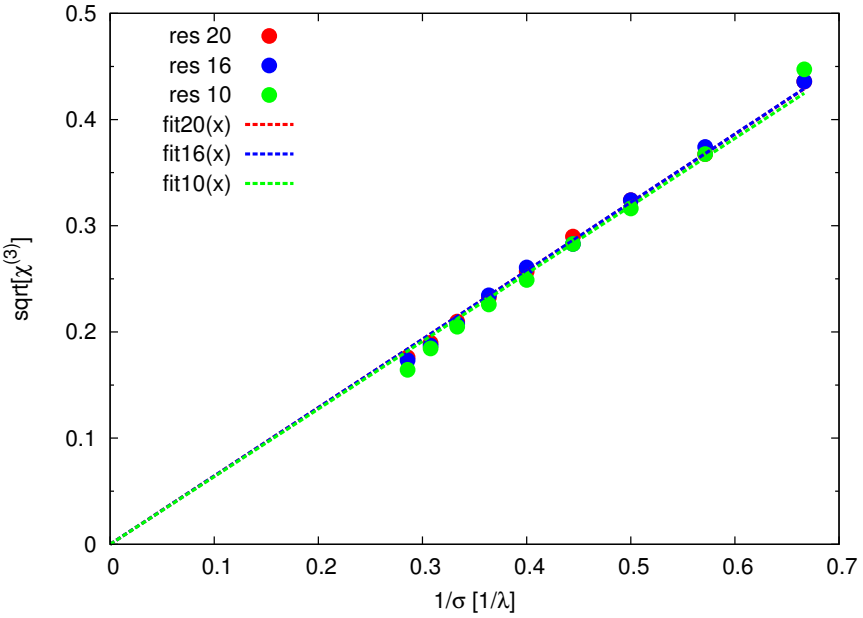

Figure F.11: Dependency of the optimal value of the nonlinear parameter $\sqrt{\chi^{(3)}(\sigma)}$ yielding a vacuum soliton with the width equal to the input width σ. The electric field amplitude $|\mathbf{E}|$ of the input beam is the same for each of the input widths σ studied.

beam is the same or even slightly larger than the width obtained for $\chi^{(3)} = 20$. These results indicate that the FDTD implementation used in MEEP may not be able to deal with high nonlinearities.

To verify the existence of this problem, we study even narrower input Gaussian beams. Figure F.13 presents the propagation results for the beam with the initial width $\sigma = 0.5\lambda$. We analyze here the values of the nonlinear parameter $\chi^{(3)}$ from 0 to 1600. For this very narrow input beam, we are not able to find the value of the $\chi^{(3)}$ parameter for which the diffraction would be fully balanced by the self-focusing nonlinear effects. The optimal value of the nonlinearity found by our method (finding the minimum of the beam width standard deviation) is $\chi^{(3)} = 70$ [panel (c)]. Nevertheless, it is clearly seen from the color map that the beam width is not constant during the propagation and therefore the solution is not stable. We notice that the solution width is oscillating (breathing soliton). The increase of the nonlinear parameter above 200 results in the field maps that become less focused during the propagation. This indicates that the MEEP implementation of the FDTD method is not capable of treating high nonlinearities. Moreover, the field profiles presented in Figs. F.13(d), (f), and (h) do not resemble a simple soliton for large propagation distances (right part of the computational domain). For high nonlinear parameters $\chi^{(3)}$, the Gaussian beam separated into two beams (for $\chi^{(3)} = 400$) or three beams ($\chi^{(3)} = 800$ and 1600). In the latter case, two side beams propagate at a certain angle with respect to the $x = 0$ axis. The field maps obtained for high nonlinearities are difficult to analyze with our method (finding the minimum of the beam width standard deviation) because it is difficult to define the half width of the beam with multiple lobes. Therefore, the optimal value of $\chi^{(3)}$ parameter for narrow input beams is not found correctly. The results presented here show that, using the excitation by a Gaussian beam we are not able to generate stationary solitons with a width equal or below $\sigma = 0.5\lambda$.

We have estimated the value of the nonlinear index modification corresponding to the formation of the beam with the width of 1λ. The soliton with the width of 1λ induces the nonlinear dielectric index change at the level $\Delta n \approx 0.1$. We conclude that this is the highest nonlinear index change that is correctly simulated using the MEEP implementation of the FDTD method.

To confirm the conclusion drawn from the visual analysis of the field maps, we have analyzed the field maps numerically. For a given input beam width σ we have analyzed the field maps for different values of the $\chi^{(3)}$ parameter. We have analyzed the value of the beam width averaged along the

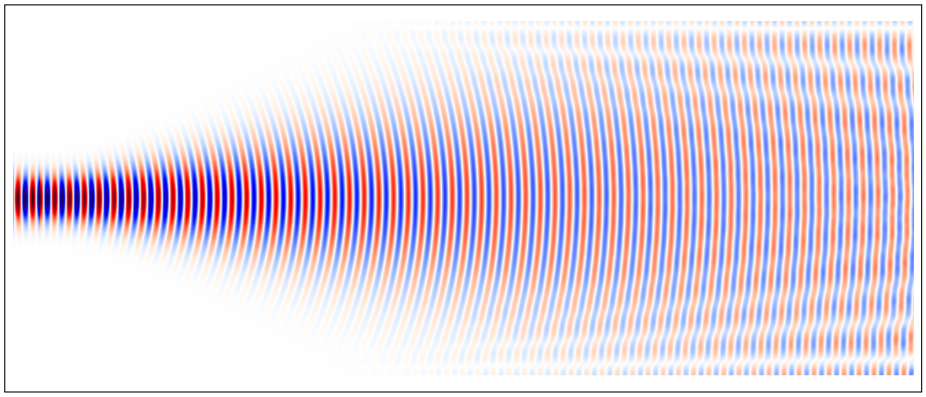

(a)

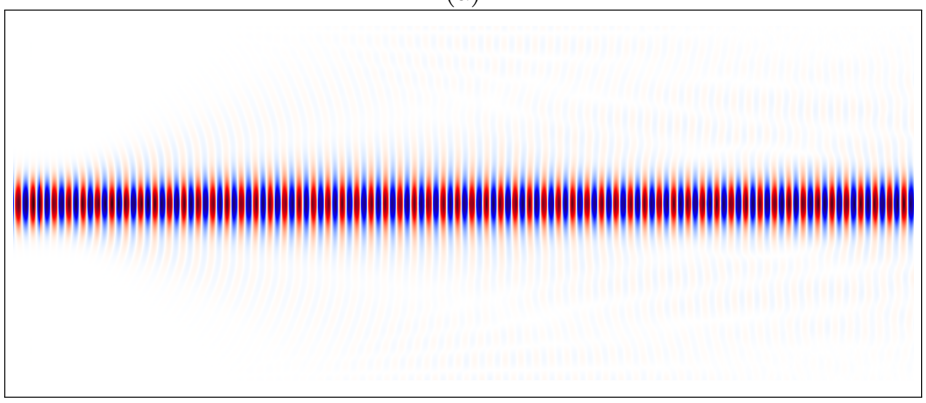

(b)

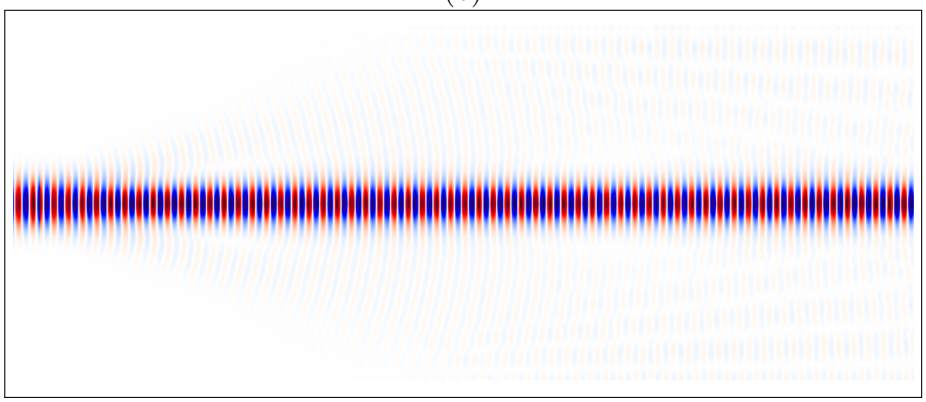

(c)

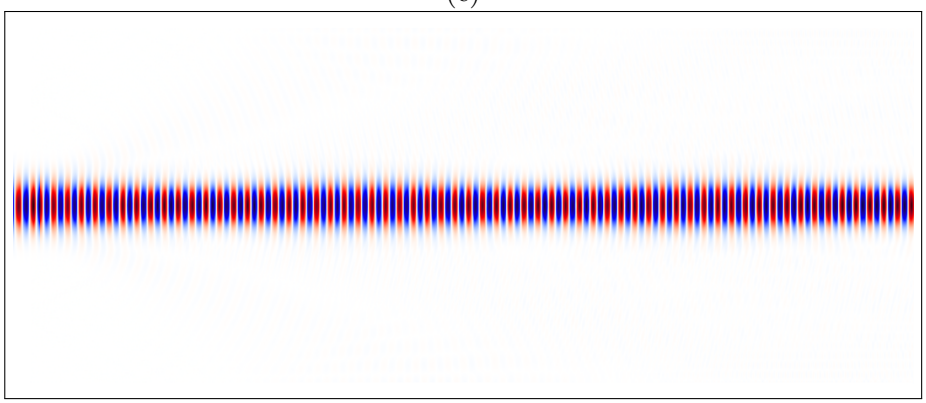

(d)

Figure F.12: Map of the electric field component $E_y(x, z)$ for the soliton propagation in media. The input beam width is $\sigma = 1\lambda$ and the snapshot is taken at the time step 305. The nonlinear parameter $\chi^{(3)}$ is equal to (a) 0, (b) 9, (c) 20, and (d) 100. The peak amplitude is equal in each subplot.

propagation ⟨FWHM⟩ (in the right part of the simulation domain in order not to take into account the beam formation close to the source; see the green rectangle in Fig. F.9). Our study, presented in Fig. F.14, shows the the dependency of the averaged width of the beam ⟨FWHM⟩ for different values of the $\chi^{(3)}$ parameter. This study was performed for four different values of the propagation length L (L denotes the computational domain size in the z direction).

The results for the linear case ($\chi^{(3)} = 0$) are not precise due to the finite size of the computational domain (in the x direction). As it can be seen in Fig. F.13(a), the field map there is influenced by the reflection from the computational domain boundaries resulting in the interference fringes. The large beam width for $\chi^{(3)} = 0$ confirms qualitatively the fact of the beam diffraction. For longer propagation lengths L, the beam diffracts more, which implies larger averaged beam width for long propagation lengths. In Fig. F.14, we observe a strong decrease of the averaged beam width for the values of the $\chi^{(3)}$ parameter between 25 and 100. Above $\chi^{(3)} = 100$ The averaged beam width remains at the constant level of 2 (MEEP units). This level is constant regardless of the length of the propagation studied.

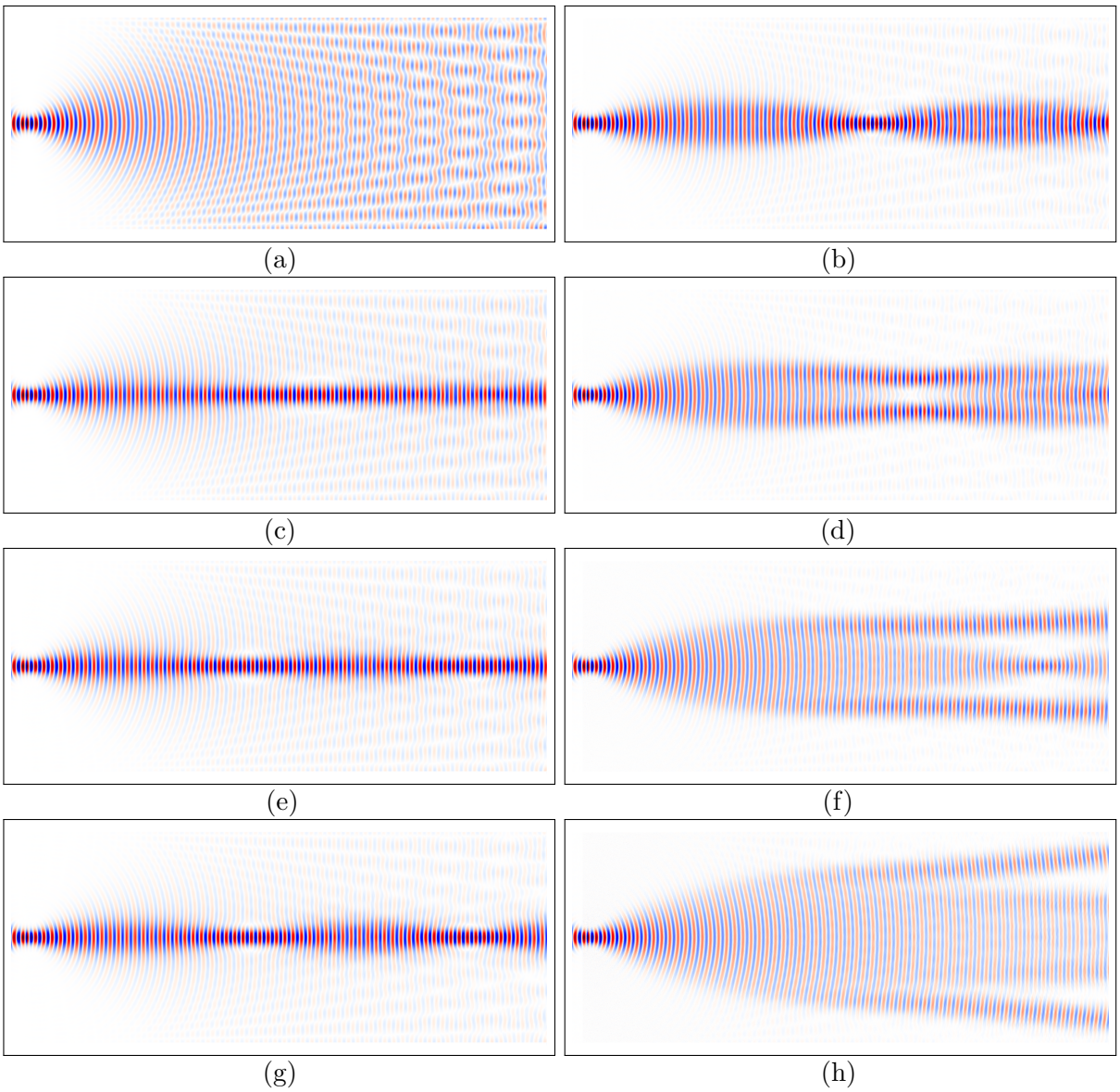

Figure F.13: Map of the electric field component $E_y(x, z)$ for the soliton propagation in media. The input beam width is $\sigma = 0.5\lambda$ and the snapshot is taken at the time step 305. The nonlinear parameter $\chi^{(3)}$ is equal to (a) 0, (c) 35, (e) 70, (g) 100, (b) 200, (d) 400, (f) 800, and (h) 1600. The peak amplitude is equal in each subplot.

Similar behavior is observed for beams with the initial width $\sigma = 0.5\lambda$ (see Fig. F.15). The strong focusing of the narrow beam occurs for higher values of the $\chi^{(3)}$ parameter that in the case of the broader beam. For $\sigma = 0.5\lambda$ the focusing occurs for the $\chi^{(3)}$ values around 250. For the values of the $\chi^{(3)}$ parameter above 450 the averaged with of the beam is equal to 2. This value is the same regardless of the propagation length studied and is identical to the value obtained for the broader beam (for the initial width $\sigma = 0.85\lambda$).

The propagation of the beam with the initial width $\sigma = 0.85$ was studied for various resolutions. The study presented in Fig. F.14 for $R = 16$ is compared with the simulation at higher resolution. The comparison of the results obtained for the propagation length $L = 100$ is shown in Fig. F.16. We observe an excellent agreement between the curves obtained for different resolutions. This proves that the resolution $R = 16$ is sufficient for the studies of solitons with the parameters we have chosen. Moreover, the results presented in Fig. F.16 confirm the fact that, for high nonlinearities the averaged beam width in our system can not be lower than 2. This means that the resolution have no influence on the way high third-order nonlinearities are treated in MEEP.

To sum up the results obtained in this section for the soliton propagation in high index media, the values of the $\chi^{(3)}$ parameter for which the standard deviation of beam width is the lowest for a given with of the input beam are presented in Fig. F.17. This figure presents the same dependency for the solitons in a high index medium, as the dependency presented in Fig. F.11 in the case of vacuum solitons. From Fig. F.17 we observe that, the linear relation given by Eq. F.4 is fulfilled for the beams with the initial width $\sigma \geqslant \lambda$. For narrower input beam, the optimal value of the $\chi^{(3)}$ parameter lays far from the dotted curve that represents the fit of the points obtained for $\sigma \geqslant \lambda$. This behavior results from the fact that, for the narrow input beams the diffraction can not be fully balanced by the nonlinearity. Therefore their field profiles do not resemble the profile of a soliton. The study presented in Fig. F.17 confirms our conclusions drawn by analyzing the field maps presented in Fig. F.13 stating that, the FDTD implementation used in MEEP has difficulties in treating high third-order nonlinearities.

One of the reasons for these difficulties is that the nonlinearity treatment implemented in MEEP uses a Padé approximation {see Eq. (20.4) in Ref. [162] or Eq. (4) in Ref. [175]}. This approximation describes well the Kerr nonlinearity for low light intensity and fails in the cases where the nonlinear

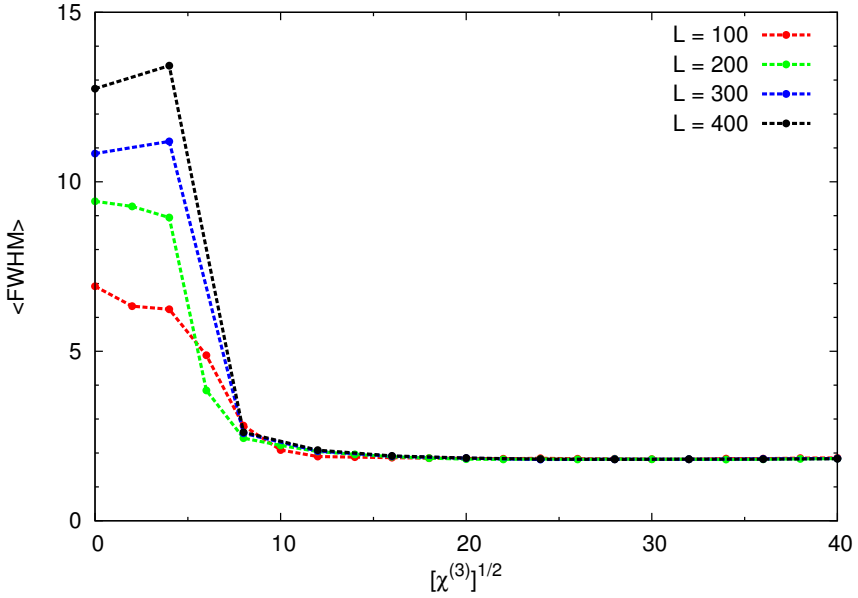

Figure F.14: Dependency of the average width of the beam on the square root of the nonlinear parameter $\chi^{(3)}$ for the beam with the initial width $\sigma = 0.85\lambda$. Results obtained at the resolution $R = 16$ for various propagation length are compared.

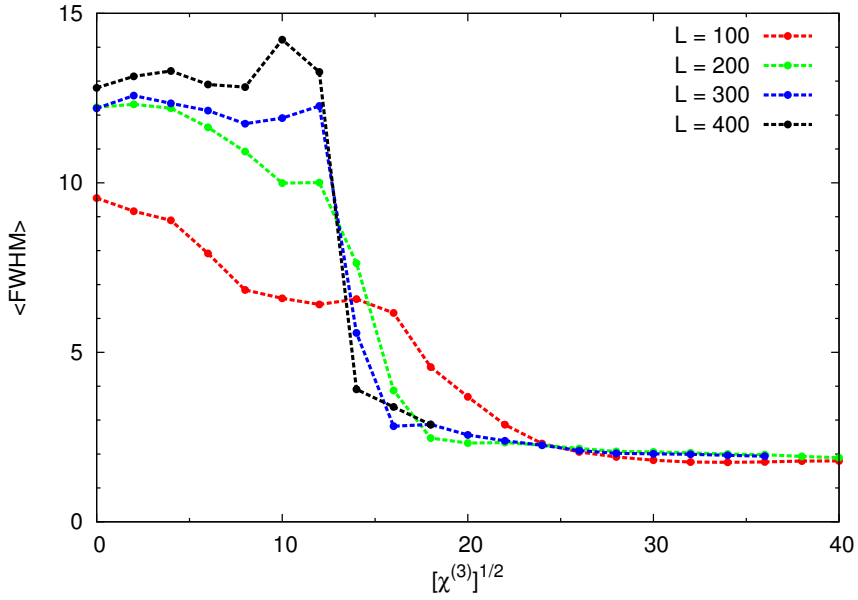

Figure F.15: Dependency of the average width of the beam on the square root of the nonlinear parameter $\chi^{(3)}$ for the beam with the initial width $\sigma = 0.5\lambda$. Results obtained at the resolution $R = 16$ obtained for various propagation length are compared.

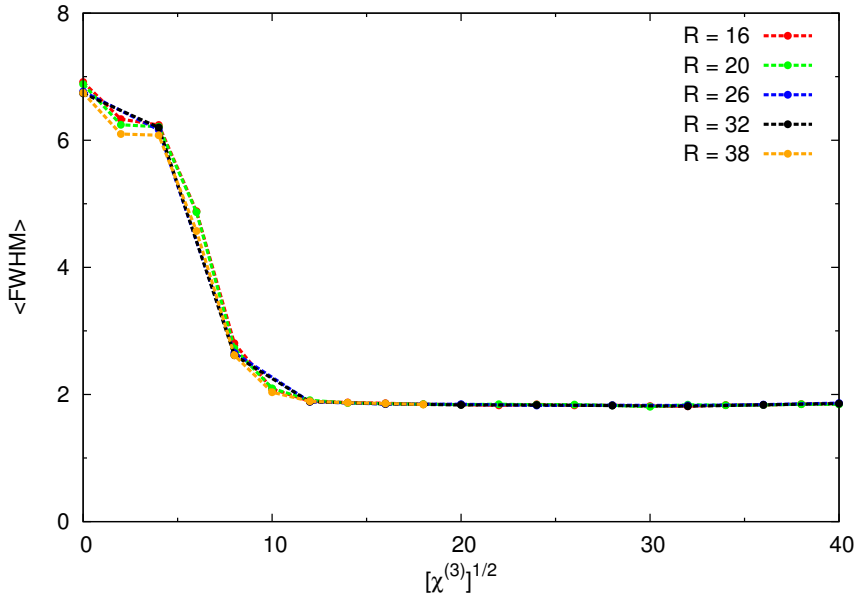

Figure F.16: Dependency of the average width of the beam $\langle \mathrm{FWHM} \rangle$ on the square root of the nonlinear parameter $\chi^{(3)}$ for a beam with an initial width $\sigma = 0.85\lambda$. Results obtained obtained for the propagation length $L = 100$ for various resolutions are compared. The results for the resolution $R = 38$ (yellow curve) are obtained only for the $\chi^{(3)}$ values lower than 300.

index modification is of the same order of magnitude as the linear part of the refractive index. One of the ways to avoid these problem could be the use of the general vector auxiliary differential equation (GVADE) method in the FDTD simulations. This method permits to model light propagation in complex media (also nonlinear) from first principles — the full-vector Maxwell's equations — and it is described in Ref. [177]. In this reference, the results of the GVADE FDTD simulations for narrow soliton beams (FWHM = 1.25λ) are also presented. These results are obtained for a beam width where

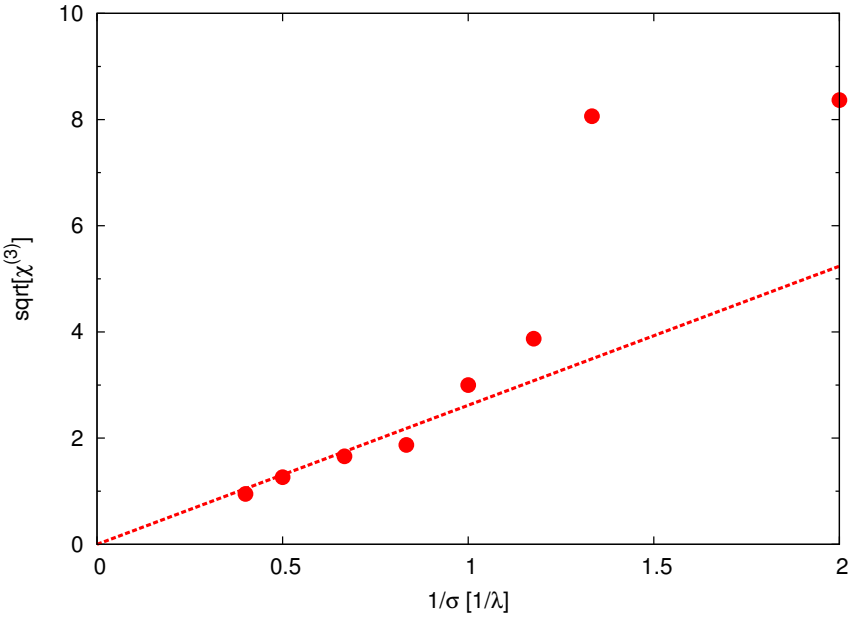

Figure F.17: Dependency of the optimal value of the nonlinear parameter $\sqrt{\chi^{(3)}(\sigma)}$ yielding a soliton with the width equal to the input width σ. The electric field amplitude $|\mathbf{E}|$ of the input beam is the same for each of the input widths σ studied.

our simulations also result in stable solitons. It would be interesting to use the GVADE FDTD for the solitons with lower beam widths to see if this method performs better in the case of high third-order nonlinearities than the standard FDTD approach implemented in MEEP.

Bibliography

[1] Y. R. Shen, *The principles of Nonlinear Optics* (Wiley, New York, 2003).

[2] R. W. Boyd, *Nonlinear Optics* (Academic, New York, 2007).

[3] G. I. Stegeman and R. A. Stegeman, *Nonlinear Optics: Phenomena, Materials and Devices* (Wiley, New York, 2012).

[4] R. Y. Chiao, E. Garmire, and C. H. Townes, "Self-trapping of optical beams," Phys. Rev. Lett. **13**, 479–482 (1964).

[5] S. Trillo and W. Torruellas, eds., *Spatial Solitons* (Springer, Berlin, 2001).

[6] Y. S. Kivshar and G. P. Agrawal, *Optical Solitons, From Fibres to Photonic Crystals* (Academic, New York, 2003).

[7] N. N. Akhmediev and A. Ankiewicz, *Solitons, Nonlinear Pulses and Beams* (Chapman & Hall, London, 1997).

[8] N. N. Akhmediev, "Spatial solitons in Kerr and Kerr-like media," Opt. Quant. Electron. **30**, 535–569 (1998).

[9] Z. Chen, M. Segev, and D. Christodoulides, "Optical spatial solitons: historical overview and recent advances," Rep. Prog. Phys. **75**, 086401 (2012).

[10] W. J. Tomlinson, "Surface wave at a nonlinear interface," Opt. Lett. **5**, 323–325 (1980).

[11] A. A. Maradudin, "s-polarized nonlinear surface polaritons," Z. Phys. B – Condensed Matter **41**, 341–344 (1981).

[12] K. M. Leung, "Propagation of nonlinear surface polaritons," Phys. Rev. A **31**, 1189–1192 (1985).

[13] H. E. Ponath and G. I. Stegeman, eds., *Modern Problems in Condensed Matter Sciences, Volume 29* (Elsevier, Amsterdam, 1991).

[14] A. D. Boardman, A. A. Maradudin, G. I. Stegeman, T. Twardowski, and E. M. Wright, "Exact theory of nonlinear p-polarized optical waves," Phys. Rev. A **35**, 1159–1164 (1987).

[15] D. Mihalache, G. I. Stegeman, C. T. Seaton, E. M. Wright, R. Zanoni, A. D. Boardman, and T. Twardowski, "Exact dispersion relations for transverse magnetic polarized guided waves at a nonlinear interface," Opt. Lett. **12**, 187–189 (1987).

[16] F. Lederer, U. Langbein, and H.-E. Ponath, "Nonlinear waves guided by a dielectric slab: I TE polarization," Appl. Phys. B **31**, 69–73 (1983).

[17] G. J. Robbins, "TE modes in a slab waveguide bounded by nonlinear media," Opt. Commun. **47**, 309–312 (1983).

[18] G. I. Stegeman, C. T. Seaton, J. Chilwell, and S. D. Smith, "Nonlinear waves guided by thin films," Appl. Phys. Lett. **44**, 830–832 (1984).

[19] F. Lederer, U. Langbein, and H.-E. Ponath, "Nonlinear waves guided by a dielectric slab: II TM polarization," Appl. Phys. B **31**, 187–190 (1983).

[20] D. Mihalache and D. Mazilu, "TM-polarized nonlinear waves guided by asymmetric dielectric layered structures," Appl. Phys. B **37**, 107–113 (1985).

[21] C. T. Seaton, J. D. Valera, B. Svenson, and G. I. Stegeman, "Comparison of solutions for TM-polarized nonlinear guided waves," Opt. Lett. **10**, 149–150 (1985).

[22] C. T. Seaton, J. D. Valera, R. L. Shoemaker, and G. I. Stegeman, "Anomalous nonlinear guided wave cut-off phenomena," Appl. Phys. Lett. **45**, 1162–1163 (1984).

[23] U. Langbein, F. Lederer, H.-E. Ponath, and U. Trutschel, "Analysis of the dispersion relations of nonlinear slab-guided waves. Part I: Asymmetrical configuration," Appl. Phys. B **36**, 187–193 (1985).

[24] U. Langbein, F. Lederer, H.-E. Ponath, and U. Trutschel, "Analysis of the dispersion relations of nonlinear slab-guided waves. Part II: Symmetrical configuration," Appl. Phys. B **38**, 263–268 (1985).

[25] N. N. Akhmediev, "Novel class of nonlinear surface waves: asymmetric modes in a symmetric layered structure," Sov. Phys. JETP **56**, 299–303 (1982).

[26] J. V. Moloney, J. Ariyasu, C. T. Seaton, and G. I. Stegeman, "Stability of nonlinear stationary waves guided by a thin film bounded by nonlinear media," Appl. Phys. Lett. **48**, 826–828 (1986).

[27] K. S. Chiang and R. A. Sammut, "Effective index-method for spatial solitons in planar waveguides with Kerr-type nonlinearity," J. Opt. Soc. Am. B **10**, 704–708 (1993).

[28] K. S. Chiang and R. A. Sammut, "Iterative methods and stability of TE modes of nonlinear planar waveguides," Opt. Commun. **109**, 59–64 (1994).

[29] N. N. Akhmediev, R. F. Nabiev, and Y. M. Popov, "Three-dimensional models of a symmetric nonlinear plane waveguide," Opt. Commun. **69**, 247–252 (1989).

[30] R. W. Micallef, Y. S. Kivshar, J. D. Love, D. Burak, and R. Binder, "Generation of spatial solitons using non-linear guided modes," Opt. Quant. Electron. **90**, 751–770 (1998).

[31] R. A. Sammut, Q. Y. Li, and C. Pask, "Variational approximation and mode stability in planar nonlinear waveguides," J. Opt. Soc. Am. B **9**, 884–890 (1992).

[32] S. Chelkowski and J. Chrostowski, "Scaling rules for slab waveguides with nonlinear substrate," Appl. Opt. **26**, 3681–3686 (1987).

[33] J. P. Torres and L. Torner, "Diagramatic analysis of nonlinear planar waveguides," J. Opt. Soc. Am. B **11**, 45–52 (1994).

[34] L. Leine, C. Wächter, and F. Lederer, "Evolution of nonlinear guided optical fields down a dielectric film with a nonlinear cladding," J. Opt. Soc. Am. B **5**, 547–558 (1988).

[35] D. Mihalache, D.-K. Baboiu, and D. Mazilu, "Propagation effects in nonlinear strip optical waveguides," Opt. Commun. **110**, 67–74 (1994).

[36] D. Mihalache, D.-M. Baboiu, D. Mazilu, L. Torner, and J. P. Torres, "Gausian-beam excitation and stability of three-dimensional nonlinear guided waves," J. Opt. Soc. Am. B **11**, 1244–1253 (1994).

[37] D. Mihalache, M. Bertolotti, and C. Sibilia, "Nonlinear wave propagation in planar structures," in "Progress in Optics," , vol. XXVII, E. Wolf, ed. (Elsevier, Amsterdam, 1989), pp. 229–313.

[38] W. R. Holland, "Nonlinear guided waves in low-index, self-focusing thin films: transverse electric case," J. Opt. Soc. Am. B. **3**, 1529–1534 (1986).

[39] A. D. Boardman and P. Egan, "Optical nonlinear waves in thin films," IEEE J. Quant. Electron. **22**, 319–324 (1986).

[40] W. Chen and A. A. Maradudin, "s-polarized guided and surface electromagnetic waves supported by a nonlinear dielectric film," J. Opt. Soc. Am. B **5**, 529–538 (1988).

[41] V. K. Fedyanin and D. Mihalache, "P-polarized nonlinear surface polaritons in layered structures," Z. Phys. B – Condensed Matter **47**, 167–173 (1982).

[42] U. Langbein, F. Lederer, and H.-E. Ponath, "A new type of nonlinear slab-guided waves," Opt. Commun. **46**, 167–169 (1983).

[43] N. N. Akhmediev, R. F. Nabiev, and Y. M. Popov, "Stripe nonlinear waves in asymmetrical planar structure," Opt. Commun. **72**, 190–194 (1989).

[44] D. Mihalache, D.-K. Baboiu, M. Ciumac, and D. Mazilu, "Propagation and stability of the stationary stripe nonlinear guided waves in a symmetric structure with a nonlinear film," Opt. Quant. Electron. **26**, S311–S319 (1994).

[45] M. Fontaine, "Scaling rules for nonlinear thin film optical waveguides," Appl. Opt. **29**, 3891–3899 (1990).

[46] U. Langbein, F. Lederer, and H.-E. Ponath, "Generalized dispersion relations for nonlinear slab-guided waves," Opt. Commun. **53**, 417–420 (1985).

[47] R. A. Sammut and C. Pask, "Gaussian and equivalent-step-index approximation for nonlinear waveguides," J. Opt. Soc. Am. B **8**, 395–402 (1991).

[48] Q. Y. Li, C. Pask, and R. A. Sammut, "Simple model for spatial optical solitons in planar waveguides," Opt. Lett. **16**, 1083–1085 (1991).

[49] R. A. Sammut, C. Pask, and Q. Y. Li, "Theoretical study of spatial solitons in planar waveguides," J. Opt. Soc. Am. B **10**, 485–491 (1993).

[50] A. D. Capobianco, B. Constantini, C. D. Angelis, G. F. Nalesso, and C. G. Someda, "Variational analysis of nonlinear channel waveguides," IEEE J. Quant. Electron. **31**, 512–519 (1995).

[51] N. A. Stathopoulos and J. D. Kanellopoulos, "Calculation of nonlinear waves guided by optical fibers with saturable nonlinear core and cladding: a resonance-technique approach," J. Opt. Soc. Am. B **14**, 1219–1227 (1997).

[52] D. Mihalache and R.-P. Wang, "Nonlinear guided waves in multilayer systems bounded by optically nonlinear media," J. Appl. Phys **69**, 1892–1900 (1991).

[53] Y.-D. Wu and M.-H. Chen, "Method for analyzing multilayer nonlinear optical waveguide," Opt. Express **13**, 7982–7996 (2005).

[54] C.-W. Kuo, S.-Y. Chen, M.-H. Chen, C.-F. Chang, and Y.-D. Wu, "Analyzing multilayer optical waveguide with all nonlinear layers," Opt. Express **15**, 2499–2516 (2007).

[55] S. A. Maier, *Plasmonics: Fundamentals and Applications* (Springer, Berlin, 2007).

[56] E. N. Economu, "Surface plasmons in thin films," Phys. Rev. **182**, 539–554 (1969).

[57] J. J. Burke, G. I. Stegeman, and T. Tamir, "Surface-polariton-like waves guided by thin, lossy metal films," Phys. Rev. B **33**, 5186–5201 (1986).

[58] H. Raether, ed., *Surface Plasmons on Smooth and Rough Surfaces and on Gratings* (Springer, Berlin, 1988).

[59] A. V. Zayats, I. I. Smolyaninov, and A. A. Maradudin, "Nano-optics of surface plasmon polaritons," Phys. Rep. **408**, 131–314 (2005).

[60] J. Homola, ed., *Surface Plasmon Resonance Based Sensors* (Springer, Berlin, 2006), chap. Electromagnetic Theory of Surface Plasmons, pp. 3–44.

[61] E. Ozbay, "Plasmonics: Merging photonics and electronics at nanoscale dimensions," Science **311**, 189–193 (2006).

[62] J. M. Pitarke, V. M. Silkin, E. V. Chulkov, and P. M. Echenique, "Theory of surface plasmons and surface-plasmon polaritons," Rep. Prog. Phys. **70**, 1–87 (2007).

[63] K. Y. Bliokh, Y. P. Bliokh, V. Freilikher, S. Savel'ev, and F. Nori, "Colloquim: Unusual resonators: Plasmonics, metamaterials, and random media," Rev. Mod. Phys. **80**, 1201–1213 (2008).

[64] P. Berini, "Long range surface plasmon polaritons," Adv. Opt. Phot. **1**, 484–588 (2009).

[65] M. Kauranen and A. V. Zayats, "Nonlinear plasmonics," Nature Photon. **6**, 737–748 (2012).

[66] B. Eggleton, B. Luther-Davies, and K. Richardson, "Chalcogenide photonics," Nature Photon. **5**, 141–147 (2011).

[67] V. M. Agranovich, V. S. Babichenko, and V. Y. Chernyak, "Nonlinear surface polaritons," JETP Lett. **32**, 512–215 (1980).

[68] G. I. Stegeman, C. T. Seaton, J. Ariyasu, R. F. Wallis, and A. A. Maradudin, "Nonlinear electromagnetic waves guided by a single interface," J. Appl. Phys. **58**, 2453–2459 (1985).

[69] A. A. Maradudin, "Nonlinear surface electromagnetic waves," in "Optical and Acoustics Waves in Solids — Modern Topics," , M. Borissov, ed. (World Scientific, Singapore, 1983), pp. 72–142.

[70] J.-H. Huang, R. Chang, P.-T. Leung, and D. P. Tsai, "Nonlinear dispersion relation for surface plasmon at a metal–Kerr medium interface," Opt. Commun. **282**, 1412–1415 (2009).

[71] K. Y. Bliokh, Y. P. Bliokh, and A. Ferrando, "Resonant plasmon-soliton interaction," Phys. Rev. A **79**, 041803 (2009).

[72] A. R. Davoyan, I. V. Shadrivov, and Y. S. Kivshar, "Self-focusing and spatial plasmon-polariton solitons," Opt. Express **17**, 21732–21737 (2009).

[73] J. Ariyasu, C. T. Seaton, G. I. Stegeman, A. A. Maradudin, and R. F. Wallis, "Nonlinear surface polaritons guided by metal films," J. Appl. Phys. **58**, 2460–2466 (1985).

[74] G. I. Stegeman and C. T. Seaton, "Nonlinear surface plasmons guided by thin metal films," Opt. Lett. **9**, 235–237 (1984).

[75] G. I. Stegeman, J. D. Valera, C. T. Seaton, J. Sipe, and A. A. Maradudin, "Nonlinear s-polarized surface plasmon polaritons," Solid State Commun. **52**, 293–297 (1984).

[76] D. Mihalache, D. Mazilu, and F. Lederer, "Nonlinear TE-polarized surface plasmon polaritons guided by metal films," Opt. Commun. **59**, 391–394 (1986).

[77] H. Yin, C. Xu, and P. M. Hui, "Exact surface plasmon dispersion relations in linear-metal-nonlinear dielectric structure of arbitrary nonlinearity," Appl. Phys. Lett. **94**, 221102 (2009).

[78] C.-C. Huang, "Pseudospectral mode solver for analyzing nonlinear optical waveguides," Opt. Express **20**, 13014–13028 (2012).

[79] W. Walasik, V. Nazabal, M. Chauvet, Y. Kartashov, and G. Renversez, "Low-power plasmon–soliton in realistic nonlinear planar structures," Opt. Lett. **37**, 4579–4581 (2012).

[80] A. Ferrando, C. Milián, and D. V. Skryabin, "Variational theory of soliplasmon resonances," J. Opt. Soc. Am. B **30**, 2507–2522 (2013).

[81] W. Walasik, G. Renversez, and Y. V. Kartashov, "Stationary plasmon-soliton waves in metal-dielectric nonlinear planar structures: modeling and properties," Phys. Rev. A **89**, 023816 (2014).

[82] C. Milián, D. E. Ceballos-Herrera, D. V. Skryabin, and A. Ferrando, "Soliton-plasmon resonances as Maxwell nonlinear bound states," Opt. Lett. **37**, 4221–4223 (2012).

[83] A. Degiron and D. R. Smith, "Nonlinear long-range plasmonic waveguides," Phys. Rev. A **82**, 033812 (2010).

[84] C.-C. Huang, "Analysis of long-range surface plasmon polaritons in nonlinear plasmonic waveguides using pseudospectral method," Opt. Express **20**, 18665–18678 (2012).

[85] E. Feigenbaum and M. Orenstein, "Plasmon-soliton," Opt. Lett. **32**, 674–676 (2007).

[86] A. W. Snyder and J. D. Love, *Optical Waveguide Theory* (Chapman and Hall, London, 1983).

[87] A. R. Davoyan, I. V. Shadrivov, and Y. S. Kivshar, "Nonlinear plasmonic slot waveguide," Opt. Express **16**, 21209–21214 (2008).

[88] W. H. Press, S. A. Teukolsky, W. T. Vetterling, and B. P. Flannery, *Numerical Recipes, The Art of Scientific Computing,* 3^{rd} *ed.* (Cambridge University Press, Cambridge, 2007).

[89] I. D. Rukhlenko, A. Pannipipitiya, and M. Premaratne, "Dispersion relation for surface plasmon polaritons in metal/nonlinear-dielectric/metal slot waveguides," Opt. Lett. **36**, 3374–3376 (2011).

[90] I. D. Rukhlenko, A. Pannipipitiya, M. Premaratne, and G. Agrawal, "Exact dispersion relation for nonlinear plasmonic waveguides," Phys. Rev. B **84**, 113409 (2011).

[91] M. A. Swillam and S. A. Tawfik, "Plasmonic slot waveguides with core nonlinearity," Plasmonics **9**, 409–413 (2014).

[92] W. Walasik, A. Rodriguez, and G. Renversez, "Symmetric plasmonic slot waveguides with a nonlinear dielectric core: Bifurcations, size effects, and higher order modes," Plasmonics, DOI: 10.1007/s11468-014-9773-5 (2014).

[93] J. R. Salgueiro and Y. S. Kivshar, "Nonlinear plasmonic directional couplers," Appl. Phys. Lett. **97**, 081106 (2010).

[94] A. Marini, A. V. Gorbach, and D. V. Skryabin, "Coupled-mode approach to surface plasmon polaritons in nonlinear periodic structures," Opt. Lett. **35**, 3532–3534 (2010).

[95] Y. Kou, F. Ye, and X. Chen, "Surface plasmonic lattice solitons," Opt. Lett. **37**, 3822–3824 (2012).

[96] F. Ye, D. Mihalache, B. Hu, and N. C. Panoiu, "Subwavelength plasmonic lattice solitons in arrays of metallic nanowires," Phys. Rev. Lett. **104**, 106802 (2010).

[97] F. Ye, D. Mihalache, B. Hu, and N. C. Panoiu, "Subwavelength vortical plasmonic lattice solitons," Opt. Lett. **36**, 1179–1181 (2011).

[98] Y. Kou, F. Ye, and X. Chen, "Multipole plasmonic lattice solitons," Phys. Rev. A **84**, 033855 (2011).

[99] A. R. Davoyan, "Plasmonic couplers with metal nonlinearities," Phys. Lett. A **375**, 1615–1618 (2011).

[100] A. R. Davoyan, I. V. Shadrivov, and Y. S. Kivshar, "Symmetry breaking in plasmonic waveguides with metal nonlinearities," Opt. Lett. **36**, 930–932 (2011).

[101] J. D. Jackson, *Classical Electrodynamics,* 3^{rd} *ed.* (Wiley, New York, 1999).

[102] D. J. Griffiths, *Introduction to Electrodynamics* (Prentice Hall, New Jersey, 1999).

[103] R. W. Boyd, ed., *Nonlinear Optics* (Academic, New York, 2007), chap. Introduction to Nonlinear Optics, pp. 1–4.

[104] B. Crosignani, A. Cutolo, and P. D. Porto, "Coupled-mode theory of nonlinear propagation in multimode and single-mode fibers: envelope solitons and self-confinement," J. Opt. Soc. Am. **72**, 1136–1141 (1982).

[105] A. Ciattoni, B. Crosignani, P. D. Porto, and A. Yariv, "Perfect optical solitons: spatial Kerr solitons as exact solutions of Maxwell's equations," J. Opt. Soc. Am. B **22**, 1384–1394 (2005).

[106] A. A. Sukhorukov, A. S. Solntsev, S. S. Kruk, D. N. Neshev, and Y. S. Kivshar, "Nonlinear coupled-mode theory for periodic plasmonic waveguides and metamaterials with loss and gain," Opt. Lett. **39**, 462–465 (2014).

[107] D. J. Griffiths, *Introduction to Electrodynamics* (Prentice Hall, New Jersey, 1999), p. 383.

[108] R. D. Ettinger, F. A. Fernandez, B. M. A. Rahman, and J. B. Davies, "Vector finite element solution of saturable nonlinear strip-loaded optical waveguide," IEEE Photon. Technol. Lett. **3**, 147–149 (1991).

[109] Q. Y. Li, R. A. Sammut, and C. Pask, "Variational and finite element analyses of nonlinear strip optical waveguides," Opt. Commun. **94**, 37–43 (1992).

[110] F. Drouart, G. Renversez, A. Nicolet, and C. Geuzaine, "Spatial Kerr solitons in optical fibres of finite size cross section: beyond the Townes soliton," J. Opt. A: Pure Appl. Opt. **10**, 125101 (2008).

[111] I. S. Gradshteyn and I. M. Ryzhik, *Table of integrals, series, and products* (Academic, New York, 1980).

[112] M. Abramowitz and I. A. Stegun, eds., *Handbook of Mathematical Functions With Formulas, Graphs, and Mathematical Tables* (Dover, New York, 1964).

[113] A. W. Snyder and J. D. Love, *Optical Waveguide Theory* (Chapman and Hall, London, 1983), chap. Modal methods for Maxwell's equations, pp. 601–622.

[114] F. Zolla, G. Renversez, A. Nicolet, B. Kuhlmey, S. Guenneau, D. Felbacq, A. Argyros, and S. Leon-Saval, *Foundations of Photonic Crystal Fibres,* 2^{nd} *ed.* (Imperial College Press, London, 2012), chap. Main properties of microstructured optical fibres, pp. 327–388.

[115] J. Jin, *The Finite Element Method in Electromagnetic,* 2^{nd} *ed.* (Wiley, New York, 2002).

[116] K. Hayata and M. Koshiba, "Full vectorial analysis of nonlinear-optical waveguides," J. Opt. Soc. Am. B. **5**, 2494–2501 (1988).

[117] B. M. A. Rahman, J. R. Souza, and J. B. Davies, "Numerical analysis of nonlinear bistable optical waveguides," IEEE Photon. Technol. Lett. **2**, 265–267 (1990).

[118] B. M. A. Rahman, F. A. Fernandez, and J. B. Davies, "Review of finite element methods for microwave and optical waveguides," Proc. IEEE **79**, 1442–1448 (1991).

[119] F. Zolla, G. Renversez, A. Nicolet, B. Kuhlmey, S. Guenneau, D. Felbacq, A. Argyros, and S. Leon-Saval, *Foundations of Photonic Crystal Fibres, 2^{nd} ed.* (Imperial College Press, London, 2012), chap. Finite Element Method, pp. 159–233.

[120] P. Dular, C. Geuzaine, F. Henrotte, and W. Legros, "A general environment for the treatment of discrete problems and its application to the finite element method," IEEE Trans. Magn. **34**, 3395–3398 (1998).

[121] C. Geuzaine, "GetDP: a general finite-element solver for the de Rham complex," in "Sixth International Congress on Industrial Applied Mathematics (ICIAM07) and GAMM Annual Meeting, Zürich 2007, Special Issue of Proc. Appl. Math. Mech.", , vol. 7 (Wiley, 2008), vol. 7, pp. 1010603–1010604.

[122] C. Geuzaine and J.-F. Remacle, "Gmsh: a three-dimensional finite element mesh generator with built-in pre- and post-processing facilities," Int. J. Numer. Meth. Eng. **79**, 1309–1331 (2009).

[123] F. Drouart, "Non-linéarité Kerr dans les fibres optiques microstructurées," Ph.D. thesis, University of Aix-Marseille III (2009).

[124] J. Homola, J. Čtyroký, M. Skalský, J. Hradilová, and P. Kolářová, "A surface plasmon resonance based integrated optical sensor," Sens. Actuat. B–Chem **38–39**, 286–290 (1997).

[125] J. Čtyroký, J. Homola, P. V. Lambeck, S. Musa, H. J. W. M. Hoekstra, R. D. Harris, J. S. Wilkinson, B. Usievich, and N. M. Lyndin, "Theory and modelling of optical waveguide sensor utilising surface plasmon resonance," Sens. Actuat. B–Chem **34**, 66–73 (1999).

[126] J. Čtyroký, J. Homola, and M. Skalský, "Modelling of surface plasmon resonance waveguide sensor by complex mode expansion and propagation," Opt. Quant. Electron. **29**, 301–311 (1997).

[127] J. Homola, ed., *Surface Plasmon Resonance Based Sensors* (Springer, Berlin, 2006).

[128] S. A. Taya, M. M. Shabat, H. M. Khalil, and D. S. Jäger, "Theoretical analysis of TM nonlinear asymmetrical waveguide optical sensors," Sens. Actuat. A–Phys **147**, 137–141 (2008).

[129] R. Jha and A. Sharma, "High-preformance sensor based on surface plasmon resonance with chalcogenide prism ans aluminium for detection in infrared," Opt. Lett. **34**, 749–751 (2009).

[130] D. Kumar and V. Singh, "Theoretical modeling of a nonlinear asymmetric metal-clad planar waveguide based sensors," Optik **122**, 1872–1875 (2011).

[131] R. Rangel-Rojo, T. Kosa, E. Hajto, P. J. S. Ewen, A. E. Owen, A. K. Kar, and B. S. Wherrett, "Near-infrared optical nonlinearities in amorphous chalcogenides," Opt. Commun. **109**, 145–150 (1994).

[132] G. Boudebs, F. Sanchez, J. Troles, and F. Smektala, "Nonlinear optical properties of chalcogenide glasses: comparison between Mach–Zehnder interferometry and Z-scan techniques," Opt. Commun. **199**, 425–433 (2001).

[133] A. Zakery and S. R. Elliott, "Optical properties and applications of chalcogenide glasses: a review," J. Non-Cryst. Solids **330**, 1–12 (2003).

[134] A. Zakery and M. Hatami, "Nonlinear optical properties of pulsed-laser-deposited GeAsSe films and simulation of a nonlinear directional coupler switch," J. Opt. Soc. Am. B **22**, 591–597 (2005).

[135] A. Zakery and S. R. Elliott, *Optical Nonlinearities in Chalcogenide Glasses and their Applications* (Springer, Berlin, 2007).

[136] J. Fatome, C. Fortier, T. N. Nguyen, T. Chartier, F. Smektala, K. Messaad, B. Kibler, S. Pitois, G. Gadret, C. Finot, J. Troles, F. Desevedavy, P. Houizot, G. Renversez, L. Brilland, and N. Traynor, "Linear and nonlinear characterizations of chalcogenide photonic crystal fibers," J. Lightwave Technol. **27**, 1707–1715 (2009).

[137] K. Narayanan and S. F. Preble, "Optical nonlinearities in hydrogenated-amorphous silicon waveguides," Opt. Express **18**, 8998–9005 (2010).

[138] B. Kuyken, H. Ji, S. Clemmen, S. K. Selvaraja, H. Hu, M. Pu, M. Galili, P. Jeppesen, G. Morthier, S. Massar, L. K. Oxenløwe, G. Roelkens, and R. Baets, "Nonlinear properties of and nonlinear processing in hydrogenated amorphous silicon waveguides," Opt. Express **19**, B146–B153 (2011).

[139] J. Matres, G. C. Ballesteros, P. Gautier, J.-M. Fédéli, J. Martí, and C. J. Oton, "High nonlinear figure-of-merit amorphous silicon waveguides," Opt. Express **21**, 3932–3940 (2012).

[140] C. Grillet, L. Carletti, C. Montat, P. Grosse, B. B. Bakir, S. Menezo, J. M. Fedeli, and D. J. Moss, "Amorphous silicon nanowires combining high nonlinearity, FOM and optical stability," Opt. Express **20**, 22609–22615 (2012).

[141] K.-Y. Wang and A. C. Foster, "Ultralow power continuous-wave frequency conversion in hydrogenated amorphous silicon waveguides," Opt. Lett. **37**, 1331–1333 (2012).

[142] C. Lacava, P. Minzioni, E. Baldini, L. Tartara, J. M. Fedeli, and I. Cristiani, "Nonlinear characterization of hydrogenated amorphous silicon waveguides and analysis of carrier dynamics," Appl. Phys. Lett. **103**, 141103 (2013).

[143] E. D. Palik, ed., *Handbook of Optical Constants of Solids Vol. 1* (Academic, New York, 1985).

[144] P. B. Johnson and R. W. Christy, "Optical constants of the noble metals," Phys. Rev. B **6**, 4370–4379 (1972).

[145] A. D. Rakic, A. B. Djurisic, J. M. Elazar, and M. L. Majewski, "Optical properties of metallic films for vertical-cavity optoelectronic devices," Appl. Opt. **37**, 5271 (1998).

[146] "Scilab," http://www.scilab.org.

[147] V. Nazabal, M. Cathelinaud, W. Shen, P. Nemec, F. Charpentier, H. Lhermite, M.-L. Anne, J. Capoulade, F. Grasset, A. Moreac, S. Inoue, M. Frumar, J.-L. Adam, M. Lequime, and C. Amra, "Chalcogenide coatings of $Ge_{15}Sb_{20}S_{65}$ and $Te_{20}As_{30}Se_{50}$," Appl. Opt. **47**, C114–C123 (2008).

[148] A. R. Davoyan, I. V. Shadrivov, and Y. S. Kivshar, "Quadratic phase matching in nonlinear plasmonic nanoscale waveguides," Opt. Express **17**, 20063–20068 (2009).

[149] N. Nozhat and N. Granpayeh, "Switching power reduction in the ultra-compact kerr nonlinear plasmonic directional coupler," Opt. Commun. **285**, 1555–1559 (2012).

[150] D. A. Smirnova, A. V. Gorbach, I. V. Iorsh, I. V. Shadrivov, and Y. S. Kivshar, "Nonlinear switchiung with graphene coupler," Phys. Rev. B **88**, 045443 (2013).

[151] A. R. Davoyan, I. V. Shadrivov, A. A. Zharov, D. K. Gramotnev, and Y. S. Kivshar, "Nonlinear nanofocusinf in tapered plasmonic waveguides," Phys. Rev. Lett. **105**, 116804 (2010).

[152] M. Abramowitz and I. A. Stegun, eds., *Handbook of Mathematical Functions With Formulas, Graphs, and Mathematical Tables* (Dover, New York, 1964), chap. Jacobian Elliptic Functions and Theta Functions, pp. 569–588.

[153] D. J. Mitchell and A. W. Snyder, "Stability of fundamental nonlinear guided waves," J. Opt. Soc. Am. B **10**, 1572–1580 (1993).

[154] M. Abramowitz and I. A. Stegun, eds., *Handbook of Mathematical Functions With Formulas, Graphs, and Mathematical Tables* (Dover, New York, 1964), chap. Elliptic Integrals, pp. 589–626.

[155] J. M. T. Thompson and H. B. Stewart, *Nonlinear dynamics and chaos,* 2^{nd} *ed.* (Wiley, New York, 2002).

[156] Y. Kivshar and A. A. Sukhorukov, "Stability of spatial optical solitons," in "Spatial Solitons," , S. Trillo and W. Torruellas, eds. (Springer, 2001), pp. 211–245.

[157] C. Weilnau, M. Ahles, J. Petter, D. Träger, J. Schröder, and C. Denz, "Spatial optical (2+1)-dimensional scalar- and vector-solitons in saturable nonlinear media," Ann. Phys. (Leipzig) **8**, 579–1629 (2002).

[158] J. V. Moloney, J. Ariyasu, C. T. Seaton, and G. I. Stegeman, "Numerical evidence for nonstationary, nonlinear, slab-guided waves," Opt. Lett. **11**, 315–317 (1986).

[159] D. Mihalache, D. Mazilu, M. Bertolotti, and C. Sibilia, "Exact solutions for nonlinear thin-film guided waves in higher-order nonlinear media," J. Opt. Soc. Am. B **5**, 565–570 (1988).

[160] A. B. Aceves, A. D. Capobianco, B. Constantini, C. D. Angelis, and G. F. Nalesso, "Two domensional variational analysis of self-trapped solutions in planar waveguides," Opt. Commun. **105**, 341–346 (1994).

[161] A. Taflove and S. C. Hagness, *Computational Electrodynamics: The Finite-Difference Time-Domain Method,* 3^{rd} *ed.* (Artech House, Boston, 2005).

[162] A. Taflove, ed., *Advances in FDTD Computational Electrodynamics* (Artech House, Boston, 2013).

[163] J. Čtyroký, P. Kwiecien, and I. Richter, "Analysis of hybrid dielectric-plasmonic slot waveguide structures with 3d fourier modal methods," J. Europ. Opt. Soc. Rap. Public. **18**, 13024 (2013).

[164] J. Petráček, "Nonlinear directional coupling between plasmonic slot waveguides," Appl. Phys. B **112**, 593–598 (2013).

[165] C. K. R. T. Jones and J. V. Moloney, "Instability of standing waves in nonlinear optical waveguides," Phys. Lett. A **117**, 175–180 (1989).

[166] M. G. Vakhitov and A. A. Kolokolov, "Stationary solutions of the wave equation in the medium with nonlinearity saturation," Radiophys. Quantum Electron. **16**, 783–789 (1973).

[167] "COMSOL," http://www.comsol.com.

[168] Y. Kou, F. Ye, and X. Chen, "Multiband vector plasmonic lattice solitons," Opt. Lett. **38**, 1271–1273 (2013).

[169] C. Huang, X. Shi, F. Ye, Y. V. Kartashov, X. Chen, and L. Torner, "Tunneling inhibition for subwavelength light," Opt. Lett. **28**, 2846–2849 (2013).

[170] X. Shi, X. Chen, B. A. Malomed, N. C. Panoiu, and F. Ye, "Anderson localization at the subwavelength scale for surface plasmon polaritons in disordered arrays of metallic nanowires," Phys. Rev. B **89**, 195428 (2014).

[171] "Meep - Abinitio," http://ab-initio.mit.edu/wiki/index.php/Meep.

[172] R. W. Boyd, ed., *Nonlinear Optics* (Academic, New York, 2007), chap. The Intensity-Dependent Refractive Index, pp. 207–252.

[173] "Maxima, a Computer Algebra System," http://maxima.sourceforge.net.

[174] "Maple," http://www.maplesoft.com/products/maple.

[175] A. F. Oskooi, D. Roundy, M. Ibanescu, P. Bermel, J. D. Joannopoulos, and S. G. Johnson, "MEEP: A flexible free-software packa ge for electromagnetic simulations by the fdtd method," Comput. Phys. Commun. **181**, 687–702 (2010).

[176] "Units and nonlinearity in Meep," http://ab-initio.mit.edu/wiki/index.php/Units_and_nonlinearity_in_Meep.

[177] Z. Lubin, J. H. Greene, and A. Taflove, "GVADE FDTD modelling of spatial solitons," in "Advances in FDTD Computational Electrodynamics," , A. Taflove, ed. (Artech House, Boston, 2013), pp. 497–516.